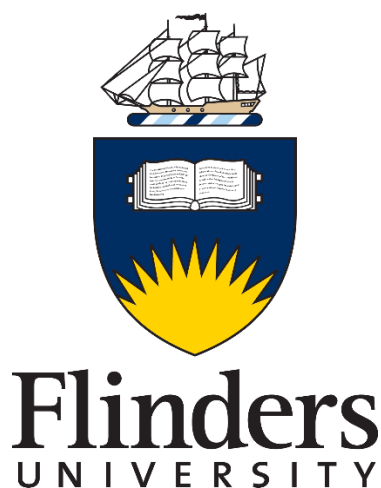# DEVELOPMENT OF A HIGH SPATIAL RESOLUTION MAPPING TECHNIQUE FOR PRISTINE AND MODIFIED CARBON SURFACES USING SCANNING AUGER MICROSCOPY

by

Jade Taylor

BSc(Hons)

Thesis

Submitted to Flinders University

For the degree of

Doctor of Philosophy

College of Science and Engineering

January 2021

CONTENTS

THESIS SUMMARY

An area of ever-increasing importance in science, particularly in nanotechnology, is the development of environmentally friendly technologies to replace current materials. Carbon-based devices are being investigated for a huge range of applications, ranging from electronic devices to biological implants to plasma facing materials in fusion reactors. The usefulness of carbon stems from the changes in its physical and electrical properties that occur when the bonding and structure of the material changes. These differences allow for devices entirely composed of carbon to be created through the use of structures of one hybridisation of carbon on top of, or even within, another hybridisation.

In order to create these devices it is necessary to control the hybridisation of the carbon present in each section, and to be able to characterise the presence of the hybridisation with spatial resolution. These two areas have been the focus of the work presented in this dissertation, with plasma utilised for the growth or modification of carbon species, and the development of a technique to characterise the hybridisation of carbon with high spatial resolution using Scanning Auger Microscopy.

Plasma modification of a surface can produce a wide range of results depending on the conditions applied. The Radio Frequency (RF) coupling power applied to ignite the plasma from the source gas, the length of time the surface is exposed to the plasma, and the composition of the source gas itself are variables that can be controlled to modify the surface to varying extents. This work has shown systematic studies of the oxygen and argon plasma modification of HOPG that produces surface oxides and hybridisation changes to varying degrees, allowing for the selection of treatment parameters that will produce the desired surface.

Similar systematic studies have been performed on the plasma deposition of diamond like carbon films. The pressure of the source gas, the RF-coupling power used to ignite the plasma, and the exposure time of the substrate to the plasma all have an effect on the thickness and growth rate of the film, however the elemental and hybridisation composition of films grown from methane gas are constant despite variation of these parameters.

Mapping of the hybridisation of carbon materials at the micro- and nano-scales has been successfully performed using the technique developed within this work. The development of this

technique involved the creation of code within MATLAB to process data obtained using Scanning Auger Microscopy, as well as the optimisation of the parameters used to acquire the data to achieve the best quality spectra in a reasonable acquisition time. This technique was expanded to include hybridisation line scanning so that higher spatial resolution in one dimension could be achieved with a shorter acquisition time than would be required for a 2D map of the same resolution, and both of these techniques have shown the ability to accurately and reproducibly determine the hybridisation of a carbon material with spatial resolution.

The development of the capabilities to grow and modify carbon materials and characterise them with spatial resolution has been established using the facilities available at Flinders University, and has provided an important step in the development carbon-based devices which is the ability to accurately determine their structure, and therefore their properties, at the micro- and nano-scales.

DECLARATION

I certify that this thesis does not incorporate without acknowledgment any material previously submitted for a degree or diploma in any university; and to the best of my knowledge and belief, does not contain any material previously published or written by another person except where due reference is made in the text.

Jade Kirsten Taylor

4/12/2019

ACKNOWLEDGEMENTS

Firstly, I would like to thank my supervisors, Professor Jamie Quinton and Associate Professor Sarah Harmer, for their support and guidance throughout this project. Without them I would not be where I am, as they have taught me many valuable lessons and provided me with many opportunities to grow as both a person and as a scientist.

To all those who have provided me with training and guidance, I thank you deeply for all you have taught me through this journey. In particular, many thanks go to Dr Alex Sibley for inspiring me to move into this field when I was just starting my research career and for providing excellent training on a range of instruments, not only in their use but also in their maintenance. I am also grateful for the advice of Dr Benjamin Chambers, whose support and guidance while writing my thesis was invaluable. Thanks also go to Dr Anders Barlow, who provided me with great advice on data processing and analysis programs. You learn so much when things go wrong, and I am grateful for the support of the Science and Engineering workshop staff, particularly Chris Price and Andrew Dunn, who have helped keep our laboratory running while also teaching me a lot about instrument maintenance.

I would like to thank my parents for all their support over the years, for always having faith in me and my abilities since I was a child, and for encouraging me to pursue my passion. Without your support and love I could not have achieved this. I would also like to thank my friends for their support and encouragement, especially towards the end, and for reminding me why I do what I do.

Finally, I would like to acknowledge that this PhD was supported by an Australian Government Research Training Program Scholarship.

1 INTRODUCTION

The applications of carbon materials are extremely diverse and are being thrust into almost every aspect of our lives. From fuel cells [1] and energy storage [2-7] to water purification [5, 8], from biomedical implants [2] and biosensors [9] to drug delivery [2, 10-13], and a wide range of electronic devices [3, 10], carbon devices have almost countless applications with more being investigated every day. This huge range of applications is possible because of the many different structures of carbon, all of which have different properties. However, the potential to create devices that entirely composed of carbon cannot be fully realised until the ability to create structures composed of different types of carbon together, and more importantly, to characterise the chemical form of this carbon with spatial resolution, has been achieved.

1.1 Carbon

Carbon exists in a range of different allotropes that are defined by their bonding structures, with materials occasionally consisting solely of either sp^2 or sp^3 hybridised carbon, and often regions of both within the one material [14-17]. Hybridisation refers to the mixing of atomic orbitals to form new hybrid orbitals that have different shapes and orientation to the originals [18, 19]. When this occurs the total number of orbitals must remain constant, for example, two sp orbitals are formed when an s orbital mixes with a p orbital, as shown in Figure 1-1 [18, 19].

Removed due to copyright restrictions.

Figure 1-1: Hybridisation of an *s* orbital and a *p* orbital of the same atom produces two *sp* orbitals, which are oriented at 180° to each other. Reproduced from [19].

Similarly, when an s orbital mixes with two p orbitals, three sp^2 hybrid orbitals are formed, and when an s orbital mixes with three p orbitals four sp^3 hybrid orbitals are formed (Figure 1-2) [18, 19].

Removed due to copyright restrictions.

Figure 1-2: (left) Orientation of three *sp²* orbitals, which are oriented at 120 ° to each other along the x-y plane. The unhybridized *p* orbital lies along the z-axis (not shown), and (right) orientation of four *sp³* orbitals, which are oriented tetrahedrally at an angle of 109.5° to each other. Reproduced from [19].

Graphite consists of sp^2 hybridised carbon in a two dimensional hexagonal lattice, while diamond consists of sp^3 hybridised carbon atoms bonded in a face centred unit cell [14-17]. Materials such as glassy carbon and amorphous carbon contain regions of both of these hybridisations [14-17].

There are also several other allotropes, including diamond-like carbon (DLC), fullerenes and nanotubes [14-17]. At ordinary temperatures and pressures the thermodynamically stable crystalline form of carbon is graphite [14-17]. Diamond can be formed at pressures over 30 kbar and will be stable at atmospheric pressures, however it will transform back to graphite if left at high temperatures [14-17, 20].

One of the unique properties of carbon is its large extent of catenation, that is, its ability to bond to itself in long order structures and chains [14, 15, 21]. Although other elements bond to themselves to varying degrees, none come close to the abilities of carbon to form potentially limitless networks [14, 15]. Carbon can form single, double, and triple bonds with itself, where the carbon atoms are sp^3, sp^2, and sp hybridised, respectively [14, 15, 21, 22]. The strength of the carbon-carbon bonds depends on this hybridisation, with the average bond energy of ~350 kJ.mol^{-1} for single bonds, ~610 kJ.mol^{-1} for double bonds, and ~840 kJ.mol^{-1} for triple bonds [14, 15].

Carbon materials are extremely useful for engineering applications due to their low density, high chemical and thermal stability, and good high temperature mechanical properties in a non-oxidising atmosphere [23]. Nanoscale carbon materials, including fullerenes, nanotubes, nanoribbons, nanofibers, graphene, nanodiamond, and nanofoams, have remarkable physical and chemical properties [23]. The geometrical constrains on nanoscale carbons result in unique properties such as field emission, pore channel diameter controlled band gap in carbon nanotubes (CNTs), helicity dependent electrical conductance (metallic or semiconductor), nanoporosity governed ultralow solid state thermal conductivity in carbon aerogels, ultra-high modulus and tensile strength of CNTs, and tailored biological activity of functionalised fullerenes [23].

1.1.1   Diamond

Carbon atoms in this form are sp^3 hybridised, with each carbon atom covalently bonded to four others in a face centred cubic structure as shown in Figure 1-3 [14, 15, 24, 25].

Removed due to copyright restrictions.

Figure 1-3: Structure of diamond.

This structure results in diamond's unique mechanical and elastic properties [14, 15, 24, 26]. Some important properties of diamond are its incredibly high mechanical hardness and Young's modulus, low friction coefficient, high wear resistance, high corrosion resistance, high atomic density, wide band gap, low dielectric losses, high dielectric breakdown strength, low friction coefficient, high

thermal conductivity, chemical inertness, inertia toward ionisation radiation, optical transparency, high refractive index, and low thermal expansion coefficient [15, 27-30]. These properties make diamond a useful material for many applications including cutting and grinding tools, heat exchangers, infrared windows, tribological coatings, microfiltration, chromatography, and high-frequency high-power electronic devices [15, 27, 29].

Diamond is also a very useful material for radiation detection in radiation harsh environments such as the innermost layers at the Large Hadron Collider (LHD) at CERN [31-46]. The bandgap of diamond is 5.47 eV, thus it can be used to detect any radiation that has an energy higher than this, including deep UV photons, X-Rays, gamma rays, as well as charged particles and neutrons with sufficient energies [31, 36]. Diamond radiation detectors have several advantages over other types such as silicon detectors [31, 36]. For example, it has a high resistance to radiation damage, will work at room temperature without cooling, has a higher resistivity by several orders of magnitude, has very low leakage current, and does not require p- or n-type junctions [31, 36].

Carbon films with nanocrystalline diamond structure are referred to as nanocrystalline diamond [47]. Nanocrystalline diamonds (50-100 nm) and ultra-nanocrystalline diamonds (2-5 nm) can be fabricated via glow discharge of plasma enhanced CVD [23, 26, 48]. They have potential applications as bright, low-voltage (cold) cathodes, as well as light emitters and electron emitters. Their properties of exceptional hardness, fracture strength, inertness, and a smooth surface makes them extremely useful for MEMS applications, as well as drug delivery vehicles and substrates for DNA attachment in biological applications [23]. Conductive Nanocrystalline Diamond (CNCD) films have electronics applications including field electron emitters for displays and thermionic emitters for energy conversion applications [48].

1.1.2   Graphene

Graphene is an allotrope of carbon composed of sp^2 hybridised carbon atoms bonded in a hexagonal lattice, as shown in Figure 1-4 [17, 23, 49-51].

Removed due to copyright restrictions.

Figure 1-4: Structure of graphene indicating two stacked layers.

This hybridisation results in each carbon atom having one *s* orbital and two *p* orbitals forming σ bonds to other carbon atoms, while the remaining *p* orbital is oriented perpendicular to the graphene plane and forms π bonds [17]. Graphene sheets can form very different materials

depending on how they are arranged. When stacked on top of each other graphite is formed, while rolling them results in nanotubes and fullerenes [17, 50-52].

A layer of graphene is approximately 0.345 nm thick, and has a high Young's modulus (1100 GPa), a fracture strength of 15 GPa, a high thermal conductivity (5000 $W.m^{-1}.K^{-1}$) and a large surface area (2630 $m^2.g^{-1}$) [23]. The physical properties of graphene include fast charge transport, excellent thermal conductivity, mechanical strength, high transparency, and flexibility [17, 53-56]. The electrical properties of graphene are also very good, including high charge carrier mobility, near-ballistic transport and tuneable charge carrier type and density [17, 52, 53, 57].

The electrical, optical, and mechanical properties of graphene make it useful for many applications such as micro- and nanomechanical systems, transparent electronics, transistors, sensors, wide band dipole antenna, electrodes for organic electronics, catalysis, spintronics, flexible and printable (opto)electronics, photonics, energy harvesters, lithium ion batteries, hydrogen storage, and reinforcing filler in high performance polymer composites [17, 50, 51, 54, 58, 59].

Graphene's use in electronic devices is related to the way it behaves as a zero band gap semi-metal and exhibits the quantum Hall effect and ambipolar electric field effect resulting from its high charge carrier mobility [17, 53, 60]. Reducing the lateral dimensions to below a few tens of nanometres changes the electronic properties from semimetallic to semiconducting [17, 53, 60]. The electronic properties of graphene nanoribbons with lateral dimensions of sub tens of nanometres are semiconducting and highly influenced by edge states and quantum confinement. Edge effects reduce the mobility of the charge carriers, which may limit the application of graphene in electronics [17, 53, 60]. It is important to find the balance between restricting the thickness to create a semiconductor and maintaining a thickness large enough to minimise the edge effects. [17, 53, 60]

Graphene is also under investigation as an alternative to indium tin oxide (ITO) for use in electronics [17, 61, 62]. The monolayer honeycomb lattice carbon material shows transmittance and conductivity that is much better than other suggested alternatives, including silver nanowires and grids [61].

Isolation or synthesis of graphene can be achieved through a variety of methods, including mechanical exfoliation of graphite, chemical reduction of graphite oxide, epitaxial growth on SiC, liquid phase ultrasonic, laser reduction of graphite oxide, and chemical vapour deposition (CVD) using C-containing gases on catalytic metal surfaces [17, 49-51, 54, 55, 60, 62]. While mechanical

exfoliation from graphite is simple and low cost, it has the disadvantage of producing flakes that are small (usually several microns) and are irregularly shaped [49]. These methods all have the problem of producing randomly distributed graphene sheets on the substrate, and these sheets can be difficult to locate for device fabrication. Other methods that allow more control over the placement of graphene sheets include transfer printing, electrostatic exfoliation, and site specific stamping of patterned graphite [60]. Patterning HOPG can be achieved by combining photolithography and reactive ion etching techniques, however these methods are time consuming and expensive [60].

Graphene can be chemically functionalised in a number of ways, including the production of graphene oxide [63]. Oxidation of the graphene allows a higher degree of tunability of the chemical and physical properties [63]. Graphene oxide can then be reduced to alter the electrical properties of the material [63]. Pristine graphene is a gapless semiconductor while graphene oxide is electrically insulating, and as the extent of oxidation is changed the electrical conductivity can be varied over several orders of magnitude [63].

1.1.3   Graphite

Graphite consists of stacked layers of sp^2 hybridised carbon atoms in a hexagonal array such that each carbon is bonded to three others [14, 15, 24]. The fourth electron for each carbon is used to form a π bond that helps to stabilise the structure [14, 15, 24]. The most common stacking format is ABAB, however there is also a rare ABCABC that results in rhombohedral graphite, both of which are shown in Figure 1-5 [14, 64, 65]. The properties of graphite are very different to those of diamond, and include being soft, having good electrical conductivity, and absorbing UV-VIS-IR light [15, 64, 66].

Removed due to copyright restrictions.

Figure 1-5: Side view showing stacking of ABAB and ABCA HOPG graphite structures. Reproduced from [64].

Nanocrystalline graphite films are carbon films with nano graphite crystals [47]. These films are usually formed by annealing at higher temperature after prolonged mechanical scrubbing, deposition at a high temperature, or high-energy post-irradiation [47]. Graphite-like carbon films can be made to have quite high hardness, as well as high toughness and wear resistance [47].

1.1.4   Highly Oriented Pyrolytic Graphite

Polycrystalline artificially formed graphite is known as pyrolytic graphite, and is formed by the pyrolysis of a carbonaceous gas at temperatures above 2000°C [14, 67, 68]. Pyrolytic graphite is

generally quite well ordered in the stacking direction, however the graphene planes are quite randomly oriented [14, 67, 68]. In order to obtain more ordered graphite, annealing of pyrolytic graphite at temperatures above 3300 K is conducted to form Highly Oriented Pyrolytic Graphite (HOPG) [14, 67, 68]. This annealing process allows for the atoms within the carbon material to diffuse to a lower energy lattice, resulting in a much more ordered structure than natural graphite [14, 67, 68].

HOPG occurs in the ABAB arrangement forming a three-dimensional hexagonal close-packed structure as shown in Removed due to copyright restrictions.

Figure 1-6 [67, 69].

Figure 1-6: Structure of HOPG

1.1.5 Amorphous Carbon

Yet another allotrope of carbon is amorphous carbon (a-C) which is usually prepared by the pyrolysis of organic polymers or hydrocarbon precursors at temperatures below 1500°C [14]. The structure of a-C is still somewhat debated in the literature, but is known to mostly contain regions of sp^2 and sp^3 hybridised carbon [22, 24, 47, 70]. The percentage of each of these hybridisations that make up an amorphous carbon film determine the structure and thus the properties of the film [47, 71-74]. Several studies state that a-C a material consists of roughly planar layers of mostly sp^2 hybridised carbon, however it differs from graphite because it also contains sp^3 hybridised carbon atoms in various ratios and lacks long range crystallinity [14, 47]. Large clusters of sp^2 hybridised carbon can be formed by fusing double bonds and rings, these rings may either coexist with each other or be deformed [22, 24, 47]. It is also possible that a-C contains some sp hybridised carbon, where the carbon atom contains two sp orbitals, forming two σ-bonds, with the remaining valence electrons forming two perpendicular π orbitals [47].

Amorphous carbon films that do not contain hydrogen are referred to as a-C films, and are generally soft films formed at low energy or high temperature [47]. If the soft film contains hydrogen it is referred to as a-C:H film. Softer amorphous carbon films with a high hydrogen content are referred to as polymeric a-C:H [47].

Although amorphous carbon does not show long distance order with either sp^2 or sp^3 hybridised

carbon, as is found in diamond and graphite, order on the nano scale is often found [47]. When the sp^2 and/or sp^3 hybridised carbon clusters become large the materials are referred to as nanocrystalline diamond or nanocrystalline graphite [47]. These nanocrystalline films are stable even after annealing, friction tests, and irradiation [47].

The bonding and structure of the amorphous carbon network is dependent on the relative concentrations of sp^2 and sp^3 carbon [73, 75]. The evaluation of this ratio and its dependence on the deposition parameters of the film (such as energy and rate of carbon atoms arriving at the surface, or the energy and dose of hydrogen ions) are two crucial steps to obtain a material with required microscopic properties [73]. This ratio can be determined quantitatively by measuring the IR absorption spectra of the films and examining the absorption bands corresponding to vibrational frequencies active in the IR region [75].

Both a-C and a-C:H have many useful optical and mechanical properties, including high hardness, thermal stability, diamond-like tribological properties, chemical inertness to acid attack (including HF), and good optical properties such as high transparency in the IR region [72, 73, 75-78]. These properties make amorphous carbon films useful for applications such as protective coatings on optical components working in the infrared region of the spectrum [22, 73], coatings to increase the life time of cutting tools [72, 73, 78], tribological coatings to improve wear resistance [22, 77], and semiconducting layers in electronic devices [72, 73].

1.1.6 Diamond-Like Carbon

Diamond-like carbon (DLC) refers to amorphous carbon with a very high sp^3 hybridised carbon fraction (up to 85%), but no unique composition, containing a mixture of diamond- and graphite-like regions [14-16, 79-85]. This unusual structure presents a range of properties that are often a mixture of those of diamond and graphite [16, 81, 83, 84, 86]. Also known as tetrahedral amorphous carbon, DLC films that have no hydrogen are referred to as ta-C films, while those that contain hydrogen are referred to as ta-C:H films [47, 87-90]. DLC films, both hydrogenated and non-hydrogenated, are metastable and their structures will become more graphitic upon thermal activation or irradiation with energetic photons or particles [91, 92].

Many of the useful properties of DLC films are the same as those of diamond, but DLC has the advantage of being much easier to synthesise [81, 90, 91, 93-95]. These properties include high hardness, high mechanical stability, excellent thermal conductivity, high photoelectric yield, low

friction coefficient, high wear resistance, electrochemical stability, good transparency in the IR region, scratch resistance, optical transparency, high electrical resistivity, low electron affinity, chemical inertness, low dielectric constant, hydrophobicity, low surface energy, endurance, and are nontoxic [15, 16, 29, 89, 91, 96-102]. The properties of the film are dependent upon the sp^2/sp^3 ratio, thus the properties of the film can be tailored by varying the deposition parameters when making the film [71, 83, 103-106]. The ability to tailor the properties of the films makes them suitable for a large range of industrial applications, including resist materials for photolithography, electronics, medical, automotive, avionics, aerospace, protective films for magnetic recording disks, cutting tools, coatings for medical devices and space applications, magnetic storage, optical windows, insulating layers in microelectronic devices, protective and antireflective coatings, thin film transistors, field emission displays, solid lubricants, gas barriers, coatings for tribological, optical, and medical applications, corrosion protection coatings for steel, and antireflective and scratch-resistant, wear and abrasion protective coatings for Ge, ZnS, or ZnSe IR optics and polycarbonate sunglasses lenses [16, 91, 102, 107-114].

The structure-dependent nature of the properties of DLC films has already been discussed, thus the properties of the material can be changed by varying deposition conditions [106, 115, 116]. DLC is generally formed as a thin film and can be produced by several methods, including chemical vapour deposition, physical vapour deposition, sputtering using a carbon beam ion source, pulsed laser deposition (PLD), DC or RF plasma deposition, dual-beam methods, laser evaporation, magnetron sputtering, and ion beam plating [16, 77, 87, 91, 94, 100, 116-123]. These methods all involve ion bombardment, and often produce DLC containing significant amounts of hydrogen [16, 116]. The DLC films are often deposited onto single-crystalline silicon substrates and are very thin [97]. On the industrial scale DLC is produced by either magnetron sputtering or plasma-enhanced chemical vapour deposition (PECVD) [115]. The method used for growth of DLC films in this work is PECVD. The properties of the DLC films grown in this way are related to the deposition conditions, including total gas pressure, input power, gas flow rate, and substrate material [90, 91, 124, 125].

The source gas and plasma deposition parameters used to grow DLC films influence the properties of the resultant films [90, 111, 125]. The properties of DLC films depends on hydrogen content and the relative amounts of sp^2 and sp^3 hybridised carbon [71, 90, 91, 126, 127]. The electrical properties of the DLC film are governed by the sp^2 carbon content, while the sp^3 carbon content controls the mechanical properties [83, 116, 126, 128, 129]. The smoothness of a DLC film is also dependent on the sp^2/sp^3 content, with a higher sp^3 content producing a smoother film [94]. Hydrogen is needed

to form and stabilise the sp^3 bonds from sp^2 bonds and passivate the dangling bonds [83, 90, 91, 116, 130-132]. Conversely, ionic bombardment can transform sp^3 bonds to sp^2 bonds during plasma growth by sputtering and/or etching or bond breaking [128]. The bombardment with various species occurs in three characteristic depths within the sample [82]. At the surface level the interactions are dominated by the reactions with hydrocarbon and hydrogen species [82]. At a depth of around 2 nm the interactions are dominated by atomic hydrogen, while at depths greater than 2 nm the reactions of hydrogen ions, which are smaller than the other species, can penetrate where atomic hydrogen and hydrocarbon species cannot [82]. The presence of oxygen in the plasma can also lead to preferential etching of sp^2 hybridised carbon over sp^3 hybridised carbon [133]. It is much more difficult to break C-C bonds (~607 kJ.mol^{-1}) than a C-H bond (337 kJ.mol^{-1}), therefore ion bombardment is likely to break C-H bonds over C-C bonds, creating dangling bonds [128]. These dangling bonds can recombine with other adjacent dangling bonds, which results in sp^2 hybridised carbon forming in place of sp^3 hybridised carbon [128].

DLC can be grown via plasma deposition using a range of carbon containing gases, such as methane, ethane, butane, propane, acetylene, ethylene, cyclohexane, octane, decane, and other hydrocarbons, sometimes as a mixture of two of these gases or with the inclusion of H_2 [90, 99, 110, 116, 129, 130, 134]. For this work methane was used as the source gas, with the pressure, RF-coupling power, and growth time varied to examine the effect on the film.

Other studies in the literature have mixed methane with hydrogen [83, 116, 135, 136], argon [113, 134, 137], or neon [134]. The inclusion of hydrogen is used to help form and stabilise the sp^3 bonds [83, 90, 116, 130-132], while the inclusion of dilution gases such as Ar or Ne in plasma deposition of DLC from CH_4 has been shown to increase the average size of the diamond crystals in the film, as well as decrease the number of crystalline defects [134]. This indicates that the inclusion of rare gases can alter the plasma composition and change the reaction paths through the addition of ion or metastable exited atom reactions [134]. Simulations have been performed that indicate that in a pure CH_4 environment the plasma is CH_3-rich, while when the plasma is CH_4 heavily diluted by Ar (1 % CH_4) the environment becomes C_2-rich [134].

1.1.7 Glassy Carbon

Glassy carbon is a form of disordered carbon that, on the micro scale, contains a mixture of graphite-like ribbons and micro fibrils. It can be thought of as having a level of microstructural order between that of amorphous carbon and single-crystal graphite [47, 138]. Produced using solid precursors

with highly disordered structures such as polymers and resins, glassy carbon is isotropic and does not form graphitic structure even when exposed to high temperatures of 2500-3000°C as a result of the high degree of crosslinking between crystalline regions [14].

Some important properties of glassy carbon are its high thermal stability and inertness to chemical attack, high hardness, abrasion resistance, corrosion resistance, durability, and low reactivity [138, 139]. It has been shown to have low rates of oxidation by oxygen, carbon dioxide, or water vapour when compared to other forms of carbon, and is highly resistant to attack by acids [139]. Recent studies into the structure of glassy carbon have revealed a structure that is fullerene related, with curved carbon sheets containing pentagons, hexagons, and heptagons [139]. The properties of GC make it suitable for similar applications to those of DLC [138].

1.1.8   Carbon Nanomaterials

In macroscopic carbon materials the mechanical properties are dominated by the size and distribution of microstructure defects, while in nano-carbon materials the particle size and interface bonding become much more important [23]. Figure 1-7 shows the structures of a variety of carbon nanomaterials [23].

Removed due to copyright restrictions.

Figure 1-7: Structures of several carbon nanomaterials. Reproduced from [23]

1.1.8.1 Fullerenes

Fullerenes are closed hollow cages of carbon that can be formed by the joining of dangling bonds from the edge of a graphene sheet [14, 23, 140]. A fullerene, F_n, has n vertices and will consist of 12 pentagons and ($n/2$-10) hexagons for all even $n \geq 20$ (except for n=22, which does not form) [23]. The pentagons must be present in order for a spherical structure to form [14, 140]. Due to its availability, high symmetry, and low price the most common fullerene is C_{60} [23]. Fullerenes can be formed in several ways, including vaporisation of graphite, laser ablation, inductively coupled RF evaporation, and hydrocarbon combustion [23]. Once synthesised, the fullerenes can then be functionalised to increase solubility in organic solvents and enhance processability [23]. Fullerenes have applications in many areas, including electrical conductivity (superconductors), artificial photosynthesis, nonlinear optics, cosmetics, surface coatings (dry lubricants, antibiofouling, and antioxidants), organic photopholtaics, catalysts for hydrocarbon upgrading, and pharmaceuticals (protease inhibitor and drug delivery vehicles) [23].

1.1.8.2 Carbon Nanotubes

Carbon nanotubes (CNTs) are formed when one or more graphene sheets roll up to form cylinders, thus they are composed of sp^2 hybridised carbon atoms bonded together hexagonally [23, 25, 136, 140-142]. Carbon nanotube behaviour is influenced by the structure that forms from the rolling of a graphene sheet into a tube [14]. The axis of rolling relative to the hexagonal structure of the graphene sheet determines the types of cylinders created (armchair, zigzag, or chiral), with the properties varying from metallic to semiconducting [14, 23, 140, 141]. Nanotubes also differ in structural characteristics such as diameter, being open-ended or closed-ended, and being single or multi-walled [14, 140-142]. The diameters of nanotubes vary from 0.8-2 nm for Single-Walled Carbon Nanotubes (SWCNT) and 5-20 nm for Multi-Walled Carbon Nanotubes (MWCNT) [23, 140, 142]. The length to diameter ratio of SWCNTs is usually about 1000, which allows them to be considered as an almost one-dimensional structure [140-142]. CNT can be prepared by arc discharge, laser ablation, and chemical vapour deposition [23, 136, 140].

Carbon nanotubes have unique structural, mechanical, and electrical properties, including low threshold voltage for electron field emission, ballistic electron transport, high mechanical strength, high elastic modulus, large elastic strain, high thermal conductivity, and high toughness [25, 136, 141, 142].

1.1.8.3 Carbon Nanofibres

Carbon nanofibres (CNF) are composed of sp^2 hybridised carbon, with high aspect ratios (over 100) and diameters of 50-100 nm [23]. They differ from normal carbon fibres or CNTs in their structure, which is truncated conical or planar layers regularly stacked along the fibre length [23]. These carbon structures have applications in high performance polymer composites, energy conversion and storage, catalysis, and biomedical applications, and can be produced by catalytic CVD or electro-spinning and thermal treatment of organic polymers [23].

1.1.8.4 Carbon Nanopillars

Carbon nanopillars of diamond can be made by depositing a diamond film and selectively etching with oxygen plasma using lithography to mask the pillar areas [143]. When doped with nitrogen vacancy defects (a nitrogen atom adjacent to a vacancy in the carbon lattice) these pillars can act as waveguides to achieve a maximum fluorescent output as sensors [143]. The properties of this material include high photostability, high brightness, and high spatial resolution by stimulated emission depletion [143].

1.1.8.5 Nanodiamonds

Nanodiamonds refer to diamonds that have a diameter of 100 nm or less [144, 145]. Nanodiamonds exhibit the same properties of regular diamond, including mechanical stability at high pressures, hydrolytical stability over the entire pH scale, high chemical inertness, high thermal stability, low coefficient of thermal expansion, and they do not shrink or swell in either aqueous or organic solvents [146]. Because of these properties nanodiamonds are being investigated for a number of applications including stationary phases for liquid chromatography, biosensors, catalysis, nanofillers, tribology and lubricants, optical filters, antibacterials, antibiotics, and drug delivery [102, 145-151]. They can be prepared by several methods, most commonly fragmentation of crystals grown under high pressure high temperature conditions or detonation of strong explosives [145, 148, 149].

1.2   Applications of Carbon Materials

As has been previously discussed, the electrical properties of diamond and graphite are very different, which allows for devices composed entirely of carbon to be possible by creating structures of one hybridisation within or on the other. There are a large variety of applications for these carbon devices, with microelectromechanical systems (MEMS) and nanoelectromechanical systems (NEMS) gaining popularity rapidly.

MEMS and NEMS are mechanical or electromechanical devices or structures that are on the micrometre or nanometre scales, respectively [152-154]. Nanometre scaled structures have different properties from their macroscale counterparts, including their optical and electrical properties [155]. These structures vary in complexity from simple structures with no moving parts to very complex structures controlled by integrated microelectronics [152]. MEMS contain sensors, actuators, and microelectronics. The sensors are used to convert mechanical signals into electrical signals, while the actuators are used to convert a source of energy (commonly electrical energy), into motion [58, 152, 155].

There is a large range of applications for MEMS and NEMS, including photonics, microfluidics, biophysics, biotechnology, medicine, communications, mechanical and aerospace engineering, electrical systems, and sensors [152, 155-157]. These sensors include microsensors that are able to detect temperature, pressure, inertial forces, chemical species, magnetic fields, and radiation. The performance of these sensors is often comparable, if not better than, that of their macro scale counterparts, while generally being low cost to create [152]. The applications in these areas include

multi-link active catheters, artificial muscles, biosensors, implants, bio-medical devices, micro-pumps, molecular motors, micro- and nano-robots, micro-manipulators, and biomimetic robots [58, 157]. There is also a growing need to create an interface between microelectrodes and tissues for applications such as neural signal sensing and stimulation in brain computer interface for sensorimotor control to chronic pain management and deep brain stimulation. Probes and electrodes for applications like these can be composed of glassy carbon due to the biocompatibility and electrical and mechanical properties of the material [158].

CNT MEMS and NEMS are being investigated for electronic applications including flat panel displays, chemical sensors, field emitters, electrochemical microgravimetry, diffractive optical elements, supercapacitors, scanning probe tips, photonic crystals, and waveguide structures [156, 157, 159-162]. Diamond radiation detectors, composed of graphitic channels within diamond, are also being investigated [163].

One of the areas where carbon has major advantages over other commonly used materials such as silicon is in biometrics, including biosensors and implants [157]. Medical implants must be biocompatible in order to re-establish biological and mechanical functions within the body [16, 80, 164, 165]. Depending on the application, the implant needs to withstand dynamical mechanical loads and perform the desired long-term biological interaction with the surrounding tissue [80, 164, 165]. These load bearing properties of the implant are mainly controlled by the bulk properties of the implant, while the implant surface affects the interaction with the surrounding tissue [80, 164]. The interaction of the body with an implant is affected by many aspects, including surface chemistry and surface texture, implant movement, biodegradation, and surgical aspects [80, 164].

Biomedical applications for carbon materials currently include DLC films for blood contact implants such as heart valves and stents, films for reducing wear in load bearing joints, protective coatings for implants, biosensors, and biochips, hip prostheses, coronary stents, heart valves, vascular prostheses, anatomic sheets, intraocular and contact lenses, surgical needles for corneal surgery, orthopaedic pins and screws, dental prostheses, medical guide wires, and rotary pumps for left ventricular assistance [16, 164-166].

1.3   Modified Carbon Surfaces

There are many ways that a carbon surface can be modified so that the surface contains more than one type of carbon hybridisation. These methods are useful for producing carbon-based devices,

and include lithography, laser modification, ion beam irradiation, and plasma etching. Plasma modification is the method that will be used in this work, however other methods are also discussed here briefly.

1.3.1 Lithography

Modifying the topography of a film surface by micro- or nano-structuring will modify the surface properties of the material, including the adhesion, wear resistance, friction, wettability, and adsorption. Applications of such textured films include nanoimprint moulds, data storage devices, gas sensors, biocompatible coatings, self-cleaning surfaces, microfluidic channels for 'lab on a chip" technology, and micro- and nanoelectromechanical systems (MEMS and NEMS) [115, 157, 167, 168]. This patterning can be carried out using a variety of lithographic techniques, including Electron Beam Lithography (EBL), Nanoimprint Lithography (NIL), Nanosphere Lithography (NSL), Colloidal Lithography (CL), Direct Channel Diffused Plasma Etching, and Hole-mask Colloidal Lithography (HCL) [115, 155, 167, 169-171].

Carbon can also be used as masks for lithography, for example, a DLC film was deposited onto a silicon substrate then exposed to pulsed excimer laser radiation through a photomask which graphitises the top layer of the DLC film [172]. The whole surface is then exposed to an oxygen plasma, which will etch the graphitised regions at a much faster rate than the DLC regions [172, 173]. In this way the graphitised areas can be completely removed, leaving the DLC with steps where the laser irradiation occurred [172]. The sample is then exposed to CF_4 plasma which will etch the silicon much faster than the DLC, resulting in the laser exposed pattern being transferred to the silicon [172].

1.3.2 Laser Modification

Microstructured diamond has many MEMS applications, including for optical memories, photonic crystal structures, photodiodes, and ultra-fast microstructured electrical high voltage devices [174]. When exposed to a laser with femtosecond pulses, CVD diamond is converted to graphite [20, 48, 70, 156, 173, 175-189]. The focal plane of the laser is set to the rear of the CVD diamond sample, and the graphitisation initially occurs at this point when the threshold laser fluence (9-12 J/cm^2) is applied [156, 174, 176]. If the irradiation is continued, the graphitised area will grow out towards the laser [156]. If the diamond is moved along the beam axis during laser exposure the graphitisation process will continue, resulting in the production of straight graphitic wires through the diamond. The diameter of these wires changes depending on the pulse energy used, with a smaller energy

resulting in a smaller wire diameter [156, 174]. The scanning speed used also impacts the wire diameter, but not in any predictable way [156].

1.3.3   Ion Beam Irradiation

Low energy ion irradiation of HOPG has been performed using argon and nitrogen for the purpose of investigating the possible formation of a carbon nitride solid phase by ion beam deposition. It is expected that argon ion irradiation will result in a purely physical disordering of the near surface region, while nitrogen ion irradiation will result in both physical and chemical effect; that is the disordering of the near-surface region and formation of chemical bonds between the implanted nitrogen and carbon atoms [190].

1.3.4   Plasma Etching

Etching of carbon by plasma can occur in two ways: physical sputtering and chemical etching. How this etching occurs will depend on the structure of the carbon material, that is, if the carbon atoms are sp^2 or sp^3 hybridised, and thus occurs differently for different carbon materials [167, 191]. The etching will also be dependent on the gas used to ignite the plasma, with oxygen, hydrogen, and water plasmas having been used previously in the literature, as well as on the plasma parameters used for the etching treatment [63, 103, 167, 168, 191-193].

The different species present in the oxygen plasma are the cause of the different etching rates of carbon in the forward and lateral directions [167]. A plasma is composed of neutral species, electrons, ions, and radicals. The latter two are the species that are responsible for the etching of the carbon surfaces [167]. A potential difference is induced between the sample and the plasma as a result of the higher mobility of electrons compared to ions, causing the oxygen ions to be accelerated towards the sample, while the electrically neutral atoms will not be influenced [167]. As a result of this the ionic species will contribute more to the etching in the forward direction, while the neutral species will contribute to isotropic etching [167].

There are three main steps in the oxygen plasma etching of carbon materials [167]. The first step is the adsorption of oxygen to the carbon surface, followed by the oxidation of the carbon surface, and finally desorption of the reaction products (CO and CO_2) [167]. The rate-determining step in this process is believed to be the desorption of the products, with the increase in the stable oxygen complexes present on the surfaces present on the carbon surface after plasma treatment supporting this theory [167].

The binding energy of reaction products at an edge or defect site is decreased by the absorption of atomic oxygen on nearby basal plane sites [167]. The rate of desorption of these reaction products is dependent on their binding energy, therefore the presence of oxygen on basal planes can influence the etch rate at the edge sites [167, 193].

Oxygen plasma is commonly used for carbon modification, however water plasma can also be used to achieve an oxidised surface [63]. Water plasma leads to a milder and more controllable modification [63].

1.4   Plasma

Plasma is colloquially referred to as an ionised gas, however this is not technically accurate as all gas is ionised to some small degree. In his textbook *Introduction to Plasma Physics and Controlled Fusion* Chen defined a plasma as 'a quasineutral gas of charged and neutral particles which exhibits collective behaviour' [194]. The term quasineutral describes the behaviour of the plasma when viewed from a large enough scale, at which point it will appear to be neutral as the positive and negative charges within the plasma will balance each other [194]. This is not the case when the plasma is viewed on a scale that is below a certain length known as the Debye length, λ_D, which is defined by [194]

$$\lambda_D = \left[\frac{k_B T_e}{4\pi e^2 n_e}\right]^{\frac{1}{2}}$$
(1.4-1)

Where k_B is Boltzmann's constant, T_e is the electron temperature, *e* is the elementary charge, and n_e is the electron density [194]. Below this length the Coulomb potentials of the ions and electrons within the plasma can be observed, and the plasma does not appear neutral [194]. The term collective behaviour relates to the behaviour of the charged species within the plasma. In a neutral gas atoms or molecules move due to their thermal motion and are not acted on by a net external force, thus they only change course if they undergo a collision with other atoms or molecules [194]. However, within a plasma the charged species are in motion, which induces currents and localised electric and magnetic fields that can act on remote particles and influence their motion [194]. This influence of the plasma on the particles within it is what is referred to as collective behaviour [194].

When energy is applied to a gas the gaseous molecules can polarise, dissociate and ionise to form a plasma [67, 193, 195, 196]. As the plasma contains ions, electrons, and radicals it is a much more

16

volatile environment than the gas, and thus a plasma will react more readily with the sample surface than a molecular gas [67, 193, 195, 196]. In this way, the sample can be forced to react with something that otherwise may not react, or only react slowly [67, 193, 195, 196].

The plasma used in this research is Radio-Frequency (RF) Inductively Coupled Plasma (ICP), which uses a radio frequency current within a coil antenna to supply energy to the source gas by inducing a changing electromagnetic field. After the molecules are ionised, the electric field present will accelerate the charged species so that they collide with other gaseous molecules, producing further ions and radicals [67, 193, 195, 196]. In this way, once a certain threshold RF-coupling power is applied to ignite the plasma, this power can be lowered and the plasma is maintained by becoming somewhat self-propagating [67, 193, 195, 196]. This self-propagating behaviour also occurs with variations in the source gas pressure, where the pressure of the source gas can be reduced to levels below that needed for ignition to occur after ignition is achieved [67, 193, 195, 196].

The nature of a plasma treatment can be changed by varying a number of experimental parameters, including the choice of source gas (or mixture of gases), source gas pressure, applied RF-coupling power, and the exposure time of the sample to the plasma [67, 193, 195, 196]. The composition of the gas/mixture determines the species present in the plasma and their abundance, which will impact how the surface is modified with the plasma [67, 193, 195, 196]. The pressure of the source gas (at a set RF-coupling power) influences the ability of the gas to be ignited into the plasma, as well as the energy of the ions in the plasma [67, 121, 193, 195, 196]. If the pressure is too high the mean free path of the electrons and ions is too small for sufficient ionisation to occur, and the plasma cannot be sustained [67, 193, 195, 196]. However, if the pressure is too low there are not enough molecules present to supply the critical density of electrons needed to ignite the plasma [67, 193, 195, 196]. Varying the RF-coupling power changes the strength and the spatial extent of the electromagnetic field [67, 193, 195, 196]. Greater RF-coupling power leads to a higher amount of dissociated molecules, which results in an increased density of chemically reactive plasma species available for surface modification [67, 193, 195, 196]. Conversely, if the RF-coupling power is lowered the number of reactive species will be decreased [67, 193, 195, 196]. The exposure time of the sample to the plasma impacts the total number of ions and radicals that will react with the surface, thus an increased treatment time can result in a higher degree of surface modification [67, 193, 195, 196].

Plasma modification has several advantages over chemical processes, including being

environmentally friendly and time efficient [63]. Plasma exposes samples to a wide variety of functional groups that can be covalently bound to the graphene surface [63]. These groups are dependent on the chemical nature of the plasma and the plasma parameters [63]. Plasma treatment is also compatible with standard microfabrication procedures and can thus be easily incorporated into current device fabrication protocols [63].

1.5   Carbon Characterisation

Due to the large range of carbon materials that exist it is important to properly characterise the structure of the material, using either direct or indirect bonding characterisation methods [47, 73]. There are a great many techniques that are useful for identifying the chemical bonds and microstructures of carbon materials, including optical characterisation, electron spectroscopy and microscopy, and surface morphology characterisation [47, 73]. It is advantageous to use multiple techniques to obtain as complete a picture of the structures as possible [47, 73]. The techniques chosen for characterisation in this work are X-ray Photoelectron Spectroscopy (XPS) and Auger Electron Spectroscopy (AES) as both can be used to provide information about both the elemental composition of the samples and the hybridisation of the carbon, with the advantage of being surface sensitive, which allows for better examination of surface modification. Scanning Electron Microscopy (SEM) is also used in this work as an in-situ addition to the Scanning Auger Microscopy (SAM) characterisation.

1.5.1   X-ray Photoelectron Spectroscopy

X-ray Photoelectron Spectroscopy is a surface sensitive technique that utilities the photoelectric effect to determine the elemental composition of a surface [197]. An x-ray source is used to excite emission of photoelectrons from the surface, which are detected and their kinetic energy measured [197]. This kinetic energy can be used to calculate the binding energy of the electron, and therefore element from which the electron was emitted can be determined [197]. Small changes in the binding energy of the electron can also be used to determine the chemical environment of the atom [197]. XPS is described in more detail in section 2.5.

1.5.2   Auger Electron Spectroscopy

After emission of a photoelectron from an atom within a sample surface an Auger electron can be emitted as the atom relaxes, and it is this electron that is detected in Auger electron spectroscopy [198]. The kinetic energy of the Auger electron is measured and is indicative of the atom from which

18

it was emitted [198]. Scanning Auger Microscopy (SAM) combines AES with SEM to provide Auger electron characterisation with spatial resolution. More detail on AES and SAM is provided in section 2.6.

1.5.3   Scanning Electron Microscopy

Scanning Electron Microscopy uses a beam of electrons to produce an image of a sample surface. The electron beam is produced by applying a voltage to an electron emitting filament that is typically made of W or LaB$_6$ [47]. The electrons are collimated and focused using optics such as an electromagnetic condenser and objective lenses, and are then rastered across the surface using a set of scanning coils to deflect the bean in a controlled manner [47]. When the electron beam interacts with the sample surface secondary electrons are emitted from the sample [47]. These electrons are detected and, using the information about the surface topography they contain, an image of the surface is formed [47].

1.6   Research Aims

The research aims of this work can be divided into two broad categories: carbon material fabrication and carbon material characterisation.

As has been outlined previously in this chapter the properties of a carbon material, and therefore its applications, are dependent on its structure, and it is therefore desirable to have the capability to change the properties of a carbon material. Plasma modification has been shown as one way to do this, and therefore the first aim of this work was to use oxygen and argon plasma to modify HOPG. The modification is expected to change the amounts of sp^2 and sp^3 hybridised carbon present on the surface of the HOPG, and the extent of modification can be varied by changing plasma treatment parameters. These parameters are the RF-coupling power used to ignite the plasma and the length of time the surface is exposed to the plasma, and both will be varied systematically to determine the parameters required to achieve a certain level of modification.

Growth of DLC films can also be performed using plasma, and the resultant film is expected to be dependent on the deposition parameters and the gas mixture used to ignite the plasma. This work aims to examine the impact of these parameters on the growth of the DLC films by using methane, as well as mixtures of methane and hydrogen and methane and argon, to ignite a plasma for deposition. The RF-coupling power, source gas pressure, and growth time will all influence the growth of films, and will therefore be varied systematically to determine their impact and find a

protocol for the growth of DLC films with required properties.

To understand the properties of a carbon material it is important to know its composition, and therefore characterisation of these materials is vital for ensuring that they have the desired characteristics. When developing carbon MEMS and NEMS this is particularly important, as the difference in the properties of different areas is vital for the functionality of the devices, and it is therefore necessary to be able to characterise the hybridisation of the carbon at the micro- and nano-scale. Some work has been completed recently in the literature that used XPS to create maps of carbon peak width [199-201], as well as some studies using Raman spectroscopy to examine the changes in D/G ratio across carbon samples [202], however no method has been developed previously using SAM. The advantages of SAM for carbon characterisation include extremely high surface sensitivity, high spatial resolution, and ease of differentiating between sp^2 and sp^3 hybridised carbon. To this end, this work has developed a method for high spatial resolution characterisation of carbon hybridisation using SAM. The development of this technique will include the optimisation of many parameters used to acquire spectra to produce carbon hybridisation maps and carbon hybridisation line scans.

The work in this dissertation therefore aims to increase the knowledge of the growth, modification, and characterisation of carbon materials with the following research aims:

  i.   To investigate the influence of experimental parameters on the modification of HOPG with oxygen or argon plasma.

  ii.   To investigate the influence of experimental parameters on the plasma deposition of DLC films.

  iii. To develop a novel characterisation technique that displays the hybridisation of a carbon material with high spatial resolution using SAM.

The first two aims of this work will utilise the surface sensitive characterisation techniques of XPS and SAM to examine the elemental and hybridisation composition of samples. SAM will also be used to achieve the third aim, with the current capabilities of the technique built upon to produce hybridisation maps and line scans.

2 EXPERIMENTAL

2.1 Preparation of Highly Oriented Pyrolytic Graphite

The surface of Highly Oriented Pyrolytic Graphite (HOPG) that has been left exposed to the atmosphere will become contaminated through the deposition of adventitious carbon and the growth of an oxide, and it is necessary to remove these contaminations before beginning any treatment of HOPG. To achieve this the HOPG is cleaved using the 'tape lift' method whereby adhesive tape is applied to the surface and rapidly peeled off [195]. The bonds between layers in HOPG are weaker than the bonds between the HOPG and sticky tape, therefore the top layers of HOPG will be removed by the tape, leaving a fresh, atomically flat surface of HOPG behind [195]. To ensure that any surface contaminations have been removed by this cleaving process X-ray photoelectron spectroscopy (which is discussed in section 2.5) was performed on the surfaces before and after cleaving to determine whether the resultant surface was free of oxidation and other contaminants. These results showed that a freshly cleaved HOPG surface does contain small amounts of oxygen adsorbed to the surface. The amount of oxygen detected using XPS after a second cleaving had not changed, thus it was concluded that small amounts of oxygen would always be present due to the exposure of the sample to the atmosphere.

2.2 Plasma Treatment of Highly Oriented Pyrolytic Graphite

The surface of HOPG was modified by exposure to a variety of plasma treatments. The plasma chamber used for this work is shown in Figure 2-1.

Figure 2-1: Plasma chamber used in this work.

A schematic showing the setup of the plasma chamber is shown in Figure 2-2.

Removed due to copyright restrictions.

a)

b

Figure 2-2: Schematic of the plasma chamber used in this work from (a) a side view and (b) the top view. Reproduced from [195].

The chamber is constructed of AISI-316 stainless steel with a diameter of 0.4 m and height of 0.3 m. A turbomolecular pump backed by a Pfeiffer rotary pump is used to maintain a base pressure of the chamber in the 10^{-5} Torr range, as monitored by an MKS Baratron pressure gauge. This gauge contains a thin diaphragm which moves with the changing pressure in the chamber [203]. This physical movement results in a change in capacitance between the diaphragm and an electrode proportional to the pressure in the chamber, which is converted to an electrical signal [203]. Gas is introduced into the chamber in two locations on opposite sides of the chamber using either a Granville Phillips 216 Automatic Pressure Controller (APC) or a manual control valve, depending on which of the two gas lines is used. Energy is supplied to produce the plasma by use of an air cooled single loop stainless steel antenna which is used to inductively couple the radio-frequency (RF) power to the plasma at a frequency of 13.56 MHz, which is an industrial, scientific, and medical band reserved (among other things) for scientific purposes.

A RF-matching unit is also present on the chamber and is shown schematically in Figure 2-3.

Removed due to copyright restrictions.

Figure 2-3: Schematic of the RF-matching unit and antenna attached to the plasma chamber. Reproduced from [195].

This unit contains two variable capacitors, labelled C_1 and C_3, which are adjusted to match the impedance of the source to that of the antenna-plasma system and minimise the reflected power. This matching is necessary for the power to be effectively transferred to the plasma. The forward and reflected power coupled to the plasma were measured using a BIRD 4381 RF-power analyst, with the total power supplied to the plasma being the difference between the reflected power from and forward power.

Freshly cleaved HOPG is placed in a plasma chamber, which is pumped to reach a vacuum with a pressure below 1×10^{-4} Torr. The sample and chamber are left at vacuum to outgas for at least 30 minutes prior to introduction of the source gas, and longer if the chamber has been at atmospheric

pressure for an extended period of time.

The source gas of choice for the plasma is let into the chamber and allowed to flow through the chamber at the desired pressure for five minutes before ignition of the plasma. As all gases will be introduced into the chamber using the same lines there may be some residual gas present in the lines from previous experiment, as well as the possibility of air being introduced into the lines when switching to a different gas, and this flushing procedure removes any contaminants from the lines and chamber.

The plasma is then ignited by supplying a RF signal to the antenna in the chamber. The colour of the plasma produced is monitored to ensure that it matches the colour expected for the source gas. If there are any leaks in the gas line, or if it hasn't been flushed sufficiently, then the plasma will be bright pink (the colour of nitrogen/air plasma) instead of the expected colour. The voltage applied to the antenna system is adjusted to reach the desired RF-coupling power. After ignition the matching unit is adjusted to maximise the forward power. While ideally the reflected power would be zero, it is typically ~10% of the forward power under practical conditions over the range of values chosen for the coupled power used in this work. After the plasma treatment is complete the plasma is extinguished by simply turning off the power to the antenna, the chamber is vented to nitrogen, the samples are removed and then mounted for characterisation.

2.3   Diamond-Like Carbon Growth

The RF-plasma growth of diamond-like carbon was first performed by Holland et. al in the 1970s [204], and many studies have been performed to expand on the technique with different gases and deposition parameters. Gases that have been studied previously in the literature include methane, ethane, butane, propane, acetylene, ethylene, cyclohexane, octane, decane, and other hydrocarbons, sometimes as a mixture of two of these gases or with the inclusion of H_2 [90, 99, 110, 116, 125, 129, 130, 205, 206].   As the bonds between the carbon and hydrogen in methane molecules are in the same orientation as the carbon-carbon bonds in diamond, methane is the most preferable for DLC growth [131]. DLC growth using plasma assisted CVD is generally accepted to occur by surface chemisorption of carbon-carrying neutral radicals [106].

It has been shown in the literature that the properties of DLC films produced by plasma deposition are influenced by the deposition parameters of the plasma used to grow them [125]. The relative amounts of CH_x radicals and atomic H determine how the DLC film grows [28, 84, 116, 129, 130,

133]. The CH radicals enhance DLC layer growth, while the H atoms enhance chemical etching, thus the deposition rate is related to these concentrations [28, 110, 116, 129, 130, 133].

For this work CH_4 was chosen as the source gas and was ignited into a plasma using a RF-antenna with a frequency of 13.56 Hz. This method has been used in the literature previously, with a range of RF-coupling powers (20-250 W) and source gas pressures ($1.5x10^{-2}$ Torr-1 Torr) [90, 111, 112, 125, 130, 207, 208]. These RF-coupling power and source gas pressure ranges are generally higher than those that can be used in the plasma chamber at Flinders University, therefore the growth of the DLC films was studied with source gas pressures in the range of 0.01-0.1 Torr and RF-coupling powers in the range of 10-60 W for treatment times ranging between 10 and 60 minutes. As the results of a plasma treatment are also dependent on the setup of the plasma chamber it is expected that even for RF-coupling power or gas pressure ranges that overlap with those used in the literature the results may be different. Specific parameters used for plasma deposition are presented before results and discussed in later chapters. The substrate used for the deposition of the DLC films is silicon, which was chosen as a readily available, flat substrate that would not itself be modified by the plasma used to grow the DLC film.

There have also been some studies that have used argon or hydrogen to change the hybridisation and properties of the DLC films [83, 113, 116, 134-137]. These studies were performed at higher RF-coupling power or source gas pressure values, and therefore these source gas compositions were also examined with a variety or ratios. These parameters are also discussed further in the appropriate results sections.

2.4   Plasma Cleaning of Silicon

There has been many examples in the literature of the use of plasma to clean surfaces, typically with oxygen or argon plasma [82, 83, 104, 111, 129, 209]. The way these two plasma interact with the surface is different due to the different species that are present in each, and therefore each have different applications. As received silicon substrates were treated with oxygen or argon plasma for a range of times and the surfaces examined using XPS to determine how each treatment impacted the carbon and oxygen present on the surfaces. Analysis of these results showed that oxygen plasma was the most effective, and therefore all films deposited in this chapter used silicon substrates that were cleaned by oxygen plasma for 5 minutes using a source gas pressure of $1x10^{-2}$ Torr and a RF-coupling power of 30 W.

2.5 X-Ray Photoelectron Spectroscopy Characterisation

2.5.1 XPS Theory

X-Ray Photoelectron Spectroscopy is used to determine which elements are present in the surface layers of a sample [47, 67, 196, 197, 210]. This technique is based on the photoelectric effect, a phenomenon where a material is exposed to high energy radiation, resulting in the photoemission of electrons from the surface of the material [47, 67, 196, 197, 210]. The X-rays used in XPS have a fixed energy (typically 500 eV - 2 keV) [47, 67, 196, 197, 210]. Because the energy of these X-rays is known (hv) and the kinetic energy of the photoelectrons is detected (E_k), the binding energy of the molecular orbital from which the photoelectrons were emitted can be calculated (E_b) [47, 67, 196, 197, 210]:

$$E_k = hv - E_b - \Phi_{sp}$$
(2.5-1)

Where Φ_{sp} is the spectrometer work function [47, 67, 196, 197, 210].

This equation is valid only when the Fermi energy level is the same for the sample as for the spectrometer [210]. If a sample is an insulator or charges then the Fermi level is not well defined and the peak position may shift from the expected energy [210]. If this occurs an electron gun can be used to help neutralise the sample surface during characterisation, shifting the peak back to its correct position [210].

XPS detects the photoelectrons that are emitted when a surface is irradiated with X-rays. This emission process is illustrated in Figure 2-4 [67, 197, 210].

Removed due to copyright restrictions.

Figure 2-4: Emission process of a photoelectron. Reproduced from [47].

X-ray photoelectron spectra are plots of intensity versus binding energy, and the peaks present in the spectrum indicate which elements are present on the surface, and in what concentrations [47, 67, 196, 197, 210]. An example of an XPS spectrum is shown in Figure 2-5 for a sample of oxygen plasma treated HOPG. This spectrum contains two prominent photoelectron peaks, the C 1*s* and O 1*s* peaks, as well as the Auger peaks of these elements.
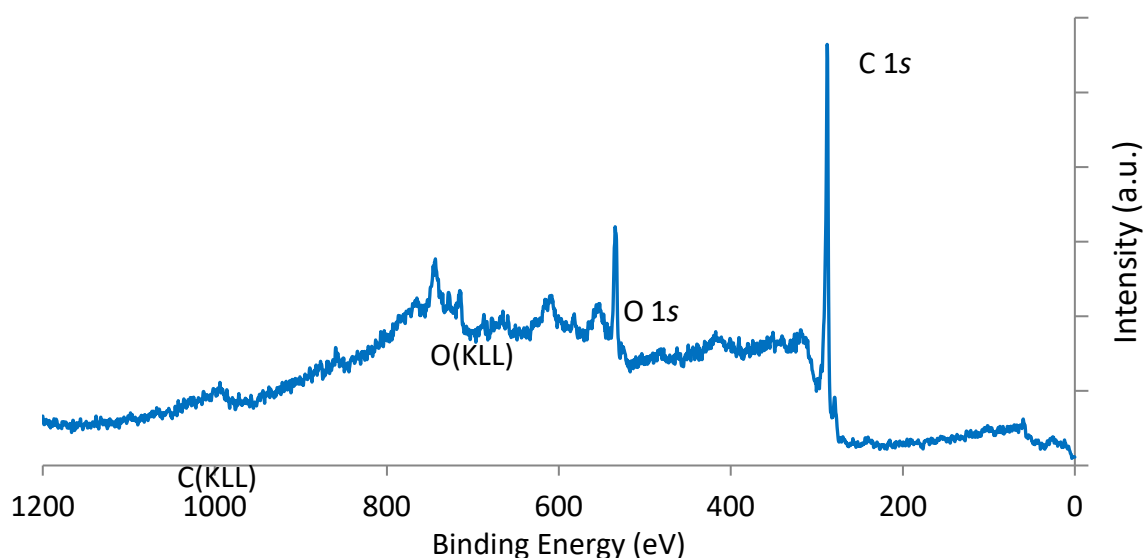
Figure 2-5: Example XPS spectrum of oxygen plasma treated HOPG.

As the binding energy of an electron is characteristic of the element from which it came, the position of peaks within the XPS spectrum allow determination of the elements present on a sample surface [47, 67, 196, 197, 210]. Variation in the binding energies of an element occur as a result of the differences in the chemical potential and polarizability of the compounds, which influence the energy levels of the electrons within the atom [47, 67, 196, 197, 210]. This variation results in a small chemical shift of the peak in the XPS spectrum, enabling identification of the chemical state of the elements on the surface [47, 67, 196, 197, 210]. The area of the peaks (after background subtraction and application of atomic sensitivity factors) allows determination of the percentage that each element contributes to the sample surface [47, 67, 196, 197, 210].

The two common x-ray sources used in laboratory XPS are Mg K$_\alpha$ radiation with an energy of 1253.6 eV and Al K$_\alpha$ radiation at 1486.6 eV. The two sources have different characteristics, which make them suitable for different applications [196]. These characteristics include flux and line width, and must be taken into account when choosing the line to be used for characterisation of a particular sample [196]. It is also important to consider which elements are expected to be present as some elements have overlapping photoelectron and Auger peaks [196]. The binding energy of a core electron is constant regardless of the X-ray energy used to cause its emission, and therefore the photoelectron peaks in an XPS spectrum with a binding energy scale will not shift when different X-ray sources are used. However, the kinetic energy of an Auger electron is constant regardless of the excitation energy, and will therefore undergo an apparent shift in binding energy when a different X-ray source is used. By changing the excitation energy the binding energy of the Auger peaks will

26

shift, aiding in the separation of overlapping peaks [196].

Although the X-rays penetrate to a large depth (~1 μm) into the sample to initiate the emission of a photoelectron, these electrons will not reach the surface as they undergo energy loss by collisions with other atoms within the solid [67, 196, 197, 210]. The Inelastic Mean Free Path (IMFP) is a measure of the distance that an electron can travel before undergoing energy loss through a collision with another particle [211]. If this energy loss is small the electron can still be emitted, however instead of contributing to spectra as a defined peak they will contribute to the background of the spectrum [211]. However, if the energy loss is large and approaches the kinetic energy of the electron it will not be able to be emitted. Seah et. al. produced a curve indicating the IMFP for electrons (in nm) as a function of the electrons kinetic energy, shown in Figure 2-4 [211]. From this plot it can be seen that there is a dramatic increase in the IMFP of electrons as their kinetic energy decreases, which is initially counterintuitive as one might expect that the lower energy will lead to a smaller escape depth [211]. However, due to a decrease in the probability of energy loss events occurring as the kinetic energy decreases the electrons can be emitted from a greater depth within the surface [211].

Removed due to copyright restrictions.

Figure 2-6: IMFP measurements (in nanometres) as a function of the kinetic energy of the electron. Reproduced from [211].

The IMFP of an electron is dependent on the atom from which it is emitted, and indeed the chemical state of that atom. Tanuma et. al. have calculated the electron IMFP of electrons from a range of elements, including carbon in its graphitic, diamond, and glassy carbon forms [212]. The IMFP curve for these carbon allotropes is shown in Figure 2-6 for electron kinetic energies between 50 eV and 30 keV [212].

Removed due to copyright restrictions.

Figure 2-7: Electron IMFP (in angstroms) as a function of electron kinetic energy for Li, Be, graphite, diamond, glassy carbon, and Na. Reproduced from [212].

The magnitude of the kinetic energy of electrons emitted in XPS allows only a few nanometres of travel within the material before all energy is lost, therefore the electrons that are detected in XPS are typically only from the top 10 nm of the sample surface [67, 196, 197, 210, 213]. This accounts for the surface sensitivity of XPS, which makes it extremely useful for the characterisation of

surfaces, in particular for thin film growth or gradual modification of a surface. [67, 196, 197, 210, 213].

There are many examples in the literature of XPS being used to characterise a variety of carbon materials [22, 73, 128, 141, 214, 215]. One disadvantage of XPS in carbon material characterisation is its inability to detect hydrogen due to its extremely low photoemission cross section and lack of core electrons [216]. However, it is very useful in its ability to differentiate between sp^2 and sp^3 hybridised carbon. As the C 1s binding energy is different for the sp^2 and sp^3 hybridised carbons, the C 1s peak position will vary by small amounts, and can be deconvoluted into two components using Gaussian-Lorentzian functions [47, 80]. These two components represent sp^2 and sp^3 hybridised carbon, and are separated by approximately 0.7 eV, with sp^2 having the lower binding energy [80, 217]. Peak fitting of these components will thus reveal the relative presence of sp^2 and sp^3 hybridised carbon and their ratio can be determined [47].

Recently, XPS imaging has allowed mapping of components of the C1s peak across a sample surface, resulting in maps of different chemical environments of the carbon in a sample surface [215]. This XPS mapping has also been performed on samples such as patterned silicon oxide by taking a spectrum at each pixel and deconvoluting the silicon and oxygen peaks [218]. In these cases of XPS image analysis various types of multivariate image analysis methods are used to extract important information from the large quantity of data obtained [219, 220].

2.5.2   XPS Instrument

The XPS system used in this work is a Leybold-Haraeus LHS-10 system, shown in Figure 2-8.
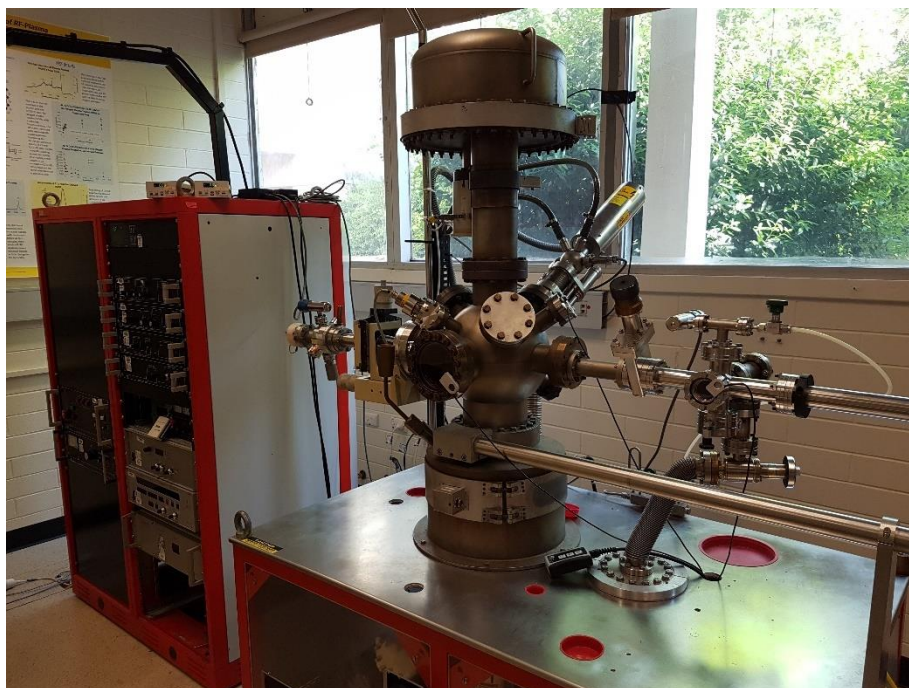
Figure 2-8: Leybold-Haraeus LHS-10 XPS system used in this work.

This system has a main analysis chamber that is kept below ~5x10^{-9} Torr at all times, separated from an introduction chamber by a gate valve. The main chamber has a base pressure of ~5x10^{-10} Torr, which is maintained by a turbomolecular pump backed by a rotary vane pump. The introduction chamber is also pumped by the same style of pumping system, and has a base pressure of less than 1x10^{-4} Torr.

Attached to the LHS-10 system is an EA-10/100 concentric hemispherical analyser (CHA) electron spectrometer, shown schematically in Figure 2-9.

Removed due to copyright restrictions.

Figure 2-9: A schematic diagram of the CHA. Reproduced from [196].

The CHA attached to the XPS consists of two concentric stainless steel hemispheres of radii r_1 and r_2, which are biased at negative voltages V_1 and V_2, respectively, where V_2 is greater than V_1 [196]. An equipotential surface exists between the two hemispheres at a radius r_0 [196]. Electrons are focused onto the entrance slit by an electrostatic lens, and will have a kinetic energy $E=eV_0$ (e is the elemental charge) as they travel along the path r_0 [196]. They are then focused onto the exit slit, and pass through to the detector [196]. If the kinetic energy is significantly greater or less than eV_0 then it will not be focused to the exit slit, and will not reach the detector [196]. Therefore by changing the values of V_1 and V_2 the CHA can select which kinetic energy it will detect [196]. The

pass energy, E_0, is defined as the kinetic energy of the electron that will traverse through the analyser to the detector [196].

The CHA has two operational modes: Constant Retarding Ratio (CRR) and Constant Analyser Energy (CAE) [196]. CRR mode sweeps both the hemisphere voltages and the lens system so that the electrons are slowed down as they enter the analyser to a constant ratio of the electron energy in order to be detected [196]. For example, if a retarding ratio of 10 is to be used to detect an electron at 500 eV then the electron must be slowed down to 50 eV and E_0 is set to 50 eV [196]. This mode maximises the signal across the entire energy range, which results in constant resolving power but does not have a constant resolution [196]. CAE mode keeps the voltage V_0 constant, therefore the pass energy E_0 is also constant [196]. The lens system then slows down the electrons to the required energy by using a retarding field [196]. If we consider the same electron with 500 eV energy, then it must be slowed by 450 eV to reach the set pass energy of 50 eV [196]. This results in constant analyser resolution across the entire energy range [196]. These differences in mode allow them to be used in different situations: CRR mode is typically used for survey scans over large energy ranges while CAE mode is used for high resolution scans over narrow energy bands where analysis required constant energy resolution and the signal to noise ratio doesn't vary too much [196].

The X-ray source used with this system is a SPECS XR50 Dual-Anode X-ray Source, mounted such that there is a 55° angle between the source and the analyser. The sample is mounted such that it is perpendicular to the analyser, and the orientation of sample, source, and analyser is chosen as a balance between increased surface sensitivity and decreased signal to noise ratio [210]. The X-ray source used in this work is a dual source that can produce both Al K_α (1586.8 eV) and Mg K_α (1253.6 eV) radiation, however for this work the Mg K_α source was used.

The spectra collection software utilised with this XPS system is XSpect, and was developed in house by Dr. Anders Barlow, a past graduate of the Quinton research group at Flinders University who upgraded the electronic hardware system to enable computer control over manual scanning. This software allows control of scan parameters, as well as averaging data sets over multiple scans, reducing post-processing requirements.

2.5.3 XPS Sample Characterisation Process

Samples were attached to a steel sample mount for XPS using adhesive copper tape. Typically, carbon tape is used for this purpose, however as the samples examined in this work are composed

of carbon an alternative is used to eliminate the possibility of mistaking carbon from the adhesive with that from the sample during characterisation. The samples are placed in the XPS introduction chamber and pumped down to below 1×10^{-4} Torr then left to outgas for between 30 minutes and 2 hours, depending on the nature of the samples and how much they outgas, that is, how long it takes for gaseous species that had been adsorbed to or trapped in the surface to be removed from the surface so that the high level of vacuum required for XPS analysis may be reached. When sufficient time has elapsed, the samples are transferred to the main (analysis) chamber of the XPS instrument. When the pressure in this chamber is below $\sim 1 \times 10^{-8}$ Torr characterisation can begin. Typically, a survey scan is performed first to determine which elements are present on the surface, followed by high resolution scans of any peaks of interest to allow for peak fitting and chemical environment analysis to be performed.

XPS characterisation is performed before SAM characterisation as it does not induce changes in the surface, while the electron beam used in SAM can result in redeposited carbon on the surface which would impact on the shape of the carbon peaks in XPS. The impact of XPS characterisation on the samples was examined by acquiring repeated scans over the same sample, which revealed no significant difference between subsequent scans.

2.5.4 XPS Sample Analysis

The spectra obtained from XPS are analysed with CasaXPS software (version 2.3.22). This software is used to determine the elemental composition of the sample and the chemical environments that the elements exist in on the surface. The areas of the peaks in the surface scan are corrected using atomic sensitivity factors to show the atomic concentrations of the elements present. XPS has different sensitivity to different elements, and this sensitivity must be taken into account when analysing the XPS spectra. The high-resolution scans of individual peaks are deconvoluted into components indicating the different chemical environments of the element. This is possible because the chemical environment of an atom affects binding energy of its electrons, including those in core levels, and thus the kinetic energy with which it is emitted. The kinetic energy of the $1s$ photoelectrons will thus be subtly different for a carbon atom bonded to an oxygen atom. The hybridisation of carbon also influences the kinetic energy of the electron, with sp^2 hybridised carbon having a lower binding energy (higher kinetic energy) than sp^3 hybridised carbon.

The high resolution XPS C $1s$ peak is deconvoluted into six components in this work. These components are a sp^2 hybridised carbon peak, a sp^3 hybridised carbon peak, three carbon-oxygen

species (ether, epoxy, and carbonyl), and a component referred to as 'vacancy', which indicates carbon atoms adjacent to lattice positions where carbon atoms have been ejected from the surface. The positions of these peaks vary slightly within the literature depending on the samples and instruments used, but all fall within distinct ranges. In this work the dominant component in most samples was the sp^2 hybridised carbon peak, thus this component was positioned first and all other components set to binding energy values relative to this. The sp^2 hybridised carbon component is typically observed at ~284.6 eV, and the sp^3 hybridised carbon component appears 0.7 eV higher [72, 81, 90, 126-128, 140, 141, 221, 222]. The three carbon-oxygen species appear at even higher binding energies, with the ether increasing by 1.2 eV [81, 90, 128, 146, 223, 224], epoxy by 1.9 eV [72, 126, 146, 225], and carbonyl by 2.6 eV [72, 126, 140, 141, 146, 224] relative to the sp^2 component. The only component to have a binding energy that is lower than the sp^2 hybridised carbon component is the vacancy component, which has a lower energy by 1.0 eV [226]. The example C 1s spectrum for a freshly cleaved HOPG surface is shown in Figure 2-10, where the pink line indicates the experimental data, with the position and intensity of each component shown in separate lines, and finally the envelope of these components is shown in the black line.
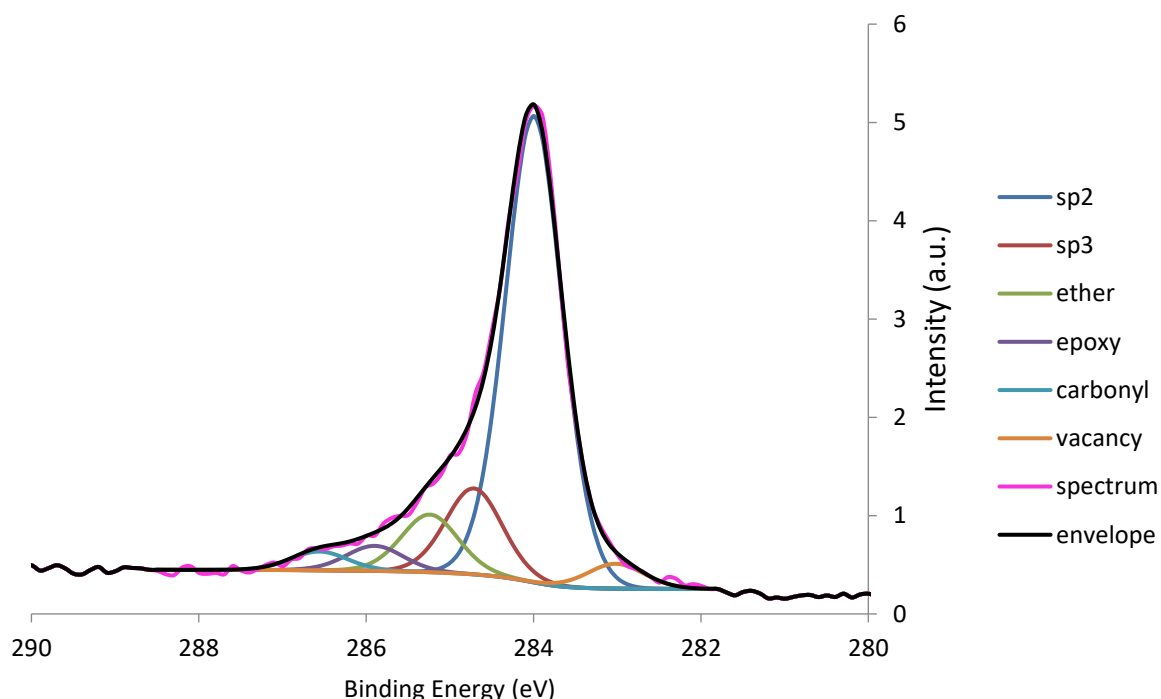
Figure 2-10: Deconvoluted C 1s peak from a sample of freshly cleaved HOPG, showing the raw spectrum, the components fit to the peak, and the envelope of these components.

Further information about factors influencing the analysis of XPS spectra is provided in Appendix A.

2.6   Scanning Auger Microscopy Characterisation

2.6.1   SAM Theory

Auger Electron Spectroscopy (AES) is a technique used to detect elements within the top several nanometres of a sample surface. During AES the sample is irradiated with a focused beam of high energy electrons (1-20 keV) from an electron gun or a field emission source [47, 200, 210, 227]. Depending on their energy, these electrons penetrate 0.1-1 µm into the sample and can then ionise target atoms by transferring their energy to core electrons within the atom, causing electron emission from different electron orbitals [47, 200, 210, 227]. In order for the ionized atom to relax, one of two things will occur [47, 200, 210, 227]. The first possibility is for the energy is released by emission of a photon, which is referred to as fluorescence. The second possibility is that an electron from a higher energy level will move down to fill the core hole produced by the emission of the photoelectron, which causes a third electron (the Auger electron) to be emitted from the atom with the excess kinetic energy from the second electron [47, 200, 210, 227]. This process is shown in Figure 2-11 [47]. The Auger and fluorescence yields, that is, the likelihood of either process occurring, are dependent on the element, and are also influenced by the chemical environment of that element [210, 228-230]. For light elements (low Z), the Auger yield is significantly higher than the fluorescence yield (over 90 %), however the fluorescence yield increases with increasing atomic number [210]. For carbon in particular, the fluorescence yield is extremely small, and is reported between 0.8 and 3.0×10^{-3} %, depending on the experiment and chemical environment of the carbon atoms [228, 231, 232].

The kinetic energy of the Auger electron is characteristic of the element from which it was emitted [47, 200, 210, 227]. The attenuation length of Auger electrons is usually between 0.3 and 3 nm due to the IMFP of the electrons, making AES extremely surface sensitive and suitable for the characterisation of thin films and surface modification [47, 200, 210, 227].

Removed due to copyright restrictions.

Figure 2-11: Energy level diagram for the emission of photoelectrons and Auger electrons upon exposure of a material to an electron beam. Reproduced from [47].

The kinetic energy with which the Auger electron is emitted is the difference between the energy of the singly ionised state and the doubly ionised final state [47, 210]. For any ABC transition in an atom with atomic number Z, the kinetic energy of the Auger electron is given by the difference in the binding energies of the energy levels A, B, and C [47, 210]:

$$E_{ABC}(Z) = E_A(Z) - E_B(Z) - E_C^*(Z) - \Phi_s \qquad (2.6\text{-}1)$$

Where Φ_s is the spectrometer work function, which is specific to the spectrometer attached to the instrument and can be taken into account with the software of the instrument, and E_C^* indicates that the energy of the C level has been altered from that of a neutral atom due to the presence of the core hole [47, 210]. Auger transitions are labelled depending on the energy levels involved. The first letter of the label corresponds to the energy level of the initial core hole, while the second and third terms are sequentially labelled from the energy levels of the two electrons involved in the Auger transition [47, 210, 227]. For example, an Auger electron emitted from the M shell after a hole in the K shell is filled via the relaxation transition of an electron in the L shell would be labelled a KLM Auger electron. The most prominent Auger peak for an element depends on its atomic number. For elements with atomic number Z=3-14 the KLL transitions will be the most prominent at room temperature, while for elements with Z = 14-40 LMM transitions are more prominent, and for heavier elements it is MNN transitions, as shown in Figure 2-12 [210, 227].

Removed due to copyright restrictions.

Figure 2-12: Principal Auger electron energies. Reproduced from [198].

Auger spectra are plots of the number of electrons detected at a specific kinetic energy against the kinetic energy [210, 227]. An example Auger spectrum is shown in Figure 2-13 (a) for an oxygen plasma treated HOPG sample, showing C(KLL) and O(KLL) peaks.
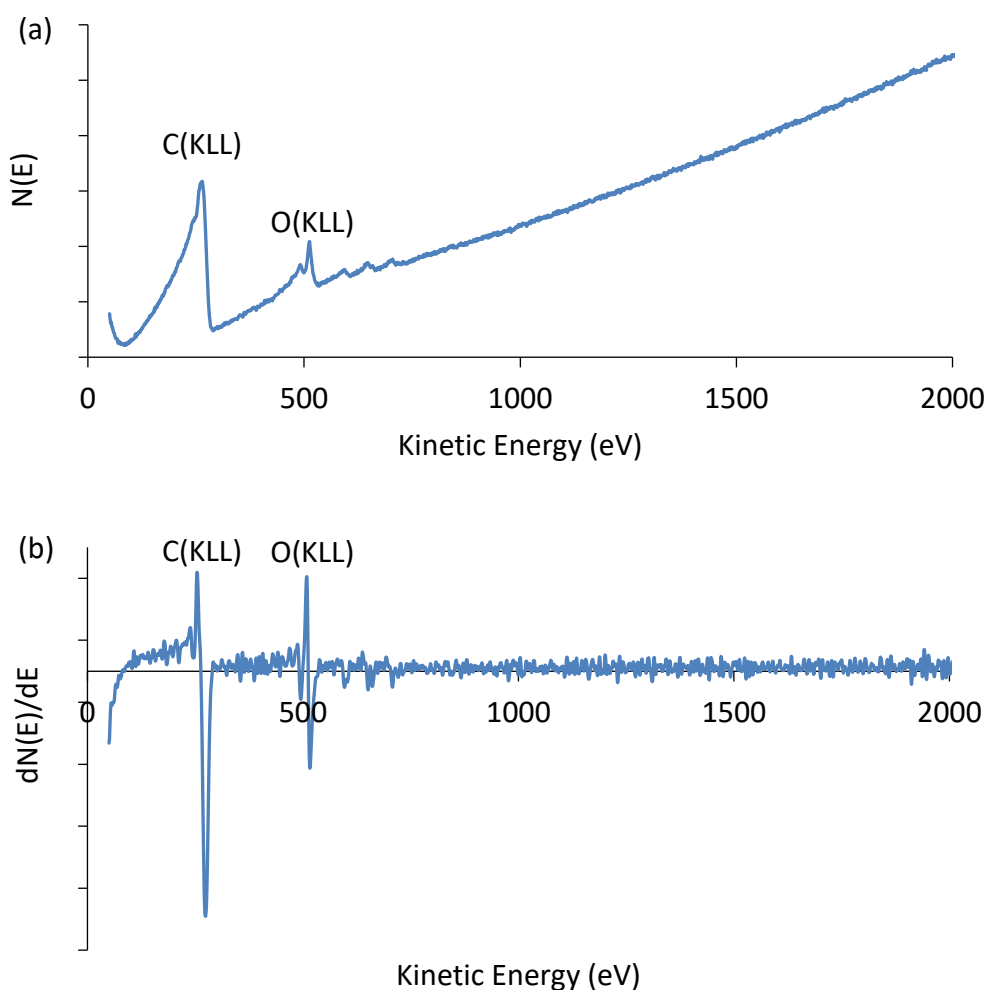
Figure 2-13: (a) Example SAM spectrum of oxygen plasma treated HOPG in undifferentiated form, and (b) the same spectrum in differentiated form.

The background of Auger spectra increases smoothly with increasing kinetic energy and is a result of inelastically scattered primary and secondary electrons [210, 227]. While it is theoretically possible for the background subtraction to be performed in the same way as is done for XPS, there is not a generally accepted procedure for the optimal background subtraction in AES [210]. In addition, as the Auger spectra background intensities often far exceed the signal intensities, there are much higher uncertainties introduced after background subtraction in AES than in XPS [210]. Instead of background subtraction the Auger spectra are generally differentiated, as shown in Figure 2-13 (b), although differentiation results in a loss of sensitivity to chemical bond influence [210]. Differentiation also increases the signal-to-noise ratio of the spectra and highlights small peaks [210, 227]. The peak energy is taken as the negative peak extension in this derivative mode, while the peak-to-peak height from the differentiated peak is proportional to the number of atoms in a volume (after taking sensitivity factors into account) [210, 227].

AES is capable of determining the surface bonding, chemistry, and details of thin film growth mechanisms [227, 233]. It can be used to determine the elemental composition of the sample surface. When combined with scanning capabilities, Auger spectroscopy can be used to produce maps illustrating the distribution of the elements over a sample surface. Ion sputtering can also be combined with Auger spectroscopy in order to produce compositional depth profiles [47, 227].

It is important to quantitatively characterise the bonding types in deposited carbon films. Carbon hybridisation information can be obtained using AES, with the binding energy width of the C (KLL) derivative spectrum from the most positive maximum to the most negative minimum providing an indication of the carbon hybridisations present [200, 217]. This width, called the D parameter, is smaller for natural diamond than it is for graphite, with amorphous carbons having D parameter values somewhere between these two extremes and being dependent on the sp^2/sp^3 ratio. There is a linear relationship between this ratio and the D parameter [22, 73, 75, 76, 92, 190, 200, 217, 224, 234-236]. Typical D parameter values for sp^3 hybridised carbon range from 11 to 15 eV, while those of sp^2 hybridised carbon are more typically around 21 – 24 eV [22, 73, 75, 76, 92, 190, 200, 217, 234-238]. There has also been investigation of how the intensity of the C(KLL) peak changes with hybridisation, with the intensity reducing with decreasing degree of hybridisation, resulting in diamond (sp^3 hybridised) having the highest intensity, followed by graphite (sp^2 hybridised), and finally carbide (sp hybridised) with the lowest intensity [239]. However, for this work only the D parameter is used to create the carbon hybridisation maps and line scans.

The difference between the differentiated C(KLL) spectra for different carbon materials is shown in Figure 2-14, which shows the X-Ray induced Auger Electron Spectroscopy (XAES) spectra derivative maxima are positioned at about 253-254 eV for diamond, graphite, and amorphous carbon [73]. The D parameter for the three samples are 14.3, 22.5, and 18.8 eV, respectively, with the D parameter being linearly related to the sp^2 hybridised carbon concentration [73].

Removed due to copyright restrictions.

Figure 2-14: Derivative dN(E)/dE XAES spectra of graphite, diamond, and ICH4 (amorphous carbon) samples. Reproduced from [73].

The general description of the energy of an emitted Auger electron can be made more specific to carbon C(KLL) transitions and becomes [22, 73, 236, 240]:

$$E_k = C(1s) - V_i - V_j \qquad\qquad (2.6\text{-}2)$$

Where E_k is the kinetic energy of Auger electrons, C(1s) is the binding energy of the carbon 1s level and $V_{i,j}$ are the binding energies of valence electrons involved in transitions referred to the Fermi level, which in the case of carbon are both L electrons [22, 73, 236, 240]. The carbon Auger peak is therefore labelled C(KLL).However, as these L electrons are also the valence electrons this peak is also often labelled as C(KVV).

At kinetic energies lower than ~255 eV the main contributions are due to the 2s electrons and it is therefore not expected that there will be any significant changes in this region of the spectrum for different carbon hybridisations [22, 73]. For kinetic energies higher than ~270 eV the main contributions are due to pπ electrons (which are present in graphitic carbon as it contains π bonds) as pσ electrons (which are present for all carbon allotropes that contain σ bond) have larger binding energies (<~5 eV and ~8 eV, respectively) [73, 75, 114]. The contributions to the spectrum in this region are the C(KV(2pπ)V(2pπ)) and C(KV(2pσ)V(2pπ)) transitions, which are transitions involving either only sp^2 bonded electrons, or both sp^2 and sp^3 bonded electrons, respectively. An increase in these contributions therefore leads to an increase in the Auger band at energies above 270 eV [22, 73, 75, 76, 114, 224]. This increase leads to the conclusion that an increase in the Auger line width results from an increase in sp^2 hybridised carbon [22, 73, 75, 76, 114, 224]. The spectra of all carbon species except diamond contain peaks at ~275 eV and ~280 eV which are assigned to pπ electrons from sp^2 coordinated carbon and are not present in diamond [22, 75, 76, 224].

There have been recent studies that used the Auger carbon peaks in XPS spectra to produce maps showing the carbon hybridisation of graphite and graphite oxide samples [199, 200]. Figure 2-15 shows a D parameter map of a graphite flake (sp^2 hybridised) on carbon tape (mixture of both sp^2 and sp^3 hybridised carbon), along with the spectra from two pixels (one on the graphite flake and one on the carbon tape) [200]. These spectra show clear differences in the width of the C(KLL) peak, which can also be seen in the D-map which shows larger D values in the area of the graphite flake, indicating sp^2 hybridised carbon, and smaller D values in the area of the carbon tape, indicating sp^3 hybridised carbon (carbon tape is composed of carbon filled acrylic, and is thus expected to be mostly sp^3 carbon) [200].

Removed due to copyright restrictions.

Figure 2-15: 800 μm D parameter image of graphite flake on carbon tape with C(KLL) spectra extracted, where the

A similar method has been developed in this work to utilise the data obtained using SAM to produce maps of carbon hybridisation.

2.6.2   SAM Instrument

The SAM system used in this work is a PHI 710 Scanning Auger Nanoprobe as shown in Figure 2-16.
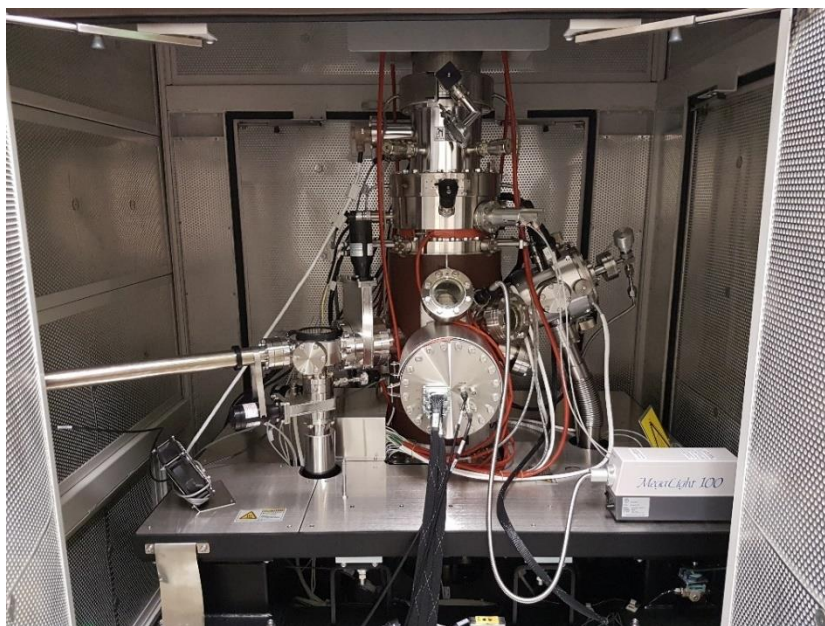
Figure 2-16: PHI 710 Scanning Auger Nanoprobe used in this work.

This instrument has a main analysis chamber kept at a pressure below 1×10^{-9} Torr separated by a gate valve from the introduction chamber. The main chamber has a base pressure of $\sim 1 \times 10^{-10}$ Torr, which is maintained by a turbomolecular drag pump backed by ion pumps. The introduction chamber is also pumped by the same pumping system, and has a base pressure of less than 1×10^{-4} Torr.

A Cylindrical Mirror Analyser (CMA) and a coaxial field emission electron gun, which are mounted coaxially to minimise shadowing of the energy analyser for rough surfaces, are the source of electrons and analyser for the instrument [227]. A schematic of the CMA is shown in Figure 2-17.

Removed due to copyright restrictions.

Figure 2-17: Schematic Diagram of a Cylindrical Mirror Analyser. Reproduced from [210].

The analyser employs two concentric cylinders which are held at different potentials, and electrons that enter are deflected in an arc by this potential so that only electrons of a certain energy will be

detected, in the same way as the CHA [227]. The energy resolution, ΔE, varies proportionally to the energy, E, and the percent resolution, ΔE/E, is constant for a fixed analyser geometry [227]. If an adjustable exit slit or aperture is included in the CMA it is possible to adjust the percentage resolution [227].

The spectra collection software utilised is SmartSoft-AES (version 5.2.0.8), also from PHI, which integrates with the PHI MultiPak data reduction software used for data analysis.

One of the disadvantages of using SAM for characterisation is that carbon deposition in areas under examination is common, as it is in SEM [241]. Although SAM is performed under UHV conditions, there remains some residual carbon containing gasses, including CO, CO_2, and various hydrocarbons, present in the system, which can be decomposed by exposure to the electron beam [241]. This enhances the adsorption sticking coefficient of the carbon containing molecules, and results in areas contaminated with carbon that can be seen on SEM images as darker areas [241]. In order to see the effect that this contamination has on the data obtained in this project, successive spectra were taken over the same area to examine any differences caused in both survey scans and high-resolution C(KLL) scans.

2.6.3 SAM Sample Characterisation Process

Samples are mounted for SAM using a mask that is placed and screwed down over the sample, allowing a small window through which to characterise the sample. The samples are placed in the SAM introduction chamber and pumped down to below 1×10^{-4} Torr, then left to outgas for 30 minutes – 1 hour, depending on the nature of the samples and how much they outgas. When sufficient time has elapsed the samples are transferred to the main chamber of the SAM instrument. When the pressure in this chamber is below $\sim 5 \times 10^{-9}$ Torr characterisation can begin. Typically, an SEM image is taken of a region of the sample, followed by survey scans of area(s) within this region and high-resolution scans of any peaks of interest. Elemental maps, line scans, and depth profiles can also be performed in this region. Multiple areas of each sample can be examined to help determine the uniformity of the surface.

Elemental map acquisition is performed by first finding an area of interest and acquiring an SEM image then acquiring the elemental maps over the same area. There are several parameters that must be chosen to acquire the scan, including the spatial resolution and acquisition mode. The spatial resolution is chosen by the number of pixels that the map is composed of, where the lowest

resolution available is 32x32 pixels and the highest is 512x512 pixels. A spectrum is acquired at each point by scanning the electron beam across the map area. These spectra can either be acquired using a 2- or 3-point acquisition mode, which detects the maximum and either one or two minima to find the peak intensity, or window mode, which takes a full spectrum of the peak of interest. The elemental maps show the intensity of an element at each pixel across the surface, and can be used to visually compare the elemental composition at different points on the sample.

This work has developed a method to produce a carbon hybridisation map from a carbon elemental map that has been acquired in window mode. By extracting the spectra obtained at each pixel of the map, differentiating them, and determining the D parameter at each pixel a new map showing the D width can be produced. This D parameter map can be converted to a carbon hybridisation map using the relationship between the magnitude of the D parameter and the sp^2 hybridised carbon percentage. Using this method micro- and nano-structures composed of different carbon hybridisations can be characterised in order to determine where each hybridisation is present across the surface.

Carbon hybridisation line scans can be produced from carbon elemental line scans in much the same way, with window mode scans acquired, D parameters extracted, and converted to a sp^2 hybridised carbon percentage which can then be plotted.

2.6.4   SAM Sample Analysis

The spectra, maps, line scans, and depth profiles obtained from SAM are analysed with the MultiPak (PHI electronics, version 9.8.0.19) software package. The peak-to-peak height of peaks within survey spectra show the atomic concentrations of the elements present (when atomic sensitivity factors are taken into account). The shape and position of peaks in high resolution spectra are examined to determine the chemical states of the elements. Elemental maps can be coloured either red, green, or blue and red-green-blue (RGB) overlays made to show where 2 or 3 elements are present on the surface simultaneously. Line scans and depth profiles can be created to show how the elemental composition of the surface changes across a line or down through the surface of the sample, respectively. Analysis of carbon elemental maps and line scans for the production of carbon hybridisation line scans is discussed in detail in later chapters.

2.7 Materials

2.7.1 Highly Oriented Pyrolytic Graphite

The Highly Oriented Pyrolytic Graphite (HOPG) used in the work was obtained from Coherent Scientific Australia (12 mm x 12 mm x 2 mm), ZYB grade). Fresh HOPG surfaces were obtained by cleaving with adhesive tape. XPS characterisation revealed no contamination from this tape.

2.7.2 Oxygen

The oxygen gas used in this work was obtained from BOC (high purity research grade, 99.95 % purity). This gas was used to treat samples, clean silicon substrates, and clean the plasma chamber.

2.7.3 Argon

The argon gas used in this work was obtained from BOC (high purity research grade, 99.997 % purity). This gas was used both to treat samples and to clean the plasma chamber.

2.7.4 Methane

The methane gas used in this work was obtained from Linde Australia (high purity research grade, 99.95 % purity). This gas was used to grow diamond-like carbon films.

2.7.5 Hydrogen

The hydrogen gas used in this work was obtained from CIG (high purity research grade, 99.99 % purity). This gas was used in the growth of diamond-like carbon films.

3 PLASMA MODIFICATION OF HIGHLY ORIENTED PYROLYTIC GRAPHITE

As the physical and electronic properties of a carbon material are strongly dependent on its structure the ability to modify the surface of a carbon material allows for the creation of a surface layer or surface structures with different properties to the bulk material. One way of modifying a surface is through exposure to plasma, which allows for control of the extent of modification through the variation of several parameters. The source gas composition, source gas pressure, radio frequency (RF)-coupling power, and exposure time to the plasma can all be varied within the radio-frequency inductively couple plasma (RF-ICP) system, and the impact of the treatment on the HOPG surface is characterised using XPS and SAM.

Previous work using this plasma system has determined that the range of modification of HOPG achieved by varying the source gas pressure and the RF-coupling power is the same [67], therefore in this work the RF-coupling power, the time exposed to the plasma, and the source gas composition are the three plasma parameters that were focused on. The samples of modified HOPG created in this manner were characterised with both XPS and SAM, and the results from both techniques are compared.

3.1 Source Gas Choice

Previous systematic studies on the modification of HOPG with oxygen plasma have been performed in the RF-ICP system used in this work, with the source gas pressure, RF-coupling power, and exposure time used for the plasma treatment all found to influence the extent of modification of the HOPG surface [67]. This work was characterised using XPS and Raman spectroscopy, however some experiments were revisited to characterise with SAM. In order to further expand the carbon modifying capabilities of the plasma system the impact of argon plasma on HOPG has also been studied.

Plasma is composed of energetic species such as ions, radicals, and electrons, all of which will interact with the sample surface in different ways depending on their size, composition, and energy. The species present in an argon plasma will not only be of a different chemical nature to those in an oxygen plasma, they will also have a different size. These differences are expected to change how the HOPG surface is modified, with the larger, more inert species in the argon plasma likely to

bombard the surface rather than chemically modifying it as the oxygen plasma is expected to do.

3.2   Oxygen Plasma Treatment of Highly Oriented Pyrolytic Graphite

Oxygen plasma that has been ignited from oxygen gas will contain different species including ions, radicals, electrons, and unionised molecules of oxygen. These species include O_2^+, O_2^-, O_3, O^+, O^-, $O\cdot$, $O_2\cdot$, and $O_3\cdot$, and result in the oxygen plasma being chemically reactive towards surfaces that it encounters. The HOPG is exposed to all of these species during the plasma treatment and as such will be oxidised, however it is also expected that some of the carbon atoms on the surface will be converted from sp^2 hybridised carbon to sp^3 hybridised carbon and thus produce a layer of modified carbon on top of the bulk HOPG. To modify the HOPG with oxygen plasma a source gas pressure of 1.0×10^{-3} Torr is used for all samples, while the treatment time and RF-coupling power are varied in an attempt to change the extent of modification to the surface.

3.2.1   Influence of Exposure Time on Plasma Modification of Highly Oriented Pyrolytic Graphite

Samples can be treated with a plasma for as long as desired and it is therefore important to understand the level of modification that is achieved when using a specific set of conditions. To this end a range of treatment times between 2 and 60 minutes are tested for oxygen plasma ignited with a 30 W or 40 W RF-coupling power.

3.2.1.1 30 W RF-Coupling Power Oxygen Plasma

Oxygen plasma ignited with a 30 W RF-coupling power was applied to samples of cleaved HOPG for times ranging between two minutes and 60 minutes, and the resultant samples were characterised using XPS and SAM to examine the chemical composition of the sample and the hybridisations of carbon present on the surface, as well as the other chemical environments of the carbon.

3.2.1.1.1   XPS RESULTS

The XPS results obtained for samples of 30 W RF-coupling power oxygen plasma treated HOPG are shown in Figure 3-1, which presents the concentration of carbon, oxygen, fluorine, iron, and nickel as a function of the time the sample was exposed to the plasma. The error bars of the data points indicate the average errors in the elemental concentration of the different elements found from the standard deviation of similar samples previously.
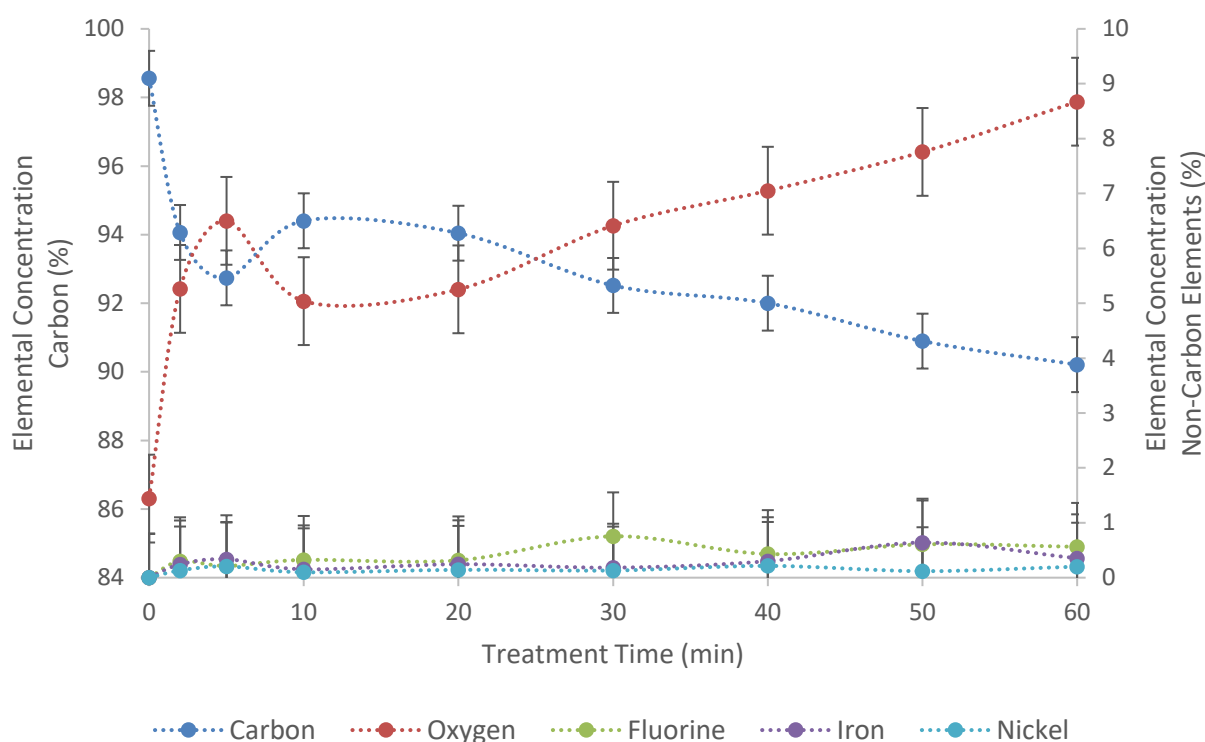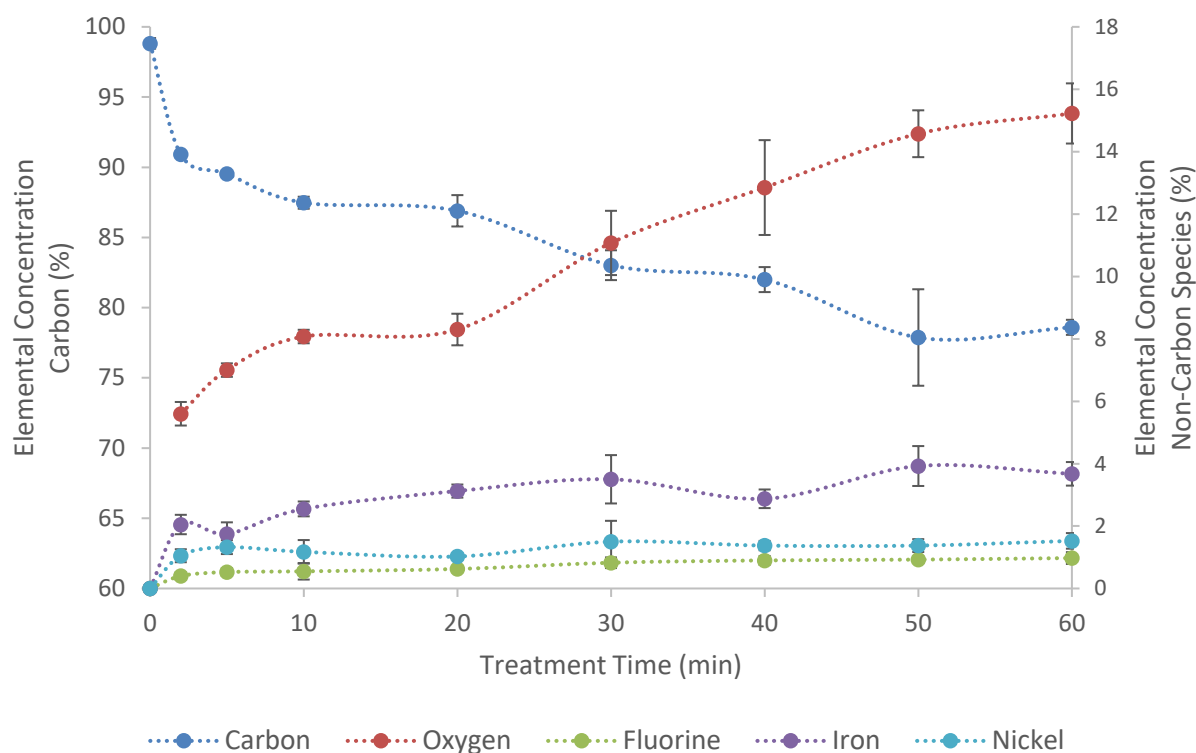
Figure 3-1: Variation in the elemental composition of 30 W oxygen plasma treated HOPG with treatment time, determined with XPS. The elemental concentration of carbon is shown on the left axis and elemental concentrations of oxygen, fluorine, iron, and nickel are shown on the right axis. Error bars indicate the error determined as the average for the plasma modification of HOPG based on previous experiments.

The elemental composition of the sample changes as the treatment time increases, indicating an increased extent of modification of the HOPG with further exposure to the oxygen plasma. The carbon percentage decreases from 98.6 % initially to 94.0 % after a 2-minute plasma treatment, and further decreases to 92.7 % after a 5-minute treatment. An increase in the treatment time to ten minutes results in an increase in the carbon percentage to 94.4 %, while further increases in treatment time beyond ten minutes produce a continually decreasing carbon percentage until a minimum of 90.2 % is reached at 60 minutes. The oxygen content of the sample shows the opposite trend, with an initial 2-minute treatment increasing the oxygen from 1.4 % on the untreated sample to 5.3 %, a 5-minute treatment results in 6.5 % oxygen, and a 10-minute treatment decreases the oxygen content to 5.0 %. After this point further increases in treatment time results in a gradual increase of oxygen until a maximum of 8.7 % after 60 minutes.

The formation of an oxide on the surface is the result of reactions between the oxygen plasma species and the HOPG. There are a variety of reactions occurring during the plasma treatment, including the breaking of bonds, the forming of new bonds, the modification of carbon groups, and

the removal of species from the HOPG surface.

The bond enthalpies of sp^2 and sp^3 hybridised carbon bonds are different, and therefore the likelihood of the bonds breaking when exposed to plasma is different. The carbon – oxygen bonds also have different enthalpies, all of which contribute to the equilibrium occurring between the plasma and the HOPG surface. The bond enthalpy values for these bond types are given in Table 3-1 [18].

Table 3-1: Bond enthalpies for different carbon-carbon and carbon-oxgyen bond types [18].

Bond Type	Bond Enthalpy (kJ.mol^{-1})
C-C	348
C=C	614
C-O	358
C=O	799

These differences in bond enthalpy show that the C-C and C-O bonds are much easier to break than the C=C bonds of the HOPG, and therefore are more likely to be broken through exposure to the plasma.

The initial modification from the plasma will cause some of the C=C bonds to break, either forming C-C bonds, C-O bonds, or dangling C bonds. The C-O and C-C bonds are both much weaker than the C=C bonds, and therefore these bonds are more likely to be broken if the energy from the plasma species is not sufficient to break further C=C bonds on the HOPG surface. When these weaker C-C and C-O bonds break it can result in the removal of species from the HOPG surface, which leaves behind carbon surface that can then be further oxidised. This equilibrium of the oxidation of the HOPG surface and the removal of carbon-oxygen species results in an equilibrium in the elemental concentrations of carbon and oxygen on the oxygen plasma modified HOPG surface.

The oxygen plasma treatment also results in the deposition of fluorine, iron, and nickel on the HOPG surface. These elements are present in the antenna used in the plasma chamber to ignite the plasma using a RF-signal. The antenna is composed of steel, which is the source of the iron and nickel, while the fluorine is the result of previous use of the plasma chamber for the fluorination of surfaces using sulphur hexafluoride. This fluorination process caused some fluorine to become implanted in the antenna, and as a result when sputtering of the antenna occurs during plasma treatments at higher

RF-coupling powers fluorine is produced along with the expected iron and nickel. The elemental concentrations of these three elements are small (less than 1 %) and therefore do not show any clear trends in their behaviour as the treatment time increases.

The change in the oxide formed on the HOPG surface as a result of the oxygen plasma treatment can be more clearly examined without interference of sputtered antenna species by considering the O:(C+O) ratio, as shown in Figure 3-2.
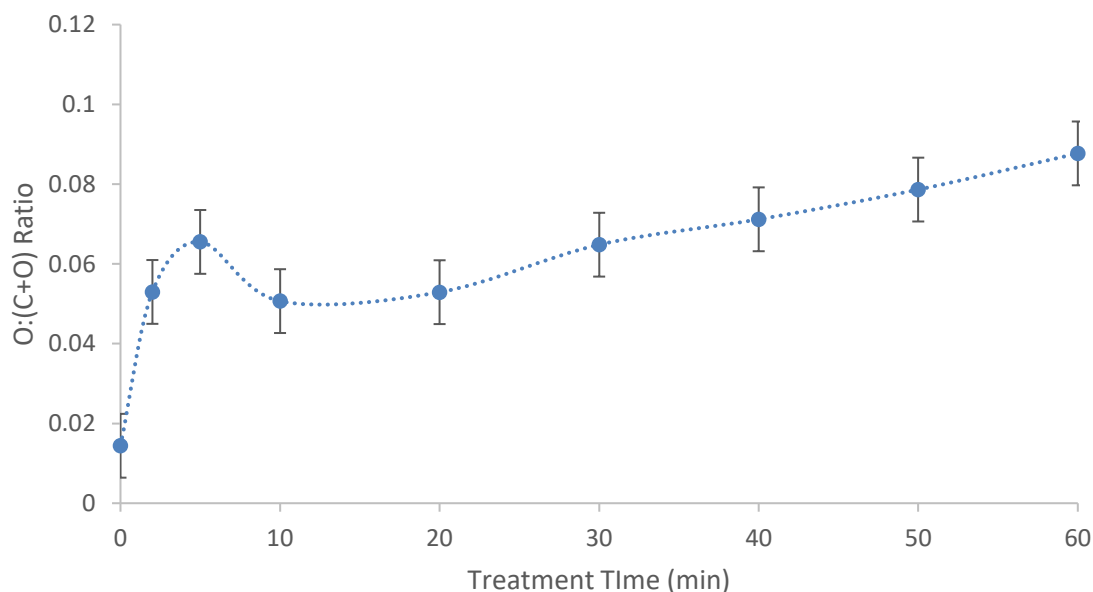
Figure 3-2: O:(C+O) ratio for 30 W oxygen plasma treated HOPG with plasma treatment times between 2 and 60 minute found with XPS. Error bars indicate the error determined as the average for the plasma modification of HOPG based on previous experiments.

The O:(C+O) ratio shown in Figure 3-2 indicates an increase in the amount of oxygen on the surface as the oxygen plasma treatment time increases. The initial increase after a 2-minute treatment is rapid, and a further increase is observed as the treatment time is increased to 5 minutes. However, a decrease in the O:(C+O) ratio occurs when the treatment is increased to 10 minutes, before the increase begins again with further increases in treatment time. The small oscillation that occurs between 2 and 5 minutes cannot conclusively be said to be a true oscillation due to the size of the error bars, which indicate that each point lies within the uncertainties of the other points and therefore may not actually be different. Further study could provide clarity on the oscillatory behaviour, or lack thereof, of the oxygen plasma modification of a HOPG surface.

The high resolution C 1s peak was deconvoluted into six components of carbon-carbon bonds,

carbon-oxygen bonds, and carbon-lattice vacancy interactions, and the percentage that each component contributes to the total C 1*s* peak is presented for each treatment time examined in Figure 3-3.
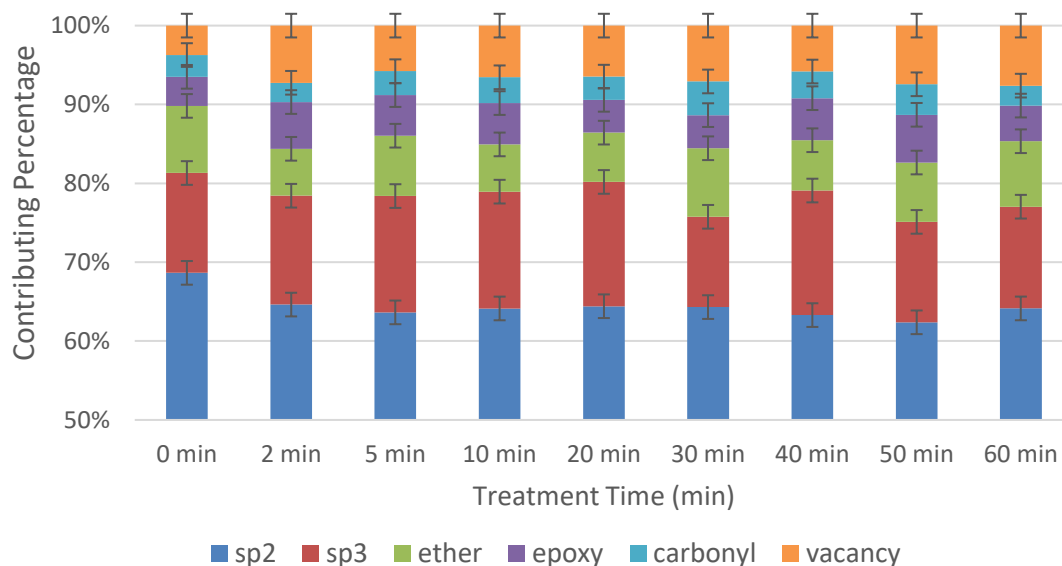
Figure 3-3: Percentages each deconvoluted component of C 1s peak contributes to the total peak for 30 W oxygen plasma treated HOPG determined with XPS. Error bars indicate the error determined as the average for the plasma modification of HOPG based on previous experiments.

The components of the C 1*s* peak show changes as the treatment time increases, with the carbon-carbon species decreasing and the carbon-oxygen species increasing. There are sp^2 hybridised carbon-carbon bonds and sp^3 hybridised carbon-carbon bonds present in the sample, and while the combination of the two decreases with treatment time the sp^3 hybridised carbon percentage increases by a small amount. The ether, epoxy, and carbonyl species all vary as the treatment time increases with the carbon-oxygen species total showing an increase, however the individual species do not show systematic changes. The other change observed in the C 1*s* peak is the increase in the vacancy component, which indicates disruption to the HOPG lattice that occurs as part of the plasma treatment. This percentage that this species contributes to the C 1*s* peak increases after a 2-minute plasma treatment and then remains reasonably constant as further plasma exposure occurs.

3.2.1.1.2   SAM RESULTS

The elemental composition found using SAM for the same 30 W oxygen plasma treated HOPG samples are is shown in Figure 3-4, which indicates the percentages of carbon, oxygen, fluorine, iron, and nickel on the sample as a function of the time the HOPG was exposed to the plasma.
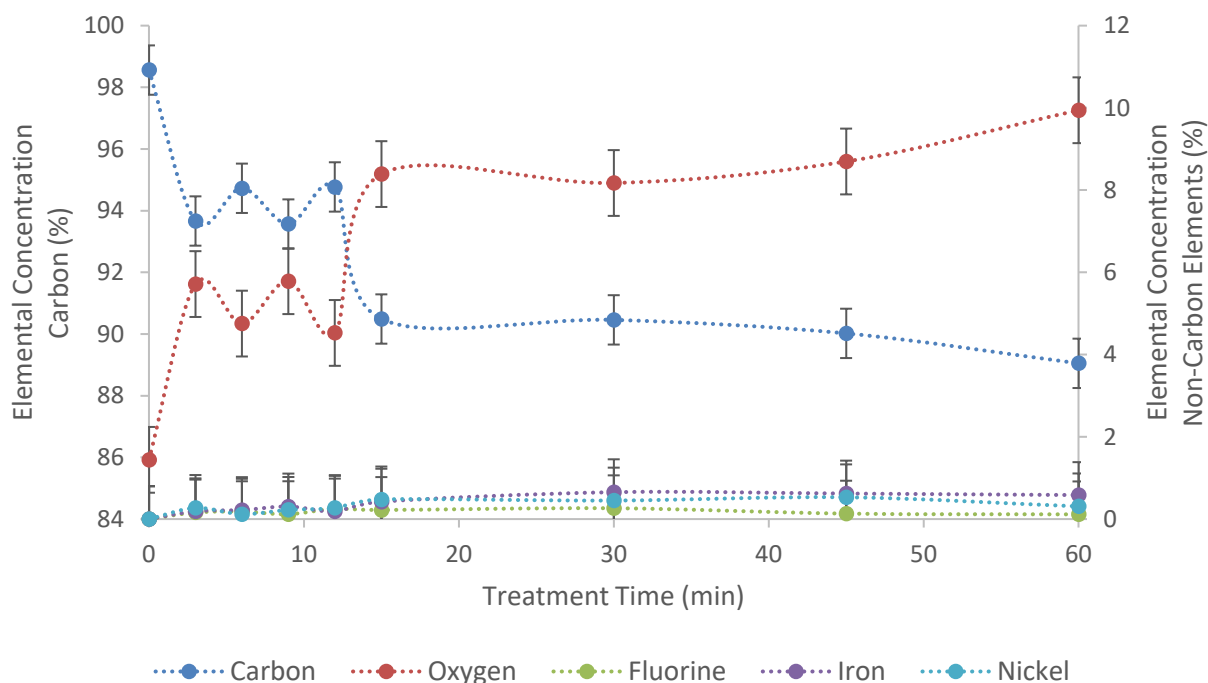
Figure 3-4: Variation in the elemental composition of 30 W oxygen plasma treated HOPG with treatment time, determined with SAM. The concentration of carbon is shown on the left axis and concentrations of oxygen, fluorine, iron, and nickel are shown on the right axis. Data points are the average of four samples, and error bars are the standard deviation from four samples.

From Figure 3-4 it can be seen that there are changes to the concentrations of all elements on the surface as the treatment time increases. The carbon concentration begins at 99 % for an untreated HOPG sample and begins to decrease after exposure to the oxygen plasma. After 2 minutes the carbon concentration has decreased to 91 % and continues to decrease with longer treatment time until a minimum of 78 % is reached after 50 minutes of plasma exposure. After 60 minutes the carbon concentration increases slightly to 79 %, however as the 50 minute point has a large error bar it is possible that with increased repetition a 50 minute treatment would result in an extent of modification between the 40 and 60 minute samples and the decreasing carbon concentration trend would continue. Iron, nickel, and fluorine are also detected for each sample that has been treated with oxygen plasma, with the iron increasing to a maximum elemental concentration of 4 %, while the nickel and fluorine have elemental concentrations of approximately 1 %. Comparison of the data in Figure 3-1 and Figure 3-4 indicate that both the XPS and SAM characterisation methods show systematic changes in the elemental composition of the surface after exposure to oxygen plasma. However, the XPS results show lower oxygen, iron, fluorine, and nickel concentrations than the results from SAM.

To examine the oxidation of the HOPG more clearly without the influence of the sputtered contaminating elements the O:(C+O) ratio is calculated for each sample and is shown in Figure 3-5.
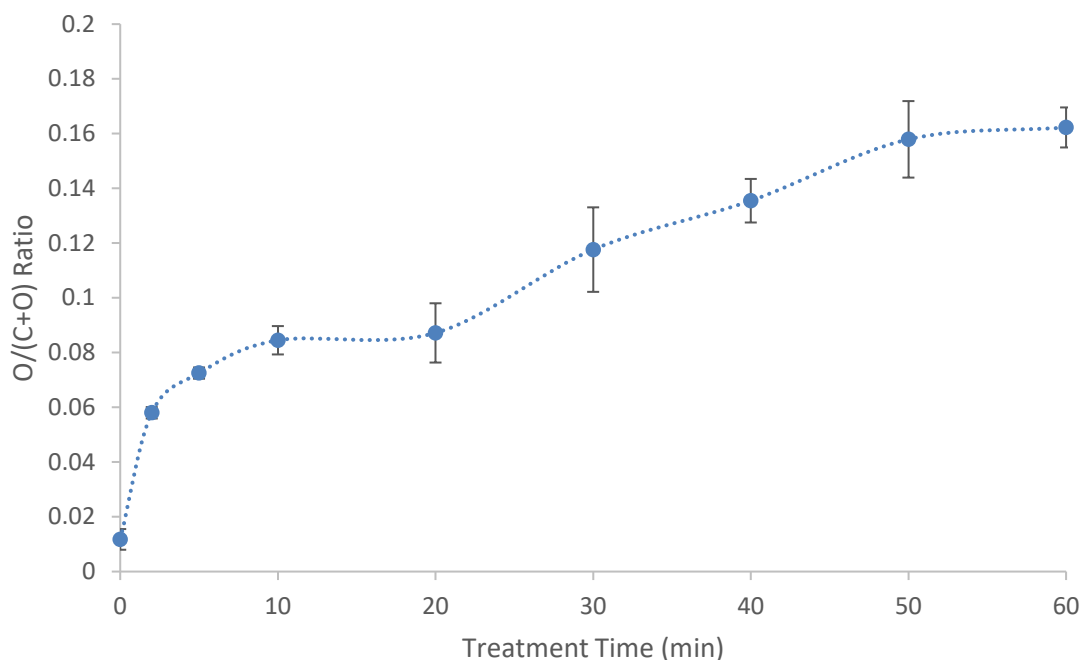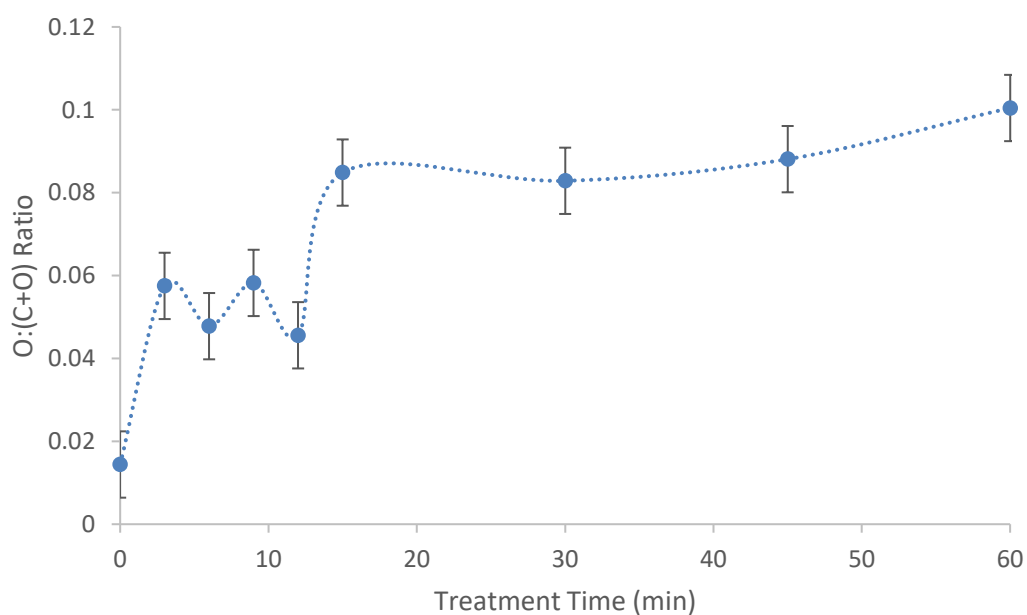

Figure 3-5: O:(C+O) ratio for 30 W oxygen plasma treated HOPG with plasma treatment times between 2 and 60 minute found with SAM. Data points are the average of four samples, and error bars are the standard deviation from four samples.

The ratio shown in Figure 3-5 is used to examine the growth of the oxide layer on the HOPG surface as the extent of treatment time increases. It can be seen from these results that as the treatment time increases the surface becomes increasingly oxidised. The initial modification is quite rapid, with a 2-minute oxygen plasma treatment increasing the ratio from 0.01 to 0.06, while it takes 30 minutes to achieve the same increase again. Beyond 30 minutes the ratio continues to increase, until the trend begins to stabilize for the 50- and 60-minute treatments with a value of 0.16. This trend is very similar to that observed from XPS in Figure 3-2, indicating consistency between the data obtained using the two techniques, however the ratio is lower for XPS, which shows that there is less oxygen being detected relative to carbon in this technique.

High-resolution C(KLL) spectra were also acquired for each sample and the width between the maximum and minimum of the differentiated spectra (the D parameter) was measured for each case. This D parameter value was then converted to a sp^2 hybridised carbon percentage using a calibration curve linking the two parameters. Both the D parameter and sp^2 hybridised carbon percentage for each sample are shown in Figure 3-6 on the left and right axes, respectively.
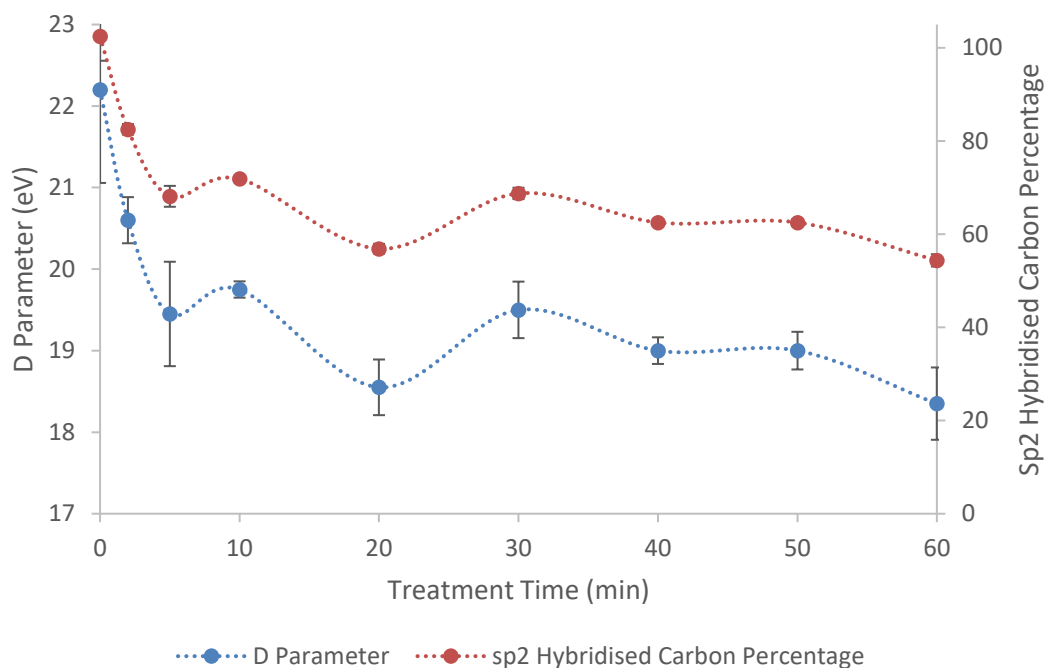
Figure 3-6: D parameter (left axis, blue points) and *sp*² hybridised carbon percentage (right axis, red points) for samples of HOPG exposed to 30 W oxygen plasma for times ranging between 2 minutes and 60 minutes. Data points are the average of four samples, and error bars are the standard deviation from four samples.

The D parameter values and sp^2 hybridised carbon percentage in Figure 3-6 follow the same trend that has been observed for the elemental concentrations described above in Figure 3-4. As the exposure time to the oxygen plasma increases the D parameter and sp^2 hybridised carbon percentage also decrease, indicating that as well as an oxide layer being formed on the surface of the HOPG there is also a conversion of sp^2 to sp^3 hybridised carbon occurring. A pristine HOPG surface should be composed entirely of sp^2 hybridised carbon, although any lattice defects on the surface will result in the presence of sp^3 carbon. As the oxygen plasma interacts with the surface and produces an oxide layer the double bonds in the HOPG are broken and replaced with single bonds, which lowers the sp^2 hybridised carbon percentage.

The first 2 minutes of oxygen plasma treatment produces a large change in D parameter from 22.2 eV to 20.6 eV, and this decreasing trend continues but at a lower rate as the exposure time of the HOPG to the plasma is increased. A 20-minute treatment time results in a D parameter of 18.5 eV, and after this further treatment results in a spike in D parameter after 30 minutes, before the values decrease again until a treatment time of 60 minutes results in a D parameter of 18.4 eV. This 60-minute oxygen plasma treatment results in a sp^2 hybridised carbon percentage of 55 %, which is the lowest percentage reached using a 30 W oxygen plasma. While there are still some changes

occurring as the treatment time increases past 20 minutes these changes are smaller, and the trend appears to be stabilizing. The trends shown in Figure 3-6 are similar to those observed in Figure 3-3 for the changes in hybridisation found using XPS, however the SAM results show a greater change in hybridisation with treatment time.

3.2.1.1.3 COMPARISON OF SAM AND XPS RESULTS

The XPS and SAM results both indicate that a 30 W oxygen plasma treatment results in modification of the HOPG surface, and that the extent of modification is influenced by the length of time that the sample is exposed to the plasma. There are, however, some differences in the numbers that the two techniques show which are due to two factors: the sampling depths and the sampling areas of the techniques.

Both XPS and SAM are surface sensitive techniques, with the sensitivity due to the low inelastic mean free path (IMFP) of electrons emitted in the photoelectron and Auger processes. The IMFP of an emitted electron is element specific, and also depends on the kinetic energy with which it is emitted. For example, C $1s$ electrons emitted from graphitic carbon atoms during XPS with an Mg K_α source will have a kinetic energy of 989 eV, and will have an IMFP of approximately 1.81 nm [212]. However, C(KLL) electrons emitted from graphitic carbon atoms during SAM will have a kinetic energy of approximately 270 eV, resulting in an IMFP of approximately 0.71 nm [212], and thus in a significantly higher surface sensitivity for SAM over XPS. The modification of HOPG with plasma is expected to occur on the surface layer of the graphite, therefore XPS will be detecting more of the unmodified graphite beneath the surface layer than SAM, and the elemental and hybridisation ratios will be different for the two techniques.

SAM also examines a smaller area on the sample surface spatially, with XPS examining an area that is approximately 5 mm x 10 mm while SAM varies with magnification level, but typically examines areas on the μm or nm scale. While multiple positions were examined and averaged for each sample using SAM and showed that the modification was quite uniform across the sample surface, when examining smaller areas it is possible that there are variations in the extent of modification that are not detected, whereas the large area examined with XPS represents the average of these variations.

The results from XPS and SAM are therefore consistent and complementary of each other despite showing different numerical values for the extent of modification.

3.2.1.1.4 CONCLUSIONS

A 30 W oxygen plasma treatment can be used to modify the surface layers of the HOPG to produce an oxide on the surface and to convert a fraction of the sp^2 hybridised carbon atoms on the surface to sp^3 hybridised carbon atoms. The extent of this modification can be controlled by varying the length of time that the sample is exposed to the plasma, with XPS and SAM both showing greater modification with increased treatment time.

3.2.1.2 40 W RF-coupling Power Oxygen Plasma

To compare the influence of RF-coupling power on the modification, the same experiments were repeated for a 40 W RF-coupling power. Oxygen plasma was used to treat cleaved HOPG for treatment times ranging between 3 minutes and 60 minutes, which were characterised with XPS and SAM.

3.2.1.2.1 XPS RESULTS

Samples of HOPG exposed to a 40 W RF-coupling power oxygen plasma were characterised using XPS to examine the elemental composition. The carbon, oxygen, fluorine, iron, and nickel elemental concentrations are shown for each treatment time tested in Figure 3-7.

Figure 3-7: Elemental composition of 40 W oxygen plasma treated HOPG with treatment time determined with XPS. The concentration of carbon is shown on the left axis and concentrations of oxygen, fluorine, iron, and nickel are shown on the right axis. Error bars indicate the error determined as the average for the plasma modification of HOPG based on previous experiments.

As the exposure time to the plasma increases the elemental composition of the sample changes, with the carbon content decreasing while the oxygen, fluorine, iron, and nickel content increases. A 3-minute treatment time results in a decrease in the carbon concentration from 98.6 % to 93.7 %, however after this further treatment up to 12 minutes does not show a clear trend and the carbon concentration hovers around 94 %. A treatment time of 15 minutes produces a further decrease in the carbon content to 90.5 %, and the decreasing trend continues up to 60 minutes when the carbon percentage is reduced to 80.0 %. The reverse trend occurs for oxygen, with the concentration increasing from 1.4 % to 10.0 % after a 60-minute treatment time. Sputtering of iron, fluorine, and nickel from the antenna also occurs during the oxygen plasma treatment, and the concentrations of these elements shows some slight increases as the treatment time increases, however these changes cannot be said to be significant due to the size of the uncertainties.

The O:(C+O) ratio more clearly indicates the trend in the oxidation of the surface without interference from the contaminating elements, as indicated in Figure 3-8.

Figure 3-8: O:(C+O) ratio for 40 W oxygen plasma treated HOPG with plasma treatment times between 2 and 60 minute found with XPS. Error bars indicate the error determined as the average for the plasma modification of HOPG based on previous experiments.

The O:(C+O) ratio found with XPS shows an increasing trend as the length of time the sample is exposed to the plasma increases. For short treatment times up to 12 minutes the ratio increases to approximately 0.5 and while there is some variation in these points it is within the uncertainty and does not indicate a true oscillation. After a 15-minute treatment the ratio increases to 0.085, and

remains around this value until a 60-minute treatment time is reached. The behaviour between 15 and 60 minutes indicates that the modification from the plasma has reached an equilibrium point and the surface is not experiencing further changes overall.

Deconvolution of the high-resolution C 1s peak from XPS produced six components with carbon-carbon bonds, carbon-oxygen bonds, and carbon-vacancy interactions. The percentage that each of these components contributes to the C 1s peak is shown for each treatment time in Figure 3-9.
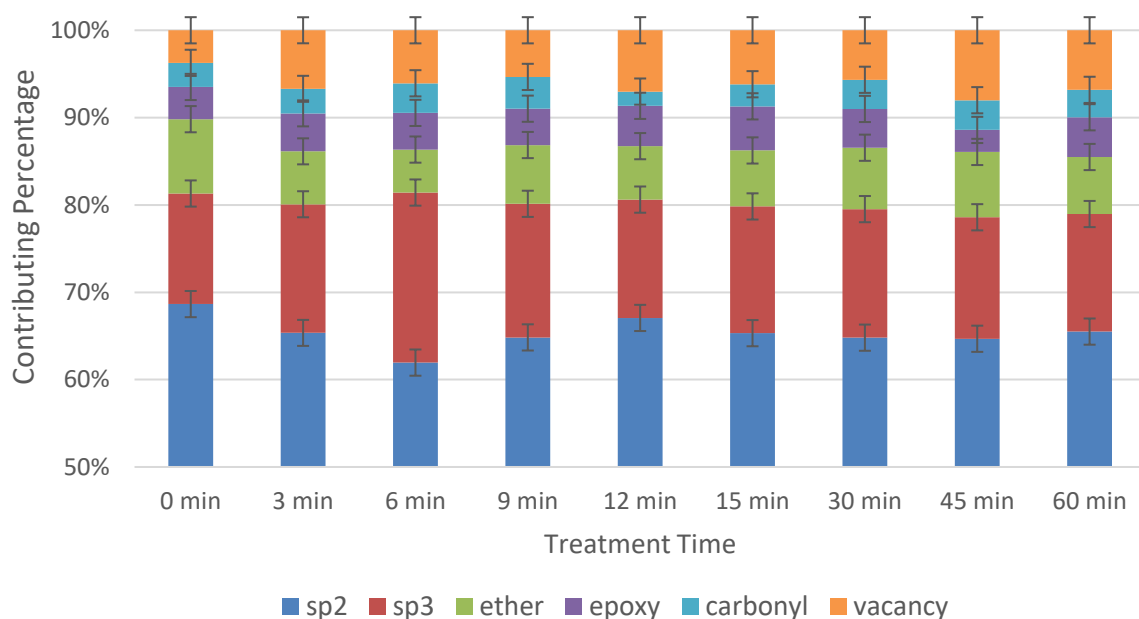
Figure 3-9: Percentages each deconvoluted component of C 1s peak contributes to the total peak for 40 W oxygen plasma treated HOPG determined with XPS. Error bars indicate the error determined as the average for the plasma modification of HOPG based on previous experiments.

The deconvolution of the C 1s peak shows a difference between an untreated HOPG sample and those treated with the oxygen plasma, however there is no clear trend in how the modification changes the carbon-carbon and carbon-oxygen species when the treatment time increases. After the 3-minute oxygen plasma treatment the largest difference observed is in the increase in sp^3 hybridised carbon bonds and carbon-lattice vacancy interactions. The total contribution from the carbon-oxygen species remains roughly the same, however the contributions from the individual species do change randomly. As the treatment time increases there is a small decrease in the carbon-carbon species overall and a small increase in the carbon-oxygen species, however this change is not significant in comparison with the size of the uncertainties. These results show that the plasma modification changes the structure of the HOPG on the surface and disrupts the sp^2

hybridised carbon lattice to form a larger percentage of sp^3 hybridised carbon bonds, but suggests that once initial modification has occurred there is an equilibrium between the plasma species and the surface and the extent of hybridisation modification does not change further with more plasma exposure.

3.2.1.2.2 SAM RESULTS

The same HOPG samples that were treated with a 40 W oxygen plasma were characterised with SAM to determine the elemental composition. The atomic percentages of carbon, oxygen, fluorine, iron, and nickel are shown in Figure 3-10 as a function of the length of time the HOPG was exposed to the plasma.
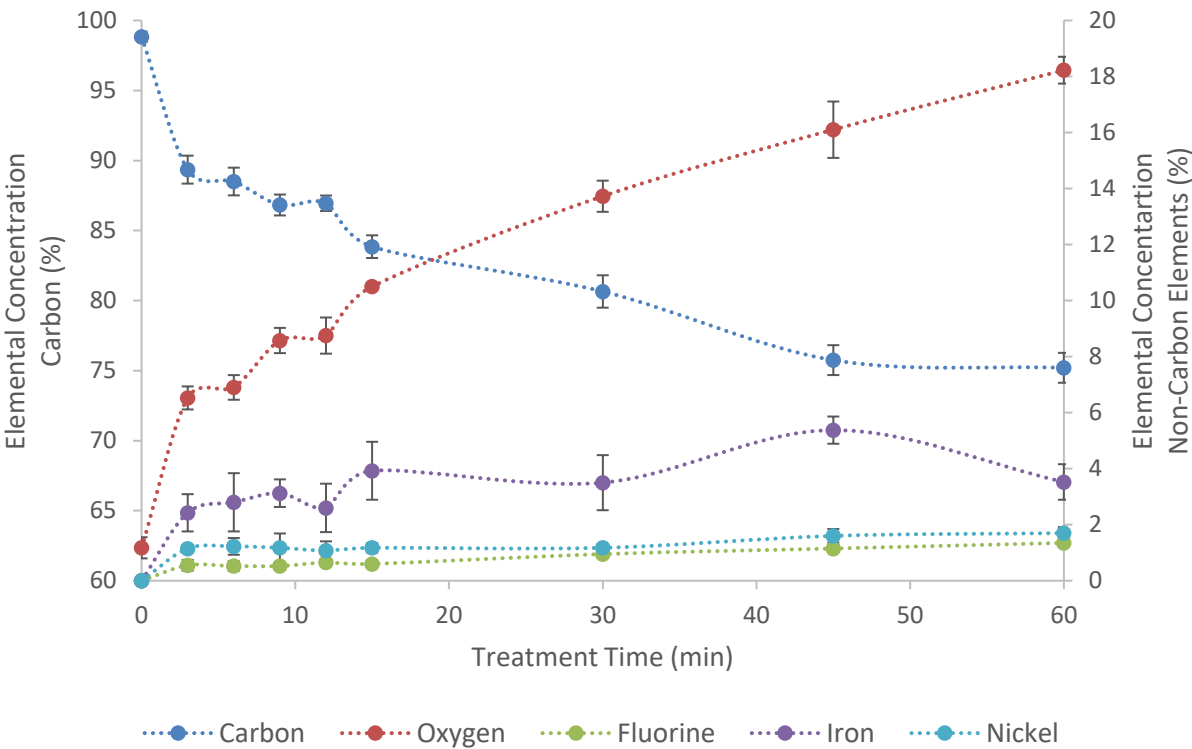
Figure 3-10: Elemental composition of 40 W oxygen plasma treated HOPG with treatment time determined with SAM. The concentration of carbon is shown on the left axis and concentrations of oxygen, fluorine, iron, and nickel are shown on the right axis. Data points are the average of four samples, and error bars are the standard deviation from four samples.

The elemental composition of the oxygen plasma treated HOPG changes with the length of time it is exposed to the plasma. Initially the HOPG is composed predominantly of carbon, with a small amount of oxygen also present. After a three-minute plasma treatment the sample shows a decrease in the amount of carbon on the surface and an increase in oxygen content, as well as the deposition of a small amount of iron, nickel, and fluorine. The source of these new elements is

55

sputtering from the antenna in the plasma chamber, which occurred in the same way as was described previously for the 30 W oxygen plasma treated samples in Figure 3-4. Further exposure to the oxygen plasma results in continued decrease in the concentration of carbon and an increase in oxygen, fluorine, iron, and nickel, however the rate of change of the elements slows as the treatment time increases. After 60 minutes the carbon percentage has decreased to 75 % and the oxygen has increased to 18 %. These trends match those observed with XPS for the same samples (Figure 3-7), however the carbon percentage is lower and the other elemental concentrations higher with SAM due to the differences in sampling area and depth, as was discussed previously (section 3.2.1.1.3).

The carbon and oxygen are considered without the other contaminating elements in Figure 3-11 by comparing the O:(C+O) ratio for each sample.
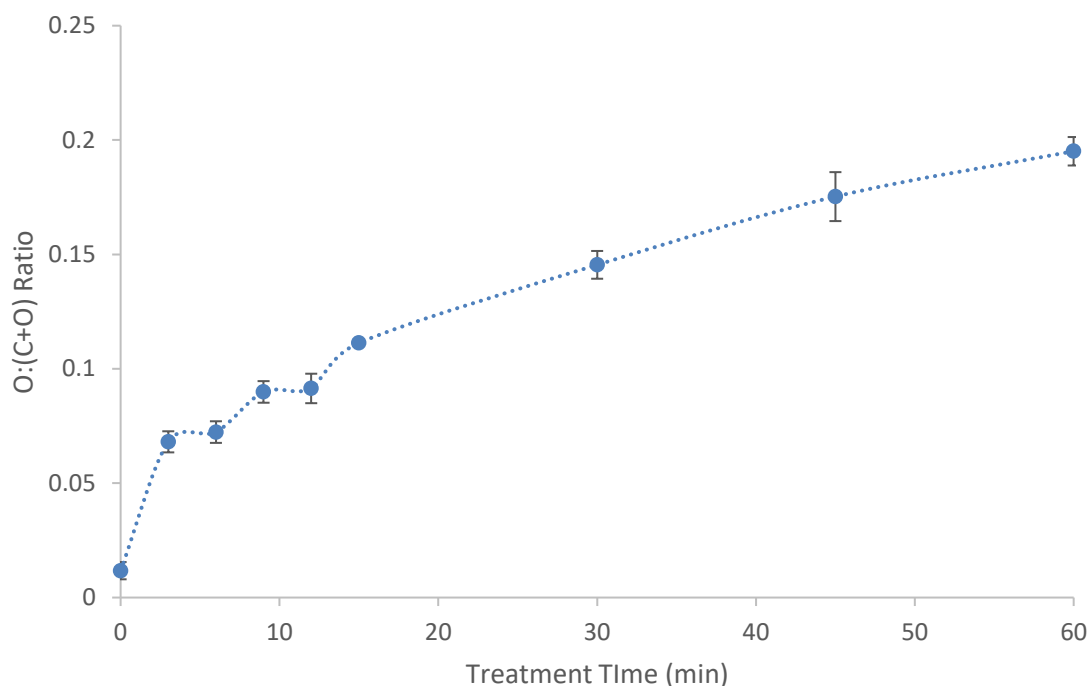
Figure 3-11: O:(C+O) ratio for 40 W oxygen plasma treated HOPG with plasma treatment times between 2 and 60 minute found with SAM. Data points are the average of four samples, and error bars are the standard deviation from four samples.

The O:(C+O) ratio for the 40 W oxygen plasma treated HOPG samples shows a clear trend as the length of the treatment increases. The initial ratio is 0.01, which increases to 0.07 after a 3-minute plasma treatment, and then continues to increase at a slower rate as the plasma treatment increases. It takes 30 minutes to achieve the same increase in the O:(C+O) ratio again, with the ratio

at 0.14 at this point, and after 60 minutes the ratio has increased to approximately 0.2. This trend does not appear to stabilize during the times tested which indicates that a larger extent of modification is possible if the sample is exposed to the plasma for longer times. The gradually increasing trend shown here from SAM is consistent with that observed previously in Figure 3-8 from XPS results, indicating further consistency between the two characterisation techniques.

High resolution C(KLL) spectra were acquired on these samples and the positions of the maxima and minima of the differentiated peaks found in order to determine the D parameter for each spectrum, with the results shown in Figure 3-12. This D parameter value was converted to a sp^2 hybridised carbon percentage which is also shown in Figure 3-12.
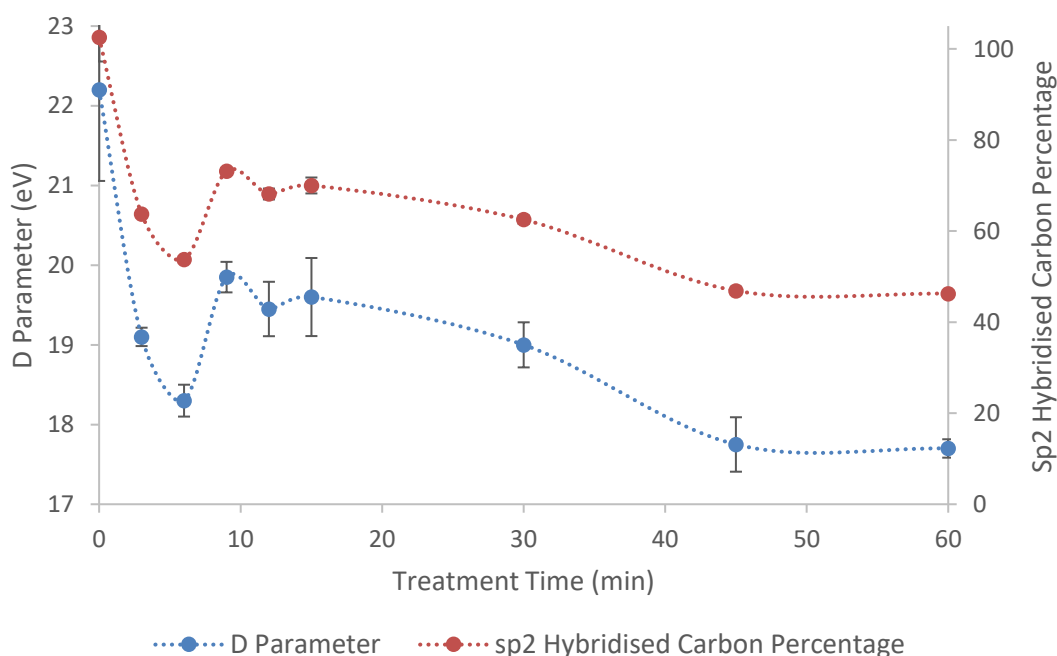
Figure 3-12: D parameter (left axis, blue points) and *sp²* hybridised carbon percentage (right axis, red points) for samples of HOPG exposed to 40 W oxygen plasma for times ranging between 3 minutes and 60 minutes. Data points are the average of four samples, and error bars are the standard deviation from four samples.

There is a change in the D parameter, and therefore in the sp^2 hybridised carbon percentage, when the HOPG surface is exposed to the 40 W oxygen plasma. After 3 minutes of plasma treatment the D parameter has decreased from 22 eV to 19 eV, which decreases the sp^2 hybridised carbon percentage to 64 %. An increase in the exposure time to 6 minutes results in a further reduction in the D parameter, and the sp^2 content is 54 %, however a further increase in the treatment time to 9 minutes results in an increase in the D parameter and sp^2 hybridised carbon percentage to 73 %.

After this point the D parameter and sp^2 hybridised carbon percentage decrease with further exposure to the oxygen plasma until a minimum of 46 % sp^2 hybridised carbon is reached after 60 minutes. These results do not follow any simple trend, but rather it appears that there may be an oscillation occurring in the changes in the hybridisation. Further studies need to be performed to investigate this, however any trend that occurs would be the result of the equilibrium kinetics of the multiple atomic and molecular processes that take place when the plasma species are breaking bonds in the carbon surface to form oxides or etch species from the surface, as has been discussed previously. The D parameter and sp^2 hybridised carbon percentage values show a clearer trend than was observed for the changes in hybridisation with XPS (Figure 3-9), which is likely due to the difference in the sampling depths as the hybridisation changes will be occurring on the outer layer of the surface, and will therefore be more easily detected with SAM.

3.2.1.2.3 CONCLUSIONS

The XPS and SAM results both show an increase in the oxygen content of the HOPG surface when exposed to the 40 W oxygen plasma, as well as a corresponding decrease in the carbon content of the surface and the appearance of iron, nickel, and fluorine. The two techniques do show differences between the numerical values for the elemental contributions which is explained by the differences in the sampling depth and sampling area as was discussed previously for the 30 W oxygen plasma treated samples. The XPS and SAM results also show a conversion of sp^2 hybridised carbon to sp^3 hybridised carbon between the untreated and treated HOPG with no clear trend in the behaviour after the initial plasma treatment as the treatment time increases.

3.2.2   Influence of RF-Coupling Power on Plasma Modification of Highly Oriented Pyrolytic Graphite

The magnitude of the RF-coupling power applied to ignite the plasma will have an impact on the type and number of species present in the plasma, and therefore will also influence the interactions between the plasma and the surface. The results from the 30 W and 40 W oxygen plasma treatment of HOPG can be compared to examine if the difference in RF-coupling power results in a different extent in modification of the surface.

3.2.2.1 XPS Results

A comparison of the O:(C+O) ratio of the 30 W and 40 W oxygen plasma treated samples found with XPS is shown in Figure 3-13. The blue points indicate the 30 W samples while the red points indicate the 40 W samples.
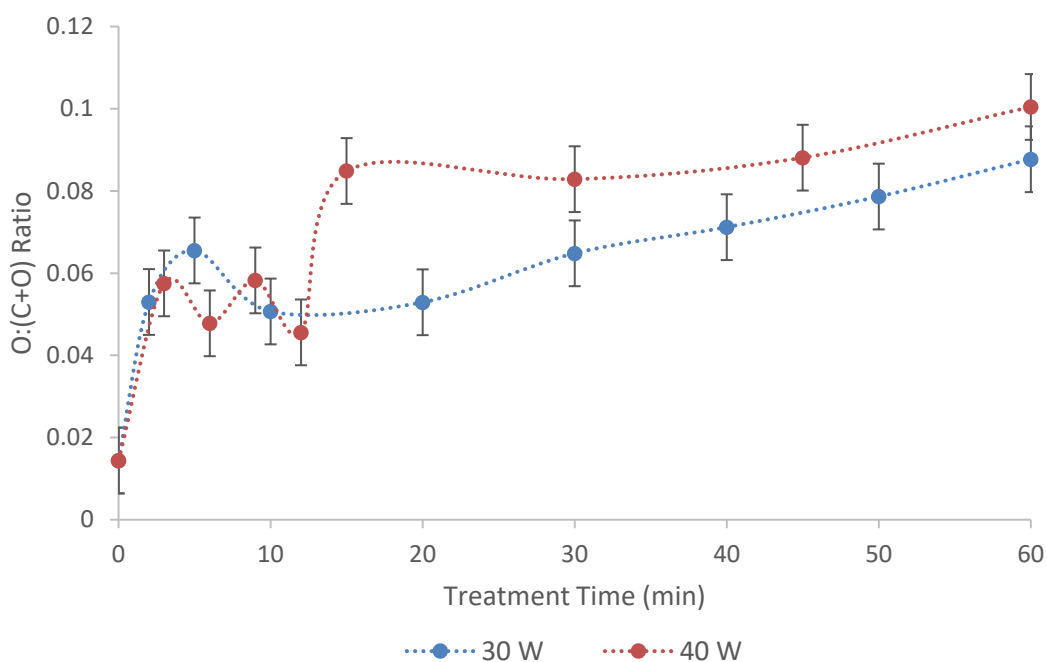
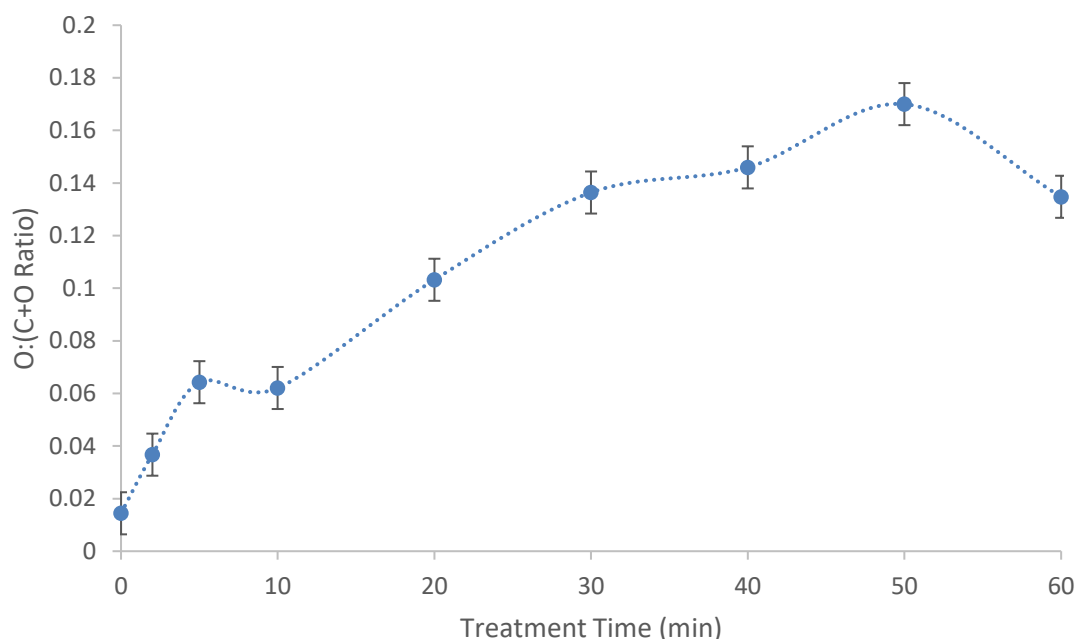**Figure 3-13: O:(C+O) ratio for 30 W (blue points) and 40 W (red points) oxygen plasma treated HOPG with plasma treatment times between 2 and 60 minute found with XPS. Error bars indicate the error determined as the average for the plasma modification of HOPG based on previous experiments.**

The O:(C+O) ratios for both the 30 W and 40 W oxygen plasma treated HOPG show an increasing trend as the treatment time increases, however the 40 W samples reach a higher value then plateaus while the 30 W samples show a more gradual increase. The 40 W samples generally appear to be higher than the 30 W samples for longer treatment times, however for the shorter treatment times the points mostly lie within each other's uncertainties and therefore it cannot be concluded that they are significantly different.

The percentage that each deconvoluted component of the high resolution C 1s peak contributes to the peak are shown in Figure 3-14 for the 30 W and 40 W oxygen plasma treated HOPG samples in circular points and triangular points, respectively.
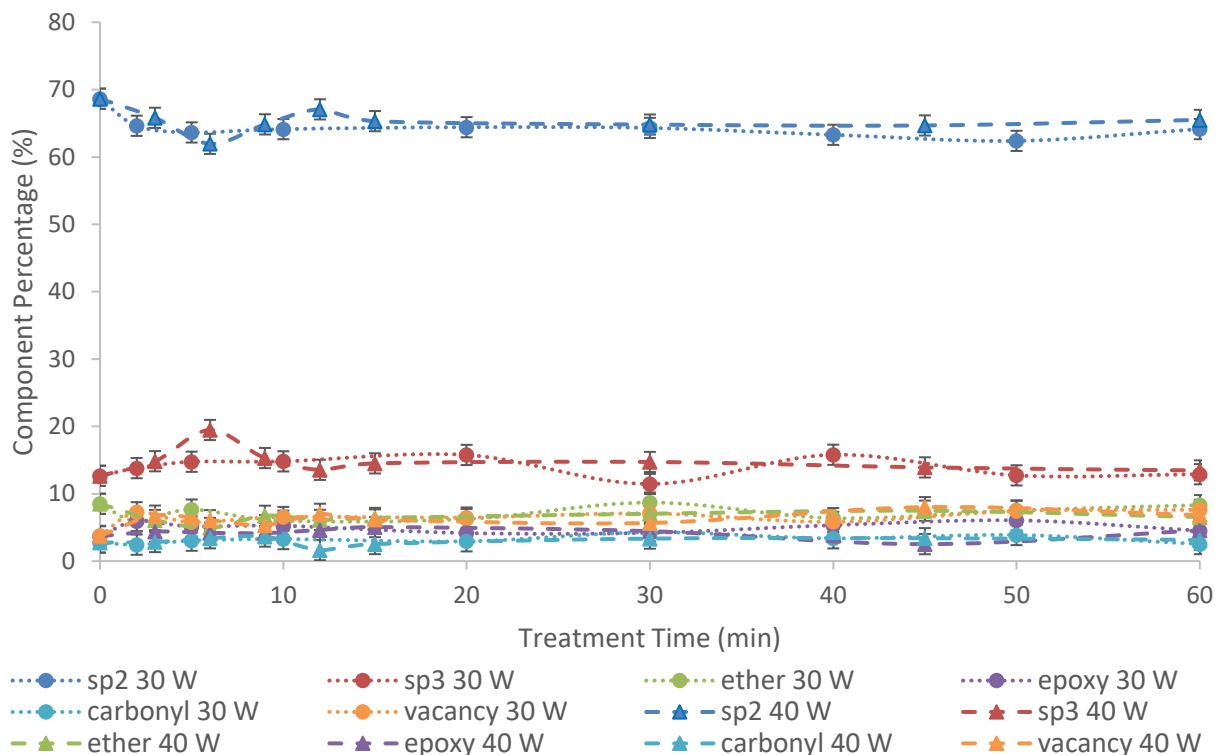
Figure 3-14: Percentages of components of C 1s peak for 30 W (circular points) and 40 W (triangular points) oxygen plasma treated HOPG determined with XPS. Error bars indicate the error determined as the average for the plasma modification of HOPG based on previous experiments.

The 30 W and 40 W points for each component of the C 1*s* peak show the same trends and very similar values, and therefore suggest that the different RF-coupling powers used to ignite the oxygen plasma do not cause differences in the way that the carbon is bonded within the HOPG.

3.2.2.2 SAM Results

The O:(C+O) ratio from the 30 W and 40 W samples found with SAM are compared in Figure 3-15, with the 30 W samples shown in red and the 40 W samples in blue for each treatment time tested.
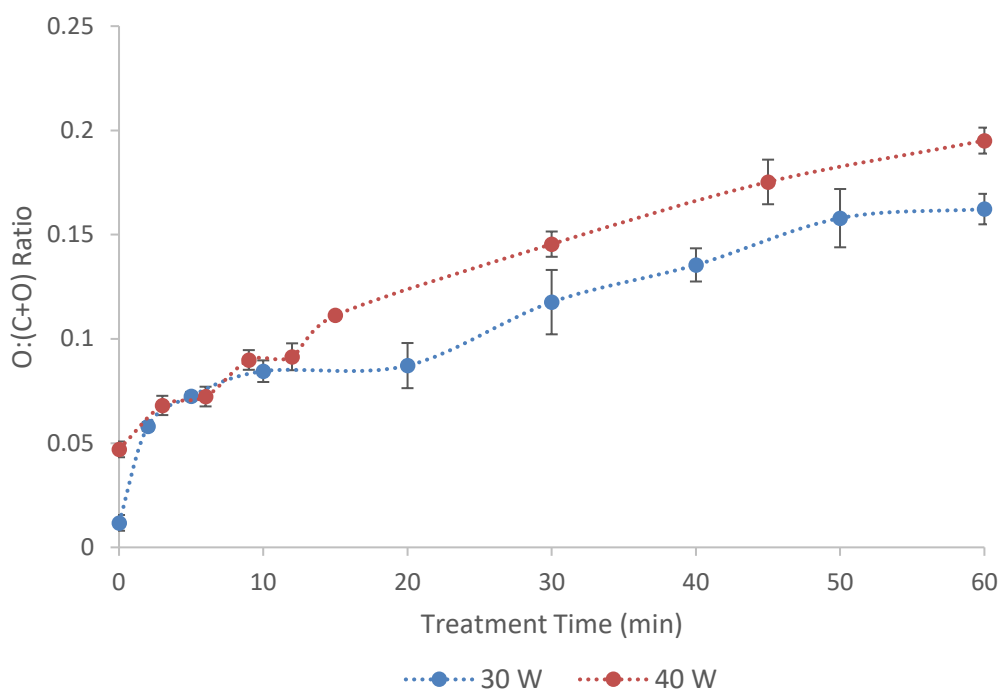
Figure 3-15: O:(C+O) ratio for 30 W (blue points) and 40 W (red points) oxygen plasma treated HOPG with plasma treatment times between 2 and 60 minute found with SAM. Data points are the average of four samples, and error bars are the standard deviation from four samples.

In Figure 3-15 it can be seen that the 30 W samples display lower O:(C+O) ratios than the 40 W samples. This trend is more pronounced for longer treatment times, which is expected due to the nature of the interactions of the plasma species with the HOPG surface. A higher power results in a higher energy of the plasma species, which will enable more species to have energies high enough to modify the surface, and this effect will increase as the treatment time increases. These results are consistent with those observed using XPS in Figure 3-13, although the ratios are numerically different due to the differences in sampling depth.

The D parameter values and sp^2 hybridised carbon percentage values from the 30 W and 40 W samples are also compared, with the circular points in Figure 3-16 indicating the 30 W samples and the triangular points the 40 W samples.
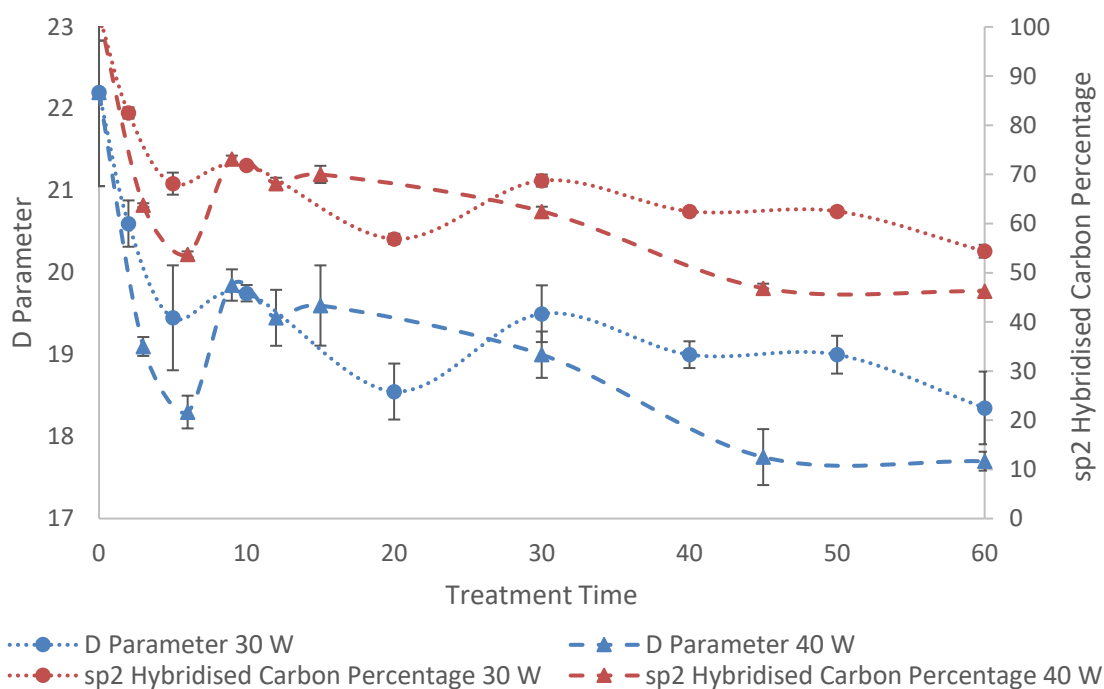
Figure 3-16: D parameter (left axis, blue points) and *sp*² hybridised carbon percentage (right axis, red points) for samples of HOPG exposed to 30 W (circle points) and 40 W (triangle points) oxygen plasma for times ranging between 3 minutes and 60 minutes. Data points are the average of four samples, and error bars are the standard deviation from four samples.

The trends in the D parameter and *sp*² hybridised carbon percentage are not as clear as those observed for the elemental compositions, especially at lower treatment times where the uncertainties are larger. However, when considering the longer treatment times the 40 W samples have a consistently lower D parameter and *sp*² hybridised carbon percentage than the 30 W samples, indicating that a longer exposure to the higher powered plasma will result in a higher extent of conversion of *sp*² hybridised carbon to *sp*³ hybridised carbon.

3.2.2.3 Conclusions

The XPS results presented show that while the extent of conversion of the *sp*² surface to its oxidised *sp*³ form is slightly more prevalent for 40 W plasma, due to the size of the uncertainties of the results these differences are quite small. The SAM results presented do show some differences between the 30 W and 40 W treatments, with the 40 W samples showing higher levels of modification. This difference is seen more clearly in the SAM results partly because of the smaller uncertainties of the results making the trends more conclusive, and also due to the differences in the sampling depth of the two techniques which makes smaller differences on the surface more prominent on the results. An increase in the RF-coupling power used to ignite the oxygen plasma for treatment of the HOPG

surface will therefore result in an increase in the extent of modification of the surface. This increased modification is more pronounced at longer treatment times, with both the oxidation of the surface and changes in the hybridisation increasing over time.

3.3 Argon Plasma Treatment of Highly Oriented Pyrolytic Graphite

Argon plasma is expected to modify the HOPG surface in a different manner to the oxygen plasma as it consists of larger and chemically inert species. The species present in the argon plasma are various argon ions and radicals, electrons, and unionised argon atoms, and these species are not chemically reactive but instead modify the surface through bombardment with relatively large particles. The influence of treatment time and RF-coupling power on the argon plasma modification of HOPG will be examined systematically to determine how the modification can be controlled to achieve a desired surface. The source gas pressure used for all plasma treatments is 1.0×10^{-2} Torr, while the treatment time is varied between 2 minutes and 60 minutes and the RF-coupling power between 30 W and 50 W.

3.3.1 Influence of Exposure Time on Plasma Modification of Highly Oriented Pyrolytic Graphite

To investigate the effect of treatment time on the extent of modification of a HOPG surface a range of treatment times between 2 and 60 minutes were tested while holding the RF-coupling power used to ignite the argon plasma constant at either 30 W, 40 W, or 50 W.

3.3.1.1 30 W RF-Coupling Power Argon Plasma

Argon plasma ignited with a 30 W RF-coupling power was used to treat samples of cleaved HOPG for times ranging between 2 minutes and 60 minutes. These samples were characterised using XPS and SAM to determine how the elemental composition and carbon hybridisations change as a result of the plasma treatment.

3.3.1.1.1 XPS RESULTS

The elemental concentrations of carbon, oxygen, iron, nickel, and fluorine from the 30 W argon plasma treated HOPG samples are shown in Figure 3-17 for treatment times ranging between 2 minutes and 60 minutes. There are no argon peaks present in the XPS spectrum for argon plasma treated HOPG, indicating that the argon species in the plasma are modifying the surface without becoming implanted within it.
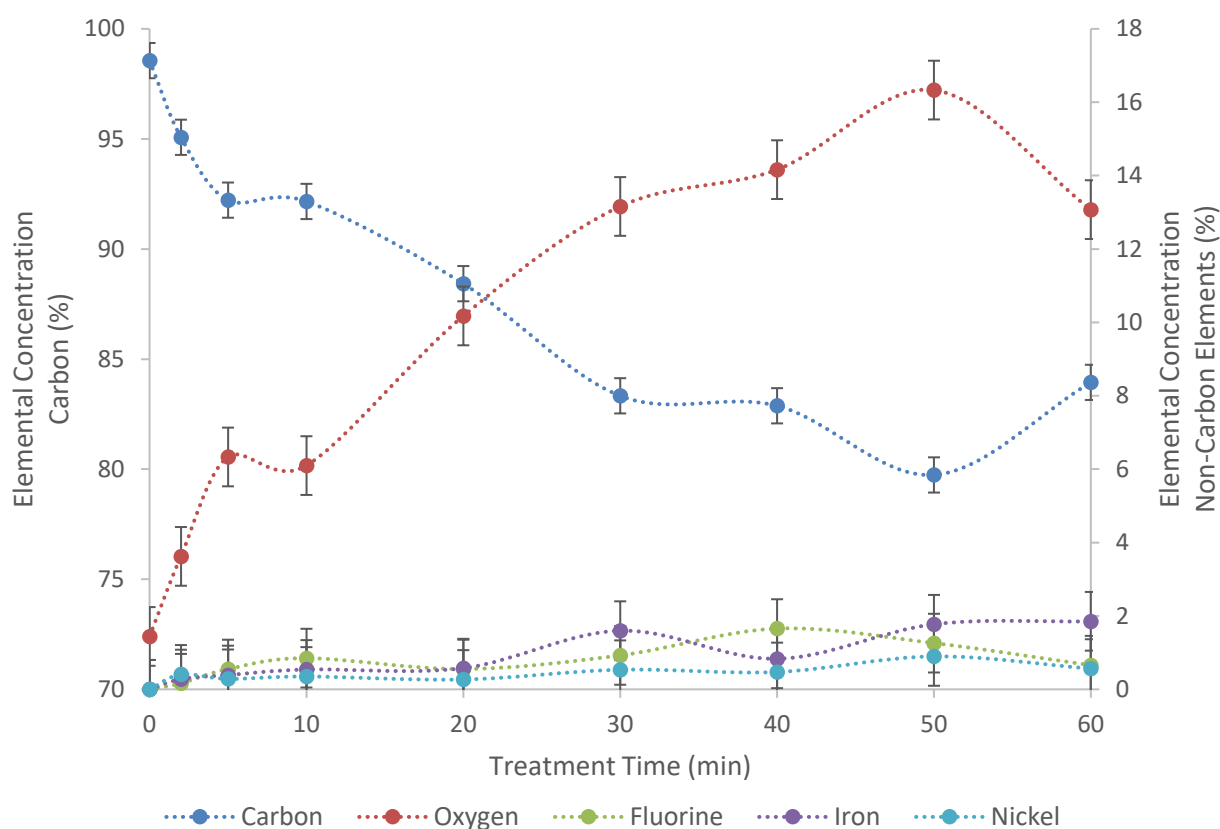
Figure 3-17: Elemental composition of 30 W argon plasma treated HOPG with treatment time determined with XPS. The concentration of carbon is shown on the left axis and concentrations of oxygen, fluorine, iron, and nickel are shown on the right axis. Error bars indicate the error determined as the average for the plasma modification of HOPG based on previous experiments.

The carbon percentage of the HOPG begins to decrease after 2 minutes of the argon plasma treatment, with the elemental concentration decreasing from 98.6 % to 95.1 %, and decreases by approximately the same amount to 92.2 % after 5 minutes. Further plasma exposure for a treatment time up to 10 minutes does not change the carbon percentage, however after this point the carbon content continues to decrease. This decreasing trend continues until 50 minutes of plasma exposure when the carbon content decreases to 79.7 %, after which further treatment to 60 minutes produces an increase to 83.9 %. The oxygen content of the samples shows the opposite trend to the HOPG, showing an increase from 1.4 % to 3.6 % after a 2-minute plasma treatment and then to 6.3 % after a 5-minute treatment, where it stays after a 10-minute treatment. Further increases in treatment time up to 50 minutes result in an increase in oxygen content to 16.3 % before a decrease to 13.1 % occurs after a 60-minute treatment. There is also deposition of iron, nickel, and fluorine as a result of sputtering from the antenna during the plasma treatment, with the concentrations of each increasing slightly as the treatment time increases. These results suggest that when the

treatment time increases from 50 minutes to 60 minutes there is actually a decrease in the extent of the modification of the surface in regards to the elemental composition, however it is thought that this sample may be an outlier from the trend of the rest of the samples due to the random nature of the plasma treatment.

To examine the growth of the oxide without interference from the contaminating elements from antenna sputtering the O:(C+O) ratio is shown in Figure 3-18 for HOPG treated with 30 W argon plasma for times between 2 minutes and 60 minutes.

Figure 3-18: O:(C+O) ratio for 30 W argon plasma treated HOPG with plasma treatment times between 2 and 60 minute found with XPS. Error bars indicate the error determined as the average for the plasma modification of HOPG based on previous experiments.

The O:(C+O) ratio increases from 0.015 to 0.037 when the HOPG is exposed to the argon plasma for 2 minutes, and increases further to 0.065 after a 5-minute plasma treatment, however a 10-minute treatment does not change the ratio. Increases between 20 minutes and 50 minutes produce increases in the O:(C+O) ratio up to a maximum of 0.17, while an increase to a 60-minute treatment time decreases the O:(C+O) ratio to 0.16. These results show that there is an increase in the O/(C+O) ratio, and hence in the extent of modification of the HOPG, as the exposure time to the plasma increases. This occurs for treatment times up to 50 minutes, however after 60 minutes there is a decrease in the ratio. Further studies for treatment times beyond 60 minutes could determine whether this is a true decrease and further modification decreases the oxygen content of the sample

or if this sample is an outlier.

The components from the deconvoluted high resolution C 1*s* peak from XPS are compared for each treatment time in Figure 3-19. The percentage that each component contributes to the C 1*s* peak is shown for the six components that were fit to the peak, including carbon-carbon, carbon-oxygen, and carbon-lattice vacancy interactions.
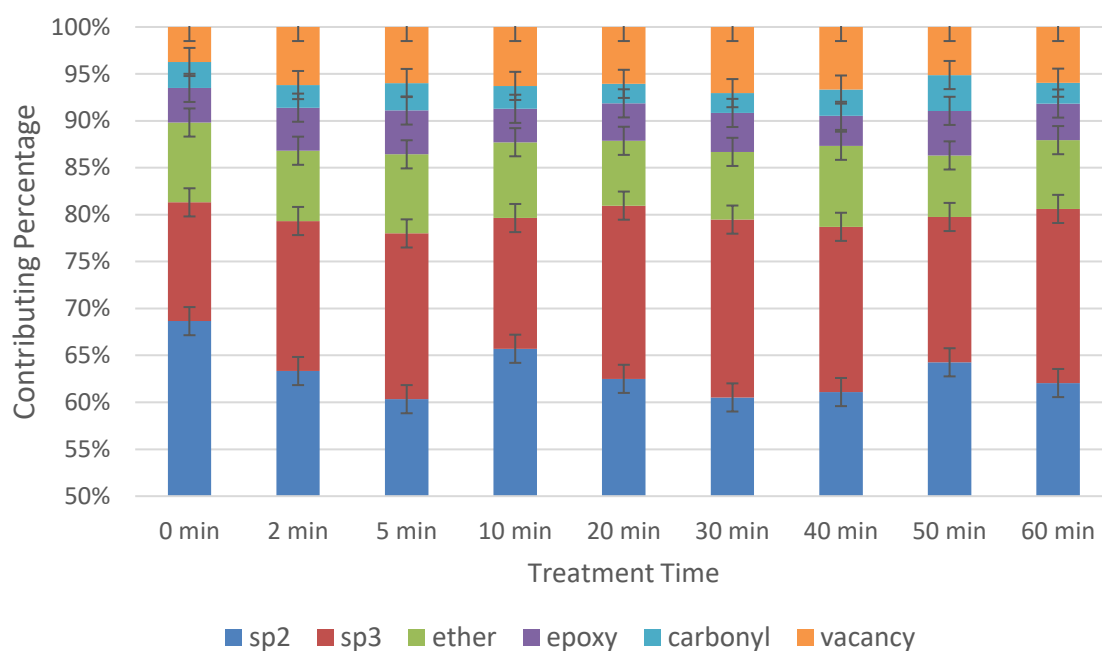
Figure 3-19: Percentages of components of C 1s peak for 30 W argon plasma treated HOPG determined with XPS. Error bars indicate the error determined as the average for the plasma modification of HOPG based on previous experiments.

A HOPG sample that has been exposed to a 30 W argon plasma for 2 minutes shows some changes in the chemical environment of the carbon atoms, with the *sp*^{2} hybridised carbon content decreasing while the *sp*^{3} hybridised carbon increases to maintain a total carbon-carbon content that is approximately the same as the untreated sample. There is a decrease in the carbon-oxygen species as a result of the argon treatment, however there is an increase in the carbon-lattice vacancy contributions, indicating that the argon plasma is removing atoms from the HOPG lattice. Further exposure to the argon plasma for times up to 60 minutes produces some changes in the magnitudes of each component, however the total carbon-carbon and carbon-oxygen species remain approximately the same and no clear trend is observed for any species. These results show that the argon plasma is changing the HOPG surface, however after initial modification there are a range of ongoing processes of oxidation, bond breaking, and removal of species on the surface that cause

66

individual components, and therefore individual carbon chemical environments, to fluctuate randomly.

3.3.1.1.2 SAM RESULTS

The elemental composition of HOPG treated with 30 W RF-coupling power argon plasma was characterised using SAM for samples with treatment times ranging between 2 minutes and 60 minutes. The elements found on the surface are carbon, oxygen, fluorine, iron, and nickel, and their variation is shown in Figure 3-20.
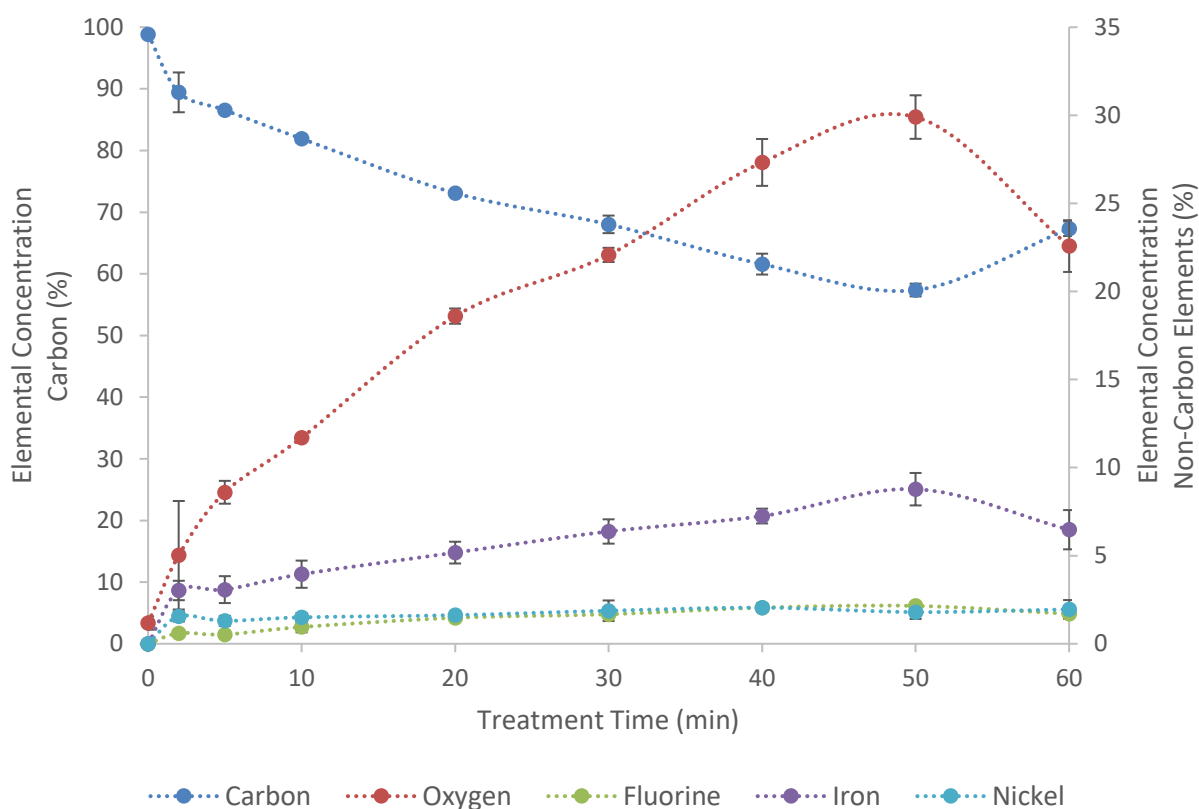
Figure 3-20: Elemental composition of 30 W argon plasma treated HOPG with treatment time determined with SAM. The concentration of carbon is shown on the left axis and concentrations of oxygen, fluorine, iron, and nickel are shown on the right axis. Data points are the average of four samples, and error bars are the standard deviation from four samples.

Untreated HOPG is predominately composed of carbon, with approximately 1 % oxygen across the surface. Exposure to the 30 W argon plasma results in an increase in the oxygen percentage on the surface, as well as the appearance of fluorine, iron, and nickel on the surface. These extra elements are the result of sputtering of the antenna, as has been explained previously for oxygen plasma treated HOPG. There is a general trend of carbon content decreasing and the other elements increasing as the length of time the sample is exposed to the plasma increases until a treatment

time of 50 minutes is reached. At this point the carbon content has decreased to 57 %, while there is also 30 % oxygen, 9 % iron, 2 % nickel, and 2 % fluorine. However, further argon plasma treatment results in an increase in carbon content to 67 %, with corresponding decreases in the oxygen, fluorine, iron, and nickel concentrations. Further repeats of the experiment need to be performed to determine whether this abrupt change in trend is a true representation of the way the HOPG behaved upon exposure to the 30 W argon plasma, however it can be said that the treatment is consistent across the surface of this sample and is consistent with the results found using XPS for this sample (Figure 3-17).

The carbon and oxygen elemental concentrations can be converted to the O:(C+O) ratio to more clearly examine the oxide film that is produced as a result of the 30 W argon plasma treatment. This ratio is shown in Figure 3-21 for samples with treatment time between 2 minutes and 60 minutes.
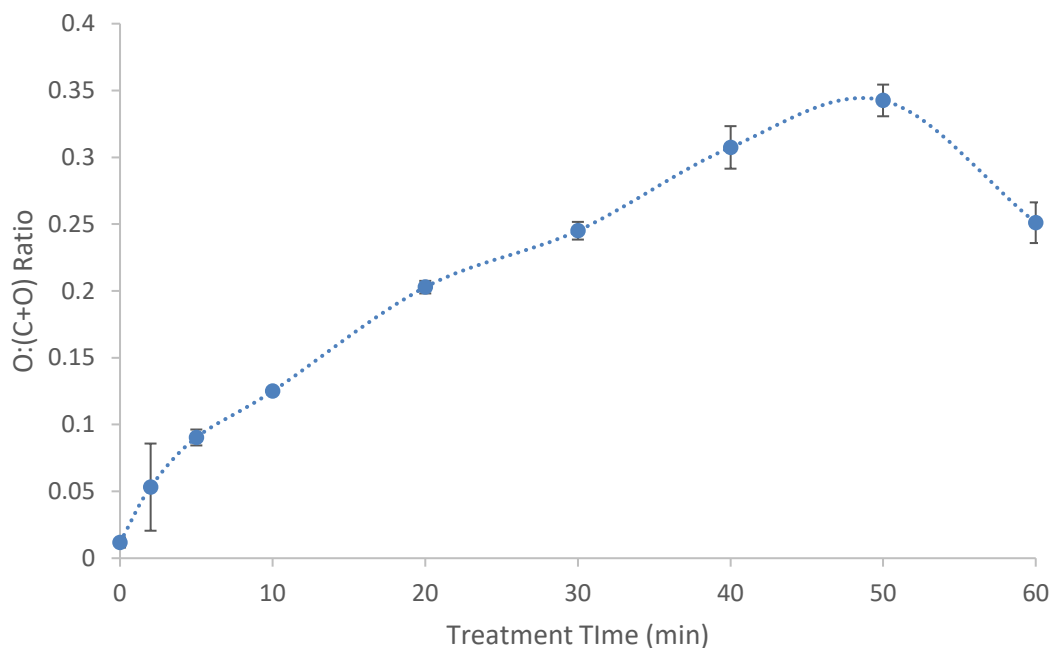
Figure 3-21: O:(C+O) ratio for 30 W argon plasma treated HOPG with plasma treatment times between 2 and 60 minute found with SAM. Data points are the average of four samples, and error bars are the standard deviation from four samples.

The O:(C+O) ratio increases with increased exposure to the 30 W argon plasma, with the ratio increasing from 0.01 for untreated HOPG to a maximum of 0.35 after 50 minutes. A 10-minute plasma treatment results in an O:(C+O) ratio of 0.12, and it takes 30 minutes for this value to be doubled, and a further increase of 0.12 is achieved after 50 minutes. After 60 minutes of plasma treatment the O:(C+O) ratio decreases to 0.25, which is the same ratio achieved with a 30-minute

plasma treatment. This trend is consistent with that observed previously using XPS (Figure 3-18).

The high-resolution C(KLL) spectra from each sample were differentiated and the distance between the positions of the maxima and minima measured to determine the D parameter for each spectrum. This D parameter was then converted to a sp^2 hybridised carbon percentage, with both values plotted in Figure 3-22 for each treatment time tested.
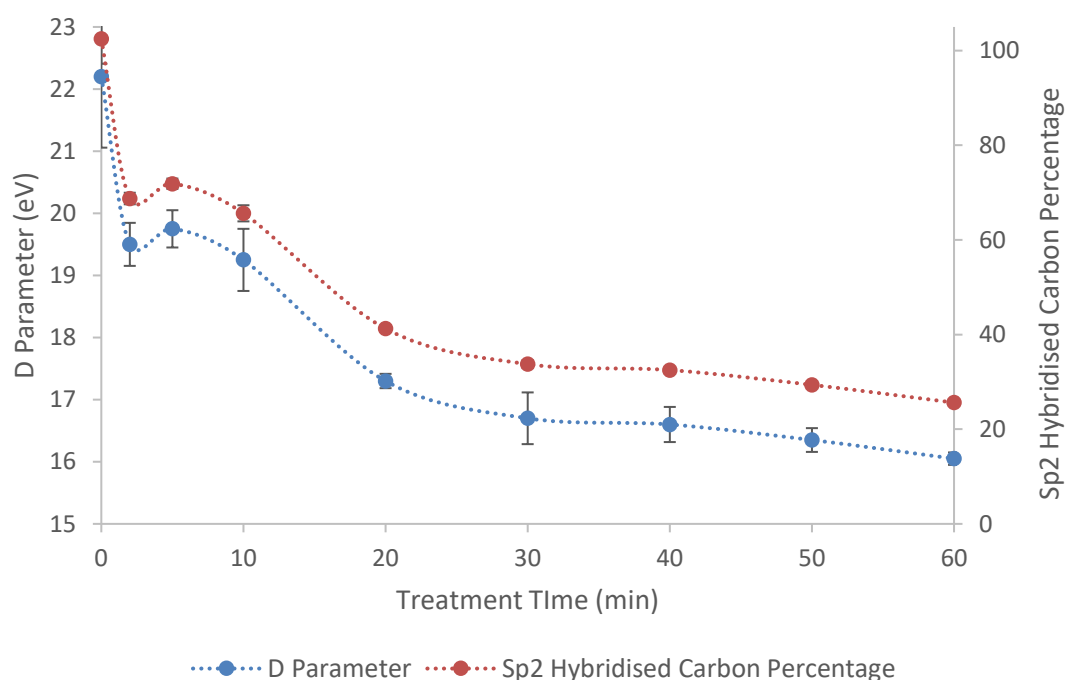
Figure 3-22: D parameter (left axis, blue points) and *sp2* hybridised carbon percentage (right axis, red points) for samples of HOPG exposed to 30 W argon plasma for times ranging between 2 minutes and 60 minutes. Data points are the average of four samples, and error bars are the standard deviation from four samples.

A 2-minute treatment of 30 W argon plasma results in the HOPG surface undergoing changes in the hybridisations present, with the D parameter decreasing from 22.2 eV for the untreated sample to 19.5 eV. A longer treatment of 5 minutes results in a slightly higher D parameter of 19.8 eV, however within the range of uncertainty of these points they cannot be said to be different. When the treatment time is increased to 10 minutes there is another slight decrease in the D parameter to 19.3 eV but with a larger uncertainty it also cannot be said to be significantly different from the previous two points. There is a larger change in D parameter observed when the treatment time is increased to 20 minutes, with a value of 17.3 eV showing a decrease in the sp^2 hybridised carbon content of the surface to 41 %. Treatment times of 30, 40, 50, and 60 minutes result in D parameter values of 16.7 eV, 16.6 eV, 16,4 eV, and 16.0 eV, respectively. This trend shows that continued

exposure to the 30 W argon plasma results in continued modification of the hybridisations of carbon present in the HOPG surface, however the rate at which this occurs decreases after the first 20 minutes. The sp^2 hybridised carbon percentage after the 60-minute treatment is 25 %, indicating significant modification of the HOPG surface. These results show a greater extent of modification and a clearer trend than that observed with XPS (Figure 3-19), which is expected due to the modification occurring on the surface and being more easily detected by the more surface sensitive SAM.

3.3.1.1.3   CONCLUSIONS

The results from the XPS and SAM characterisation of HOPG treated with 30 W argon plasma both show the same trend of increasing extent of modification as the treatment time increases. The modification to the surface includes an increase in oxygen as well as the deposition of iron, nickel, and fluorine due to sputtering from the antenna in the plasma chamber. There is also a conversion of sp^2 hybridised carbon to sp^3 hybridised carbon when the HOPG is exposed to the argon plasma, which is observed in both XPS and SAM, however the SAM results show the trend of modification with time more clearly as it is examining only the carbon-carbon bonds and is more surface sensitive.

3.3.1.2 40 W RF-Coupling Power Argon Plasma

To examine how HOPG is modified when the RF-coupling power used to ignite the plasma is increased to 40 W samples of HOPG were treated with argon plasma for times ranging between 3 and 60 minutes, and then characterised with XPS and SAM to find the elemental composition and carbon hybridisations present on the surface after each treatment.

3.3.1.2.1   XPS RESULTS

The carbon, oxygen, iron, nickel, and fluorine elemental concentrations found using XPS for the 40 W argon plasma treated HOPG are shown in Figure 3-23.
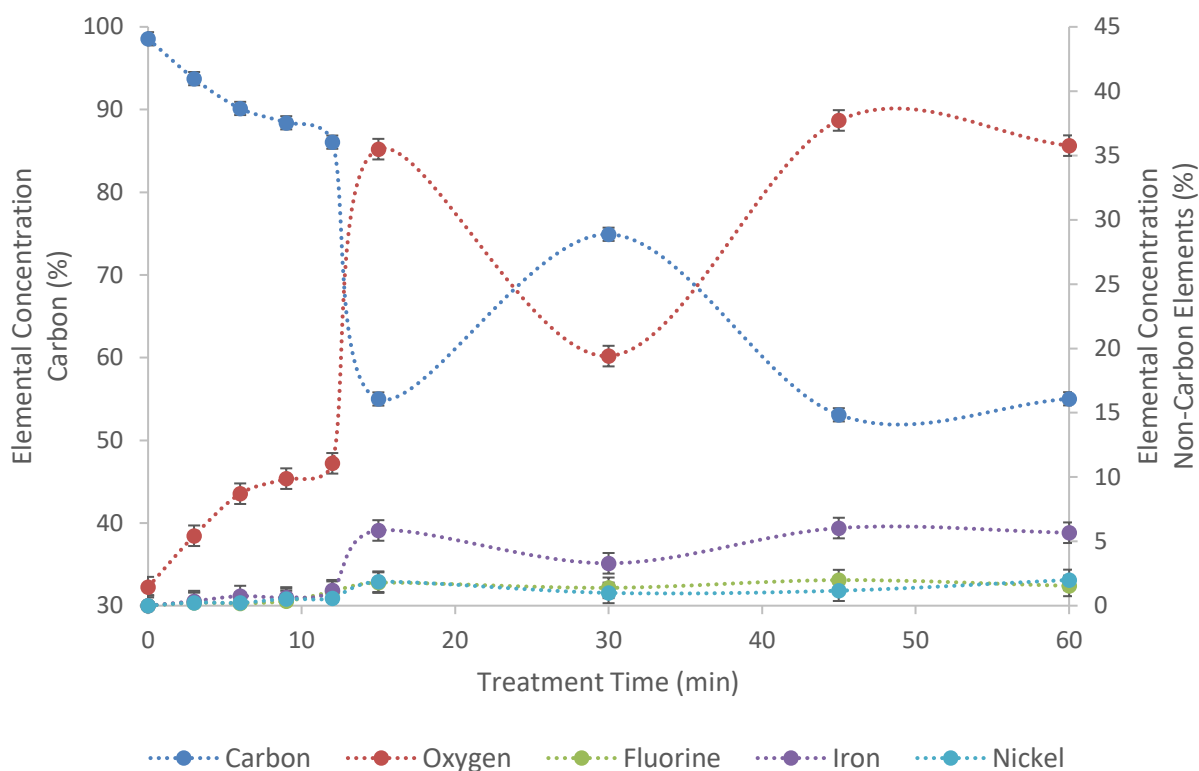
Figure 3-23: Elemental composition of 40 W argon plasma treated HOPG with treatment time determined with XPS. The concentration of carbon is shown on the left axis and concentrations of oxygen, fluorine, iron, and nickel are shown on the right axis. Error bars indicate the error determined as the average for the plasma modification of HOPG based on previous experiments.

The carbon content of the argon plasma treated HOPG decreases as the exposure time of the sample to the plasma increases, while the oxygen content increases correspondingly. These changes occur quite smoothly for the first 12 minutes, however after 15 minutes the carbon content drops from 86.1 % to 55.0 % before increasing to 74.9 % after 30 minutes and then continuing the decreasing trend. The anomalous sample shows a higher oxygen content to compensate for the decrease in carbon, and shows an elemental composition similar to the 45-minute sample, suggesting that this sample is an outlier and that something unusual occurred during the treatment of this sample. There is also deposition of iron, nickel, and fluorine on the HOPG surface as a result of sputtering from the antenna. The iron concentration increases as the treatment time increases, however the nickel and fluorine concentrations remain relatively constant.

To consider how the oxide of the sample changes with exposure to the argon plasma without interference from the sputtered elements the O:(C+O) ratio is considered in Figure 3-24.
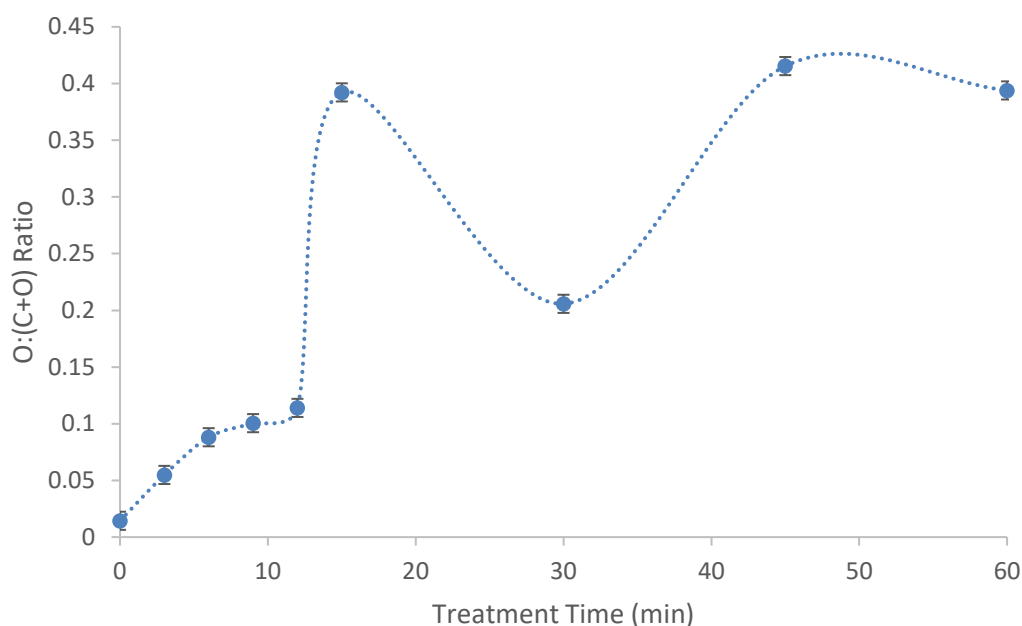
Figure 3-24: O:(C+O) ratio for 40 W argon plasma treated HOPG with plasma treatment times between 2 and 60 minute found with XPS. Error bars indicate the error determined as the average for the plasma modification of HOPG based on previous experiments.

The O:(C+O) ratio for the 40 W argon plasma treated HOPG increased from 0.014 to 0.055 after a 3-minute treatment, and increased further by similar amounts until a ratio of 0.14 is reached after a 12-minute treatment. After 15 minutes the O:(C+O) ratio is 0.39, which is much larger than the previous and following samples as the 30-minute treatment produces a ratio of 0.21. Treatments of 45 minutes and 60 minutes produce samples with an O:(C+O) ratio of 0.42 and 0.39, respectively, indicating that the increasing trend is levelling off and an equilibrium between the competing processes may have been reached at this point.

The high resolution C 1*s* peak was deconvoluted into six carbon-carbon, carbon-oxygen, and carbon-vacancy peaks and the percentage that each component contributes to the total peak is presented in Figure 3-25 for each treatment time tested.
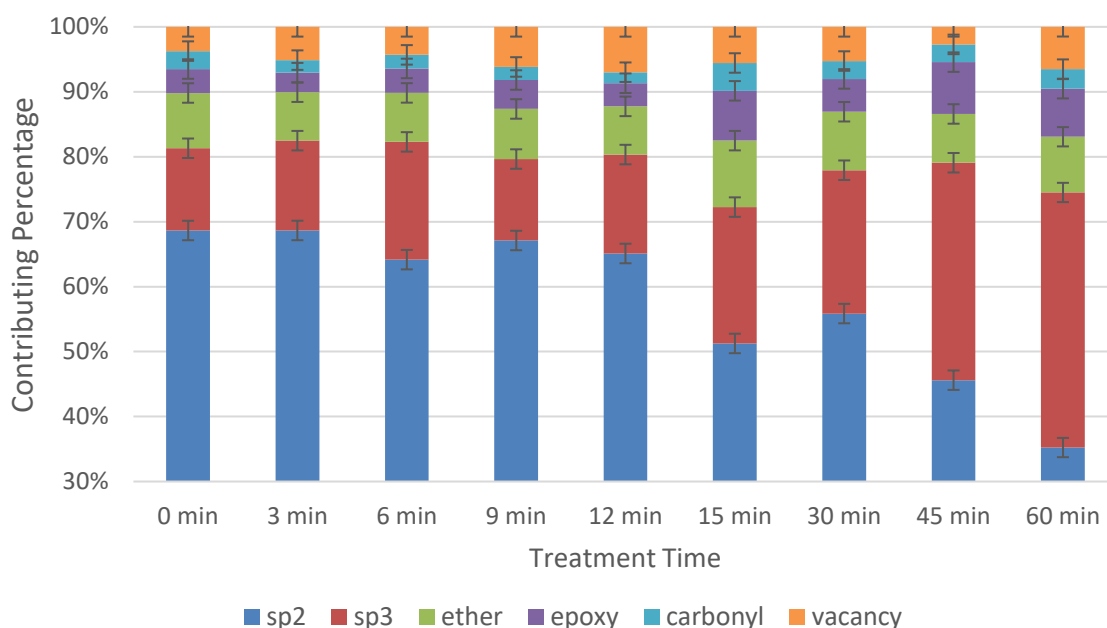
Figure 3-25: Percentages of components of C 1s peak for 30 W argon plasma treated HOPG determined with XPS. Error bars indicate the error determined as the average for the plasma modification of HOPG based on previous experiments.

A 3-minute 40 W argon plasma treatment of HOPG shows some small changes in the contributions of different components to the C 1s peak, with the carbon-lattice vacancy component showing the largest change as it increases while the carbon-oxygen components all decrease slightly. As the treatment time increases larger changes are observed in the components of the C 1s peak. There is an overall decrease in carbon-carbon bonds with the sp^2 hybridised carbon percentage decreasing to 35 % after a 60-minute treatment, however the sp^3 hybridised carbon percentage increases to 40 %. The carbon-oxygen components also increase as the treatment time increases, although there is no trend in the changes in individual components with treatment time. There is an increase in the component indicating carbon atoms adjacent to a lattice vacancy as the treatment time increases, with these results all combining to indicate that the argon plasma is having a larger impact on the hybridisation of the carbon of the HOPG surface than it is on the species within the oxide layer.

3.3.1.2.2 SAM RESULTS

HOPG exposed to 40 W argon plasma for times between 3 minutes and 60 minutes were characterised using SAM to determine the elemental composition of the samples. The elements found on the surface were carbon. oxygen, fluorine, iron, and nickel, and their elemental concentrations are shown for each treatment time in Figure 3-26.
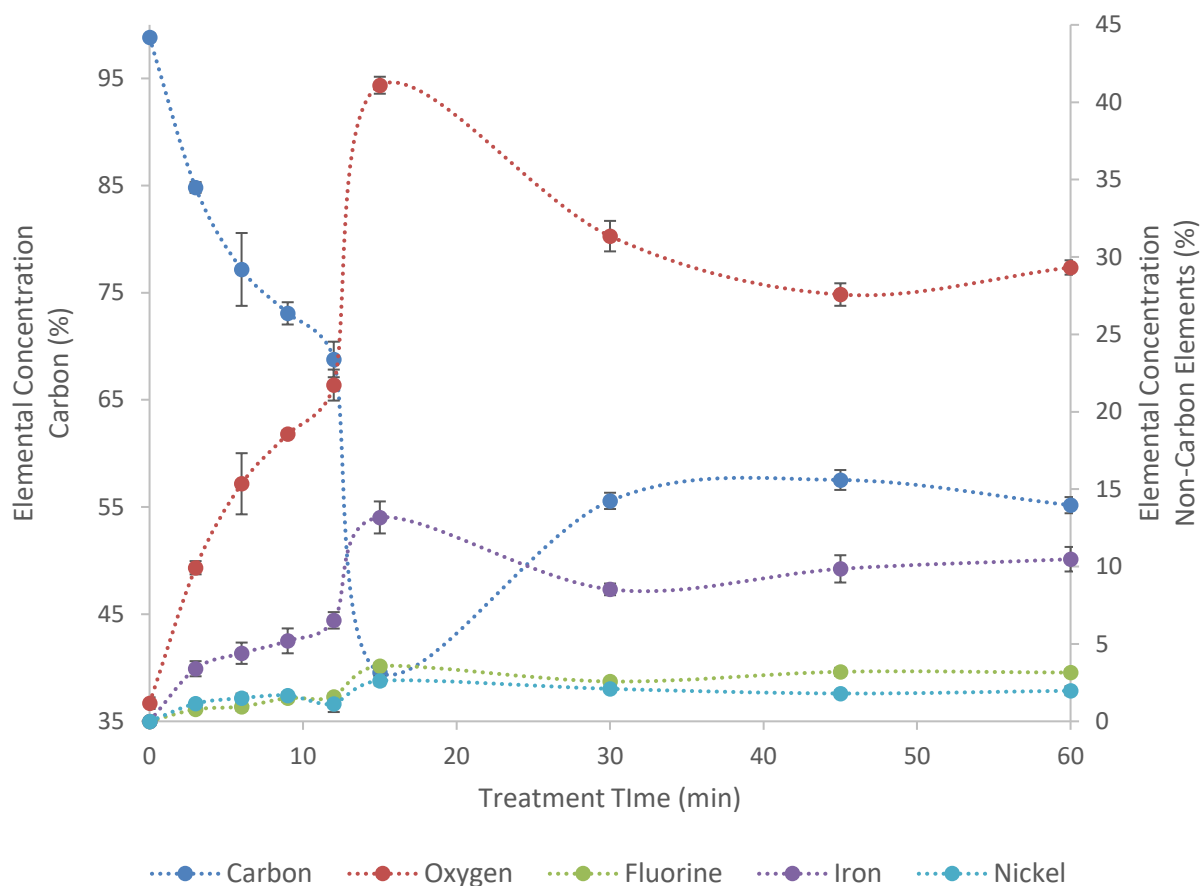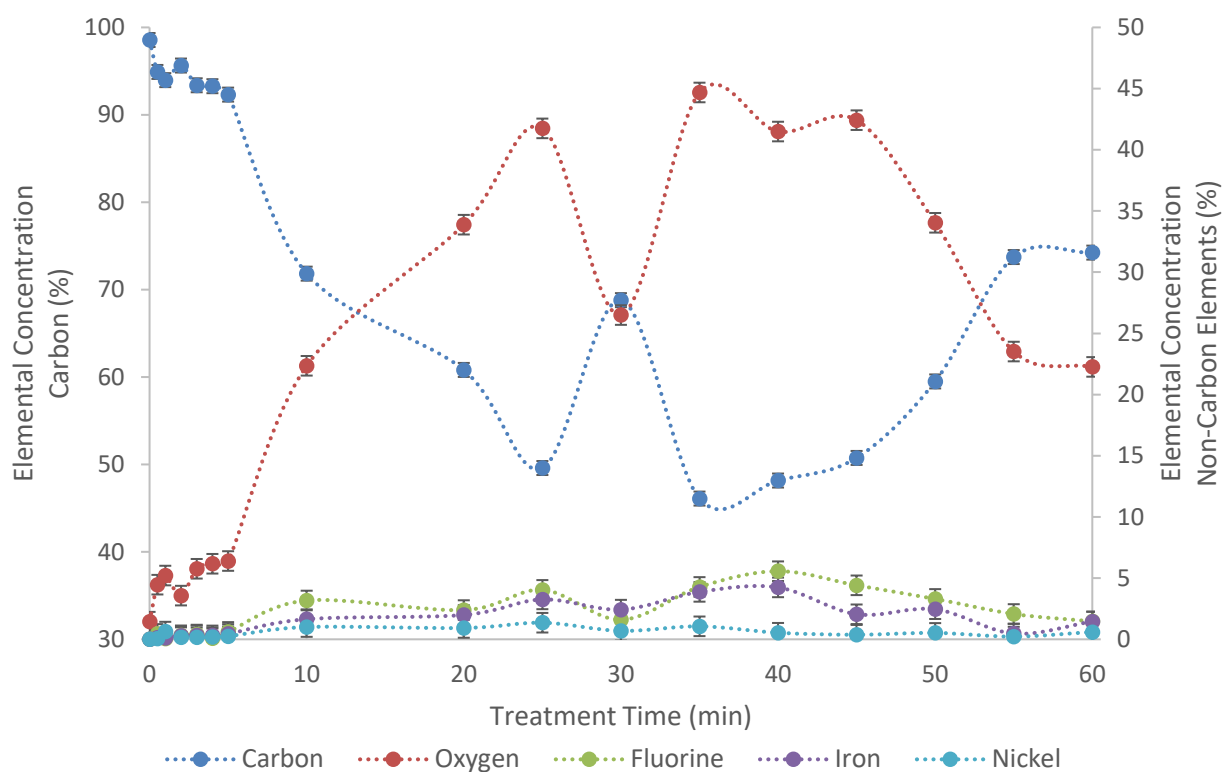
Figure 3-26: Elemental composition of 40 W argon plasma treated HOPG with treatment time determined with SAM. The concentration of carbon is shown on the left axis and concentrations of oxygen, fluorine, iron, and nickel are shown on the right axis. Data points are the average of four samples, and error bars are the standard deviation from four samples.

It can be seen from Figure 3-26 that as the time that the HOPG is exposed to the argon plasma is increased the elemental concentrations of the sample changes, with a general trend showing the decrease in the elemental concentration of carbon while those of other elements decreases. The untreated HOPG sample is composed of 99 % carbon and 1 % oxygen while a 3 minute 40 W argon plasma treated HOPG sample has only 85 % carbon, while oxygen is increased to 10 % and iron, nickel, and fluorine appear on the surface with elemental concentrations of 3 %, 1 %, and 1 %, respectively. The iron, nickel, and fluorine deposited on the surface are the result of sputtering from the steel antenna in the plasma chamber during the argon plasma treatment. The oxygen on the surface is the result of residual oxygen in the plasma chamber that interacts with the surface during the argon plasma treatment, and also due to exposure to the atmosphere after the plasma treatment has been completed and before characterisation can occur.

As the argon plasma treatment time is increased to 6, 9, and 12 minutes the carbon percentage in

the sample decreases to 77 %. 73 %, and 68 %, respectively, while the oxygen and iron increase and the nickel and fluorine elemental concentrations remain approximately the same. There is a very large change in the elemental composition of the sample when the treatment time is increased to 15 minutes, with the carbon decreasing to 40 % while the oxygen increases to 41 %. There are also larger amounts of iron, nickel, and fluorine present, with elemental concentrations of 13 %, 3 %, and 4 %, respectively. However, when the treatment time is further increased to 30 minutes the elemental concentrations return to levels that align with the trend that may be expected based on the trends observed for other plasma treatments discussed previously. Treatment times of 30 minutes, 45 minutes, and 60 minutes result in carbon elemental concentrations of 31 %, 28 %, and 29 %, respectively, which suggest that further increases of treatment time beyond 30 minutes do not result in a large change in the elemental composition of the surface. The oxygen, fluorine, iron, and nickel also show this trend, settling at elemental percentages of around 56 %, 3 %, 10 %, and 2 %, respectively. While the 15 minute sample appears to be anomalous when compared to the rest of the treatment times, the results obtained from SAM are consistent with those found using XPS (Figure 3-23).

To more closely examine the behaviour of the oxygen and carbon species without interference of the other contaminating elements the O:(C+O) ratio of each sample was determined and is shown in Figure 3-27 for each treatment time of the argon plasma on the HOPG.
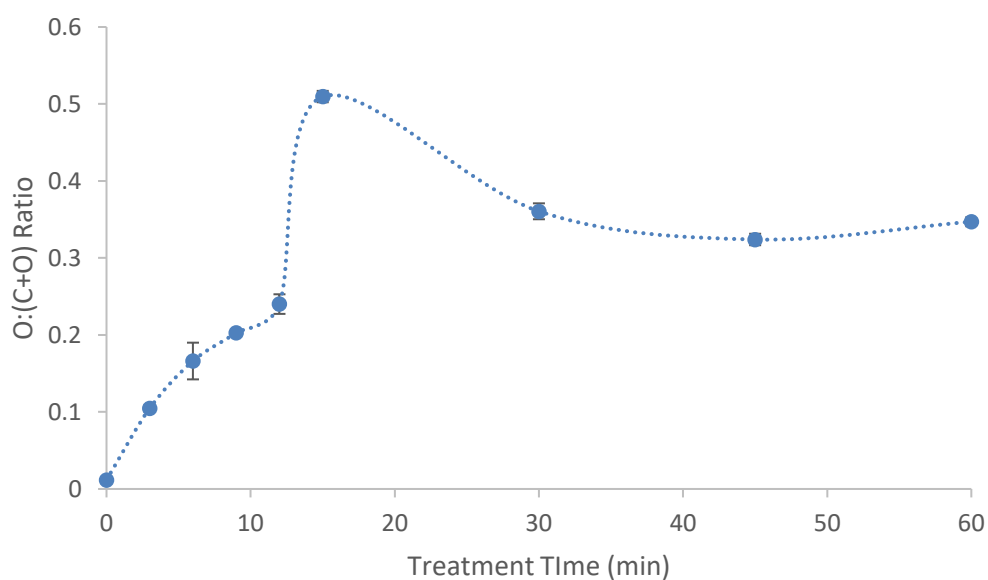
Figure 3-27: O:(C+O) ratio for 40 W argon plasma treated HOPG with plasma treatment times between 2 and 60 minute found with SAM. Data points are the average of four samples, and error bars are the standard deviation from four samples.

The O:(C+O) ratios for the 40 W argon plasma treated samples show an overall increasing trend with the treatment time increases, with the exception of the 15-minute sample, which is much higher than the other samples. The initial O:(C+O) ratio is 0.01, while after 3 minutes it has increased to 0.10 but then takes until 9 minutes to double this value to 0.20. A 12-minute plasma treatment results in a slight increase in the O:(C+O) ratio to 0.24, however after 15 minutes the ratio increases to 0.51 then decreases to 0.36 after 30 minutes. Further exposure to the argon plasma beyond 30 minutes only presents small changes to the O:(C+O) ratio, with 45 minutes and 60 minutes having values of 0.32 and 0.35, respectively. These results suggest that after 30 minutes further exposure to the argon plasma does not change the formation of the oxide on the surface, and that the large increase in the oxygen content resulting from a 15 minute treatment is an anomalous result that would likely not occur again when the experiments are repeated.

The D parameter for each sample was determined by finding the positions of the maxima and minima from the differentiated C(KLL) high resolution spectrum for each sample. These D parameter values and the resultant sp^2 hybridised carbon percentages are shown in Figure 3-28 for each treatment time examined.
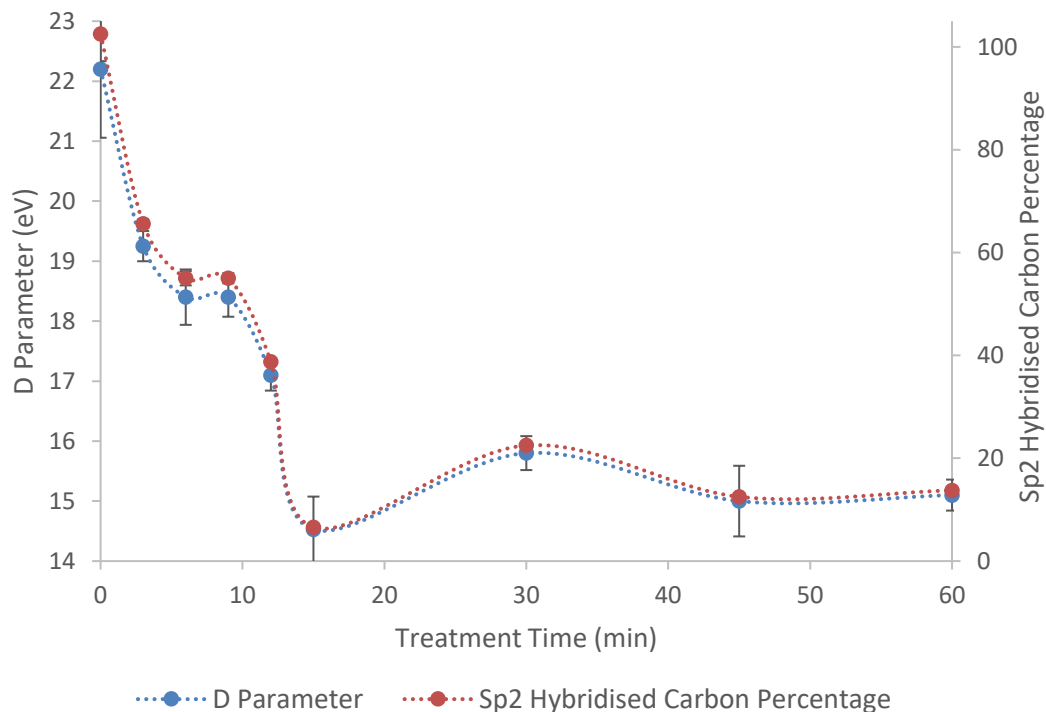
Figure 3-28: D parameter (left axis, blue points) and sp^2 hybridised carbon percentage (right axis, red points) for samples of HOPG exposed to 40 W argon plasma for times ranging between 2 minutes and 60 minutes. Data points are the average of four samples, and error bars are the standard deviation from four samples.

The 3-minute argon plasma treatment results in a decrease in the D parameter from 22.2 eV to 19.2 eV, which leads to a decrease in the sp^2 hybridised carbon percentage. Increasing the treatment time to 6 minutes or 9 minutes results in a further decrease in the D parameter to 18.4 eV, while a 12-minute treatment produces a D parameter value of 17.1 eV. The D parameter decreases to the lowest value observed for the 40 W argon plasma treatment after a 15-minute treatment time, with the value dropping to 14.5 eV and the sp^2 hybridised carbon percentage is at 6.6 %. Further treatment after this point results in an increased D parameter value of 15.8 eV after 30 minutes, 15.0 eV after 45 minutes, and 15.1 eV after 60 minutes. These treatment times result in sp^2 hybridised carbon percentages of 22.5 %, 12.5 %, and 13.8 %, which indicates that almost all of the carbon on the surface has become sp^3 hybridised as a result of the argon plasma treatment. The trend occurring in the D parameters and sp^2 hybridised carbon percentages appears to be stabilising as the treatment time increases past 30 minutes as the changes observed become much smaller in both data sets. The trends observed in Figure 3-28 may initially seem to contradict those observed previously in Figure 3-25, which showed increasingly large changes in hybridisation as the treatment time increases. However, due to the differences in sampling depths of the two techniques it is sensible that a larger change in the sp^2 hybridisation content at or near the surface is needed to show the larger changes in XPS, which is detecting a larger amount of bulk HOPG under the modified surface.

3.3.1.2.3 CONCLUSIONS

Both XPS and SAM results show an increase in the extent of modification to the surface as the exposure time to the 40 W argon plasma increases in respect to both the elemental composition and the carbon chemical environments of the HOPG. As well as an increase in the oxygen content on the surface as treatment time increases there is also a deposition of iron, nickel, and fluorine as the result of sputtering from the antenna, however these elements are present in lower amounts than the oxygen. There are also significant changes to the hybridisation of the carbon on the HOPG surface when exposed to the argon plasma for increasing lengths of time, with the sp^3 hybridised carbon content increasing and showing a significant portion of the HOPG lattice has been disrupted by the plasma.

3.3.1.3 50 W RF-Coupling Power Argon Plasma

The third RF-coupling power used to ignite the argon plasma was 50 W, and samples of HOPG were exposed to this plasma for times ranging between 0.5 minutes and 60 minutes. These samples were characterised with XPS and SAM to determine the elemental composition and carbon hybridisations

present on the surface of each sample and hence determine the extent of modification caused by the 50 W argon plasma.

3.3.1.3.1   *XPS RESULTS*

The HOPG samples exposed to a 50 W argon plasma were characterised with XPS to determine the changes in elemental composition with respect to treatment time. The elemental concentration of carbon, oxygen, iron, nickel, and fluorine on each sample are shown in Figure 3-29.

Figure 3-29: Elemental composition of 50 W argon plasma treated HOPG with treatment time determined with XPS. The concentration of carbon is shown on the left axis and concentrations of oxygen, fluorine, iron, and nickel are shown on the right axis. Error bars indicate the error determined as the average for the plasma modification of HOPG based on previous experiments.

The elemental composition of HOPG treated with 50 W argon plasma for various times shows a different trend to that observed for the lower RF-coupling power argon plasma treated samples. For treatment times up to 25 minutes the carbon elemental concentration of the sample decreases down to 49.6 %, before increasing to 68.8 % after 30 minutes, and then decreasing down to 46.1 % after 35 minutes. After this point the carbon content gradually increases as the treatment time increases further until a maximum is reached at 74.2 % after 60 minutes. The oxygen content of the sample shows the reverse trend, including the sample at 30 minutes which appears to be the outlier

to the trend. The iron, nickel, and fluorine sputtered onto the HOPG from the antenna in the plasma chamber also follow this trend of an initial increase followed by a decrease with further exposure to the plasma. The unusual trend observed for the 50 W plasma treatment indicates that after 35 minutes an increased exposure to the argon plasma results in a decrease in the modification of the surface in regard to the elemental composition, and that oxygen and other species are being removed from the surface. This result is surprising, as the plasma parameters are consistent for all treatment times, and therefore the plasma species should also be consistent. While a 50 W plasma may produce more species with sufficient energies to break the stronger C=O bonds (Table 3-1), these species would be present from the moment of ignition, and not appear after 30 minutes of plasma treatment. Previous results have indicated that an equilibrium between the modification of the surface and the removal of species from the surface may be occurring, resulting in a surface that does not change significantly with further increases in treatment time. If the plasma species are not changing then another factor must be altering the balance of the equilibrium to cause a net removal of oxygen containing species from the surface of the sample when longer treatment times are used, however the cause of this change is not clear.

To further examine the oxide on the surface without the influence of the contaminating sputtered elements the O:(C+O) ratio is shown for each treatment time in Figure 3-30.
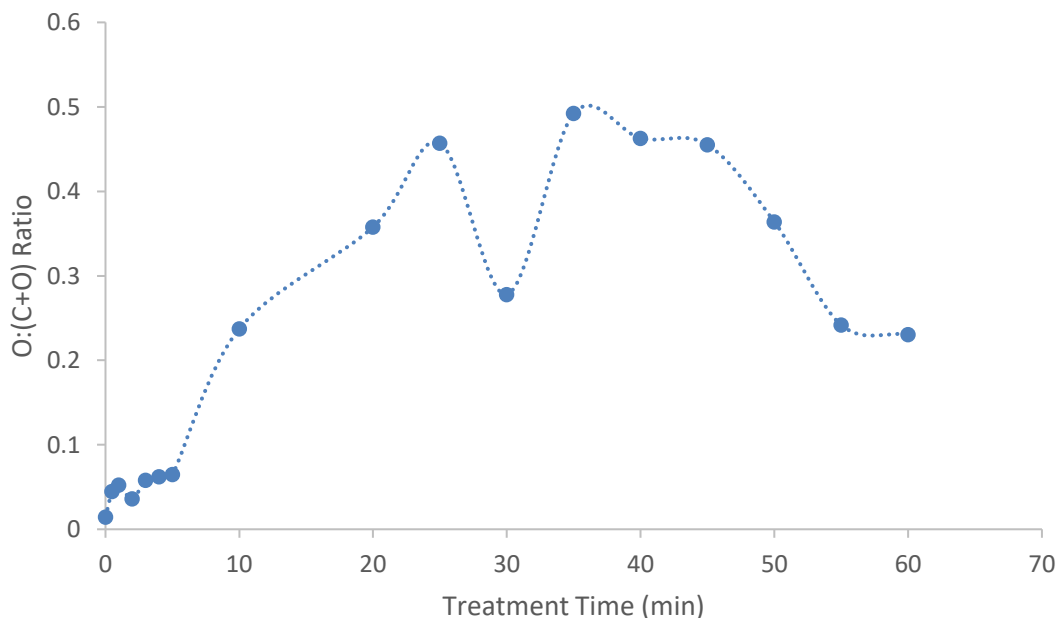
Figure 3-30: O:(C+O) ratio for 40 W argon plasma treated HOPG with plasma treatment times between 2 and 60 minute found with XPS. Error bars indicate the error determined as the average for the plasma modification of HOPG based on previous experiments.

The O:(C+O) ratio of the 50 W argon plasma treated HOPG shows an increase for every treatment time up to 25 minutes to reach a maximum of 0.46, followed by a decrease to 0.28 after 30 minutes, and an increase up to 0.49 after 35 minutes, indicating that the 30 minute sample is an outlier and does not follow the trend of the rest of the samples. For treatment times longer than 35 minutes the O:(C+O) ratio begins to decrease until a time of 60 minutes produces a ratio of 0.23. These results agree with the previous suggestion that increased exposure to 50 W argon plasma results in the removal of oxygen containing species from the HOPG surface, but does not provide further insight into the cause of this phenomenon.

The percentage to which each component of the deconvoluted high resolution C 1s peak contributes to the peak is shown in Figure 3-31 for each treatment time examined. There are six components fit to the C 1s peak, including two carbon-carbon species, three carbon-oxygen species, and one component indicating carbon-lattice vacancy interactions.
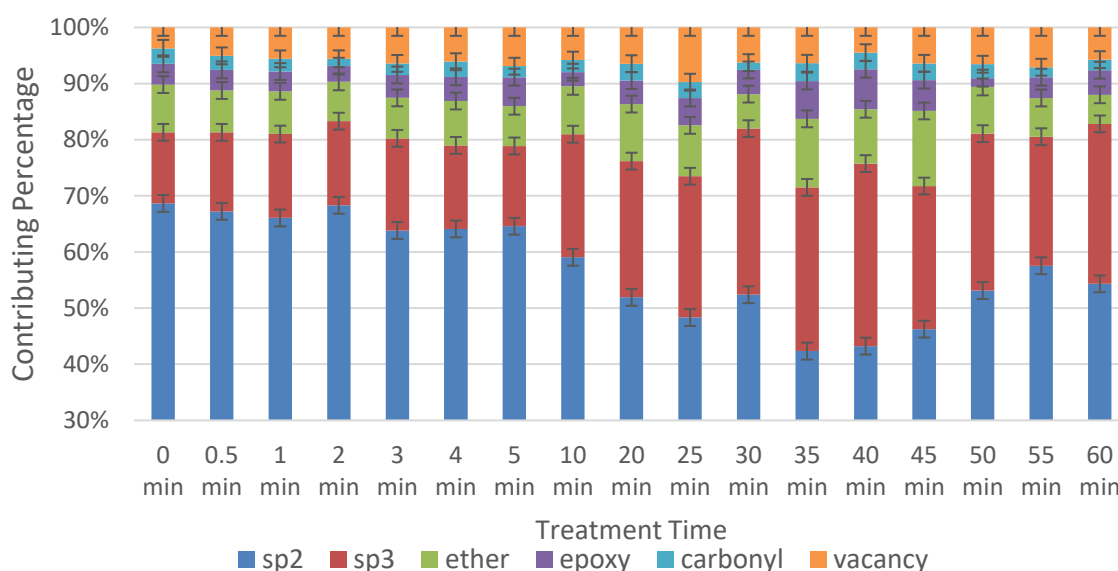
Figure 3-31: Percentages of components of C 1s peak for 30 W argon plasma treated HOPG determined with XPS. Error bars indicate the error determined as the average for the plasma modification of HOPG based on previous experiments.

The components of the C 1s peak show the same unusual trend as the elemental composition, with the carbon-carbon components decreasing and carbon-oxygen components increasing as the argon plasma treatment time increases for times up to 25 minutes before showing a large increase in carbon-carbon bonding for the 30 minute sample. The 35-minute sample shows a decrease in carbon-carbon bonding, and then a gradual increase occurs as the treatment time increases beyond this point up to 60 minutes. These results suggest that there is a decrease in the oxygen content on

80

the sample at higher treatment times, which agrees with the elemental composition results, however it does not conclude that no further modification is occurring as there is an increase in the carbon-carbon bonding, with the sp^3 hybridised carbon content remaining approximately the same after 35 minutes while the carbon-oxygen components are reduced and the sp^2 hybridised carbon increases. These results suggest that for 50 W argon plasma treatments for times longer than 35 minutes the dangling bonds that occur in the HOPG lattice as a result of bonds being broken are either reformed as sp^2 hybridised bonds or converted to sp^3 hybridised bonds, thus reducing the number of dangling bonds available to react with oxygen upon exposure to the atmosphere. However, the reason for the equilibrium shifting in this way after 35 minutes of plasma treatment is not clear and needs to be investigated further.

3.3.1.3.2   SAM RESULTS

HOPG was exposed to a 50 W argon plasma for treatment times ranging between 0.5 minutes and 60 minutes and characterised using SAM to find the elemental composition of each sample. Carbon, oxygen, fluorine, iron, and nickel were all found on the samples after plasma treatment, and the percentages of each as a function of treatment time are presented in Figure 3-32.
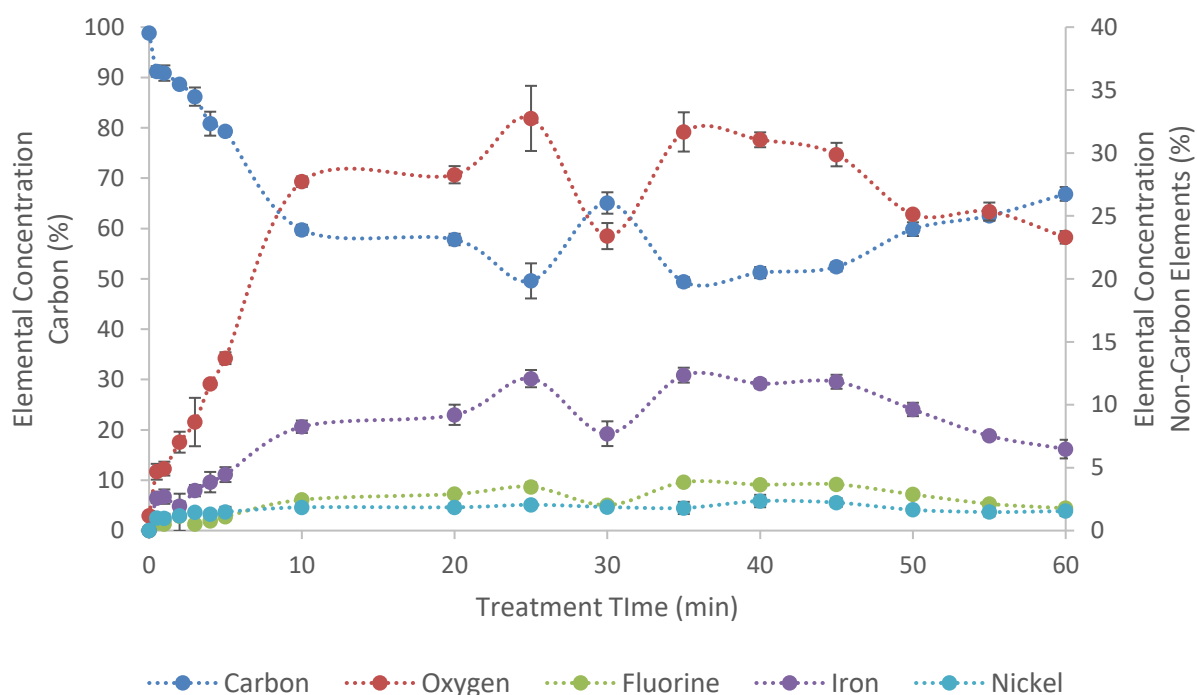
Figure 3-32: Elemental composition of 50 W argon plasma treated HOPG with treatment time determined with SAM. The concentration of carbon is shown on the left axis and concentrations of oxygen, fluorine, iron, and nickel are shown on the right axis. Data points are the average of four samples, and error bars are the standard deviation from four samples.

81

The composition of the 50 W argon plasma treated HOPG varies significantly with the length of time the sample is exposed to the plasma. The untreated sample shows 99 % carbon and 1 % oxygen, however after 0.5 minutes of plasma exposure the carbon percentage has decreased to 91 %, while the oxygen increases to 5 %. There is also a deposition of iron, nickel, and fluorine on the sample after plasma treatment, with elemental concentrations of 2 %, 1 %, and 1 %, respectively, which are the result of sputtering from the antenna in the plasma chamber during the plasma treatment.

As the treatment time increases the carbon content of the surface decreases, and after 5 minutes the carbon percentage has decreased to 79 % while the other elements increase to compensate for this. The oxygen percentage increases the most, at 14 %, and iron, nickel, and fluorine increase to 4 %, 2 %, and 1 %, respectively. Doubling the treatment time to 10 minutes also results in a doubling of the oxygen and iron percentages, while the nickel and fluorine increase by a small amount and the carbon percentage drops to 60 %. The changes that occur after a 20-minute plasma exposure are very small compared to the 10-minute plasma treatment, however after 25 minutes there is a further decrease in the carbon content and increase in oxygen, iron, nickel, and fluorine. After a 30-minute plasma treatment there is an increase in the carbon percentage and corresponding decreases in the other elements, however after 35 minutes the percentages are almost identical to the 25-minute sample. Further increase in treatment time results in a trend of increasing carbon and decreases in the other elements, which is unexpected as other argon and oxygen plasma treatments have not shown this reversal of elemental composition changes, but is consistent with the results obtained using XPS in Figure 3-29. The reason for this trend is not clear, and should be studied further to investigate the repeatability of the trend.

The O:(C+O) ratio is considered to examine the modification of the surface without the influence of the contaminating elements. This value is shown for each plasma treatment time in Figure 3-33.
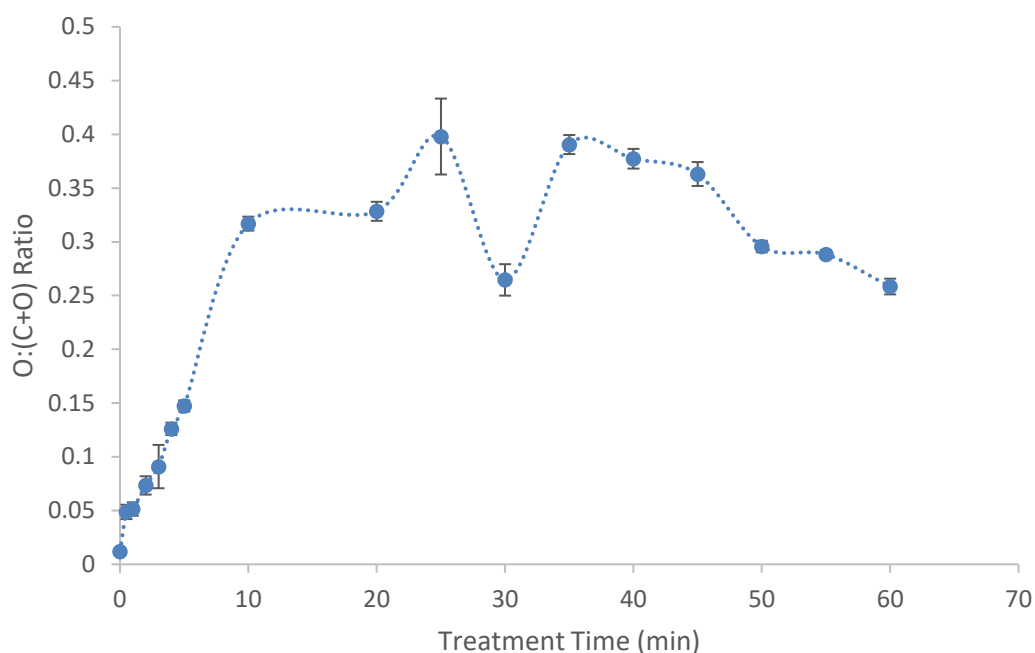
Figure 3-33: O:(C+O) ratio for 50 W argon plasma treated HOPG with plasma treatment times between 2 and 60 minute found with SAM. Data points are the average of four samples, and error bars are the standard deviation from four samples.

The O:(C+O) ratio in Figure 3-33 shows a fairly rapid increase initially, with the ratio increasing from 0.01 to 0.05 after 1 minutes, and to 0.09 after 3 minutes. This rate of increase continues after 5- and 10-minute treatments, with O:(C+O) ratios of 0.15 and 0.32, respectively. After this point a doubling of the treatment time to 20 minutes results in only a very small increase in the ratio to 0.33, and then increases to 25- and 30-minutes produce O:(C+O) ratios of 0.40 and 0.26, respectively, which is where the increasing trend stops. A 35-minute treatment brings the ratio back up to 0.39, and after this point further treatment results in a decrease in the O:(C+O) ratio until a value of 0.26 is reached after 60 minutes. As with the total elemental concentrations shown in Figure 3-32 the reason for this is not clear, and should be investigated further by repeating the experiment and further investigating the kinetics involved once more data verifies the trend.

High resolution C(KLL) spectra were acquired for each sample and differentiated to find the positions of the maxima and minima and the D parameter value, which is then used to determine the sp^2 hybridised carbon percentage. Both of these values are plotted against treatment time in Figure 3-34.

83
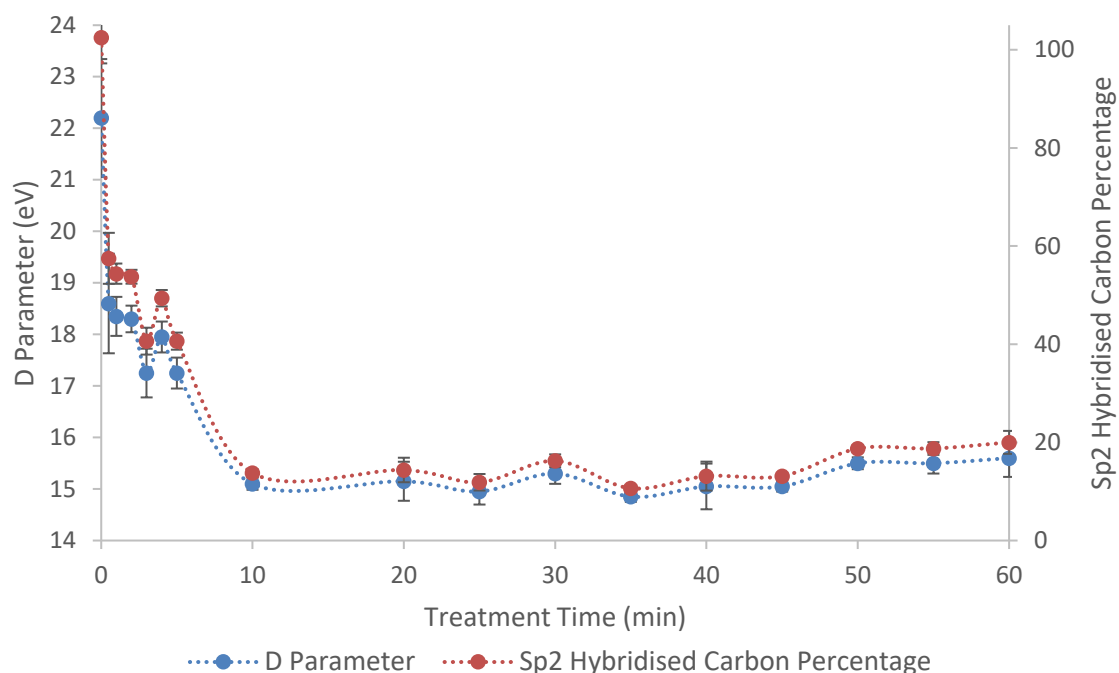
Figure 3-34: D parameter (left axis, blue points) and *sp*² hybridised carbon percentage (right axis, red points) for samples of HOPG exposed to 50 W argon plasma for times ranging between 2 minutes and 60 minutes. Data points are the average of four samples, and error bars are the standard deviation from four samples.

The D parameter changes significantly from the untreated sample to the 0.5 minutes 50 W argon plasma treated sample, with the value decreasing from 22 eV to 19 eV, however after this point the rate of change is much slower, with a 5-minute treatment time only producing a decrease to 17 eV. After a 10-minute treatment the D parameter has decreased to 15 eV, and it varies between 14 eV and 16 eV for treatments between 10 minutes and 60 minutes with a slightly increasing trend. These D parameter values result in *sp*² hybridised carbon percentages between 10 % and 20 % indicating that the majority of the carbon on the HOPG surface has been converted to *sp*² hybridised carbon after 10 minutes of 50 W argon plasma treatment. These results are consistent with those observed previously with XPS in Figure 3-31.

3.3.1.3.3   CONCLUSIONS

The results from the XPS and SAM characterisation of 50 W argon plasma modified HOPG indicate that there is a large amount of modification of the surface in terms of the elemental composition for exposure times up to 30 minutes, however after this point there appears to be less modification on the surface and oxygen species are reduced, suggesting that after this time more carbon-carbon bonds are reformed after HOPG lattice disruption. The modification of the carbon hybridisations present does not reverse after 30 minutes to a large extent, although there are some variations in

the sp^2 and sp^3 hybridised carbon percentages observed for these longer treatment times.

3.3.2 Influence of RF-Coupling Power on Plasma Treatment of Highly Oriented Pyrolytic Graphite

Argon plasma ignited with a 30 W, 40 W, or 50 W RF-coupling power has been used to treat HOPG and the impact of each of these treatments on the HOPG surface has been considered in the preceding sections. The three treatments are now compared to each other to examine the influence of the RF-coupling power has on the modification of the HOPG.

3.3.2.1 XPS Results

The O:(C+O) ratio of the argon plasma treated HOPG samples are shown in Figure 3-35 to consider impact of the RF-coupling power on the oxidation of the HOPG. The 30 W samples are shown in blue points, while the 40 W and 50 W samples are shown in red and green, respectively.
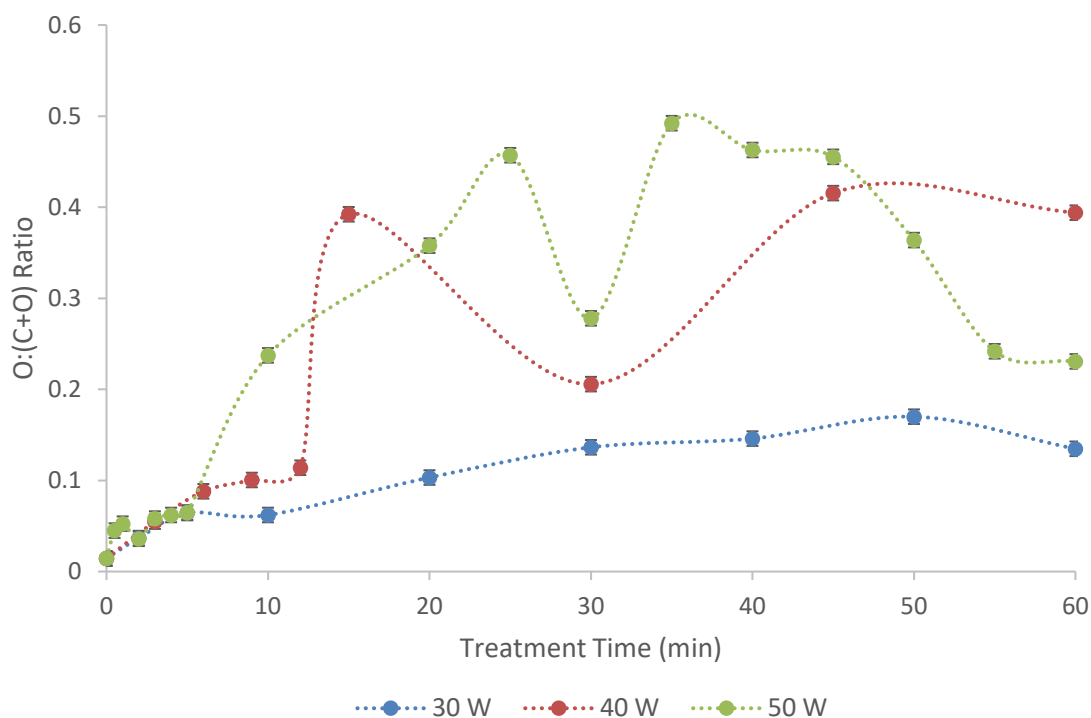
Figure 3-35: O:(C+O) ratio for 30 W (blue points) and 40 W (red points) oxygen plasma treated HOPG with plasma treatment times between 2 and 60 minute found with XPS. Error bars indicate the error determined as the average for the plasma modification of HOPG based on previous experiments.

The O:(C+O) ratios of the 30 W, 40 W, and 50 W argon plasma treated HOPG are very similar for treatment times below 5 minutes, however as the treatment time increases past 5 minutes differences occur between the three plasma treatments. The 30 W samples show O:(C+O) ratios that are lower than those of the 40 W and 50 W samples for all times between 10 minutes and 60 minutes. The trends from the 40 W and 50 W samples are less clear and overlap with each other.

For times below 45 minutes the 40 W samples show O:(C+O) ratios lower than the 50 W samples with the exception of the 15-minute sample, which shows a higher ratio. However, this sample has been presumed to be an outlier in previous analysis and it is likely that the value should be lower. For treatment times longer than 45 minutes the O:(C+O) ratio for the 50 W samples is decreasing and has a lower value than the 45 W samples. Further study should be conducted in the behaviour of the 40 W and 50 W samples for a larger range of treatment times to determine with more clarity the influence of the RF-coupling power on the modification of the HOPG.

The percentage that each component of the deconvoluted high resolution C 1s peak contributes to the peak is presented in Figure 3-36 for the 30 W, 40 W, and 50 W argon plasma treated HOPG using circular points, triangular points, and square points, respectively.
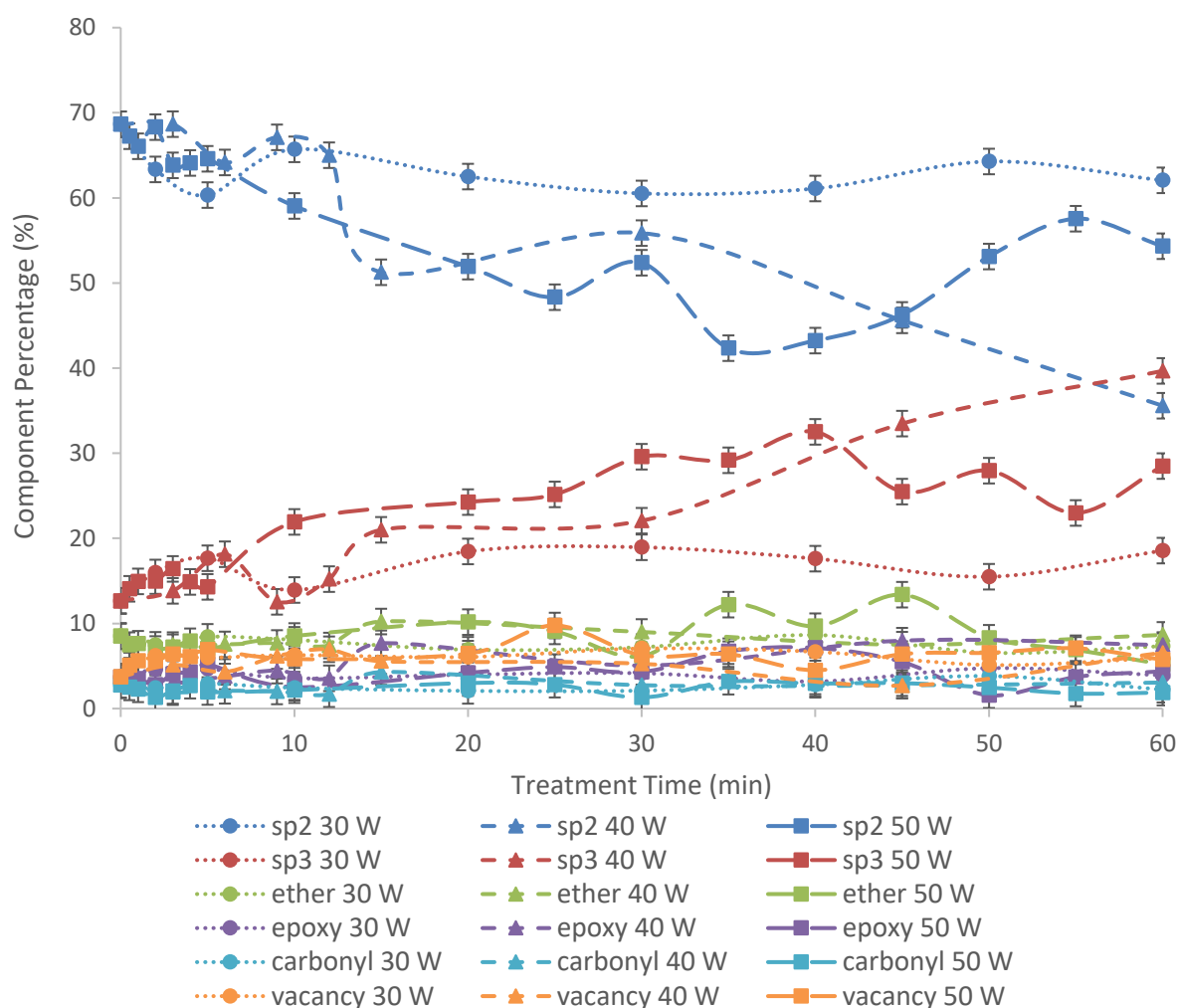
Figure 3-36: Percentages of components of C 1s peak for 30 W (circular points), 40 W (triangular points), and 50 W (square points) oxygen plasma treated HOPG determined with XPS. Error bars indicate the error determined as the average for the plasma modification of HOPG based on previous experiments.

There is no clear trend observed in the behaviour of the components of the deconvoluted high-resolution C 1s peak as the RF-coupling power changes. The carbon-oxygen and carbon-lattice vacancy components do not show significant differences as the RF-coupling power increases, although there are some samples that show higher contributions of various components than others this does not occur with any regularity with regard to the RF-coupling power. The sp^2 and sp^3 hybridised carbon percentages show the largest amount of variation with the treatment time, as has been described previously for the individual RF-coupling powers. Despite these larger variations there is no discernible trend in these component percentages as some samples display higher sp^2 hybridised carbon with lower RF-coupling powers while others display lower sp^2 carbon content. These results suggest that the modification of the chemical environments present on the HOPG surface as a result of exposure to argon plasma is not dependent on the RF-coupling power used to ignite it.

3.3.2.2 SAM Results

The O:(C+O) ratio for the 30 W, 40 W, and 50 W argon plasma treated HOPG is shown in Figure 3-37 for all three RF-coupling powers, with 30 W shown in blue points, 40 W in red points, and 50 W in green points, for treatment times up to 60 minutes.
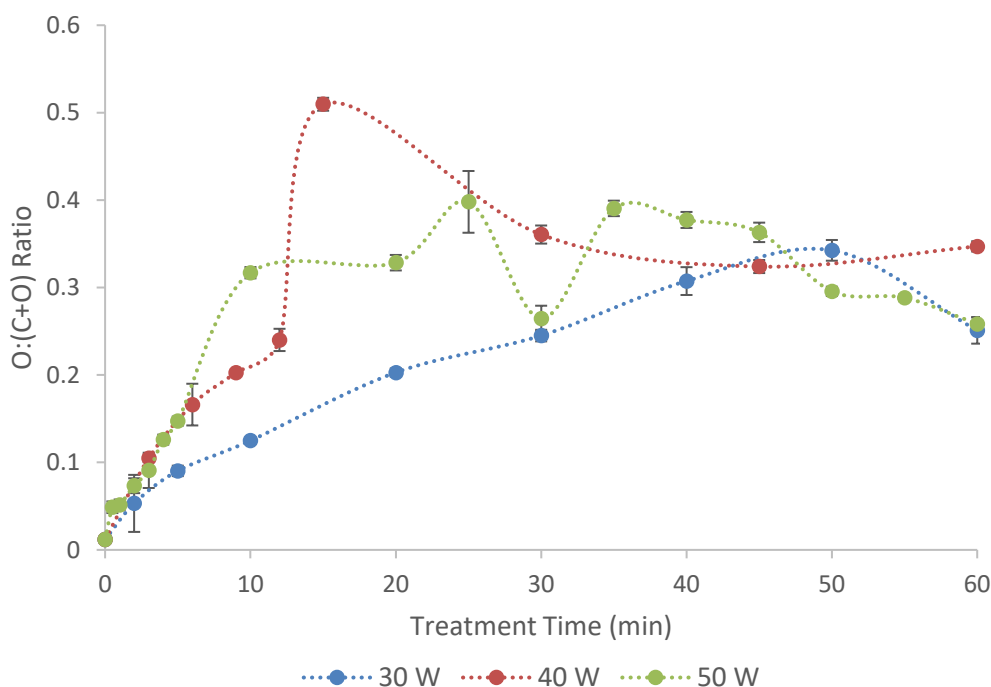
Figure 3-37: O:(C+O) ratio for 30 W (blue points), 40 W (red points), and 50 W (green points) argon plasma treated HOPG with plasma treatment times between 2 and 60 minute found with SAM. Data points are the average of four samples, and error bars are the standard deviation from four samples.

The O:(C+O) ratio for the 30 W argon plasma treated samples is lower than the 40 W and 50 W samples for treatment times up to 40 minutes, after which the data sets cross each other and no longer show a clear trend. For treatment times below 10 minutes the 40 W and 50 W samples have very similar O:(C+O) ratios but differ for treatment times between 10 minutes and 40 minutes with the 50 W generally being higher. These trends indicate that for low- to mid- range treatment times an increase in RF-coupling power used to ignite the plasma results in an increased extent of modification of the surface, however after 40 minutes the RF-coupling power used does not change the modification in a predictable way. The uncertainties in these measurements are generally very small, and are likely not impacting on the trends observed. However, there are several data points between the three data sets that have much larger uncertainties, as shown in Figure 3-37. These larger uncertainties are likely the result of random variations in the plasma treatment, or the examination of atypical areas on the sample surfaces while performing SAM characterisation. The second cause is less likely, as the in-situ SEM was used to find areas that appeared to be typical of the majority of the surface, therefore it is expected that the plasma treatment is the main cause. However, the few samples that have these larger uncertainties are not showing large impacts on the overall trends observed, and therefore the trends are thought to be valid. These results are similar to those found using XPS (Figure 3-35), however the 40 W and 50 W trends overlap more in the SAM results.

The modification of the carbon hybridisation of the HOPG occurs to a different extent when the RF-coupling power of the argon plasma treatments is changed. The D parameter values in Figure 3-38 are shown in the blue points, while the sp^2 hybridised carbon percentage values are shown in the red points. The 30 W plasma treated samples are indicated by circular points, the 40 W samples by triangular points, and the 50 W samples by square points.
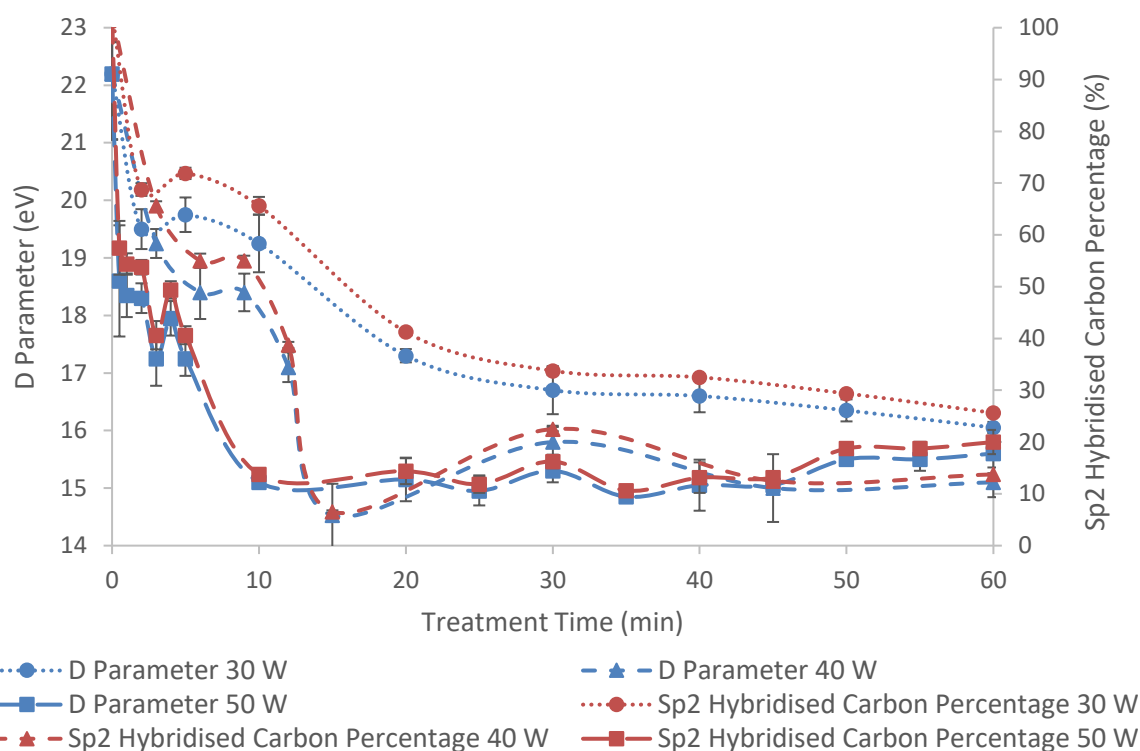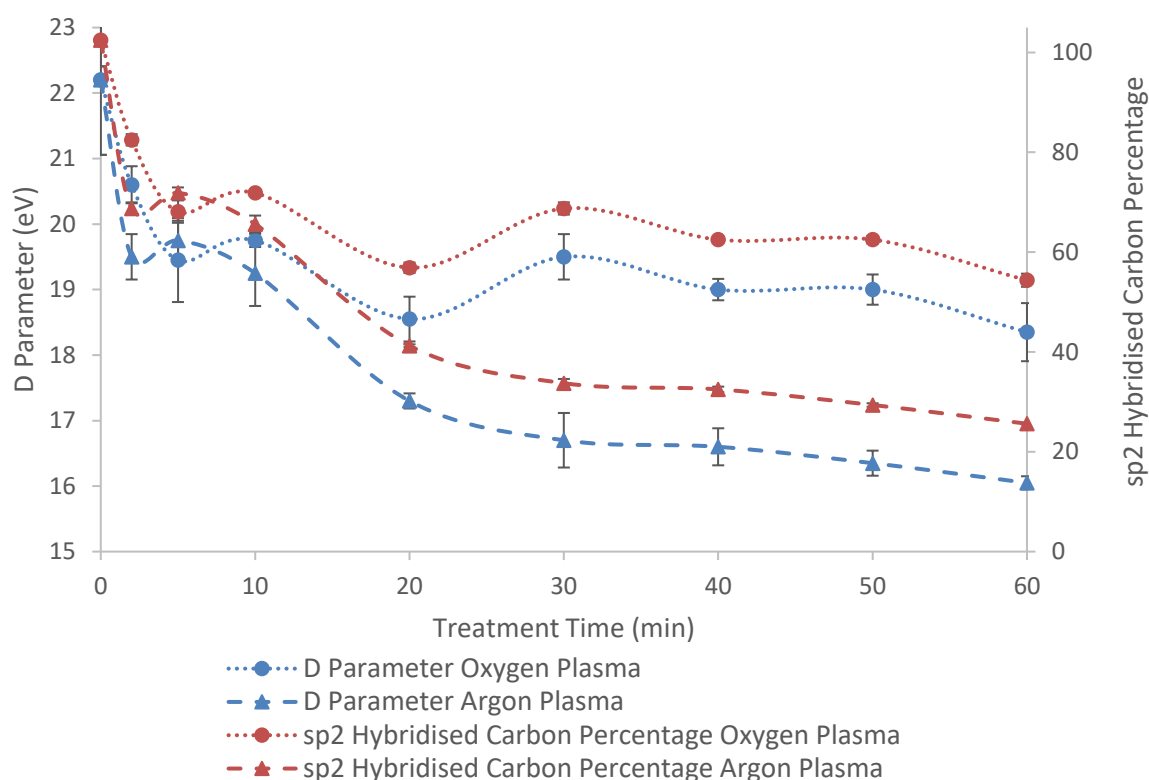
Figure 3-38: D parameter (left axis, blue points) and *sp²* hybridised carbon percentage (right axis, red points) for samples of HOPG exposed to 30 W (circle points), 40 W (triangle points), and 50 W (square points) argon plasma for times ranging between 3 minutes and 60 minutes. Data points are the average of four samples, and error bars are the standard deviation from four samples.

There is a clear trend in the D parameter of the argon plasma treated HOPG as the RF-coupling power of the plasma increases above 30 W, with the higher RF-coupling power resulting in a greater extent of modification of the HOPG surface. The lowest D parameter value achieved with a 30 W plasma is 16.0 eV, while that found with a 40 W plasma as 14.5 eV, and that from a 50 W plasma is 15.0 eV. While the 40 W treatment produces the lowest treatment time this sample appears to be an outlier from the trend of the other 40 W samples. This range of D parameter values results in *sp²* hybridised carbon percentages as low as 26 %, 7 %, and 11 % for the 30 W samples, 40 W samples, and 50 W samples, respectively. It can be seen from Figure 3-38 that the lattice of the HOPG surface can be almost entirely disrupted and converted to *sp³* hybridised carbon, and modification resulting in different *sp²* hybridised carbon percentages can be achieved by varying the RF-coupling power and treatment time of the argon plasma used to modify the surface. The uncertainties for these data sets indicate some variation between samples, which is expected to be the result of the random nature of the plasma treatment. While the plasma parameters may be held constant, the individual movements of the particles within the plasma will be random and interact

with the surface differently during different treatments, resulting in some variation in the changes to the hybridisation of the carbon on the surface. The uncertainties for some data points in Figure 3-38 have the largest impact on the 40 W and 50 W data sets, and as these trends overlap in many places they are not concluded to show any clear difference within the experimental uncertainty level.

3.3.2.3 Conclusions

The XPS and SAM results for the elemental composition of 30 W, 40 W, and 50 W argon plasma treated HOPG are in agreement that the trends in changes in modification with RF-coupling power are not clear, particularly between the 40 W and 50 W samples. However, the results pertaining to the hybridisation of the carbon on the surface are not in agreement, with the XPS results not showing any clear trends with a change in RF-coupling power while the SAM results indicate that an increase in RF-coupling power results in a decrease in the sp^2 hybridised carbon content on the surface. These differences are a result of the differences in the sampling depth of the two techniques, with the increase in sp^3 hybridised carbon having a higher impact on the SAM results because of the smaller sampling depth.

3.4 Comparison of Oxygen and Argon Plasma Modification of Highly Oriented Pyrolytic Graphite

Previous results in this chapter have indicated that changing the RF-coupling power used to ignite a plasma and the length of time a sample is exposed to the plasma influences the extent of modification of the HOPG surface. The impact of the plasma species on the modification of HOPG is now examined through comparison of oxygen and argon plasma treated HOPG ignited using both 30 W and 40 W RF-coupling powers.

3.4.1 30 W RF-Coupling Power Plasma

HOPG was exposed to both oxygen and argon plasma ignited with a 30 W RF-coupling power for treatment times ranging between 2 minutes and 60 minutes, and subsequently characterised using XPS and SAM to examine the elemental composition and the carbon hybridisations present.

3.4.1.1 XPS Results

The O:(C+O) ratio for the 30 W oxygen and 30 W argon plasma treated HOPG found using XPS is shown in Figure 3-39 as blue points and red points, respectively.
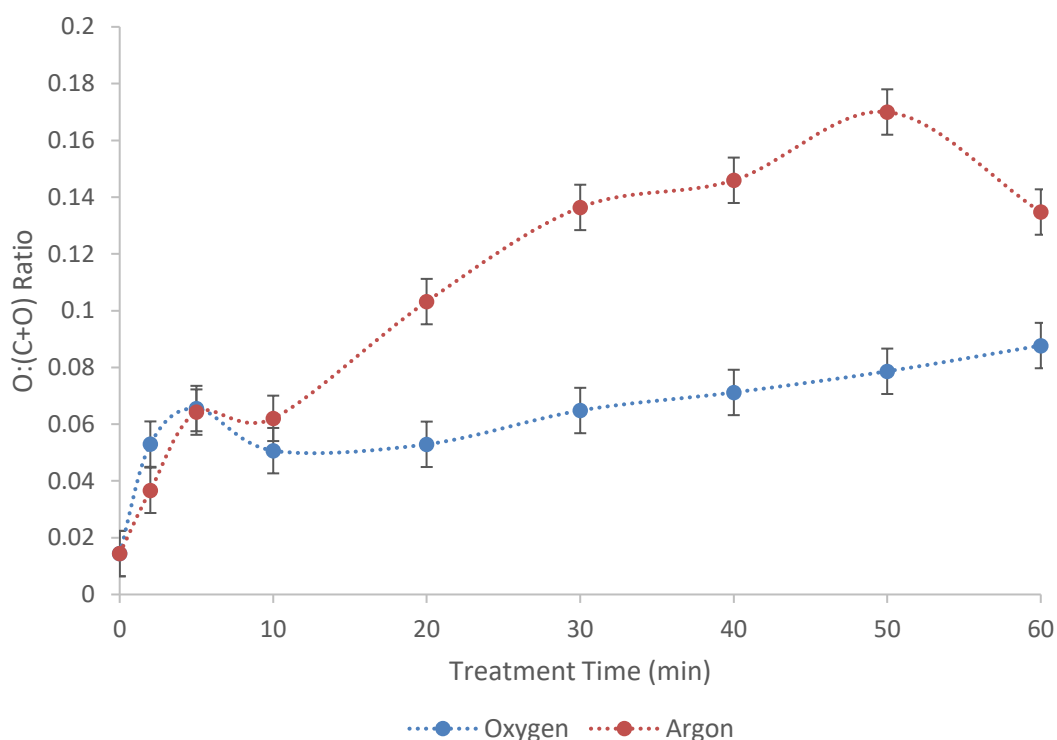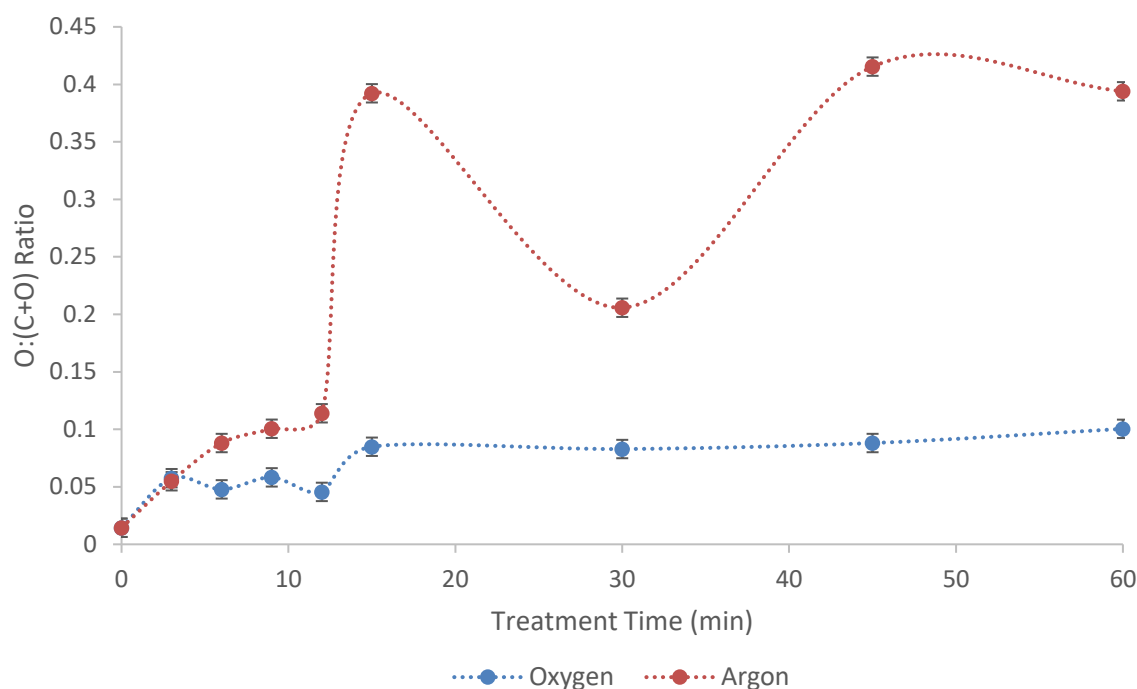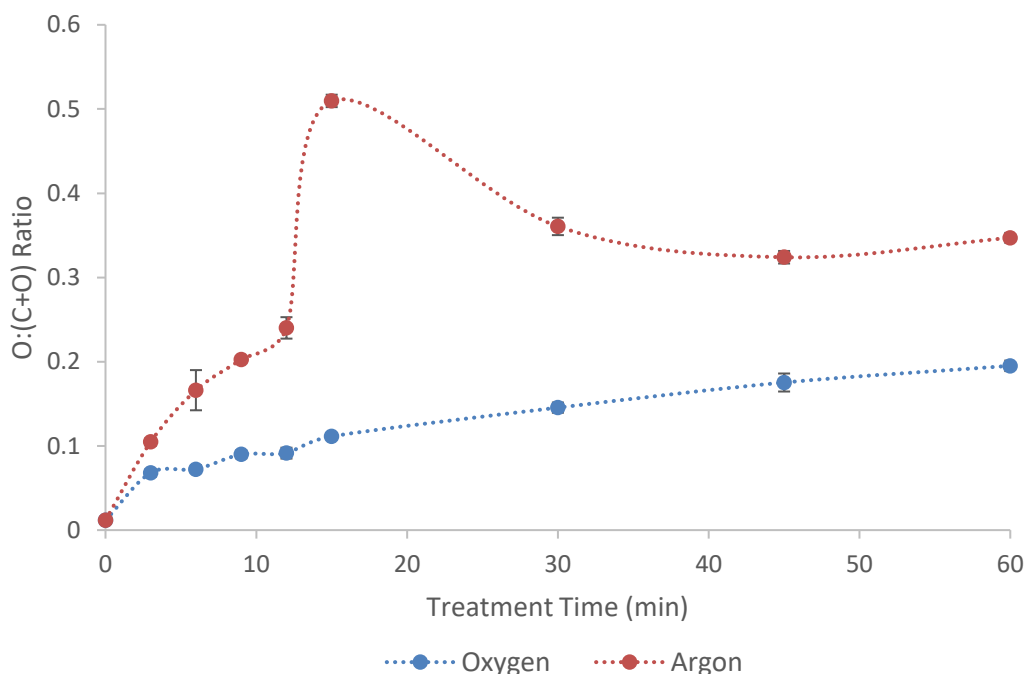
Figure 3-39: O:(C+O) ratio for 30 W oxygen plasma (blue points) and 30 W argon plasma (red points) treated HOPG with plasma treatment times between 2 and 60 minutes found with XPS. Error bars indicate the error determined as the average for the plasma modification of HOPG based on previous experiments.

There is a clear difference between the O:(C+O) ratio of the 30 W oxygen and argon plasma treated HOPG for treatment times longer than 20 minutes, however the trend is not so clear for shorter treatment times. For a 2-minute treatment the oxygen plasma produces a higher O:(C+O) ratio than the argon plasma, while for a 5-minute treatment both produce the same results and for a 10-minute treatment the argon plasma produces a higher O:(C+O) ratio, although the error bars for these samples overlap and it cannot be concluded that they are different. For the treatment times longer than 20 minutes the plasma treatments results in an increasingly large difference between the argon and oxygen plasma treatments, with the maximum difference reached at 50 minutes with ratios of 0.17 and 0.079 for the argon and oxygen plasma treated samples, respectively. The O:(C+O) ratios for the 60-minute samples are closer together as the argon plasma treated ratio decreases while the oxygen plasma treated sample continues to increase. These results show that the argon plasma produces a higher level of modification to the HOPG surface than the oxygen plasma in terms of the oxide grown on the surface.

It is counterintuitive that the argon plasma treatment would result in a higher oxygen content on the sample than the oxygen plasma treatment, however the way that the two plasma types interact

91

with the HOPG is different. As has been discussed previously the oxygen plasma interacts chemically with the HOPG and causes carbon-oxygen bonds to form, as well as breaking the sp^2 hybridised carbon bonds on the surface to remove carbon atoms or change their hybridisation. The argon plasma acts differently and will not induce the formation of carbon-oxygen bonds during the plasma treatment but will instead break carbon bonds on the HOPG surface, changing the hybridisation and leaving dangling bonds that react with any oxygen that remains within the plasma chamber as well as atmospheric oxygen once the sample is removed from the vacuum chamber after plasma treatment. The oxygen plasma treatment therefore terminates the bonds broken on the surface during the plasma treatment while the argon plasma doesn't and has many sites available on the surface to react with atmospheric oxygen. The iron that is sputtered from the antenna during the argon plasma treatment is also likely in the form of iron oxides, which will result in additional oxygen being deposited onto the HOPG surface during the plasma treatment. This could be further investigated through high resolution XPS of the O $1s$ peak, however these peaks were not of sufficient resolution to be successfully deconvoluted within this work.

The high-resolution C $1s$ peaks were deconvoluted into six components including carbon-carbon species, carbon-oxygen species, and a carbon-lattice vacancy interaction. The contribution of each of these components to the peak is shown in Figure 3-40 for the oxygen plasma treated samples (circular points) and the argon plasma treated samples (triangular points).
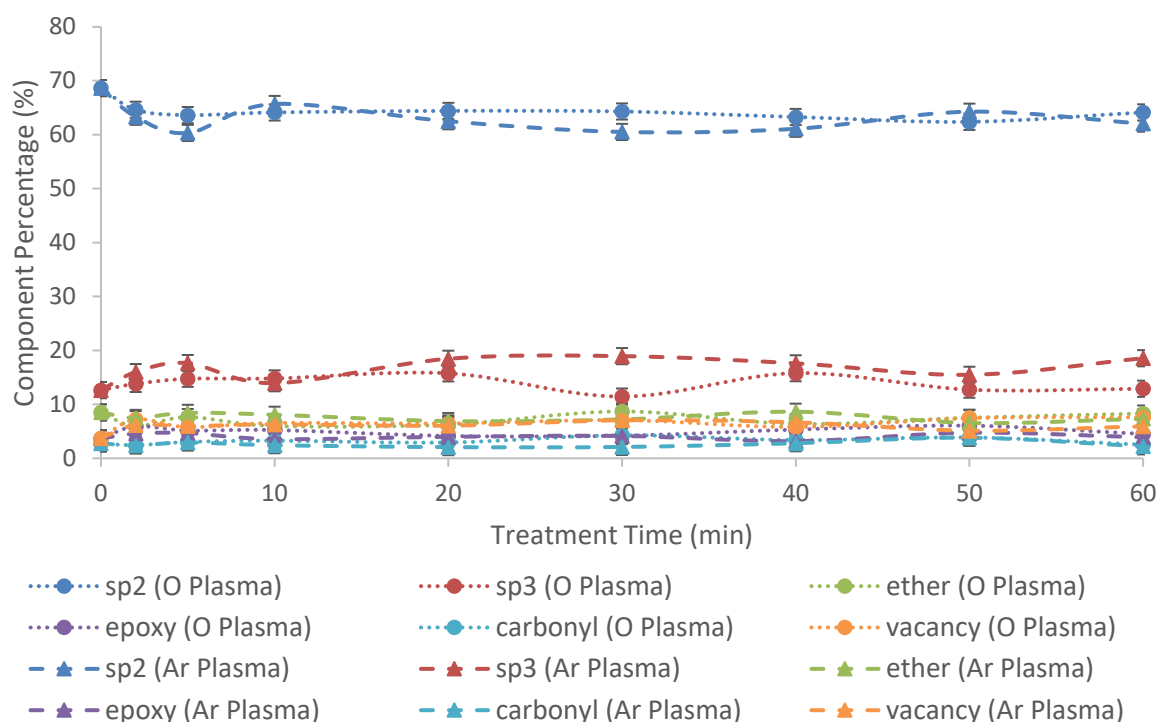
Figure 3-40: Percentages of components of C 1s peak for 30 W oxygen plasma (circular points) and 30 W argon plasma (triangular points) treated HOPG determined with XPS. Error bars indicate the error determined as the average for the plasma modification of HOPG based on previous experiments.

There is no clear trend in the difference between the components of the C 1*s* peak of samples treated with a 30 W oxygen plasma or a 30 W argon plasma. Both plasma treatments show the same trends in how each component changes with increasing treatment time in the plasma, and there is very little difference between the percentage that each component contributes to the total peak area for the oxygen and argon plasma treated samples. These results show that the changes to the chemical environment of the carbon in the HOPG that occur as a result of exposure to either oxygen or argon plasma are the same when a 30 W RF-coupling power is used to ignite the plasma.

3.4.1.2 SAM Results

The O:(C+O) ratio of the samples exposed to the two plasmas as found with SAM are shown in Figure 3-41 for oxygen and argon treated HOPG with treatment times ranging up to 60 minutes.
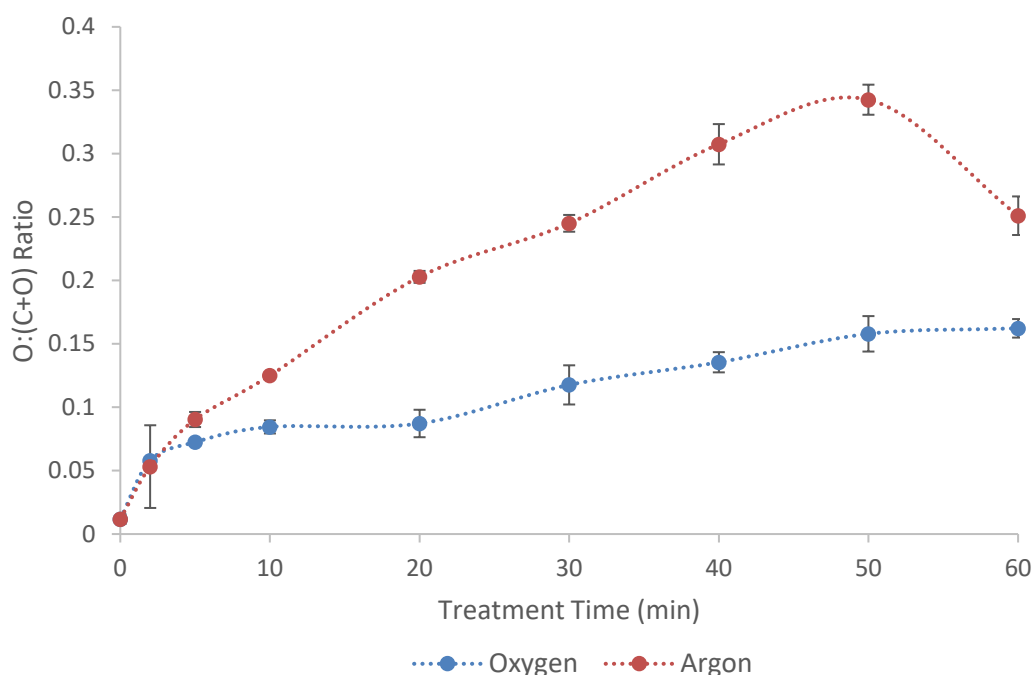
Figure 3-41: O:(C+O) ratio for 30 W oxygen plasma (blue points) and 30 W argon plasma (red points) treated HOPG with plasma treatment times between 2 and 60 minutes found with SAM. Data points are the average of four samples, and error bars are the standard deviation from four samples.

The difference in the O:(C+O) ratio of samples treated with oxygen plasma or argon plasma is clear in Figure 3-41. For both types of plasma the O:(C+O) ratio increases as the treatment time increases, however that of argon plasma treated HOPG increases at a much faster rate. This supports the theory described previously that the different action of the argon plasma compared to the oxygen plasma and the increased rate of sputtering from the antenna are causing the increase in oxygen on the surface. The species in the argon plasma bombard the surface and cause disruption of the HOPG lattice but do not bond to the carbon, which results in the carbon-carbon bonds reforming as sp^2 or sp^3 hybridised carbon bonds or remaining as dangling bonds. These dangling bonds can bond to oxygen when the sample is exposed to atmosphere between plasma treatment and characterisation, which may result in an increase in oxygen on the surface compared to that achieved with oxygen plasma, which is interacting terminating bonds during the plasma treatment.

The increased oxygen content on samples treated with argon rather than oxygen plasma seems counterintuitive, but as was discussed previously for the XPS results (Figure 3-39) it is likely the result of the difference between the way the argon and oxygen plasmas interact with the sample surface and the increased presence of iron which may be in the form of iron oxides. Further study of the samples performed using sufficient resolution for high-resolution examination of the iron and

94

oxygen peaks could provide further detail on the types of oxygen present on the surface, however the high-resolution oxygen spectral data obtained thus far was not able to be deconvoluted to provide this information.

The D parameter value and sp^2 hybridised carbon percentages of samples exposed to oxygen or argon plasma are shown in Figure 3-42 as circular points and triangular points, respectively, to show the extent of modification of the hybridisation of the carbon with the two plasma treatments.

Figure 3-42: D parameter (left axis, blue points) and *sp*² hybridised carbon percentage (right axis, red points) for samples of HOPG exposed to 30 W oxygen plasma (circle points) and 30 W argon plasma (triangle points) for times ranging between 3 minutes and 60 minutes. Data points are the average of four samples, and error bars are the standard deviation from four samples.

It can be seen from Figure 3-42 that there is a difference between the D parameter values for HOPG modified with oxygen or argon plasma when treated for the same length of time, with the argon treated samples showing a lower D parameter value than the oxygen treated samples. The argon plasma treated samples have D parameters as low as 16 eV, while the lowest observed for oxygen plasma treated samples is 18 eV. This results in sp^2 hybridised carbon percentages of 26 % and 54 %, respectively, which shows that the argon plasma treatment has a much larger effect on the hybridisation of the HOPG than the oxygen plasma. The difference is likely due to the difference in

the ways the two plasma interact with the surface, with oxygen likely to form chemical bonds with carbon atoms on the surface while the argon species do not, and instead break apart carbon-carbon double bonds which results in dangling bonds and the reformation of carbon-carbon single bonds.

3.4.1.3 Conclusions

The results indicating the elemental composition of HOPG exposed to 30 W oxygen or argon plasma from both XPS and SAM indicate that the argon plasma results in a greater extent of modification to the HOPG surface. This is shown by the increase in the oxygen content of the argon treated samples compared to the oxygen plasma treated samples, which is due to a combination of a larger extent of iron oxides deposited on the HOPG surface as a result of sputtering from the antenna and the production of dangling bonds on the argon plasma treated samples reacting with oxygen when the samples are exposed to the atmosphere. The XPS and SAM results do not agree on the modification of the hybridisation of the carbon due to the oxygen and argon plasma treatments as the SAM results show a large difference in the hybridisations while the XPS show very similar results for the two types of plasma. This is expected to be due to the difference in sampling depth of the two techniques, with the surface modification being more prominent in the SAM results than the XPS results.

3.4.2   40 W RF-Coupling Power Plasma

To compare the oxygen and argon plasma treatments at a higher RF-coupling power both types of plasma were ignited with a 40 W RF-coupling power and applied to HOPG surfaces for treatment time ranging between 3 and 60 minutes, with the resultant modification characterised using XPS and SAM to examine the elemental composition and carbon hybridisations present.

3.4.2.1 XPS Results

The O:(C+O) ratio for the 40 W oxygen plasma and 40 W argon plasma treated HOPG are shown in Figure 3-43 for treatment times between 3 minutes and 60 minutes as blue points and red points, respectively.

Figure 3-43: O:(C+O) ratio for 40 W oxygen plasma (blue points) and 40 W argon plasma (red points) treated HOPG with plasma treatment times between 2 and 60 minute found with XPS. Error bars indicate the error determined as the average for the plasma modification of HOPG based on previous experiments.

After a 3-minute treatment with either oxygen or argon plasma the O:(C+O) ratio increases to 0.055, however for treatment times longer than 3 minutes the ratio is different for the different plasma treatments. For all samples with treatment times between 6 minutes and 60 minutes the O:(C+O) ratio is higher for the argon plasma treated samples than the oxygen plasma treated samples, and the ratio of the argon treated samples increases at a faster rate than the oxygen samples. This shows that the argon plasma results in a higher extent of modification of the HOPG surface with respect to the oxide growth on the surface.

The deconvolution of the C 1*s* peak into its constituent components was performed for the oxygen and argon plasma treated HOPG samples, with the results presented in Figure 3-44 as circular points and triangular points, respectively.
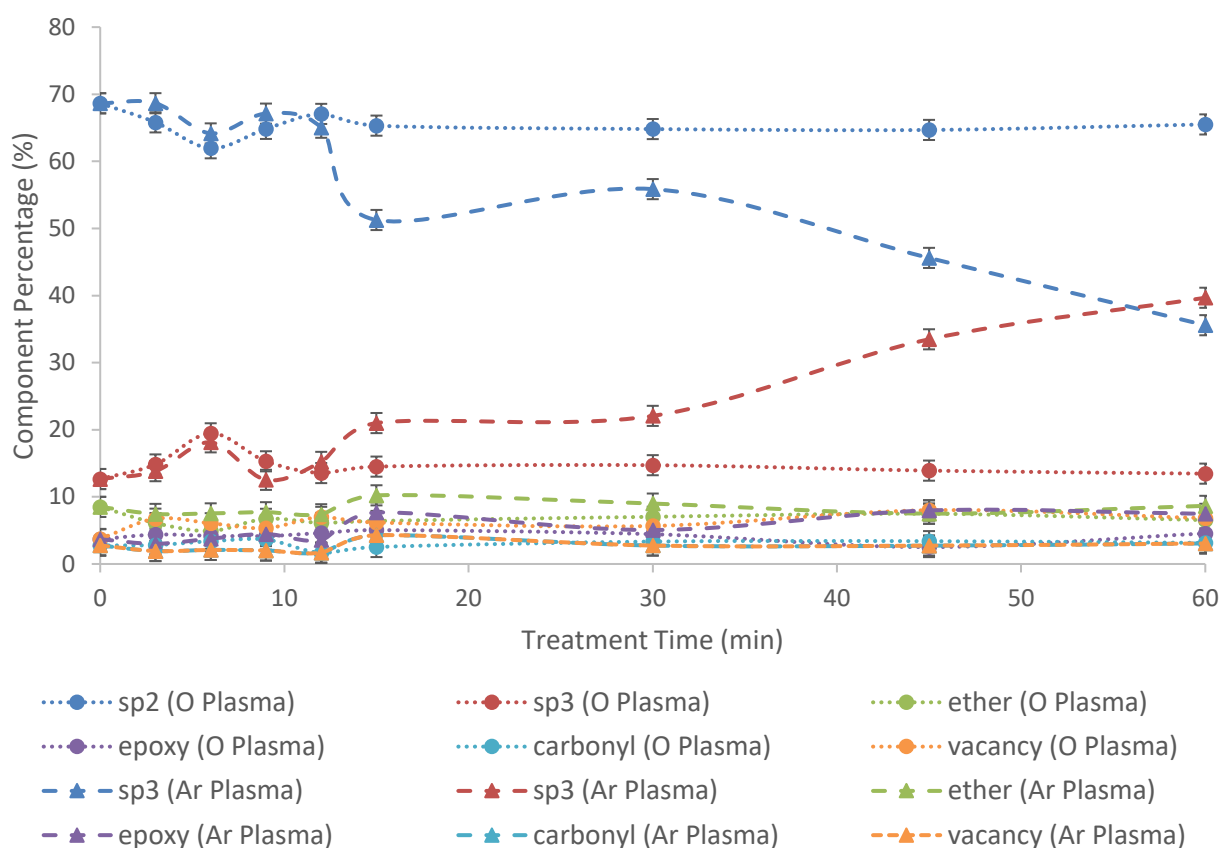
Figure 3-44: Percentages of components of C 1s peak for 40 W oxygen plasma (circular points) and 40 W argon plasma (triangular points) treated HOPG determined with XPS. Error bars indicate the error determined as the average for the plasma modification of HOPG based on previous experiments.

For treatment times of 12 minutes or less there is no clear difference between the 40 W argon and oxygen plasma treated HOPG in the percentage that any of the components contribute to the C 1s peak, however there are differences that occur for treatment times longer than this. For the longer treatment times the argon plasma shows a lower sp^2 hybridised carbon percentage than the oxygen plasma treated samples, with the difference between the two generally increasing as the treatment time increases. While this occurs the sp^3 hybridised carbon percentage is changing in the opposite direction, with the argon plasma treated samples showing higher sp^3 hybridised carbon percentages than the oxygen plasma treated samples. These results show that the argon plasma treatment results in a higher extent of modification to the HOPG lattice and a higher conversion of sp^2 hybridised carbon to sp^3 hybridised carbon. This difference is the result of the difference in the way the argon and oxygen plasma interact with the HOPG, where the argon plasma is causing a higher level of disruption to the sp^2 hybridised carbon lattice.

3.4.2.2 SAM Results

The growth of the oxide species on the HOPG surface can be more clearly examined through the O:(C+O) ratio as shown in Figure 26 for the oxygen plasma treated samples (blue points) and the argon plasma treated samples (red points).

Figure 3-45: O:(C+O) ratio for 40 W oxygen plasma (blue points) and 40 W argon plasma (red points) treated HOPG with plasma treatment times between 2 and 60 minute found with SAM. Data points are the average of four samples, and error bars are the standard deviation from four samples.

The argon plasma treated HOPG samples consistently show a higher O:(C+O) ratio than the oxygen plasma treated samples. For each treatment time considered the argon sample shows a higher ratio, often by a factor of 2, although both plasma treatments show an increasing O:(C+O) ratio with increasing treatment time. These results support the previous conclusion that the argon plasma treated HOPG results in a higher extent of modification of the HOPG surface, with the higher oxygen content of the argon samples likely due to a combination of the dangling bonds created by argon bombardment and the iron oxides present from the antenna sputtering. These trends are consistent with those observed previously using XPS in Figure 3-43.

The D parameter values measured for the oxygen and argon plasma treated samples are shown in Figure 3-46, along with the resultant sp^2 hybridised carbon percentages. The oxygen plasma treated samples are indicated by circular points while the argon plasma treated samples are indicated by triangular points.
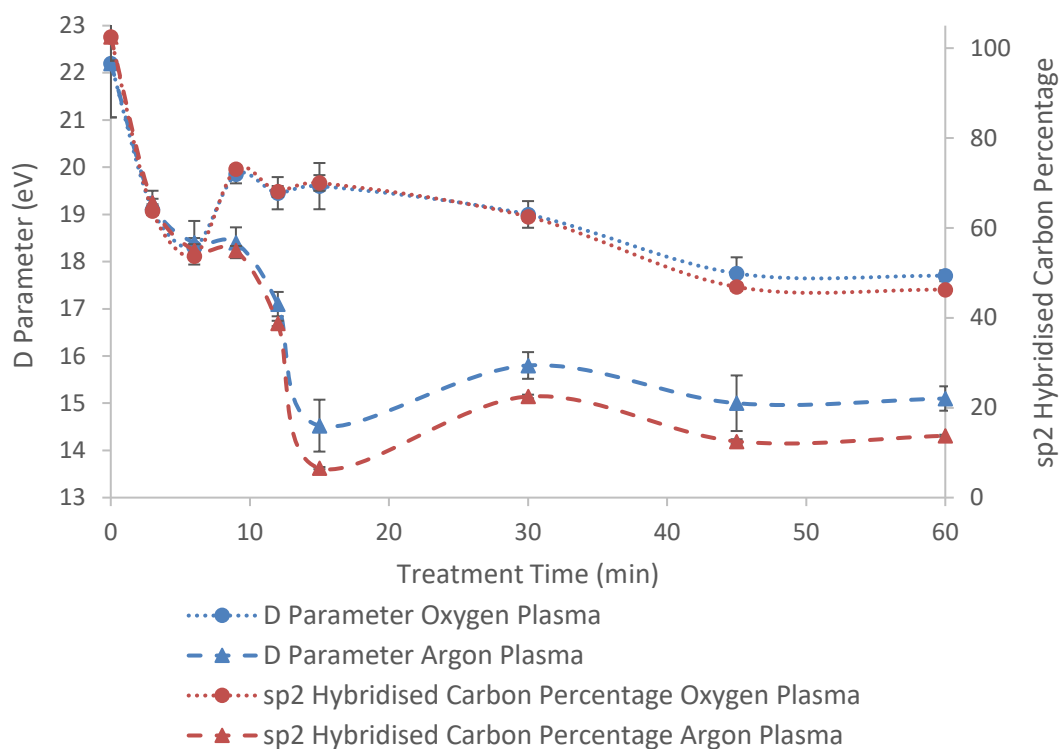
Figure 3-46: D parameter (left axis, blue points) and *sp*² hybridised carbon percentage (right axis, red points) for samples of HOPG exposed to 40 W oxygen plasma (circle points) and 40 W argon plasma (triangle points) for times ranging between 3 minutes and 60 minutes. Data points are the average of four samples, and error bars are the standard deviation from four samples.

There is a difference between the D parameters of the samples that are treated with oxygen or argon plasma, with argon samples exhibiting a lower D parameter value for all samples with treatment times of 9 minutes or longer, while treatment times shorter than 9 minutes show very similar D parameter values. The lowest D parameter achieved for the oxygen plasma treated samples is 17.5 eV while that of the argon plasma treated samples is 14.5 eV, which results in sp^2 hybridised carbon percentages of 46 % and 14 %, respectively. These results show that the argon plasma treatment has a larger impact on the hybridisation of the HOPG, and results in much of the sample being converted from sp^2 hybridised carbon to sp^3 hybridised carbon, which is consistent with the results observed in Figure 3-44 from XPS characterisation.

3.4.2.3 Conclusions

The XPS and SAM results for the chemical composition of the 40 W oxygen and argon plasma treated HOPG both show that the argon plasma results in a higher extent of modification of the surface than the oxygen plasma. There is a higher level of oxygen on the argon plasma treated samples, as well as a higher level of sputtering from the antenna resulting in higher levels of iron, nickel, and fluorine.

Both techniques also show a larger conversion of sp^2 hybridised carbon to sp^3 hybridised carbon with argon plasma than oxygen plasma, which is also due to the differences in the interactions of the oxygen and argon plasma with the HOPG.

3.5 Conclusion

Both the chemical composition and carbon hybridisations of HOPG can be modified by treating the sample surface with oxygen or argon plasma. The extent of the modification can be varied by changing the choice of source gas or the other parameters involved in the plasma treatment, that is, the length of time the sample is exposed to the plasma and the RF-coupling power used to ignite the plasma.

XPS and SAM have been used to characterise the elemental composition of each sample and have indicated that an increase in RF-coupling power produces an increase in the extent of modification of the HOPG when the source gas is argon, however a change in the RF-coupling power used to ignite oxygen plasma does not significantly change the extent of modification. When comparing the samples treated with argon and oxygen plasma it was found that an argon plasma produces a more modified HOPG surface than the oxygen plasma in terms of the chemical composition. This is the result of the differences in the species present in the two plasma and how these species interact with the HOPG surface, and also due to the deposition of iron oxides that have been sputtered from the antenna in the plasma chamber, which occurs to a larger extent with the argon plasma than the oxygen plasma.

The carbon hybridisations present on the surface of the plasma treated samples was also characterised using XPS and SAM, and it was found that an increase in the RF-coupling power used to ignite the oxygen plasma does not result in large differences in the hybridisations of carbon present on the surface. There was, however, differences noted for argon plasma ignited with different RF-coupling powers, with the higher power plasma inducing larger changes in the hybridisation of the carbon atoms and producing higher levels of sp^3 hybridised carbon. It was also observed that the argon plasma resulted in a larger change in hybridisation of the HOPG than the oxygen plasma due to the differences in the reactions that occur between the two plasma and the HOPG.

These studies have shown that it is possible to modify the surface of HOPG to produce an oxide layer while also changing the hybridisations of carbon that are present, and as a result changing the

properties of the sample surface. The extent of this modification can be controlled by changing the source gas, the applied RF-coupling power, or the exposure time of the HOPG to the plasma, and the desired properties can therefore be imparted to the surface through the use of plasma treatment.

4 DIAMOND-LIKE CARBON GROWTH

Diamond-like carbon (DLC) is becoming increasingly important for a variety of applications, particularly for medical implants and plasma facing materials in fusion reactors, as has been discussed in chapter 1.1.6. The electrical and mechanical properties of DLC films depend on the amounts of sp^2 and sp^3 hybridised carbon present within the film, which can typically be varied by controlling the deposition parameters when the film is grown by Plasma Enhanced Chemical Vapour Deposition (PECVD) [16, 90, 91, 99, 111, 114, 125, 127, 129, 130, 137, 207, 242, 243]. This growth has been achieved using a variety of conditions in the literature, however no studies have been found that use the same conditions available in the equipment at flinders university. A well as the deposition parameters, the growth of the film depends on the shape and size of the plasma chamber and the relative positions of the plasma source and sample within the chamber.

All plasma deposited films in this chapter were on silicon wafer substrates that were cleaned in oxygen plasma for 5 minutes using a carrier gas pressure of 1×10^{-2} Torr and an RF-coupling power of 30 W.

There are four experimental parameters that can be varied to influence the growth of a DLC film in this system, namely: source gas composition; pressure; RF-coupling power; and growth time. Each of these parameters was investigated systematically to determine the practical range of DLC film compositions that can be produced in this system.

4.1 Influence of Source Gas Pressure

Using methane as the source gas, the pressure of the plasma used for DLC growth was varied from 0.01 – 0.1 Torr with an Automatic Pressure Controller (APC). For these experiments the RF-coupling power was held fixed at 30 W and a growth time of 30 minutes was used. The pressure of the source gas impacts the spatial extent of the plasma sheath throughout the chamber. Consequently, the plasma density of reactive species changes at the sample, which is placed at a fixed distance from the antenna, when other parameters are held constant. At higher pressures the plasma remains more localised around the antenna, while at lower pressures the plasma spreads through the chamber. This is directly due to the different mean-free paths of the plasma species with variation in pressure. At higher pressure the mean-free path is short, thus the plasma is condensed around the antenna, while at lower pressure the mean-free path is increased and the spatial extent of the

plasma increases. While the spatial extent could potentially be monitored quantitatively through the use of a Langmuir probe to measure the electron temperature and positive ion density, for this study it was examined visually as the plasma is easily observed due to its bright colour. This variation in the spatial extent of the plasma will impact the number of plasma species impacting on the substrate surface during the plasma treatment, and is therefore expected to change the growth rate of the DLC film, with the lowest pressures expected to produce the highest growth rate.

4.1.1 XPS Results

The atomic concentrations of carbon, oxygen, and silicon from DLC samples that have been produced at various source gas pressure values are shown in Figure 4-1.
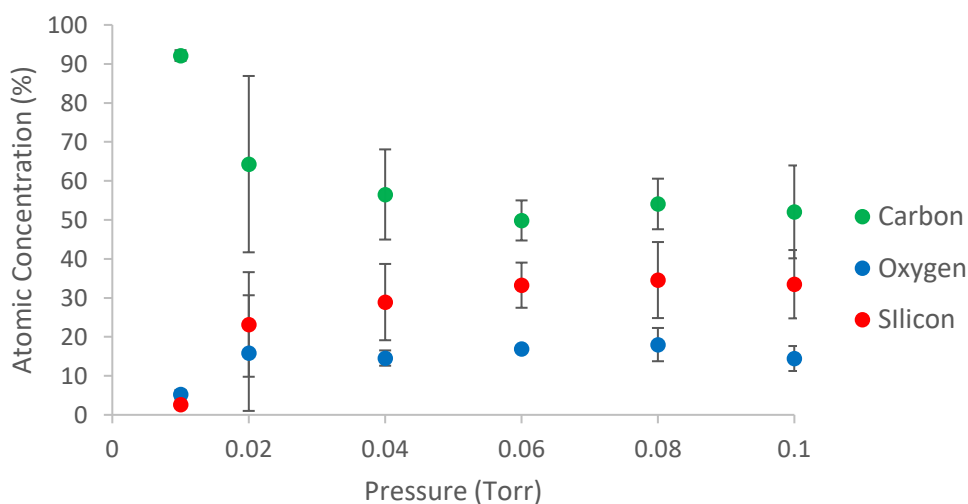
Figure 4-1: The influence of source gas pressure on atomic concentrations of carbon (green), oxygen (blue), and silicon (red) in PECVD DLC films deposited on silicon as found by XPS. Data shown is the average of three samples for each point, with the error bars showing the standard deviation calculated from these three samples.

At 0.01 Torr the sample contains 92 % carbon, 5 % oxygen, and 3 % silicon, indicating that on average the film is approximately 10 nm thick as the silicon oxide layer and silicon substrate are barely visible, or that the film may have greater thickness than this but is not completely uniform across the surface. As the source gas pressure is increased the carbon presence decreases asymptotically to 50 % at 0.06 Torr, beyond which the carbon concentration on the treated surface stays quite uniform with larger pressure values. The concentrations of oxygen and silicon vary in a similar way, with both increasing until they plateau at 0.06 Torr with values of 17 % and 33 %, respectively. This behaviour is similar to that seen in previous studies in the plasma chamber, where the effect of source gas pressure on the oxygen plasma modification of HOPG was investigated [67].

The high-resolution spectrum of the C 1s peak region of these samples was deconvoluted as described previously, with the results shown in Figure 4-2.
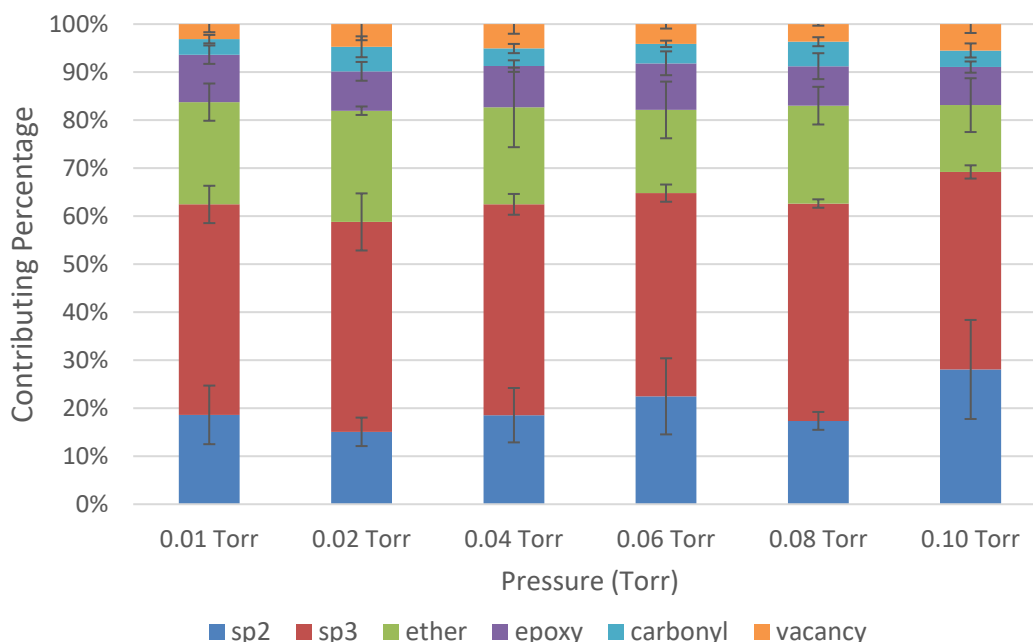
Figure 4-2: The influence of source gas pressure on the components of high resolution C 1s spectral peaks. Components are sp^2 hybridised carbon (dark blue), sp^3 hybridised carbon (red), ether (green), epoxy (purple), C=O (light blue), and carbon-vacancy (orange). Data shown is the average of three samples for each point, with the error bars showing the standard deviation calculated from these three samples.

While there is some variation in the percentage contribution of each component within the C 1s peak for the different source gas pressure values, there is no clear overall trend and the differences fall within the error bars for each component. This suggests that the composition of the film does not vary with pressure, and therefore the source gas pressure does not appear to be an experimental parameter that can be used to control the types of species present in the surface film, or perhaps even within the plasma itself. This is also consistent with other research performed over this pressure range in the chamber, although prior investigations of the oxygen plasma modification of HOPG showed that as the oxygen source gas pressure dropped below 5×10^{-3} Torr the components of the C 1s peak varied [67].

This consistency in the composition of the film is an unexpected result. On the one hand, it means that slight variations in the supply pressure during film growth will not cause large deviations in the structure or properties of the deposited film, increasing ease of replication and the ability to grow films consistently. However, it also makes it difficult to tailor the properties of the DLC if a different

sp^2/sp^3 ratio is desired.

4.1.2 SAM Results

The atomic concentrations of carbon, oxygen, and silicon were calculated for DLC samples at various pressures using the peak heights from the survey scans taken with SAM, these results are shown in Figure 4-3 as green, blue, and red data points, respectively.
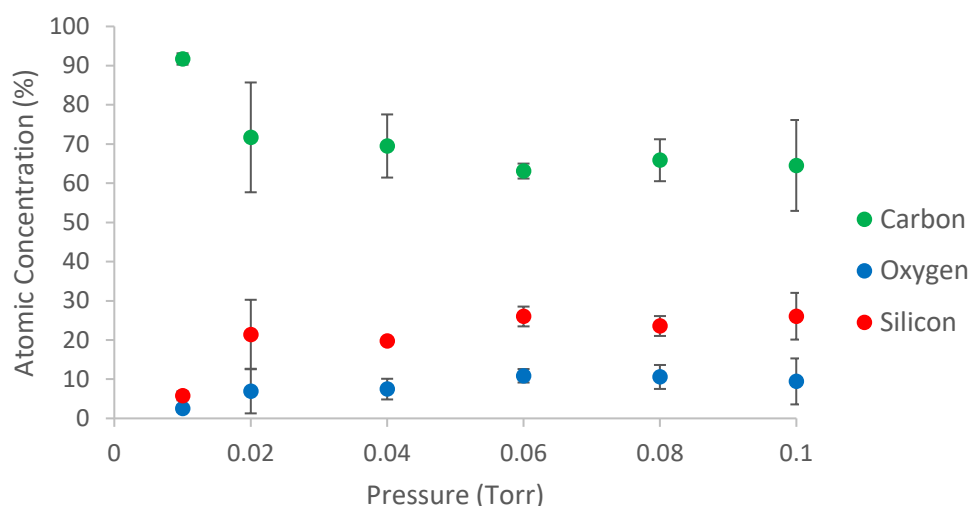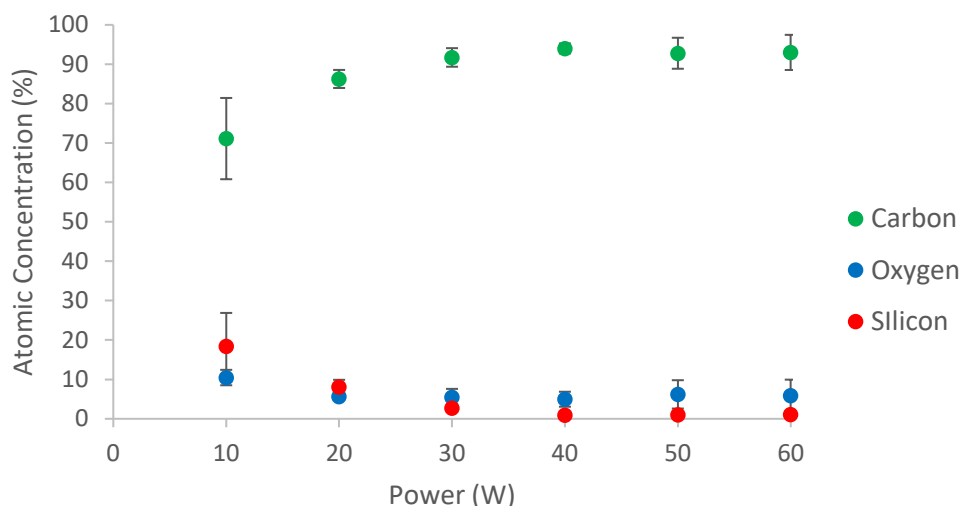

Figure 4-3: The influence of source gas pressure on atomic concentrations of carbon (green), oxygen (blue), and silicon (red) in PECVD DLC films deposited on silicon as found by SAM. Data shown is the average of three samples for each point, with the error bars showing the standard deviation calculated from these three samples.

At a source gas pressure of 0.01 Torr the surface of the plasma-modified sample contains 92 % carbon, 2 % oxygen, and 6 % silicon, with atomic concentrations changing asymptotically with pressure until 0.06 Torr, at which point the concentrations of carbon, oxygen, and silicon are 63 %, 11 %, and 26 %, respectively. This trend closely agrees with the XPS results, although the values are somewhat different. This difference is likely due to the difference in sampling depths and areas examined by the two techniques. As SAM is more surface sensitive than XPS, as has been discussed previously in section 3.2.1.1.3, the film must be thinner before the silicon content is observed to increase. Additionally, in XPS the sample area examined is approximately 10 mm x 5 mm, while in SAM the area examined is usually 535 μm x 535 μm. The area examined by XPS thus takes the average of the surface composition over a large area, while the area examined by SAM may show variations that are not averaged out.

High-resolution spectra of the C (KLL) peak were also acquired to examine the width of the differentiated peak and obtain the value for the D parameter for the different source gas pressures,

which is shown in Figure 4-4.
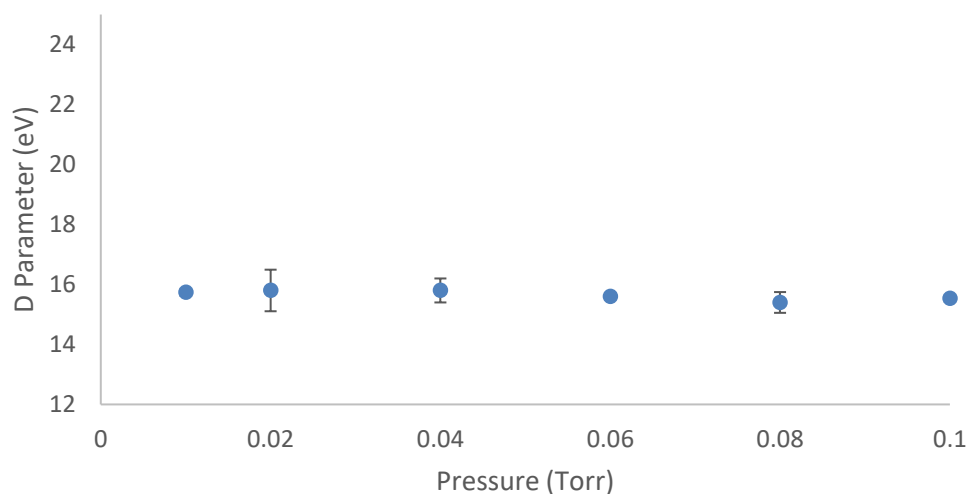
Figure 4-4: The influence of source gas pressure on the width of the differentiated C (KLL) peak (D) from high resolution SAM spectra. Data shown is the average of three samples for each point, with the error bars showing the standard deviation calculated from these three samples.

The results in Figure 4-4 show that the value of D remains quite constant, varying slightly around 15.6 eV, for each pressure tested. These results show that the sp^2/sp^3 ratio does not change with pressure over the range of values tested, and agrees with the XPS results shown in Figure 4-2.

In understanding the behaviour of the growing films it is important to understand not only the elemental or carbon hybridisation composition but also the thickness and morphology. While varying the pressure of the source gas may not be changing the composition of the film, it does change the spatial extent of the plasma sheath within the deposition chamber and this will impact on the number of reactive species reaching the substrate, and therefore the film thickness. To investigate this relationship depth profiles were performed on each sample, with the film thickness measured for each sample and displayed as a function of the source gas pressure in Figure 4-5.
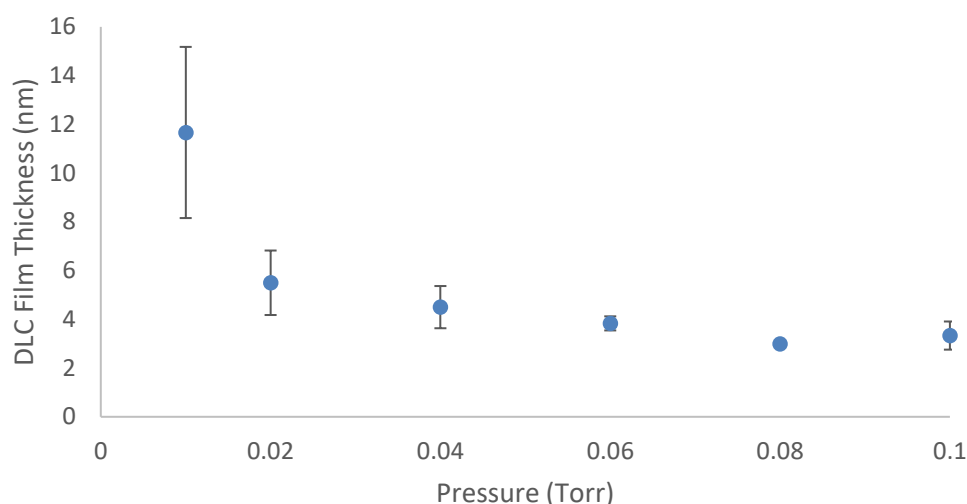
Figure 4-5: The influence of source gas pressure on the DLC film thickness as determined from depth profiling with SAM. Data shown is the average of three samples for each point, with the error bars showing the standard deviation calculated from these three samples.

As shown in Figure 4-5, the film thickness at a pressure of 0.01 Torr is ~12 nm, but the error for this pressure is large, suggesting that at this low pressure either the composition of the plasma or the spatial extent of the plasma within the chamber is not always consistent. As the pressure of the plasma is lowered, it will eventually reach a point where the reactions cannot be sustained due to the mean-free path of the plasma species becoming too large for gas molecules to continue being ionised. As the pressure approaches this point the plasma is likely to become less uniform and the growth of the film will also be less consistent. The DLC film thickness is roughly halved when the pressure is doubled to 0.02 Torr, then continues to show small decreases as the pressure continues to increase to 0.1 Torr. The errors associated with the data points also decrease as the pressure increases, suggesting that the plasma density stabilises at higher pressures. The thicknesses determined from these depth profiles agree with the depths suggested by the XPS results in Figure 4-1. However, these results do not indicate the level of uniformity of the films.

In order to examine the uniformity of the films elemental maps were acquired for the samples and are shown in Figure 4-6 for one set of these samples. First, a SEM image is acquired over the area under examination, as shown in Figure 4-6, before carbon, oxygen, and silicon elemental maps were acquired over the same area, as shown in green, blue, and red, respectively. A red-green-blue (RGB) overlay of these three elemental maps is also presented in Figure 4-6, which helps indicate the areas where the different elements are more prevalent.
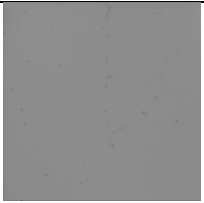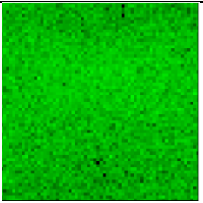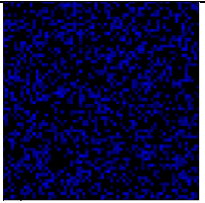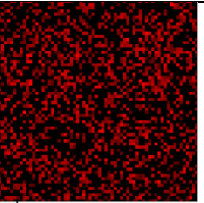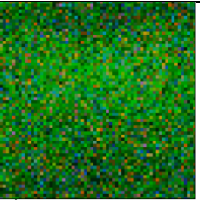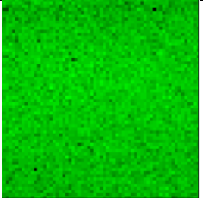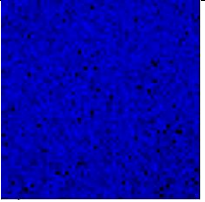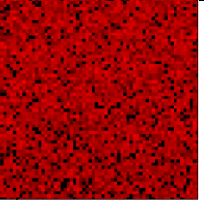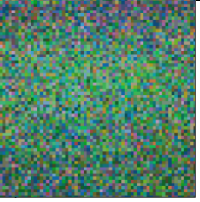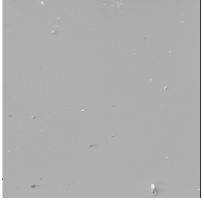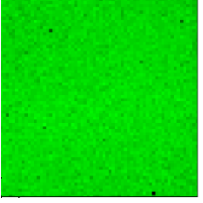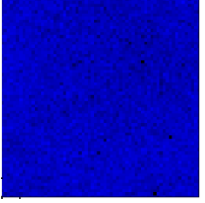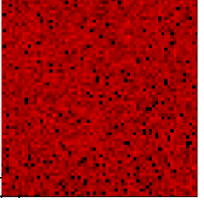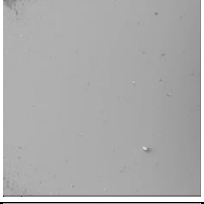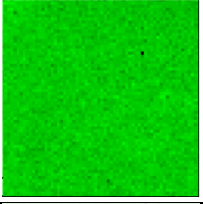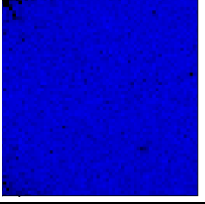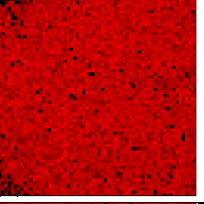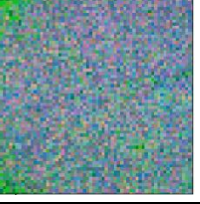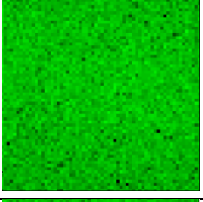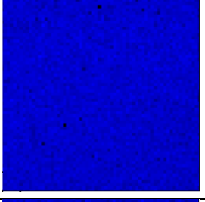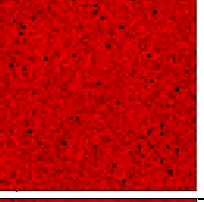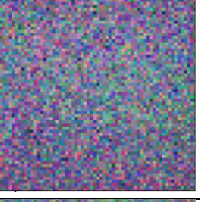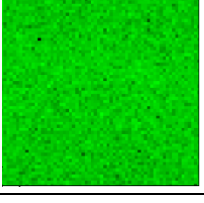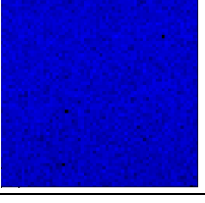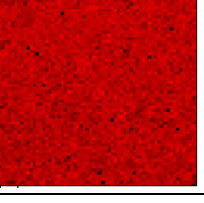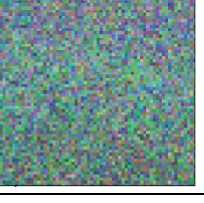
Pressure (Torr)	SEM	Carbon	Oxygen	Silicon	Overlay
0.01					
0.02					
0.04					
0.06					
0.08					
0.1					

Figure 4-6: SEM images of DLC films deposited at various source gas pressures, and carbon, oxygen, and silicon elemental maps of the same area, and the RGB overlay showing the relative amounts and positions of the elements.

The maps in Figure 4-6 indicate that the carbon, oxygen, and silicon are uniformly distributed across the sample surface. The maps for all pressures show the same level of uniformity, although there is some variation in the relative concentration of the elements with pressure, as is expected from the elemental composition results determined with both XPS and SAM shown in Figure 4-1 and Figure 4-3, respectively. The maps from other sample sets are consistent with these samples, and support the conclusion that the plasma deposition of DLC results in growth of a uniform film.

4.1.3   Conclusions

The combination of the results from both XPS and SAM show that variation in the source gas pressure used during PECVD growth of DLC from methane results in variation in film thickness, however the carbon hybridisation composition of the film remains constant. The observed variation in thickness is expected based on the change in spatial extent of the plasma throughout the deposition chamber as the pressure is varied, while the constant film composition suggests that the variation in pressure does not cause a change in the types of species present in the plasma.

4.2   Influence of RF-Coupling Power

Using methane as the source gas, the RF-coupling power used to ignite the plasma for DLC film growth was varied from 10 – 60 W, while a source gas pressure of 0.01 Torr and a growth time of 30 minutes were used for control values. The RF-coupling power can influence the type and number of species present in the plasma, depending on the source gas(es) present. In the case of methane, there is a limited number of species that can be created as all bonds in the molecule have the same bond strength. It is therefore not unreasonable to expect that altering the RF-coupling power will not significantly affect the composition of the plasma and hence the deposited surface film. However, the number of species present within the plasma will change, and thus the thickness of the DLC film grown could vary with RF-coupling power.

4.2.1   XPS Results

The atomic concentrations of carbon, oxygen, and silicon as found using XPS are shown in Figure 4-7 for films grown with RF-coupling power values between 10 W and 60 W as green, blue, and red points, respectively.
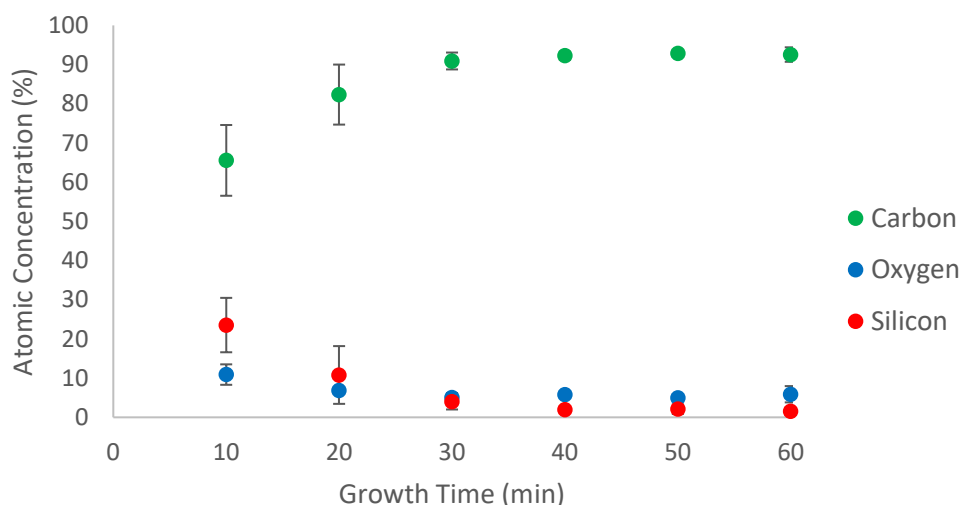
Figure 4-7: The influence of RF-coupling power on atomic concentrations of carbon (green), oxygen (blue), and silicon (red) in PECVD DLC films deposited on silicon as found by XPS. Data shown is the average of three samples for each point, with the error bars showing the standard deviation calculated from these three samples.

At a RF-coupling power of 10 W the deposited film contains elemental concentrations of carbon, oxygen, and silicon of 71 %, 10 %, and 19 %, respectively. The oxygen percentage increases with increasing power until a maximum of 94 % at a RF-coupling power of 40 W, after which further increases in power do not result in a higher carbon percentage. Similarly, the oxygen and silicon percentages decrease with increasing power until minima of 5 % and 1 % are reached, respectively, after which further increases in RF-coupling power do not result in lower concentrations. As the RF-coupling power increases there is an increase in the quantity of ionic and radical species in the chamber as more of the source gas is ionised. The results here showing an increase in the amount of carbon present on the sample are consistent with this theory as an increased quantity of reactive species will result in more reactive species interacting with the substrate per unit time, and therefore more carbon will be deposited on the substrate over the same length of time and the film thickness increases.

The high-resolution C 1*s* peaks were deconvoluted to show the chemical environments of the carbon atoms within the DLC films, with the results shown in Figure 4-8.
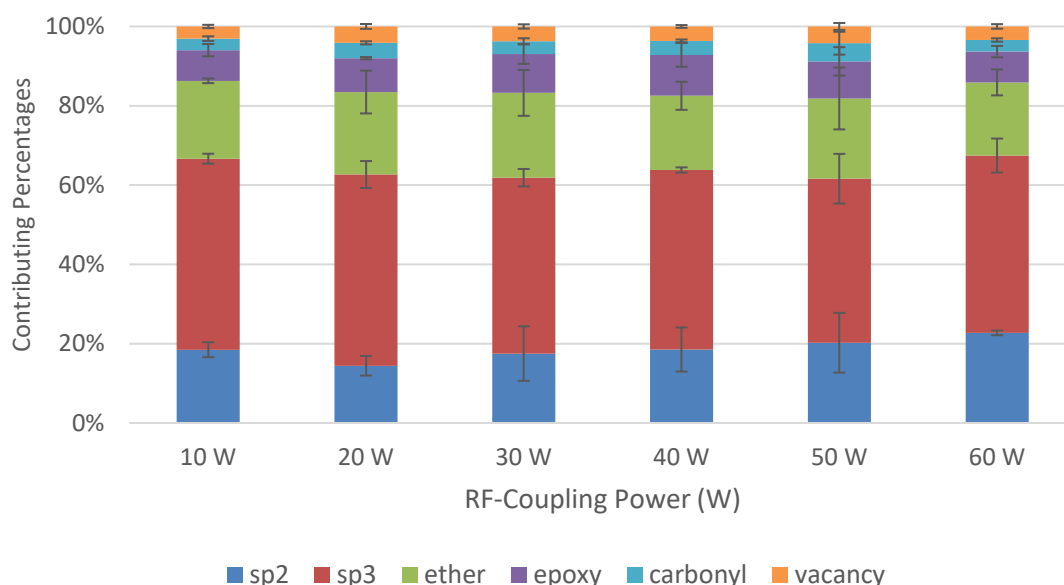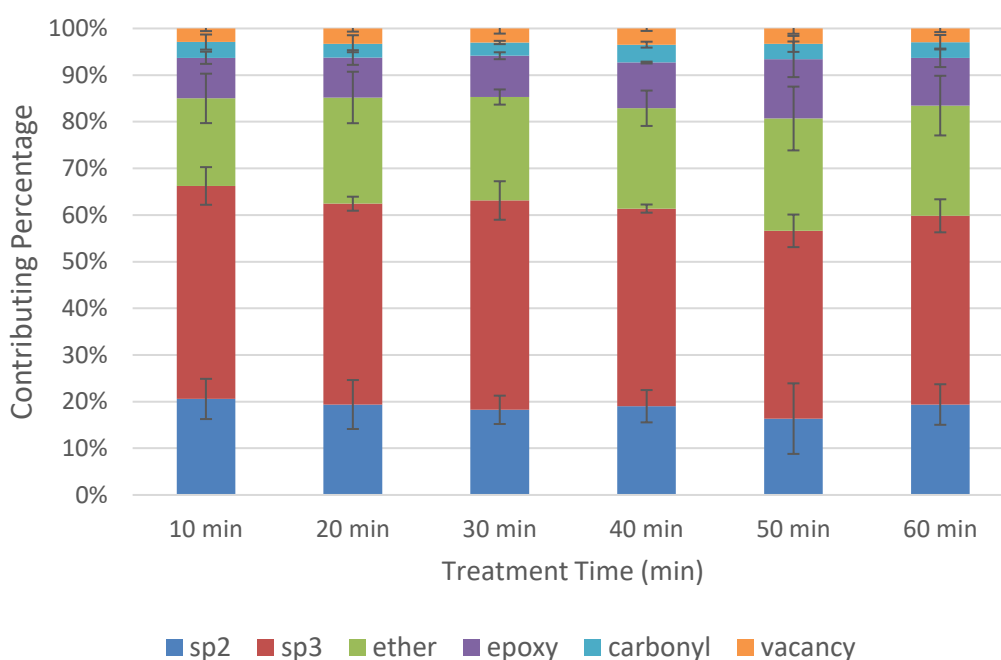
Figure 4-8: The influence of RF-coupling power on the components of high resolution C 1s spectral peaks. Components are *sp*² hybridised carbon (dark blue), *sp*³ hybridised carbon (red), ether (green), epoxy (purple), C=O (light blue), and carbon-vacancy (orange). Data shown is the average of three samples for each point, with the error bars showing the standard deviation calculated from these three samples.

The percentages that each component contributes to the C 1*s* peak are quite constant when the RF-coupling power is varied. Generally, an increase in power could be expected to change the proportion of *sp*² and *sp*³ hybridised carbon present in the DLC film due to the increased ability to break bonds within a molecule of source gas, therefore the ionic species and radicals in the plasma may be different and the composition of the film will change. However, as the source gas used in this experiment is methane and there is only one type of bond within the molecule to break, it is not surprising that the increase in RF-coupling power does not significantly change the *sp*² and *sp*³ hybridised carbon concentrations in the film.

This result indicates that the plasma chamber has the capability to consistently produce DLC films, with any small variations in RF-coupling power not causing any significant changes in the composition of the film. However, it does again lead to a difficulty in tailoring the composition of the film to suit different applications.

4.2.2   SAM Results

The elemental atomic concentrations of carbon, oxygen, and silicon found using SAM are shown in Figure 4-9 as green, blue, and red points, respectively, for each RF-coupling power value tested.
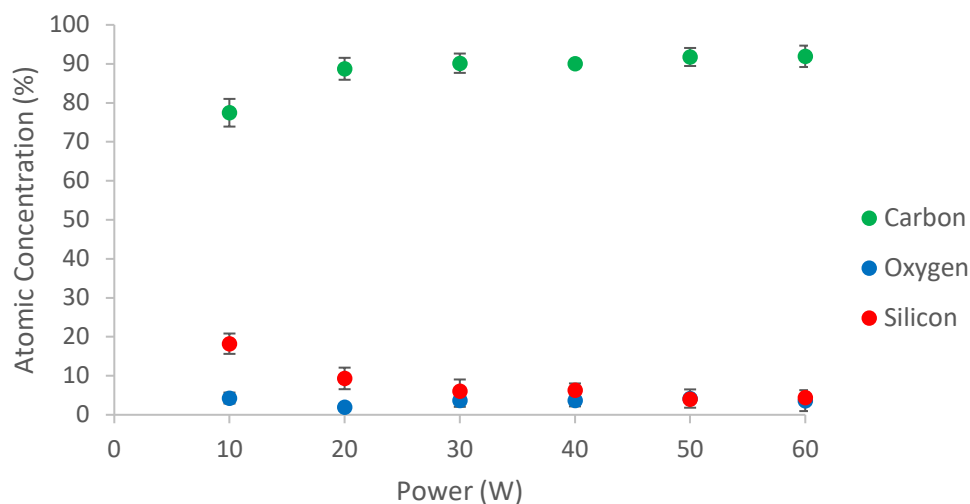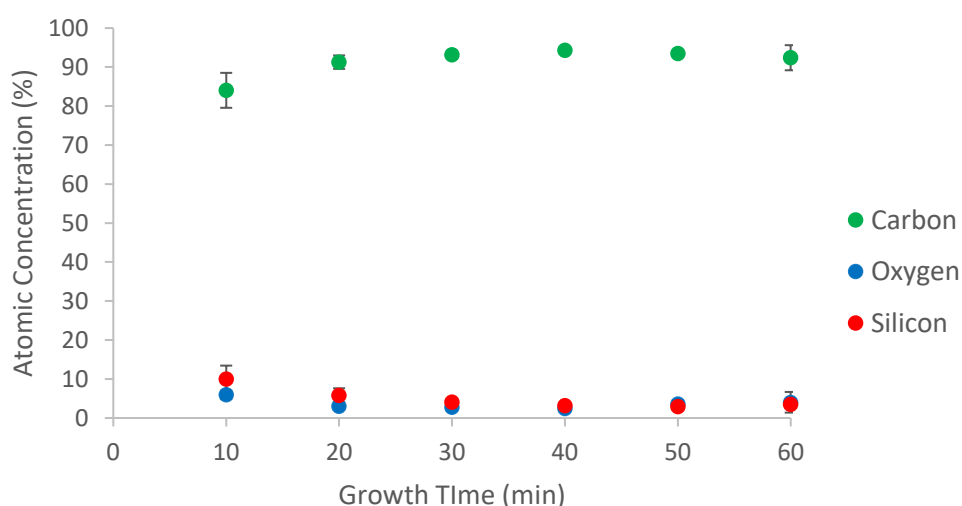
Figure 4-9: The influence of Rf-coupling power on atomic concentrations of carbon (green), oxygen (blue), and silicon (red) in PECVD DLC films deposited on silicon as found by SAM. Data shown is the average of three samples for each point, with the error bars showing the standard deviation calculated from these three samples.

The atomic percentages of carbon, oxygen, and silicon are 78 %, 4 %, and 18 %, respectively, at a RF-coupling power of 10 W. As the power increases to 30 W, the carbon atomic percentage increases to 90 % and remains approximately constant as the power increases further. Similarly, the silicon concentration decreases to about 6 % by 30 W, while the oxygen concentration remains quite constant at around 4 %. This trend corresponds to those seen in the XPS results in Figure 4-7, although the SAM results show a plateau at a lower power. This is likely to be due to the different sampling depths and sample areas examined using the two techniques. The standard deviation for all measurements is low, indicating good reproducibility in the chemical composition obtained through plasma deposition of the DLC films.

The width of the differentiated high-resolution C (KLL) peaks were also examined, with the D values shown in Figure 4-10 for RF-coupling power values between 10 W and 60 W.
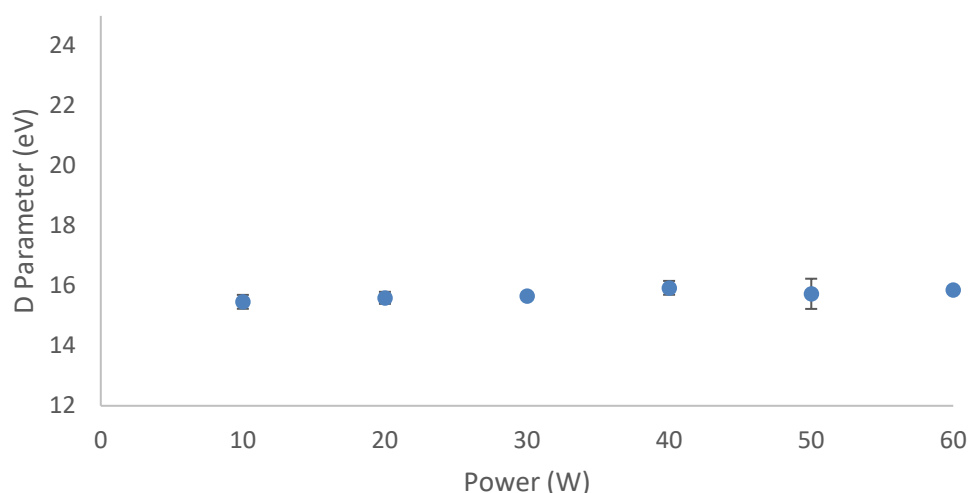
Figure 4-10: The influence of RF-coupling power on the width of the differentiated C (KLL) peak (D) from high resolution SAM spectra. Data shown is the average of three samples for each point, with the error bars showing the standard deviation calculated from these three samples.

The values for the D parameter remain at 15.6 eV for all RF-coupling powers tested, showing that the RF-coupling power does not influence the sp^2/sp^3 hybridised carbon ratio when methane is the source gas. These results agree with the results found using XPS as shown in Figure 4-8. The standard deviation is small, indicating that the reproducibility of the films is high and the films are deposited with a constant sp^2/sp^3 hybridised carbon ratio.

The film thickness was examined by performing depth profiles. Figure 4-11 shows how the DLC film thickness changes with RF-coupling power.
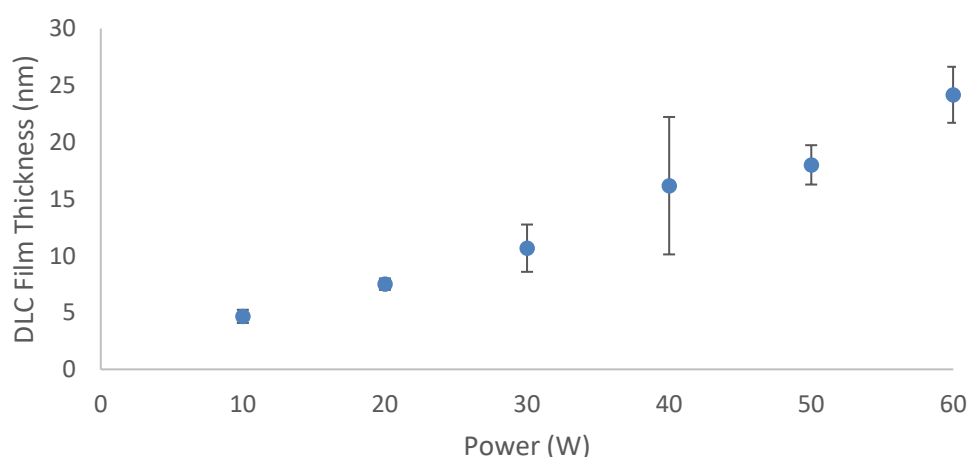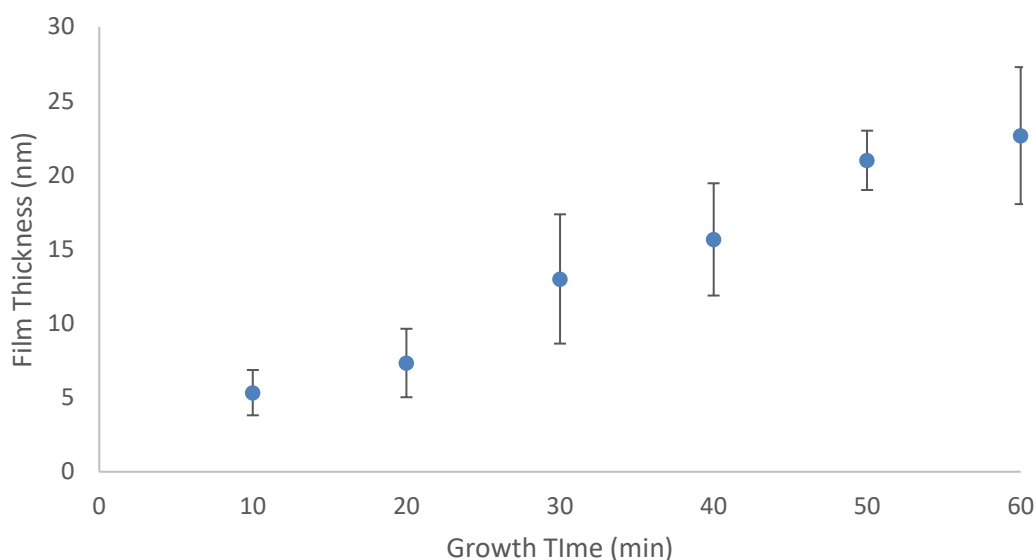

Figure 4-11: The influence of RF-coupling power on the DLC film thickness as determined from depth profiling with SAM. Data shown is the average of three samples for each point, with the error bars showing the standard deviation calculated from these three samples.

114

At a power of 10 W the film is ~4.5 nm thick, with the film thickness increasing linearly with coupling power to reach a thickness of ~24 nm when the RF-coupling power is 60 W. These results further demonstrate that while the increase in RF-coupling power does not change the identity of the species present, it increases the overall number of reactive species present in the plasma, resulting in more species reacting with the substrate per unit time and a thicker film deposited per unit time, as was expected from the nature of the plasma as discussed previously. These results agree with the atomic concentrations found using both SAM (Figure 4-9) and XPS (Figure 4-7), which indicated an initial increase in the carbon present on the surface, but after a certain thickness was reached (at powers of 30 W and 40 W, respectively), could give no further information about the increased film thickness. The standard deviation for most of these samples is small, indicating a high level of reproducibility, however the 40 W samples have a much larger standard deviation, as there were some issues with reproducibility at that power setting.

Carbon, oxygen, and silicon elemental maps were acquired for these samples to examine the uniformity of the film. The SEM image of the area examined for each sample is shown in Figure 4-12, along with the carbon (green), oxygen (blue), and silicon (red) elemental maps and RGB overlay of the three elemental maps.

The maps for all RF-coupling powers tested show that the DLC film is mostly uniform across the surface. While each element appears to be uniformly distributed across the sample surface, there are some variations in the relative concentrations of the elements with changing RF-coupling power, as was expected from the elemental compositions of the samples as determined by XPS and SAM survey scans and shown in Figure 4-7 and Figure 4-9.

Power (W)	SEM	Carbon	Oxygen	Silicon	Overlay
10					
20					
30					
40					
50					
60					
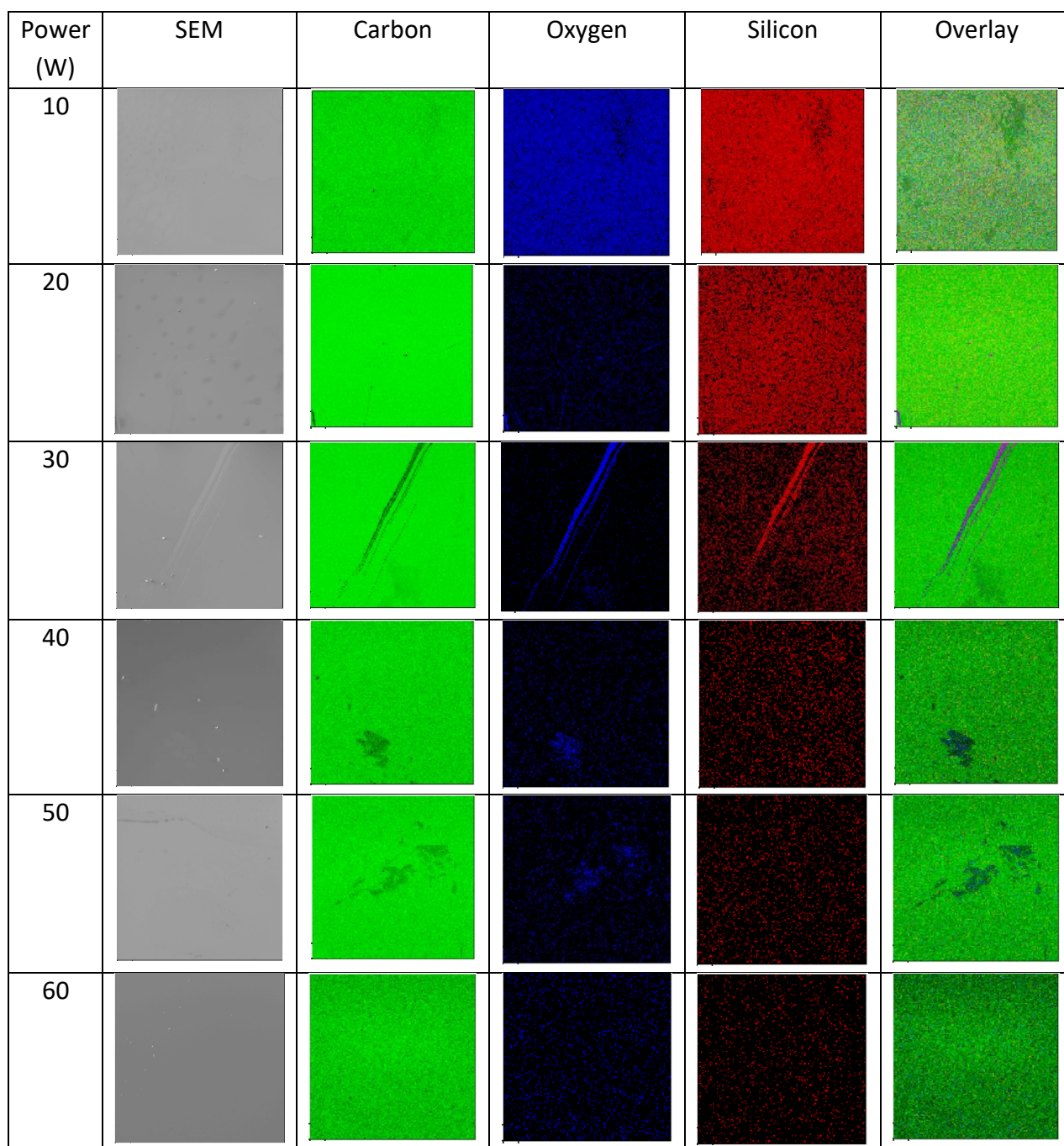
Figure 4-12: SEM images of DLC films deposited at various RF-coupling powers, and carbon, oxygen, and silicon elemental maps of the same area, and the RGB overlay showing the relative amounts and positions of the elements.

4.2.3   Conclusions

Examining the results obtained from XPS and SAM has shown that the variation in the RF-coupling power used during the PECVD growth of DLC using methane results in a variation in the thickness of the film, however the composition of the film remains constant, with very little variation in the sp^2 and sp^3 hybridised carbon concentrations. These results show that an increase in RF-coupling power results in a higher proportion of the source gas molecules being ionised within the plasma, however as the source gas is methane the composition of the plasma does not significantly change as there

is only one type of bond that can be broken. These results allow for the growth of DLC films of varying thickness without concern that the elemental or hybridisation composition of the film is unintentionally changing.

4.3   Influence of Growth Time

In order to study the influence of growth time on the deposition of DLC films control values of 30 W RF-coupling power and 1.0×10^{-2} Torr source gas pressure were used, while the length of time the substrate was exposed to the plasma was varied between 10 and 60 minutes. This is not expected to change the elemental composition or hybridisation of carbon present as the source gas remains constant, however the growth time is expected to influence the thickness of the deposited DLC film.

4.3.1   XPS Results

The atomic concentrations of carbon, oxygen, and silicon found using XPS for DLC films grown with varying plasma deposition times are shown in Figure 4-13 as green, blue, and red points, respectively.

Figure 4-13: The influence of growth time on atomic concentrations of carbon (green), oxygen (blue), and silicon (red) in PECVD DLC films deposited on silicon as found by XPS. Data shown is the average of three samples for each point, with the error bars showing the standard deviation calculated from these three samples.

The elemental concentration of carbon after a 10-minute growth time is 65 %, while that of oxygen and silicon are 11 % and 24 %, respectively. As the growth time of the film is increased the carbon percentage increases until a time of 30 minutes, at which point the carbon percentage becomes 91 % and does not change significantly with further increase in growth time. The opposite trend is

117

observed in the oxygen and silicon concentrations, which decrease asymptotically to 5 % and 4 %, respectively. These results suggest that after 30 minutes the DLC film is more than 10 nm thick as silicon and oxygen presence is attenuated. It is expected that as the growth time continues to increase the film thickness will also continue to increase, however this effect cannot be confirmed from this data. The standard deviation indicated by the error bars is larger for samples with growth times of 10 and 20 minutes, and decreases for higher growth times. However, the reproducibility here is still high, especially if slightly thicker films are desired.

The high-resolution C 1s peaks were again deconvoluted, with the percentage each component contributes to the C 1s peak shown in Figure 4-14.

Figure 4-14: The influence of growth time on the components of high resolution C 1s spectral peaks. Components are sp^2 hybridised carbon (dark blue), sp^3 hybridised carbon (red), ether (green), epoxy (purple), C=O (light blue), and carbon-vacancy (orange). Data shown is the average of three samples for each point, with the error bars showing the standard deviation calculated from these three samples

It can be seen that while there are some small variations in the component percentages, there is no trend with increasing growth time. It is not expected that the species present in the plasma will change with growth time as the RF-coupling power and source gas pressure are constant, thus it is not surprising that the composition of the film does not change with growth time. The standard deviation for these samples varies with each component, however the small variation in the components fall within the standard deviations, indicating that the films can be created with a

reasonably high level of reproducibility in terms of their carbon hybridisation.

The combination of the XPS results shows that an increase in growth time does not impact the carbon hybridisations present in the film, however it does increase the thickness of the DLC film.

4.3.2   SAM Results

The atomic concentration of carbon, oxygen, and silicon present in the film as found using SAM are shown in Figure 4-15 in green, blue, and red points, respectively.

Figure 4-15: The influence of growth time on atomic concentrations of carbon (green), oxygen (blue), and silicon (red) in PECVD DLC films deposited on silicon as found by SAM. Data shown is the average of three samples for each point, with the error bars showing the standard deviation calculated from these three samples.

The elemental concentrations of carbon, oxygen, and silicon after a 10-minute deposition time are 84 %, 6 %, and 10 %, respectively. At 20 minutes the concentration of carbon has increased to 91 %, and only slightly increases to 94 % with further increases of growth time. Similarly, the concentrations of oxygen and silicon decrease to 3 % and 6 %, respectively, at 20 minutes growth time, and the silicon content further decreases to 3 % with no further change in oxygen content with higher growth times. This indicates that after 20 minutes the DLC film thickness is greater than 5 nm, and is in agreement with the results from XPS in Figure 4-13. It is expected that the film thickness will continue to increase with further increases in growth time, however this cannot be confirmed from these results and further investigation with SAM is needed. The standard deviation for all samples is quite low, indicating that the elemental composition of the DLC film is reproducible for all growth times.

119

The C(KLL) peak width, D, is shown for the varying growth times in Figure 4-16.
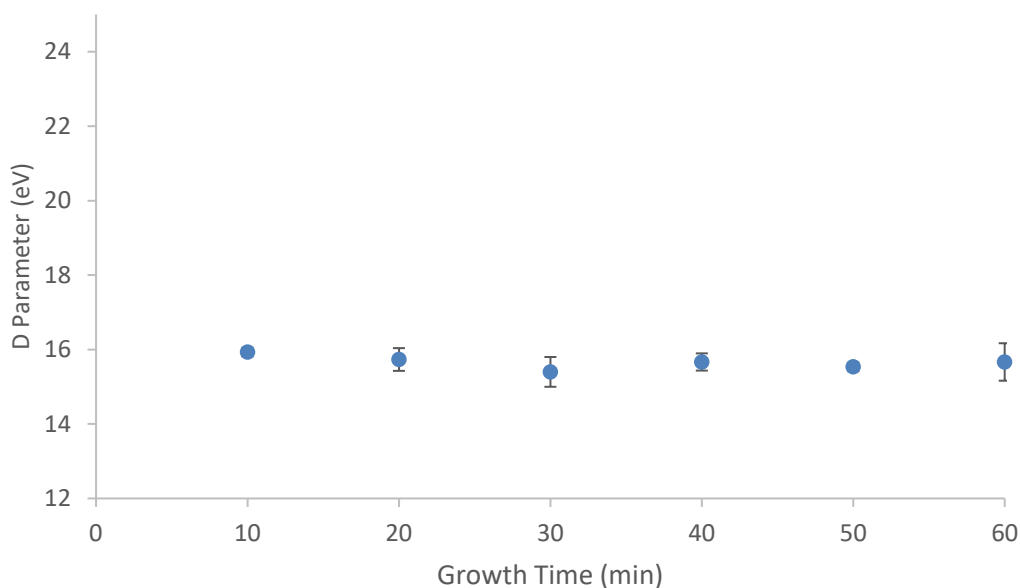
Figure 4-16: The influence of growth time on the width (D) of the differentiated C (KLL) peak. Data shown is the average of three samples for each point, with the error bars showing the standard deviation calculated from these three samples.

It can be seen in Figure 4-16 that D does not change with growth time, which is as expected based from the deconvolution of the C 1s peak as shown in Figure 4-14. The species present in the methane plasma are not expected to change as the growth time changes, thus the composition of the DLC film is not expected to change, only the thickness. The standard deviation is again very small, indication a high level of reproducibility in the carbon hybridisations present in the plasma grown DLC films at all deposition times tested.

The thickness of the DLC film with varying growth time is shown in Figure 4-17.

Figure 4-17: The influence of growth time on the DLC film thickness as determined from depth profiling with SAM. Data shown is the average of three samples for each point, with the error bars showing the standard deviation calculated from these three samples.

The depth profile results show a linearly increasing trend in the DLC film thickness as the growth time increases, with a thickness of 5.5 nm after a ten-minute growth time increasing to 23 nm after 60 minutes. These results agree with the XPS film elemental composition results shown in Figure 4-13, as after 30 minutes growth time the film is thicker than 10 nm, and with the SAM film elemental composition results shown in Figure 4-15, as after 20 minutes growth time the film is thicker than 5 nm.

Elemental maps of carbon. oxygen, and silicon were acquired for these samples to study how the uniformity of the film changes with increasing growth time. The maps for all growth times investigated are shown in Figure 4-18, where the carbon, oxygen, and silicon maps are coloured green, blue, and red, respectively. The RGB overlay is also shown for each sample.

At all growth times the distribution of the elements is quite uniform across the surface, however as the growth time increases the amount of carbon present on the surface is seen to increase, as shown by the increasing amount of green in the RGB overlays. This correlates with the atomic percentages observed with both XPS and SAM, as shown in Figure 4-13 and Figure 4-15, respectively.
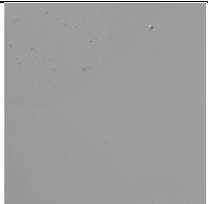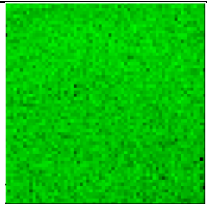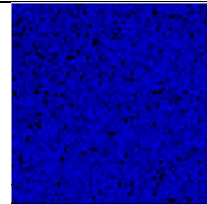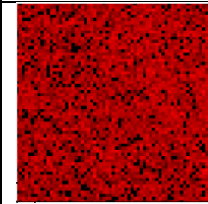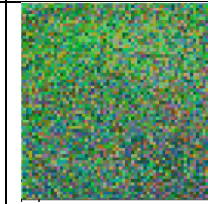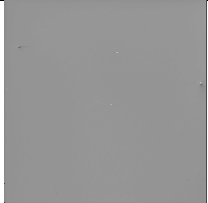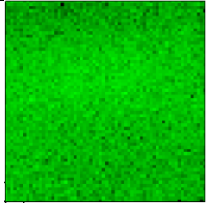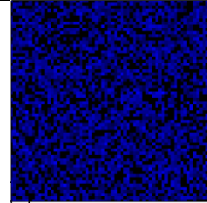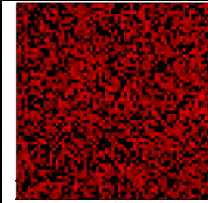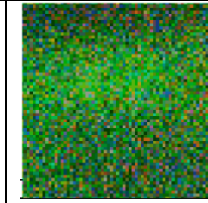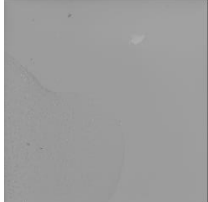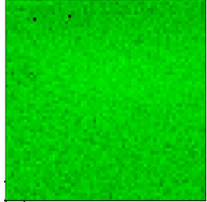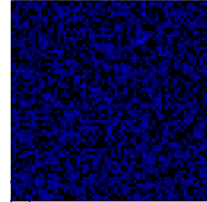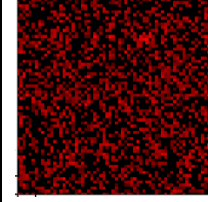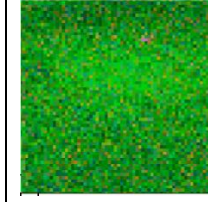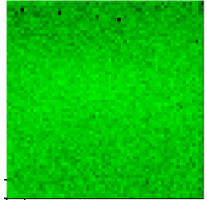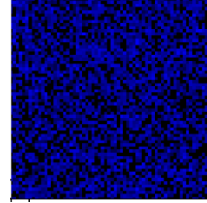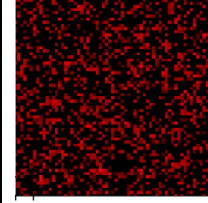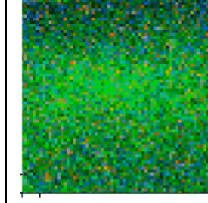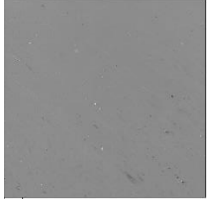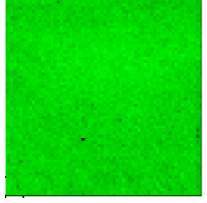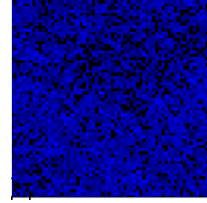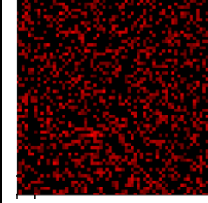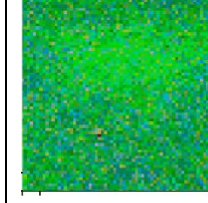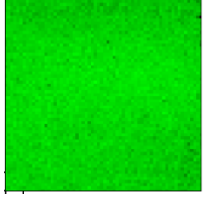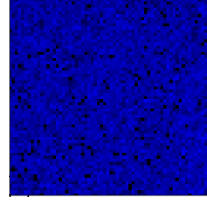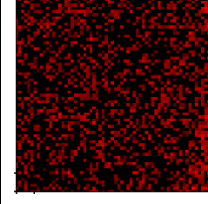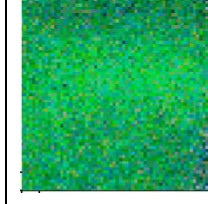
Growth Time (min)	SEM	Carbon	Oxygen	Silicon	Overlay
10					
20					
30					
40					
50					
60					

Figure 4-18: SEM images of DLC films deposited with various growth times, and carbon, oxygen, and silicon elemental maps of the same area, and the RGB overlay showing the relative amounts and positions of the elements.

4.3.3   Conclusions

Through examination of the results from XPS and SAM it has been shown that an increase in the growth time of the DLC film results in an increase in the film thickness, however the composition of the film does not change. This result is supported by the plasma composition, which is expected to be constant with variation in the growth time as no variables that influence the plasma conditions are changed, the sample is simply exposed to that plasma for longer. However, there is some

variation in the film composition, which is likely due to the nature of plasma, where the precise species, and movements of those species, are never identical.

4.4   Influence of Source Gas Composition

Plasma deposited DLC films have been produced with a range of gas compositions in the literature, including mixing methane with argon or hydrogen in various concentrations to vary the properties of the resultant film [83, 113, 116, 134-137]. In order to examine the influence of methane concentration when diluted with argon or hydrogen a series of different concentrations were tested using control values of 30 minute growth time, 30 W RF-coupling power, and 1×10^{-2} Torr total pressure, with the different concentrations tested by changing the partial pressures of methane and diluting gas within the plasma.

4.4.1   Methane and Argon Gas Mixture

The impact of diluting the methane source gas with argon is expected to be observed in the growth and composition of the DLC film. The species within an argon plasma are large, and so argon plasma can be used for cleaning surfaces by bombarding the surface and knocking away impurities. Argon plasma has also been used to modify the surface of graphite to create a sp^3 hybridised layer, which it does by bombarding the surface and breaking sp^2 carbon bonds. It was thus expected that the argon plasma will change the overall growth rate of the DLC film by bombarding the surface causing some removal of deposited carbon. As sp^3 C-C bonds are weaker than sp^2 C-C bonds it could also be expected that the sp^3 carbon bonds will be broken preferentially, thus decreasing the sp^3 hybridised carbon content.

The DLC films are deposited with a 30-minute growth time, a total pressure of 0.01 Torr, and a RF-coupling power of 30 W while the partial pressures of the methane and argon within the plasma were varied to achieve mixes containing between 10 % and 100 % methane.

4.4.1.1 XPS Results

The concentrations of methane and argon within the plasma were varied systematically, with concentrations of methane ranging between 10 % and 100 %. The atomic concentrations of carbon, oxygen, and silicon as found using XPS are shown in Figure 4-19 as green, blue, and red points,
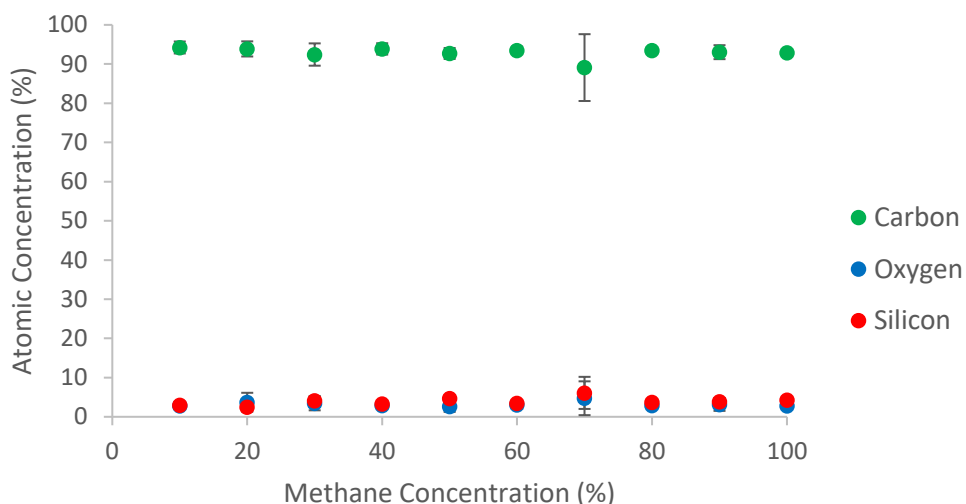
respectively.
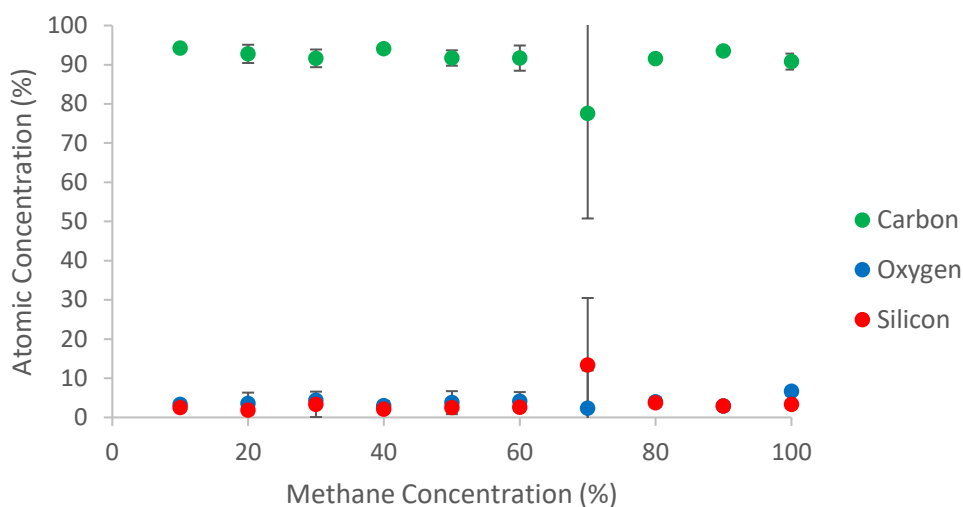
Figure 4-19: The influence of argon and methane concentration on atomic concentrations of carbon (green), oxygen (blue), and silicon (red) in PECVD DLC films deposited on silicon as found by XPS. Data shown is the average of two samples for each point, with the error bars showing the standard deviation calculated from these two samples.

It can be seen from Figure 4-19 that the elemental concentrations are quite constant across the different methane concentrations, with concentrations of 93 %, 5 %, and 2 % for carbon, oxygen, and silicon, respectively. There is an exception at 70 % methane, where the average carbon percentage is considerably lower at 78 % due to one of the samples having a much lower carbon percentage than the other. However, given the consistency within all the other concentrations tested it is expected that there was some issue with that one sample, and the other sample better reflects the actual composition of the film grown at 70 % methane. These results show that there is no change in the film composition with decreasing methane concentration, and also that the film remains thicker than 10 nm as the underlying substrate is not detected.

The high-resolution C 1s peak from XPS was deconvoluted, with the percentage that each component contributes to the peak given in Figure 4-20.
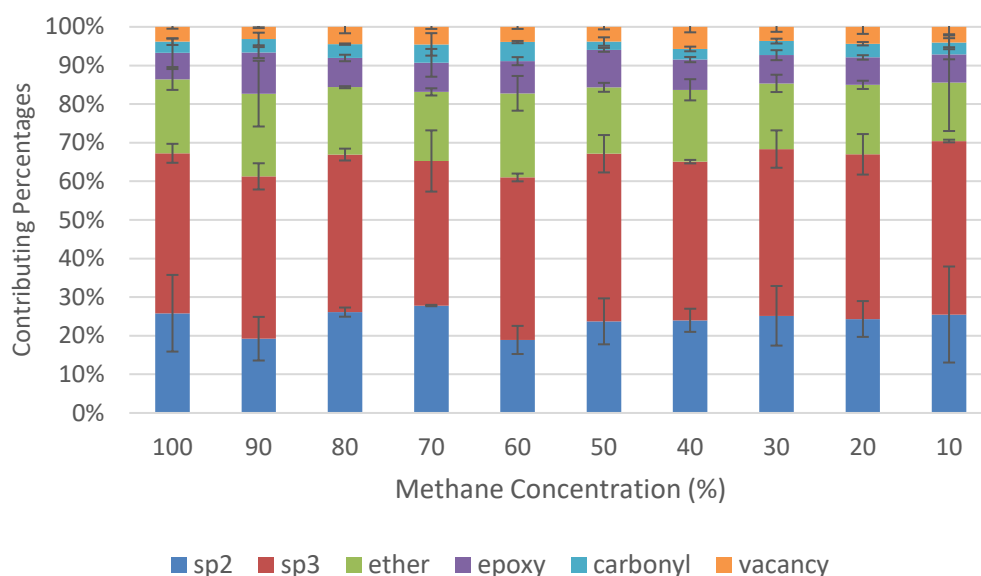
Figure 4-20: The influence of argon and methane concentration on the components of high resolution C 1s spectral peaks. Components are sp^2 hybridised carbon (dark blue), sp^3 hybridised carbon (red), ether (green), epoxy (purple), C=O (light blue), and carbon-vacancy (orange). Data shown is the average of two samples for each point, with the error bars showing the standard deviation calculated from these two samples

There are some small variations in the percentages of these components, however there is no observable trend across the partial pressures of the methane and argon are varied. These results show that the carbon chemical environments do not change with variation in methane concentration. This result suggests that the addition of argon species to the plasma does not change the hybridisation of carbon within the film, although it was expected that there would be some change based on the bombarding nature of argon species on the carbon surface.

The results from XPS combine to indicate that the presence of argon to dilute the concentration of methane within the plasma does not significantly impact film growth in terms of either the elemental composition or carbon hybridisations present in the film, regardless of whether the methane is diluted to a 9:1 ratio or a 1:9 ratio with argon.

4.4.1.2 SAM Results

The effect of diluting the methane plasma with argon was also examined with SAM, with the atomic concentrations of carbon, oxygen, and silicon shown in Figure 4-21 as green, blue, and red points, respectively, for all partial pressures examined.

Figure 4-21: The influence of argon and methane concentration on atomic concentrations of carbon (green), oxygen (blue), and silicon (red) in PECVD DLC films deposited on silicon as found by SAM. Data shown is the average of three samples for each point, with the error bars showing the standard deviation calculated from these three samples.

The concentrations of carbon, oxygen, and silicon are quite constant at 94 %, 3 %, and 3 %, respectively, across all methane concentrations tested. The exception is the 70 % methane sample, which has a lower carbon percentage of 89 % and higher oxygen and silicon concentrations of 5 % and 6 %, respectively. These results are in agreement with the XPS results shown earlier in Figure 4-19, however the effect has been slightly minimised by the use of three samples, two of which show carbon concentrations of 94 % while the other one 80 %. This supports the supposition that the sample of lower carbon concentration was anomalous in some way and does not represent the treatment that usually occurs with the 70 % methane plasma.

The D parameter values for each these samples was measured using SAM and is shown in Figure 4-22 as a function of methane concentration.
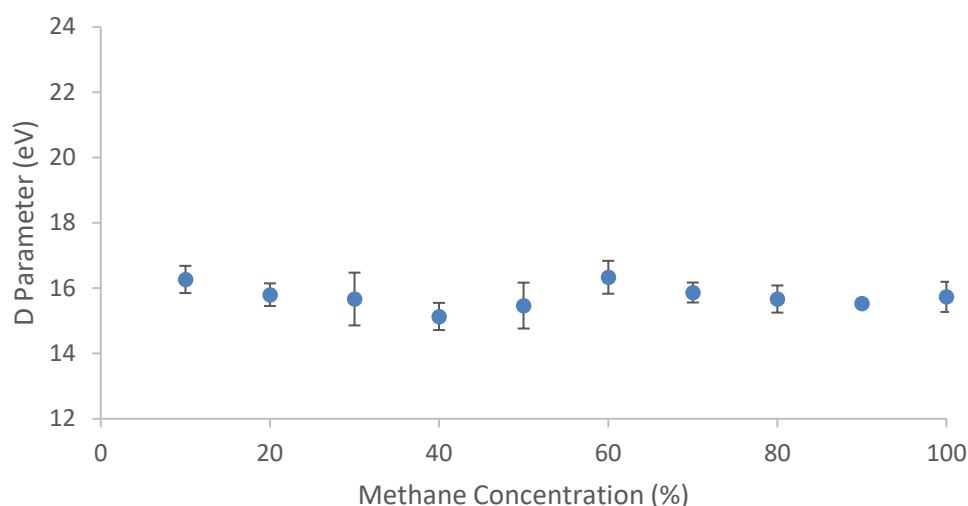
Figure 4-22: The influence of argon and methane concentration on the width of the differentiated C (KLL) peak (D) from high resolution SAM spectra. Data shown is the average of three samples for each point, with the error bars showing the standard deviation calculated from these three samples.

From these results it can be seen that there are some small variations in the D parameter, and hence the hybridisation, of the DLC film as the methane concentration changes. However, these variations do not occur in any systematic way, and the error bars are larger than those exhibited in other data sets and account for these variations, thus it can be concluded that there is no effect on the carbon hybridisation with changing methane concentration. These results are in agreement with the results from the deconvolution of the C 1*s* peak from XPS shown in Figure 4-20. The increase in the size of the error bars indicates that while there is no systematic change, there is more variation between individual samples and it may be more difficult to reproducibly create DLC films with a methane and argon mixture.

The thickness of the DLC film with varying methane and argon concentration is shown in Figure 4-23.
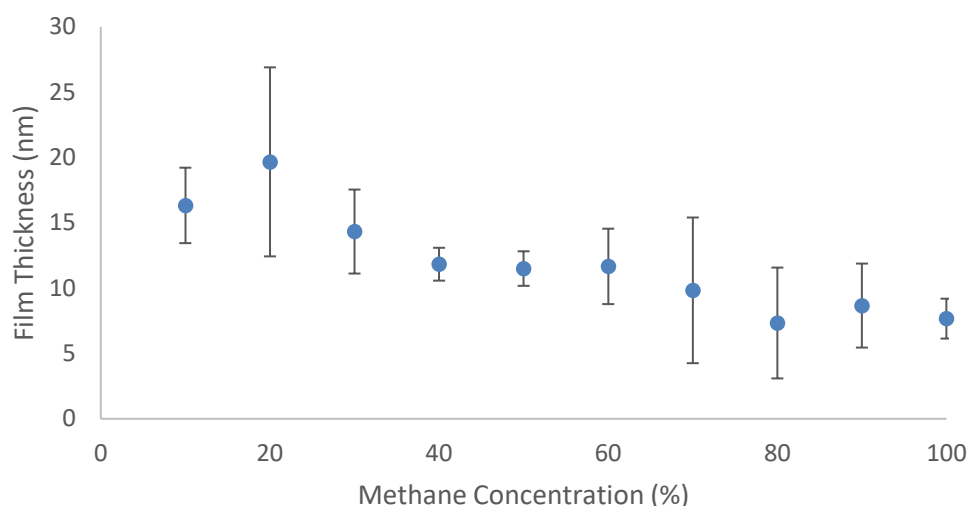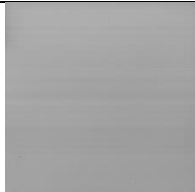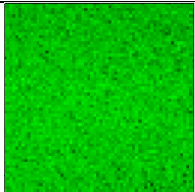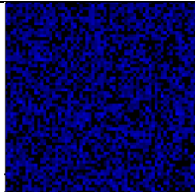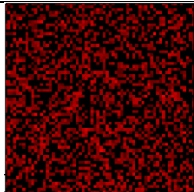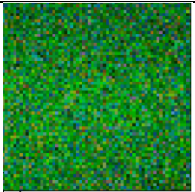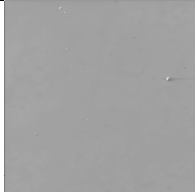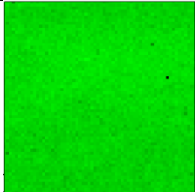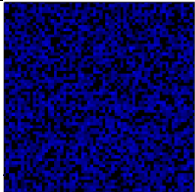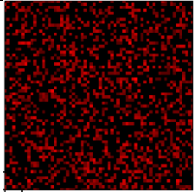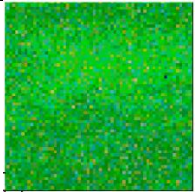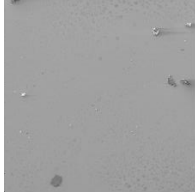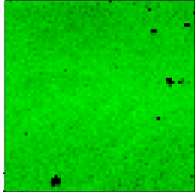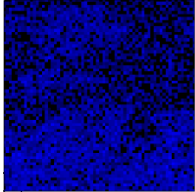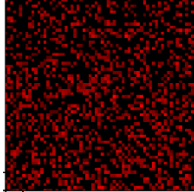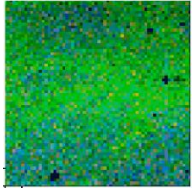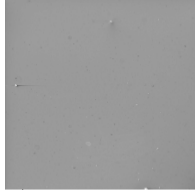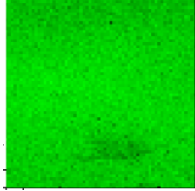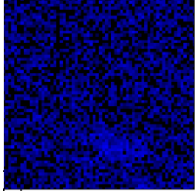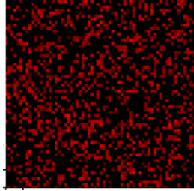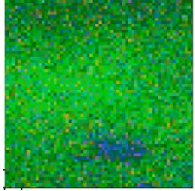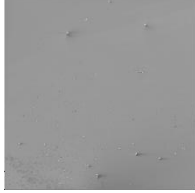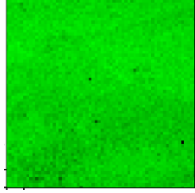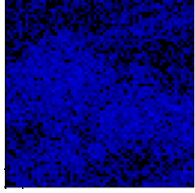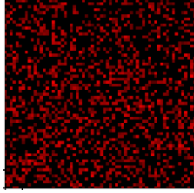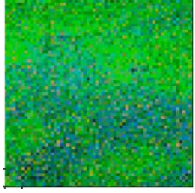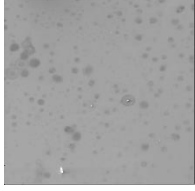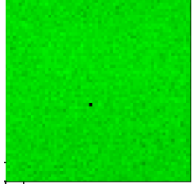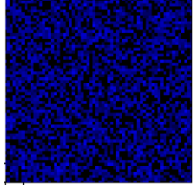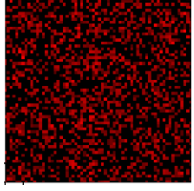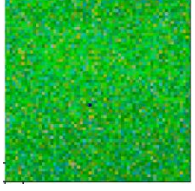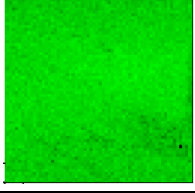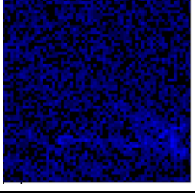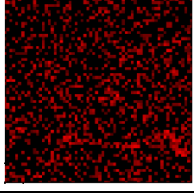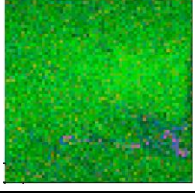
Figure 4-23: The influence of argon and methane concentration on the DLC film thickness as determined from depth profiling with SAM. Data shown is the average of three samples for each point, with the error bars showing the standard deviation calculated from these three samples.

There is a slight trend of increasing film thickness with decreasing methane concentration, however the error bars on these samples are large and many values lie within each other's uncertainties and therefore this trend cannot be stated with any certainty. It is also highly likely that any trend observed is a result of the method used to obtain the correct partial pressures. As the plasma apparatus used for this research only has one automatic flow rate controller, when two gases are used one must be supplied through a manual control valve. When a gas is ignited into a plasma the pressure recorded by the baratron gauge changes, and the flow rate must be adjusted to maintain the correct pressure while the plasma is ignited. When the gas is introduced through the automatic flow controller this occurs automatically, however when the manual control value is used this process must be performed by hand, which takes a short period of time (usually less than one minute). As a result of this, there is an introduction of a thin layer of DLC that is grown from an entirely methane-based plasma before the film grown under methane and argon is started. The thickness of this methane grown film expected to be 1-2 nm based on the previous results with methane deposited films shown in in Figure 4-17, which is only 12-25 % of the thickness of the thinnest films deposited with methane and argon (Figure 4-23). This methane only film will not be the same thickness for each sample as there is some variation in the time taken to manually adjust the pressure, however this variation is expected to be random as there is no trend in the length of time required to achieve the correct partial pressure manually. It has been shown previously that a lower methane concentration results in the plasma having a larger spatial extent throughout the plasma chamber, and therefore results in a higher deposition rate, as was shown in Figure 4-5. This

will cause a thicker methane grown layer beneath the methane-argon grown layer when the partial pressure of methane is lower, increasing the overall DLC film thickness, and resulting in the slight trend of thicker DLC films grown with lower methane concentrations.

Elemental maps of carbon, oxygen, and silicon were also taken for these samples, and are shown in Figure 4-24 in green, blue, and red, respectively, along with the RGB overlay of these elemental maps.

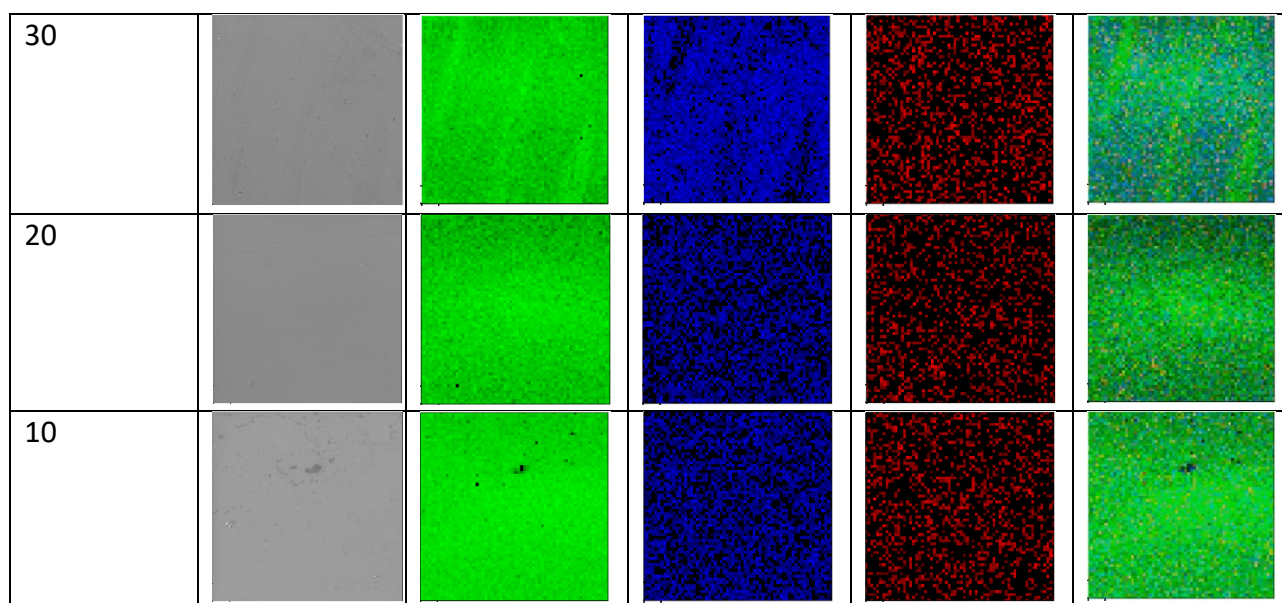| Methane Percentage	SEM	Carbon	Oxygen	Silicon	Overlay
100					
90					
80					
70					
60					
50					
40					

Figure 4-24: SEM images of DLC films deposited with various methane and argon concentrations, and carbon, oxygen, and silicon elemental maps of the same area, and the RGB overlay showing the relative amounts and positions of the elements.

There are some small variations in the concentrations of carbon, oxygen, and silicon observed in the elemental maps in Figure 4-24, but no overall trend is observed. This matches the atomic concentrations found using XPS and SAM, as shown in Figure 4-19 and Figure 4-21, respectively.

4.4.1.3 Conclusions

The combined results from XPS and SAM indicate that at the source gas pressure and RF-coupling power tested there was no impact on the film growth when argon was introduced into the methane plasma, at any ratio concentration between 10 % and 90 %. These results are not what was expected based on previous work that has been performed with argon plasma, which showed that an increase in the argon content in the plasma results in a decrease in the deposition rate of the DLC film [137]. As has been previously discussed the plasma deposition parameters have an effect on the deposition rate, and hence the thickness, of the DLC film, and the parameters used in the literature include much higher RF-coupling power values (50 − 350 W) and source gas pressures (0.3 Torr) [137] than those used in this study (30 W RF-coupling power and 0.01 Torr). Along with the different construction of the plasma chamber causing different spatial distributions of the plasma, these factors are likely the cause of the difference between the DLC film depositions. It has also been shown in the literature that the presence of argon changes the dominant carbon containing species within the methane-argon plasma from CH_x to C_2 as the amount of methane present decreases to as low as 1 %, which could have been expected to change the carbon hybridisation content of the DLC film [134]. However, this work did not find any changes in carbon hybridisation with changing

methane:argon ratio, likely as a result of the higher methane fractions used. Due to the precision of the pressure gauges and flow rate controllers used for this work a methane percentage below 10 % cannot be accurately achieved, therefore the differences between the hybridisations of the DLC films grown in this work and the literature values are likely a result of the differing deposition conditions.

4.4.2 Methane and Hydrogen Gas Mixture

Mixing methane and hydrogen as the source gas for depositing DLC films is expected to influence both the growth and composition of the film. The presence of excess hydrogen has been shown in the literature to stabilise the formation of sp^3 hybridised carbon by terminating dangling bonds and preventing the formation of sp^2 hybridised carbon [83, 116].

The DLC films are deposited with a 30-minute growth time, a total pressure of 0.01 Torr, and a RF-coupling power of 30 W while the partial pressures of the methane and hydrogen within the plasma were varied to achieve mixes containing between 20 % and 100 % methane.

4.4.2.1 XPS Results

A series of methane and hydrogen concentrations were tested, ranging from 20 % to 100 % methane diluted with hydrogen. The atomic concentrations of carbon, oxygen, and silicon were found using XPS and are shown in Figure 4-25 as green, blue, and red points, respectively, for each ratio.
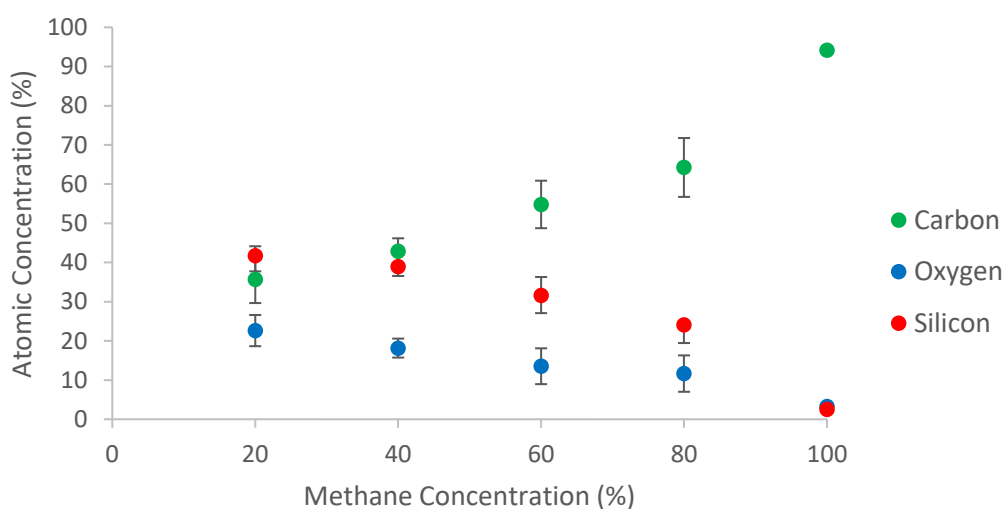

Figure 4-25: The influence of hydrogen and methane concentration on atomic concentrations of carbon (green), oxygen (blue), and silicon (red) in PECVD DLC films deposited on silicon as found by XPS. Data shown is the average of three samples for each point, with the error bars showing the standard deviation calculated from these two samples.

131

It can be seen that by diluting methane plasma with hydrogen the percentage of carbon in the surface film decreases from 94 % for pure (i.e. 100 %) methane to 36 % when the methane concentration is diluted to 20 % methane. Conversely, oxygen and silicon percentages increase as the methane concentration decreases, with oxygen changing from 3 % to 23 % and silicon from 3 % to 42 %. This trend suggests that the presence of excess hydrogen inhibits film growth.

Deconvolution of the C 1s peak from XPS into components shows a trend in the changing percentages of the components, as shown in Figure 4-26.
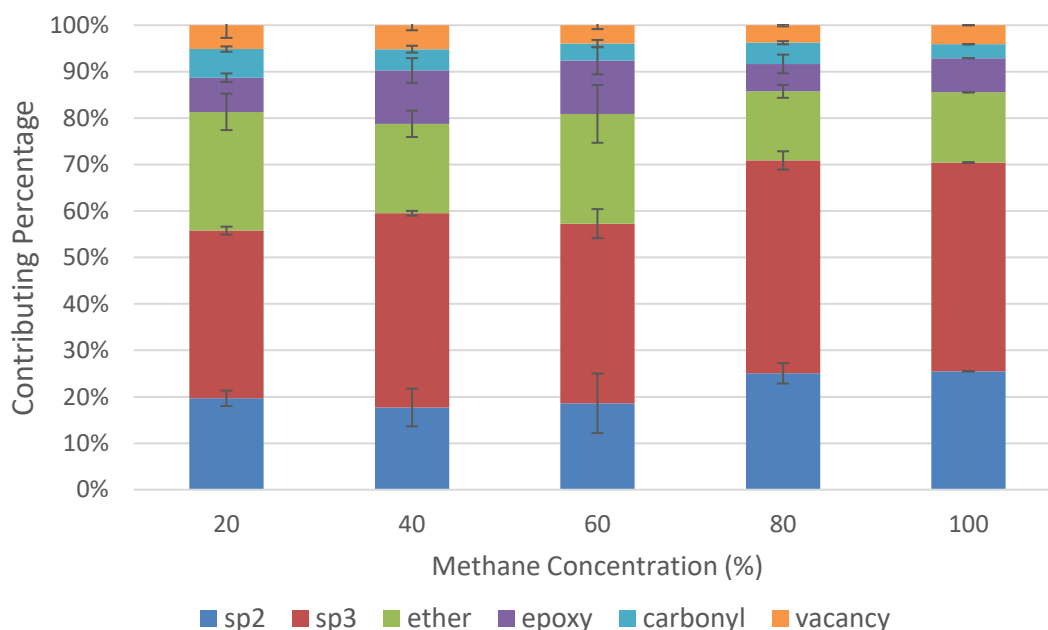

Figure 4-26: The influence of hydrogen and methane concentration on the components of high resolution C 1s spectral peaks. Components are sp^2 hybridised carbon (dark blue), sp^3 hybridised carbon (red), ether (green), epoxy (purple), C=O (light blue), and carbon-vacancy (orange). Data shown is the average of three samples for each point, with the error bars showing the standard deviation calculated from these three samples

It can be seen that as the methane concentration decreases, the overall amount of C-C bonds decreases and the C-O species, mainly from the ether component, increase. However, the ratio of sp^2 to sp^3 hybridised C-C bonds does not change, indicating that the introduction of hydrogen results in the incorporation of more oxygen into the film without disrupting the carbon hybridisations present. This is possibly due to the hydrogen capping the remaining bonds on the oxygen atoms after they bond to the carbon surface.

Overall the XPS results show that an increase in the hydrogen content within the plasma used to grow DLC films results in a thinner film with a lower oxygen concentration, however the carbon

hybridisation in the film does not vary. This suggests that the hydrogen composition of the film is increasing, and the presence of hydrogen capping carbon atoms prevents the further attachment of carbon, and thus hindering the growth of the carbon film.

4.4.2.2 SAM Results

The atomic concentrations of carbon, oxygen, and silicon found with SAM are shown in Figure 4-27 as green, blue, and red, respectively.
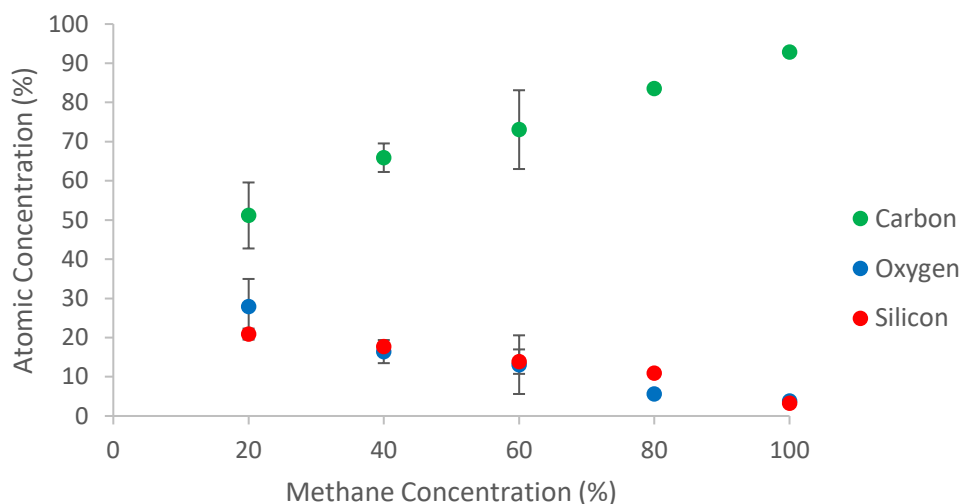

Figure 4-27: The influence of hydrogen and methane concentration on atomic concentrations of carbon (green), oxygen (blue), and silicon (red) in PECVD DLC films deposited on silicon as found by SAM. Data shown is the average of three samples for each point, with the error bars showing the standard deviation calculated from these three samples.

These results show a similar trend to those observed with XPS (Figure 4-25), although the trends appear to be slightly more linear in the SAM results. The carbon concentration decreases from 93 % to 52 % as the methane concentration decreases from 100 % to 20 %, while the oxygen increases from 4 % to 28 % and the silicon content increases from 3 % to 21 %. These results support the supposition that excess hydrogen in the plasma results in a thinner DLC film forming.

The D parameter for these samples is shown in Figure 4-28 for each methane concentration tested.
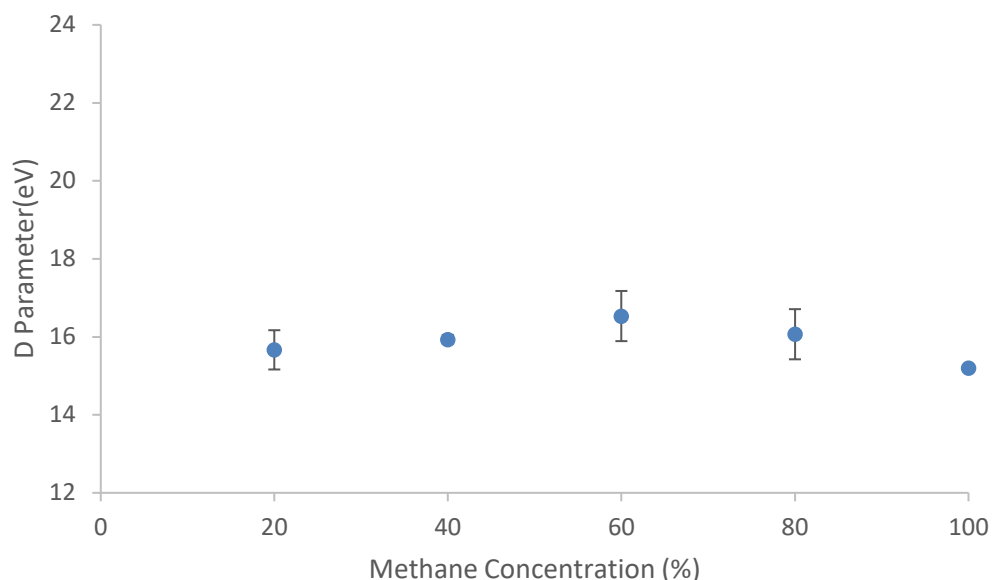
Figure 4-28: The influence of hydrogen and methane concentration on the width of the differentiated C (KLL) peak (D) from high resolution SAM spectra. Data shown is the average of three samples for each point, with the error bars showing the standard deviation calculated from these three samples.

These results show that the D parameter does not systematically change with methane and hydrogen concentrations. This supports the XPS data in Figure 4-26, which indicated that the carbon hybridisation does not change when methane plasma is diluted with hydrogen. However, the error bars for the samples from the diluted methane are larger than those of the straight methane plasma grown DLC films, which suggests that the presence of excess hydrogen creates a less constant plasma than the straight methane, and impacts the reproducibility of the DLC growth.

The thickness of the DLC film with varying methane and hydrogen concentrations in the plasma varies as shown in Figure 4-29.
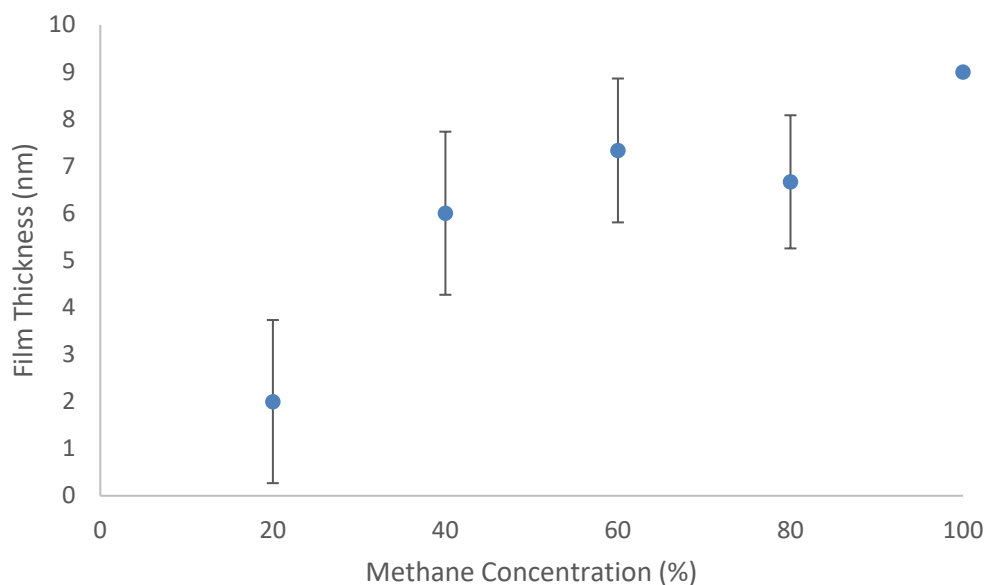
Figure 4-29: The influence of hydrogen and methane concentration on the DLC film thickness as determined from depth profiling with SAM. Data shown is the average of three samples for each point, with the error bars showing the standard deviation calculated from these three samples.

As the methane concentration decreases, there is a decrease in the film thickness from 9 nm at 100 % methane to 2 nm at 20 % methane. This correlates with the decrease in carbon atomic percentage observed from both XPS (Figure 4-25) and SAM (Figure 4-27), and supports the theory that the presence of excess hydrogen inhibit DLC film growth. There are again large error bars, which indicates that the plasma is not as constant when hydrogen is mixed with the methane, and thus reproducibility is reduced.

Elemental maps of carbon, oxygen, and silicon were acquired for these samples, and are shown in Figure 4-30 in green, blue, and red respectively, along with the SEM image of the area examined and the RGB overlay of the elemental maps.

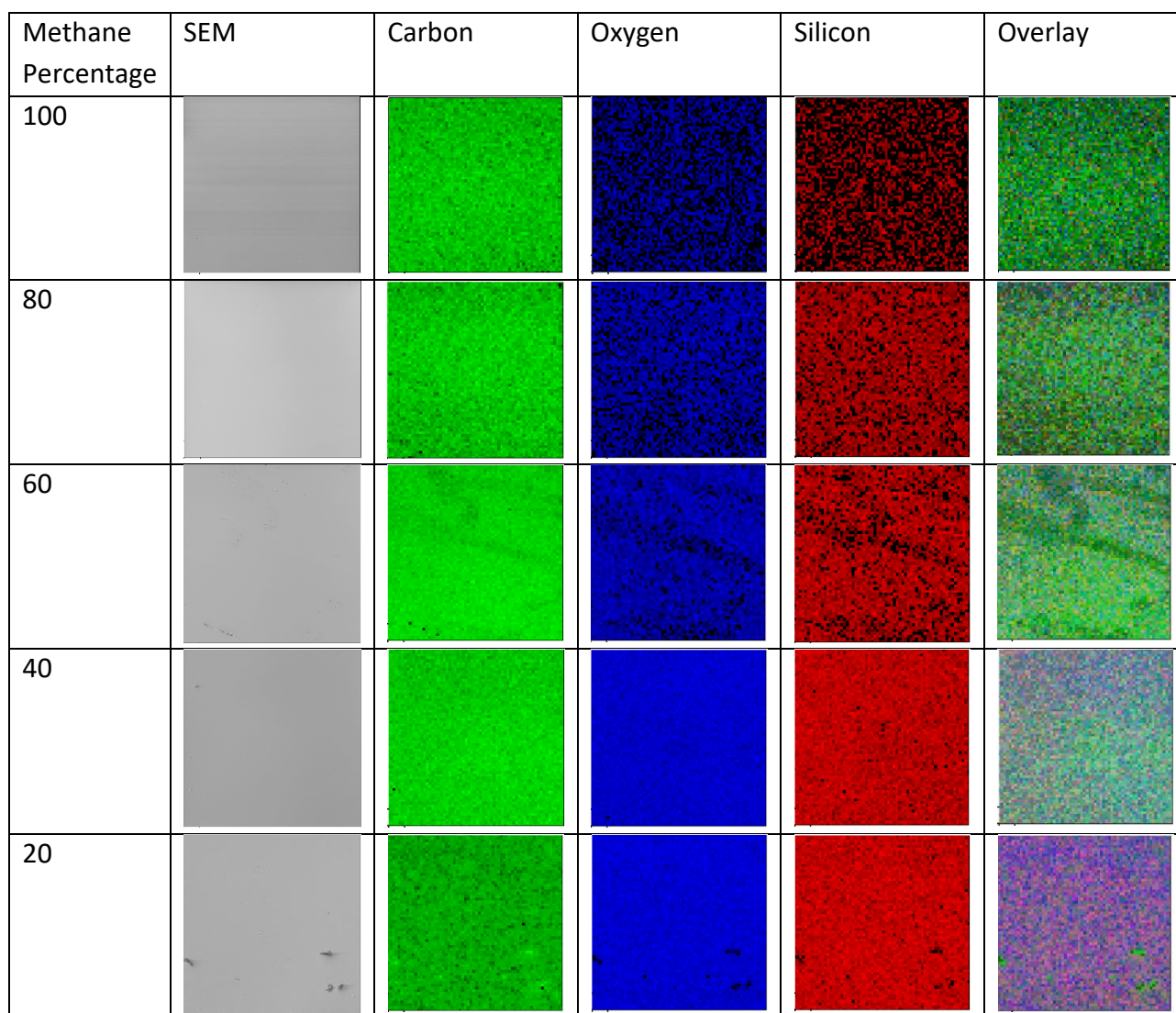| Methane Percentage	SEM	Carbon	Oxygen	Silicon	Overlay
100					
80					
60					
40					
20					

Figure 4-30: SEM images of DLC films deposited with various methane and hydrogen concentrations, and carbon, oxygen, and silicon elemental maps of the same area, and the RGB overlay showing the relative amounts and positions of the elements.

These maps show that as the methane concentration decreases and the hydrogen concentration increases the amount of carbon present on the surface decreases, indicating that the deposited film is getting thinner, however it remains uniformly distributed across the sample surface. These results correspond with the elemental concentrations found using XPS and SAM, as shown in Figure 4-25 and Figure 4-27, respectively.

4.4.2.3 Conclusions

The combined XPS and SAM results suggest that diluting methane plasma with hydrogen inhibits film growth, but does not significantly change the relative amounts of carbon hybridisation present in the DLC film. There has been varying results in the literature from the inclusion of hydrogen with the methane for DLC film growth, with some results showing an increase in the sp^3 hybridised

carbon and others showing a decrease [83, 116]. The deposition conditions of these literature studies are generally different to those used in this work, with much higher RF-coupling power values (up to 300 W) applied to the plasma [83, 116]. Combined with the differences in the orientation of the plasma chamber changing the spatial distribution of the plasma these differences in deposition conditions are likely to be the reason for the disagreement between literature results and those obtained in this work. The addition of excess hydrogen species in the plasma should stabilise the formation of the sp^3 bonds by preferentially etching the sp^2 bonds, which could result in a decrease in the film thickness [116]. This agrees with the film thickness data obtained in Figure 4-29, however it would also suggest that there should be a higher sp^3 content, which is not observed experimentally.

One possible reason for this difference is that with the parameters used for the DLC film deposition from pure methane the amount hydrogen produced from the methane molecules will etch the sp^2 hybridised carbon to the highest extent that is possible within this system. This would result in the additional hydrogen producing no significant difference in the hybridisations of carbon present in the film and the hybridisation of the DLC film remains constant when the methane:hydrogen ratio is changed. The increase in hydrogen and decrease in methane plasma results in fewer carbon containing species impinging on the sample surface, and hence the film will grow at a decreased rate.

4.5   Conclusion

The impact of four plasma parameters on the deposition of DLC films have been examined. As the pressure of the source gas increases, the thickness of the deposited film decreases, which is due to the change in spatial extent of the plasma within the chamber. As pressure increases, the plasma becomes more localised around the RF-antenna, thus fewer plasma species reach the substrate to grow the film, which is held at a constant distance from the antenna. However, the sp^2/sp^3 hybridised carbon ratio is not significantly changed by changing the source gas pressure.

An increase in the RF-coupling power applied to ignite the plasma increases the deposition rate of the DLC film due to an increase in the number of ionised species present. However, as there is only one type of bond present in methane the composition of the plasma does not change, and thus the sp^2/sp^3 hybridised carbon ratio does not change significantly with a change in RF-coupling power.

The length of the time the substrate is exposed to the methane plasma influences the thickness of

the deposited film, with an increase in the time resulting in a linearly dependent increase in the film thickness. This again does not impact the sp^2/sp^3 hybridised carbon ratio of the DLC film, as the composition of the plasma does not change with treatment time.

Finally, mixing argon and methane to create the source gas for DLC deposition is not observed to impact the growth rate, chemical composition, or film thickness in any significant way. However, the inclusion of hydrogen with the methane source gas does change the DLC deposition. As the methane concentration decreases the film thickness decreases, but the sp^2/sp^3 ratio does not change significantly.

These results combine to show that the chemical and hybridisation composition of DLC films grown within the plasma chamber do not significantly change over the range of plasma deposition parameters tested, which allows for the reproducible production of DLC films. The thickness of the deposited film can be tailored by changing either the RF-coupling power, source gas pressure, or growth time used to grow the film. In order to change the chemical or hybridisation composition of the film other conditions must be examined, including the use of other source gas(es), and this should be examined in future work to enable the tailoring of films to meet desired properties.

5 CARBON HYBRIDISATION MAPPING

The ability to produce a carbon hybridisation 'map' of a surface composed of structures created from different carbon hybridisations will help break down one of the barriers preventing the creation of carbon MEMS and NEMS, which is the accurate determination of the properties of each part of the sample. By mapping the hybridisation present on each part of the sample the physical and electronic properties of each part can be determined, and the manufacturing and tailoring of the device can be improved.

Scanning Auger Microscopy (SAM) provides a unique ability to create these hybridisation maps. The combination of an in-situ Scanning Electron Microscopy (SEM) capability, high spatial and energy resolution elemental maps, and a large variation between the spectra of sp^2 and sp^3 hybridised carbon that is not influenced by other chemical effects, allow for the production of a carbon hybridisation map from a carbon elemental map.

5.1 Development of Carbon Hybridisation Mapping Technique

The creation of the hybridisation maps occurs via three main steps: map acquisition, preparation of the data so that it is a form that MATLAB will accept, and then processing in MATLAB to create the hybridisation map. These processes, along with the application of the smoothing and differentiation algorithms applied during data processing within the MATLAB environment, are detailed in this chapter.

The carbon elemental maps acquired using the PHI710s SmartSoft program that form the basis of this hybridisation mapping technique need to be acquired in 'window' mode, whereby each pixel of the carbon map contains an entire spectrum of the carbon (KLL) peak. This is necessary to have sufficient data to perform the smoothing and differentiation that are needed to obtain the D parameter for determining the colour value at each pixel. Unfortunately, this approach requires a significantly increased acquisition time over the 'two-point' or 'three-point' modes which are normally used for elemental maps, which only measure a maximum and one or two minima of the peak at each point to determine the peak intensity at each pixel. An increased acquisition time means that sacrifices in the counting time need to be made to acquire the maps within a reasonable time, and the optimisation of the scanning parameters used to do this will be discussed further later in this chapter in section 5.2.

As the elemental mapping technique is not designed to undergo the type of processing necessary to produce a hybridisation map the data is acquired using the instruments native SmartSoft software and then further processed using the programs CasaXPS and MATLAB, rather than using PHI's MultiPak to analyse the SAM data as has been performed in previous chapters. The standard procedure for acquiring the data used in this chapter is to locate a region of interest using the in-situ SEM, acquire an SEM image, and then acquire the relevant elemental maps. For the samples presented in this work this means taking 'three-point' carbon, oxygen, and silicon elemental maps to examine the distribution of elements across the surface, and then acquiring a 'window mode' carbon elemental map over the same area. This map is then processed according to the methods outlined below.

5.1.1 Data Preparation

In order to create maps of carbon hybridisation from a window mode carbon elemental map there are several data processing steps that need to be undertaken to convert the data to the format necessary to import into MATLAB. The data is acquired in the form of a .map file which, when opened in the PHI SmartSoft or MultiPak software, produces a carbon elemental map and shows the average spectra of the entire map region. However, the individual spectra for each pixel of the carbon elemental map are contained within this .map file. It is these spectra that need to be extracted to ultimately produce the carbon hybridisation map. Neither SmartSoft nor MultiPak allow for extraction of the spectra within these elemental maps, therefore an intermediate program must be used before importing into MATLAB. The steps necessary for the conversion and importing of the data to MATLAB are outlined in Appendix B. The MATLAB code used to create the hybridisation maps is outlined in the following section.

5.1.2 MATLAB Code for Hybridisation Map Creation

The code used to produce hybridisation maps, which are two-dimensional images indicating the sp^2 hybridised carbon percentage at each pixel, from SAM carbon elemental maps was developed in MATLAB for maps of dimensions 32x32, 64x64, and 128x128 pixels as these were the three dimensions used in this work. While the code for smoothing and differentiation and the determination of the D parameter and sp^2 hybridised percentage is the same regardless of the dimensions of the map other areas of the code need to be updated to suit the dimension used. All three codes are therefore presented here and in Appendix C, however only the code for the 32x32 pixel map is described in detail, while the other dimensions are discussed only in how they are

different to the 32x32 pixel map code. Instructions on how to modify the code to suit maps with higher spatial resolution are also given in Appendix C.

5.1.2.1 32x32 Pixel Map

The code used to create a 32x32 pixel sp^2 hybridised map from a SAM carbon elemental map of the same dimensions is presented below:

```
%%Select Spectra Columns from Map File%%
Data = Map(:,2:3:end);
X = XValues(20:end-20,:);

%%Smoothing%%
%%sgolayfilt(Data,order,number of points)%%

SmQuadratic41 = sgolayfilt(Data,2,41);

%%Differentiation%%

for k = 11:289
    DerivativeLinear(k,:)   =   (1/(770*0.2))*((-10*SmQuadratic41(k-
10,:))+(-9*SmQuadratic41(k-9,:))+(-8*SmQuadratic41(k-8,:))+(-
7*SmQuadratic41(k-7,:))+(-6*SmQuadratic41(k-6,:))+(-
5*SmQuadratic41(k-5,:))+(-4*SmQuadratic41(k-4,:))+(-
3*SmQuadratic41(k-3,:))+(-2*SmQuadratic41(k-2,:))+(-
1*SmQuadratic41(k-
1,:))+(0*SmQuadratic41(k,:))+(1*SmQuadratic41(k+1,:))+(2*SmQuadrat
ic41(k+2,:))+(3*SmQuadratic41(k+3,:))+(4*SmQuadratic41(k+4,:))+(5*
SmQuadratic41(k+5,:))+(6*SmQuadratic41(k+6,:))+(7*SmQuadratic41(k+
7,:))+(8*SmQuadratic41(k+8,:))+(9*SmQuadratic41(k+9,:))+(10*SmQuad
ratic41(k+10,:)));
end

%%Map Creation%%

%%Find Max and Min of Each Spectra%%
[MaxY,IndexMaxY] = max(DerivativeLinear(20:end-20,:));
[MinY,IndexMinY] = min(DerivativeLinear(20:end-20,:));

%%Find Corresponding X Values%%
XValuesMap = [X(IndexMaxY), X(IndexMinY)];

%%Create Matrix of D%%
DAll = XValuesMap(:,1) - XValuesMap(:,2);
DAllRow = DAll.';
D = reshape(DAllRow,32,32).';

%%Make D positive and Convert to sp2 percentage%%
DPositive = D.*-1;
Dminus12 = DPositive-12;
sp2 = Dminus12./0.12;

%%Create D parameter Map - Reverse y axis once plot is created%%
[A,B] = meshgrid(1:1:32,1:1:32);
```

```
Dmap = pcolor(A,B,DPositive);
```
```
%%Create sp2 Map - Reverse y axis once plot is created%%
figure
[A,B] = meshgrid(1:1:32,1:1:32);
map = pcolor(A,B,sp2);
```

Each section of this code will now be reviewed and its purpose explained. The first section of the code is used to create a matrix of the y-values of the spectra from the carbon elemental map.

```
%%Select Spectra Columns from Map File%%
Data = Map(:,2:3:end);
X = XValues(20:end-20,:);
```

The imported matrix 'Map' contains a set of three repeating columns: x-values, y-values, and a blank column. In order to perform the necessary processing, the y-values need to be extracted from 'Map' and used to form a new matrix 'Data', which is created by taking every third column from 'Map', starting with the second column, and collating them.

The next line of code creates a matrix 'X' which takes the matrix 'XValues' (the x values for each spectrum in the map) and removes the first and last 20 values. This is necessary so that the x-values and y-values continue to correspond with each other correctly after the differentiation of the y-values has been performed. The differentiation process removes the first and last 20 data points from the y-values, therefore the x-values matrix must be modified to match.

The second section of the code is used to smooth the data in 'Map'.

```
%%Smoothing%%
%%sgolayfilt(Data,order,number of points)%%
SmQuadratic41 = sgolayfilt(Data,2,41);
```

The smoothing that is performed is a 41-point Savitzky-Golay (SG) smoothing, which is undertaken using MATLABs inbuilt 'sgolayfilt' function, which is written as sgolayfilt(x,order,framelen), where x is the data to be smoothed, order is the polynomial order, and framelen is the number of points over which the smoothing is to be performed. For the smoothing process applied here, the order is 2 as a quadratic function is used and framelen is 41 to use 41 points. The smoothed data is labelled as 'SmQuadratic41'. The SG smoothing and differentiation process is described and derived in Appendix D.

The third section of code is used to apply a 21-point Savitzky-Golay differentiation to 'SmQuadratic41'. To do this a 'for' loop is required. The loop has the form:

142

```
    for index = values
        statements
    end
```

In the code for differentiation the 'index = values' section takes the form k = initialValue:endValue, which will result in the statement being performed for the initial index value, then increment the index value by one and repeat the execution of the statement until the end value is completed.

```
%%Differentiation%%
for k = 11:289
    DerivativeLinear(k,:)   =   (1/(770*0.2))*((-10*SmQuadratic41(k-
10,:))+(-9*SmQuadratic41(k-9,:))+(-8*SmQuadratic41(k-8,:))+(-
7*SmQuadratic41(k-7,:))+(-6*SmQuadratic41(k-6,:))+(-
5*SmQuadratic41(k-5,:))+(-4*SmQuadratic41(k-4,:))+(-
3*SmQuadratic41(k-3,:))+(-2*SmQuadratic41(k-2,:))+(-
1*SmQuadratic41(k-
1,:))+(0*SmQuadratic41(k,:))+(1*SmQuadratic41(k+1,:))+(2*SmQuadrat
ic41(k+2,:))+(3*SmQuadratic41(k+3,:))+(4*SmQuadratic41(k+4,:))+(5*
SmQuadratic41(k+5,:))+(6*SmQuadratic41(k+6,:))+(7*SmQuadratic41(k+
7,:))+(8*SmQuadratic41(k+8,:))+(9*SmQuadratic41(k+9,:))+(10*SmQuad
ratic41(k+10,:)));
End
```

In this code each column of the matrix has 301 data points. The first point to which a 21-point Savitzky-Golay differentiation can be applied is the 11th point, as it requires 10 data points either side of the specific data point (making 21 in total, with the 11th in the centre) to perform the calculation, thus the 'initialValue' used is 11. By applying the same logic, the 'endValue' used is 289. The statement used here is an equation for the 21-point Savitzky-Golay differentiation of the data, labelled 'DerivativeLinear' to indicate that a linear form of the 21-point SG derivative is used. DerivativeLinear(k,:) is used so that the statement is applied to every column for each 'k' value specified by the index. In this way the derivative formula is applied sequentially to the columns of the matrix 'SmQuadratic21'. The result of this is 'DerivativeLinear', which is a matrix composed of columns of the derivative from each column of 'SmQuadratic41', and thus forms a set of derivative spectra. This formula is followed by 'end' to close the loop. The data is now in the form necessary to extract the width between the maxima and minima of the differentiated peak and convert this value to a sp^2 hybridised carbon percentage.

The next section of the code finds the maxima and minima values of each column in 'DerivativeLinear', excluding the first and last 20 data points to negate the values ignored in the smoothing and derivative processes. These are stored in the 'MaxY' and 'MinY', respectively, as

matrices of the maximum and minimum values from each column.

```
%%Find Max and Min of Each Spectra%%
[MaxY,IndexMaxY] = max(DerivativeLinear(20:end-20,:));
[MinY,IndexMinY] = min(DerivativeLinear(20:end-20,:));

%%Find Corresponding X Values%%
XValuesMap = [X(IndexMaxY), X(IndexMinY)];

%%Create Matrix of D%%
DAll = XValuesMap(:,1) - XValuesMap(:,2);
DAllRow = DAll.';
D = reshape(DAllRow,32,32).';
```

Also created are the matrices 'IndexMaxY' and 'IndexMinY', which are the positions of the maximum and minimum values from each column. In order to find the corresponding x-values for the max and min values a new matrix is created, 'XValuesMap', which applies the 'IndexMaxY' and 'IndexMinY' to 'X' to create a matrix with the x values corresponding to the maxima (XValues(:,2)) and minima (XValues(:,1)) values from each spectrum. The parameter 'DAll' is a matrix of the width between the maxima and minima by subtracting the larger of the x values (XValuesMap(:,2)) from the smaller (XValuesMap(:,1)), resulting in a column matrix of D values from all spectra. This column of data needs to be reformatted to become a 32x32 matrix that matches the position of the D value to the spectrum it was extracted from in the initial carbon map. To do this the column matrix 'DAll' needs to be converted to a row matrix, 'DAllRow', which is then reshaped to be a 32x32 matrix and transposed to obtain the correct order for the elements, labelled 'D'.

As the D values obtained are negative, the matrix 'D' is multiplied by -1 to obtain 'Dpositive', before using a calibration curve to convert the D values to a sp^2 hybridised carbon percentage by subtracting 12 and dividing by 0.12 (the values from the calibration curve) to obtain the matrix 'sp2', which is a matrix of the sp^2 hybridised carbon percentage at each pixel of the carbon elemental map based on the width of the C(KLL) peak.

```
%%Make D positive and Convert to sp2 percentage%%
DPositive = D.*-1;
Dminus12 = DPositive-12;
sp2 = Dminus12./0.12;
```

This step results in a sp^2 hybridised carbon percentage from each pixel of the map, and therefore the carbon hybridisation map created using this code will be a sp^2 hybridised carbon percentage map. Further code could be added to also create a sp^3 hybridised carbon percentage map by either changing the calibration curve to be in terms of sp^3 hybridised carbon or by subtracting the

sp^2 hybridised percentage from 100 to obtain the sp^3 hybridised carbon percentage, and then adding a further plot using the same method described below.

Sometimes a map of the D values may be desired, so the next part of the code creates this map by creating a frame using the 'meshgrid' function, where [A,B] is a two-dimensional grid based on the coordinates x and y.

```
%%Create D parameter Map - Reverse y axis once plot is created%%
[A,B] = meshgrid(1:1:32,1:1:32);
Dmap = pcolor(A,B,DPositive);
```

For this code, both x and y are given as 1:1:32, creating a 32x32 grid with lines evenly spaced every 1 unit, thus [A,B] has a length of 32 rows and 32 columns, which matches the dimensions of the original carbon elemental map. The D map is plotted on this meshgrid using 'pcolor(X,Y,C)', where X and Y are A and B from the meshgrid, respectively, and C is the data 'DPositive'. A figure window is now opened showing the D map, and the axes and colour scale can now be modified. It is important to reverse the direction of the y axis so that it plots the first line of pixels at the top of the plot and matches the order of the original carbon map and the orientation of the corresponding SEM image. The colourmap editor is then opened and the range of values can be modified to remove any outliers so that a clear map is obtained (for example, if the range of D across the majority of the map is 18-20 eV but there are several outliers at 30 eV, the upper limit can be set to 20 eV to best show the distribution in the majority of the map). Different colourmaps can be chosen to display the data, however for this work the 'jet' map has been chosen as it has the largest range of different colours over a full rainbow scale, so that it is intuitive when looking at the map that the red pixels are at one extreme of the data, and blue at the other, with yellows and greens in between.

The final step of the code is to create the new map showing the sp^2 hybridised carbon percentage. In order to produce a second figure and not overwrite the one already created for the D parameter map the command 'figure' must be included in the code.

```
%%Create sp2 Map - Reverse y axis once plot is created%%
figure
[A,B] = meshgrid(1:1:32,1:1:32);
map = pcolor(A,B,sp2);
```

The carbon hybridisation map is again plotted on the meshgrid using 'pcolor(X,Y,C)', where X and Y are A and B from the meshgrid, respectively, and C is the data 'sp2'. After the new figure is opened with the hybridisation map it is again necessary to reverse the Y axis to match the original carbon

145

map. The colourmap editor is then opened to adjust the maximum and minimum values to be 100 and 0, respectively, to ensure that colour scale represents the full range of sp^2 hybridised carbon percentages possible. The 'jet' colour scale is again chosen for this data to best show an intuitive and clear difference in the hybridisations present.

The MATLAB code for creating hybridisation maps with higher spatial resolution, that is, higher pixel numbers, is shown in Appendix C, along with the explanations of the modifications needed to adjust the code for larger pixel numbers.

5.2   Carbon Hybridisation Mapping Optimisation

As in any spectroscopy technique, it was necessary to find the optimum scan parameters to produce the best hybridisation maps with a reasonable scan acquisition time. There are several scan parameters that need to be examined to find the optimal combination, including the energy step width, time per step, and the number of averaged scans. These parameters were tested using both HOPG and DLC samples, and the results of both will be discussed here. The impact of the level of magnification at which the maps are acquired is also investigated.

5.2.1   Repeated Scans

When testing the impact of the carbon elemental map scan parameters on the spectra within the maps and the resultant hybridisation maps it is desirable to acquire all maps over the same area so that any differences observed are due to the changes in scan parameter and not a result of a different area having a different hybridisation. However, it is possible that electron beam induced changes may occur on the surface while acquiring the spectra and could influence the peak shape and resultant hybridisation map, therefore to examine the impact of beam damage from repeated scans in the same area four carbon maps were acquired sequentially for both HOPG and DLC films.

5.2.1.1 Repeated Scans – HOPG

To investigate whether exposure to the electron beam is causing changes to the hybridisation of the HOPG surface four carbon elemental maps were acquired sequentially over the same area. The SEM image of the area over which these maps were acquired is shown in Figure 5-1, along with the carbon elemental maps, the resultant hybridisation maps, and the signal to noise ratio (SNR) values for each of the four scans. All other scan parameters were held constant, thus any changes to the results can be concluded to be the result of electron beam damage to the surface.

The 20 µm field of view (FOV) SEM image for this area shows a HOPG surface that appears to contain two distinct graphite flakes, shown by the difference in colour of two large regions on the top and bottom of the image. The images obtained in SEM are sensitive to both the composition and morphology of the surface, enabling these different structures to be observed in the images. The surface also shows regions that the graphene flakes appear to be disrupted in some way, as indicated by the small areas that appear lighter and darker than the surrounding surface. The carbon elemental map for the first scan acquired shows some variation in intensity due to the morphology of the surface, however this variation is not significant as it only indicates the maximum intensity of the carbon peak, which does not provide useful information about the sample unless compared to the intensity of other peaks using atomic sensitivity factors. The hybridisation map produced from this carbon elemental map is also shown in Figure 5-1, and is not sensitive to the morphology as the calculation performed to obtain the mapped values is independent of the intensity of the peak. This map shows a surface that is quite uniform in carbon hybridisation, as evidenced by the uniformity in the colour of the map. The surface of the HOPG has an average sp^2 hybridised carbon percentage of approximately 90 %, however there is some variation that occurs across the surface. This variation appears to be random and does not align with any features in the SEM image, indicating that the areas of different colour in the SEM image are indeed areas of HOPG with differences in morphology. To quantify the extent in this variation the SNR is considered. The SNR value for the hybridisation map is calculated by dividing the average sp^2 hybridised carbon percentage value from the map by the standard deviation calculated from the values in the map, and shows a value of 20.4 for the first scan.

The second sequentially acquired carbon elemental map and hybridisation map in Figure 5-1 show some variations in carbon intensity and hybridisation occurring across the surface with no clear trend, which is very similar results to the first scan. The SNR value for this scan (21.0) is very similar to the first scan, showing that despite some small changes in the positions of higher or lower sp^2 hybridised carbon percentage pixels the surface is very similar after the first and second scans. The third and fourth sequentially acquired scans show very similar results again for both the hybridisation map and the SNR values.

The consistency in the carbon hybridisation maps shown in Figure 5-1 suggest that there is no significant beam damage that will impact on the scan parameter tests, however the SNR values will be considered more closely to examine any changes in the variance.
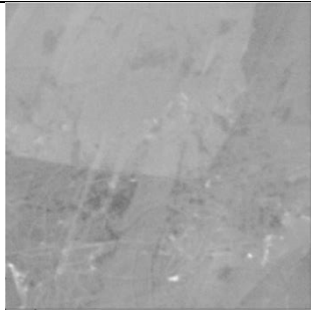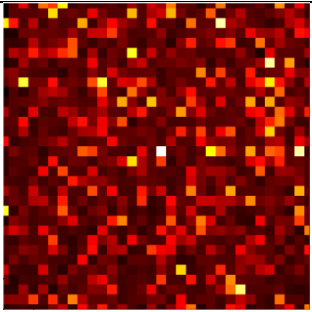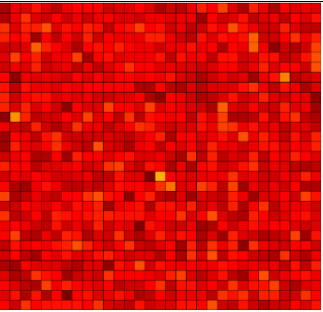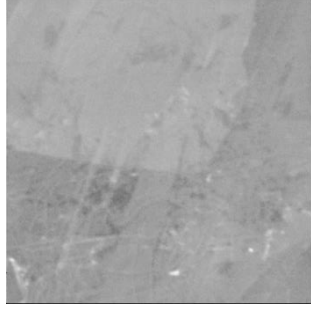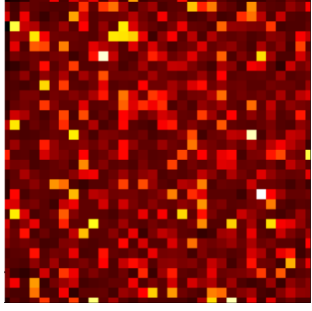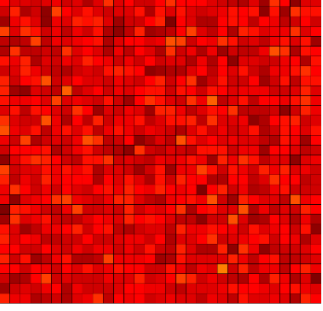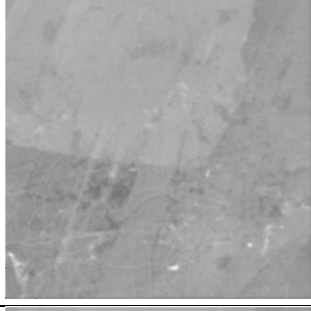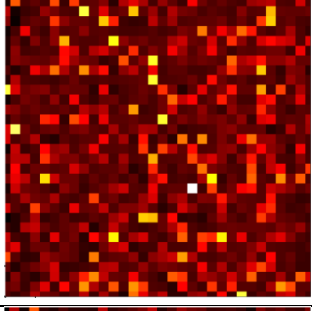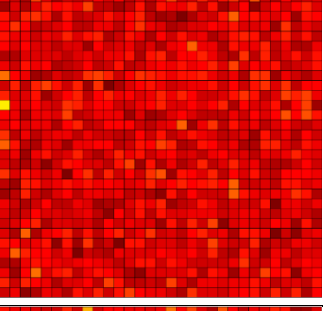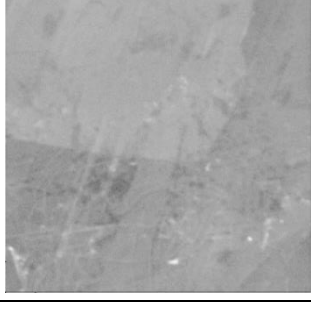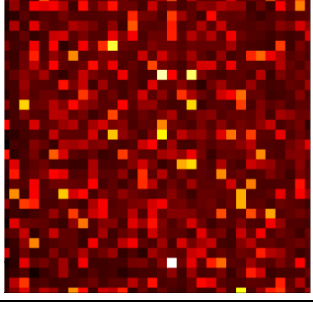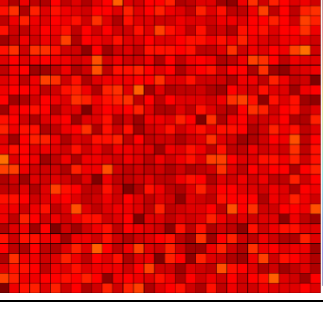
Scan Number	SEM	Carbon Elemental Map	Hybridisation map	SNR
1				20.4
2				21.0
3				20.3
4				20.0

Figure 5-1: SEM images (20 μm FOV), C(KLL) elemental map, and hybridisation maps of four scans of HOPG taken sequentially in the same area.

The SNR values are plotted against the sequential scan number in Figure 5-2 to examine if there is any trend in the variance of the hybridisation map when the maps are acquired sequentially over the same area. It can be seen from Figure 5-2 that there is some variation in the SNR values as maps are acquired sequentially over one area, however this variation does not occur with any trend. This indicates that the average sp^2 hybridised carbon percentage and the variance in the hybridisation
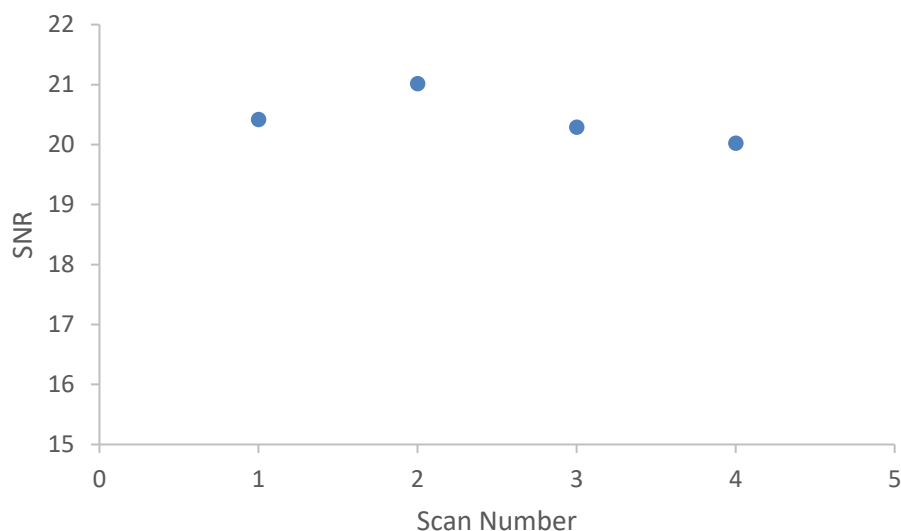
Figure 5-2: SNR for the four sequentially acquired hybridisation maps on HOPG from Figure 5-1.

values is quite similar for all four scans, and while there are some small changes that occur to the surface upon electron beam exposure they do not occur systematically.

To further examine how the electron beam exposure impacts the HOPG surface the spectra that make up the window mode carbon elemental map will be examined to observe any changes in the peak shapes. The spectrum calculated by averaging the spectra from each pixel within the carbon elemental map from Figure 5-1 is shown in Figure 5-3 (a) for sequentially acquired scans 1, 2, 3, and 4 as blue, red, green, and purple lines, respectively. The results from scans 1 through 4 appear to be extremely similar, showing no differences in the fine structure of the peak or the positions of the maxima and minima, and a consistent D parameter value of 22.6 eV (Table 5-1).

Spectra extracted from individual pixels of the map are also considered as they will show more variation than the averages. Pixels 272, 588, and 784 were chosen as they are distributed evenly through the map but are spaced far enough apart across the sample that any small local effects that may produce an unexpected result in a one pixel will not impact on the others. The spectra from these points are shown in Figure 5-3 (b), (c), and (d), respectively. Some small changes in the fine structure of these spectra is observed, however the energy positions of the maxima and minima do not appear to shift significantly. The variation that does occur, as shown in Table 5-1, does not follow any systematic trend for any of the pixels. Pixel 272 has D parameter values that vary between 22.0 eV and 22.8 eV, which is a reasonably large difference considering the 0.2 eV uncertainty in the measurements. The D parameter values from pixel 784 show a similar range, again with no trend as the sequential scan number increases, while pixel 588 has D parameter values of 22.6 eV or 22.8 eV,

149

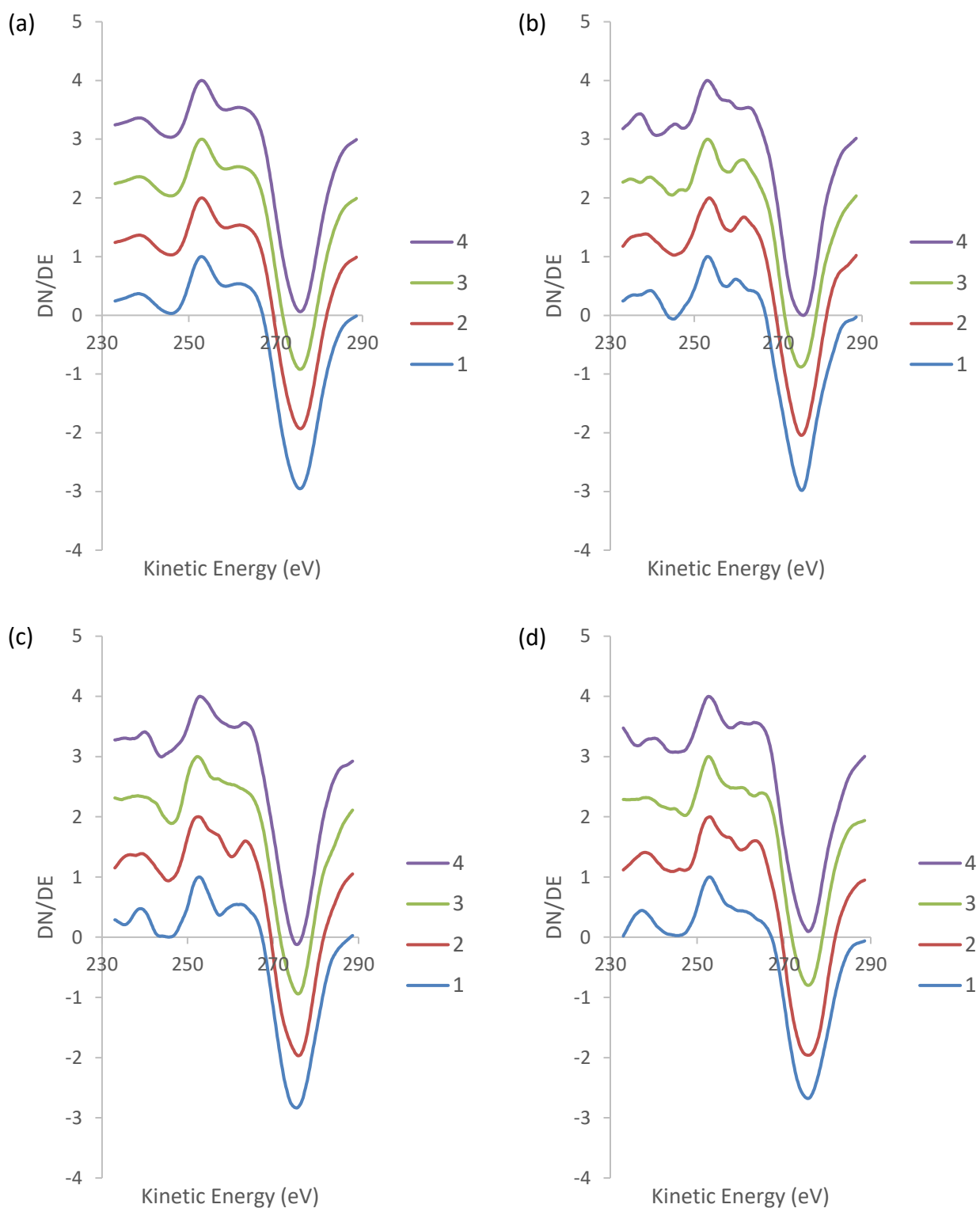which is not a significant difference.

Figure 5-3: C(KLL) spectra taken from (a) the average of all spectra in the map, and pixel (b) 272, (c) 558, and (d) 784 of the 32x32 pixel carbon elemental maps. Each plot shows spectra from four maps taken sequentially in the same place on the HOPG sample.

Table 5-1: D Parameter values from each spectrum in Figure 5-3. The uncertainty in D parameter measurements is ±0.2 eV.

Scan Number	D Parameter (eV) (Average)	D Parameter (eV) (Pixel 272)	D Parameter (eV) (Pixel 558)	D Parameter (eV) (Pixel 784)
1	22.6	22.4	22.8	22.8
2	22.6	22.0	23.6	22.4
3	22.6	22.2	23.6	23.0
4	22.6	22.8	22.8	23.0

From comparison of the data in Figure 5-1, Figure 5-2, Figure 5-3, and Table 5-1 it can be seen that by sequentially acquiring carbon elemental maps over the same area there are some small changes to the hybridisation of the carbon on a HOPG surface. However, these changes are small and do not occur systematically, and average across the surface so that the average sp^2 hybridised carbon percentage from the map remains approximately constant. Based on these results it can be concluded that the scanning parameter optimisation tests can be performed on HOPG by acquiring all maps over the same area of the sample, and any significant changes that are observed will be the result of the variation in parameter rather than changes in the sample surface.

5.2.1.2 Repeated Scans – DLC

The scan parameter optimisation tests were also performed on DLC films as the films will not necessarily react to the exposure to the electron beam in the same way as HOPG. Four carbon elemental maps were acquired sequentially over the same area of DLC at a FOV of 20 µm to examine the impact of electron beam exposure on this type of sample. All scanning parameters were held constant for each of these maps, therefore any changes that are observed in the hybridisation maps can be expected to be a result of electron beam induced changes to the carbon hybridisation.

The SEM image of the area examined in this test is presented in Figure 5-4 and shows a DLC film surface that appears to be mostly smooth and uniform, with several patches of slightly darker coloured areas. The first of the sequentially acquired carbon elemental maps is also shown in Figure 5-4, along with its resultant hybridisation map and the SNR of that map. The carbon elemental map shows a range of intensities distributed randomly across the DLC surface, while the corresponding hybridisation map consists of mainly red pixels, indicating a high sp^2 hybridised carbon percentage. Within the hybridisation map there is also a number of pixels ranging from light blue to orange

indicating regions of lower sp^2 hybridised carbon percentage, which are distributed randomly across the surface with no correlation to the differently coloured areas on the SEM image. This shows that the different coloured areas on the SEM image are all DLC and the difference in colour is related to the morphology of the surface. The SNR is quite low (7.03) and provides some quantification on the variation in the sp^2 hybridised carbon percentages across the surface.

A second map was acquired over the same area, increasing the amount of electron beam exposure the surface has experienced, and the carbon elemental map is shown in Figure 5-4. This map shows a range of carbon intensities randomly distributed randomly across the surface in a way that is very similar to that shown in the first map. The hybridisation map for the second scan shows fewer blue, green, and yellow pixels than the previous scan, while the most frequently observed red colour appears to be consistent with the first scan. The reduction in the number of pixels indicating lower sp^2 hybridised carbon percentages increases the average sp^2 hybridised carbon percentage used to calculate the SNR, resulting in a value of 8.28.

The third map indicates a further decrease in the number of blue, green, and yellow pixels, while further exposure to the electron beam by acquiring a fourth map does not appear to result in further changes in the hybridisation percentages present. These results suggest that exposure of the DLC film to the electron beam results in the surface becoming more sp^2 hybridised, and this result must be taken into consideration in the following analysis of scan parameter optimisation. The SNR values will be examined to provide further insight into the variation in the hybridisation across the surface.

The SNR values are plotted against the sequentially acquired scan number in Figure 5-5 to examine how the variance in the data changes with increased electron beam exposure.
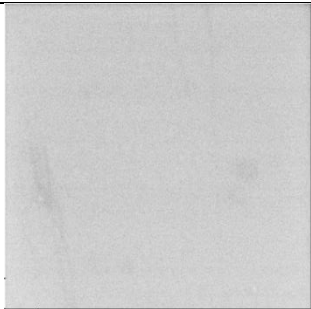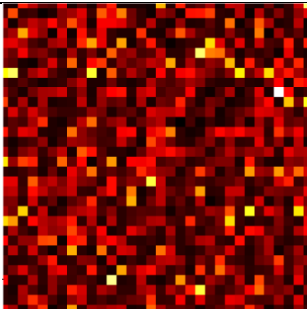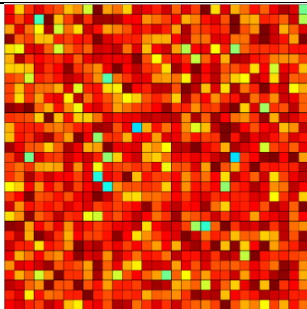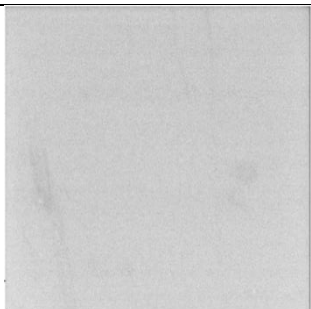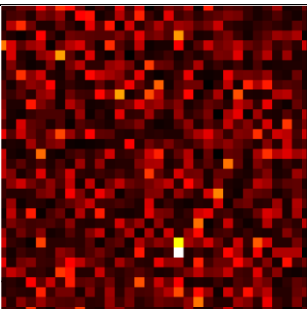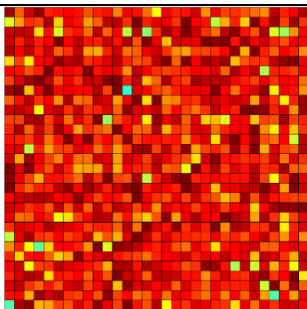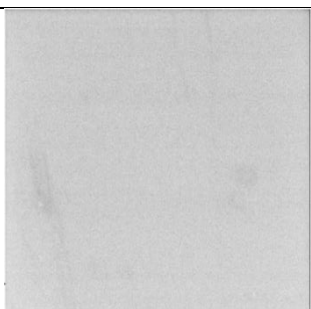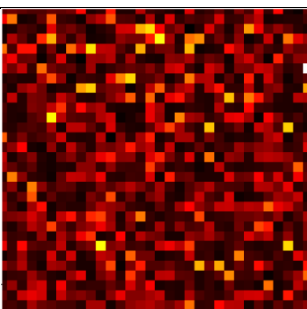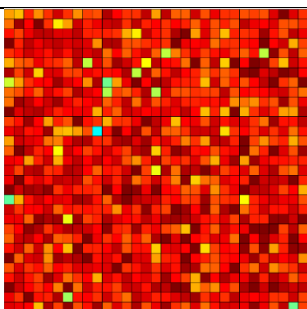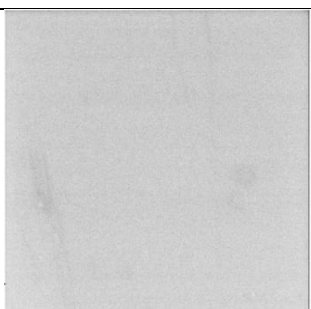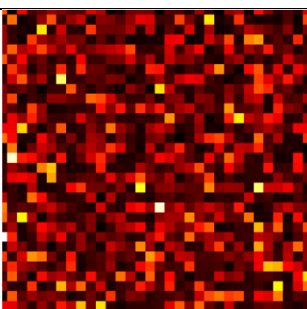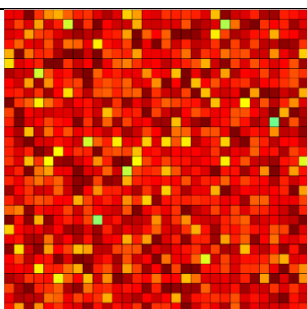
Scan Number	SEM	Carbon Elemental Map	Hybridisation map	SNR
1				7.03
2				8.28
3				9.11
4				9.10

Figure 5-4: SEM images (20 μm FOV), C(KLL) elemental map, and hybridisation maps of four scans of DLC taken in the same area.
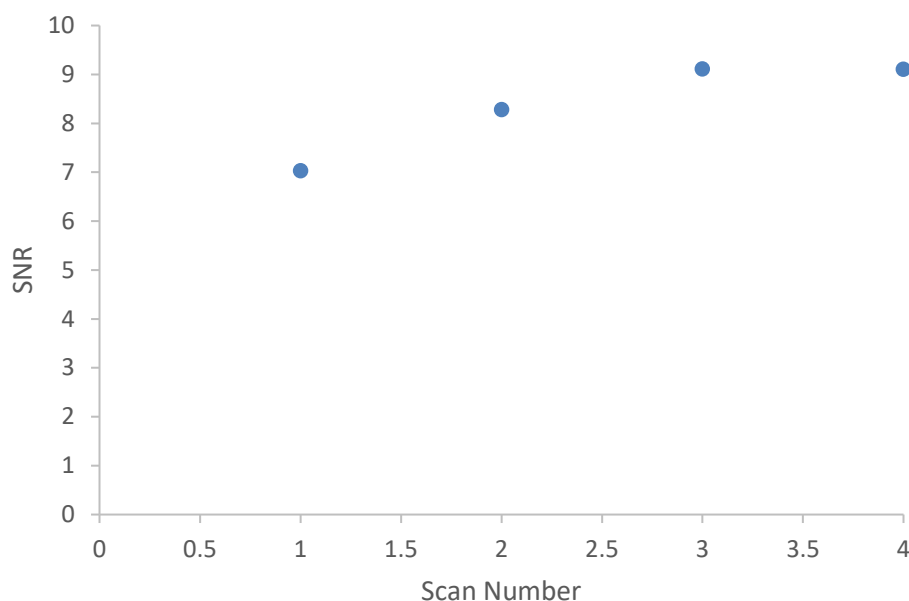
Figure 5-5: SNR for the four sequentially acquired hybridisation line scans on DLC from Figure 5-4.

An increasing trend in the SNR is shown in Figure 5-5 when the sample experiences increased exposure time to the electron beam. This change in SNR occurs partly because of the reduction in the standard deviation within the map, but also because of an increase in the average sp^2 hybridised carbon percentage. These results show that the electron beam is changing the hybridisation of carbon present in the DLC film by graphitizing the areas that initially had low sp^2 hybridised carbon percentages, which is not ideal for performing scanning parameter optimisation tests as the impact of changing the parameter will need to be separated from the electron beam induced changes.

The spectra obtained by averaging all pixels of each of these maps is shown in Figure 5-6 (a), where the first, second, third, and fourth scan spectra are shown in blue, red, green, and purple, respectively. The shape of these spectra are quite similar, however the D parameter increases slightly from 22.0 eV to 22.4 eV as the scan number increases from 1 to 2, and remains at 22.4 eV for scans 3 and 4. (Table 5-2). While this difference is small, it is larger than the uncertainty in the measurements (0.2 eV) and is therefore a significant change, and this change correlates with the differences observed in the hybridisation maps.

Spectra were also extracted from three individual pixels of each map and are compared in Figure 5-6 (b), (c), and (d). These spectra were taken from the same place in each map, therefore the large differences in shape that can be observed are expected to be a result of the electron beam induced damage. Some of the pixels show larger changes in the D parameter than others as the scan number increases (Table 5-2), with a gradually increasing trend observed for pixels 558 and 784. Pixel 272

154

shows no clear trend, which is related to the lack of sharp maxima and minima in some of the spectra for this point.
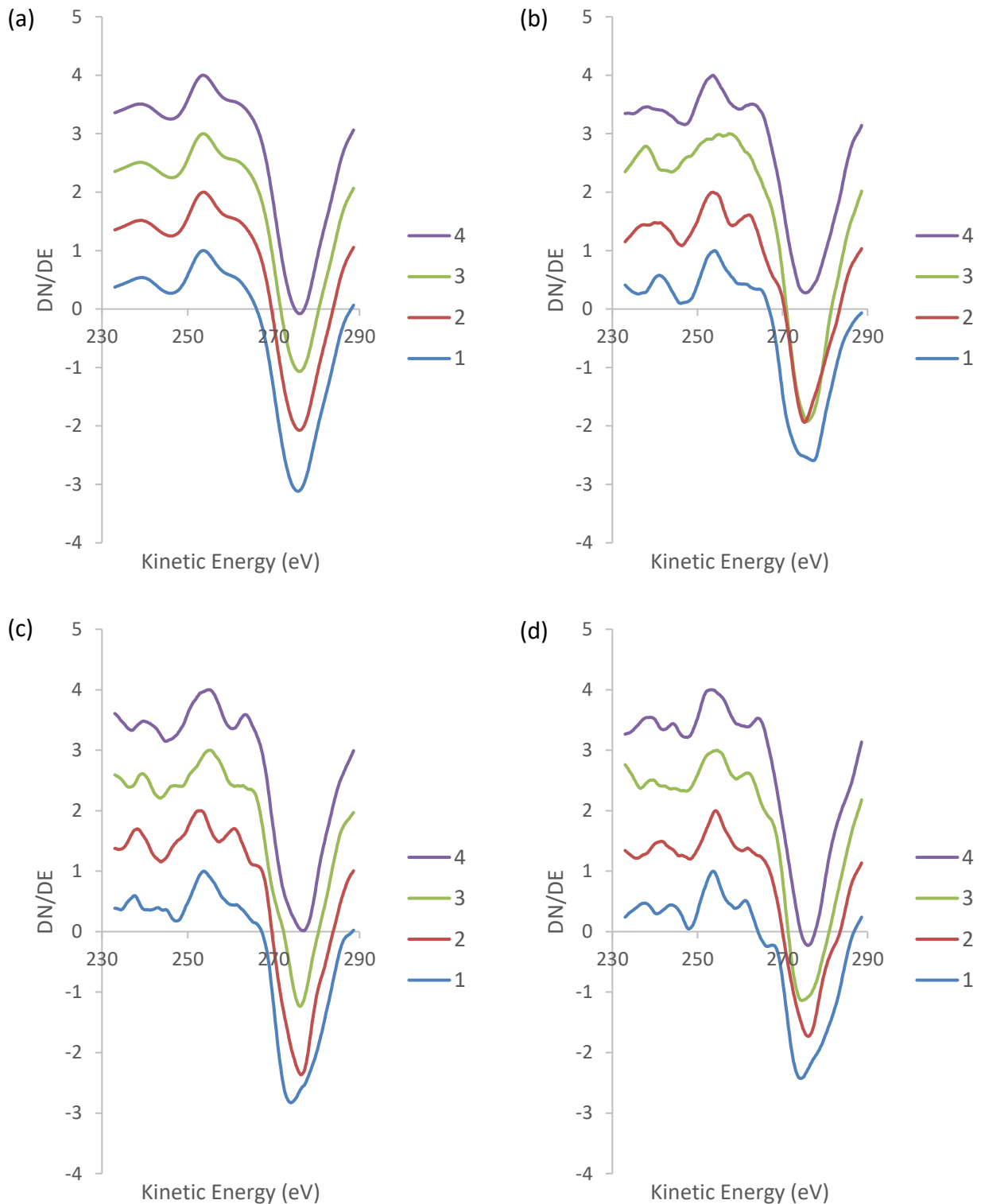

Figure 5-6: C(KLL) spectra taken from (a) the average of all spectra in the map, and pixel (b) 272, (c) 558, and (d) 784 of the 32x32 pixel carbon elemental maps. Each plot shows spectra from four maps taken sequentially in the same place on the DLC sample.

Table 5-2: D Parameter values from each spectrum in Figure 5-6. The uncertainty in the D parameter measurements is ±0.2 eV.

Scan Number	D Parameter (eV) (Average)	D Parameter (eV) (Pixel 272)	D Parameter (eV) (Pixel 558)	D Parameter (eV) (Pixel 784)
1	22.0	23.2	20.2	20.6
2	22.4	21.6	23.4	21.8
3	22.4	18.4	21.0	20.0
4	22.4	21.8	22.0	22.8

Examination of the data in Figure 5-4, Figure 5-5, Figure 5-6, and Table 5-2 shows that there are changes in the hybridisation of the carbon on the surface of DLC films that occur as the result of exposure to the electron beam, and this damage increases as the length of time the sample is exposed to the beam is increased. This is not ideal for testing the impact of changing scanning parameters, as the changes that occur may be hidden by the changes that occur due to the graphitisation.

5.2.1.3 Repeated Scans – Conclusions

Hybridisation maps produced by sequentially acquiring maps over the same area of samples of both HOPG and DLC has shown that the two samples behave differently under exposure to the electron beam. HOPG does not undergo significant changes in hybridisation after electron beam exposure, and sequential maps can be acquired over the same area without impacting the sample and the results. However, DLC does exhibit changes in the hybridisation of the surface, and these changes become larger as the exposure time to the electron beam increases. While this is not ideal for the scanning parameter optimisation process as it becomes difficult to separate the electron beam induced changes from any changes that occur with variation in the scanning parameters it is still preferred that the optimisation occurs over the same area. To minimise the impact of this electron beam exposure the parameter tests will be acquired in order of increasing acquisition time so that the previous exposure is minimised for each new scan.

5.2.2 Step Width Optimisation

When acquiring a spectrum the step width is an important parameter to optimise as it determines the energy resolution of that spectrum. The Scanning Auger Nanoprobe used in this work allows for step widths ranging between 0.1 eV and 10 eV for elemental maps, with the standard used for most

applications being 1.0 eV. However, in order to obtain a scale of sp^2 hybridised carbon percentage with smaller increments it is desirable to reduce this step width and measure smaller variations in D parameter. Appropriate choice of this variable is critical for the hybridisation determination, but if the step width is chosen to be too small variations in spectral noise may result in determining a false maximum or minimum during analysis. Decreasing the step width value also results in an increased acquisition time, therefore any improvement to the data must be balanced against the time cost.

To examine the influence of the step width on the results carbon elemental maps of both HOPG and DLC surfaces were acquired using step widths of 1.0 eV, 0.5 eV, 0.2 eV, and 0.1 eV, and converted to hybridisation maps using the method described in section 5.1.2. The hybridisation maps and spectra extracted from each map are compared to examine how the step width effects the data and determine the best step width value to use.

5.2.2.1 Step Width Optimisation – HOPG

The four step width values were tested by acquiring carbon elemental maps over the same area of a HOPG sample, which can be seen in the SEM image Figure 5-7. The SEM image shows the 20 µm FOV area that appears largely featureless, with the exception of several faint ridges that indicate flake edges, a small flake sitting above the surrounding surface, and a thick raised line running through the upper right corner. From the image it is not clear whether this line is a structure composed of HOPG or if it is a form of contamination on the surface.

The carbon elemental map acquired with a step width of 1.0 ms is presented in Figure 5-7 and shows some variation in the carbon intensity, however these variations do not correlate with any of the features observed in the SEM image. The resultant hybridisation map also shows variation across the surface which does not match up to features in the SEM image, indicating that the features observed are all graphitic despite their different appearance in the SEM. The hybridisation map is mainly composed of red pixels, indicating a high sp^2 hybridised carbon content, but also has pixels of blue, green, and yellow scattered through the image, indicating areas of lower sp^2 content. This variation produces a SNR value of 6.43, indicating a high level of variance across the surface.

The carbon elemental map acquired using a step width value of 0.5 eV, and the resultant hybridisation map, are shown in Figure 5-7. This hybridisation map shows a lower number of blue, green, and yellow pixels, indicating an average higher sp^2 content across the surface and less

variance, which results in a higher SNR value. Further decrease in the step width value to 0.2 eV produces a hybridisation map that has a very consistent hybridisation across the whole area, with almost all of the pixels showing a shade of red, indicating a high sp^2 hybridised carbon percentage, and only a few orange pixels indicating areas of lower sp^2 content. The SNR value from this map is almost double that of the 0.5 eV map, indicating a significant reduction in the variance across the map. While there is variation in the hybridisation indicated by this map, the variations do not correlate with any of the features observed in the SEM image. This indicates that the features are all graphitic and appear differently coloured in the SEM due to their different morphology.

When the step width is further reduced to 0.1 eV the hybridisation map shows an increase in the variation in the pixel colours over the 0.2 eV step width map. There is an increase in the number of both dark red pixels (indicating the top of the sp^2 hybridised carbon percentage scale, and quite possibly exceeding the maximum value of the scale) and orange and yellow pixels, indicating lower sp^2 content, which has resulted in a decrease in the SNR value.

As the step width is decreased from 1.0 eV to 0.2 eV the number of pixels that appear to be outliers is decreased, and it is clear that the use of the large step width is impacting on the scale used to create the hybridisation map. As the increments of the D parameter become larger the colour scale becomes separated into large segments, resulting in the starkly different coloured pixels. As the step width is decreased the energy resolution of the spectra is improved and the uncertainty in the D parameter become smaller and the values are rounded to a smaller extent. This results in smaller increments in the D parameter scale, and hence in the sp^2 hybridised carbon percentage scale, and the variations in the map will more accurately reflect the differences in hybridisation. However, the results from a 0.1 eV step width map show an increased variation in the map when compared to the maps with larger step widths, which suggests that this smallest step width may result in artefacts from false maxima and minima in the data.
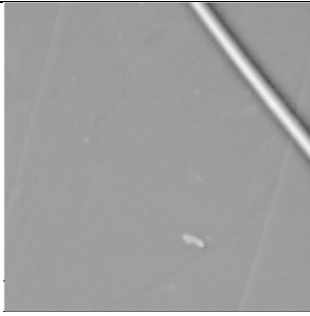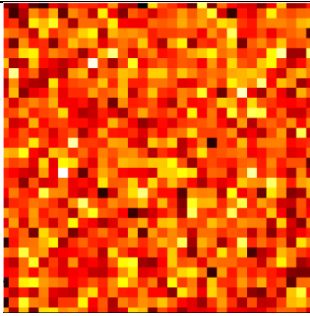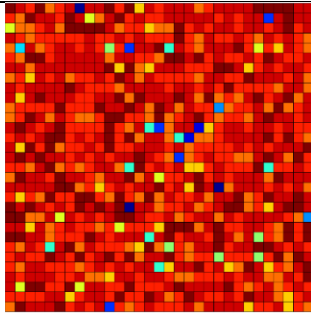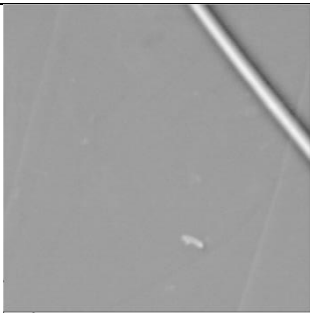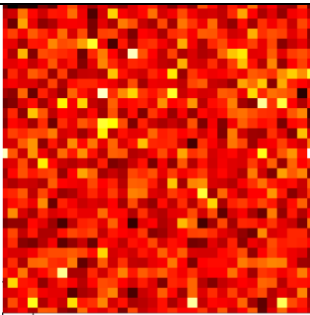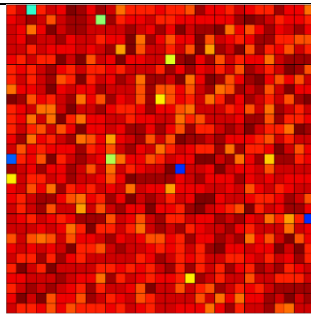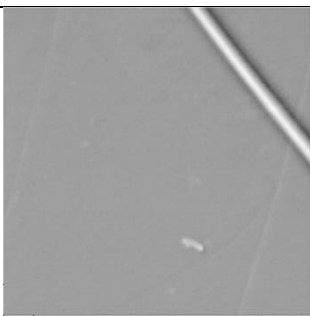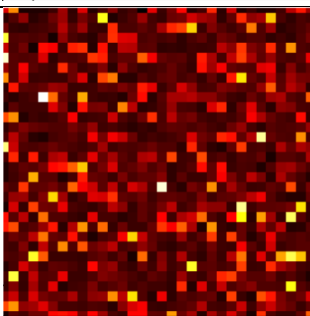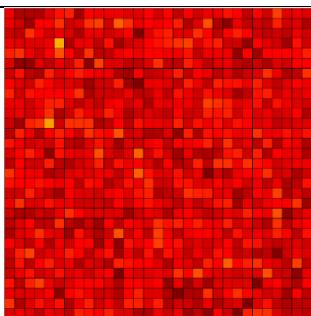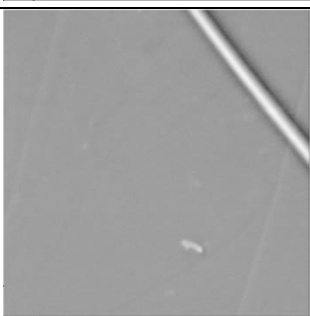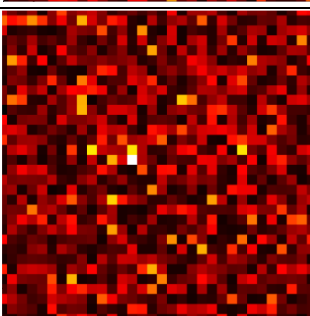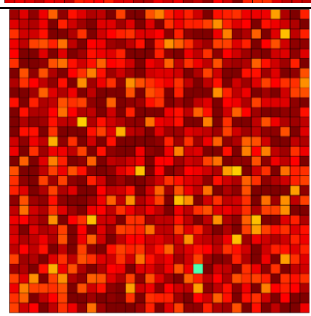
Step Width (eV)	SEM	Carbon Elemental Map	Hybridisation map	SNR
1.0				6.43
0.5				11.0
0.2				20.3
0.1				9.93

Figure 5-7: SEM images (20 µm FOV), C(KLL) elemental map, and hybridisation maps for HOPG taken with step width of 1.0 eV, 0.5 eV, 0.2 eV, and 0.1 eV.

The SNR values from Figure 5-7 are plotted against the step width used to acquire the carbon elemental maps in Figure 5-8.
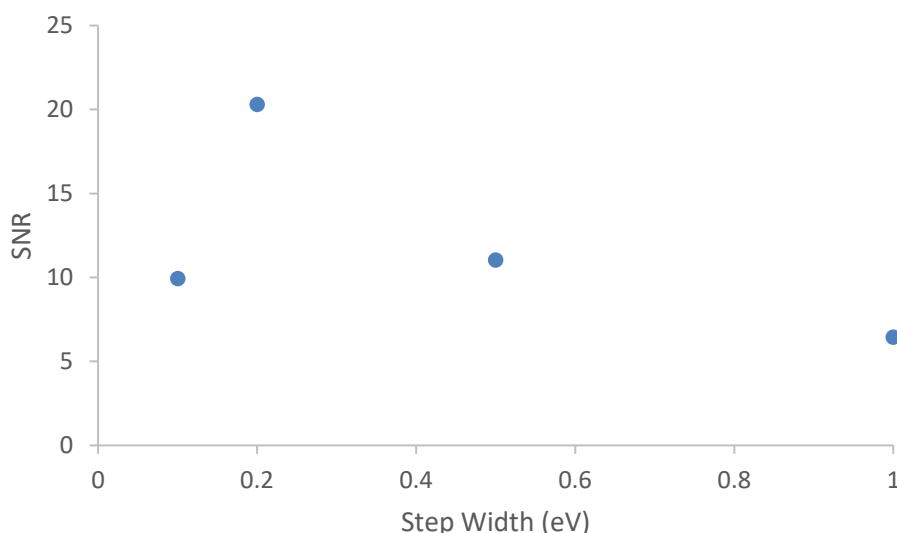
Figure 5-8: Variation in SNR value from hybridisation line scans in Figure 5-7 plotted against the step width of the C(KLL) spectra used to calculate the hybridisation.

Comparison of the SNR values in Figure 5-8 show that there is a significant increase in the SNR when the step width used to acquire the carbon elemental map is 0.2 eV, with a value that is almost double that of any other step width. This result shows that to produce a hybridisation map that shows the most consistent values of the hybridisation content of HOPG a step width of 0.2 eV should be used to acquire the carbon elemental map.

The average spectrum from across the entirety of each map in Figure 5-7 are shown in Figure 5-9 (a). The spectra acquired with step widths of 1.0 eV, 0.5 eV, and 0.2 eV show similar fine structure, but do vary in the positions of the maxima and minima, as shown in Table 5-3. The spectrum acquired with a step width of 0.1 eV shows larger variations in the fine structure but a similar D parameter value to the other spectra, with all values varying between 22.5 eV and 23.0 eV. The uncertainty in these values changes depending on the step width used to acquire the spectra, with the uncertainty being equal to the step width. The uncertainty therefore decreases when the step width decreases.

Spectra extracted from three individual pixels of the maps in Figure 5-7 are shown in Figure 5-9 (b), (c), and (d). When a step width of 1.0 eV is used (blue line) there is a loss of fine structure within each of the spectra acquired at all three pixels examined. The maxima and minima appear broad and rounded, which will negatively impact the ability to extract an accurate value for the D parameter, as shown by the variations in the D parameter in Table 5-3, which vary between 21.0 eV and 23.0 eV with an uncertainty of 1.0 eV.
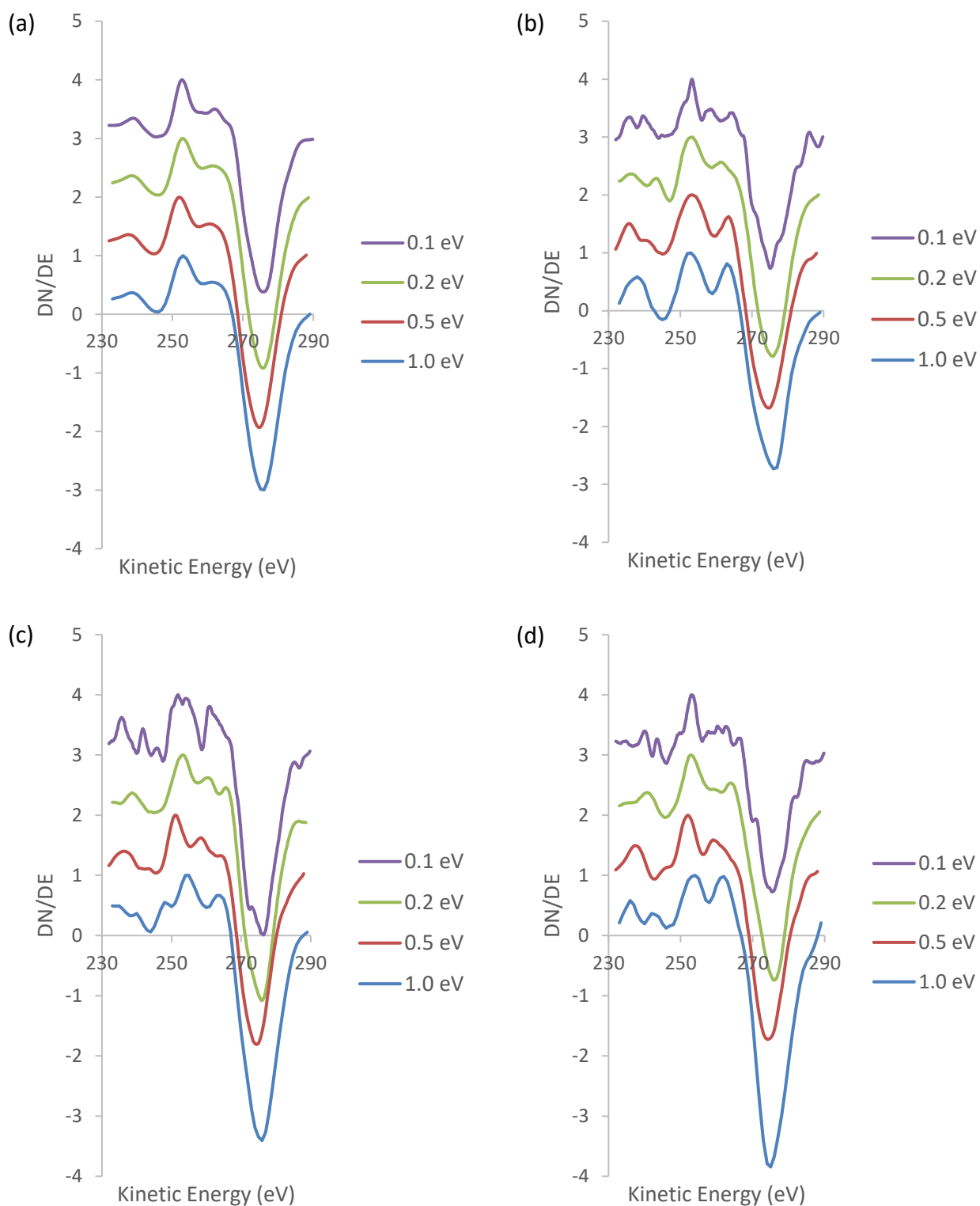
Figure 5-9: C(KLL) spectra taken from (a) the average of all spectra in the map, and pixel (b) 272, (c) 558, and (d) 784 of the 32x32 pixel carbon elemental maps of HOPG. Each plot shows a spectrum with a step width of 1.0 eV (blue), 0.5 eV (red), 0.2 eV (green), and 0.1 eV (purple).

As the step width is decreased the maxima and minima in the spectra become more clearly defined, with the maxima and minima becoming quite sharp peaks at a step width of 0.1 eV (purple line in Figure 5-9). While this may seem desirable, further examination of the spectra show that decreasing

the step width to this level actually introduces more noise into the spectra, with smaller variations in the intensity becoming more dominating to the overall peak shape, and possibly impacting on the accuracy of the value of the D parameter extracted from that spectrum. This is one of the reasons that a step width of 0.1 eV is deemed to not be suitable for the purposes of carbon hybridisation map creation. Using a step width of 0.1 eV also greatly increases the acquisition time for collecting the data to a time that is unreasonable for any scan with a spatial resolution higher that 32x32 pixels, as an increase in the spatial resolution for a given set of scanning parameters results in a fourfold increase in acquisition time, while decreasing the step width from 0.2 eV to 0.1 eV doubles the acquisition time.

Comparison of the D parameter values from Table 5-3 show that there is a lot of variation in the D parameter values when the step width changes. The uncertainty in each measurement is the same as the step width value used to acquire it, and the uncertainty is therefore decreasing as the step width decreases. While there is a lot of variation that does not show a clear increasing or decreasing trend with a decrease in step width, the values of the D parameter are most consistent for the step width of 0.2 eV, indicating that this may be the optimum value for the creation of hybridisation maps.

Table 5-3: D Parameter values from each spectrum in Figure 5-9. The uncertainty of each value is the same as the step width used to acquire it.

Step Width (eV)	D Parameter (eV) (Average)	D Parameter (eV) (Pixel 272)	D Parameter (eV) (Pixel 558)	D Parameter (eV) (Pixel 784)
1.0	23.0	23.0	21.0	21.0
0.5	22.5	21.5	23.5	22.0
0.2	22.6	22.6	22.6	23.2
0.1	23.0	21.8	24.5	22.2

Based on the hybridisation maps shown in Figure 5-7, the SNR values in Figure 5-8, the spectra in Figure 5-9, and the D parameter values in Table 5-3, it appears that the optimal step width to use for carbon elemental maps collected to create carbon hybridisation maps is 0.2 eV. This value results in an increased resolution of the D parameter, and therefore improves the gradient of colours in the hybridisation maps in a reasonable timeframe without introducing further noise to the spectral data.

5.2.2.2 Step Width Optimisation – DLC

The impact of step width on the hybridisation maps of DLC films was also examined, with step widths of 1.0 eV, 0.5 eV, 0.2 eV, and 0.1 eV used to acquire carbon elemental maps. In order to keep the impact of electron beam induced graphitisation as low as possible during these tests the maps with the shortest acquisition times were acquired first, thus the first map examined has a step width of 1.0 eV.

Figure 5-10 shows the 20 µm FOV SEM image of the area over which the maps were acquired, which is a surface that is almost entirely uniform in both colour and texture, with the exception of several small darker spots in the upper left and centre right of the image. The carbon elemental map and resultant hybridisation maps acquired with all step widths are also shown in Figure 5-10.

Using a step width of 1.0 eV, the hybridisation map shows a range of colours, indicating a range of sp^2 hybridisation percentages being present (Figure 5-10), although these variations do not correspond to the features in the SEM image. However, the increments in the scale of hybridisation percentages are large, and thus there is a lot of uncertainty and rounding errors present in the percentage values, which is likely to be causing the hybridisations to appear different to what the actual values are. When a step width of 0.5 eV is used the number of vastly differently coloured pixels in the hybridisation map is reduced, but there is also an increased range of colour shades indicating hybridisation percentages between those that were found using a step width of 1.0 eV. Further reduction of the step width to 0.2 eV results in further decrease in the size of the increments of the sp^2 hybridised carbon percentage scale, giving a larger range of shades of colour in the map. However, the map also now appears to have a higher sp^2 hybridised carbon percentage overall, as was expected based on the electron beam induced graphitisation shown in Figure 5-4 and Figure 5-6. A further reduction in step width to 0.1 eV results in more changes in the hybridisation map, with the appearance of pixels indicating the maximum of the hybridisation percentage scale is being exceeded, while simultaneously showing the presence of pixels of colder colours indicating lower sp^2 percentages. The increase in variance in this final hybridisation map may be the result of increased noise in the spectra introducing false maxima or minima to the spectra.
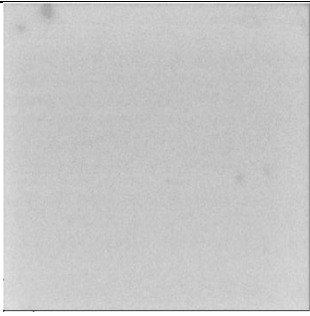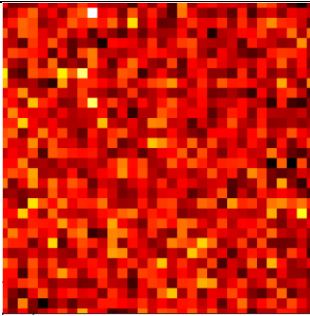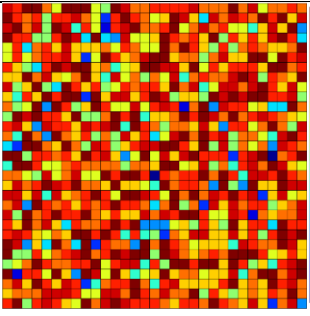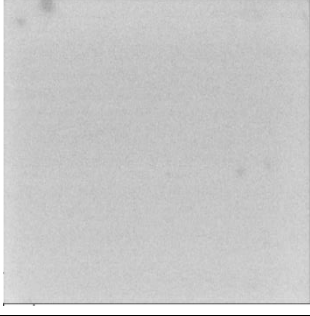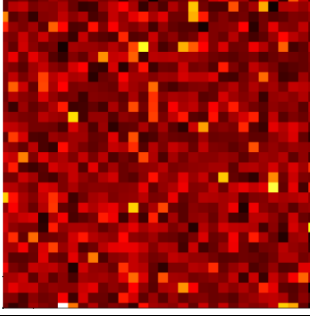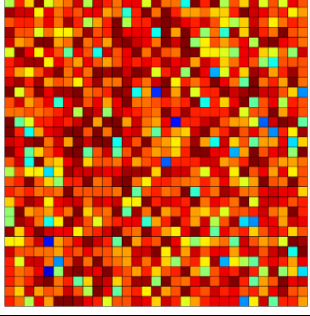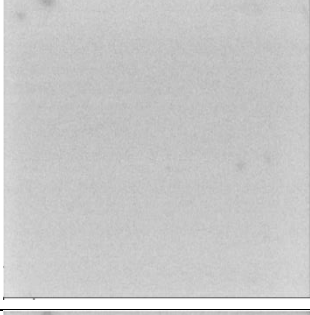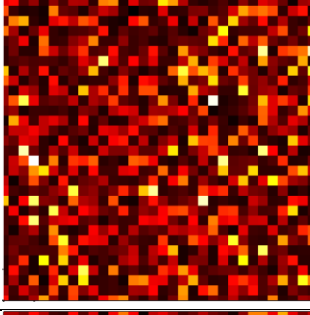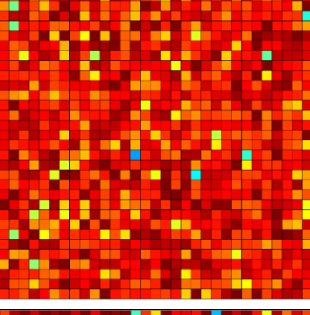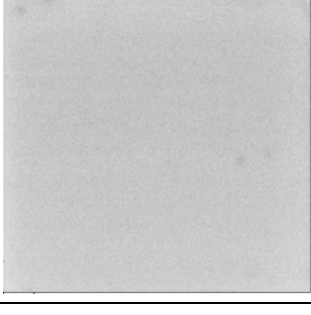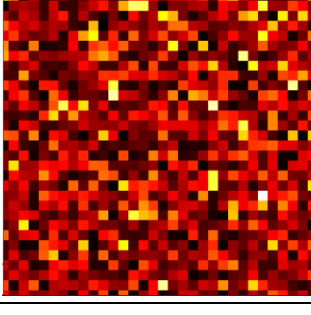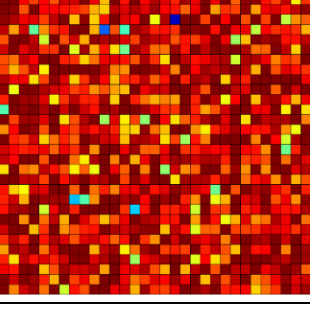
Step Width (eV)	SEM	Carbon Elemental Map	Hybridisation map	SNR
1.0				2.29
0.5				4.04
0.2				7.89
0.1				5.82

Figure 5-10: SEM images (20 μm FOV), C(KLL) elemental map, and hybridisation maps for DLC taken with step width of 1.0 eV, 0.5 eV, 0.2 eV, and 0.1 eV.

The SNR values from the hybridisation maps in Figure 5-10 are plotted against the step width value used to acquire the carbon elemental maps in Figure 5-11.
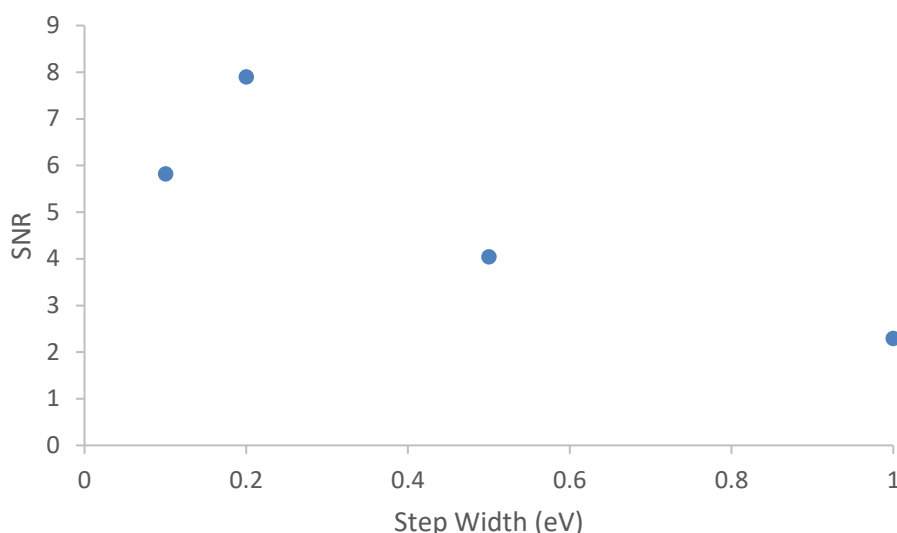
Figure 5-11: Variation in SNR value from hybridisation line scans in Figure 5-10 plotted against the step width of the C(KLL) spectra used to calculate the hybridisation.

The hybridisation map that shows the highest SNR value is that from the carbon map with a 0.2 eV step width, which is at least 25 % higher than that from any other maps. This increase in the SNR value is a result of both an increase in the average hybridisation across the surface and a decrease in variance, part of which is due to the electron beam induced graphitisation. The decreased variance is also a result of the decreased uncertainty associated with a smaller step width value. To further examine the impact of changing the step width value the spectra from the carbon maps are also examined.

An average spectrum obtained from the spectra in each pixel of the carbon elemental map is shown for each of the step width values tested in Figure 5-12 (a). The D parameter from these spectra is slightly increased as the step width decreases (Table 5-4), however this occurs to a similar extent to that observed in Figure 5-6, indicating that this change may be a result of electron beam induced graphitisation. Apart from this change in D parameter all of the step widths show a similar peak shape and very good signal to noise ratio.

However, this is not the case when spectra from individual pixels are extracted and compared. Figure 5-12 (b), (c), and (d) show spectra from three individual pixels, and a much clearer trend is observed. When a step width of 1.0 eV is used (blue lines) the spectra appear quite smooth, but do not show much fine structure and it is very likely that the true positions of the maxima and minima of the peak lie between the measured data points. The D parameter values for these spectra vary between 21.0 eV and 24.0 eV, with an uncertainty of 1.0 eV.
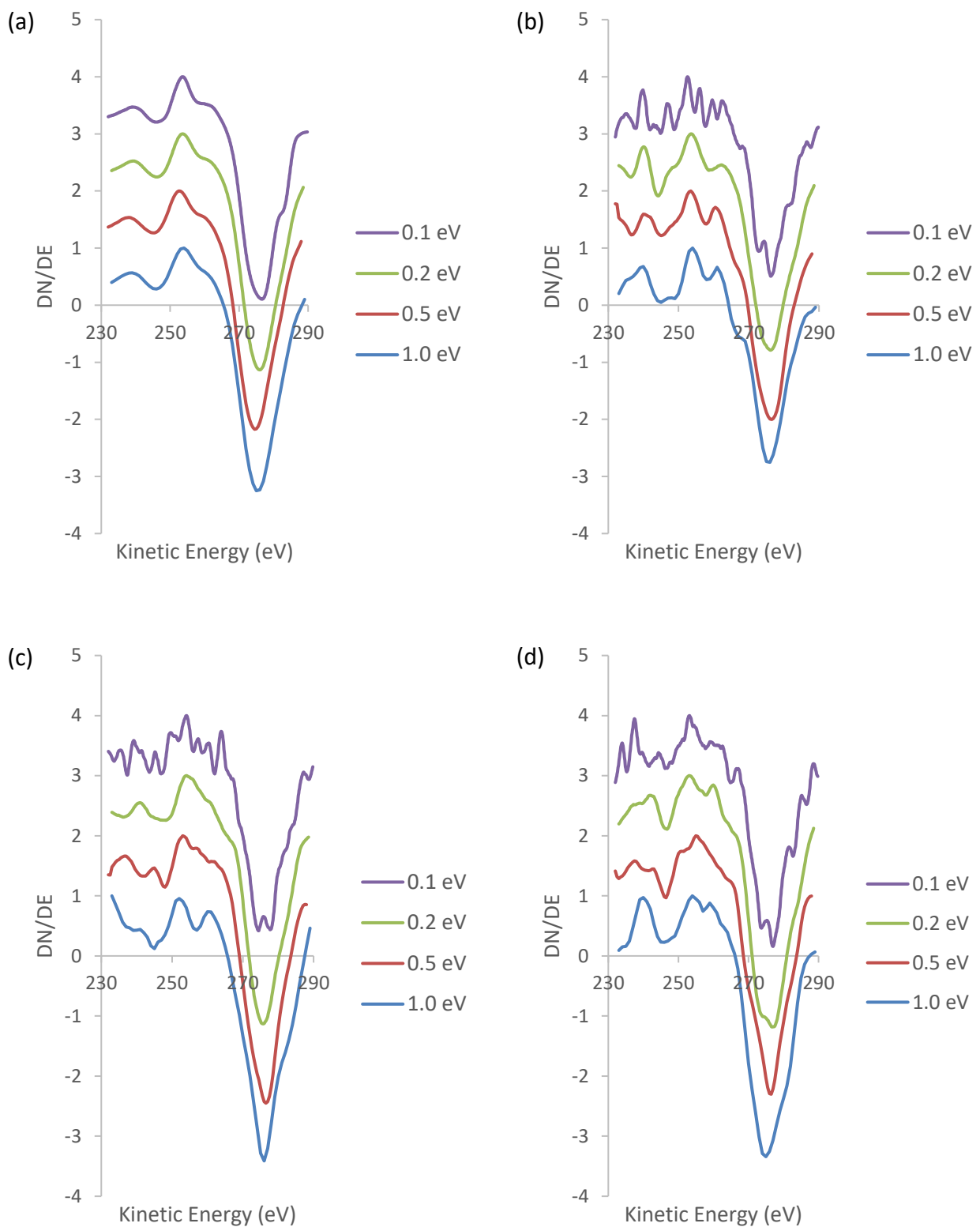
Figure 5-12: C(KLL) spectra taken from (a) the average of all spectra in the map, and pixel (b) 272, (c) 558, and (d) 784 of the 32x32 pixel carbon elemental maps of DLC. Each plot shows a spectrum with a step width of 1.0 eV (blue), 0.5 eV (red), 0.2 eV (green), and 0.1 eV (purple).

As the step width is reduced to 0.5 eV (red line) and 0.2 eV (blue line) the fine structure of the peaks becomes increasingly visible, although there is again an increase in the D parameter that is likely to

be due to the electron beam induced graphitisation. These results match the changes observed in the hybridisation maps in Figure 5-10, both in the small peak shape changes that influence the D parameter and in the overall graphitisation trend, and can be seen numerically in Table 5-4. When a smaller step width of 0.1 eV is used the spectra change quite dramatically and the signal to noise ratio is greatly decreased, making accurate determination of the maxima and minima less likely.

Table 5-4: D Parameter values from each spectrum in Figure 5-12. The uncertainty in each D parameter measurement is the same as the step width used to acquire the spectrum.

Step Width (eV)	D Parameter (eV) (Average)	D Parameter (eV) (Pixel 272)	D Parameter (eV) (Pixel 558)	D Parameter (eV) (Pixel 784)
1.0	21.0	22.0	24.0	21.0
0.5	22.0	23.0	23.5	21.5
0.2	22.4	22.6	21.8	23.8
0.1	23.0	23.7	20.3	23.8

The results from the hybridisation maps, SNR values, and spectra in Figure 5-10, Figure 5-11, and Figure 5-12, respectively, indicate that the best step width value to use for this data collection is 0.2 eV, as it improves the spectra obtained without introducing false maxima and minima from low signal to noise ratios.

5.2.2.3 Step Width Optimisation – Conclusions

Hybridisation maps acquired on both HOPG and DLC using step widths ranging between 0.1 eV and 1.0 eV are presented in Figure 5-7 and Figure 5-10, respectively, and show that there are changes in the quality of the map when the step width changes. The results from both HOPG and DLC show that a step width of 0.2 eV is necessary to acquire maps with a sufficient energy resolution to accurately determine the true value of the D parameter, and therefore the true value of the sp^2 hybridised carbon percentage. All carbon elemental maps acquired for the purpose of creating a hybridisation map will therefore be acquired using a step width of 0.2 eV.

5.2.3   Time Per Step Optimisation

The second SAM scan parameter that needs to be examined is the acquisition time per step, which is a measure of the dwell time at each energy point of the spectrum, and has pre-set allowable values ranging from 0.1 ms to 10 ms that can be chosen from a selection box. A larger time per step

value is desired to improve spectral quality by improving the counting statistics of the data collection, however this improvement must be balanced with the accompanying acquisition time. To find this balance time per step values of 0.2 ms, 0.5 ms, and 1.0 ms were examined, as anything larger than this results in acquisition times that are not feasible for maps of spatial resolution higher than 32x32 pixels.

5.2.3.1 Time Per Step Optimisation – HOPG

The impact of changing the time per step was first examined for HOPG, with Figure 5-13 showing the SEM image of the area where the tests were performed. This area is uniform in colour and texture across most of the surface, however there are some small areas of either darker or lighter colours in the image. The carbon elemental maps and the resultant hybridisation maps acquired with time per step values of 0.2 ms, 0.5 ms, and 1.0 ms are also shown in Figure 5-13. As these maps are acquired over the same area of the same sample any variations that are observed should be the result of changes in the time per step value rather than changes in the sample.

The hybridisation map acquired using a time per step of 0.2 ms (Figure 5-13) shows a surface that is predominantly sp^2 hybridised, as indicated by the majority of the pixels in the map being red. There are, however, several pixels scattered throughout the map that are yellow, green, and blue, indicating small regions with a lower sp^2 hybridised carbon content. It can be seen in Figure 5-13 that as the time per step is increased the number of pixels that show colours that appear to be different from the rest of the surface decreases, and the surface begins to look more uniform. This is to be expected as the longer counting times will help reduce the impact of random errors on the spectra and improve the signal to noise ratio. The improvement from a time per step value of 0.2 ms to 0.5 ms is quite significant, while the improvement gained using 1.0 ms time per step appears smaller, despite a doubling of acquisition time. The SNR of the hybridisation maps can provide quantification to this variance in the hybridisation maps.
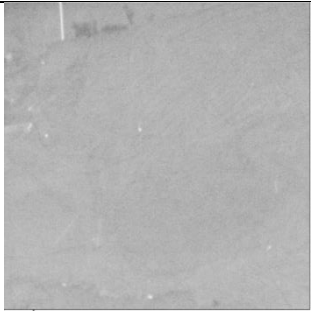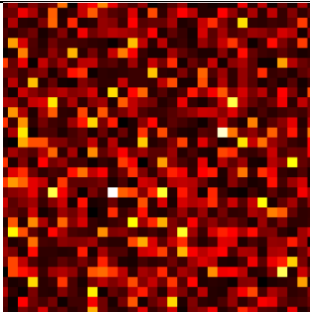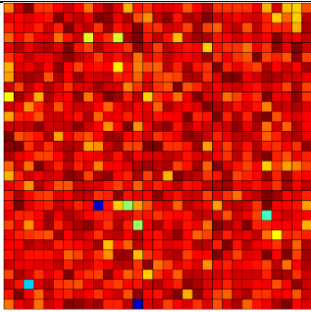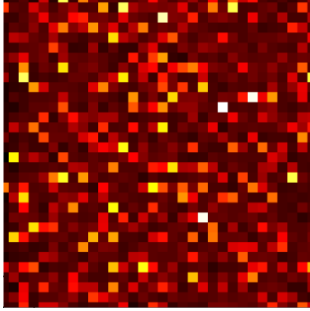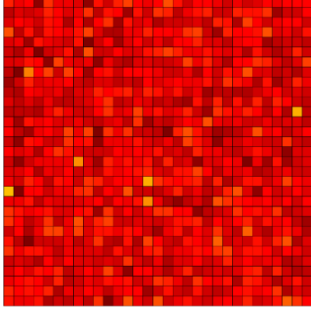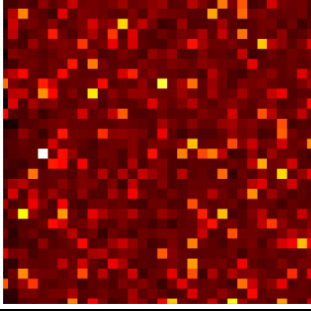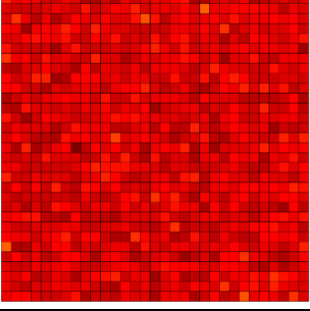
TPS (ms)	SEM	Carbon Elemental Map	Hybridisation map	SNR
0.2				9.66
0.5				19.5
1.0				28.6

Figure 5-13: SEM images (20 μm FOV), C(KLL) elemental map, and hybridisation for HOPG taken with time per step of 0.2 ms, 0.5 ms, and 1.0 ms.

The SNR values are plotted against the time per step value used to acquire them in Figure 5-14.

Figure 5-14 y-axis: SNR, x-axis: Time Per Step (ms)
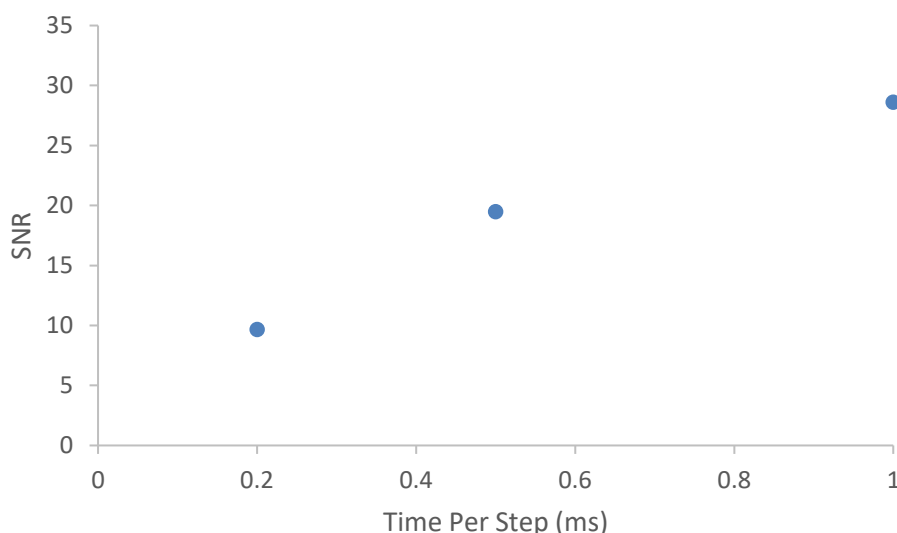
Figure 5-14: Variation in SNR value from hybridisation line scans in Figure 5-13 plotted against the time per step of the C(KLL) spectra used to calculate the hybridisation.

It can be seen in Figure 5-14 that an increase in the time per step results in an increase in the SNR value, with the 1.0 ms map producing a SNR of 28.6. This suggests that the best time per step value to use is 1.0 ms, however the spectra extracted from the carbon elemental map need to be examined to determine how the peak shape changes.

When the average spectra from all of the pixels from the map of each step width tested are compared (Figure 5-15 (a)) there is very little difference between the spectra due to the reduction of random fluctuations in the spectra that occurs with the large sample size. This can be seen in Table 5-5 where the D parameter values for the average spectrum of all time per step values are the same (22.6 eV).

However, examination of the spectra extracted from three individual pixels in the map reveals some differences (Figure 5-15 (a), (b), and (c)). The spectra with 0.2 ms time per step (blue line in Figure 5-15) have higher spectral noise than both the 0.5 ms (red line) and 1.0 ms (green line), which appear quite similar. This suggests that very little improvement is gained by increasing the time per step from 0.5 ms to 1.0 ms, despite the doubled acquisition time. The D parameter values for the spectra at different pixels do not show the same trends, however they do all approach a value of 22.8 eV with a time per step of 1.0 ms.

170

Figure 5-15: C(KLL) spectra taken from (a) the average of all spectra in the map, and pixel (b) 272, (c) 558, and (d) 784 of the 32x32 pixel carbon elemental maps of HOPG. Each plot shows a spectrum with a time per step of 0.2 ms (blue), 0.5 ms (red), and 1.0 ms (green).

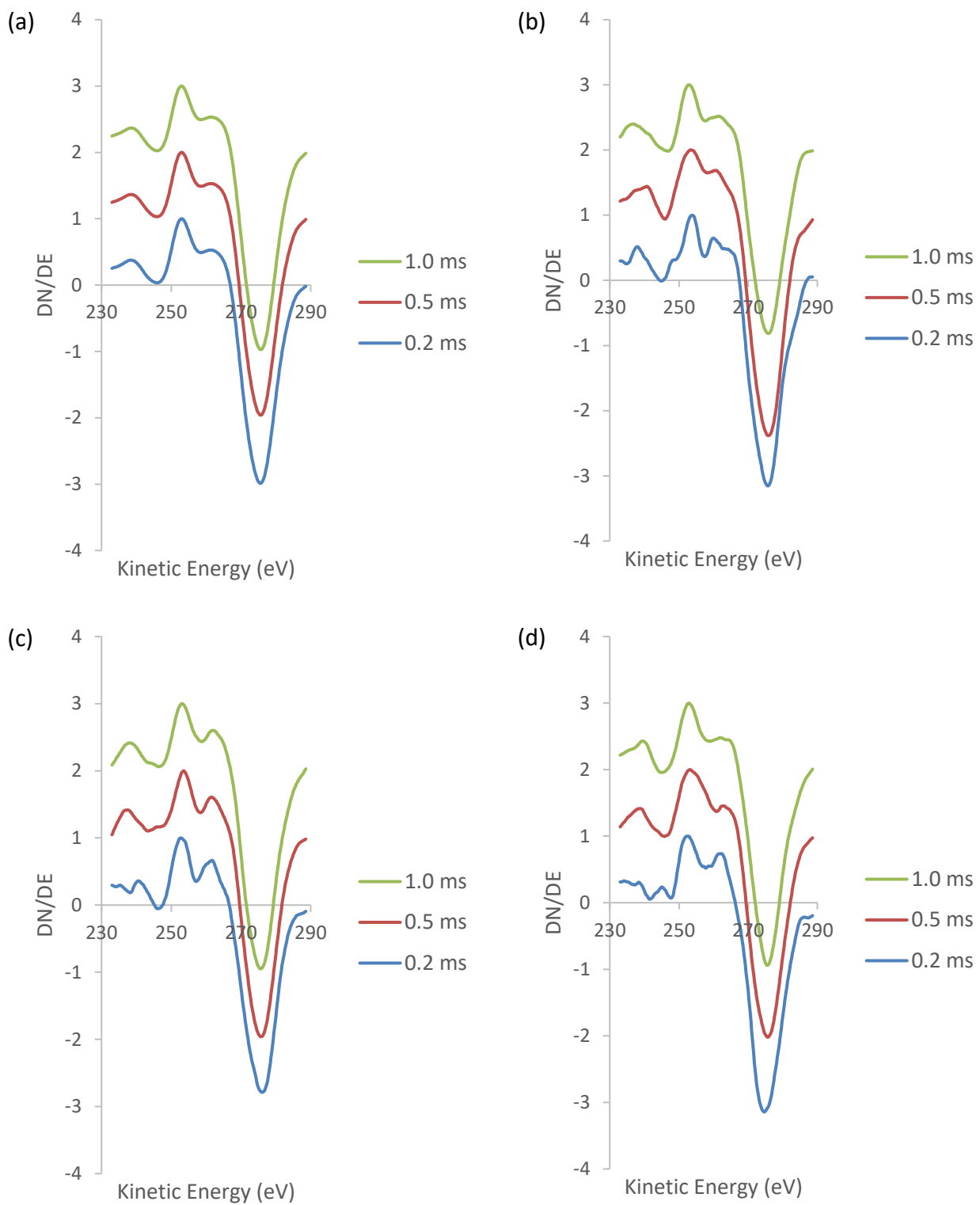| Time Per Step (ms)	D Parameter (eV) (Average)	D Parameter (eV) (Pixel 272)	D Parameter (eV) (Pixel 558)	D Parameter (eV) (Pixel 784)
0.2	22.6	21.8	23.4	22.2
0.5	22.6	22.8	22.2	22.4
1.0	22.6	23.0	22.6	22.8

The results from Figure 5-13, Figure 5-14, Figure 5-15, and Table 5-5 combine to show that an increase in the time per step used to acquire the carbon elemental maps results in an increase in the quality of the data, with the hybridisation map showing less variance and a higher SNR. However, using a time per step of 1.0 ms requires an acquisition time that is double that of a 0.5 ms map, and a decision must be made about the reasonableness of this acquisition time. A longer time will also result in more electron beam exposure on the sample surface, which could influence the hybridisations detected on the surface. Taking these factors into consideration, along with the improvements to the data when increasing the time per step from 0.5 ms to 1.0 ms, it is concluded that a time per step of 0.5 ms is the optimal choice for carbon elemental map acquisition.

5.2.3.2 Time Per Step Optimisation – DLC

The effect of changing the time per step when acquiring window mode carbon elemental maps was also examined for the DLC film. The four maps were taken over the same area, and therefore it is expected that there will be some electron beam induced graphitisation of the sample. To reduce the impact of this the maps were taken in order of increasing acquisition time. The SEM image of the area under examination is presented in Figure 5-16, and shows a surface that is mostly uniform in both colour and texture, with the exception of two darker spots and one lighter spot that appears to be a particle on the surface.

The window mode carbon elemental maps acquired with the different values of time per step and the resultant hybridisation maps are also shown in Figure 5-16. A time per step of 0.1 ms results in a carbon hybridisation map showing pixels across the full colour scale, indicating that the sample has regions ranging from 0 % to 100 % sp^2 hybridised carbon, with the variations not corresponding to any of the features in the SEM image. This high level of variance results in a low SNR value of 2.36. Increasing the time per step to 0.2 ms results in a map that shows a higher number of red

pixels, indicating a surface that is more uniform, and also that there may have been some electron beam induced graphitisation. This decreased variation in the hybridisations present results in a higher SNR value of 3.97. Further increases in the time per step to 0.5 ms and 1.0 ms result in further increases in the amount of sp^2 hybridised carbon present in the hybridisation maps, with fewer cooler coloured pixels observed.
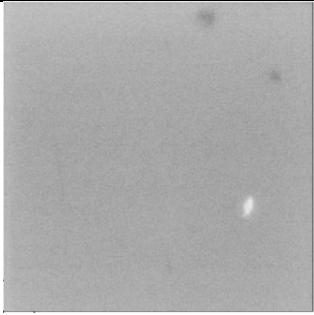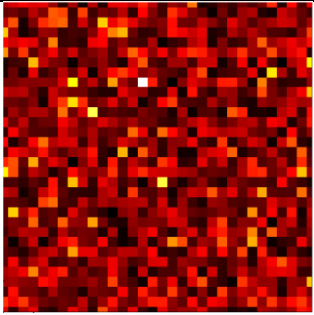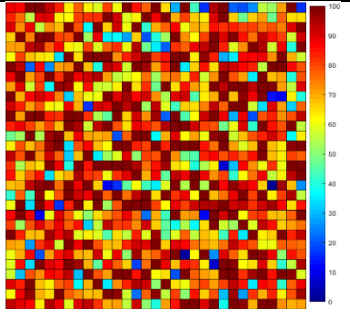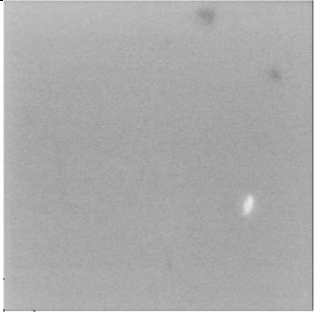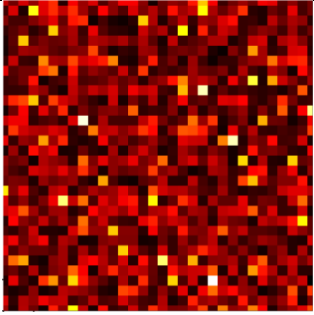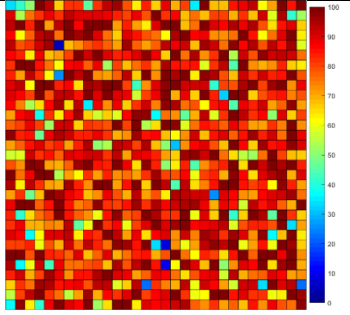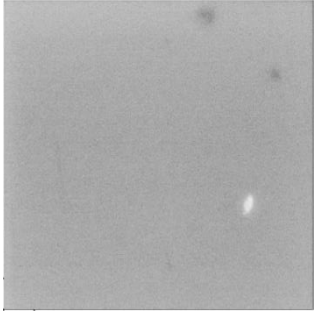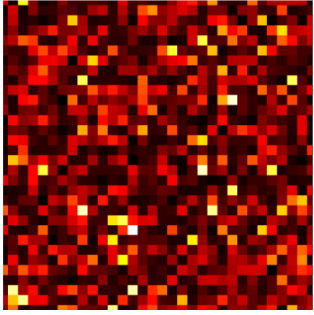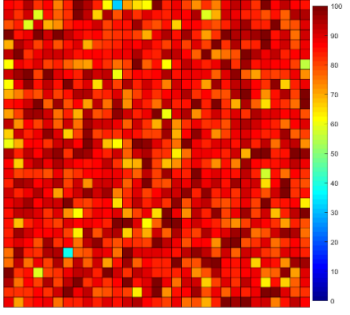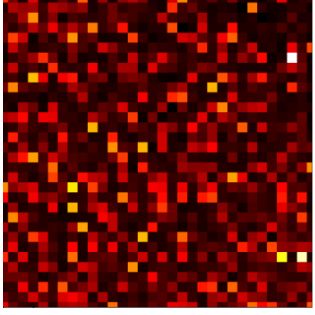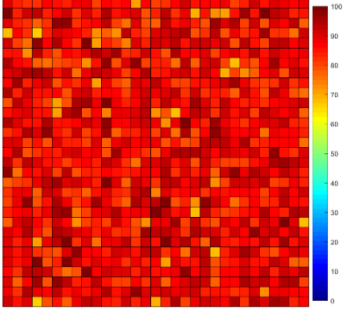
TPS (ms)	SEM	Carbon Elemental Map	Hybridisation map	SNR
0.1				2.36
0.2				3.97
0.5				9.00
1.0				13.7

Figure 5-16: SEM images (20 µm FOV), C(KLL) elemental map, and hybridisation maps for DLC taken with time per step of 0.1 ms, 0.2 ms, 0.5 ms, and 1.0 ms.

The SNR value from each of the hybridisation maps in Figure 5-16 is plotted Figure 5-17 against the

time per step value used to acquire the carbon elemental maps.
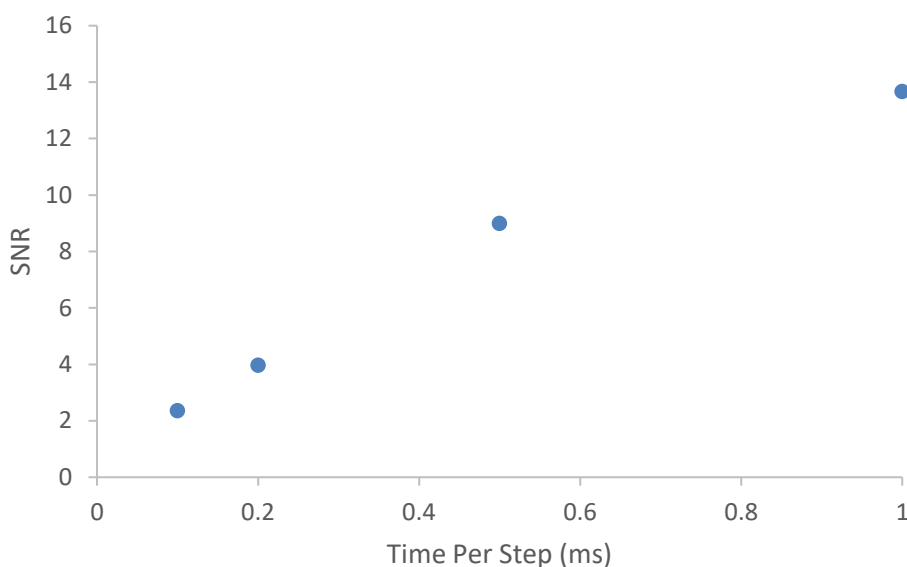
Figure 5-17: Variation in SNR value from hybridisation line scans in Figure 5-16 plotted against the time per step of the C(KLL) spectra used to calculate the hybridisation.

An increase in the SNR is observed when the time per step value increases, with a 1.0 ms time per step resulting in the highest SNR value of 13.7. This increase is due to both an increase in the average hybridisation across the surface and a decrease in the variance, which may be due to the increased graphitisation or the changes that occur with the changes in time per step value. To determine which of these cases is correct the spectra from the carbon elemental maps must be examined.

Figure 5-18 (a) shows spectra composed of the average spectra from each pixel across the entirety of each map presented in Figure 5-16. The spectra all have a similar shape and signal to noise ratio, however as the time per step increases there is an increase in the D parameter from 21.8 eV to 22.4 eV (Table 5-6). Since the energy resolution is the same in each map, the results indicate that there is indeed electron beam induced graphitisation that has occurred and influences the results.

When spectra from individual pixels are examined in Figure 5-18 (b), (c), and (d) the impact of changing the time per step is more easily observed. The spectra acquired using a time per step of 0.1 ms (blue line) have higher noise levels than those with longer time per step and are more likely to result in inaccurate D parameter values due to this noise as it is more difficult to accurately find the positions of the maxima and minima. This noise is lower in the 0.2 ms (red line), 0.5 ms (green line) and 1.0 ms (purple line), however as the time per step increases the extent of electron beam induced graphitisation is increased. This graphitisation introduces another factor into the

174

optimisation process, which is related to but not identical to the increased acquisition time with increased time per step.
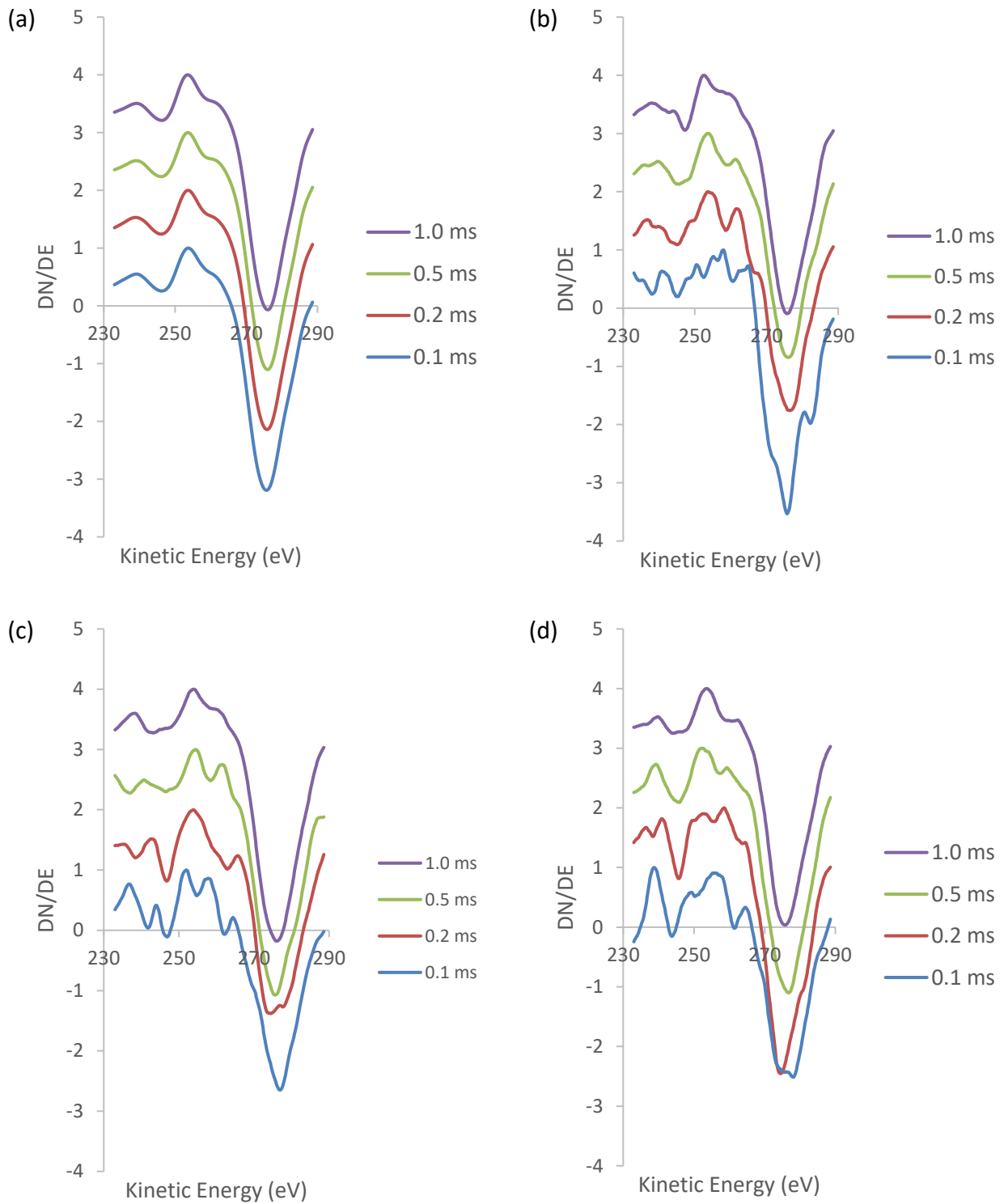
Figure 5-18: C(KLL) spectra taken from (a) the average of all spectra in the map, and pixel (b) 272, (c) 558, and (d) 784 of the 32x32 pixel carbon elemental maps of DLC. Each plot shows a spectrum with a time per step of 0.1 ms (blue), 0.2 ms (red), 0.5 ms (green), and 1.0 ms (purple).

Table 5-6: D Parameter values from each spectrum in Figure 5-18. The uncertainty in each D parameter value is ±0.2 eV.

Time Per Step (ms)	D Parameter (eV) (Average)	D Parameter (eV) (Pixel 272)	D Parameter (eV) (Pixel 558)	D Parameter (eV) (Pixel 784)
0.1	21.8	17.8	25.0	22.8
0.2	22.2	22.8	20.6	16.0
0.5	22.4	22.0	21.2	24.0
1.0	22.4	23.2	22.2	22.2

The extent of graphitisation and acquisition time prohibit the use of 1.0 ms time per step, suggesting that the best improvement in counting statistics balanced with these other factors is achieved with a time per step of 0.5 ms. The D parameter values from these samples are inconclusive (Table 5-6) due to the random noise fluctuations and spectral fine structure changes from the graphitisation, so in this case the conclusion must be drawn from the hybridisation maps, SNR, and spectra, in Figure 5-16, Figure 5-17, and Figure 5-18, respectively. These results suggest that 0.5 ms is the optimal value of time per step for acquiring the window mode carbon elemental maps on DLC to achieve high quality data without inducing excessive electron beam induced graphitisation.

5.2.3.3 Time Per Step – Conclusions

The time per step value used during acquisition of the carbon elemental maps for the purpose of producing hybridisation maps was found to have an effect on the maps for both HOPG and DLC (Figure 5-13 and Figure 5-16). The hybridisation maps, the SNR values, and the spectra from the elemental maps show that an increase in time per step produces higher quality maps, however the acquisition time is significantly increased when the time per step increases. The electron beam induced changes that occur on the DLC surface is also a factor that must be considered, as the increased acquisition time produces a higher extent of modification. Balancing these factors, a time per step of 0.5 ms is the optimum choice for the acquisition of carbon elemental maps for the purpose of producing hybridisation maps.

5.2.4 Number of Scans Optimisation

For each pixel within the map the number of scans acquired and averaged to obtain the final spectrum will have a very strong influence on the signal to noise ratio, and therefore on the quality of the data and its usefulness in creating hybridisation maps. It is expected that the signal to noise

ratio will improve as the scan number increases, however there are time restrictions on data acquisition and a compromise must be found between time taken and number of scans. To investigate the impact of this variable carbon elemental maps were taken sequentially over the same area using, 10, 20, 30, or 40 scans for both HOPG and DLC films.

5.2.4.1 HOPG Number of Scans Optimisation

The SEM image of the 20 µm FOV area examined for the tests examining the impact of the number of scans appears to be mostly uniform in colour and texture (Figure 5-19), with the exception of what appears to be several small, lighter coloured particles scattered across the lower half of the image. The carbon elemental maps acquired with 10, 20, 30, and 40 scans averaged are also shown in Figure 5-19, along with the resultant hybridisation maps and their SNR values.

The hybridisation map created from the average of 10 scans is composed mostly of red pixels, indicating a high level of sp^2 hybridised carbon, but also contains pixels of blue, green, yellow, and dark red, indicating that there are areas of lower sp^2 hybridised carbon percentage as well as areas where the maximum of the sp^2 hybridised carbon percentage scale is being exceeded. These areas showing a different hybridisation level are scattered randomly across the surface and do not align with any of the features in the SEM image, indicating that the small particle like features on the surface are graphitic in nature but have a different morphology. When the number of scans averaged to create the hybridisation map is doubled to 20 there is a decrease in the number of pixels with colours other than red, indicating a surface with less variation in hybridisation. This is reflected in the SNR value, which is higher than that from the 10 scans hybridisation map.

As the number of scans averaged to produce the maps is increased to 30 and 40 scans there are some small differences in the hybridisation maps, and the surface looks more uniformly sp^2 hybridised. However, the difference between 20, 30, and 40 scans is quite small despite the large increase in acquisition time (which doubles from 20 to 40 scans). This suggests that using 20 scans is sufficient to achieve high spectral quality and therefore obtain high quality carbon hybridisation maps.
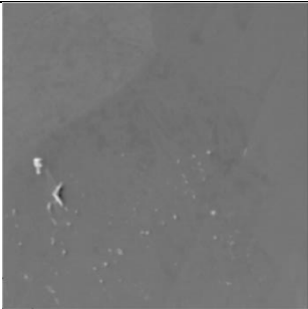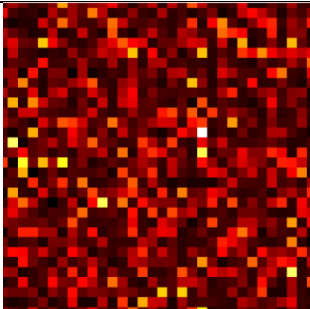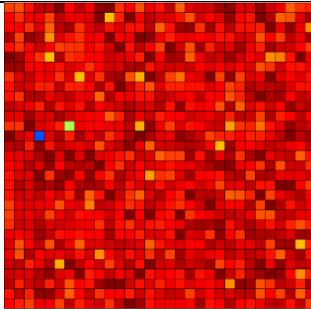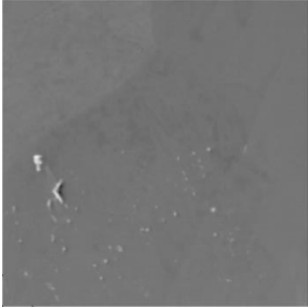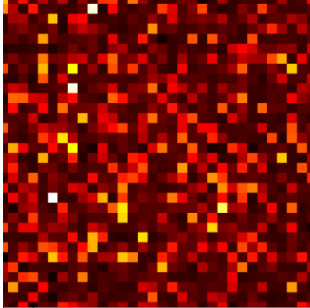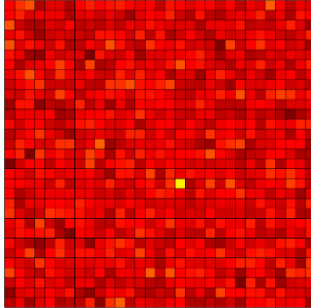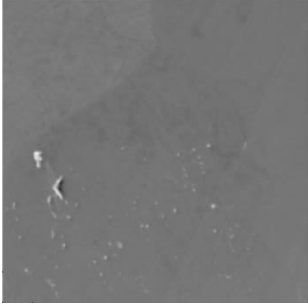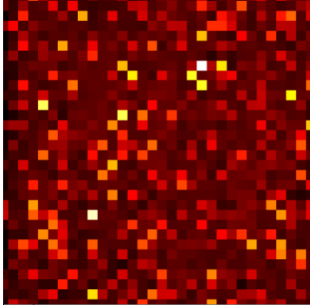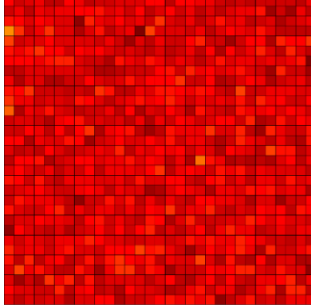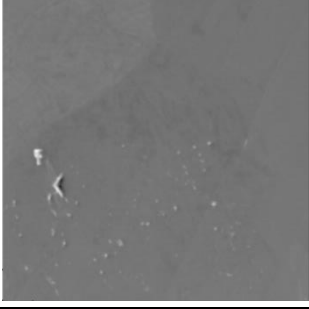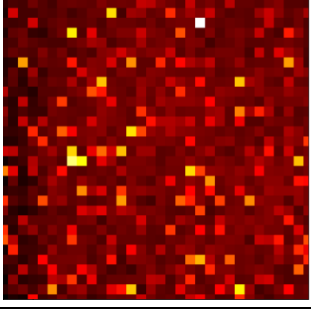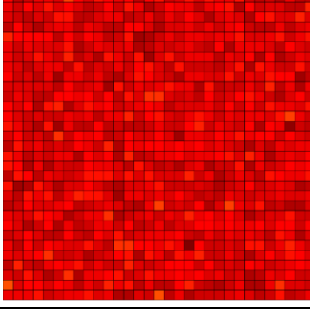
No. of Scans	SEM	Carbon Elemental Map	Hybridisation map	SNR
10				13.1
20				20.69
30				25.5
40				28.3

Figure 5-19: SEM images (20 μm FOV), C(KLL) elemental map, and hybridisation maps for HOPG taken with time per step of 0.2 ms and 10, 20, 30, and 40 scans.

The SNR values from Figure 5-19 are plotted in Figure 5-20 against the number of scans averaged to obtain the maps.
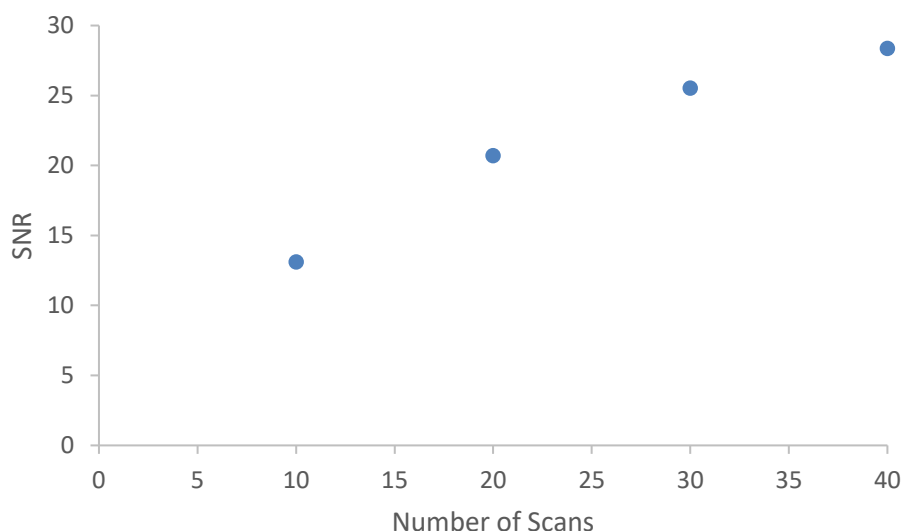
Figure 5-20: Variation in SNR value from hybridisation line scans in Figure 5-19 plotted against the number of scans averaged in the acquisition of the C(KLL) spectra used to calculate the hybridisation.

It can be seen in Figure 5-20 that the SNR value continues to increase as the number of scans averaged increases, however the improvement is smaller with each increase in scan numbers, as was expected from a visual examination of the hybridisation maps. Based on these results a minimum of 20 scans is needed to acquire hybridisation maps that are consistent and show little variance across a surface that should be constant, although increasing to 30 or 40 scans would provide further improvement. To further examine the impact of changing the number of scans the spectra from the carbon elemental maps are considered.

When the average spectra from all pixels of the carbon elemental maps are examined (Figure 5-21 (a)) the differences between the spectra obtained with varying scan numbers is small, with D parameter values of 22.6 eV for scan numbers up to 30, and a value of 22.8 eV for 40 scans (Table 5-7). The differences between the D parameter values is not significant as the uncertainty in the measurement is 0.2 eV, however the uniformity in the spectra is thought to be due to the averaging of a large number of spectra.

When individual spectra are extracted from the pixels of the hybridisation maps some differences are observed (Figure 5-21 (b), (c), and (d)). These differences are largest between the spectra for 10 scans (blue line in Figure 5-21) and 20 scans (red line), with the 20 scans spectra showing improved signal to noise ratio. The differences between the 20 scans, 30 scans, and 40 scans lines are much smaller, and suggest that increasing scan numbers beyond 20 scans does not produce sufficient increases in spectral quality to justify the increase in acquisition time. The D parameter values show some small variations between the scan numbers, but not with any trend (Table 5-7).

179

Figure 5-21: C(KLL) spectra taken from (a) the average of all spectra in the map, and pixel (b) 272, (c) 558, and (d) 784 of the 32x32 pixel carbon elemental maps of HOPG. Each plot shows a spectrum with 10 scans (blue), 20 scans (red), 30 scans (green), and 40 scans (purple).

Table 5-7: D Parameter values from each spectrum in Figure 5-21. The uncertainty in each D parameter value is ±0.2 eV.

Number of Scans	D Parameter (eV) (Average)	D Parameter (eV) (Pixel 272)	D Parameter (eV) (Pixel 558)	D Parameter (eV) (Pixel 784)
10	22.6	22.8	22.4	22.0
20	22.6	22.0	22.8	23.0
30	22.6	22.4	22.8	22.8
40	22.8	22.8	22.2	22.6

Consideration of the data presented in Figure 5-19, Figure 5-20, Figure 5-21, and Table 5-7 shows that there is significant improvement to the quality of the data obtained when the number of scans averaged to acquire the carbon elemental maps is doubled from 10 to 20 scans. If the number of scans is increased beyond this there is some further improvement observed, however this improvement must be balanced against the increase in acquisition time. It is therefore concluded that the optimal number of scans to acquire high quality data within a reasonable timeframe is 20 scans.

5.2.4.2 Number of Scans Optimisation – DLC

The number of scans averaged to obtain the carbon elemental maps was also tested with DLC films. The tests were performed over the same area, with the shortest acquisition time scan taken first to minimise the impact of the electron beam induced damage. The SEM image of this 20 µm FOV area is shown in Figure 5-22 and presents a surface that is almost entirely uniform in colour and texture. The exceptions to this are a small, round, bright area on the lower centre of the image that appears to be a particle on the surface, and a larger darker area on the upper centre of the image that also contains a small, bright particle.

The window mode carbon elemental maps are also shown in Figure 5-22, along with the resultant hybridisation maps. When 10 scans are averaged the hybridisation map shows a mixture of differently coloured pixels, which would indicate that a range of sp^2 hybridised carbon percentages are present. When the scan number is increased to 20, the hybridisation map changes to show a higher density of red pixels, indicating that the surface appears more graphitic. Further increases in scan number to 30 and 40 scans results in further increases in the density of red pixels, indicating even further graphitisation of the surface has occurred.
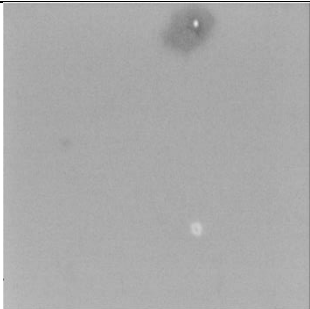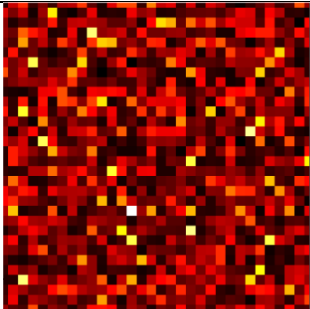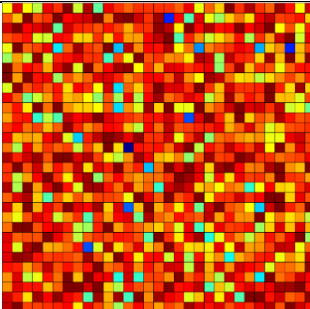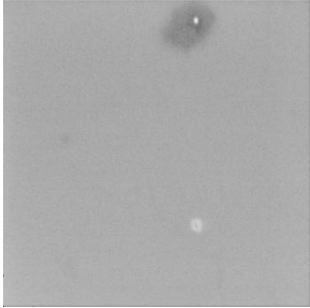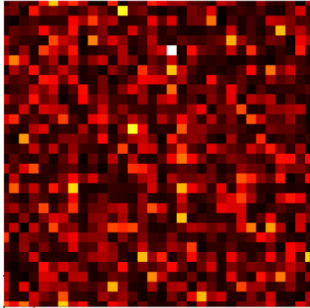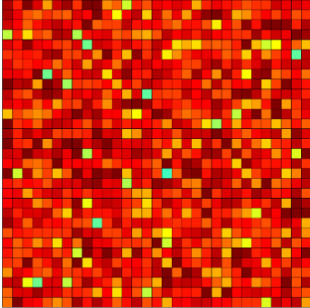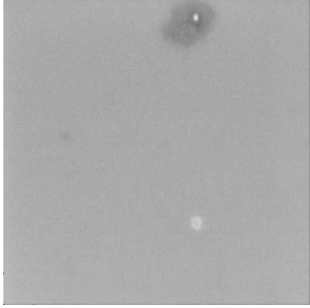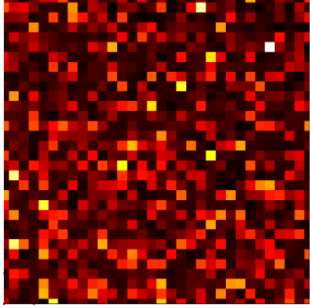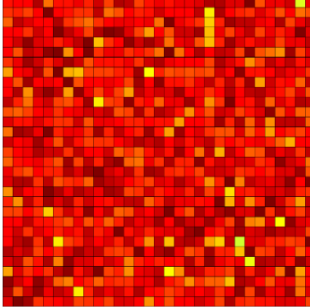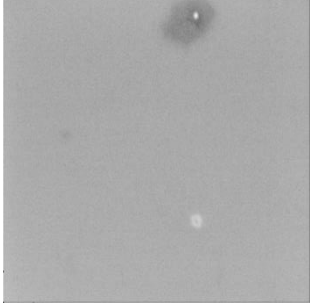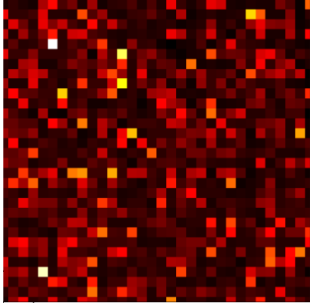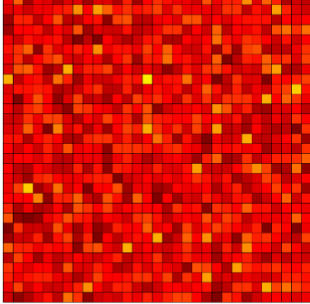
No. of Scans	SEM	Carbon Elemental Map	Hybridisation map	SNR
10				3.78
20				8.15
30				11.4
40				14.0

Figure 5-22: SEM images (20 μm FOV), C(KLL) elemental map, and hybridisation maps for DLC taken with time per step of 0.2 ms and 10, 20, 30, and 40 scans.

The SNR values from the hybridisation maps shown in Figure 5-22 can be examined to determine any trend in the variance across the surface with averaged scan number, and are plotted against this scan number in Figure 5-23. The SNR value increases when the number of scans averaged increases, indicating that a higher number of scans is better for the production of hybridisation maps. This increase in the SNR value is due to both an increase in the average sp^2 hybridised carbon percentage and a decrease in the variance in the data. These results follow the same trend of graphitisation observed in Figure 5-4. To determine if there are also changes occurring as a result of
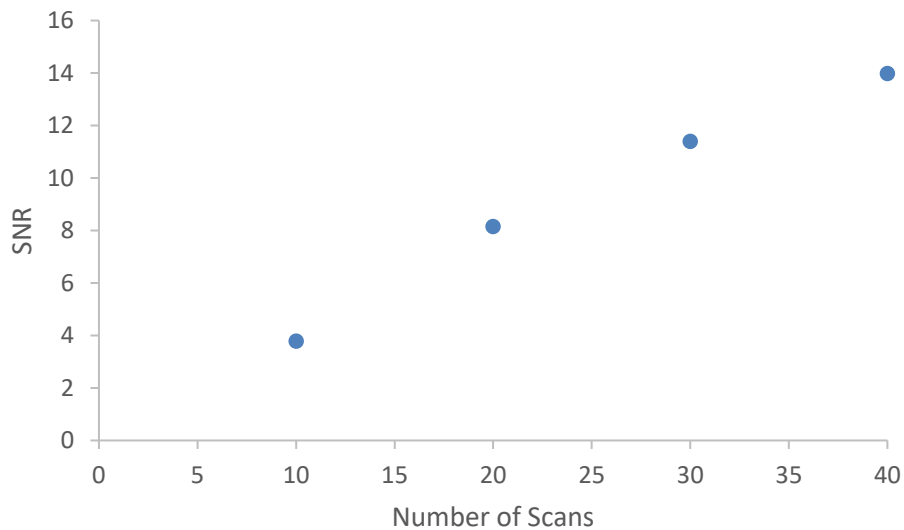
Figure 5-23: Variation in SNR value from hybridisation line scans in Figure 5-22 plotted against the number of scans averaged in the acquisition of the C(KLL) spectra used to calculate the hybridisation.

changing the number of scans the spectra from the carbon elemental map must again be examined to see the impact of changing scan numbers on the peak shape in the individual spectra.

The spectra averaged over each of the maps in Figure 5-22 are shown in Figure 5-24 (a) for 10, 20, 30, and 40 scans. The shapes of these spectra are very similar, although there is an increase in D parameter from 21.8 eV to 22.4 eV as the number of scans increases from 10 to 20, with further increases in scan numbers not showing changes to the D parameter (Table 5-8).

When spectra from individual pixels are examined in Figure 5-24 (b), (c), and (d) it can be seen that there are further differences in the peak shape and D parameter as the number of scans changes (Table 5-8), but there is no systematic variation among them. When 10 scans are averaged (blue line) the spectra have a higher noise level than that achieved with 20 scans (red line), 30 scans (green line), or 40 scans (purple line), and this can result in shifted energy positions of the observed maxima and minima, resulting in an inaccurately determined D parameter value. When the scan number is increased to 20 or higher the maxima and minima are more clearly defined, suggesting that at least 20 scans should be used for collecting the carbon elemental maps. There are some further improvements to the signal to noise ratio when the scan number is increased again, however the acquisition time is also increased, and there is the potential for further electron beam induced graphitisation of the DLC surface.
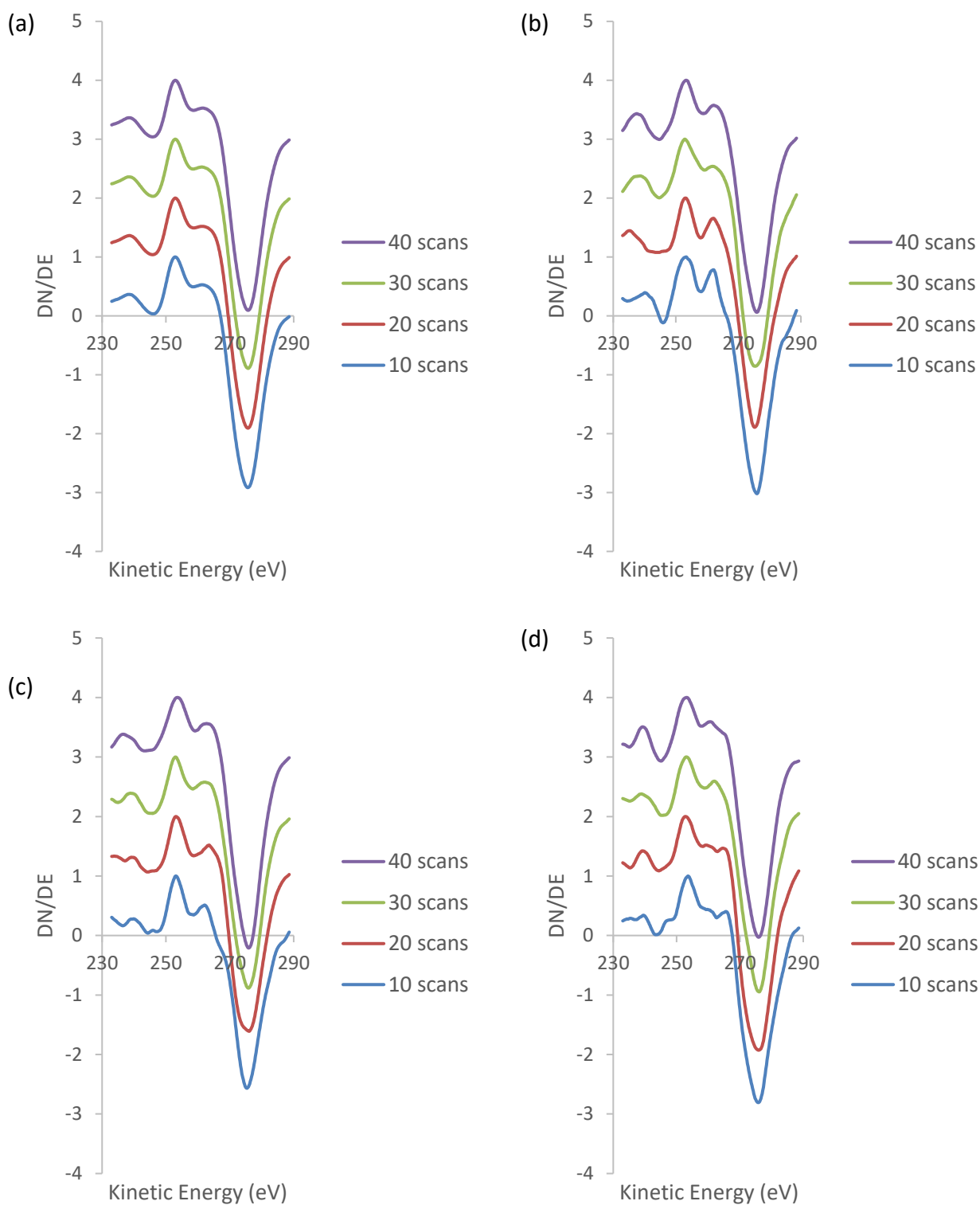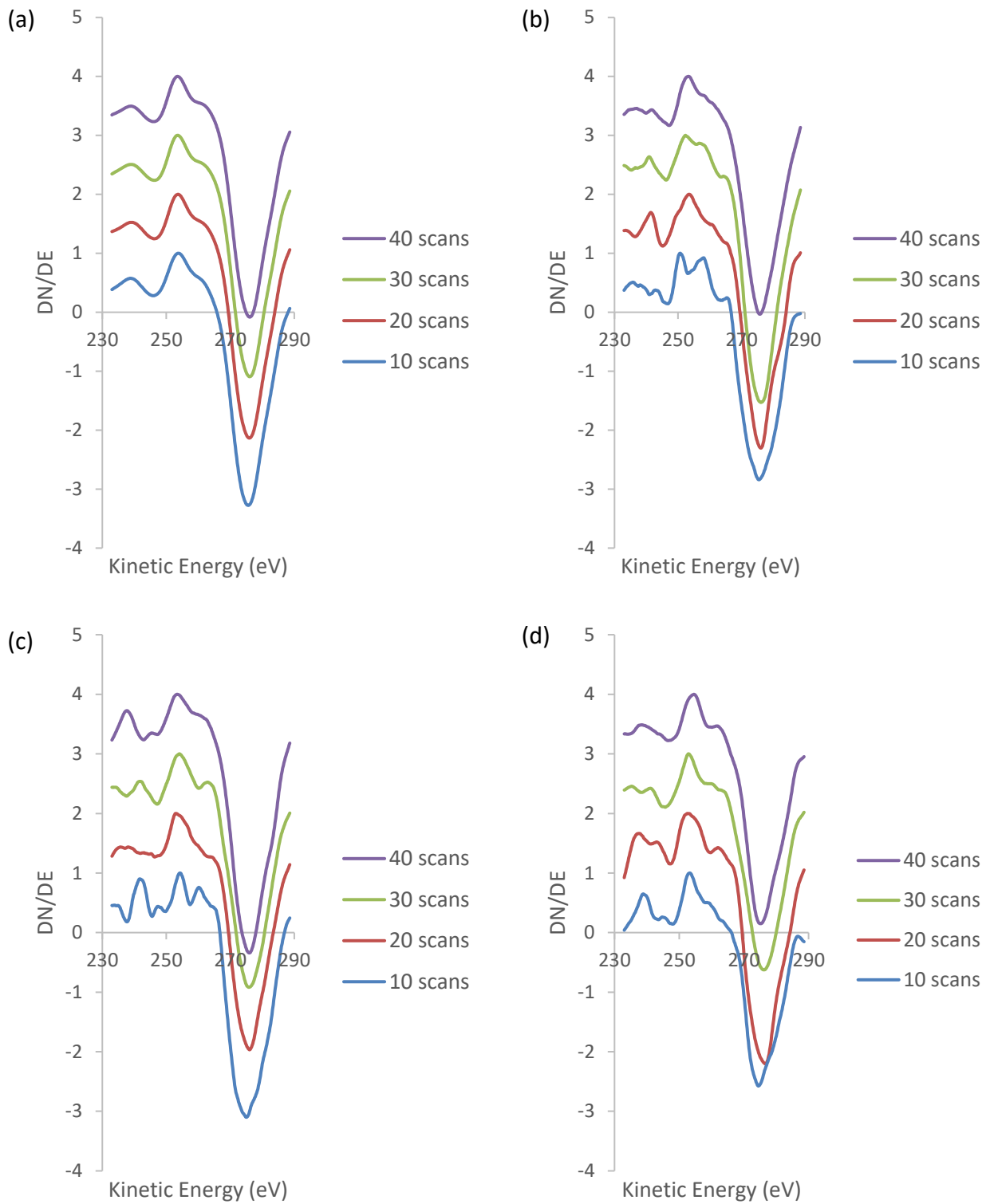
Figure 5-24: C(KLL) spectra taken from (a) the average of all spectra in the map, and pixel (b) 272, (c) 558, and (d) 784 of the 32x32 pixel carbon elemental maps of DLC. Each plot shows a spectrum with 10 scans (blue), 20 scans (red), 30 scans (green), and 40 scans (purple).

Table 5-8: D Parameter values from each spectrum in Figure 5-24. The uncertainty in each D parameter value is ±0.2 eV.

Number of Scans	D Parameter (eV) (Average)	D Parameter (eV) (Pixel 272)	D Parameter (eV) (Pixel 558)	D Parameter (eV) (Pixel 784)
10	21.8	24.6	20.6	21.0
20	22.4	22.8	23.0	24.0
30	22.4	23.8	21.8	23.2
40	22.4	22.6	22.6	20.4

The hybridisation maps (Figure 5-22), SNR values (Figure 5-23), spectra (Figure 5-24), and D parameter values (Table 5-8) from maps acquired over DLC films sequentially with an increase in the number of scans averaged to obtain the final scan show that this number has an impact on the quality of the data obtained. The improvements that are made to the data when the number of scans is increased must be balanced with the electron beam induced changes that occur to the DLC surface, which increase with the increased exposure, as well as the increase in acquisition time. Taking all of these factors into account, it seems that for DLC films 20 scans averaged is a reasonable choice that gives a well-defined peak without unnecessarily increasing the acquisition time or beam damage.

5.2.4.3 Number of Scans - Conclusions

Data from hybridisation maps produced of both HOPG (Figure 5-19) and DLC (Figure 5-22) has shown that by increasing the number of scans that are averaged to produce a carbon map results in improved data quality that is observed in the decrease in variation within the maps and decrease in SNR. However, this improvement needs to be balanced against the increased time it takes to acquire these maps and the increased electron beam exposure that this brings. Combining these factors with the data it is concluded that 20 scans averaged is the best choice for acquiring carbon elemental maps for the purpose of producing hybridisation maps.

5.2.5 Constant Total Scan Time
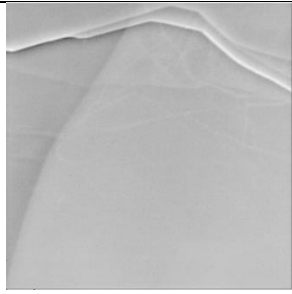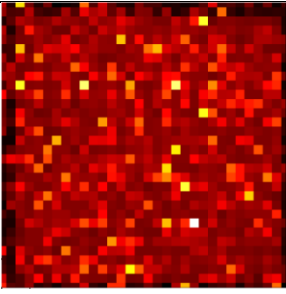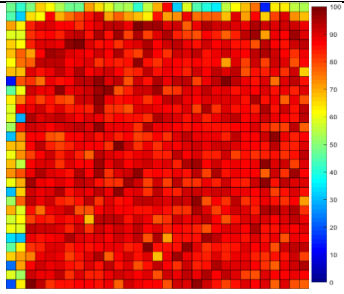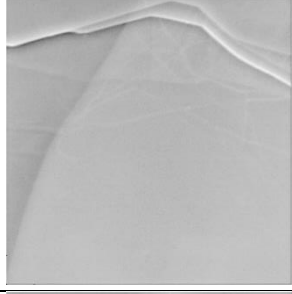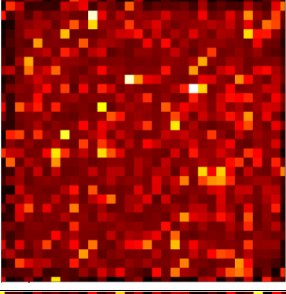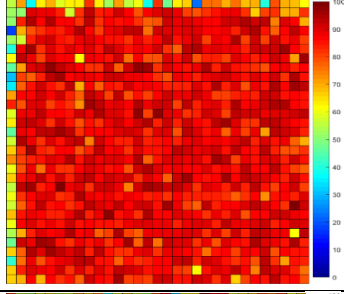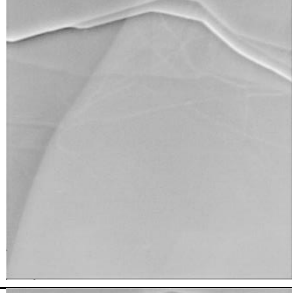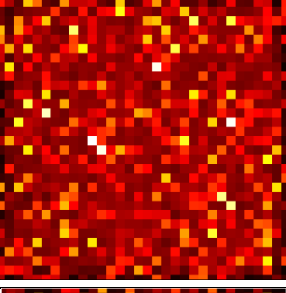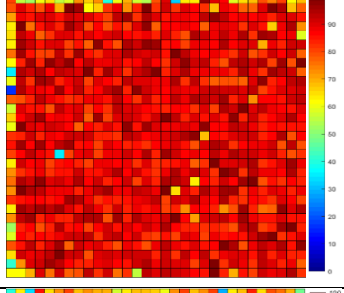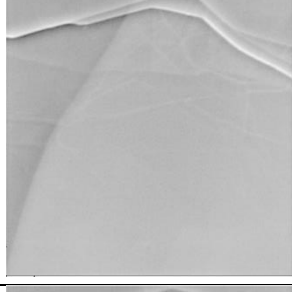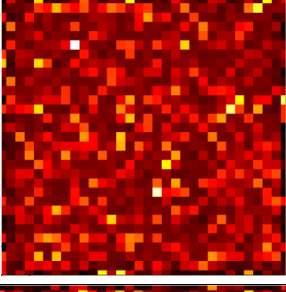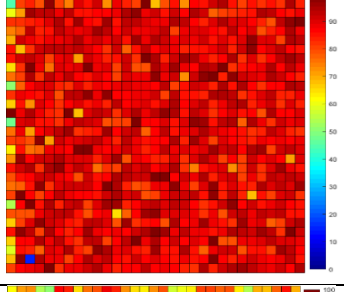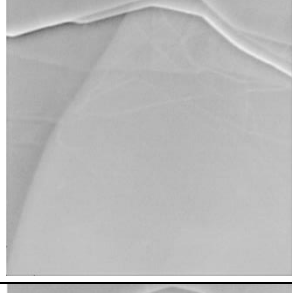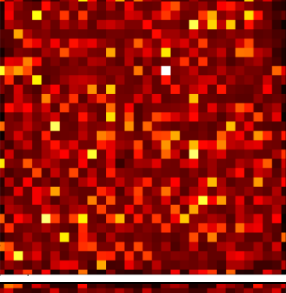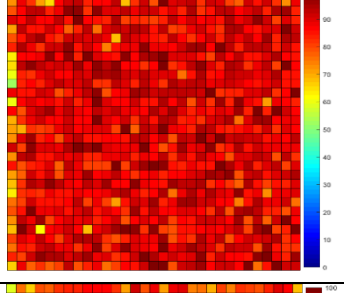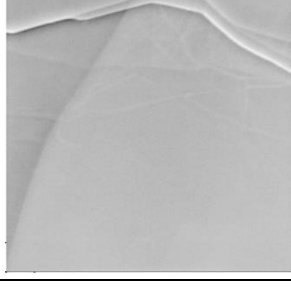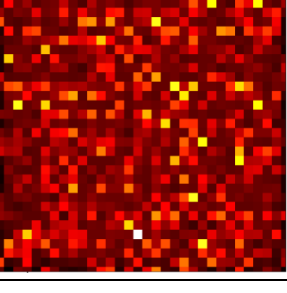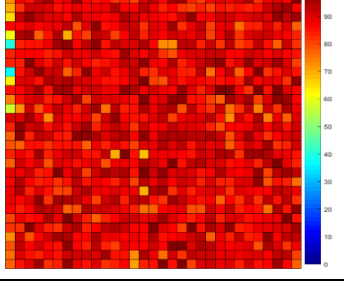
So far in this chapter each of the scan parameters for the acquisition of the window mode carbon elemental maps has been tested and the values that appear to be optimal for the best practical outcomes have been determined, however when combined together they may not necessarily be the best choice. The parameters so far deemed to be most suitable are a time per step of 0.5 ms, a

step width of 0.2 eV, and 20 scans. What this means is that for each energy value in the spectrum, a total integrated count time of 10 ms is needed. However, the time per step and number of scans can be altered to achieve this total time, and while theoretically these combinations should be equivalent, it should be tested to determine if any practical implications exist, and then choose optimal conditions to cater for them.

5.2.5.1 Constant Total Scan Time – HOPG

The 20 μm FOV SEM image of the area examined in this test (Figure 5-25) shows two graphite flake edges along the top of the image, as well as another running down the left of the image. The window mode carbon elemental map, hybridisation map, and SNR value for each of the time per step and scan number combinations tested are also shown in Figure 5-25. Each of these maps was acquired sequentially over the same area and are presented in the order taken. It is not expected that this sequential acquisition will result in significant changes to the hybridisations present based on the results of the tests in Figure 5-1.

The first combination tested is a 10 ms time per step and 1 scan, which results in a hybridisation map that is almost entirely red in the centre, but with some pixels of all other colours along the top and left sides of the map. It appears that the majority of the surface is almost entirely sp^2 hybridised, while there are some areas at the edge that have lower percentages of sp^2 hybridised carbon. The next combination examined is a 5 ms time per step and 2 scans, which results in a hybridisation map that is very similar to the first, but with fewer pixels indicating lower sp^2 hybridised carbon content around the top and left edges. Using a 2 ms time per step and 5 scans also results in a similar hybridisation map, but with fewer differently coloured pixels around the edges. This map indicates very similar hybridisations to those using 1 ms time per step and 10 scans, 0.5 ms time per step and 20 scans, 0.2 ms time per step and 50 scans, and 0.1 ms time per step and 100 scans. The changes in the hybridisation of the areas on the upper and left edges of the image in the sequentially acquired scans may indicate that the edges are truly less sp^2 hybridised than the rest of the area but are becoming increasingly graphitic due to exposure to the electron beam, in a similar way to the changes occurred for DLC in Figure 5-1, or it may be a strange artefact of the technique that is distorting the spectra. Spectra were extracted from the first row of the maps, where the lower sp^2 hybridised carbon percentage is observed, and several rows down the map, where the expected high sp^2 percentage is observed, to examine the peak shapes.

186

TPS (ms)	No. of Scans	SEM	Carbon Elemental Map	Hybridisation map	SNR
10	1				6.12
5	2				7.25
2	5				8.29
1	10				8.14
0.5	20				10.3
0.2	50				10.7

187

0.1	100				10.7
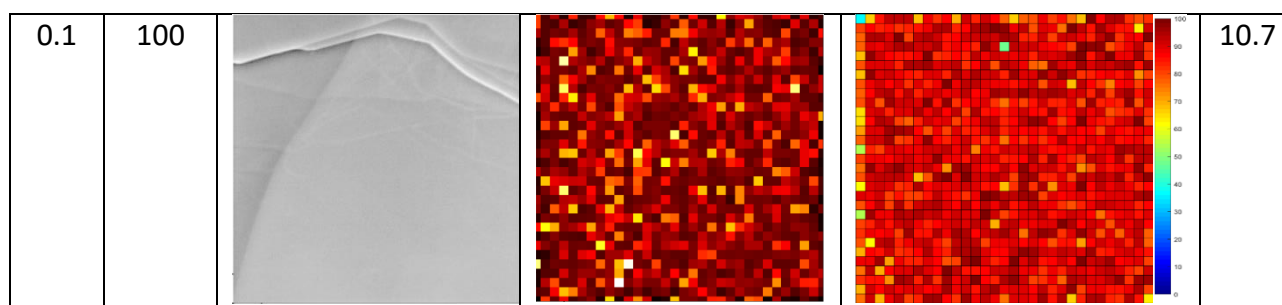
Figure 5-25: SEM images (20 μm FOV), C(KLL) elemental map, and hybridisation maps for HOPG taken with various values of time per step and repeat scan numbers such that the total scan acquisition time remains constant.

The spectra from a pixel on the top row of the map (showing lower sp^2 hybridised carbon percentage) and a pixel from several rows down the map (showing a higher sp^2 hybridised carbon percentage) are shown in Figure 5-26 for several of the maps in Figure 5-25 to determine if the pixels presenting lower sp^2 content than expected are showing typical peak shapes for low sp^2 content.

The two spectra in Figure 5-26 (a) show very different peak shapes for the positions and shapes of the maxima and minima and the fine structure, leading to D parameter values of 16.8 eV for the blue line and 23.4 eV for the red line. These differences show that the upper edge of the area examined in the map has a lower sp^2 hybridised carbon content than the rest of the area, although it does not provide a reason for this unusual result, which has not been observed for previous HOPG samples or any other samples. Figure 5-26 (b) shows peak shapes that are very similar to those in Figure 5-26 (a) and lead to similar D parameter values, indicating that the hybridisation of the sample is consistent. However, a difference is observed when the spectra in Figure 5-26 (c), where the blue line taken from the area that previously indicated a low sp^2 hybridised carbon percentage has a peak shape that is closer to that of the red line from the centre of the image, indicating that this area has become more graphitised. This trend is continued in Figure 5-26 (d), where the blue and red lines are even more similar and have D parameter values of 22.4 eV and 23.0 eV, respectively. While this trend does not explain the cause of the anomaly of the lower sp^2 hybridised carbon content along the edges of the maps, it does indicate that this area is gradually becoming graphitised due to exposure to the electron beam in a similar way to that observed for DLC films previously. One possible reason for this artefact may be if the maps were acquired over an area that is at the edge of the spatial range of the analyser of the instrument. This cannot be confirmed with the data shown, and further investigation needs to be performed to determine the cause of the artefact.
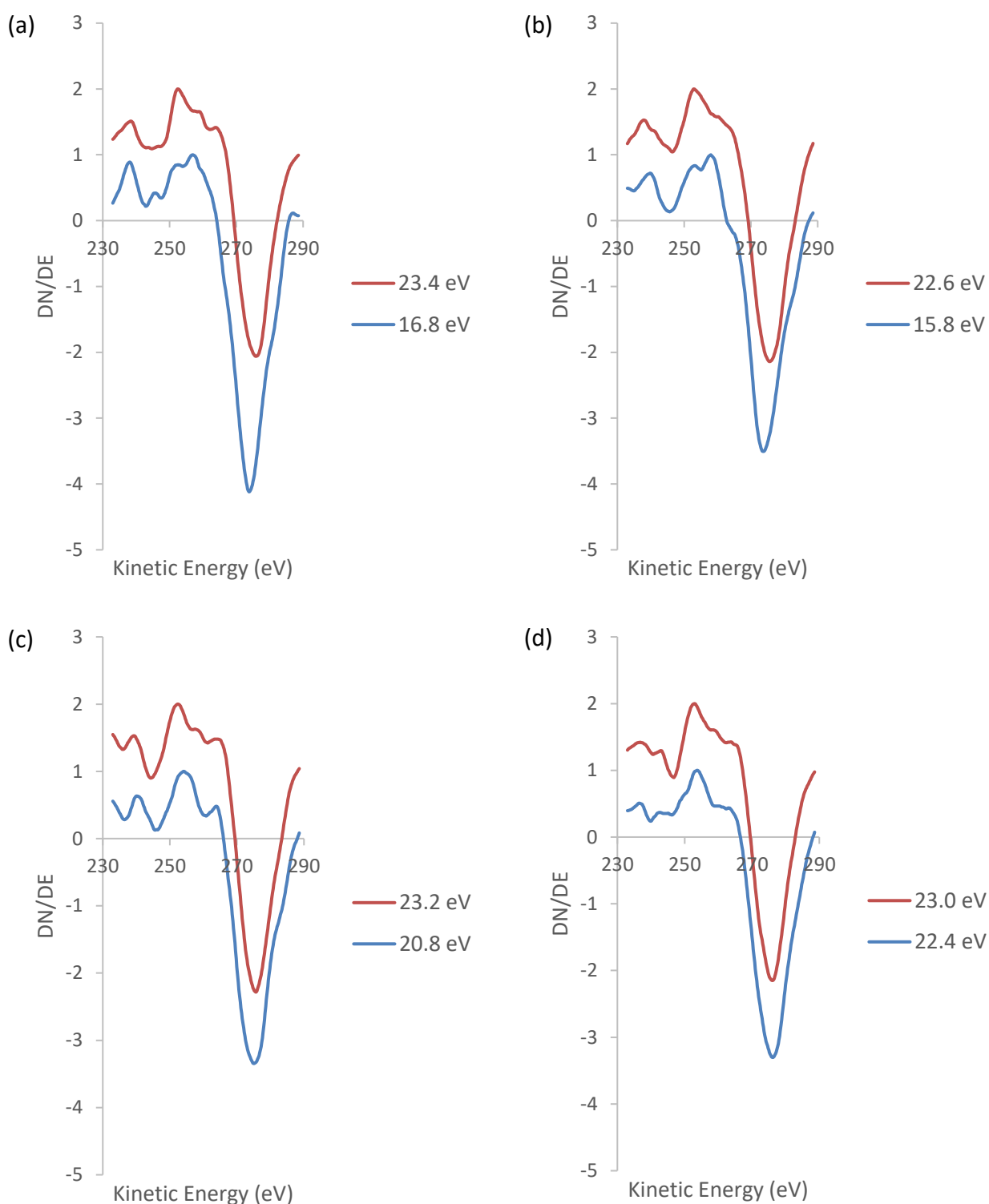
Figure 5-26: C(KLL) spectra taken from the carbon elemental maps in Figure 5-25 acquired with (a) 10 ms TPS 1 scan, (b) 2 ms TPS 5 scans, (c) 0.5 ms TPS 20 scans, and (d) 0.1 ms TPS 100 scans, with the blue line indicating a spectrum from the top row of the map where the _sp²_ hybridised carbon content is lower than expected, and the red line a spectrum from lower in the map where the hybridisation is consistent.

The SNR ratio provides further insight into the variation of the hybridisation as the time per step and number of scans used to acquire them changes, and is plotted against the time per step in Figure

5-27 (the choice of which parameter to plot against is arbitrary, the important aspect is the trend that occurs).

Figure 5-27: Variation in SNR value from hybridisation line scans in Figure 5-25 plotted against the time per step of the C(KLL) spectra used to calculate the hybridisation.

The SNR value increases as the time per step increases (and the number of scans decreases) until a value of 10-11 is reached for time per step values between 0.5 ms and 0.1 ms. This would suggest that the best combinations of time per step and number of scans includes a time per step in this range, however as the colours of the pixels through the centre of the maps is consistent across all of the maps in Figure 5-25 this variation in the SNR value is thought to be the result of the changes in the hybridisation at the upper and left sides of the image. These results, combined with the hybridisation maps, suggest that in collecting data, the total time is important but the way in which it is collected via time per step and number of scans is not. However, the spectra from which these maps are composed will also be examined to more closely validate this.

The average spectra obtained from the spectra within each pixel of each of the maps in Figure 5-25 are shown in Figure 5-28 (a). Examination of these spectra shows that all of the time per step and scan number combinations tested show almost identical spectra. There are some small variations in the D parameter values, as shown in Table 5-9, with values ranging between 22.2 eV and 22.6 eV with an increasing trend for the sequentially acquired scans. This matches what was expected based on the hybridisation maps in Figure 5-25, however previous results have shown that although the average spectra may be very similar, there may be differences that can only be seen in the spectra from individual pixels.
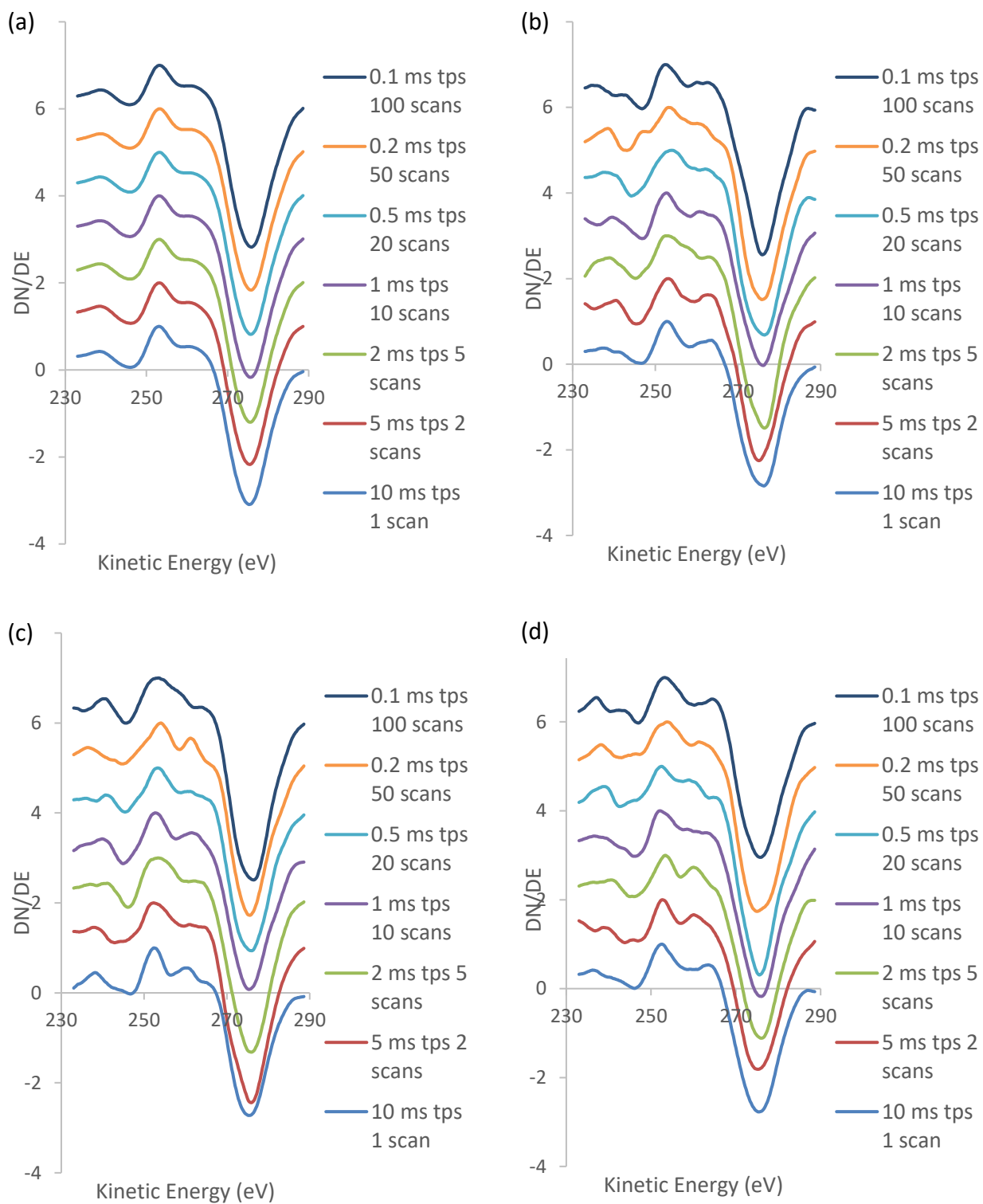
Figure 5-28: C(KLL) spectra taken from (a) the average of all spectra in the map, and pixel (b) 272, (c) 558, and (d) 784 of the 32x32 pixel carbon elemental maps of HOPG. Each plot shows spectra with various values of time per step and repeat scan numbers such that the total scan acquisition time remains constant.

To observe this the spectra from three individual pixels throughout each map were extracted and are shown in Figure 5-28 (b), (c), and (d). From these spectra it can be seen that there are small variations in the fine structure of the peaks at these individual pixels, however the overall peak

shape is very similar. The D parameter for each of these spectra are shown in Table 5-9 and show no systematic trend that can be attributed to the variations in the time per step and number of scans used to achieve the same total acquisition time.

These results show that for a given total time per point the way at which this time is arrived at is not important. However, the spectra that correspond to the mid-range values of both time per step and number of scans provide the most reliable spectra in terms of the fine structure, which can be seen in the spectra in Figure 5-28 to show very similar fine structure across each pixel.

Table 5-9: D Parameter values from each spectrum in Figure 5-28. The uncertainty in each D parameter value is ±0.2 eV.

Time Per Step (ms)	Number of Scans	D Parameter (eV) (Average)	D Parameter (eV) (Pixel 272)	D Parameter (eV) (Pixel 558)	D Parameter (eV) (Pixel 784)
10	1	22.4	23.4	22.8	22.8
5	2	22.2	21.8	23.4	22.6
2	5	22.4	22.2	22.4	22.6
1	10	22.4	23.4	22.6	23.8
0.5	20	22.6	22.4	22.7	23.2
0.2	50	22.6	22.6	21.8	21.2
0.2	100	22.6	23.4	23.0	22.6

Consideration of the hybridisation maps (Figure 5-25) and SNR values (Figure 5-27) show that the data obtained is very similar despite the difference in time per step and number of scans used to reach the same total scanning time per point. However, there are some variations in the fine structure of the spectra in Figure 5-28 that indicate that the most consistent results will be achieved when the time per step and number of scan values are within the middle of the ranges tested. Based on this it is concluded that the best choice of the scanning parameters are a time per step of 0.5 ms and 20 scans averaged.
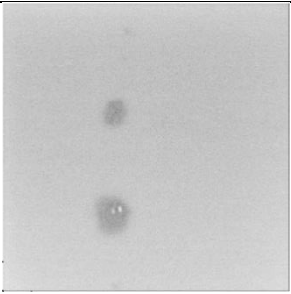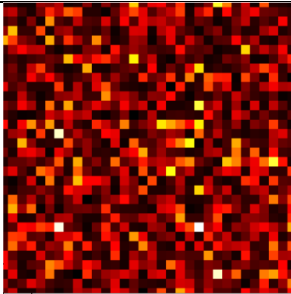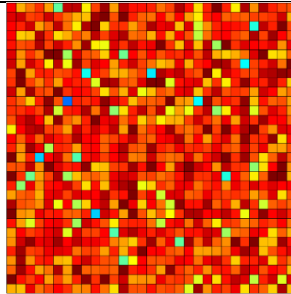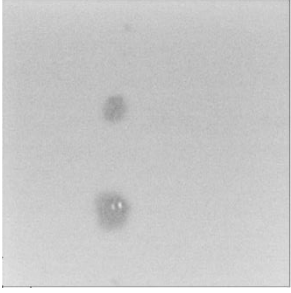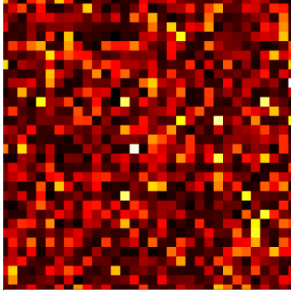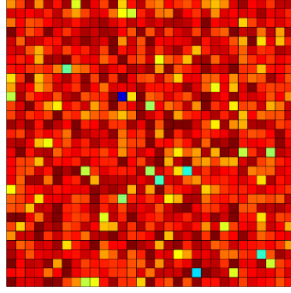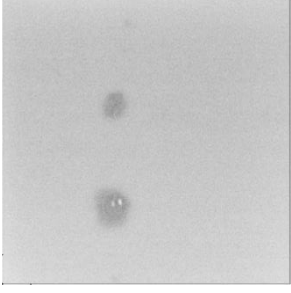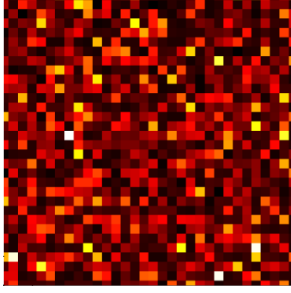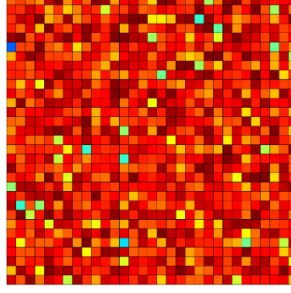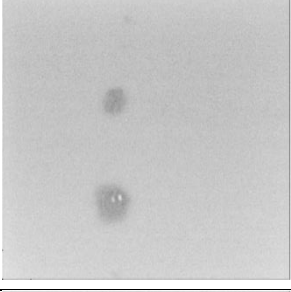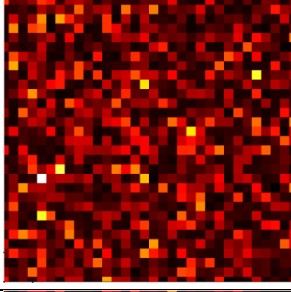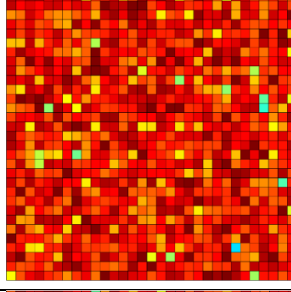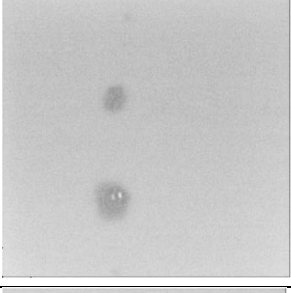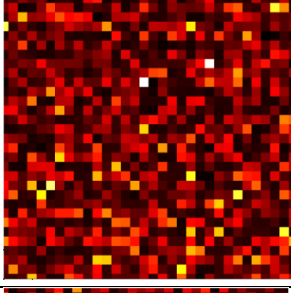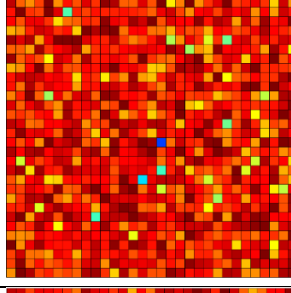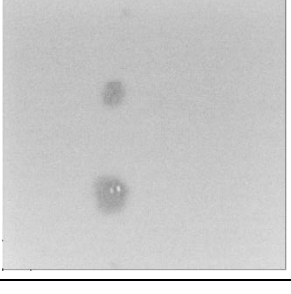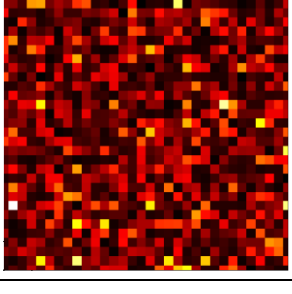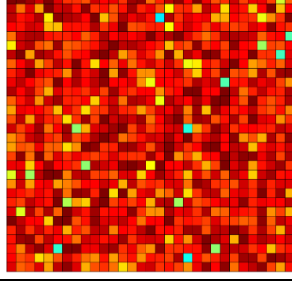
5.2.5.2 Constant Total Scan Time – DLC

The tests to determine whether the same total scan acquisition time achieved in different ways produce the same results were repeated using a DLC film. These maps were all acquired over the

same area, and therefore the DLC is expected to undergo electron beam induced graphitisation as was shown previously for DLC film characterisation in Figure 5-4. A range of time per step values and scan numbers was tested to achieve a total scan time of 10 ms per point, with time per step varying from 10 ms to 0.1 ms and step number between 1 and 100. The results of these tests are shown in Figure 5-29 in the order of which they were acquired.

The SEM image in Figure 5-29 shows the 20 µm FOV area of the DLC film over which the window mode carbon elemental maps were acquired. The DLC film is mostly smooth and featureless, with the exception of two small circular regions that appear darker than their surroundings in the SEM image, one of which contains two small particles.

The hybridisation map acquired using a 10 ms time per step and 1 scan shows a surface that is predominantly red, indicating high sp^2 hybridised carbon percentage, with pixels of orange, yellow, green, and blue interspersed randomly, indicating areas of lower sp^2 hybridised carbon percentage. These areas of lower sp^2 hybridisation do not correlate with the positions of the features in the SEM image, indicating that these features are part of the DLC film but different morphology from the surrounding areas. This result is consistent with those observed previously for DLC films, as is the next map that was acquired using a 5 ms time per step and averaging 2 scans, which has fewer pixels indicating lower sp^2 hybridised carbon and suggests that the electron beam induced graphitisation has occurred. The rest of the hybridisation maps in Figure 5-29 show results similar to the 2 ms 5 scan map, indicating that the change in the two parameters is not changing the results achieved provided that the total scan time is constant.

TPS (ms)	No. of Scans	SEM	Carbon Elemental Map	Hybridisation map	SNR
10	1				6.16
5	2				7.44
2	5				7.58
1	10				7.50
0.5	20				7.56
0.2	50				8.02

| 0.1 | 100 | | | | 8.58 |
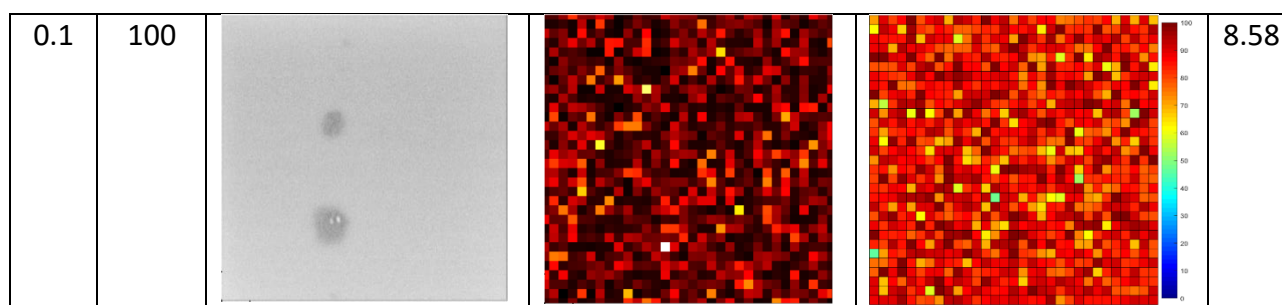
Figure 5-29: SEM images (20 μm FOV), C(KLL) elemental map, and hybridisation maps for DLC taken with various values of time per step and repeat scan numbers such that the total scan acquisition time remains constant.

The SNR values from Figure 5-29 are plotted against the time per step values used to acquire the carbon map in Figure 5-30.
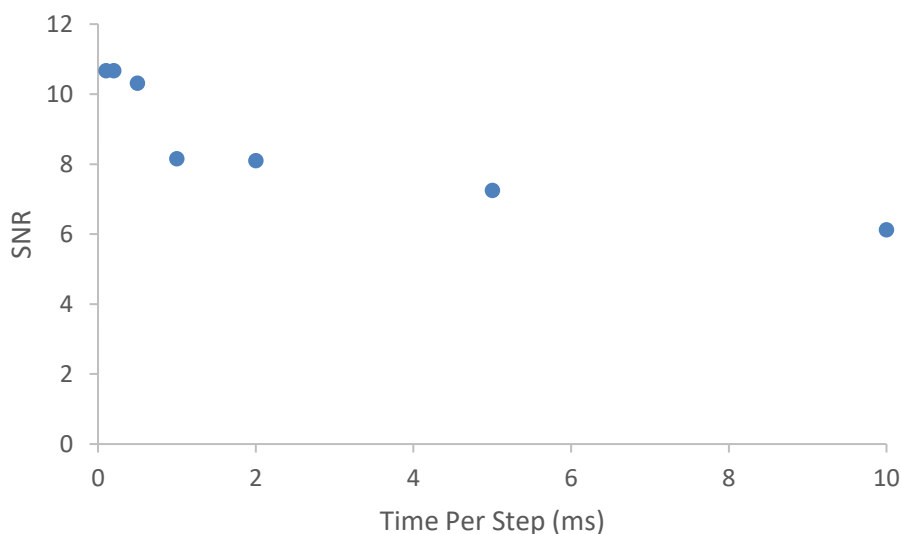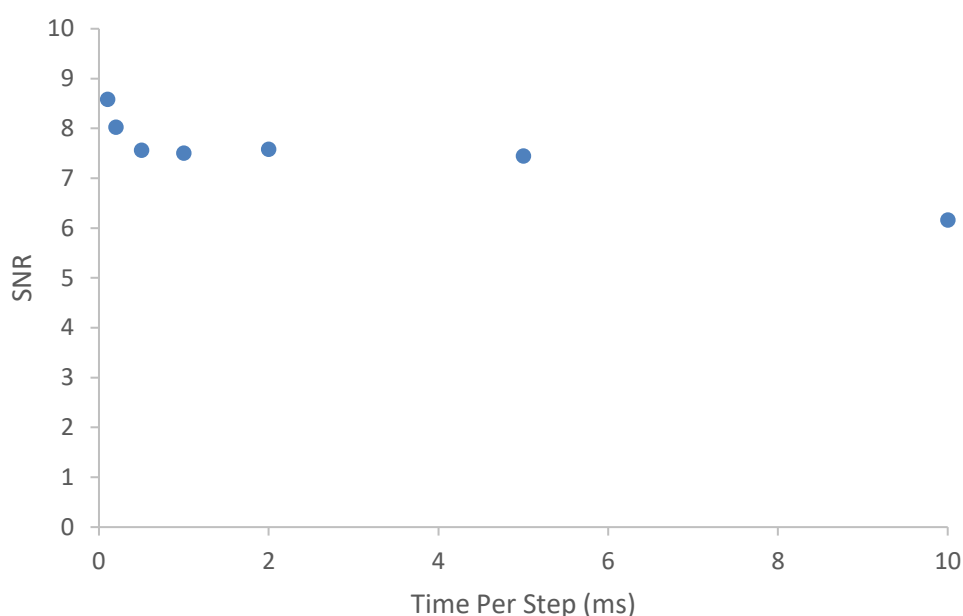

Figure 5-30: Variation in SNR value from hybridisation line scans in Figure 5-29 plotted against the time per step of the C(KLL) spectra used to calculate the hybridisation.

The SNR values in Figure 5-30 from samples using time per step values between 0.5 ms and 5 ms are very similar at approximately 7.5, however the values from either end of the plot are different. While normally a higher SNR value would be preferred, the increases here are thought to be the result of the electron beam induced graphitisation of the sample rather than changes from the scanning parameters. These SNR values therefore show that for consistent results a time per step in the centre of the range of values should be chosen, with the corresponding number of scans value also lying in the middle of its range. However, the spectra from the carbon elemental maps need to be examined to determine how variation in the time per step and number of scans changes the peak shapes.

Figure 5-31: C(KLL) spectra taken from (a) the average of all spectra in the map, and pixel (b) 272, (c) 558, and (d) 784 of the 32x32 pixel carbon elemental maps of DLC. Each plot shows spectra with various values of time per step and repeat scan numbers such that the total scan acquisition time remains constant.

The average spectrum for each map is obtained by averaging the spectra from each pixel in the carbon elemental map, and is shown in Figure 5-31 (a) for each of the maps in Figure 5-29. These

spectra show a slight trend of shifting of the maxima and minima, while the fine structure of the peaks remains quite constant. The D parameter values were calculated for these spectra and are shown in Table 5-10. The first spectrum, acquired with a 10 ms time per step and 1 scan, shows a D parameter value of 22.0 eV, while the rest of the spectra all have D parameter values of 22.4 eV. This slight increase is likely to be due to the graphitisation that occurs when these scans are acquired sequentially.

Examination of the spectra extracted from individual pixels in Figure 5-31 (b), (c), and (d) shows that there are a larger range of peak shapes observed, particularly in the fine structure and D parameter values, that does not show a clear trend (Table 5-10). This is thought to be due to the changes in the surface caused by continued exposure to the electron beam. The spectra obtained using the mid-range values for time per step and scan number are the most consistent in terms of both the peak shape and the D parameter, which suggests that these mid-range values are the best choice for the carbon elemental map acquisition.

Table 5-10: D Parameter values from each spectrum in Figure 5-31. The uncertainty of each D parameter value is ±0.2 eV.

Time Per Step (ms)	Number of Scans	D Parameter (eV) (Average)	D Parameter (eV) (Pixel 272)	D Parameter (eV) (Pixel 558)	D Parameter (eV) (Pixel 784)
10	1	22.0	24.0	23.6	22.0
5	2	22.4	21.4	22.4	21.6
2	5	22.4	21.4	23.0	21.4
1	10	22.4	22.2	20.0	20.6
0.5	20	22.4	20.0	22.6	23.0
0.2	50	22.4	23.0	23.6	20.8
0.2	100	22.4	21.3	21.6	23.6

The hybridisation maps and SNR values from these maps, shown in Figure 5-29 and Figure 5-30, respectively, indicate that it is the total acquisition time at each point that is important and the time per step and number of scans values used to achieve that total time do not matter. However, the fine structure of the spectra extracted from the carbon maps (Figure 5-31) shows some variation that depends on the acquisition values. As the values from the middle of the ranges provide the

most consistent spectra, it is concluded that a time per step of 0.5 ms and 20 scans averaged is the best choice for the acquisition of the carbon elemental maps.

5.2.5.3 Constant Total Scan Time – Conclusions
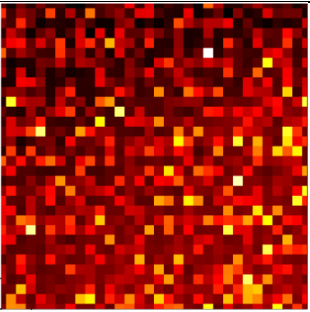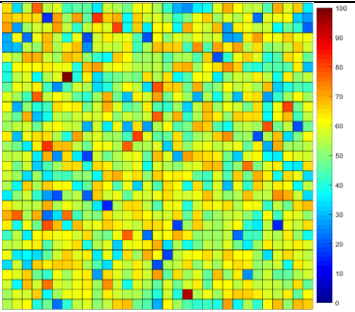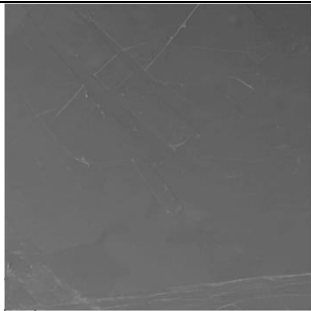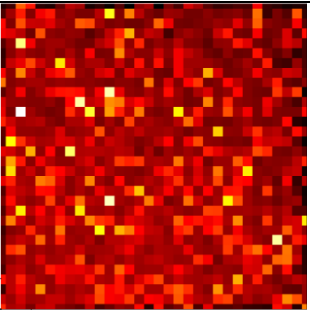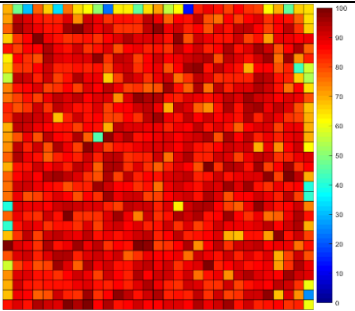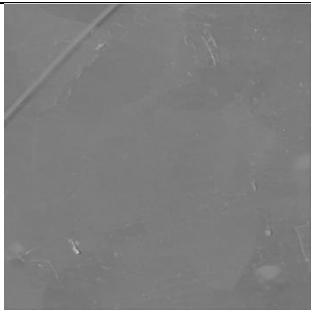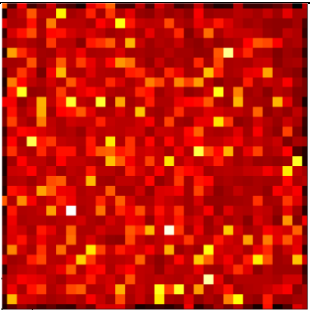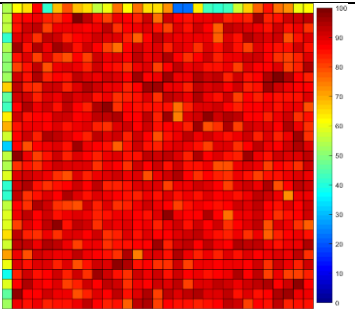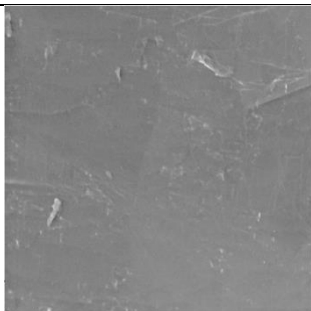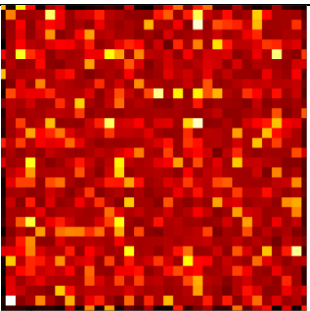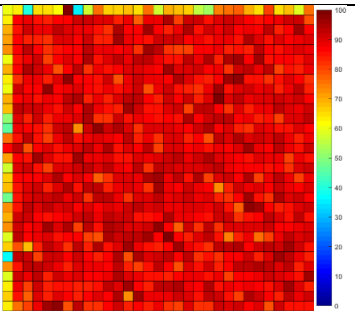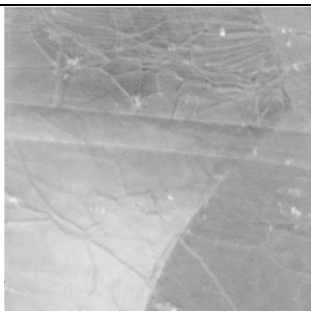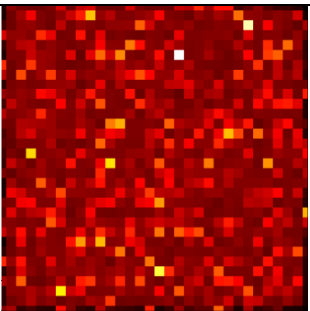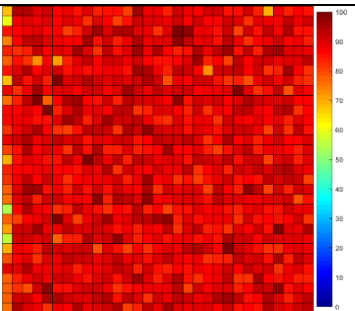
When acquiring an elemental map the total acquisition time at a point on a spectrum should theoretically provide the same results, regardless of the values of time per step and the number of scans that are averaged to reach this total time. However, examination of maps acquired for both HOPG (Figure 5-25) and DLC (Figure 5-29) have shown that there are some small differences that occur in practice, particularly in the fine structure of the spectra from the elemental map. Values of time per step and number of scans were varied, and it was found that when the values used were in the middle of the possible ranges the spectra produced the most consistent results. Based on this it is concluded that the best choices for the variables are 0.5 ms time per second and 20 scans averaged, and these are the values that were chosen for acquisition of carbon elemental maps for the purpose of producing hybridisation maps for this work.

5.2.6 Magnification Level Dependence

The data shown so far within this chapter has been collected using a FOV of 20 um, as this is the level of magnification that is most commonly needed to examine carbon structures such as graphene flakes and nanodiamonds. However, it was observed that the level of magnification at which the window mode carbon elemental maps are acquired influences the spectra obtained. To examine this further, carbon elemental maps were collected with FOVs of 500, 200, 100, 50, 20, and 10 μm for both HOPG and DLC.

5.2.6.1 Magnification Level Dependence – HOPG

It has been shown previously in this chapter that carbon hybridisation maps of HOPG produced at a FOV of 20 μm appear consistent with each other when the same scan parameters are used. Figure 5-32 shows the SEM images, carbon elemental maps, hybridisation maps, and SNR values acquired at FOV values between 500 μm and 10 um. The maps in Figure 5-32 were all acquired on the same sample, however due to the changes of the FOV were not taken over the same areas, and thus the spectra in each pixel cannot be compared directly as they could when the scan parameters were examined. Nonetheless, the sample is expected to be consistently sp^2 hybridised, and therefore examination of the shape of the spectra and the D parameter still allows comparison of the maps and spectra obtained at different magnifications.

FOV (um)	SEM	Carbon Elemental Map	Hybridisation map	SNR
500				4.16
200				6.38
100				7.06
50				9.04
20				13.8
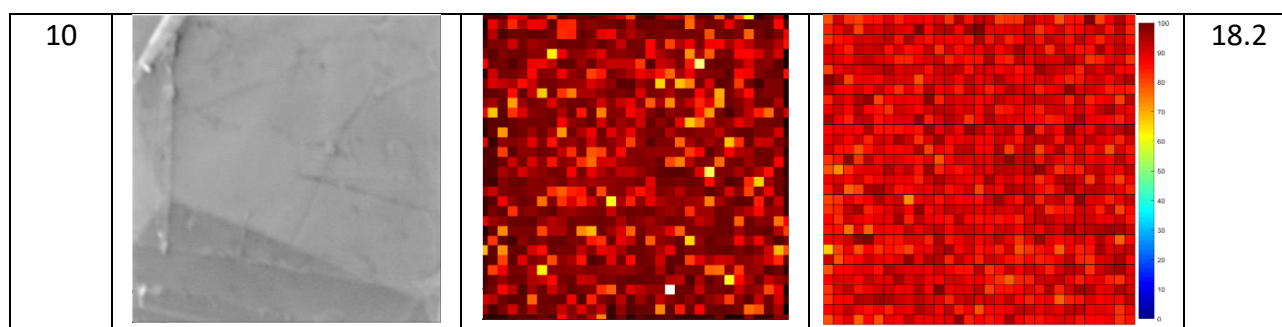
Figure 5-32: SEM images, C(KLL) elemental map, and hybridisation maps for HOPG taken with FOV of 500 um, 200 um, 100 um, 50 um, 20 um, and 10 um.

The carbon hybridisation map acquired at a FOV of 500 μm appears to have a composition that is approximately 50-60 % sp^2 hybridised carbon, which is not at all what is expected from HOPG as it should be highly sp^2 hybridised. When a hybridisation map with a FOV of 200 μm on the same sample is compared, very different hybridisations are observed. In the 200 μm FOV map, most of the map shows highly sp^2 hybridised carbon.

As the FOV is decreased further to 100 um, there is a further increase in the concentration of sp^2 hybridised carbon shown in the hybridisation map. At this magnification it appears that the entire centre of the area under examination is sp^2 hybridised, however there are areas of lower hybridisation observed on the upper and left edges of the map. This is the same artefact that was seen previously in section 5.2.5.1, and will impact on the SNR values in the same way.

At a FOV of 50 μm the hybridisation map appears very similar to that at 100 um, but with some small differences at the edges, which appear to be slightly more sp^2 hybridised. Further decreases to a 20 μm FOV sees a reduction in the number of pixels showing lower sp^2 hybridised carbon percentage, with only several pixels on the edge showing what seem to be outliers compared to the rest of the map. At the highest magnification of 10 μm this edge effect has disappeared, and the surface appears to be uniformly highly sp^2 hybridised.

The SNR values from these hybridisation maps are plotted against the FOV of the map in Figure 5-33 to examine how the average sp^2 hybridised carbon percentage and variance within the map change with the magnification level. The SNR value increases with decreasing FOV, which is expected from the visual comparison of the hybridisation maps in Figure 5-32, and this change is the result of both an increase in the average hybridisation and a decrease in the variance across the sample. Due to the edge effects on the samples acquired at FOV values between 200 μm and 50 μm the variance is larger for those samples than might be expected based on examination of the centre of the images,
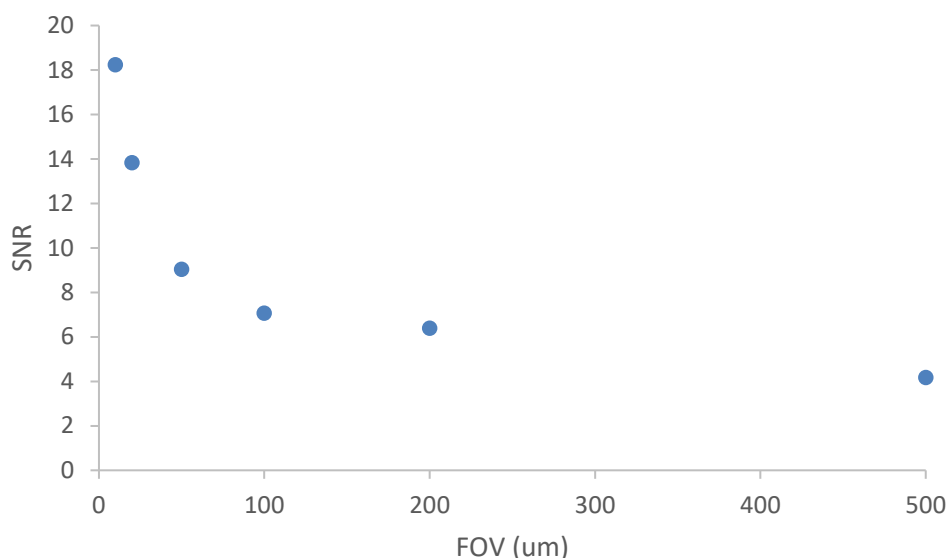
Figure 5-33: Variation in SNR value from hybridisation line scans in Figure 5-32 plotted against the FOV of the hybridisation line scan.

which is quite uniform, and thus it appears that this affect is causing the SNR values for these samples to be lower than expected.

To determine whether this magnification level dependence is due to the sample, and changes that may be occurring due to beam exposure, or the hybridisation mapping method itself the spectra from the carbon elemental maps are examined.

The average spectra taken from all pixels in the maps in Figure 5-32 are shown in Figure 5-34 (a). The spectrum corresponding to the 500 µm FOV carbon hybridisation map (dark blue line) shows a smaller D parameter (19.0 eV) than the rest of the spectra (22.4-22.6 eV), as well as a shoulder on the higher energy side of the peak (~280 eV). This spectrum appears much more diamond-like than is expected for HOPG, which matches the hybridisations observed in the hybridisation map in Figure 5-32.

The spectrum for the 200 µm FOV map (red line in Figure 5-34) shows a larger D parameter (Table 5-11), and also includes a shoulder at approximately 264 eV, which was not present in the spectrum for the 500 µm map. This trend corresponds to that observed in the maps in Figure 5-32, which showed a dramatic increase in the amount of sp^2 hybridised carbon present as the FOV was decreased from 500 µm to 200 um. The 100 µm (green line), 50 µm (purple line), 20 µm (light blue line), and 10 µm (orange line) spectra from the whole map have the same shape as that of the 200 µm spectrum, indicating no significant change in the D parameter with further increases of magnification (Table 5-11). This trend also matches the hybridisation maps shown in Figure 5-32,

201

which, apart from some small differences at the edges of the maps, appear quite consistent.
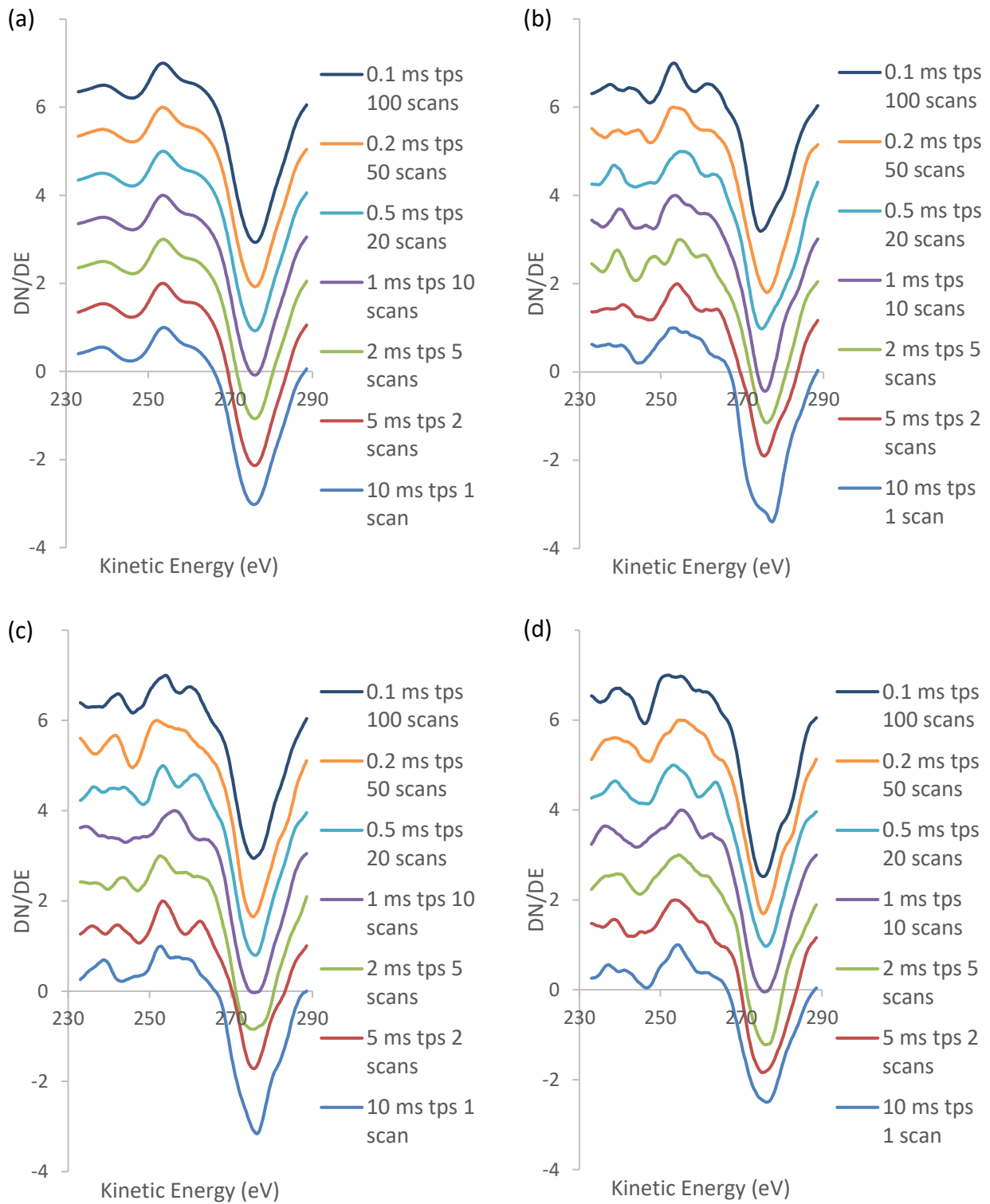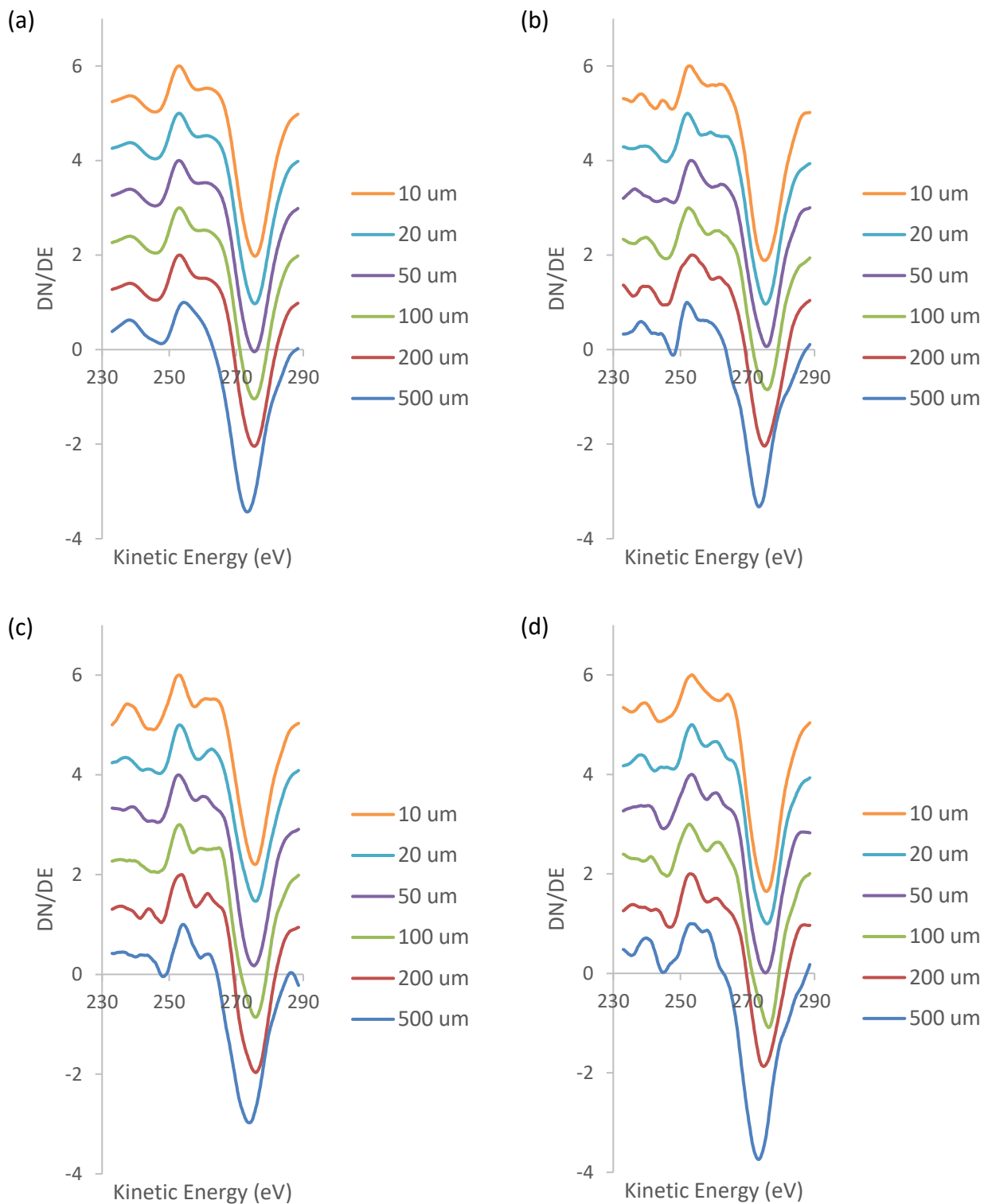

Figure 5-34: C(KLL) spectra taken from (a) the average of all spectra in the map, and pixel (b) 272, (c) 558, and (d) 784 of the 32x32 pixel carbon elemental maps of HOPG. Each plot shows a spectrum from an elemental map with a FOV of 500 μm (dark blue line), 200 μm (red line), 100 μm (green line), 50 μm (purple line), 20 μm (light blue line), and 10 μm (orange line).

Examination of individual spectra extracted from the maps in Figure 5-32 (b), (c), and (d) show a

similar trend to that observed in the spectra averaged across the entire carbon hybridisation map. In all three pixels examined the spectrum at 500 μm shows a different shape and a smaller D parameter than those obtained at smaller FOVs, which all appear to be quite consistent with each other. There are also some changes in the fine structure of the spectra extracted at individual spectra, which is a result of the different positions of the pixels within the sample when the different FOVs were examined.
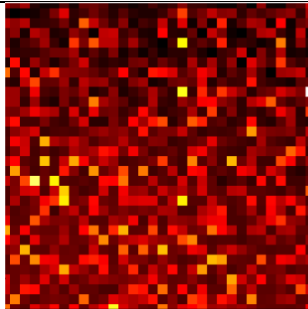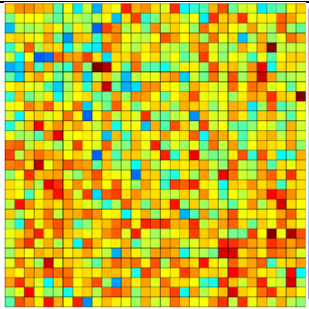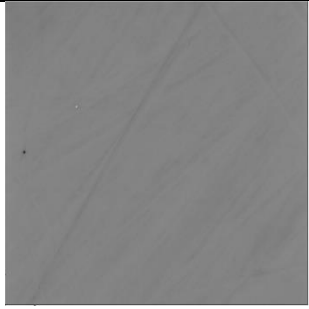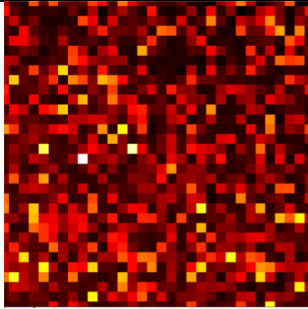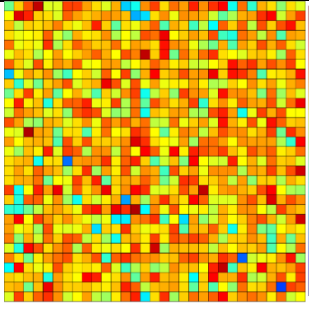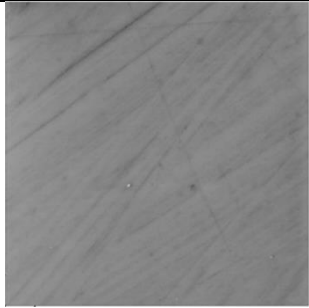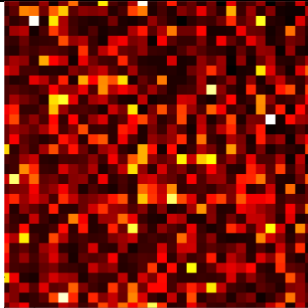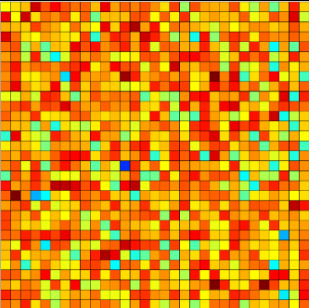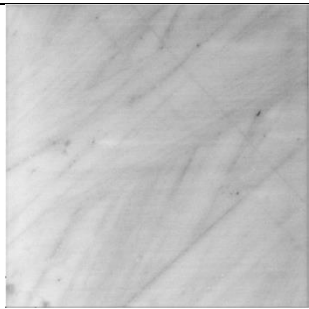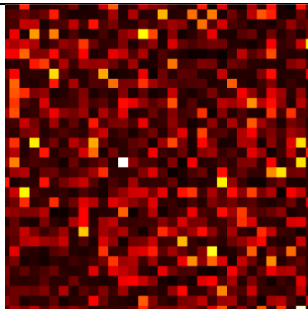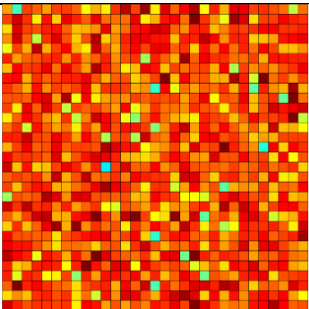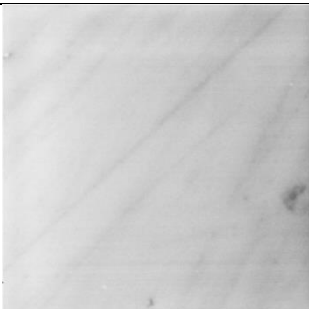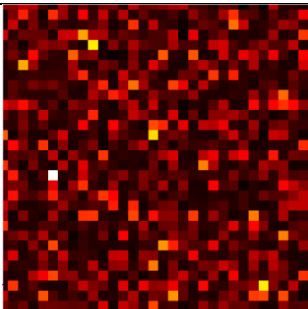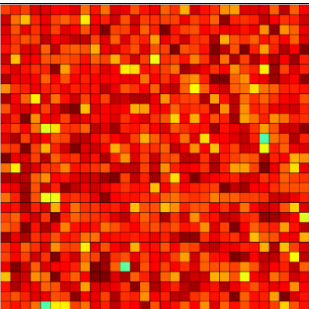
Table 5-11: D Parameter values from each spectrum in Figure 5-34. The uncertainty in each D parameter value is ±0.2 eV.

Field of View (um)	D Parameter (eV) (Average)	D Parameter (eV) (Pixel 272)	D Parameter (eV) (Pixel 558)	D Parameter (eV) (Pixel 784)
500	19.0	21.4	19.8	20.2
200	22.4	21.4	22.0	21.6
100	22.4	23.6	22.8	21.8
50	22.4	22.6	22.6	22.0
20	22.6	23.2	22.6	22.4
10	22.6	22.4	22.6	22.0

Through examination of both the spectra obtained from the carbon maps and the resultant hybridisation maps, it is clear that there is a vast difference between the peak shapes obtained at a FOV of 500 μm than at any higher magnification, despite all other scan parameters being consistent. This suggests some difference in how the Scanning Auger Nanoprobe acquires spectra at the different FOV values, even though there is no change in settings and there are no indications within the SmartSoft software that there should be any differences. To examine if this phenomenon is unique to HOPG, and therefore an artefact of the sample type, the same tests were performed on DLC.

5.2.6.2 Magnification Level Dependence – DLC

Hybridisation maps were produced for DLC at FOV values between 500 μm and 10 μm to determine if there are changes in the data due to the level of magnification. The maps were not acquired over the same area due to the changing FOV, and therefore are not expected to show an increased level of electron beam induced graphitisation with sequentially acquired scans, but have all other scanning parameters set to the same values.

FOV (um)	SEM	Carbon Elemental Map	Hybridisation map	SNR
500				4.14
200				5.68
100				5.36
50				7.53
20				10.1
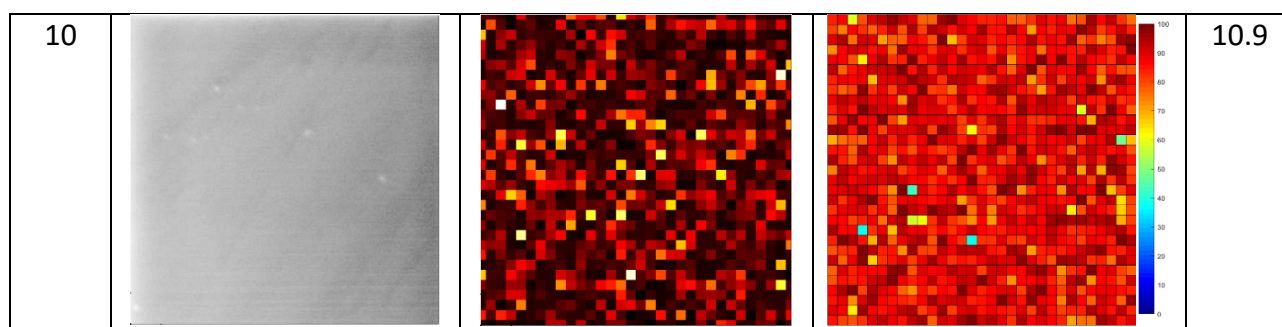
Figure 5-35: SEM images, C(KLL) elemental map, and hybridisation maps for DLC taken with FOV of 500 um, 200 um, 100 um, 50 um, 20 um, and 10 um.

The SEM images of the areas examined, along with the window mode carbon elemental maps, resultant hybridisation maps, and SNR values are shown in Figure 5-35. At a FOV of 500 μm the DLC film appears much as it would be expected to based on previous XPS and SAM characterisation, with a range of hybridisation percentages present across the surface. As the magnification is increased to a FOV of 200 μm the sample appears somewhat more sp^2 hybridised, with an increase in the number of red and orange pixels. This trend continues as further increases in magnification are made, until at 20 μm and 10 μm FOV the samples look quite similar and highly sp^2 hybridised, results which are consistent with the other hybridisation maps of DLC acquired at a FOV of 20 um. These results suggest that, as well as the differences that appear to occur due to changes in how the Scanning Auger Nanoprobe acquires spectra at different magnifications, there may also be an increased extent of electron beam induced graphitisation as the beam rasters over a smaller area at higher magnifications.

The SNR values from Figure 5-35 are plotted against the FOV of the hybridisation maps in Figure 5-36 to examine how the variance in the samples changes with level of magnification.
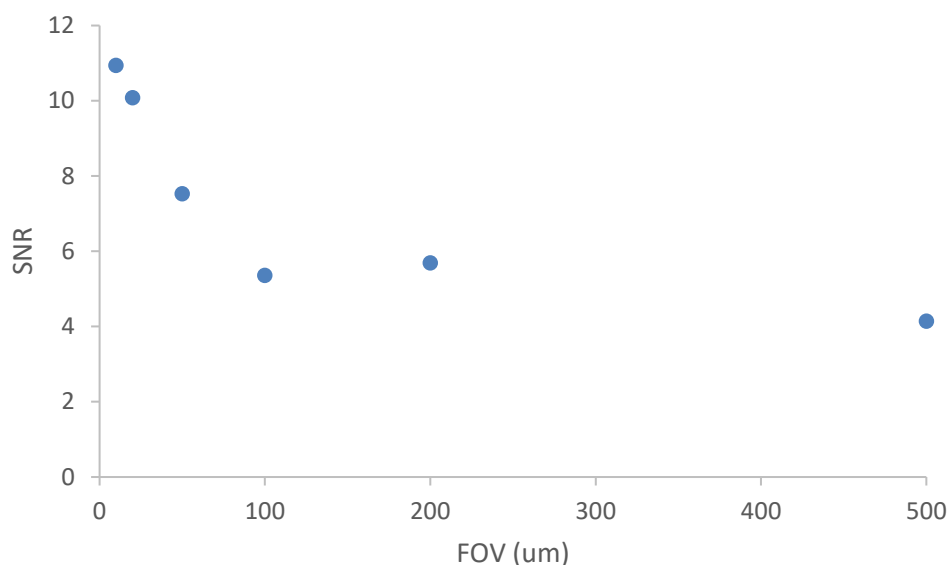
Figure 5-36: Variation in SNR value from hybridisation line scans in Figure 5-35 plotted against the FOV of the hybridisation line scan.

From Figure 5-36 it can be seen that there is an increase in the SNR value as the FOV decreases, which is due to both an increase in the average sp^2 hybridised carbon percentage and a decrease in the variation in the percentages across the surface. The edge effects that were observed in section 5.2.6.1 are not observed here, therefore the SNR values are more reflective of the entire area under examination. However, while the SNR values indicate that there is a change with FOV they do not explain why. The spectra extracted from the carbon elemental map are examined to provide further insight into how the data changes with magnification level.

The average spectra for the maps acquired at each FOV are shown in Figure 5-37 (a). Unlike those shown previously for the parameter tests, these spectra do not have a similar shape, and are not expected to have an increased extent in graphitisation due to increasing electron beam exposure time as each map is taken over a different location. However, as well as the appearance of a shoulder at the low kinetic energy side of the peak as the magnification is increased, there is also a trend in increasing D parameter from 19.8 eV to 22.4 eV (Table 5-12).

The spectra extracted from individual pixels, which are also shown in Figure 5-37 (b), (c), and (d), show some smaller variations in the peak shapes but also show trends of increasing D parameter as is seen in Table 5-12.
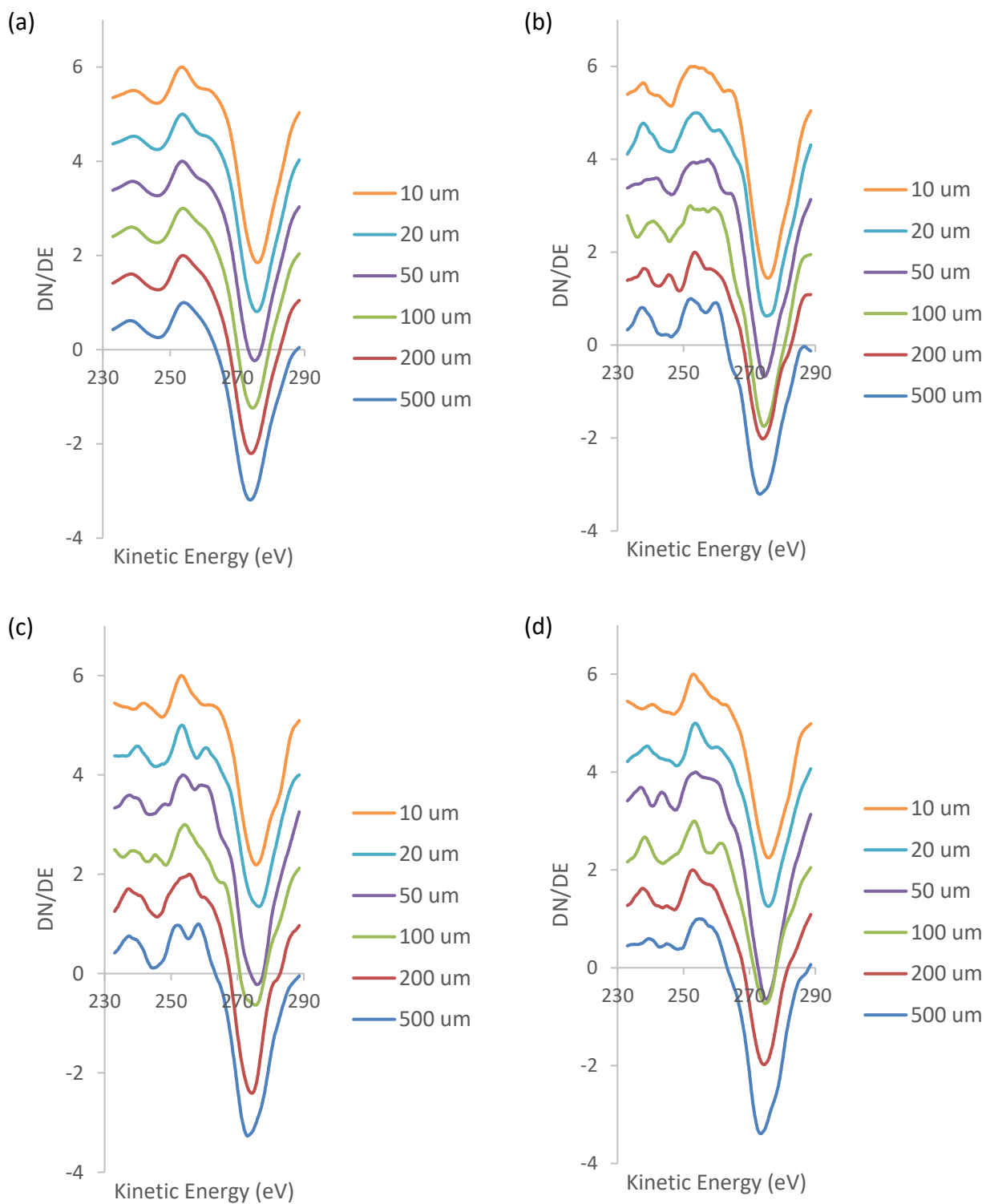
Figure 5-37: C(KLL) spectra taken from (a) the average of all spectra in the map, and pixel (b) 272, (c) 558, and (d) 784 of the 32x32 pixel carbon elemental maps of DLC. Each plot shows a spectrum from an elemental map with a FOV of 500 μm (dark blue line), 200 μm (red line), 100 μm (green line), 50 μm (purple line), 20 μm (light blue line), and 10 μm (orange line).

Table 5-12: D Parameter values from each spectrum in Figure 5-37. The uncertainty of each D parameter value is ±0.2 eV.

Field of View (um)	D Parameter (eV) (Average)	D Parameter (eV) (Pixel 272)	D Parameter (eV) (Pixel 558)	D Parameter (eV) (Pixel 784)
500	19.8	20.8	14.8	18.6
202	21.2	20.6	18.8	21.8
100	20.8	22.0	21.4	21.6
50	21.6	17.0	22.4	21.4
20	22.2	21.2	23.2	22.2
10	22.4	22.4	22.4	22.6

The change in the shape of the peaks in Figure 5-37 suggests that there are some differences in the way the Scanning Auger Nanoprobe acquires spectra at different magnifications, which agrees with the HOPG results shown previously in Figure 5-32 and Figure 5-34. However, as the differences in the HOPG spectra are decreased when the FOV is below 200 um, these results suggest that the increases in magnification also result in an increase in the electron beam induced graphitisation of the DLC films, which is likely the result of an increase in the intensity of the electron beam when it is focused on smaller areas.

5.2.6.3 Magnification Level Dependence - Causes

It has been shown in sections 5.2.6.1 and 5.2.6.2 that the hybridisation maps of both HOPG and DLC exhibit a dependence on the level of magnification at which they are acquired. There are two possibilities for the causes of this dependence. The first is the sample, however as the phenomenon was observed in the same way for both HOPG and DLC this can be ruled out. The second possible cause is the technique itself. Each of the maps was acquired with all scanning parameters held constant, and the only change was the magnification level, which suggests that the changes are due to an artefact of the technique. As all user-controlled settings were the same it is thought that the internal mechanisms of the scanning technique are causing this magnification level dependence, rather than any user input, suggesting that there is a difference in how the instrument acquires data at different magnification levels. Further information is required to determine exactly what the cause of this artefact is, however it appears to be beyond user control with the current interface to the instrument, and to overcome the problem the technique is applied only at high magnification

levels resulting in a FOV of 100 μm or lower.

5.2.6.4 Magnification Level Dependence – Conclusions

Hybridisation maps of both HOPG (Figure 5-32) and DLC (Figure 5-35) have been acquired at a variety of magnification levels, ranging from a FOV of 500 μm down to 10 um, and both samples indicate that there is a dependence of the data on the level of magnification at which it is acquired. However, for both samples any maps acquired at a FOV of 100 μm or lower show consistency, indicating that whatever is causing this phenomenon is stable at this magnification range. For the purpose of creating hybridisation maps for this work all maps will therefore be acquired at a FOV of 100 μm or lower, as the data obtained at this level provides consistent and sensible results.

5.3   Carbon Hybridisation Maps

Maps of carbon hybridisation have been produced for a range of carbon samples of differing hybridisation composition using the method described above with the optimal scanning parameters. Initially standards of one hybridisation were examined to gain an understanding of how the hybridisation varies across the surface even in a material that is should be consistent, such as Highly Oriented Pyrolytic Graphite (HOPG) and Diamond Like Carbon (DLC) films. Carbon tape was also examined as it has been used as a substrate for mounting other carbon samples in this work. After the scan parameters were optimised and several uniform surfaces examined, more complicated samples composed of different carbon hybridisations were studied. To determine the reliability of the hybridisation mapping technique in reproducibly determining the hybridisations present multiples of each sample type are examined.

5.3.1   Highly Oriented Pyrolytic Graphite

HOPG is a highly-ordered form of graphite, and as such is composed almost entirely of sp^2 hybridised carbon, although any imperfections or damage to the HOPG lattice across the surface will cause small areas of sp^3 hybridised carbon, as has been seen in section 5.2. Because of its consistent structure HOPG is used as a standard for many applications. It has already been used in this work as a model substrate to examine the oxygen and argon plasma treatment of carbon surfaces, and is now considered as a control sample and a substrate for carbon hybridisation mapping. Samples of freshly cleaved HOPG were characterised using SAM using the method described previously, and the maps processed in MATLAB using the code described previously. The 'rainbow' colour scheme has been chosen for the colour maps, with 100 % sp^2 hybridised carbon being the darkest red and 100 % sp^3 hybridised carbon being the darkest blue, and the colour varying through the rainbow

between. The carbon hybridisation maps are therefore expected to be mostly dark red, with occasional areas of orange, yellow, or even green and blue, where there are areas of lattice disruption.

Some examples of HOPG hybridisation maps have already been shown in previous sections of this chapter where the optimal elemental map scanning parameters were determined, and now samples of freshly cleaved HOPG acquired with the chosen scan parameters at a higher spatial resolution are presented. Figure 5-38 shows such a sample, with a SEM image taken at a FOV of 50 µm shown in Figure 5-38 (a). At this level several sheet edges can be seen across the HOPG surface, as indicated by the bright and dark lines across the surface produced by changes in morphology. Three-point elemental maps of carbon (green) and oxygen (blue) are shown in Figure 5-38 (b) and (c), respectively. These maps show that both carbon and oxygen are quite uniformly distributed across the surface, regardless of the presence of step edges where variations could be expected to appear due to passivation of their high surface energy. Figure 5-38 (d) shows an overlay of the two elemental maps and indicates that the dominant species on the surface is carbon, although there is a small amount of oxygen distributed quite evenly across the surface. A window mode carbon elemental map was also acquired over this area, and is shown in Figure 5-38 (e) along with the
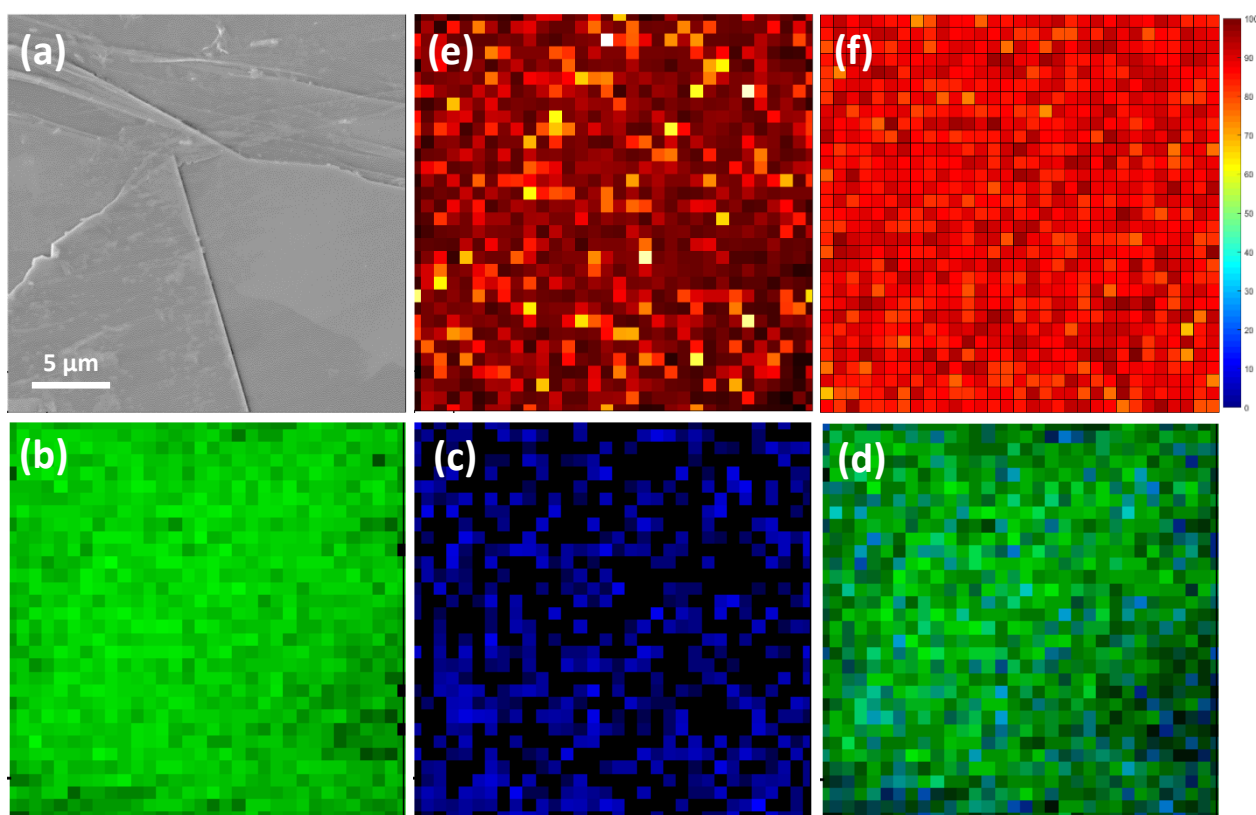
Figure 5-38: (a) SEM image of HOPG (FOV 50 µm), (b) 3 point carbon map, (c) 3 point oxygen map, (d) RGB overlay of (b) and (c), (e) window mode carbon map, and (f) hybridisation map.

resultant hybridisation map (Figure 5-38 (f)). As expected, the hybridisation map shows almost entirely red pixels, indicating a surface that is composed of highly sp^2 hybridised carbon, with several pixels indicating small areas with a lower sp^2 hybridised carbon percentage and defects in the lattice. These areas of lower sp^2 hybridised carbon content do not correspond to the step edges visible in the SEM image, suggesting that there may be small areas of lattice disruption that are not visible in the image.

As has been shown previously, the D parameter from the spectra of the carbon elemental map are used to determine the D parameter value at each pixel, which is then used to create the hybridisation map. Two spectra have been extracted from the carbon elemental map in Figure 5-38 (e) as examples of the range of peak shapes present across this map, and are shown in Figure 5-39.

Figure 5-39: Spectra extracted from pixels of the carbon elemental map in Figure 5-38 (e) showing examples of the peak shapes exhibited in this map that have different D parameter values, leading to the different coloured pixels in the corresponding hybridisation map.

The two spectra in Figure 5-39 have D parameter values of 22.6 eV and 23.2 eV, and which are values that are seen distributed across the map consistently. These spectra show very similar peak shapes, including the positions of peaks within the fine structure, however they have slightly different maxima and minima positions, leading to the difference in D parameter. This similarity is expected, as the structure of HOPG should be quite consistent, with small local disruptions to the lattice causing the small peak differences.

HOPG was also examined at a higher magnification to check for any changes that may occur in the data. An SEM image with a 20 μm FOV is presented in Figure 5-40 (a), where several sheet edges
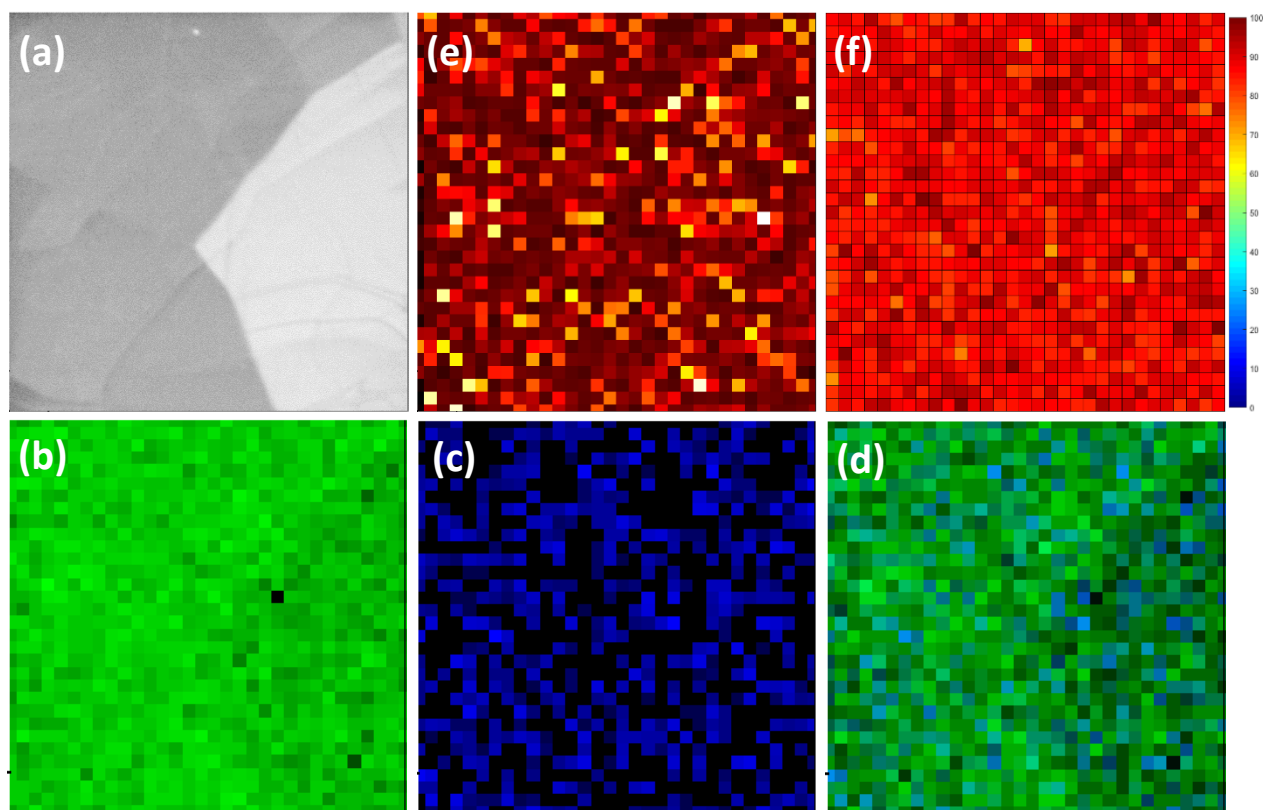
Figure 5-40: (a) SEM image of HOPG (FOV 20 µm), (b) 3 point carbon map, (c) 3 point oxygen map, (d) RGB overlay of (b) and (c), (e) window mode carbon map, and (f) hybridisation map.

can be seen in the image, with one sheet appearing to be folded over and sitting on top of the rest of the surface. The three-point elemental maps of carbon and oxygen are shown in Figure 5-40 (b) and (c), respectively, and indicate that the intensity of carbon on this higher graphite sheet is slightly reduced. This is affirmed in the overlay of these two elemental maps, shown in Figure 5-40 (d). The window mode carbon elemental map and resultant hybridisation map are shown in Figure 5-40 (e) and (f), respectively. The hybridisation map shows a surface that is almost entirely composed of sp^2 hybridised carbon, which is consistent with the surface observed at 50 um.

The results presented in this section combine to show that the surface of HOPG is composed predominately of carbon with a small amount of oxygen across the surface. The carbon present is almost entirely sp^2 hybridised, with occasional small areas of greater sp^3 hybridised carbon concentration where there are disruptions to the graphite lattice. All of these results match what was expected for HOPG based on its structure, and provide evidence that the carbon hybridisation mapping technique produces sensible and reproducible results.

5.3.2 Diamond Like Carbon

DLC films deposited on silicon substrates have been used as substrates for other carbon materials

for the purpose of carbon hybridisation mapping, and are therefore considered individually here so that they can be discerned from the other carbon species. These films were characterised in chapter 4 using both XPS and SAM and found to be highly sp^3 hybridised, however the previous results in this chapter where DLC films were used to determine the optimal scanning parameters suggested that the DLC films are significantly graphitised upon prolonged exposure to the high intensity electron beam that is required for carbon hybridisation mapping. As a result of this, the DLC films shown in this section are expected to exhibit a much larger sp^2 hybridised carbon percentage than the ideal case that had been expected from the SAM and XPS results in chapter 4.

The SEM image of a DLC film examined at a 50 μm FOV is shown in Figure 5-41 (a), and appears to be a mostly uniform surface, although there are several darker regions where fewer secondary electrons are emitted. Carbon, oxygen, and silicon three point elemental maps are shown in Figure 5-41 (b), (c), and (d), respectively, and the overlay of the three maps is shown in Figure 5-41 (e). The carbon and oxygen maps show a quite uniform distribution of elements across the surface, while the overlay shows that carbon is the dominant species. There are also small amounts of silicon observed, which suggests that the film may not be completely uniform in thickness and the silicon substrate is also being detected. These areas do not correspond to any observable defects in the SEM image, thus it is important to take the silicon elemental map at each location to ensure the

Figure 5-41: (a) SEM image of a DLC film (FOV 50 μm), (b) 3 point carbon map, (c) 3 point oxygen map, (d) 3 point silicon map, (e) RGB overlay of (b), (c) and (d), (f) window mode carbon map, and (g) hybridisation map.

surface under examination is truly the DLC film.

A window mode carbon elemental map is shown in Figure 5-41 (f), and the hybridisation map that was created from it is shown in Figure 5-41 (g). The hybridisation map shows a range of different coloured pixels, but still predominantly yellow, orange, and red, indicating that the surface is highly sp^2 hybridised. There are some pixels showing cooler colours of greens and blues, indicating areas with more sp^3 hybridised carbon, that are distributed reasonably evenly across the map, but do not correlate spatially with any of the darker areas in the SEM, nor the areas with a greater silicon content. The lack of correlation with the features in the SEM image or the elemental maps indicates that the DLC film may not be completely uniform in the distribution of the hybridisations across its surface.

Spectra were extracted from the carbon elemental map in Figure 5-41 (f) to show the range of peak shapes and D parameter values that occur across this map. These spectra are shown in Figure 5-42. The blue and red spectra in Figure 5-42 have D parameter values of 17.0 eV and 20.8 eV, respectively, indicating a wide range of sp^2 hybridised carbon percentages. As well as the differences in the positions of the maxima and minima of the two peaks the fine structure is also different, which further indicates the differences in the hybridisation of the surface at different points.
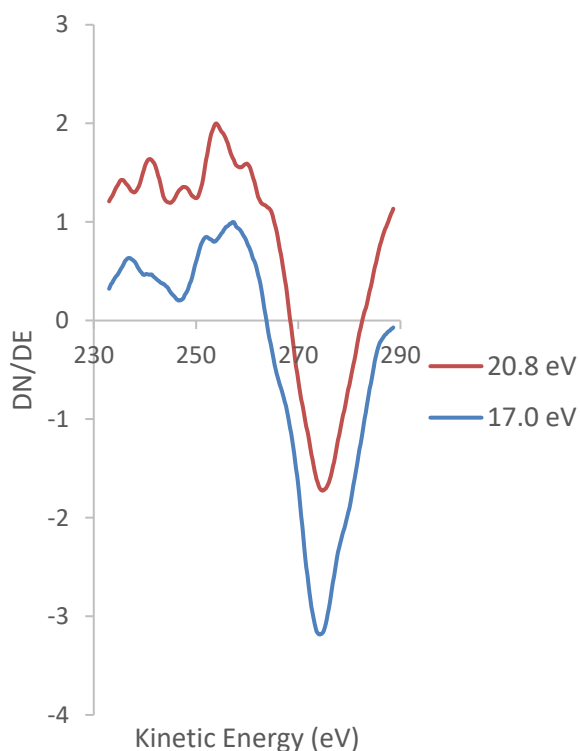
Figure 5-42: Spectra extracted from pixels of the carbon elemental map in Figure 5-41 showing examples of the peak shapes exhibited in this map that have different D parameter values, leading to the different coloured pixels in the corresponding hybridisation map.

DLC films were also examined at a higher magnification level with a 20 µm FOV to examine the consistency of the technique between different magnification levels. The SEM image in Figure 5-43
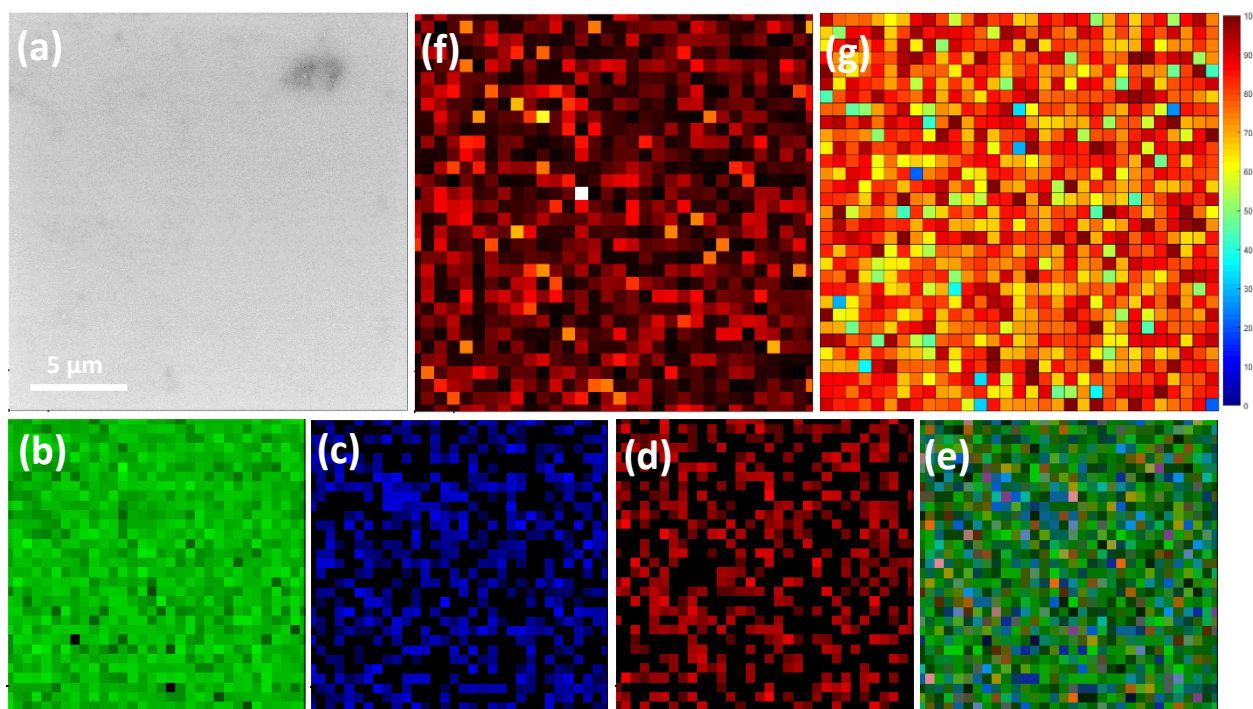
Figure 5-43: (a) SEM image of a DLC film (FOV 20 µm), (b) 3 point carbon map, (c) 3 point oxygen map, (d) 3 point silicon map, (e) RGB overlay of (b), (c) and (d), (f) window mode carbon map, and (g) hybridisation map.

(a) shows this area, and presents a surface that appears to be quite uniform, with several small and one larger dark area scattered across the surface. Carbon, oxygen, and silicon three-point elemental maps were acquired over this area and are shown in Figure 5-43 (b), (c), and (d), respectively. These maps indicate a uniform distribution of all three elements, and the RGB overlay (Figure 5-43 (e)) indicates that carbon is the dominant element, with smaller amounts of oxygen and silicon.

A window mode carbon elemental map was also acquired over the same area (shown in Figure 5-43 (f)) and was converted to a hybridisation map (Figure 5-43 (g)). The hybridisation map shows the majority of pixels to be red and orange, which indicates that the surface is largely sp^2 hybridised, however there are also pixels of yellow, green, and blue interspersed through the map that indicate areas of lower sp^2 hybridised carbon content. This map shows a higher sp^2 hybridised carbon content overall than those taken with a FOV of 50 µm (Figure 5-41) which supports the earlier conclusion that as the magnification level is increased the electron beam induced graphitisation of the DLC film is also increased.

The results shown here are different to those were initially expected for a DLC film based on the SAM and XPS characterisation performed in chapter 4 as they show a higher percentage of sp^2 hybridised carbon than the previous studies. However, it is thought that these differences are caused by electron beam induced graphitisation of the DLC film, which occurs to a significant extent

at higher magnification levels as the electron beam is at a higher intensity when focused over a smaller area. The results do show a consistent surface between different DLC samples, with the overall surface having a high sp^2 hybridised carbon content but also areas of lower sp^3 hybridised carbon percentage scattered randomly across the surface. The hybridisation maps of DLC films therefore provide evidence for the ability of this carbon hybridisation mapping technique to reliably determine the hybridisations present and their uniformity across the surface.

5.3.3 Carbon Tape

Carbon tape has been used as a substrate for the examination of graphene flakes and nanodiamonds in this work, thus it is examined here individually so that it can be compared to these other materials when they are shown together in the same sample. Carbon tape has been observed using AES to be mostly carbon, with oxygen and silicon also present. The hybridisation of the carbon in the tape is expected from the high-resolution AES to be mostly sp^3 hybridised, but it is likely that this hybridisation will not be consistent across the whole surface. This would result in the full 'rainbow' spectrum of the colour scale being present in the hybridisation maps. Carbon tape is characterised here at FOVs of 50 μm and 20 um, as these were the magnifications chosen to examine graphene flakes and nanodiamonds on carbon tape, and it is also expected that at this magnification level the calibration curve will be able to be applied accurately, as per the magnification level dependence experiments discussed in section 5.2.6.

The first sample of carbon tape was examined at a 50 μm FOV, with the SEM image presented in Figure 5-44 (a). The image shows a potentially rough surface that is highly textured across the greater portion of the examined area, with a large region of approximately 10 μm x 20 μm in size that appears to be less textured about midway down the image. This texture is indicated by the brighter and darker areas of the image, which are indicative of changes in morphology when the surface elemental composition is relatively uniform. Three-point carbon, oxygen, and silicon elemental maps are presented in Figure 5-44 (b), (c), and (d), respectively. The carbon map shows a higher intensity on the top half of the map than the bottom, while the oxygen map shows the reverse trend. The silicon map is also slightly more intense on the lower half, although its intensity is lower across the whole surface than the other elements. The RGB overlay of these three maps is shown in Figure 5-44 (e) and shows that the top half of the image is composed predominantly of carbon, while the lower half of the image is dominated by the oxygen and, to a lesser extent, silicon.

A window mode carbon elemental map was also acquired over this area and then converted into a

Figure 5-44: (a) SEM image of carbon tape (FOV 50 µm), (b) 3 point carbon map, (c) 3 point oxygen map, (d) 3 point silicon map, (e) RGB overlay of (b), (c) and (d), (f) window mode carbon map, and (g) hybridisation map.

hybridisation map, which are shown in Figure 5-44 (f) and (g), respectively. The hybridisation map shows the full range of colours in the rainbow scale, which indicates that the sp^2 hybridised carbon content ranges from 0 % to 100 % throughout the map. However, overall there are more pixels in the red and orange areas of the scale, indicating that the surface is more sp^2 hybridised overall. As the AES high resolution spectra indicated a surface that is highly sp^3 hybridised, it is likely that the carbon tape is experiencing some electron beam induced graphitisation similar to that observed in the DLC films.

Spectra were extracted from the carbon elemental map in Figure 5-44 (f) to examine the peak shapes that are common across the map. Two spectra indicating the range of D parameter values in the map are shown in Figure 5-45.

The two spectra in Figure 5-45 show large differences between the blue line, with a D parameter of 16.8 eV, and the red line, with a D parameter of 22.6 eV. The positions of the minima are quite similar for both spectra, however the positions of the maxima are very different due to the different peak shapes and fine structure around that area of the spectra. The differences between these spectra are typical for those observed across the carbon elemental map, and demonstrate the cause of the differences observed across the hybridisation map.
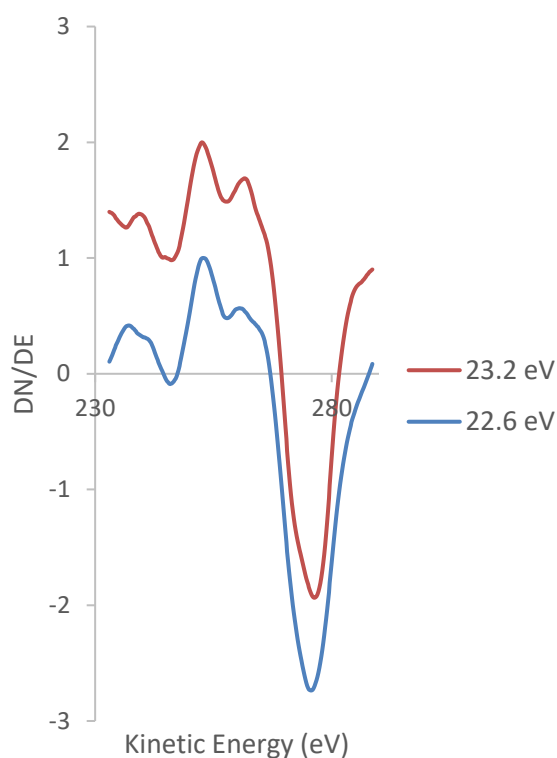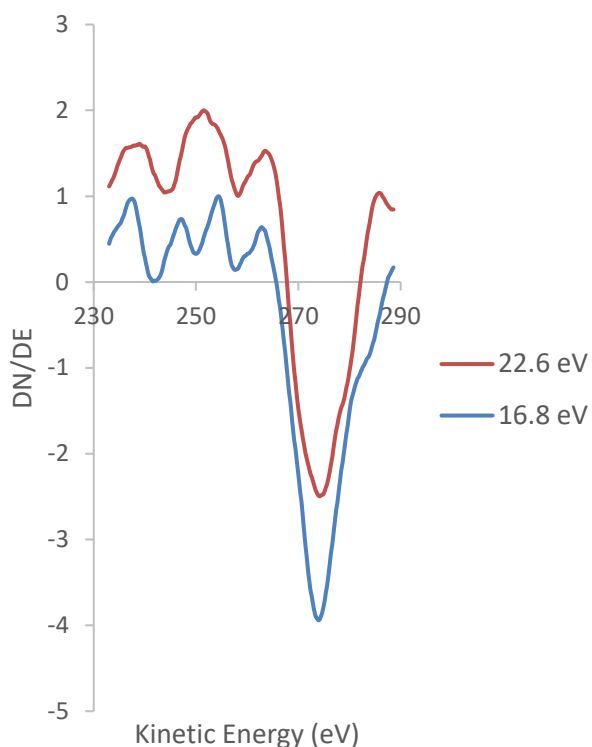
Figure 5-45: Spectra extracted from pixels of the carbon elemental map in Figure 5-44 showing examples of the peak shapes exhibited in this map that have different D parameter values, leading to the different coloured pixels in the corresponding hybridisation map.

Samples of carbon tape were also characterised with a higher level of magnification to determine if carbon tape experiences any changes similar to those undergone by the DLC films when exposed to a higher intensity electron beam. The sample is shown in the 20 μm FOV SEM image in Figure 5-46 (a). The SEM image shows a surface that appears to be very uneven and textured, with a smoother
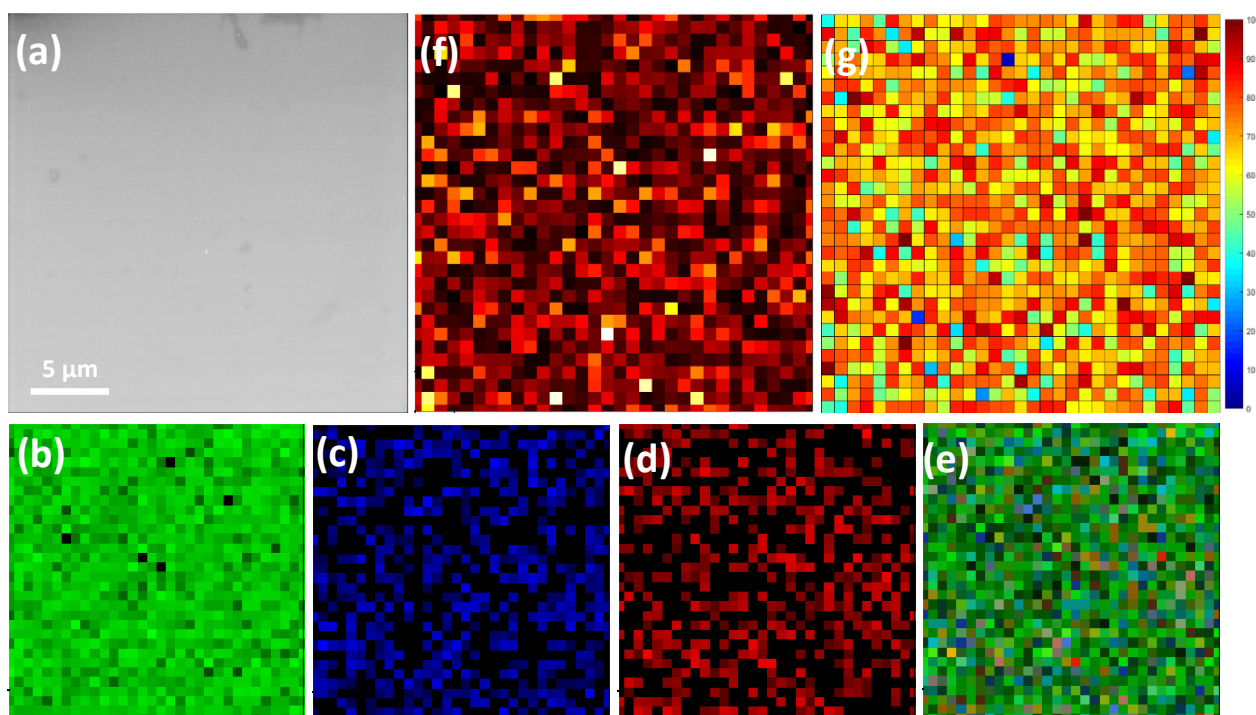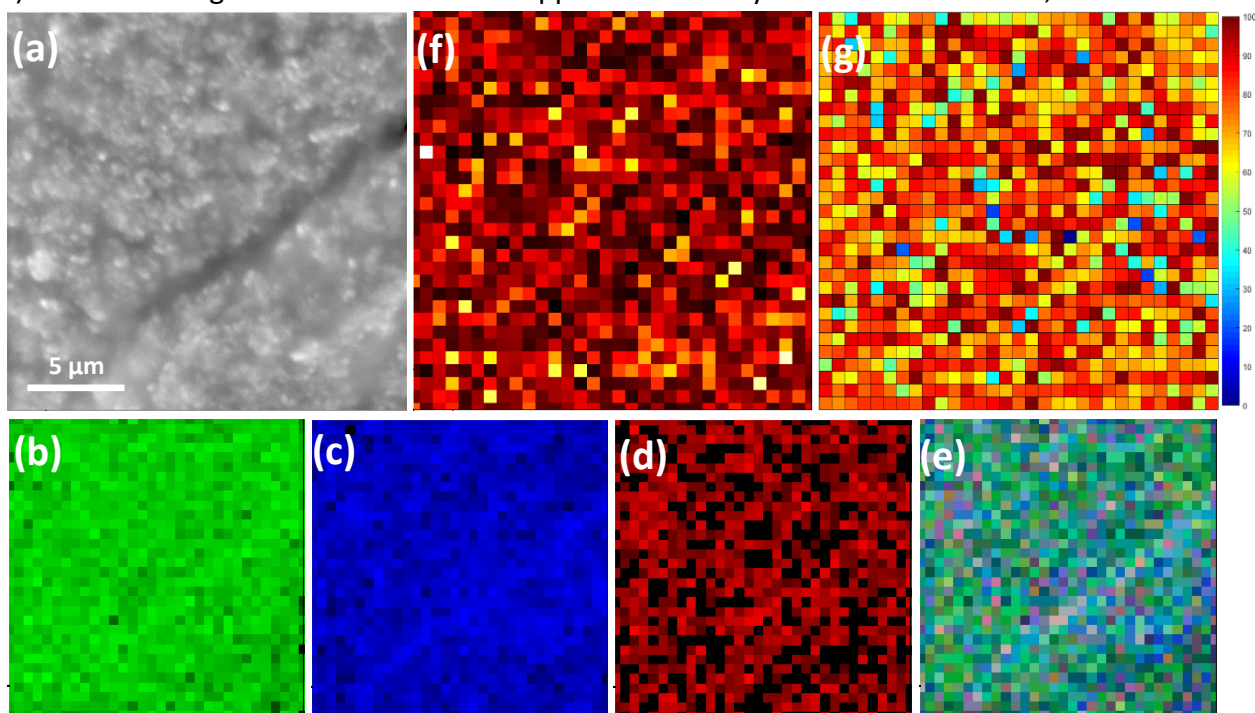

Figure 5-46: (a) SEM image of carbon tape (FOV 20 μm), (b) 3 point carbon map, (c) 3 point oxygen map, (d) 3 point silicon map, (e) RGB overlay of (b), (c) and (d), (f) window mode carbon map, and (g) hybridisation map.

line running through diagonally. Carbon, oxygen, and silicon three-point elemental maps (Figure 5-46 (b), (c), and (d), respectively) show mostly uniform distributions, although the oxygen has a slightly higher intensity in the area matching the smoother line in the SEM image. The RGB overlay in Figure 5-46 (e) shows that carbon is the most dominant element across most of the area examined, although the areas of slightly higher oxygen concentration can be seen in the overlay.

The window mode carbon elemental map (Figure 5-46 (f)) was converted to a hybridisation map (Figure 5-46 (g)), which shows a surface that has areas ranging through the full scale of sp^2 hybridised carbon percentages. The surface appears to have an overall higher sp^2 hybridised carbon content than those observed at the 50 μm FOV level of magnification (Figure 5-44), suggesting that the extent of electron beam induced graphitisation of the carbon tape increases as the magnification increases, in the same manner as that observed previously for DLC films (section 5.2.6.2).

The hybridisation maps of carbon tape show a surface that is uniformly uneven in its distribution of hybridisations, but overall shows a high sp^2 carbon content that is increased as the FOV increases, likely as a result of electron beam induced graphitisation. The similar results presented across these examples show that carbon tape is quite consistent in its chemical and hybridisation compositions, and provides further evidence that the carbon hybridisation mapping technique is working consistently for a range of samples.

5.3.4 Graphene on Carbon Tape

So far within this chapter samples composed of one material have been examined with the hybridisation mapping technique and have been found to produce reproducible results, therefore the next step in testing the technique is to apply it to a sample composed of more than one hybridisation, that is, a sample of one hybridisation sitting on a substrate of the other. To achieve this samples composed of graphene flakes deposited on carbon tape were produced. The graphene flakes are expected to be predominantly sp^2 hybridised, and thus appear to be red in the hybridisation maps, as shown in the HOPG maps previously (section 5.3.1). However, the carbon tape will have a larger range of hybridisations present as was shown in section 5.3.3, and is expected to show a range of colours from blue to red in the map, indicating sp^2 hybridised carbon percentages ranging from 0 % to 100 %. Maps of these samples were taken at 128x128 pixels, providing sufficient spatial resolution to demonstrate the method, with all other scan parameters held at the values found to be optimal previously in section 5.2 of this chapter. The FOV of each map is 50 μm and was

chosen both to provide maps of an appropriate size to include both the graphene flakes and carbon tape substrate, and also so that the calibration curve relating the D parameter to the sp^2 hybridised carbon percentage shown earlier in section 5.2.6 is expected to hold.

The first example of a sample of graphene flakes on carbon tape is shown in Figure 5-47, where the SEM image (Figure 5-47 (a)) shows multiple graphene flakes on the left side and centre of the image, while the upper and lower right of the image is the uncoated carbon tape substrate. Three-point elemental maps of carbon (green), oxygen (blue), and silicon (red) are shown in Figure 5-47 (b), (c), and (d), respectively. As expected, the carbon appears as the dominant element across the sample area, however there is a higher intensity of carbon in the areas that appear to be graphene flakes than in the surrounding carbon tape. The oxygen distribution shows the inverse relationship to this, with a higher oxygen presence detected in the areas showing carbon tape and a lower amount present in the graphene areas. The quantity of silicon was also examined due to its presence in the carbon tape, with the amount being very low across the whole area under examination. Figure 5-47 (e) shows an RGB overlay of carbon, oxygen, and silicon three-point elemental maps, and highlights the areas where the elemental composition varies. It can be seen in this map that the colour contrast clearly illustrates the areas that correspond to the graphene flakes in the SEM image (Figure 5-47
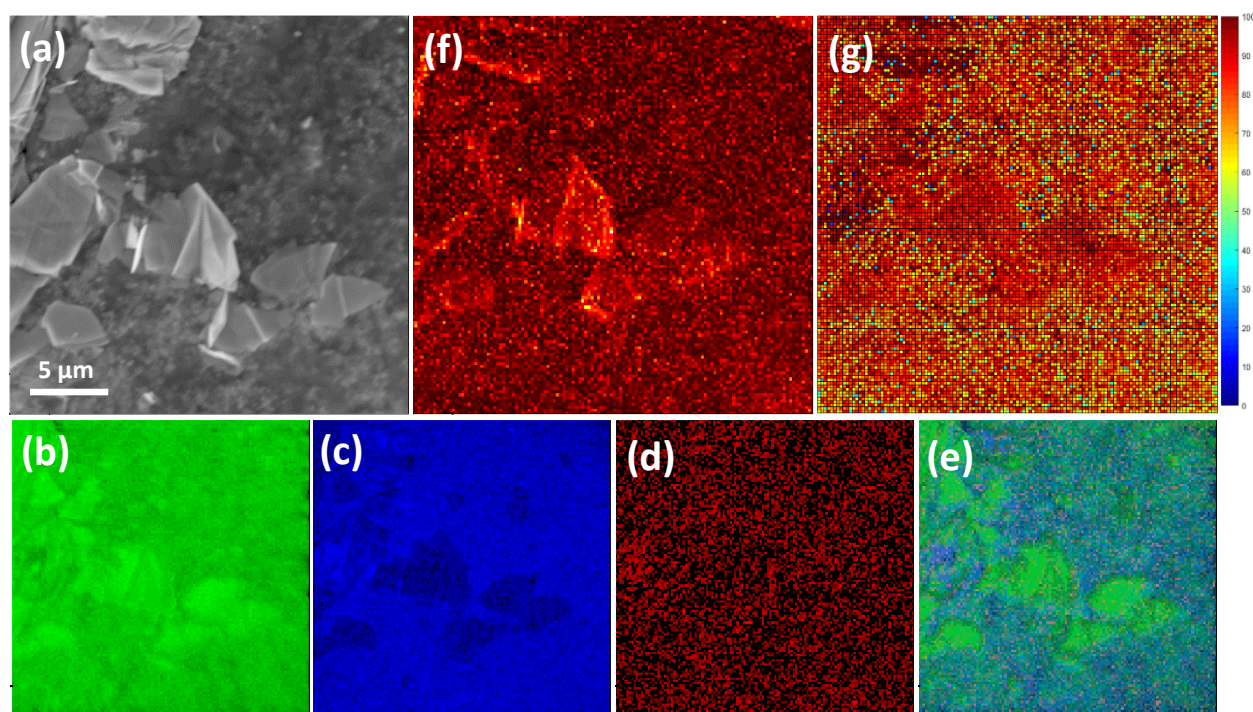
Figure 5-47: (a) SEM image of graphene flakes on carbon tape (FOV 50 μm), (b) 3 point carbon map, (c) 3 point oxygen map, (d) 3 point silicon map, (e) RGB overlay of (b), (c) and (d), (f) window mode carbon map, and (g) hybridisation map.

220

(a)). These areas show strong carbon presence, and relatively little oxygen or silicon, while the carbon tape areas show a much higher oxygen concentration, but still very little silicon.

A window mode carbon map was also acquired over the same area (Figure 5-47 (f)), and was subsequently converted to a hybridisation map, shown in Figure 5-47 (g). This hybridisation map shows several important features. First, there are regions of mostly solid red across the left side and centre of the map. These features correspond with the shapes and positions of the graphene flakes in the SEM image (Figure 5-47 (a)), and indicate that the graphene flakes are highly sp^2 hybridised, as expected. The remaining areas of the hybridisation map show a range of colours in a random fashion, as expected for carbon tape, which indicates that the tape is composed of a variety of different hybridisations. Finally, there are several small regions of dark red interspersed with several pixels of dark blue in Figure 5-47 (g), indicating that the sp^2 hybridised carbon percentage scale has been exceeded in both directions in the same area. The presence of darkest red and darkest blue pixels in the same area usually indicates that the sample was experiencing charging under the influence of the electron beam, which leads to distortion of the spectra and therefore inaccurate D parameter measurements. It is noted that while the features in hybridisation map are the same shape and size as those in the SEM image, they are slightly shifted from their expected positions. Although image registration was used to try and avoid drift in the images, the carbon tape has a tendency to move slightly as the electron beam impacts it, causing the sample to distort and the shapes to move slightly without the image registration failing. This is an effect that will be observed in all samples using a carbon tape substrate in this work.

Spectra were extracted from the carbon elemental map (Figure 5-47 (f)) in positions that correlate with both the graphene flakes and the carbon tape in the SEM image in Figure 5-47 (a). These spectra are shown in Figure 5-48 to examine the differences in the peak shape that occur from the different features. The peak shape of the two spectra from Figure 5-48 show clear differences in both the positions of the maxima and minima, as well as the fine structure of the peaks. The more graphitic peak (from the graphite flake area) has a D parameter value of 23.6 eV, and shows a peak shape that is consistent with other graphitic peaks shown previously, while the other (from the carbon tape area) has a D parameter of 17.4 eV and has a similar peak shape to that shown in Figure 5-45 for carbon tape. The spectra for both areas match what is expected based on the composition of the sample at each point.

To further examine the reliability of the hybridisation mapping technique another sample of
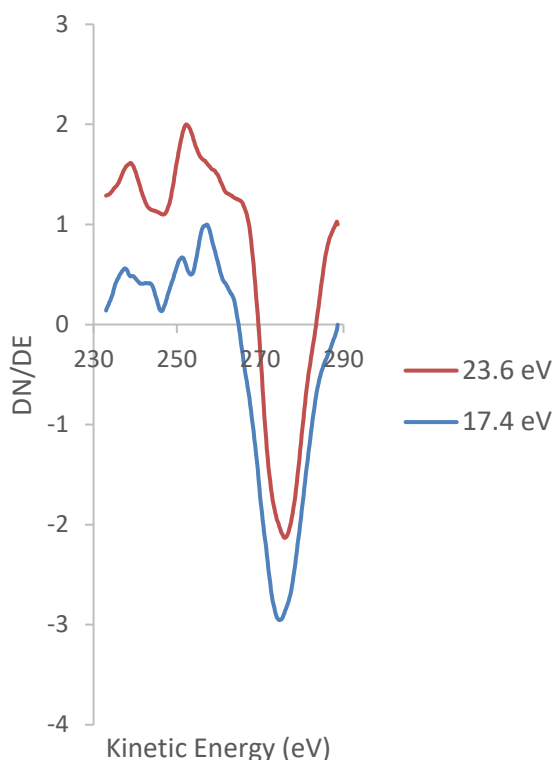
Figure 5-48: Spectra extracted from pixels of the carbon elemental map in Figure 5-47 showing examples of the peak shapes exhibited in this map that have different D parameter values, leading to the different coloured pixels in the corresponding hybridisation map.

graphene flakes on carbon tape was examined, with the results shown in Figure 5-49. The SEM image (Figure 5-49 (a)) shows a folded over graphene flake on a carbon tape substrate. The carbon (green), oxygen (blue), and silicon (red) three-point elemental maps are shown in Figure 5-49 (b), (c), and (d), respectively, and show clear differences between the graphene flake and carbon tape. The carbon has a higher intensity in the area corresponding to the graphene flake, while the oxygen map shows the inverse trend and is more intense in the carbon tape areas. These differences are highlighted in the RGB overlay in Figure 5-49 (e), where the carbon is the dominant species present in the area of the graphene flake, while the carbon tape is a mixture of carbon and oxygen, with very little silicon present anywhere.

A window mode carbon map was also taken of the sample (Figure 5-49 (f)), and was converted to the hybridisation map shown in Figure 5-49 (g). There are two distinctive areas in the hybridisation map: the area that is mostly red, which corresponds to the position of the graphene flake, and an area surrounding it that is a mixture of red, yellow, and green, which corresponds to the carbon tape. Both these regions show the hybridisations of carbon that were expected, with the graphene flake being mostly sp^2 hybridised and the carbon tape showing a random mix of hybridisations.

The above results show clear differences between the graphene flakes and carbon tape in the hybridisation maps. This is the first example of the hybridisation mapping technique being applied to a sample that is expected to have clearly defined regions of different hybridisations, and the

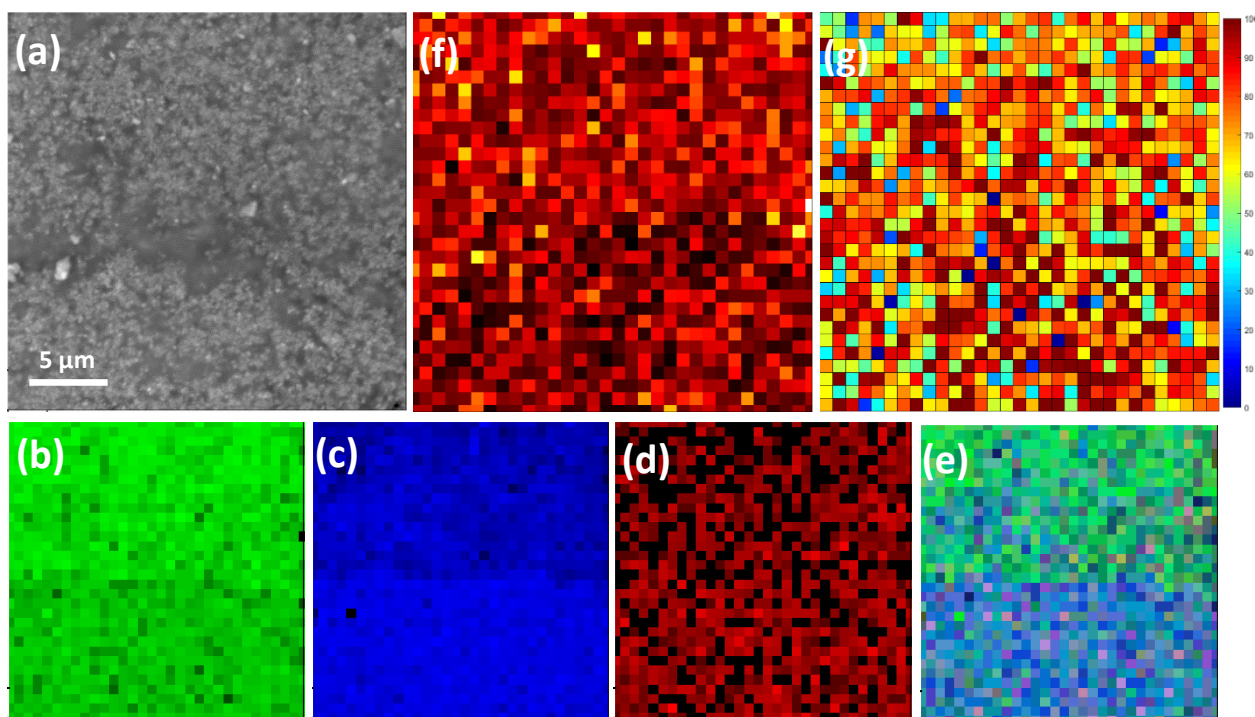**Figure 5-49: (a) SEM image of graphene flakes on carbon tape (FOV 50 μm), (b) 3 point carbon map, (c) 3 point oxygen map, (d) 3 point silicon map, (e) RGB overlay of (b), (c) and (d), (f) window mode carbon map, and (g) hybridisation map.**

results are exactly as expected. The carbon hybridisation mapping technique is therefore demonstrating the ability to identify the regions of different carbon hybridisation across the surface. The contrast evident in the hybridisation maps and their correlation with features observed on the surface in the SEM image clearly demonstrates that the hybridisation mapping technique is successful. This technique provides a valuable means to examine structures of a particular type of hybridisation on the surface, or discern mixed carbon hybridisations when they exist together.

5.3.5   Nanodiamonds

To further test the abilities of the hybridisation mapping technique to distinguish between materials of one hybridisation deposited on a substrate of the other hybridisation, samples containing nanodiamonds were created. The nanodiamonds are an example of a sp^3 hybridised carbon material, and were deposited on substrates of HOPG, DLC, and carbon tape, which should all show distinctly different hybridisations to the nanodiamonds, and therefore produce hybridisation maps with clearly defined regions.

5.3.5.1 Nanodiamonds on Highly Oriented Pyrolytic Graphite

A sample of nanodiamonds on HOPG is expected to show the largest contrast in the hybridisation map as the nanodiamonds should be predominantly sp^3 hybridised while graphite has been shown

to be predominantly sp^2 hybridised, therefore this sample was chosen to examine first. Figure 5-50 (a) shows an SEM image of several variously sized clusters of nanodiamonds on HOPG at a FOV of 20 um. Three point carbon (green) and oxygen (blue) elemental maps of this area are shown in Figure 5-50 (b) and (c), respectively, along with the RGB overlay in Figure 5-50 (d). From these elemental maps it can be seen that the entire sample is predominately carbon, with small amounts of oxygen present across the surface and in higher concentrations at the edges of the nanodiamond clusters, where the surface energy would be greater and any reaction with oxygen more likely to occur to reduce it.

A window mode carbon elemental map of the area presented in Figure 5-50 (e) shows a greater intensity in the areas corresponding to the nanodiamonds, and its corresponding hybridisation map is shown in Figure 5-50 (f). This map shows areas of different coloured pixels, indicating areas of different hybridisations. The areas corresponding to nanodiamonds show pixels near the dark blue end of the rainbow colour palette, indicating very little sp^2 hybridised carbon content, interspersed with pixels ranging from light blue to yellow in colour, indicating larger sp^2 content within the total signal obtained in those areas. The surrounding areas, which correspond to the HOPG substrate, show pixels that are near the red end of the rainbow colour palette indicating a high sp^2 hybridised
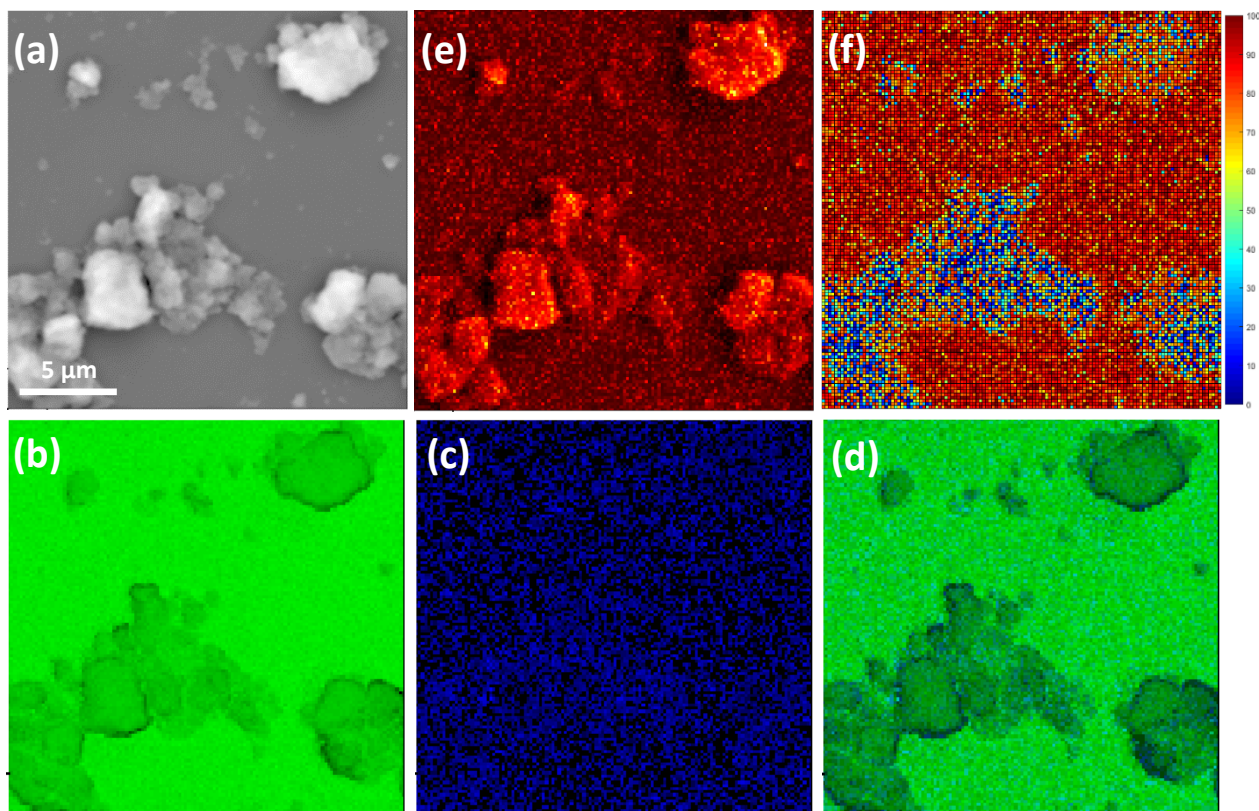
Figure 5-50: (a) SEM image of nanodiamonds on HOPG (FOV 20 μm), (b) 3 point carbon map, (c) 3 point oxygen map, (d) RGB overlay of (b) and (c), (e) window mode carbon map, and (f) hybridisation map.

carbon percentage. These results are what was expected based on the materials involved, and provide good evidence for the validity of this technique for carbon hybridisation mapping.

Spectra were extracted from the carbon elemental map in Figure 5-50 (e) in areas corresponding to nanodiamonds and HOPG shown in the SEM image in Figure 5-50 (a). These spectra are shown in Figure 5-51 to examine the differences in peak shape that lead to the differences in the hybridisation map.
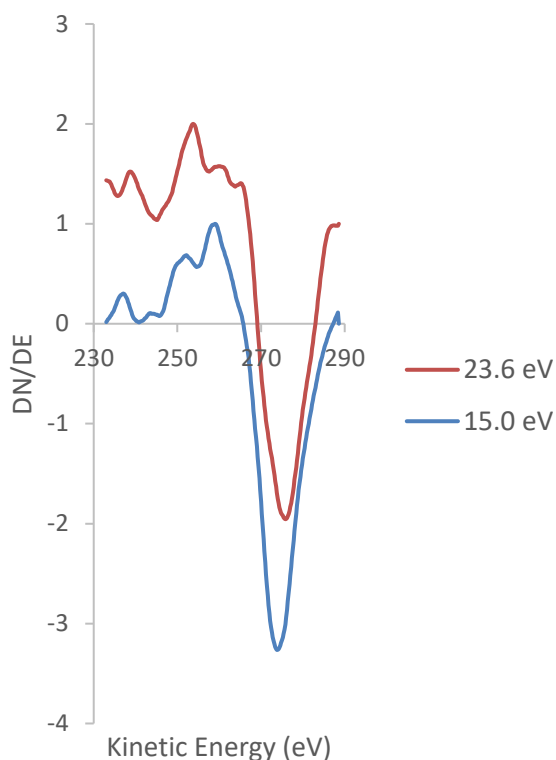
Figure 5-51: Spectra extracted from pixels of the carbon elemental map in Figure 5-50 showing examples of the peak shapes exhibited in this map that have different D parameter values, leading to the different coloured pixels in the corresponding hybridisation map.

The blue line in Figure 5-51 was extracted from an area of the sample composed of nanodiamond and has a D parameter value of 15.0 eV, while the red line was extracted from an area of HOPG and has a D parameter of 23.6 eV. As well as the differences in the positions of the maxima and minima, there are also differences in the fine structure of the peaks, both on the high and low kinetic energy sides of the peak. These spectra are typical of those obtained across their respective areas of the sample, and demonstrate the differences in peak shape that show the different sp^2 hybridised carbon percentage values at the different points.

To further examine the consistency of the hybridisation mapping technique a second sample of nanodiamonds on HOPG is shown in Figure 5-52, with the SEM image showing nanodiamond clusters of various sizes on a HOPG substrate (Figure 5-52 (a)). Three point elemental maps of carbon (green) and oxygen (blue) are shown in Figure 5-52 (b) and (c), respectively, along with the RGB overlay of the two elements (Figure 5-52 (d)). These maps show the surface to be predominantly
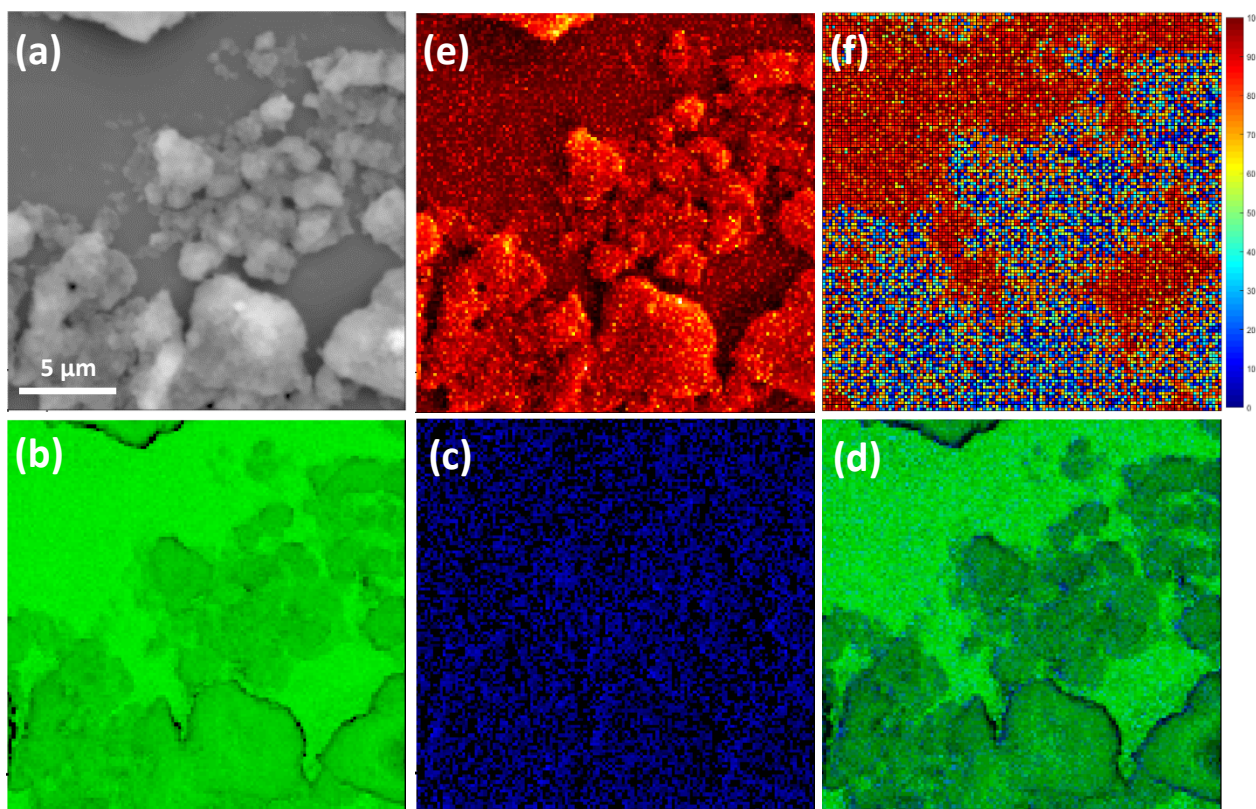
Figure 5-52: (a) SEM image of nanodiamonds on HOPG (FOV 20 μm), (b) 3 point carbon map, (c) 3 point oxygen map, (d) RGB overlay of (b) and (c), (e) window mode carbon map, and (f) hybridisation map.

carbon, with a slightly greater oxygen content in the areas corresponding to the nanodiamonds. These results match those shown in the first sample of nanodiamonds on HOPG discussed in Figure 5-50, including the higher concentration of oxygen along the edges of the nanodiamonds.

The window mode carbon elemental map is presented in Figure 5-52 (e), with the brighter areas corresponding to the nanodiamond particles on the surface. The resultant hybridisation map is shown in Figure 5-52 (f) and shows areas of stark hybridisation contrast, with areas showing either (mostly) red or (mostly) blue pixels. The red areas correspond to the HOPG substrate in the SEM image (Figure 5-52 (a)) and indicate a high sp^2 hybridised carbon content, as is expected based on the structure of HOPG and previous experimental results (section 5.3.1). These are interspersed with some pixels of yellow, indicating regions with reduced sp^2 hybridised carbon percentage (or conversely, an increase in the presence of sp^3 hybridised carbon species), thus illustrating places where the HOPG lattice has been disrupted or is occupied by the presence of small nanodiamond particles that are not visible in the SEM at this scale. The blue areas in Figure 5-52 (f) correspond to the larger nanodiamonds, and indicate regions where a very low sp^2 hybridised carbon percentage is present. This is as expected, with some 'noise' apparent through the red pixels indicating an enhanced sp^2 carbon content, which may be from the adsorbate or from the substrate underneath

226

if there are impurities. These results show clear differences between the various types of carbon that are present on the surface of the sample, and replicate the results in Figure 5-50 for a similar sample.

The hybridisation maps for samples of nanodiamonds on HOPG show very clear differences in hybridisation between nanodiamonds and the HOPG substrate, with both areas showing the hybridisations that were expected based on the composition of the materials. These maps are good examples of the validity and reproducibility of the carbon hybridisation mapping method developed in this work.

5.3.5.2 Nanodiamonds on Diamond-Like Carbon

To further examine the validity of this technique and its ability to distinguish variations in carbon hybridisations across a sample nanodiamonds were deposited on a DLC film in the same way that they were deposited on the HOPG. These samples are expected to appear very similar to the HOPG substrate samples in Figure 5-50 and Figure 5-52, but with a larger range of hybridisations present on the substrate to match the results obtained for DLC films in section 5.3.2.

A sample of nanodiamonds on DLC is examined in Figure 5-53, where clusters of nanodiamonds of various sizes can be seen scattered across the right side of the SEM image (Figure 5-53 (a)). Three point elemental maps of carbon (green), oxygen (blue), and silicon (red) were obtained (Figure 5-53 (b), (c), and (d), respectively), with the silicon examined to ensure that the DLC film is complete and the silicon substrate is not visible. It can be seen in the elemental maps that while most of the sample surface is predominately carbon, there is a small area at the bottom of the image that appears to be silicon oxide, indicating an area where the film is not complete. However, there is still some carbon present in this area and therefore a carbon hybridisation map can still be obtained in this region.

The window mode elemental map of this area is shown in Figure 5-53 (f), with the resultant hybridisation map in Figure 5-53 (g). The hybridisation map shows areas with largely different hybridisations, indicated by the difference in the colours of the pixels. The areas corresponding with nanodiamonds in the SEM image (Figure 5-53 (a)) appear mostly dark blue, with some pixels of light blue, green, and yellow interspersed, predominately around the edges of the features. This indicates that the nanodiamonds are mostly sp^3 hybridised, as is expected, but with some areas showing a larger amount of sp^2 hybridised carbon. The surrounding area, corresponding to the DLC film,
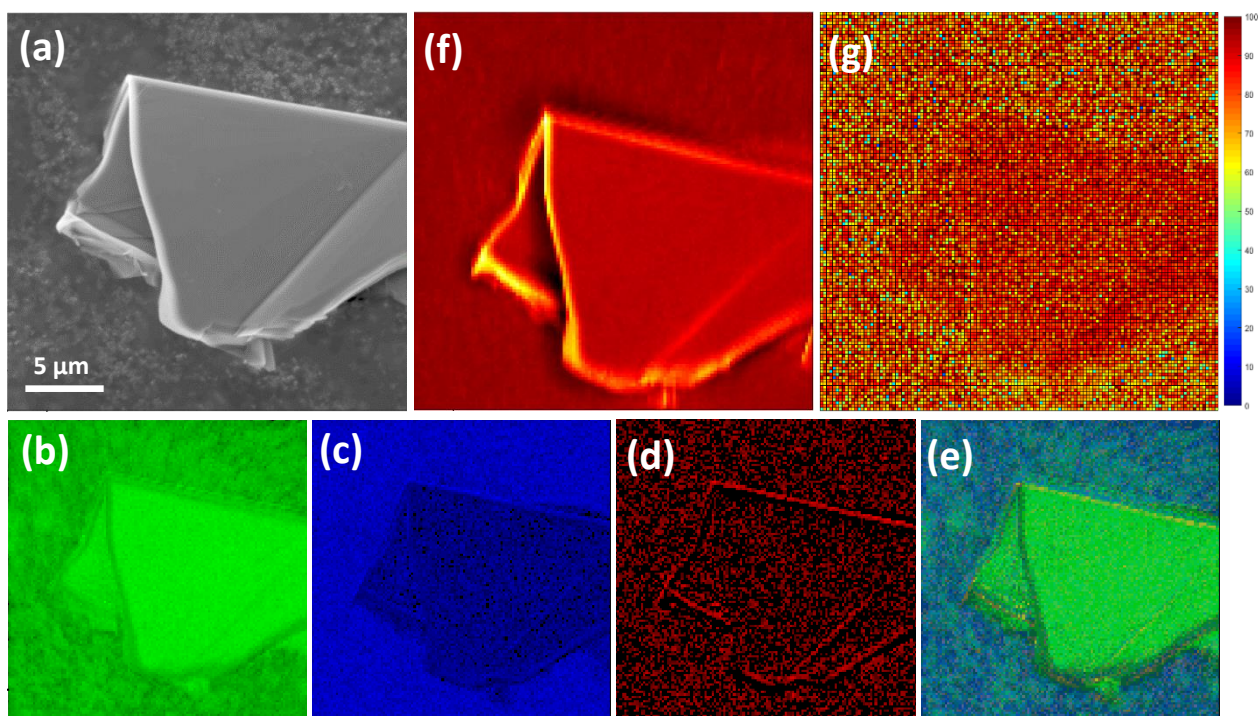
Figure 5-53: (a) SEM image of nanodiamonds on DLC film (FOV 20 µm), (b) 3 point carbon map, (c) 3 point oxygen map, (d) 3 point silicon map, (e) RGB overlay of (b), (c) and (d), (f) window mode carbon map, and (g) hybridisation map.

appears to be a mixture of red and yellow pixels, indicating an area that is mostly carbon with a high sp^2 hybridisation percentage, as is expected for these DLC films based on previous results presented in this chapter. This sample therefore shows a smaller contrast in hybridisations than the previous samples with HOPG substrate, yet the difference between the two substrates can still clearly be visualised by the hybridisation mapping technique.

Spectra extracted from the carbon elemental map in Figure 5-53 (f) in areas that correspond with both the nanodiamonds and DLC film in Figure 5-53 (a), and are shown in Figure 5-54. The red line in Figure 5-54 indicates a spectrum from the DLC film in Figure 5-53 and has a D parameter of 23.6 eV, with a fine structure that is consistent with the DLC films examined previously. Conversely, the blue line shows a spectrum from the nanodiamonds with a D parameter of 14.4 eV, with different fine structure than that observed in the previous nanodiamond sample (Figure 5-51). This difference indicates that there is some small difference in the hybridisation at this point compared to that shown with different nanodiamonds, which is consistent with the differences across the nanodiamonds in both Figure 5-50 and Figure 5-53.

A second sample of nanodiamonds on DLC was examined to check the reliability of the mapping technique for this type of sample. The SEM image (Figure 5-55 (a)) shows nanodiamond clusters in

Figure 5-54: Spectra extracted from pixels of the carbon elemental map in Figure 5-53 showing examples of the peak shapes exhibited in this map that have different D parameter values, leading to the different coloured pixels in the corresponding hybridisation map.

a range of sizes on the DLC substrate. Three-point elemental maps of carbon (green), oxygen (blue), and silicon (red) are shown in Figure 5-55 (b), (c). and (d), respectively, along with the RGB overlay in Figure 5-55 (e). These maps show a surface that is almost entirely carbon, with small amounts of oxygen present across the sample. There is no silicon observed, indicating that the DLC film is complete in this area.

A window mode carbon elemental map was taken over the same area (Figure 5-55 (f)) and converted to a hybridisation map (Figure 5-55 (g)). This map shows regions of clear differences in hybridisation, indicated by the different colours of the pixels in these areas. The areas of predominantly dark blue pixels correspond to the nanodiamonds seen in the SEM image (Figure 5-55 (a)), while the areas of predominantly red and yellow correspond to the DLC film. These colours indicate that the DLC film is composed of a mixture of sp^2 and sp^3 hybridised carbon, but with a higher sp^2 content, while the nanodiamonds are mostly composed of sp^3 hybridised carbon, with small amounts of sp^2 carbon, particularly around the edges of the clusters.

The samples of nanodiamonds on DLC have different hybridisations for the different materials, and the hybridisation mapping technique has been able to reliably distinguish between the two materials on the same sample. These results provide further validation for the usefulness of the hybridisation mapping technique, especially in determining differences when there is a thin layer of one hybridisation on top of the other.
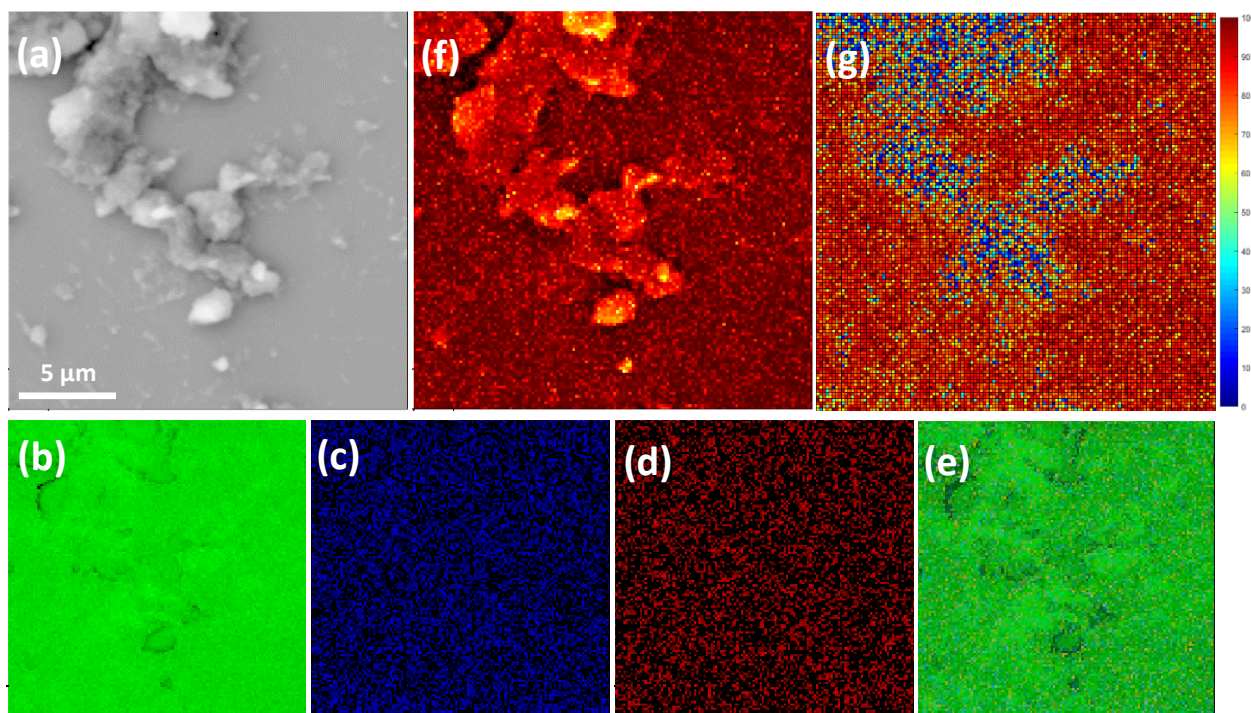
Figure 5-55: (a) SEM image of nanodiamonds on DLC film (FOV 20 μm), (b) 3 point carbon map, (c) 3 point oxygen map, (d) 3 point silicon map, (e) RGB overlay of (b), (c) and (d), (f) window mode carbon map, and (g) hybridisation map.

5.3.5.3 Nanodiamonds on Carbon Tape

To provide one more level of contrast to examine with the carbon hybridisation mapping technique nanodiamonds were also deposited on carbon tape, which should provide a slightly different background hybridisation to the DLC film. In this case the nanodiamonds are simply scattered across a piece of carbon tape that is mounted on silicon and can then be mounted for characterisation using SAM.

A sample of nanodiamonds on carbon tape was characterised with SAM, beginning with the SEM image shown in Figure 5-56 (a) which shows various sized clusters of nanodiamonds on the carbon tape substrate. Three-point elemental maps of this area were acquired for carbon (green), oxygen (blue), and silicon (red), shown in Figure 5-56 (b), (c), and (d), respectively. These maps, together with the RGB overlay in Figure 5-56 (e), indicate a surface that is predominantly carbon, with small amounts of oxygen present across the surface. The amount of silicon detected in the adhesive of the carbon tape is low.

The window mode carbon map and the resultant hybridisation map are shown in Figure 5-56 (f) and (g), respectively. The nanodiamonds are shown in the hybridisation map as areas of blue pixels, with some green and yellow pixels mixed in, while the surrounding area of the carbon tape shows a range

230
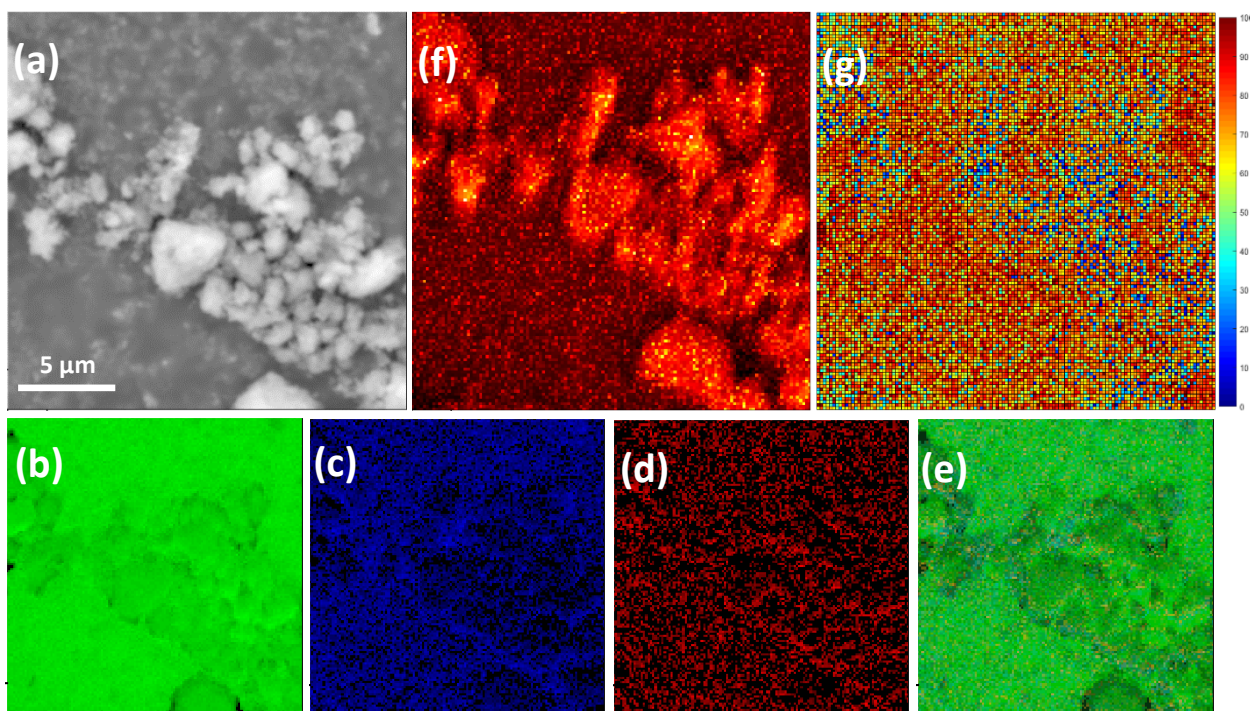
Figure 5-56: (a) SEM image of nanodiamonds on carbon tape (FOV 20 μm), (b) 3 point carbon map, (c) 3 point oxygen map, (d) 3 point silicon map, (e) RGB overlay of (b), (c) and (d), (f) window mode carbon map, and (g) hybridisation map.

of colours from blue through to red. This indicates that the nanodiamonds are mostly composed of sp^3 hybridised carbon, as is expected, while the carbon tape displays a mixture of hybridisations, as has been shown previously. The hybridisation mapping technique is thus able to distinguish areas of higher sp^3 content even when the surrounding areas also contain a large sp^3 fraction.

The spectra extracted from regions of the carbon elemental map in Figure 5-56 (f) corresponding to the nanodiamonds and carbon tape areas in Figure 5-56 (a) are shown in Figure 5-57. The shape of the red and blue lines in Figure 5-57 are quite similar, with the main difference being in the shape of the peak at the maximum. This difference produces D parameter values of 20.8 eV and 15.8 eV for the red and blue lines, respectively, and the spectra are representative of those found across the map in their respective areas. The similarity in these peaks makes differentiating between the regions of nanodiamonds and carbon tape more difficult than was observed for the previous samples of nanodiamonds on HOPG and DLC, however the differences are still significant and indicate a difference in hybridisation.

A second sample of nanodiamonds on carbon tape is examined in Figure 5-58 to test the reproducibility of the hybridisation mapping technique. The SEM image shows nanodiamond clusters of varying sizes on the carbon tape substrate, with some areas in the centre of the SEM
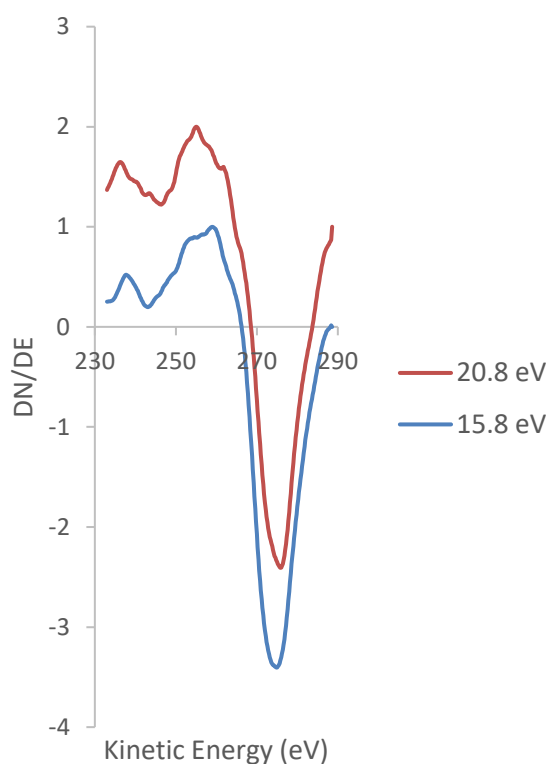
Figure 5-57: Spectra extracted from pixels of the carbon elemental map in Figure 5-56 showing examples of the peak shapes exhibited in this map that have different D parameter values, leading to the different coloured pixels in the corresponding hybridisation map.

image being difficult to distinguish between the two types of carbon visually. The three-point carbon (green), oxygen (blue), and silicon (red) elemental maps and the RGB overlay are shown in Figure 5-58 (b), (c), (d), and (e), respectively. These maps show a surface that is mostly carbon, with some
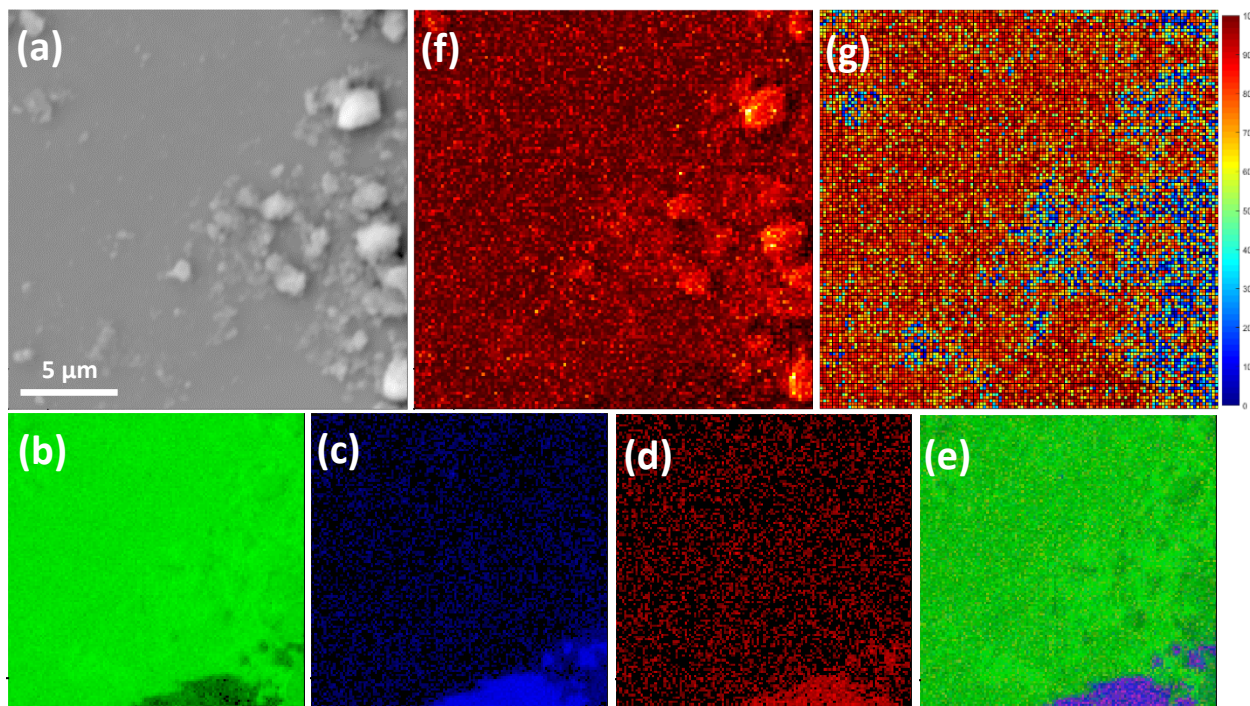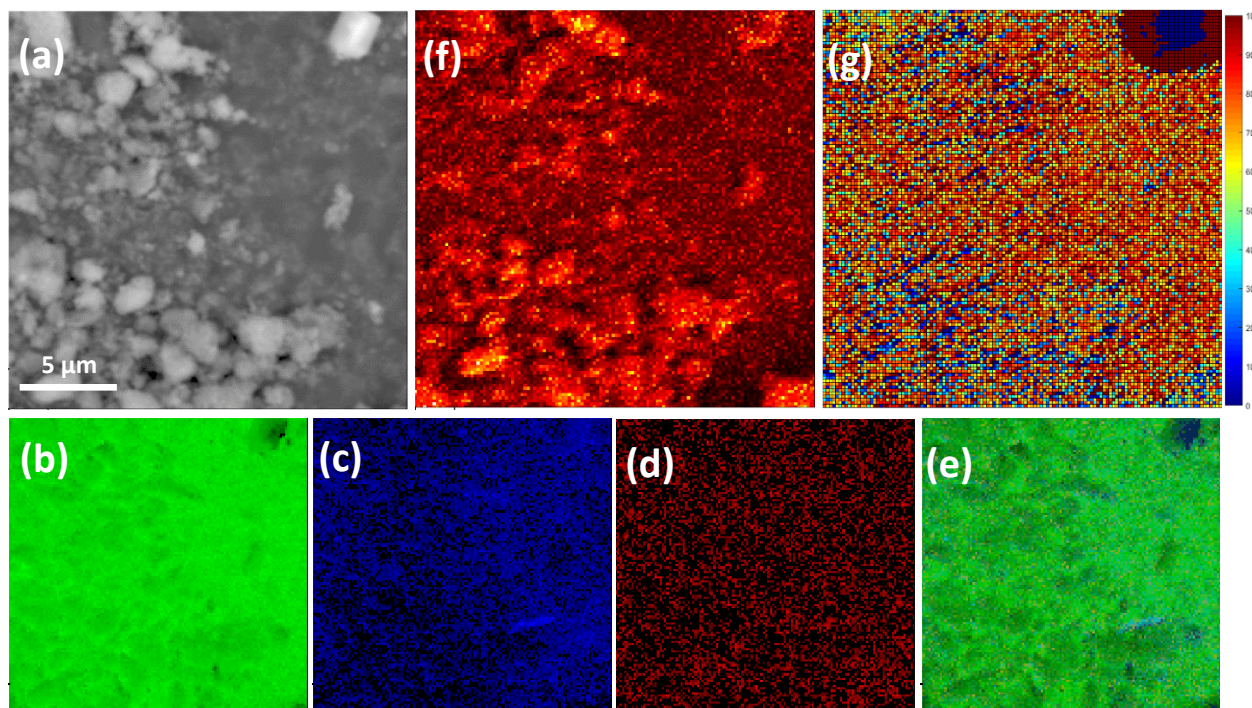

Figure 5-58: (a) SEM image of nanodiamonds on carbon tape (FOV 20 μm), (b) 3 point carbon map, (c) 3 point oxygen map, (d) 3 point silicon map, (e) RGB overlay of (b), (c) and (d), (f) window mode carbon map, and (g) hybridisation map.

oxygen present particularly on the areas corresponding to the carbon tape.

The window mode carbon map (Figure 5-58 (f)) was acquired over this area and converted to a hybridisation map (Figure 5-58 (g)). The hybridisation map shows that the areas corresponding to the nanodiamonds in the SEM image (Figure 5-58 (a)) appearing mostly dark and light blue, with some green and yellow pixels interspersed, while the surrounding carbon tape shows a mixture of colours from blue to red. This indicates that the nanodiamonds are primarily sp^3 hybridised, while the carbon tape shows a mix of hybridisations, which matches with previous results. However, there is one additional feature of interest in this hybridisation map. In the upper right corner there is a cluster of dark blue pixels surrounded by an area of dark red pixels. This indicates that the sp^2 scale, and therefore the D parameter scale, has been exceeded in both directions in this area. This has been observed to occur in regions where the sample is charging, which disrupts the shape of the carbon peak and therefore influences the magnitude of the D parameter. This area corresponds to the bright white area in the SEM image, which appears to be charging, but is slightly larger than the cluster appears in the SEM image, suggesting that the charging of the cluster is influencing the area around it. However, beyond this area the hybridisation map appears as expected, showing that although some areas in a map may be disrupted if there is an irregularity in the sample, the surrounding area can still be mapped and the hybridisations determined accurately.

Spectra from the carbon elemental map (Figure 5-58 (f)) in the area that appears to be charging in the SEM image in Figure 5-58 (a) were extracted and are shown in Figure 5-59 to determine why the hybridisation map exceeds the maximum and minimum sp^2 hybridisation on the scale in this area. Lines from areas corresponding to the dark blue and dark red areas in the hybridisation map are shown in blue and red, respectively, and have D parameter values of 7.0 eV and 29.4 eV. However, it can be seen from Figure 5-59 that these spectra are nonsensical and look nothing like the usual carbon peak. This unusual shape is due to the sample charging at the positions where these spectra were acquired, which results in the inability to record true spectra at these points.

Nanodiamonds have been deposited onto three different substrates, namely HOPG, DLC, and carbon tape, which have varying sp^2 hybridised carbon percentages. The carbon hybridisation mapping technique has been able to clearly identify the regions of the sample that are nanodiamonds and those that are substrate, even when the substrate has a high proportion of sp^3 hybridised carbon. The identification of different regions in this sample shows the effectiveness of the hybridisation mapping technique, and the reproducibility has also been established, showing
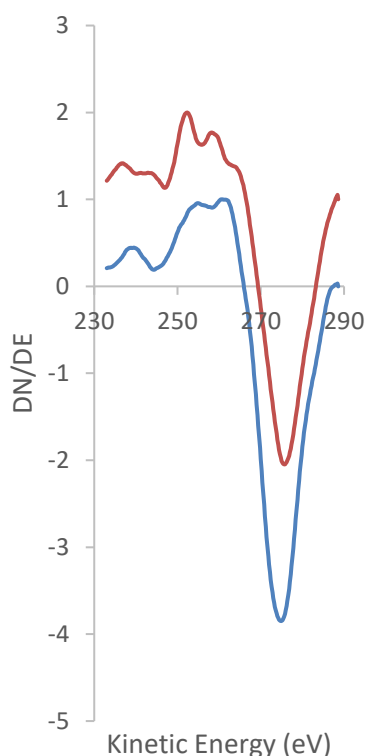
233

Figure 5-59: Spectra extracted from pixels of the carbon elemental map in Figure 5-58 showing examples of the peak shapes exhibited in this map that have different D parameter values, leading to the different coloured pixels in the corresponding hybridisation map.

that this technique is a valuable tool for the identification of carbon hybridisation with high spatial resolution.

5.3.6 Piranha Solution Treated Nanodiamonds

Nanodiamonds treated with piranha solution were also examined using the carbon hybridisation mapping technique. These nanodiamonds were obtained from Nick Adamson from the Department of Chemical Engineering at the University of Melbourne, who performed a treatment of piranha solution on the nanodiamonds. The treatment applied was a solution containing H_2SO_4 (conc.) and H_2O_2 (30 %) in a ratio of 4:1 v/v at a concentration of 5 mg.mL^{-1}. The nanodiamonds were treated in this solution at 65 °C for 4.5 hours, stirring every 0.5 hours, before the solution was diluted in approximately 500 mL of water and filtered under vacuum filtration through a polyvinylidene fluoride membrane (0.2 µm pore size) and washed twice with high purity water and dried under vacuum. To examine any difference these treated nanodiamonds may have from the untreated nanodiamonds they were deposited on the same substrates using the same methods.

5.3.6.1 Piranha Solution Treated Nanodiamonds on Highly Oriented Pyrolytic Graphite

A sample of piranha solution treated nanodiamonds deposited on a HOPG substrate is shown in Figure 5-60. The SEM image (Figure 5-60 (a)) shows clusters of nanodiamonds of varying sizes, with larger clusters appearing in the upper right of the image, and smaller clusters across the lower half of the image. Carbon (green) and oxygen (blue) three-point elemental maps are shown in Figure

5-60 (b) and (c), respectively, along with the RGB overlay in Figure 5-60 (d). The carbon can be seen to be the dominant species across the entire species, with the oxygen becoming slightly more intense in the areas corresponding to the piranha treated nanodiamonds.

The window mode carbon elemental map and resultant hybridisation map of this area are shown in Figure 5-60 (e) and (f), respectively. The hybridisation map shows distinct differences across the surface, with areas of almost completely red pixels, which correspond with the areas of HOPG in the SEM image, and areas of mostly dark blue pixels with light blue, green, and yellow interspersed that correspond to the areas of piranha treated nanodiamonds on the sample surface. The red areas indicate sp^2 hybridised carbon, which is expected for HOPG, while the blue areas indicate sp^3 hybridised carbon. The colours present in the piranha treated nanodiamond areas indicate sp^3 hybridised carbon, and are the same as those seen for the untreated nanodiamonds in Figure 5-50. This suggests that the piranha treatment of the nanodiamonds has not significantly altered the hybridisation of the carbon present.

A previous study on piranha solution treated nanocrystalline diamond has shown that there is very little change in the extent of oxidation measured by XPS after exposure to piranha solution at 373 K

Figure 5-60: (a) SEM image of piranha solution treated nanodiamonds on HOPG (FOV 20 μm), (b) 3 point carbon map, (c) 3 point oxygen map, (d) RGB overlay of (b) and (c), (e) window mode carbon map, and (f) hybridisation map.

for 5 hours [244]. Similarly, the hybridisation of the nanodiamonds was determined by deconvolution of the high resolution XPS C 1*s* peak and was found to be very similar for untreated and treated nanodiamonds [244]. However, a separate study has shown that nanocrystalline diamond under almost identical treatment conditions experienced an increase in oxygen content [245]. The changes in hybridisation of the nanodiamonds was not determined in this study [245], however the difference between these two studies indicates that some other factor, for example the morphology of the nanodiamond, may be influencing the extent of oxidation on the surface.

Spectra were extracted from the carbon elemental map in Figure 5-60 (e) from areas that correspond with both the piranha solution treated nanodiamonds and HOPG shown in Figure 5-60 (a). These spectra are shown in Figure 5-61.

The red line in Figure 5-61 was extracted from an area of HOPG and has a D parameter of 22.8 eV.
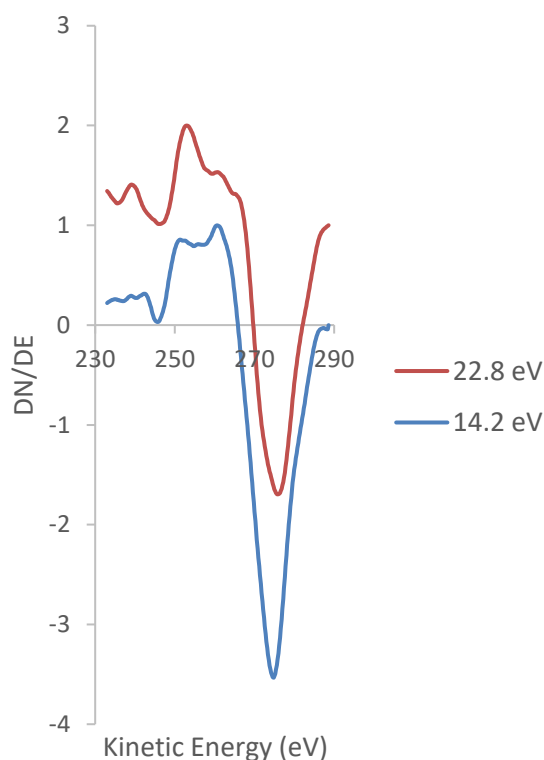
Figure 5-61: Spectra extracted from pixels of the carbon elemental map in Figure 5-60 showing examples of the peak shapes exhibited in this map that have different D parameter values, leading to the different coloured pixels in the corresponding hybridisation map.

This peak has the shape that was expected based on previous examination of HOPG, and is representative of the spectra from across the HOPG areas of this sample. The blue line was extracted from the treated nanodiamond area, and shows difference in the fine structure as well as the positions of the maximum and minimum, leading to a D parameter value of 14.2 eV. This peak is representative of spectra from across the treated nanodiamond areas, and is also very similar to the peaks observed previously for untreated nanodiamonds, indicating that the piranha solution treatment has not significantly altered the hybridisation of the nanodiamonds.

A second sample of piranha solution treated nanodiamonds on HOPG is shown in Figure 5-62. The SEM image in Figure 5-62 (a) shows quite large clusters of the treated nanodiamonds grouped together across the centre of the image, plus several individual clusters. Carbon (green) and oxygen (blue) three-point elemental maps of this area are shown in Figure 5-62 (b) and (c), respectively. These maps, along with the RGB overlay in Figure 5-62 (d), show that carbon is the most dominant species across the surface. Oxygen is also present across the surface, but with a higher intensity in the areas corresponding to the piranha solution treated nanodiamonds.

The window mode carbon map and the resultant hybridisation map of this area are shown in Figure 26 (e) and (f), respectively. The areas in this map that correspond to the piranha treated nanodiamonds in the SEM image Figure 5-62 (a)) appear mostly dark blue, with some light blue and green pixels interspersed, indicating that these areas are mostly sp^3 hybridised carbon. The surrounding areas, expected to be HOPG, are mostly red pixels, with several yellow pixels, indicating a highly sp^2 hybridised surface.

Several examples of samples composed of piranha solution treated nanodiamonds on HOPG have been examined with the hybridisation mapping technique, which has reliably distinguished the

Figure 5-62: (a) SEM image of piranha solution treated nanodiamonds on HOPG (FOV 20 μm), (b) 3 point carbon map, (c) 3 point oxygen map, (d) RGB overlay of (b) and (c), (e) window mode carbon map, and (f) hybridisation map.

areas of different hybridisation with high spatial resolution, providing further evidence for the reproducibility of the technique.

5.3.6.2 Piranha Solution Treated Nanodiamonds on Diamond-Like Carbon

The piranha solution treated nanodiamonds were also deposited on a DLC film, with the SEM image in Figure 5-63 (a) showing variously sized clusters of nanodiamonds scattered across the DLC surface, as well as several areas that appear to have a thin covering of smaller nanodiamond particles. Once again, three point elemental maps of carbon (green), oxygen (blue), and silicon (red) are acquired over the area shown in the SEM (Figure 5-63 (b), (c), and (d)). Carbon appears to be the dominant species across most of the surface, however the oxygen intensity is higher in the areas corresponding to the nanodiamonds in the SEM image (Figure 5-63 (a)). The RGB overlay of these three maps is shown in Figure 5-63 (e), and shows this trend more clearly, as well as indicating that the amount of silicon present is extremely low, confirming that the DLC film is a complete film that is thicker than 5 nm.

The window mode carbon elemental map and corresponding hybridisation map over this area are shown in Figure 5-63 (f) and (g), respectively. The hybridisation map shows areas corresponding to the nanodiamonds in the SEM image to be mostly blue and green, indicating that the piranha
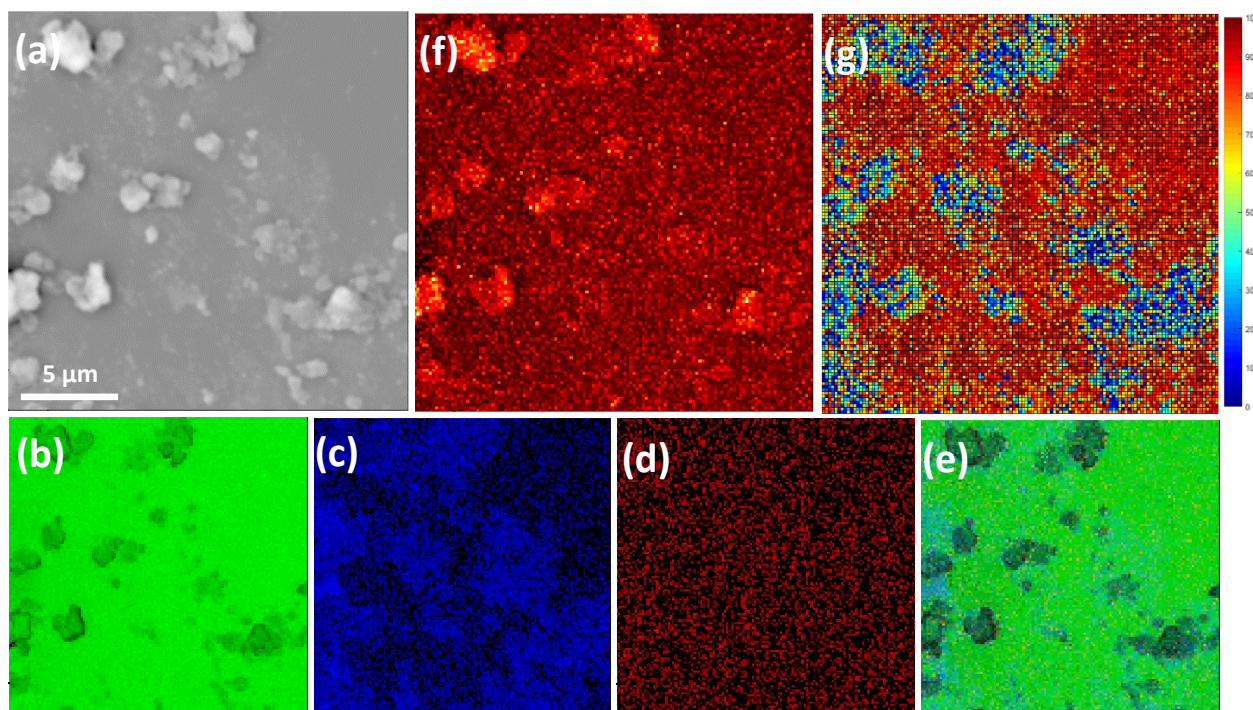
Figure 5-63: (a) SEM image of piranha solution treated nanodiamonds on DLC film (FOV 20 µm), (b) 3 point carbon map, (c) 3 point oxygen map, (d) 3 point silicon map, (e) RGB overlay of (b), (c) and (d), (f) window mode carbon map, and (g) hybridisation map.

treated nanodiamonds are highly *sp*³ hybridised, and the surrounding areas appearing mostly *sp*²

hybridised, which matches the results from the DLC films examined previously (Figure 5-43). There

is, however, some difference in the hybridisations of these piranha treated nanodiamonds to those

examined previously on a HOPG substrate. The piranha treated nanodiamonds here appear to have

a higher *sp*² hybridised carbon percentage, as shown by the higher prevalence of light blue and

green pixels. The reason for this is unclear, but may be the result of the clustering of the

nanodiamonds during the piranha treatment. Before deposition the untreated nanodiamonds

appear to be a fine powder, while the piranha treated nanodiamonds were clumped in large groups

with diameters of 1-2 mm. While these clumps were easily broken apart when the samples were

prepared, it is possible that nanodiamonds at the edges of these clumps undergo larger changes

from the treatment than those in the centre of the clumps, hence there are treated nanodiamonds

present with different hybridisations.

Spectra extracted from the piranha solution treated nanodiamonds and DLC film in Figure 5-63 (f)

are shown in Figure 5-64 to compare the shape of the peaks in these areas. The differences in the

shape of the spectra can be observed in the positions of the maxima and minima, as well as changes

in the fine structure, resulting in D parameters of 14.8 eV and 23.0 eV for the blue and red lines,

respectively. These peaks are very similar to those observed previously for both DLC and treated
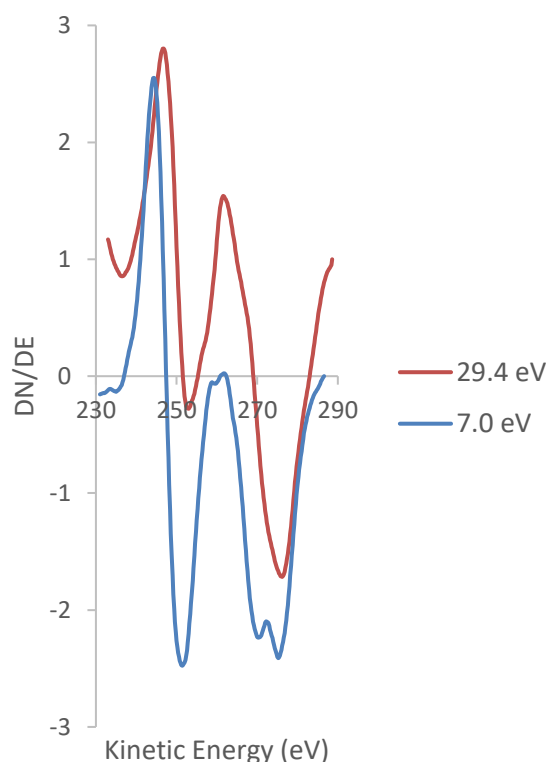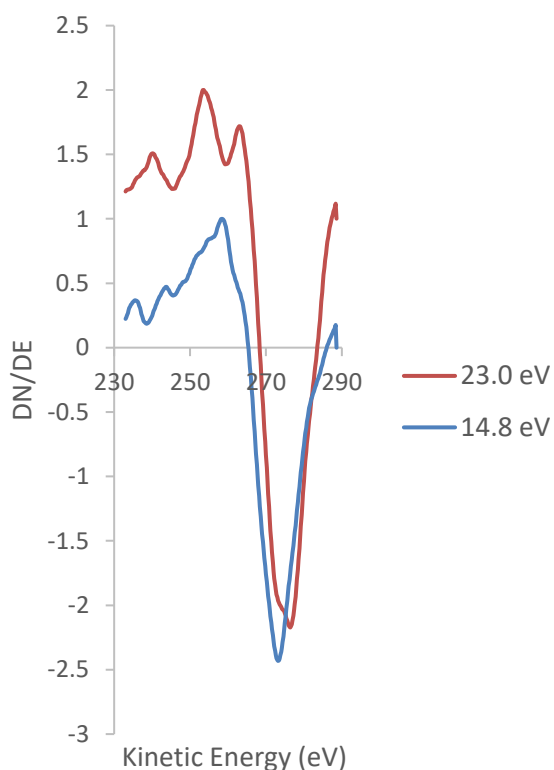

Figure 5-64: Spectra extracted from pixels of the carbon elemental map in Figure 5-63 showing examples of the peak shapes exhibited in this map that have different D parameter values, leading to the different coloured pixels in the corresponding hybridisation map.

nanodiamonds, and are representative of the peaks observed in similar areas across the map.

To further examine the consistency of the hybridisation mapping technique a second example of a sample of piranha treated nanodiamonds on a DLC film is shown in the 20 µm FOV SEM image in Figure 5-65 (a). This image shows small nanodiamond clusters of a range of sizes, as well as one very large cluster that appears to be charging significantly. Carbon, oxygen, and silicon three-point elemental maps are shown in Figure 49 (b), (c), and (d), respectively. Most of the surface shows an intense carbon presence, with the exception of the areas that are charging in the SEM image, which shows very little signal. The oxygen and silicon maps show quite low intensities across the sample, although there are small areas of high oxygen intensity at the edges of the charging features. The same trends are observed in the RGB overlay in Figure 5-65 (e), which confirms that carbon is the dominant element across the surface.

The window mode carbon elemental map taken over the same area is shown in Figure 5-65 (f), and was converted to a hybridisation map which is shown in Figure 5-65 (g). This hybridisation map shows areas that correspond to the nanodiamonds and are composed of dark blue pixels, and the surrounding areas being mostly red or yellow, indicating sp^3 hybridised areas and sp^2 hybridised areas, respectively. However, the area corresponding to the large, charging cluster in the SEM image
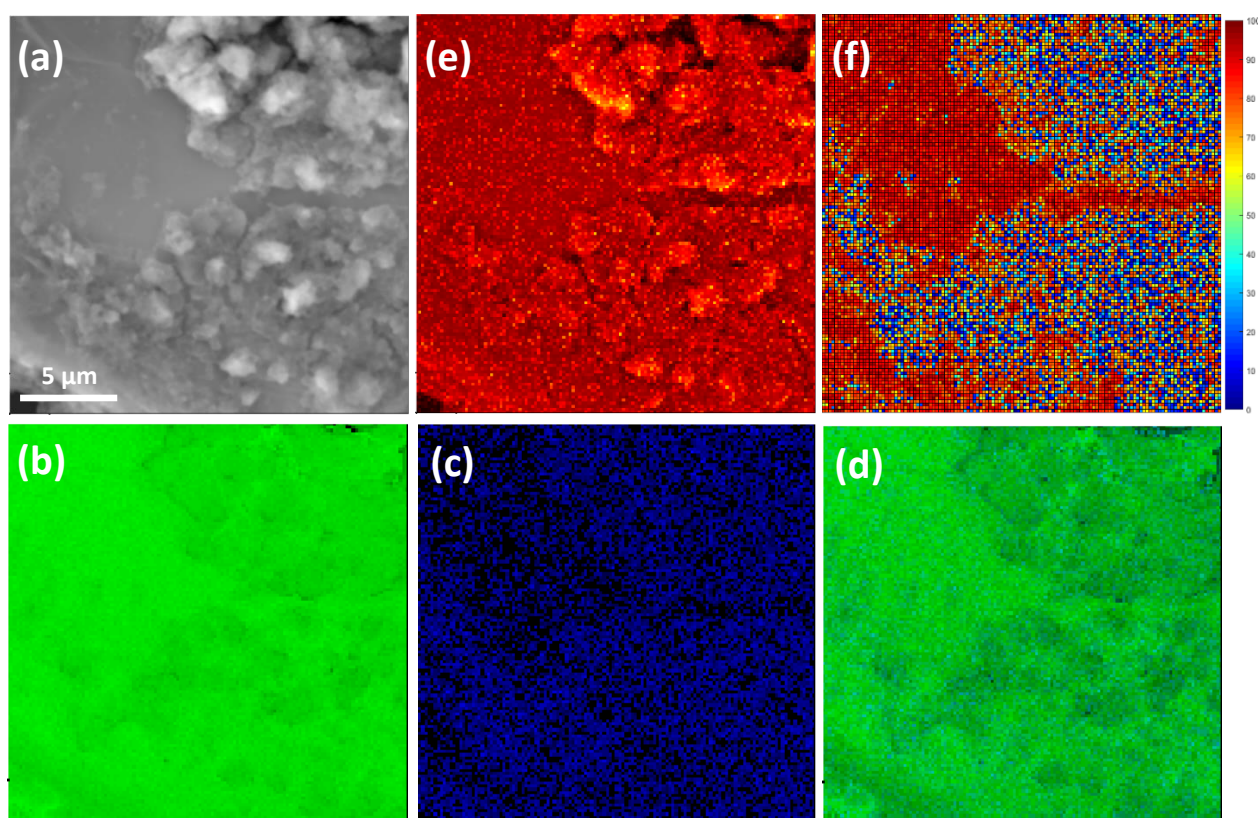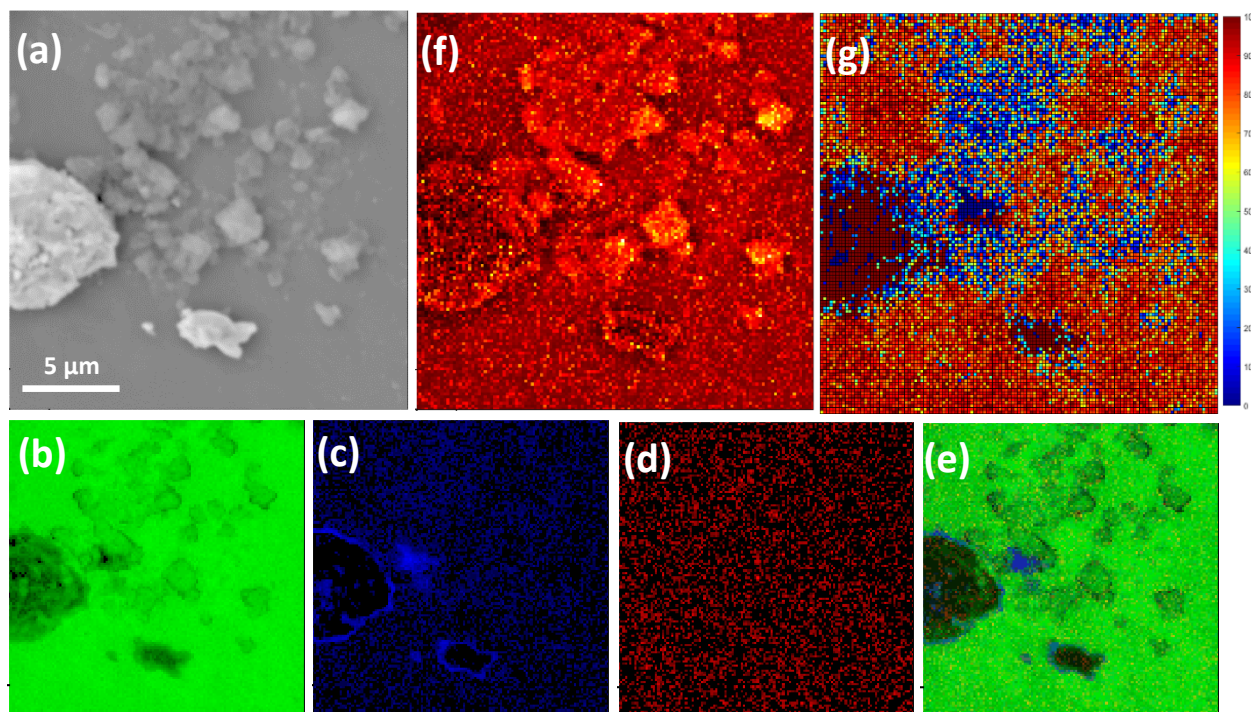

Figure 5-65: (a) SEM image of piranha solution treated nanodiamonds on DLC film (FOV 20 µm), (b) 3 point carbon map, (c) 3 point oxygen map, (d) 3 point silicon map, (e) RGB overlay of (b), (c) and (d), (f) window mode carbon map, and (g) hybridisation map.

appears to be almost completely dark red, with several pixels of dark blue interspersed, which is consistent with what has been seen previously with areas that are highly charged in the SEM. There are two other areas that also appear to be charging, however past the edges of these features the hybridisation map appears to be accurate, which provides evidence for the ability of this hybridisation mapping technique to work accurately even when the surface is less than ideal. The nanodiamonds in this sample appear more highly sp^3 hybridised than the previous sample in Figure 5-63. This supports the theory that the nanodiamonds have not been exposed to the piranha solution evenly, so that some of the piranha treated nanodiamonds have a higher sp^3 hybridised carbon content than others.

Spectra were extracted from the carbon elemental map (Figure 5-65 (f)) in the areas that correspond with the large charging area in Figure 5-65 (a), and are shown in Figure 5-66.
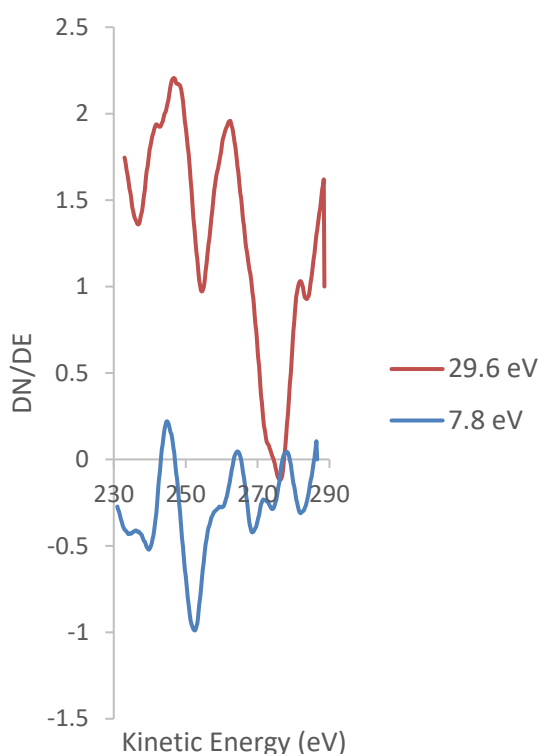
Figure 5-66: Spectra extracted from pixels of the carbon elemental map in Figure 5-65 showing examples of the peak shapes exhibited in this map that have different D parameter values, leading to the different coloured pixels in the corresponding hybridisation map.

The peaks from Figure 5-66 do not show the shape that is expected for a carbon peak, and instead show a shape that is indicative of a sample that is charging. These unusual spectra are the reason for the areas in the hybridisation map that appear to exceed the maximum and minimum of the sp^2 hybridised carbon percentage scale, and are consistent with spectra shown previously for an area that appears very similar in the SEM image and hybridisation map.

These samples of piranha treated nanodiamonds on DLC again show clear hybridisation differences

between the two types of carbon, providing further evidence for the validity of the carbon hybridisation mapping technique.

5.3.6.3 Piranha Solution Treated Nanodiamonds on Carbon Tape

In order to examine another level of contrast between different carbon materials the piranha treated nanodiamonds were also deposited on carbon tape and characterised using the carbon hybridisation mapping technique. The nanodiamonds were mounted on the carbon tape by scattering them across the surface and lightly pressing them down onto the adhesive.

The SEM image in Figure 5-67 (a) shows several clusters of nanodiamonds scattered across the top half of the image at a 20 μm FOV. In some areas of the SEM image it is difficult to determine whether some of the small particles are nanodiamonds or part of the carbon tape, which is itself quite textured. The carbon, oxygen, and silicon three-point elemental maps taken over the same area are shown in Figure 5-67 (b), (c), and (d), respectively. The carbon map shows a high intensity across most of the map, but some areas of lower intensity in some of the regions of the nanodiamonds, while the oxygen map shows the reverse trend and the silicon has very low intensity across the whole area. These results are also clear in the RGB overlay of the three elemental maps, as shown in in Figure 5-67 (e).
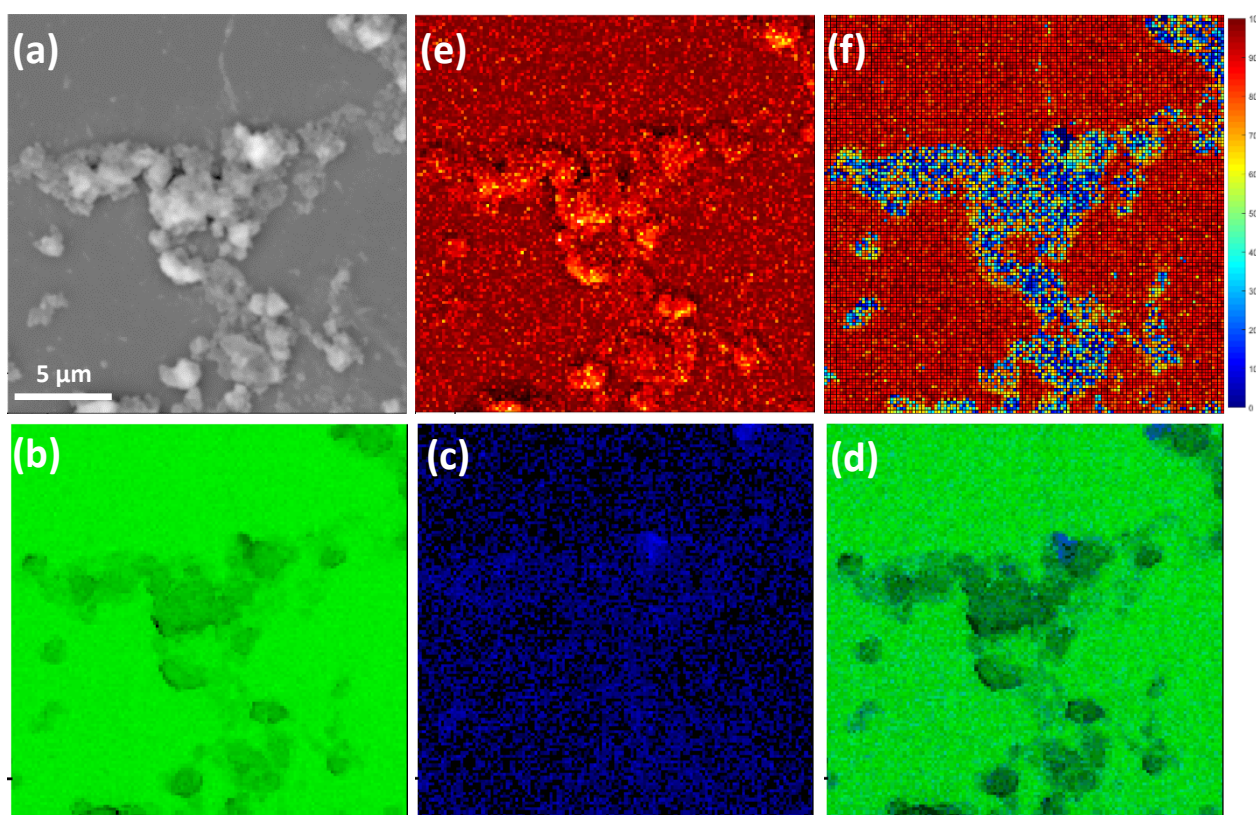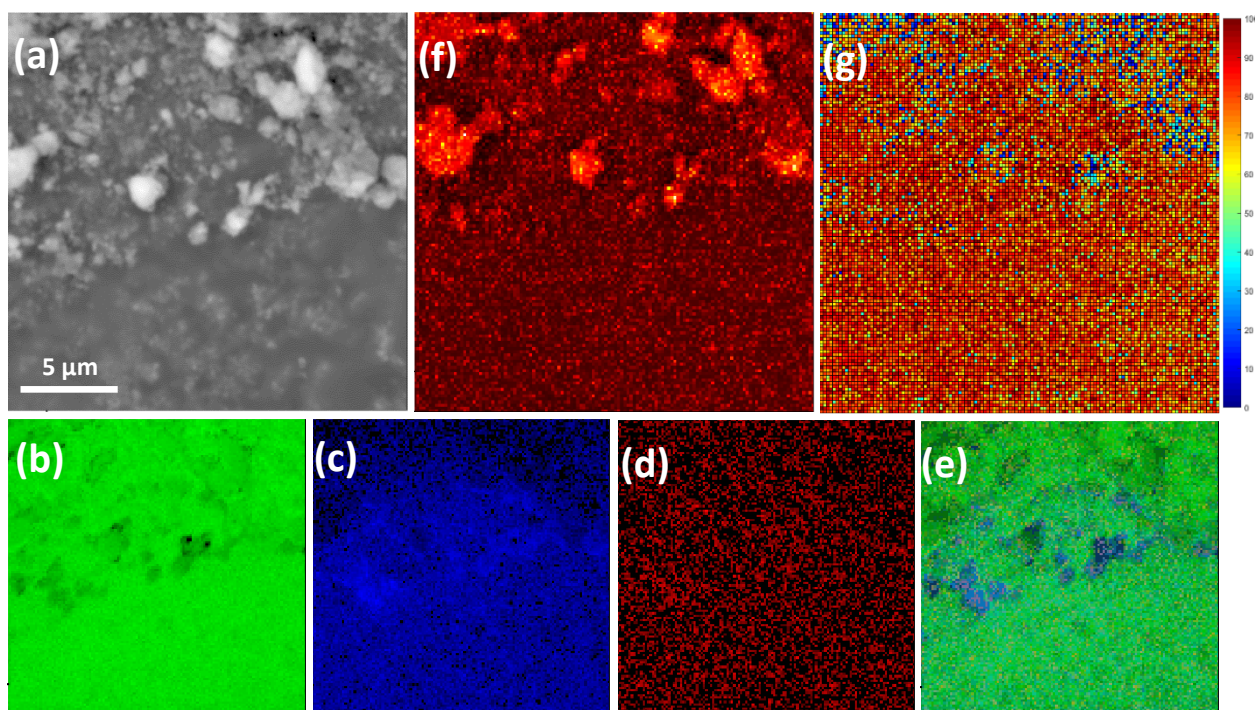

Figure 5-67: (a) SEM image of piranha solution treated nanodiamonds on carbon tape (FOV 20 μm), (b) 3 point carbon map, (c) 3 point oxygen map, (d) 3 point silicon map, (e) RGB overlay of (b), (c) and (d), (f) window mode carbon map, and (g) hybridisation map.

A window mode carbon elemental map was also acquired over the same area (Figure 5-67 (f)), and was converted to a hybridisation map (Figure 5-67 (g)). The hybridisation map does show some differences between the areas in the SEM that appear to be nanodiamond clusters and the area that is the carbon tape. The differences are less distinct in this map due to the higher sp^3 hybridised carbon content in the carbon tape compared to the HOPG of DLC, but they are still visible. The areas that correspond to the nanodiamonds show a mixture of blue, green, and yellow pixels, indicating that these areas are mostly sp^3 hybridised, while the surrounding areas that correspond to the carbon tape are a mixture of red, yellow, and green pixels, indicating a surface that is mostly sp^2 hybridised, as was expected from carbon tape.

Spectra were extracted from areas of the carbon elemental map (Figure 5-67 (f)) that correlate with the piranha solution treated nanodiamonds and carbon tape areas in Figure 5-67 (a), and are shown in Figure 5-68 to examine the differences in the peak shape.
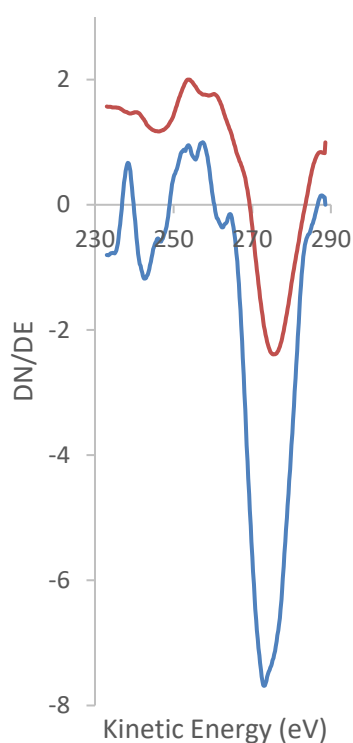
Figure 5-68: Spectra extracted from pixels of the carbon elemental map in Figure 5-67 showing examples of the peak shapes exhibited in this map that have different D parameter values, leading to the different coloured pixels in the corresponding hybridisation map.

The red line in Figure 5-68 indicates the spectrum extracted from a carbon tape area, and has a D parameter of 23.2 eV. The blue line has different positions for the maxima and minima, as well as different fine structure, and presents a D parameter value of 14.6 eV. These peaks are representative of the areas from which they were extracted in the map, and are consistent with the peaks shown previously for carbon tape and nanodiamond samples.

Piranha solution treated nanodiamonds deposited on three substrates with varying sp^2 hybridised

carbon percentages have been successfully imaged using the carbon hybridisation mapping technique, with clear differences observed between the nanodiamonds and the HOPG, DLC, and carbon tape. These samples have shown evidence for the reproducibility and reliability of the hybridisation mapping technique and its ability to produce maps showing the hybridisation of multiple materials within the same surface.

5.4 Conclusions

This chapter has shown the development of a carbon hybridisation mapping technique, including the optimisation of scanning parameters used to acquire data. These parameter include step width, time per step, and number of scans averaged, all of which influence the signal to noise ratio of the data and therefore the resultant hybridisation maps. The parameter values found to be the best choice to acquire high quality data with a reasonable acquisition time were a step width of 0.2 eV, a time per step of 0.5 ms, and 20 scans averaged. A dependence of the peak shape, and therefore the sp^2 hybridised carbon percentage, on the level of magnification at which they were acquired was observed, and was found to be an artefact of the way the instrument collects data that cannot be controlled by the user.

The carbon hybridisation mapping technique described in this chapter has been successfully applied to a range of samples, including both standards and surfaces with varying carbon hybridisations. HOPG, DLC, and carbon tape were examined, and it was observed that the materials with higher sp^3 hybridised carbon content experience some electron beam induced graphitisation. Samples with different patterns of carbon hybridisations, including graphene flakes deposited on carbon tape and nanodiamonds deposited on several substrates, were successfully characterised with the hybridisation mapping technique and differences in the hybridisations on the sample were clearly visible. This result was achieved with a high level of reproducibility for all samples examined, and provides evidence for the ability of this technique to accurately determine the hybridisation of a carbon material with high spatial resolution.

6 CARBON HYBRIDISATION LINE SCANS

The importance of characterising the hybridisations present in a carbon-based structure with spatial resolution has already been established, with a technique for the production of a carbon hybridisation map having been developed in the previous chapter. However, as in any spectroscopy, the scanning parameters must be optimised to collect the highest quality data in a reasonable timeframe. The hybridisation maps shown previously are extremely useful to examine how the hybridisation changes across features on a sample surface, but the time required to obtain them is large, and maps larger than 128x128 pixels are not able to be collected in a reasonable time as a doubling of the spatial resolution results in a four-fold increase in the acquisition time. If resolution higher than 128 pixels is required an alternative can be achieved in the form of a line scan. By acquiring a line scan (or several line scans) across a feature a much higher spatial resolution can be achieved in a shorter acquisition time, with the compromise that this high resolution is only achieved in one dimension.

6.1 Development of Carbon Hybridisation Line Scanning Technique

The creation of these hybridisation line scans involves two steps: line scan acquisition and data processing in MATLAB. The process is simpler than that for the hybridisation maps as the data can be extracted from MultiPak in a form that can directly imported into MATLAB without needing to be processed in CasaXPS first. The code written in MATLAB then allows for the carbon line scans to be converted to carbon hybridisation scans. These processes are detailed in this chapter.

The acquisition requirements of carbon line scans for the creation of a hybridisation line scan are similar to those needed for a hybridisation map. Line scans of the carbon peak are acquired in 'window' mode, where each point on the line contains an entire spectrum of the carbon (KVV) peak. This allows for the smoothing and differentiation of the peak to be performed at each point along the line, enabling the D parameter to be calculated for that point. This results in an increased acquisition time over a 'two-point' or 'three-point' elemental line scan, which only measure a maximum and one or two minima at each point to calculate the peak intensity and find relative atomic concentrations. This high acquisition time means that some sacrifices need to be made in terms of the signal to noise ratio of the data, and the scanning parameters must be optimised to find the best compromise between these two needs. This optimisation process is discussed in further detail in section 6.2.

As the elemental line scan technique from the Scanning Auger Nanoprobe is not designed to undergo the processing necessary to produce a hybridisation line scan the data is acquired using the instruments SmartSoft software and then further processed using MATLAB, in a similar way to that done for the hybridisation mapping in the previous chapter.

Each sample examined in this chapter was characterised and analysed following the same procedure, which begins with locating a region of interest using the in-situ SEM and acquiring a SEM image of the area. The location of the line(s) over which the line scans will be taken is set, and an elemental line scan of the elements of interest is acquired using the window mode line scans. For the samples in this chapter the elements of interest are carbon, oxygen, and silicon, and the atomic percentages of each of these elements across the line scan is determined using MultiPak. A higher resolution window mode carbon elemental line scan is then acquired over the same line(s) and is processed according to the methods outlined in sections 6.1.1 and 6.1.2.

6.1.1   Data Preparation

The data preparation for the hybridisation line scans is a much simpler process than that for the hybridisation map. Once the 'window' mode line scan is acquired it can be opened in MultiPak, which will show both the line scan, which shows the intensity of the peak at each point, and the spectra from each point of the line scan as a stack plot. The spectra can be saved together as a .csv file, which is formatted such that the first column of the file is the x-values of the spectra (the kinetic energy values) and the following columns are the intensity values that form the spectra at each point of the line scan. This file can be opened in MATLAB, and the data imported in the same way as was done for the hybridisation maps in the previous chapter. The x-values column should be imported as a matrix and renamed as 'XValues', and the remainder of the columns imported as a second matrix and renamed as 'Line', as shown in Figure 6-1. The MATLAB code can then be run and a hybridisation line scan produced.
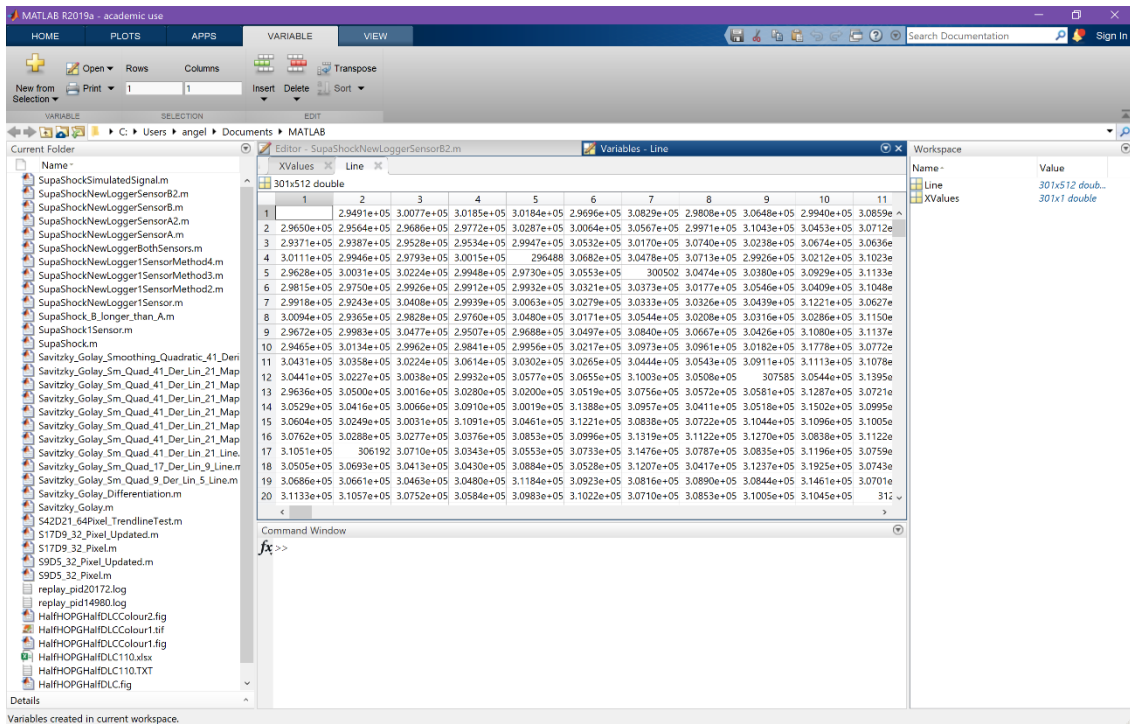
Figure 6-1: Line scan data imported into MATLAB as two separate variables: 'Line' and 'XValues'.

6.1.2   MATLAB Code

In the absence of user input to determine the spatial resolution there cannot be any single code created in MATLAB that can be used for the processing all possible line scans that the end-user could create if the x-axis is to be a measure of the scale of the line scan (equal to the FOV). This is due to the large number of combinations of FOV and point per scan numbers that could possibly be chosen, which will influence the position of the data points along the x-axis. However, by making simple modifications to the code the necessary changes can be made for any line scan. The MATLAB code used to create the hybridisation line scans in this chapter is given below, along with instructions for modifying the code for the FOV and point per scan number used in any given line scan.

```
%%Smoothing%%
%%Use the function sgolayfilt(Data,order,number of points)%%

SmQuadratic41 = sgolayfilt(Line,2,41);

%%Differentiation%%
for k = 11:288
    DerivativeLinear21(k,:) = (1/(770*0.2))*((-10*SmQuadratic41(k-
10,:))+(-9*SmQuadratic41(k-9,:))+(-8*SmQuadratic41(k-8,:))+(-
7*SmQuadratic41(k-7,:))+(-6*SmQuadratic41(k-6,:))+(-
5*SmQuadratic41(k-5,:))+(-4*SmQuadratic41(k-4,:))+(-
3*SmQuadratic41(k-3,:))+(-2*SmQuadratic41(k-2,:))+(-
1*SmQuadratic41(k-
1,:))+(0*SmQuadratic41(k,:))+(1*SmQuadratic41(k+1,:))+(2*SmQuadrat
```

247

```
ic41(k+2,:))+(3*SmQuadratic41(k+3,:))+(4*SmQuadratic41(k+4,:))+(5*
SmQuadratic41(k+5,:))+(6*SmQuadratic41(k+6,:))+(7*SmQuadratic41(k+
7,:))+(8*SmQuadratic41(k+8,:))+(9*SmQuadratic41(k+9,:))+(10*SmQuad
ratic41(k+10,:)));
end

%%Remove end x values to match Derivative Matrix Length%%
X = XValues(20:end-20,:);

%%Find Max and Min of Each Spectra%%
[MaxY,IndexMaxY] = max(DerivativeLinear21(20:end-20,:));
[MinY,IndexMinY] = min(DerivativeLinear21(20:end-20,:));

%%Find Corresponding X Values%%
XValuesSpectra = [X(IndexMaxY), X(IndexMinY)];

%%Create Matrix of D%%
DAll = XValuesSpectra(:,1) - XValuesSpectra(:,2);
D = DAll.';

%%Make D positive and Convert to sp2 percentage%%
DPositive = D.*-1;
Dminus12 = DPositive-12;
sp2 = Dminus12./0.12;

%%Create X-Axis for Plots to match scale of Line Scan%%
%%Set PointNo to be the number of points of the line scan%%
%%FieldOfView to be the scale of the field of view(units can be set
in the axis label)%%
PointNo = 512;
FieldOfView = 50;
XInterval = PointNo/FieldOfView;
XValuesLine = [1:1:PointNo]';
XValuesLineLength = XValuesLine./XInterval;

%%Create D parameter Line Scan Plot%%
figure
plot(XValuesLineLength,DPositive(:));

%%Create sp2 Line Scan Plot%%
figure
plot(XValuesLineLength,sp2(:));
```

The code will now be revisited and each section of the code examined in depth, and its purpose clarified. The first section of the above code is used to apply a 41-point Savitzky-Golay (SG) smoothing to the spectral data.

```
%%Smoothing%%
%%Use the function sgolayfilt(Data,order,number of points)%%

SmQuadratic41 = sgolayfilt(Line,2,41);
```

This is achieved using the 'sgolayfilt' function in MATLAB, which is written as

248

sgolayfilt(x,order,framelen), where x is the data to be smoothed, order is the polynomial order, and framelen is the number of points over which the smoothing is to be performed. The smoothing to be applied to this data uses a quadratic function, thus the order is 2, and framelen is set to 41 to perform the 41-point derivative. The data to be smoothed is the matrix 'Line', and the resultant smoothed data is labelled as 'SmQuadratic41'.

The next section of the code applies a 21-point Savitzky-Golay differentiation to the smoothed data 'SmQuadratic41'. To do this a 'for' loop is required. This loop has the form:

```
for index = values
    statements
end
```

The code for the 21-point SG differentiation the 'index = values' section of the 'for' loop takes the form k = initialValue:endValue, which will result in the statement being performed for the initial index value, then increment the index value by one and repeat the execution of the statement until the end value is completed.

```
%%Differentiation%%
for k = 11:288
    DerivativeLinear21(k,:) = (1/(770*0.2))*((-10*SmQuadratic41(k-
10,:))+(-9*SmQuadratic41(k-9,:))+(-8*SmQuadratic41(k-8,:))+(-
7*SmQuadratic41(k-7,:))+(-6*SmQuadratic41(k-6,:))+(-
5*SmQuadratic41(k-5,:))+(-4*SmQuadratic41(k-4,:))+(-
3*SmQuadratic41(k-3,:))+(-2*SmQuadratic41(k-2,:))+(-
1*SmQuadratic41(k-
1,:))+(0*SmQuadratic41(k,:))+(1*SmQuadratic41(k+1,:))+(2*SmQuadrat
ic41(k+2,:))+(3*SmQuadratic41(k+3,:))+(4*SmQuadratic41(k+4,:))+(5*
SmQuadratic41(k+5,:))+(6*SmQuadratic41(k+6,:))+(7*SmQuadratic41(k+
7,:))+(8*SmQuadratic41(k+8,:))+(9*SmQuadratic41(k+9,:))+(10*SmQuad
ratic41(k+10,:)));
End
```

The matrix 'SmQuadratic41' has 300 data points in each column, and the first data point to which a 21-point SG differentiation can be applied is the 11th point, as it requires 10 previous points to perform the calculation, thus the 'initialValue' is 11. By applying the same logic, the 'endValue' used in the code is 288. The statement used in this 'for' loop is the equation for the 21-point SG differentiation of the data, labelled 'DerivativeLinear21' to indicate that a linear form of the 21-point SG derivative is used. DerivativeLinear21(k,:) is used so that the statement is applied to every column for each 'k' value specified by the index. This causes the derivative formula to be applied sequentially to the columns of the matrix 'SmQuadratic21'. The result of this is 'DerivativeLinear21',

which is a matrix composed of the columns of the derivative from each column of 'SmQuadratic41', and thus shows a set of derivative spectra. This formula is followed by 'end' to close the loop. This data is now in the correct form for the D parameter, that is, the width between the maxima and minima of the differentiated peak, to be calculated and then to a sp^2 hybridised carbon percentage.

The next sections of the code find the maxima and minima values of each column in the matrix 'DerivativeLinear21', excluding the first and last 20 data points to negate the values ignored in the smoothing and derivative processes. These values from each column are stored in the matrices 'MaxY' and 'MinY', respectively.

```
%%Remove end x values to match Derivative Matrix Length%%
X = XValues(20:end-20,:);

%%Find Max and Min of Each Spectra%%
[MaxY,IndexMaxY] = max(DerivativeLinear21(20:end-20,:));
[MinY,IndexMinY] = min(DerivativeLinear21(20:end-20,:));

%%Find Corresponding X Values%%
XValuesSpectra = [X(IndexMaxY), X(IndexMinY)];

%%Create Matrix of D%%
DAll = XValuesSpectra(:,1) - XValuesSpectra(:,2);
D = DAll.';
```

The matrixes 'IndexMaxY' and 'IndexMinY' are also created, which contain the positions of the maximum and minimum values from each column. A new matrix 'XValuesSpectra' is then created, which applies the 'IndexMaxY' and 'IndexMinY' to the matrix 'X' to create a matrix with the x values corresponding to the maxima and minima. The parameter 'DAll' is a matrix of the D parameter and is obtained by extracting the larger of the x values(XValuesSpectra(:,2)) from the smaller((XValuesSpectra(:,1)), resulting in a column matrix of D values from all of the spectra. This column of data needs to be reformatted to a row matrix 'D' so that the calibration curve for converting from D parameter to sp² hybridisation percentage can be applied.

As the values of the D parameter in 'D' are negative, 'D' is multiplied by -1 to obtain 'DPositive', before the calibration curve is applied by subtracting 12 and dividing by 0.12 (the values from the calibration curve) to obtain the matrix 'sp2', which is a matrix of the sp^2 hybridised carbon percentage at each point of the carbon elemental line scan based on the width of the C(KLL) peak.

```
%%Make D positive and Convert to sp2 percentage%%
DPositive = D.*-1;
Dminus12 = DPositive-12;
sp2 = Dminus12./0.12;
```

The *sp*^{2} hybridised carbon percentage can now be plotted against the length of the line, however the length of the line, and the number of pixels within it, can change for each line scan. The next section of the code therefore needs to be edited to suit the scan parameters of each line scan.

```
%%Create X-Axis for Plots to match scale of Line Scan%%
%%Set PointNo to be the number of points of the line scan%%
%%FieldOfView to be the scale of the field of view(units can be set
in the axis label)%%
PointNo = 512;
FieldOfView = 50;
XInterval = PointNo/FieldOfView;
XValuesLine = [1:1:PointNo]';
XValuesLineLength = XValuesLine./XInterval;
```

The first parameter to be edited is 'PointNo', which is the number of points in the line scan. The second parameter is 'FOV', which is the field of view of the area analysed and therefore the length of the line scan. These numbers are then used to find the distance between each point in the line scan and create an x-axis against which the *sp*^{2} hybridised carbon percentages can be plotted.

The final two sections of the code create line scans in terms of the D parameter and the *sp*^{2} hybridised carbon percentage, that is, plots of D parameter or *sp*^{2} carbon content against the length of the line. This will now be of the same form as the original elemental line scan, with *sp*^{2} content instead of the peak intensity.

```
%%Create D parameter Line Scan Plot%%
figure
plot(XValuesLineLength,DPositive(:));

%%Create sp2 Line Scan Plot%%
figure
plot(XValuesLineLength,sp2(:));
```

When this process is complete the result is two line scans, the first a plot of D parameter against position, and the second a plot of *sp*^{2} hybridised carbon percentage against position.

6.2 Carbon Hybridisation Line Scanning Optimisation

Line scans of carbon hybridisation percentage have been produced for carbon samples of differing hybridisation composition using the method described above. These samples include standards that are ideally composed of one hybridisation to gain an understanding of how the hybridisation of a carbon material may vary across a surface even when the material should be of a consistent composition, such as Highly Oriented Pyrolytic Graphite (HOPG) and Diamond Like Carbon (DLC)

films. Carbon tape is often used as a substrate for mounting other carbon materials, therefore it is also examined individually so that it can be compared to these other materials. Once these simple samples were analysed more complicated samples with multiple hybridisations across a single surface were examined.

Before beginning characterisation of multiple hybridisation samples it is necessary to optimise the scan parameters for carbon in order to obtain the best resolution of hybridisation across the line scans with a reasonable scan acquisition time. This was done following the same procedures as for the hybridisation maps in the section 5.2. Samples of HOPG and DLC were examined to optimise the step width, time per step, and number of scans, and the results will be discussed here. The influence of the magnification level on the spectra and line scans is also investigated.

The width of the line scan is approximately 0.2 um, while the line spans across the entire width of the image, and therefore the length of the line is the same as the FOV of the SEM image. The lines can be acquired either vertically or horizontally, and multiple lines can be acquired over the same area simultaneously.

The data collection process for all hybridisation line scans begins with using the in-situ SEM to find a suitable area for characterisation. For the parameter optimisation process this area should be representative of the sample as a whole, that is, one that shows the same features (or lack thereof) as the majority of the sample. A line is then chosen within this area over which the scans will be acquired, which is displayed as a yellow line on the SEM image. An example is shown in Figure 6-2 (a), which shows a 20 μm FOV SEM image of a HOPG surface. The window mode carbon elemental line scan is then acquired, and results in a plot of intensity versus distance (um). The intensity is that of the maximum intensity of the carbon peak at that position along the line. An example of this carbon elemental line scan in shown in Figure 6-2 (b), and appears to show a surface with a large amount of variation in the carbon intensity. However, this intensity is a raw and arbitrary value, which must be contextualised with the other peaks and their sensitivity factors to provide useful information on the amount of carbon present at that point. While not quantitatively useful at this point, the carbon elemental line scan is included to show the data that is then converted into a carbon hybridisation line scan such as that shown in Figure 6-2 (c). The hybridisation line scan is a plot of sp^2 hybridised carbon percentage as a function of length (um), and displays the sp^2 hybridised carbon percentage determined using the method outlined in section 6.1.2 for each point of the original carbon elemental line scan.
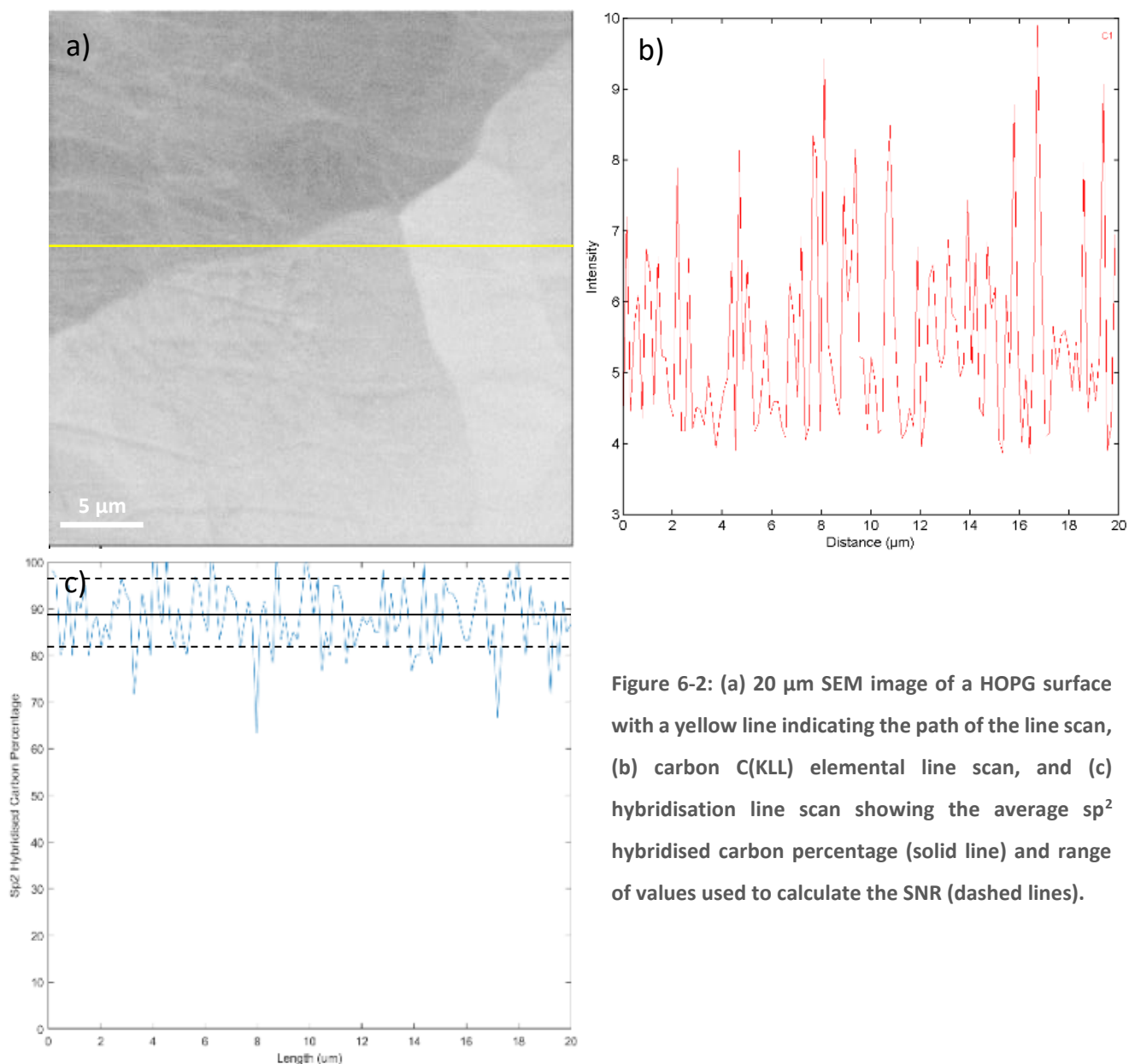
Figure 6-2: (a) 20 μm SEM image of a HOPG surface with a yellow line indicating the path of the line scan, (b) carbon C(KLL) elemental line scan, and (c) hybridisation line scan showing the average sp^2 hybridised carbon percentage (solid line) and range of values used to calculate the SNR (dashed lines).

The average hybridisation across the line and the spread of the hybridisation percentage values is expected to change when the line scan acquisition parameters are varied and the quality of the spectral data changes, so to help provide a quantitative description of the data a signal-to-noise ratio (SNR) is calculated for each hybridisation line scan. To calculate this value the average sp^2 hybridisation percentage value from the line scan is divided by the range in the data, which is determined by finding the highest and lowest values that are present across the line scan (while ignoring any outliers). For example, the solid line in Figure 6-2 (c) indicates the average sp^2 hybridised carbon percentage across the line while the two dashed lines indicate the highest and lowest values, that is, the range of the data. The SNR for the hybridisation line scan in Figure 6-2 (c)

is therefore calculated to be

$$SNR = \frac{89}{(97 - 82)} = 5.93$$

By comparing the SNR values from hybridisation line scans acquired over the same path across the sample with a variation in scanning parameters any changes in the consistency of the results obtained across the line can be numerically compared to help find the optimal acquisition parameters that provide high quality data in a reasonable timeframe. The SEM images, carbon elemental line scans, and hybridisation line scans for each sample examined in the optimisation process are presented in a table with the SNR values to allow for easy comparison of the differences that occur when scanning parameters are varied.

6.2.1   Repeated Scans

In order to determine the impact of changing the scanning parameters for the carbon elemental line scans on the spectra, and therefore on the resultant hybridisation line scans, it is desirable to acquire each line scan in the same place on the sample. This would mean that any changes observed would be the result of changes in the scan parameters rather than any differences that may occur in different areas of the sample. However, there is a possibility that when the first line scan is taken there may be electron beam induced changes to the sample, which will change the results. To determine if this is occurring several scans were taken over the same line sequentially for both HOPG and DLC films.

6.2.1.1 Repeated Scans – HOPG

To investigate the effect of electron beam induced damage on the surface of HOPG four carbon elemental line scans were acquired sequentially over the same line, with the line scans presented and SNR ratios calculated in the way described in section 6.2. The SEM image (20 μm FOV) in Figure 6-3 shows the HOPG surface over which the repeated scans tests were performed. Inspection of the image shows a textured surface, with slightly lighter and darker areas streaked across the surface indicating that the top graphene sheet appears to be wrinkled. The yellow line in the SEM image shows the line across which the line scans were taken and spans an area of the HOPG sample that is contains some of the wrinkles, but otherwise has no significant features. The window mode carbon elemental line scan acquired over the path of the yellow line in the SEM image shows the intensity of the carbon peak at each point along the 128 point line, with the distance along the line shown on the x-axis (Figure 6-3). The resultant hybridisation line scan is also shown in Figure 6-3,

along with the SNR value calculated for each line scan.

Scan Number	SEM	Carbon Elemental Line Scan	Hybridisation Line Scan	SNR
1				12.7
2				15.0
3				11.4
4				12.9

Figure 6-3: SEM images (20 μm FOV), C(KLL) elemental line scans, and hybridisation line scans of four line scans of HOPG taken sequentially in the same area.

The hybridisation line scan for the first scan in Figure 6-3 (sequential scan number 1) shows that the surface across the line analysed is quite uniform in the hybridisations present. The average sp^2 hybridised carbon percentage across the line is approximately 90 %, however the percentage varies between approximately 85 % to 95 % across the line. This trend is repeated for the second, third, and fourth of the sequential scan, although the precise percentages at each point vary slightly from

scan to scan. This suggests that while there were some small variations from scan to scan that are likely due to electron beam induced changes to the surface, there is no significant trend of increasing damage to the HOPG surface under continual exposure to the electron beam. The SNR for each of these hybridisation line scans does show some variation, and must therefore be considered further to understand how the data is influenced by electron beam induced damage.

By plotting the SNR for each sequential scan any trend in the variation within the data can be observed, as shown in Figure 6-4.
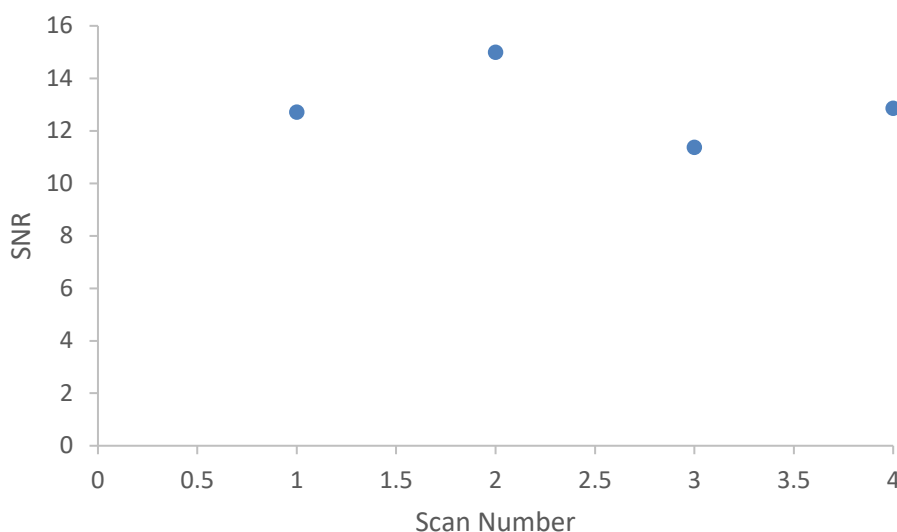
Figure 6-4: SNR for the four sequentially acquired hybridisation line scans on HOPG from Figure 6-3.

From Figure 6-4 it can be seen that while the SNR ratio changes when sequential scans were acquired over the same line they do not do so with any trend, with the final scan having almost exactly the same SNR as the first scan. In combination with the visual comparison of the hybridisation line scans these results suggest that repeating scans over the same line is not impacting the hybridisation of the surface, however some spectra were extracted from points of the carbon elemental line scan (Figure 6-3) to examine the spectral shape, these are shown in Figure 6-5.

The average differentiated spectrum from across the entire line scan for the sequentially acquired lines 1, 2, 3, and 4 from Figure 6-3 are shown in Figure 6-5 in blue, red, green, and purple, respectively. These spectra have been normalised to have a maximum intensity of 1 to allow for comparison of the magnitudes of the features of the spectra. The main feature of interest in these peaks is the position of the maxima and minima, which provides us with the D parameter values, and the signal to noise ratio, which impacts the ability to accurately determine the position of these

maxima and minima. The shape of the peak, evidenced by 'shoulders' present in the differentiated spectra, varies depending on the types of hybridisation present and the field of view (FOV) at which the scans are acquired, as has been discussed in sections 2.6.1 and 5.2.6. This fine structure does not impact on the D parameter calculation and therefore does not influence the sp^2 hybridised carbon percentage line scans and will not be discussed further in this chapter. The spectral shape and signal to noise ratio appears to be the same for each of these lines, and examination of the D parameter from each differentiated spectrum (Table 6-1) shows that the D parameter is 22.6 eV for each of the spectra, which indicates that there is no trend in changing hybridisation from electron beam induced changes to the surface. The uncertainty in the D parameter measurements is 0.2 eV at minimum, as this is the energy step width used to acquire the scans, however the peak shape of individual samples may make it more difficult to find a clearly defined maxima and minima position, in which case this uncertainty may be slightly larger.

The differentiated spectra extracted from three individual points across each line (points 32, 64, and 96 of 128) are also shown in Figure 6-5 for the sequentially acquired lines 1, 2, 3, and 4 (blue, red, green, and purple spectra, respectively). These points were chosen as points that were distributed across the entire line, far enough apart that they may be lie on different features or hybridisation areas within the sample. The differentiated spectra from point 32 show some small variations between the positions of the maxima and minima of sequential lines but no clear trend, with very similar signal to noise ratios. This is also observed in the D parameter values shown in Table 6-1, which vary between 22.8 eV and 23.0 eV randomly, which is not a significant difference as the uncertainty is 0.2 eV. The differentiated spectra from point 64 (Figure 6-5) show larger variations in the spectral line shape and positions of the maxima and minima than the previously examined point, leading to D parameter values ranging between 21.6 eV and 23.4 eV (Table 6-1), which is a much larger and more significant variation. However, there is no trend in how these values change with the sequential acquisition of the line scans and there is no change in the signal to noise ratio, suggesting that the carbon at this point has experienced some changes as a result of the beam damage but also these changes occur randomly. The final point examined (point 96) in Figure 6-5 shows similar behaviour to point 32, with smaller variations in the positions of the maxima and minima resulting in D parameter values ranging between 22.6 eV and 23.0 eV (Table 6-1).
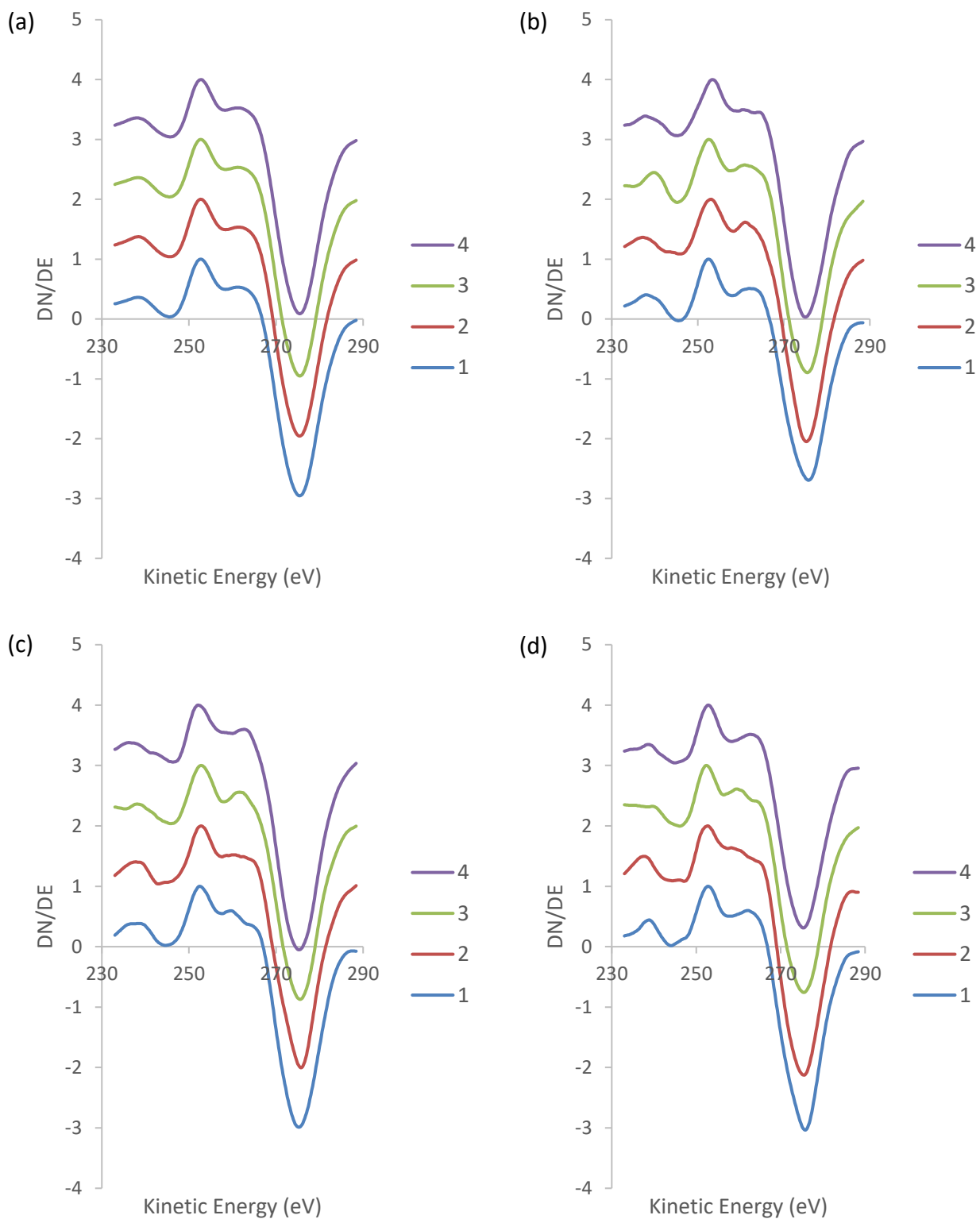
Figure 6-5: C(KLL) spectra taken from (a) the average of all spectra in the line scan, and point (b) 32, (c) 64, and (d) 96 of the carbon elemental line scans. Each plot shows spectra from four successive line scans taken sequentially in the same place on the HOPG sample.

Table 6-1: D Parameter values from each spectrum in Figure 6-5.

Scan Number	D Parameter (eV) (Average)	D Parameter (eV) (Point 32)	D Parameter (eV) (Point 64)	D Parameter (eV) (Point 96)
1	22.6	22.8	23.4	23.0
2	22.6	23.0	22.2	22.8
3	22.6	22.8	22.8	23.0
4	22.6	23.0	21.6	22.6

The results shown in Figure 6-3, Figure 6-4, Figure 6-5, and Table 6-1 combine to show that there may be some small electron beam induced changes that occur on a HOPG surface when several sequential line scans are acquired over the same line, however these changes do not occur systematically and do not significantly impact the average percentage or range of percentages of sp^2 hybridised carbon detected across the surface. The optimisation of the parameters used to acquire the window mode carbon elemental line scans can therefore be carried out over the same areas and any changes that occur systematically can be concluded to be a result of the change in parameter and not to electron beam induced changes.

6.2.1.2 Repeated Scans – DLC

The same tests to examine the impact of electron beam induced damage were performed on a DLC sample as it was expected that the beam would interact with the DLC in a different way to HOPG, with the results shown in Figure 6-6. The SEM image (20 μm FOV) shows a surface that is mostly uniform but includes several small areas that appear darker in colour or show small particles on the surface. Previous results using the hybridisation mapping technique have indicated that these small areas of differing colours or particles do not show any difference in carbon hybridisation from the rest of the film, and are therefore likely areas of DLC that have a differing morphology. The yellow line in the SEM image shows the line over which the four sequential line scans were acquired and runs through the uniform part of the sample. The window mode carbon elemental line scan acquired over this line for each of the sequential line scans acquired are also shown in Figure 6-6, along with the resultant hybridisation line scans and the SNR values from those line scans.

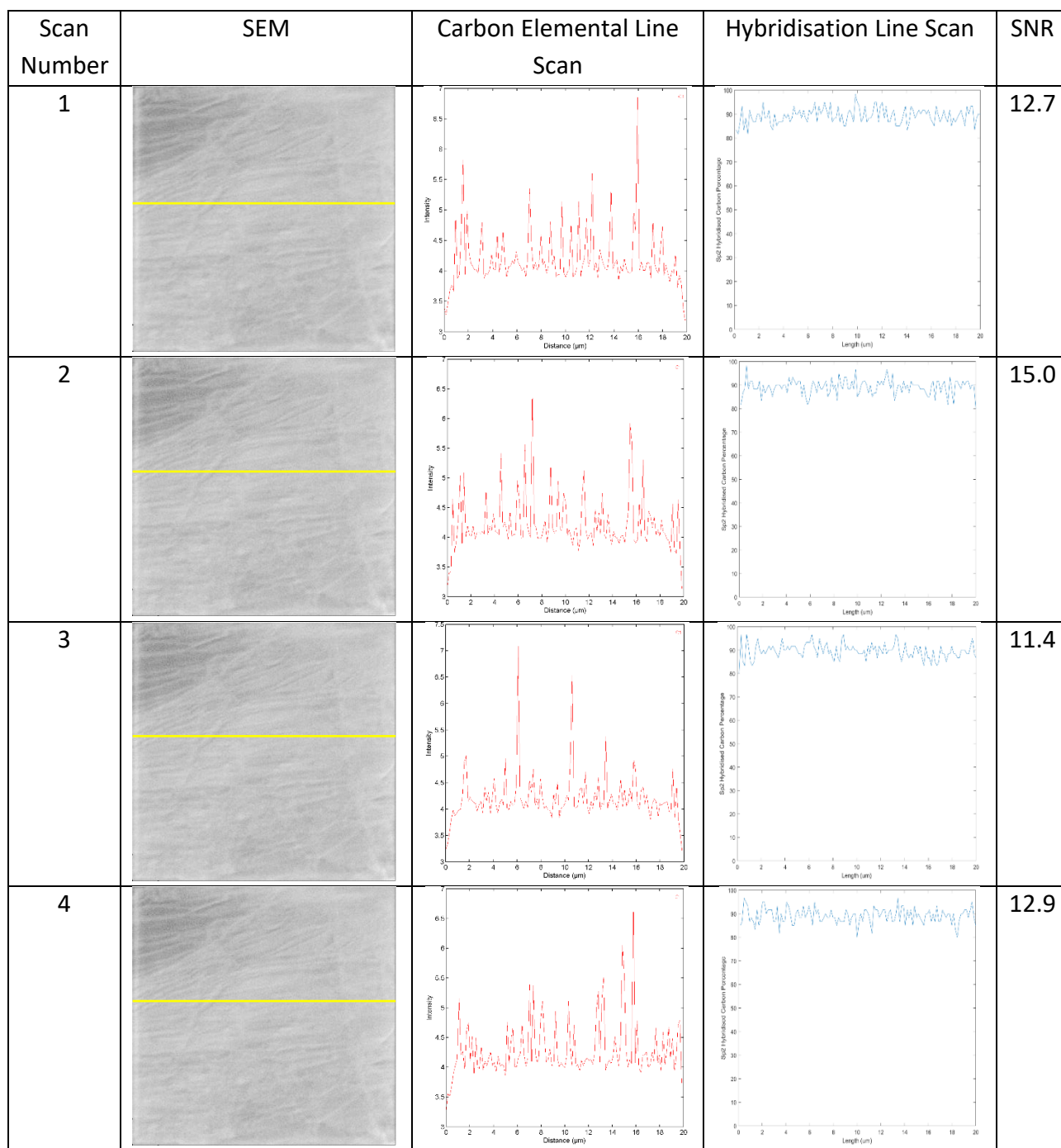| Scan Number	SEM	Carbon Elemental Line Scan	Hybridisation Line Scan	SNR
1				5.93
2				6.42
3				6.13
4				6.13
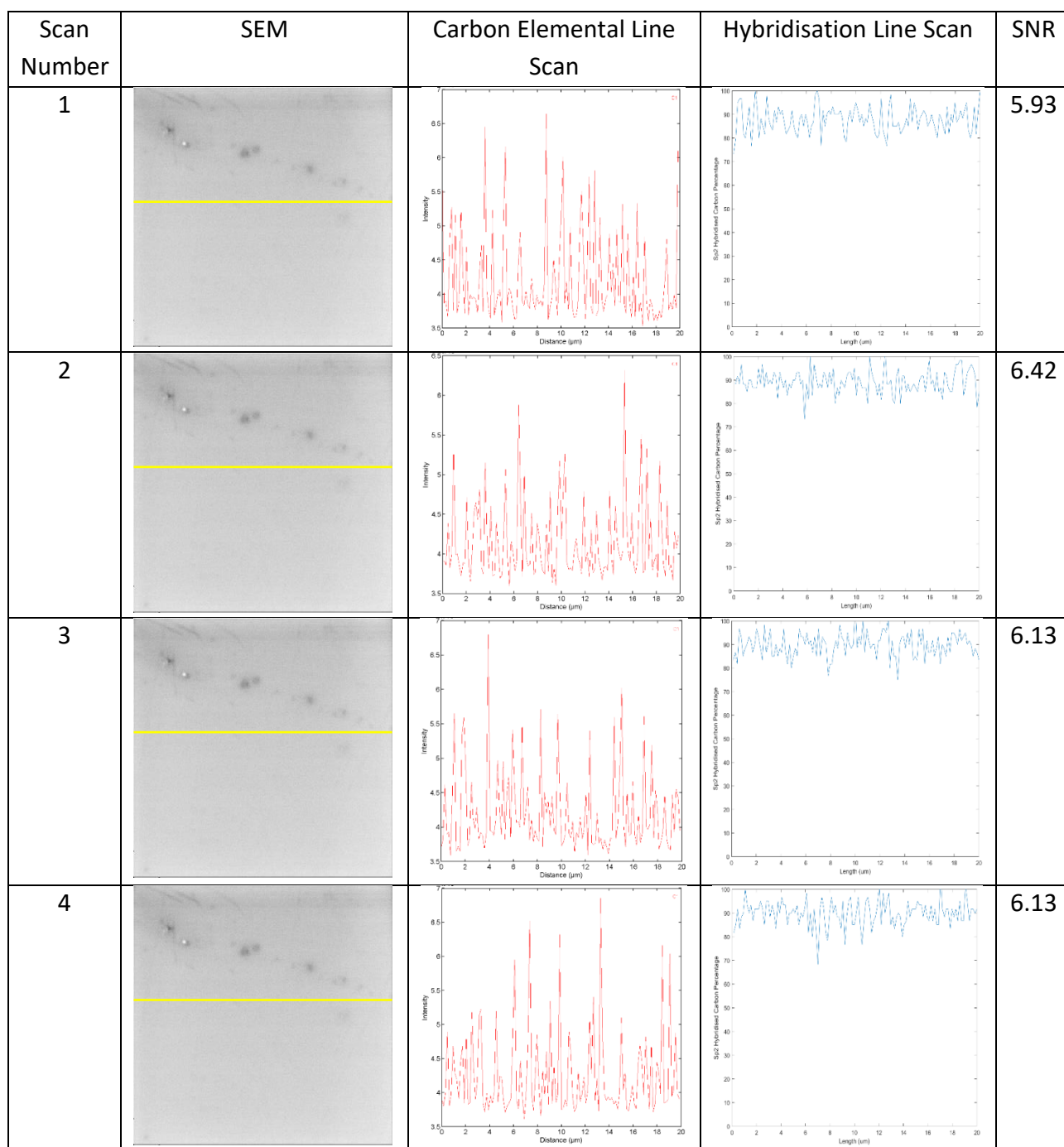
Figure 6-6: SEM images (20 μm FOV), C(KLL) elemental line scans, and hybridisation line scans of four sequentially acquired line scans of DLC taken sequentially in the same area.

The hybridisation line scan for the first scan acquired (Figure 6-6) shows an average sp^2 hybridised carbon percentage of approximately 89 %, which is similar to that of the HOPG sample, however the spread of the values is larger, ranging between 75 % and 100 %. The second scan results in a hybridisation line scan that is similar to the first, but with slightly less spread in the percentages. The third and fourth scans show similar hybridisation percentage ranges, but with a slightly higher average sp^2 hybridised carbon percentage. This suggests that there may be some electron beam induced graphitisation occurring over the area where the line scans were taken, however the extent

is smaller than that observed when the hybridisation maps were produced in the previous chapter. This is likely due to the much smaller acquisition time for these line scans than the maps, thus the exposure to the electron beam is less. The SNR values shown in Figure 6-6 will be considered to provide a semi-quantitative indication of any beam damage that is occurring.

SNR ratios from the sequentially acquired hybridisation line scans are plotted against the scan number to investigate any trends that may occur from electron beam exposure in Figure 6-7.
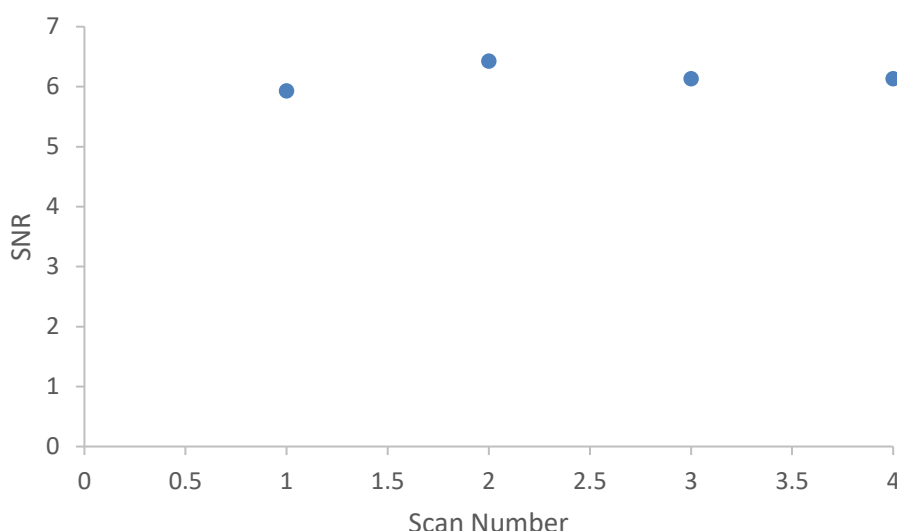
Figure 6-7: SNR for the four sequentially acquired hybridisation line scans on HOPG from Figure 6-6.

Figure 6-7 shows that there is very little variation in the SNR ratio in the sequentially acquired hybridisation line scans, which suggests that there is no significant electron beam induced damage occurring when multiple lines are acquired over the same path. To gain further insight in the impact of the electron beam on the sample the spectra extracted from the carbon elemental line scans in Figure 6-6 are also examined.

The average spectrum taken across the entire of each carbon elemental line scan in Figure 6-6 is shown in Figure 6-8, with scans 1, 2, 3, and 4 shown with the blue, red, green, and purple lines, respectively. The spectra all appear to have a similar shape, but with some slight changes in the positions of the maxima and minima. This is supported by the D parameter values in Table 6-2, which vary between 22.6 eV and 23.0 eV, with a slightly increasing trend observed with increasing scan number. However, as the uncertainty in the D parameter values is 0.2 eV this trend cannot be stated with certainty.
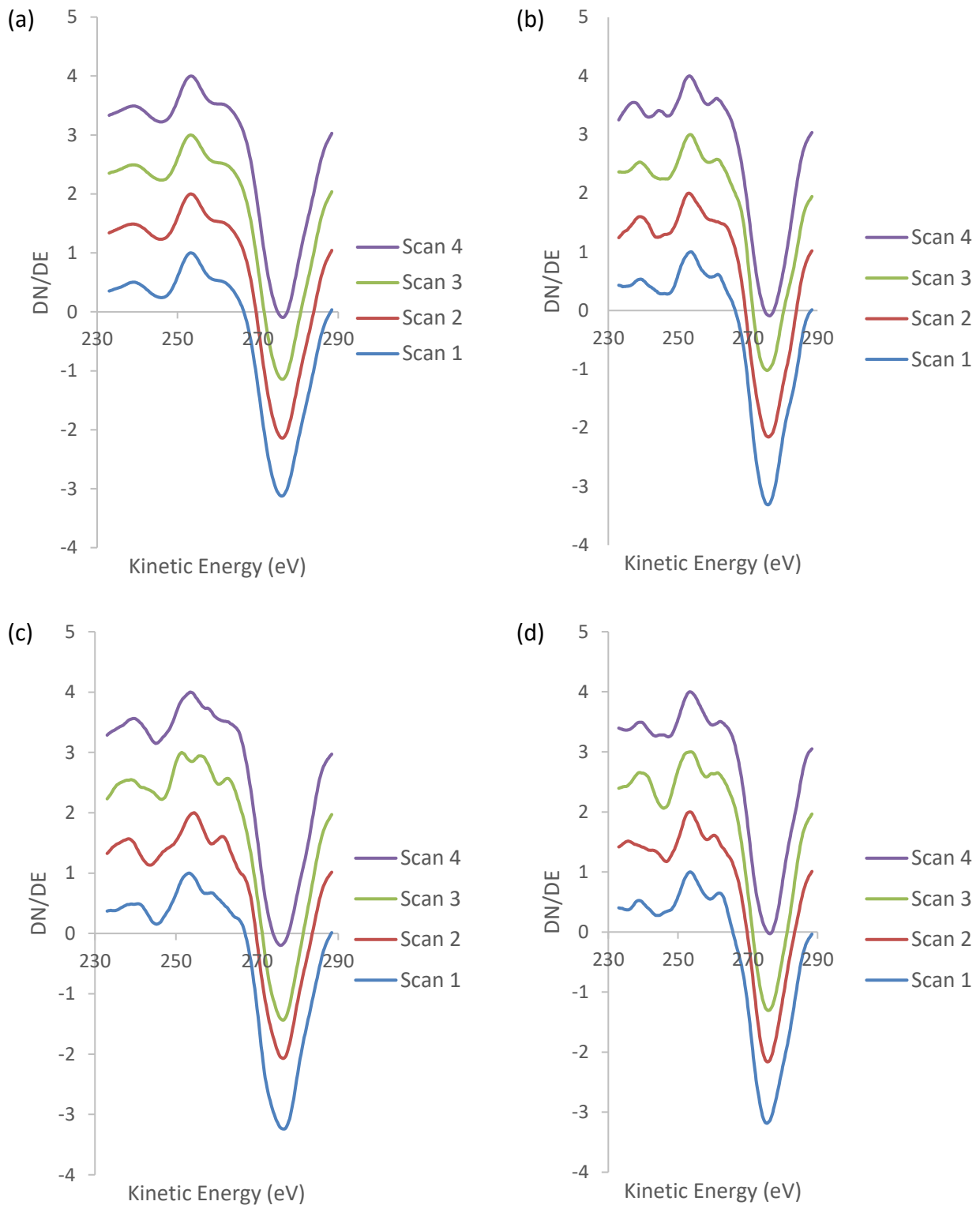
Figure 6-8: C(KLL) spectra taken from (a) the average of all spectra in the line scan, and point (b) 32, (c) 64, and (d) 96 of the carbon elemental line scans. Each plot shows spectra from four line scans taken sequentially in the same place on the DLC sample

Spectra from several points of the carbon elemental line scans (Figure 6-6) were extracted and are also shown in Figure 6-8 to further examine the effect of the electron beam exposure on the sample. This same trend of slightly changing maxima and minima position is observed for two of the

individual points examined in each scan (points 32 and 96), while the spectra from point 64 shows larger changes in the spectral line shape and maxima and minima positions but with no trend. The D parameter values extracted from each of these spectra are shown in Table 6-2 and support the conclusions drawn from the spectra. The D parameter values for the spectra at point 32 vary between 22.2 eV and 23.0 eV, with a trend of increasing D parameter as the sequential scan number increases. This trend is larger than the uncertainty of 0.2 eV, and can be stated with more confidence. The same trend is observed for the values at point 96, although the range is slightly larger as the values vary between 22.0 eV and 23.0 eV. The D parameter values from point 64 show no clear trend, with values between 22.2 eV and 25.0 eV. The spectrum that produces a D parameter value of 25.0 eV shows the largest variation in the spectral shape, with two maxima observed rather than one clear maximum point making the D parameter value inaccurate. With the exception of the spectra acquired at point 64 of the line the results shown here indicate that there is a small amount of electron beam induced graphitisation occurring when multiple line scans are acquired sequentially over the same line on the same sample.

Table 6-2: D Parameter values from each spectrum in Figure 6-8.

Scan Number	D Parameter (eV) (Average)	D Parameter (eV) (Point 32)	D Parameter (eV) (Point 64)	D Parameter (eV) (Point 96)
1	22.6	22.2	23.4	22.0
2	22.6	22.8	22.0	22.2
3	23.0	22.2	25.0	22.0
4	22.8	23.0	22.2	23.0

The results from Figure 6-6, Figure 6-7, Figure 6-8, and Table 6-2 appear to show some slightly conflicting data about the electron beam induced changes to the DLC surface, with the SNR indicating very little difference between the sequentially acquired scans while the D parameter values do show some variation. This conflict can be resolved by considering how these numbers are calculated. The SNR values are a measure of the variance within the data and show that this variance does not undergo any large changes overall across the entire line scan. However, the D parameter values are calculated at specific points along the line for each scan, and are therefore showing small, localised changes within the sample as electron beam exposure increases. The results therefore do show that there is a small amount of electron beam induced changes occurring when line scans are

repeatedly acquired over the same line, but these changes are random in nature and when the values from across the entire line are averaged produce a similar result. This complicates the following analysis as any changes in the D parameter that occur as a result of changing scan parameters must be separated from changes that occur as a result of this electron beam modification. However, as it is still preferred to have the scan parameter optimisation tests performed on the same area of the sample for all tests the line scans will be acquired in the order of shortest to longest acquisition time in order to minimise the impact of these changes to the sample surface.

6.2.1.3 Impact of Electron Beam Exposure

Through repeatedly acquiring scans over the same line on samples of both HOPG and DLC samples the impact of continued exposure to the electron beam has been established for both carbon types. HOPG has been shown to experience little electron beam induced damage, although small changes do occur in a non-systematic way when scans are repeated over the same area. However, DLC films exhibit a small amount of electron beam induced modification as the exposure to the electron beam increases. This modification is undesirable, however it is still preferable to acquire multiple scans over the same line when examining the effect of changing scanning parameters. To minimise this problem the scans will be acquired in the order of lowest to highest acquisition time for both HOPG and DLC.

6.2.2 Step Width Optimisation

The step width refers to the energy resolution of the spectra obtained in each line scan, and is an important parameter to optimise as it will have a large impact on the signal to noise ratio, and therefore the spectral quality, of the data obtained and the acquisition time. Step widths values between 0.1 eV and 10 eV can be chosen to obtain window mode elemental line scans with the Scanning Auger Nanoprobe used in this work. A step width of 1.0 eV is generally used for obtaining elemental line scans as normal use doesn't require any higher resolution than this. However, when determining the D parameter of a carbon peak it is preferred to have a higher energy resolution to find the D parameter with a higher resolution. This leads to a more accurate determination of the hybridisations present on the surface. The drawback of increasing the energy resolution is that the scan acquisition time is increased, thus it is important to find a balance between the acquisition time and energy resolution to achieve the optimal result.

To examine the impact of changing the step width carbon elemental line scans were acquired for

both HOPG and DLC using step widths of 1.0 eV, 0.5 eV, and 0.2 eV. For each sample a SEM image was acquired before a carbon elemental line scan was performed over the path shown in the SEM. These scans were converted to hybridisation line scans using the method outlined in section 6.1.2 and are presented in the same way shown previously in Figure 6-2 so that comparisons can be made between the scans acquired with different step width values.

6.2.2.1 Step Width Optimisation – HOPG

Using step widths of 1.0 eV, 0.5 eV, and 0.2 eV window mode carbon elemental line scans were acquired for a HOPG surface and are shown in Figure 6-9, along with the resultant hybridisation line scans, the SNR values from the hybridisation line scans, and the SEM image showing the area under examination. The SEM image shows that the surface of the HOPG has step edges and ridges running horizontally across the 20 µm FOV but otherwise appears to be quite uniform. The yellow line in the SEM image indicates the line over which the window mode carbon elemental line scans were acquired and passes across one step edge of the HOPG. All of the line scans were acquired sequentially over this line in order of increasing acquisition time such that the 1.0 eV step width carbon line scan was acquired first, followed by 0.5 eV and 0.2 eV, and are presented in this order in Figure 6-9.

The window mode carbon elemental line scan and resultant hybridisation line scan acquired using a step width of 1.0 eV are shown in Figure 6-9. The average sp^2 hybridised carbon content across the line is approximately 88 %, however there is a large amount of variance around this average, with the range of sp^2 carbon percentages varying between approximately 76 % and 100 %. This variance is due to the step width for obtaining the carbon elemental line scan being large, which results in the increments in the sp^2 hybridised carbon percentage scale being large and percentage values being rounded up or down. While there are some changes in the range of percentage values across the line, they do not correlate with the position of any features observed in the SEM image in Figure 6-9 which indicates that the features are areas of HOPG with different morphology.

When the step width is reduced to 0.5 eV this variance can be seen to decrease significantly (Figure 6-9) and the average sp^2 hybridised carbon percentage is increased to approximately 90 %. The percentages now vary between approximately 80 % and 95 %, and while this variation is not constant across the entire line the changes do not correlate with any features in the SEM image and therefore the results do not suggest that there is significant changes in the hybridisation present at step edges and ridges across the HOPG surface. A further decrease in the step width to 0.2 eV results

in a further reduction in the variance in the data (85 % to 95 %), however the average percentage remains at approximately 90 %. This reduction in the range of the sp^2 hybridised carbon percentages is a result of the decrease in the size of the increments in the percentage scale as the step width decreases. The increased resolution thus achieved in the percentage scale allows for a more accurate determination of the sp^2 hybridised carbon percentage at each point along the line as the errors due to rounding are reduced. These results therefore suggest that to obtain data of sufficiently high quality to be of use in characterising systems with differing carbon hybridisations a step width of 0.2 eV is required. The SNR values in Figure 6-9 will now be considered to determine how the step width impacts on the variance of the data.

Step Width (eV)	SEM	Carbon Elemental Line Scan	Hybridisation Line Scan	SNR
1.0				5.18
0.5				9.0
0.2				12.7
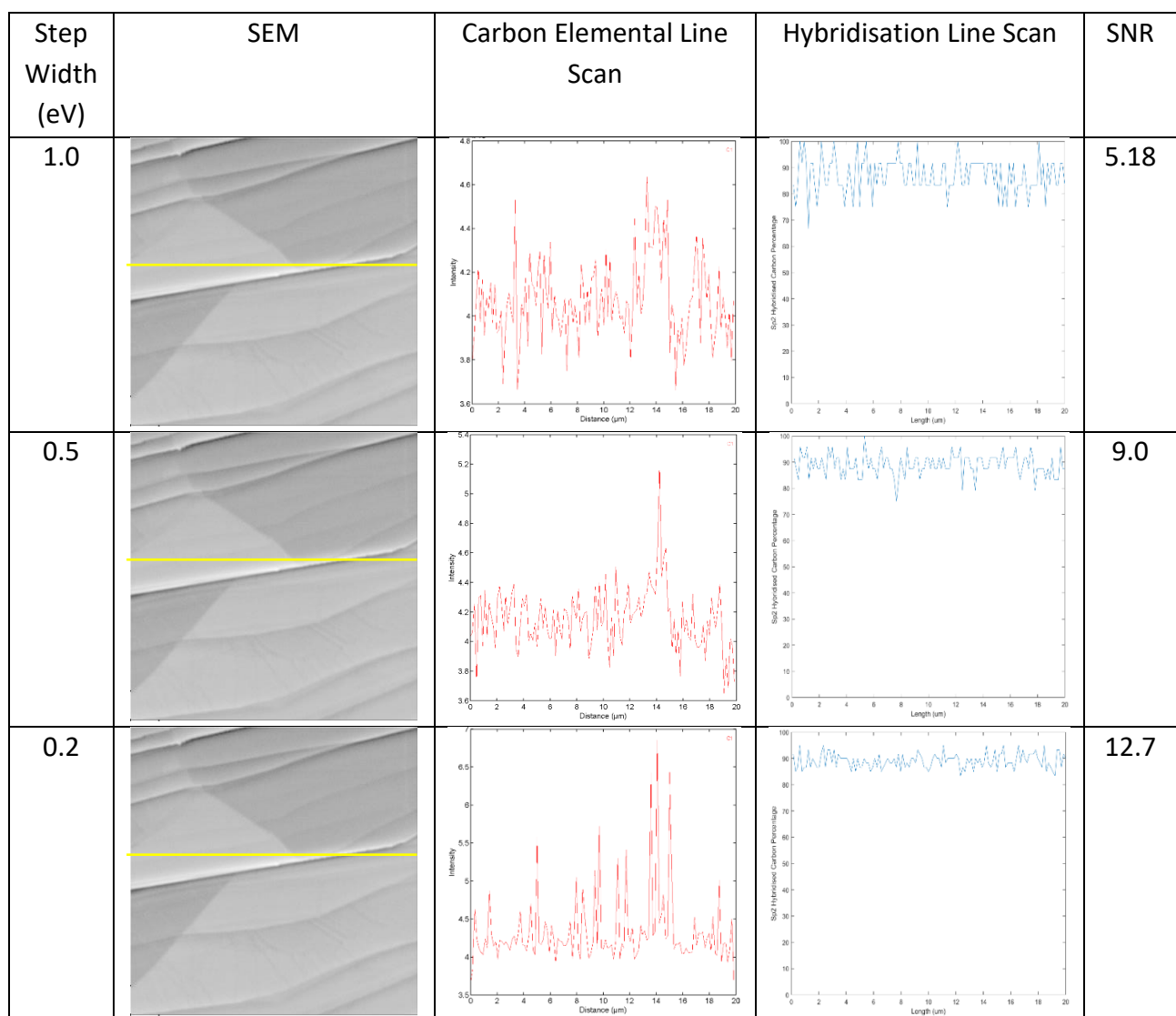
Figure 6-9: SEM images (20 μm FOV), C(KLL) elemental line scans, and hybridisation line scans of HOPG with step widths of 1.0 eV, 0.5 eV, and 0.2 eV step width.

The SNR values from each of the hybridisation line scans in Figure 6-9 are plotted against the step width used to acquire the line scans in Figure 6-10.
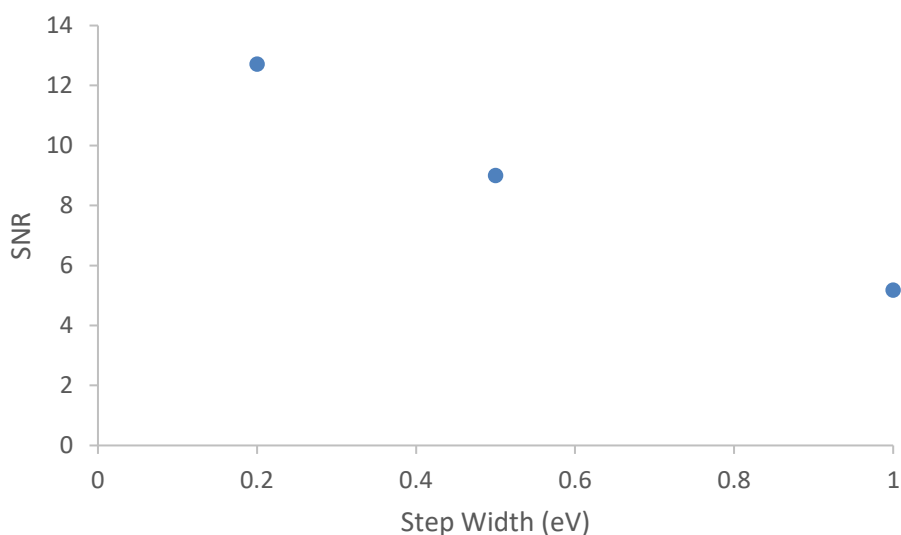
Figure 6-10: Variation in SNR value from hybridisation line scans in Figure 6-9 plotted against the step width of the C(KLL) spectra used to calculate the hybridisation.

There is a clear trend evident in the variation of the SNR when the step width changes, with the SNR increasing as the step width decreases. This trend is expected, as a smaller step width leads to smaller increments in the scale of the D parameter, and therefore also in the scale of the sp^2 hybridised carbon percentage values. Smaller increments will result in the values being rounded to a smaller extent, which will in turn reduce the range in the values and produce a more consistent line scan. Based on these results it is clear that a step width of 0.2 eV results in large improvement of the SNR over the larger step width values, which supports the conclusions made from visual examination of the line scans in Figure 6-9. However, the line scans cannot be considered alone to make the decision about the best step width value to use, and spectra from the elemental line scans will be examined to determine if the changes in spectral shape support this conclusion.

The average spectrum from across each point of the entire elemental line scan in Figure 6-9 is shown in Figure 6-11, with spectra using step widths of 1.0 eV, 0.5 eV, and 0.2 eV shown in blue, green, and red, respectively. Although these spectra show a similar shape overall, they do exhibit some differences in the positions and shape of the maxima and minima, which is also seen in Table 6-3, where the D parameter appears to be approaching its true value as the extent of rounding is decreased with the decrease in step width. A step width of 1.0 eV, 0.5 eV, and 0.2 eV result in a D parameter value of 23.0 eV, 22.5 eV, and 22.6 eV, respectively. These values suggest that the true value of the D parameter is 22.6-22.7 eV, which, due to the uncertainty in the measurements, has been rounded to the closest 1.0 eV in the first scan, the closest 0.5 eV in the second scan, and the closest 0.2 eV in the third scan. From these results it can be concluded that a step width of 0.2 eV is

necessary to obtain D parameter values with the high accuracy required to characterise carbon samples composed of different hybridisations.
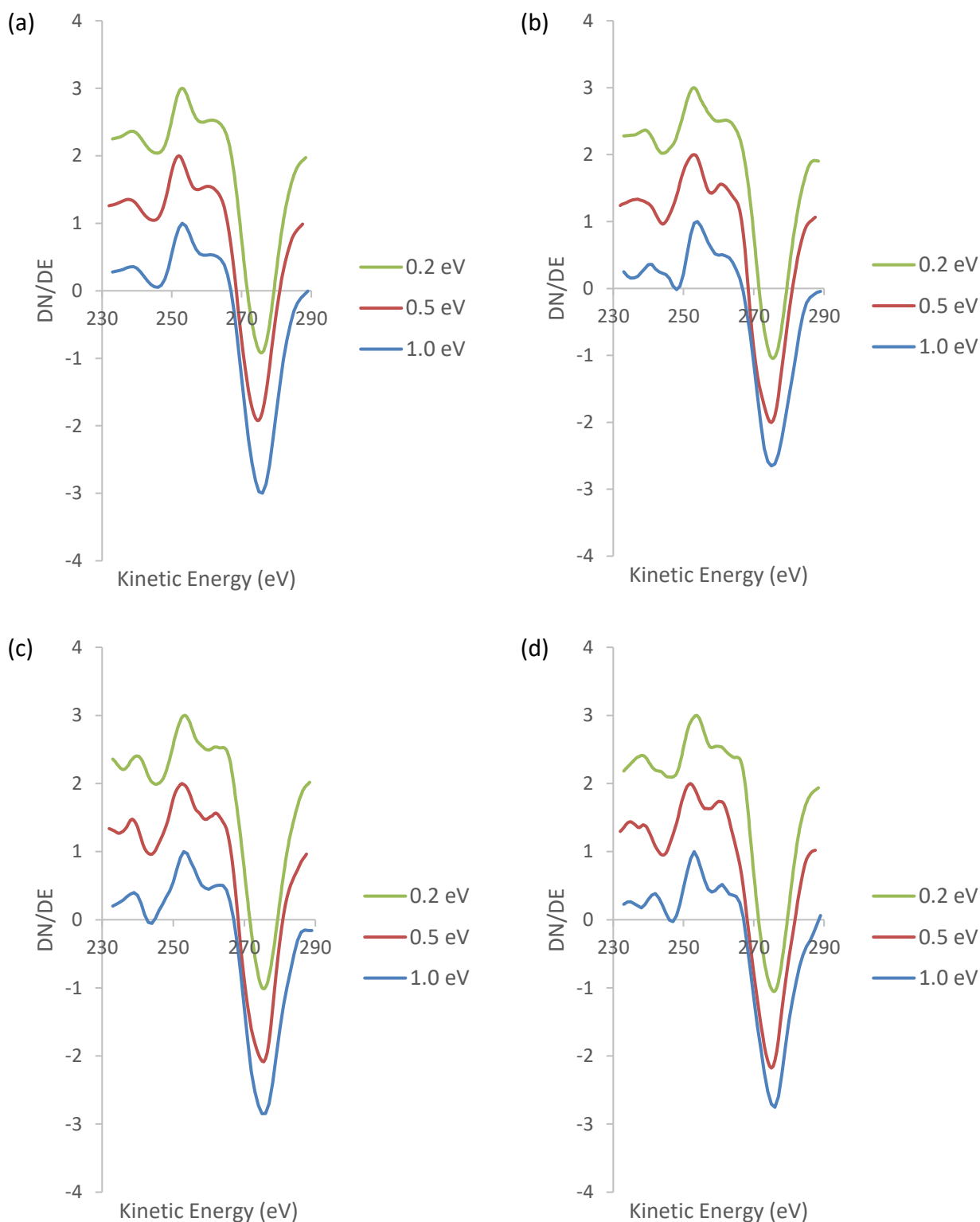
Figure 6-11: C(KLL) spectra taken from (a) the average of all spectra in the line scan, and point (b) 32, (c) 64, and (d) 96 of the carbon elemental line scans. Each plot shows spectra from line scans of HOPG with step widths of 1.0 eV (blue), 0.5 eV (red), and 0.2 eV (green).

The trend is not as easy to observe in the spectra extracted from individual points of each elemental line scan (Figure 6-11) or the D parameters that these spectra produce (Table 6-3). The spectra at point 32 show some small differences in spectral shape and the positions of the maxima and minima, however the most significant change is in the sharpness of the peaks. There is a small increase in the sharpness of the peaks as the step width decreases, which is a result of the increased energy resolution leading to a more accurate determination of the highest and lowest points of the spectra. The D parameter values are 22.0 eV for the 1.0 eV and 0.5 eV step widths and 22.4 eV for the 0.2 eV step width spectra. These values alone do not show a clear trend, however when taken with the spectral shapes in Figure 6-11 and line scans in Figure 6-9 it is clear that decreasing the step width of the window mode carbon elemental line scan increases the accuracy of the D parameter value by reducing the impact of rounding errors caused by the uncertainty in the measurements. Looking at all three aspects together is also necessary when examining the data from points 64 and 96 of the line scans. At point 64 the D parameter for spectra with step widths of 1.0 eV, 0.5 eV, and 0.2 eV are 22.0 eV, 23.0 eV, and 22.2 eV, respectively, while at point 96 they are 23.0 eV, 23.0 eV, and 22.2 eV. These three points all show a trend towards 22.2-22.4 eV as the step width decreases, and hence as the energy resolution increases, which suggests that despite the increased acquisition time a step width of 0.2 eV is necessary to obtain data of sufficient accuracy to characterise systems with different carbon hybridisation present.

Table 6-3: D Parameter values from each spectrum in Figure 6-11.

Step Width (eV)	D Parameter (eV) (Average)	D Parameter (eV) (Point 32)	D Parameter (eV) (Point 64)	D Parameter (eV) (Point 96)
1.0	23.0	22.0	22.0	23.0
0.5	22.5	22.0	23.0	23.0
0.2	22.6	22.4	22.2	22.2

The results from Figure 6-9, Figure 6-10, Figure 6-11, and Table 6-3 combine to show that a step width of 0.2 eV is necessary in order to determine the D parameter, and therefore the sp^2 hybridised carbon percentage, of HOPG with a high level of accuracy as step widths wider than this result in significant rounding of the D parameter and introduce large uncertainties in the data.

6.2.2.2 Step Width Optimisation – DLC

The above tests examining the impact of the step width used to acquire window mode carbon

elemental line scans were repeated with a DLC film. The SEM image showing the 20 µm FOV area over which these tests were performed is shown in Figure 6-12, along with the window mode carbon elemental line scans acquired with the different step width values, their resultant hybridisation line scans, and the SNR values for each scan. From the SEM image it can be seen that the area examined is largely uniform, however it does contain a dark streak that runs diagonally through the image. The yellow line in the SEM image runs through the uniform area of the sample and the darker streak and indicates the line over which the window mode carbon elemental line scans were acquired.

Step Width (eV)	SEM	Carbon Elemental Line Scan	Hybridisation Line Scan	SNR
1.0				2.93
0.5				4.4
0.2				9.0
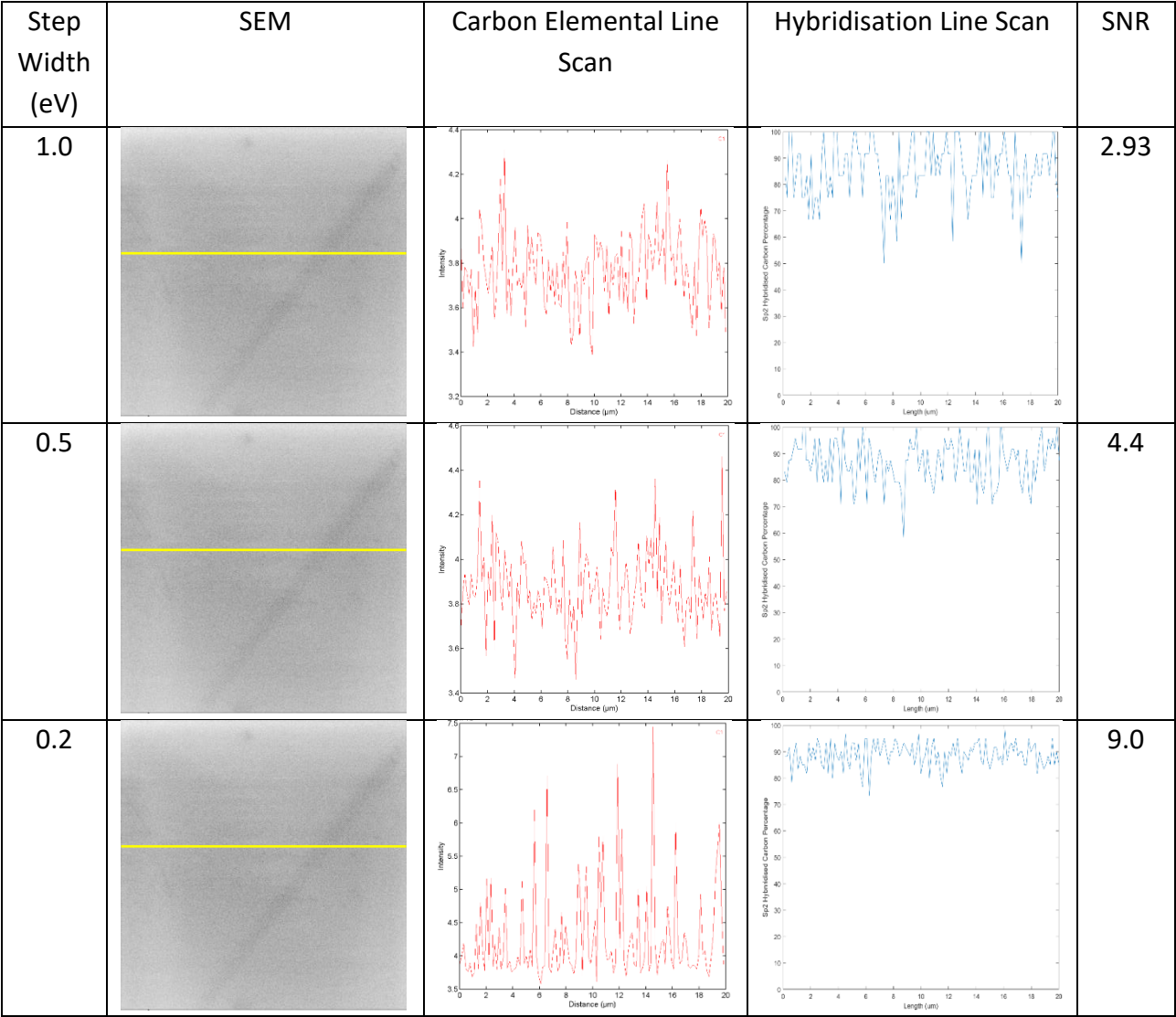
Figure 6-12: SEM images (20 µm FOV), C(KLL) elemental line scans, and hybridisation line scans of a DLC film with step widths of 1.0 eV, 0.5 eV, and 0.2 eV step width.

The hybridisation line scan produced from the elemental line scan with a 1.0 eV step width (Figure 6-12) shows an average percentage of approximately 85 % with points ranging between approximately 50 % and 100 %, resulting in a low SNR value of 2.93. This scan clearly shows how large the increments in the sp^2 hybridised carbon percentage scale are when a step width of 1.0 eV

is used and suggests that these values are not very accurate and large amounts of rounding are occurring in the determination of the position of the maxima and minima. A decrease in the step width to 0.5 eV results in a smaller range of sp^2 hybridised carbon percentages, an increased SNR, and an average percentage of approximately 88 %. This trend continues when the step width is further decreased to 0.2 eV, with the range of values decreasing further around the average of approximately 89 %. As the step width is decreased there is a significant decrease in the range of values obtained, as well as an increase in the average sp^2 hybridised carbon percentage across the line. By examining the smoothness of the lines in the three sp^2 hybridised carbon line scans the differences that occur as a result of the step width changing can be seen, with a step width of 0.2 eV providing a much smoother line with smaller increments in the scale, leading to a more accurate determination of the average sp^2 hybridised carbon percentage. The SNR values presented in Figure 6-12 provide further detail on the variance when the step width is varied, and need to be examined more closely.

A plot of the SNR against the step width used to acquire the carbon elemental line scan is shown in Figure 6-13.
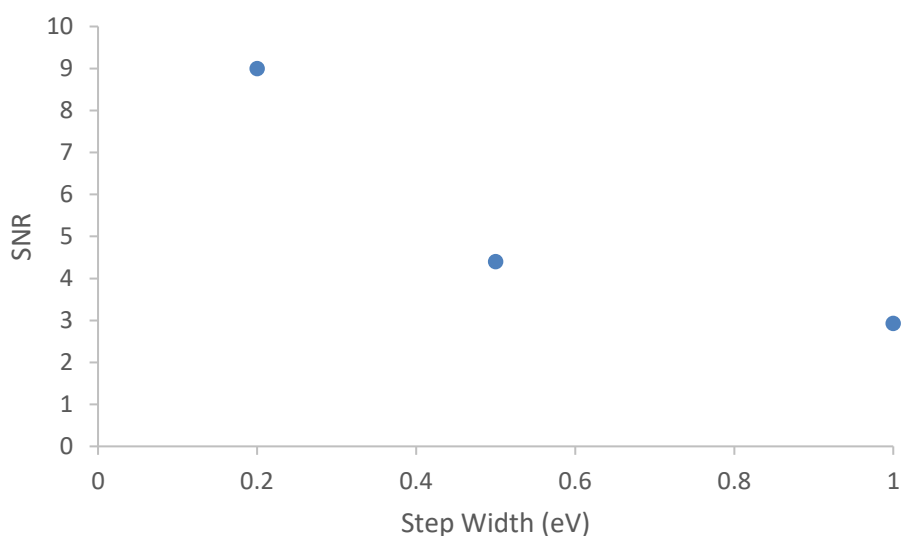
Figure 6-13: Variation in SNR value from hybridisation line scans in Figure 6-12 plotted against the step width of the C(KLL) spectra used to calculate the hybridisation.

There is a clear trend in the SNR from the hybridisation line scans when it is plotted against the step width, with a smaller step width producing a higher SNR. This result is expected due to the rounding in the D parameter value and sp^2 hybridised carbon percentage value that occurs when the step width is increased, as has been discussed previously. These results show that a step width of 0.2 eV results in a significantly improved SRN value, and therefore more accurate sp^2 hybridised carbon

concentrations, however the spectra from the window mode carbon elemental line scan will also be examined to provide further insights to the optimisation process.

The average spectrum taken across the entire line for each of the three elemental line scans in Figure 6-12 is shown in Figure 6-14, where the spectra taken with step widths of 1.0 eV, 0.5 eV, and 0.2 eV are shown in blue, red, and green, respectively. The spectra all show a similar shape, but with some variation in the positions of the maxima and minima and a slight increase in the sharpness of the maxima and minima, which is also shown in the D parameter values in Table 6-4. Using a step width of 1.0 eV the D parameter is 23.0 eV, while a decrease in step width to 0.5 eV results in a D parameter of 22.5 eV. Further decrease of the step width to 0.2 eV results in a D parameter value of 22.6 eV, thus the D parameter for the average spectra appears to approach its true value as the step width is decreased and the uncertainty caused by the rounding of the value becomes less significant.

The spectra from individual points from within the elemental line scans are also shown in Figure 6-14 and show some differences in the spectral shape with a change in step width, although it is difficult to discern any trend in these changes. As the step width decreases it can be seen that the positions of the maxima and minima change slightly, and the minima tend to become sharper, and thus the D parameter can be determined more accurately. However, this does not translate to a clear trend in the D parameter values, as shown in Table 6-4. At point 32 the D parameter values obtained using a step width of 1.0 eV, 0.5 eV, and 0.2 eV are 23.0 eV, 22.5 eV, and 23.2 eV, respectively, while at point 64 the D parameter values are 22.0 eV, 22.5 eV, and 21.8 eV. Neither of these data sets show a trend, however at point 96 the D parameter values are 24.0 eV, 22.5 eV, and 22.0 eV for spectra obtained with step widths of 1.0 eV, 0.5 eV, and 0.2 eV, respectively, which shows a decrease in D parameter as the step width increases. While these datasets do not show clear and consistent trends in the D parameter, when the D parameter values are combined with the spectral shapes, the hybridisation line scans, and SNR values it is clear that to obtain an accurate D parameter value, and therefore an accurate sp^2 hybridised carbon percentage value, a small step width of 0.2 eV is required to obtain sp^2 hybridised carbon percentage line scans with sufficient accuracy to differentiate between areas composed of different hybridisations.
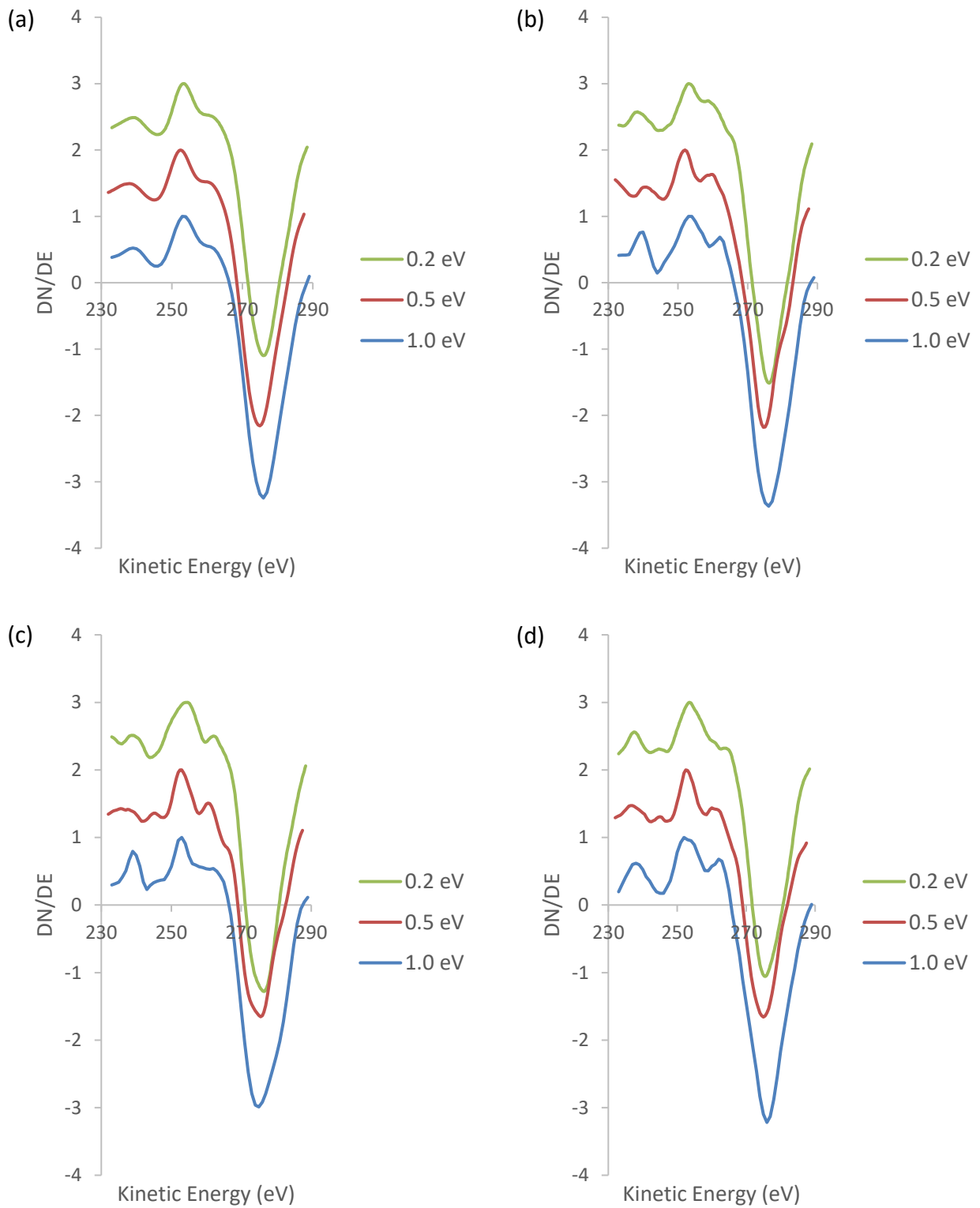
Figure 6-14: C(KLL) spectra taken from (a) the average of all spectra in the line scan, and point (b) 32, (c) 64, and (d) 96 of the carbon elemental line scans. Each plot shows spectra from line scans of a DLC film with step widths of 1.0 eV (blue), 0.5 eV (red), and 0.2 eV (green).

Step Width (eV)	D Parameter (eV) (Average)	D Parameter (eV) (Point 32)	D Parameter (eV) (Point 64)	D Parameter (eV) (Point 96)
1.0	23.0	23.0	22.0	24.0
0.5	22.5	22.5	22.5	22.5
0.2	22.6	23.2	21.8	22.0

The impact of changing the step width is observed in Figure 6-12, Figure 6-13, Figure 6-14, and Table 6-4 for a DLC film. The results combine to show that a step width of 0.2 eV is necessary to obtain more accurate D parameter values, and therefore more accurate sp^2 hybridised carbon percentage values, to reliably characterise the hybridisation of the sample.

6.2.2.3 Choice of Step Width

Through changing the step width used to acquire the window mode carbon elemental line scans shown in Figure 6-9 and Figure 6-12 it has been found that the step width, and therefore the energy resolution, has a large impact on the D parameter values found for each spectrum. The positions of the maxima and minima, as well as the sharpness of the peaks, are impacted by the choice of step width and it was found for both HOPG and DLC that a step width of 0.2 eV is necessary to obtain data with sufficient resolution to find accurate sp^2 hybridised carbon percentages. All window mode carbon elemental line scans acquired for the purpose of determining carbon hybridisations will therefore be acquired with a step width of 0.2 eV.

6.2.3 Time Per Step Optimisation

The SAM line scan parameter of time per step refers to the length of time that the analyser dwells at each energy point of the spectra during acquisition, and can have values between 0.1 ms and 10 ms. A larger time per step is desirable to improve the counting statistics and therefore the spectral quality of the line scans. However, once again any improvement made must be balanced against the increase in acquisition time needed. Time per step values between 0.1 ms and 5 ms were examined as reasonable values for use in producing hybridisation line scans of both HOPG and DLC.

6.2.3.1 Time Per Step Optimisation – HOPG
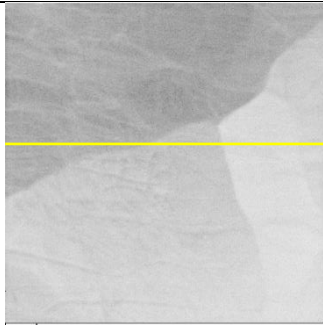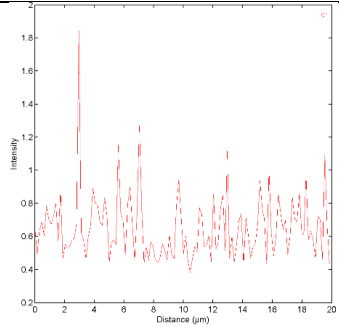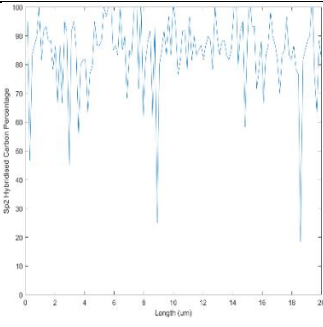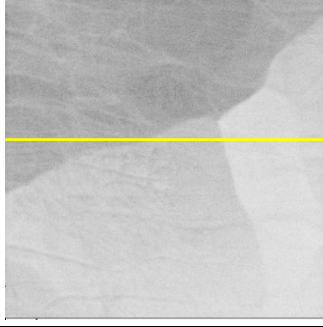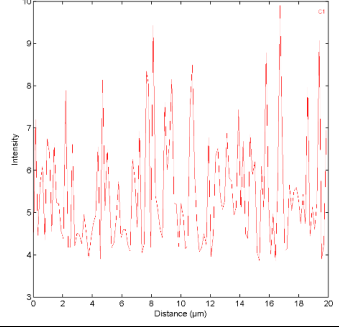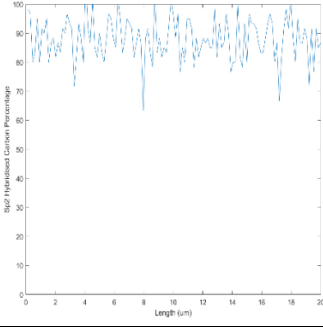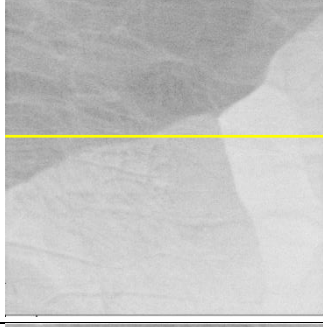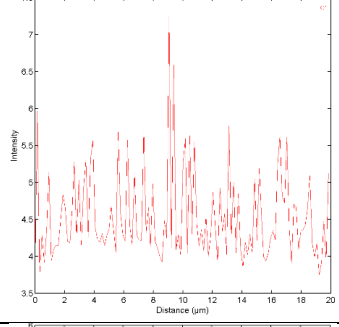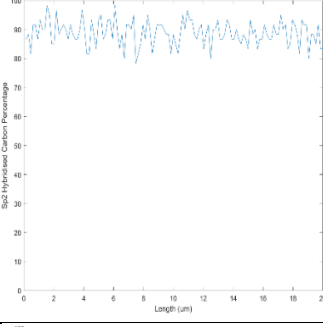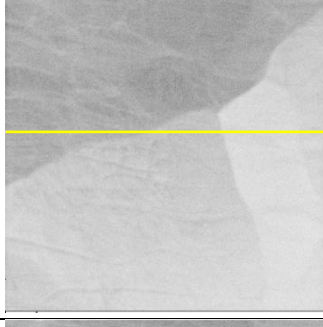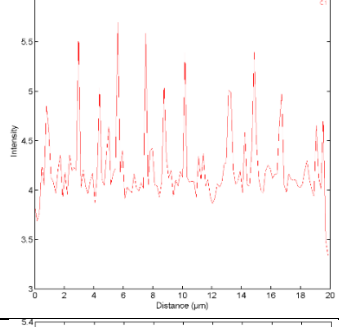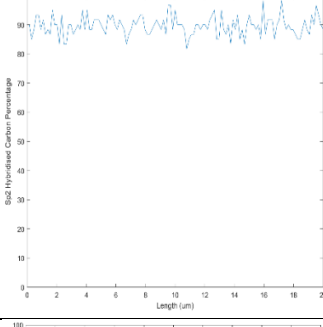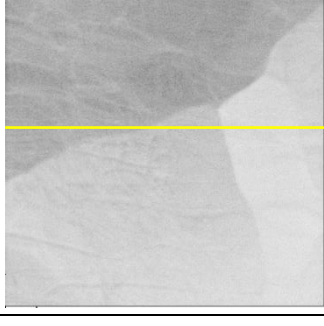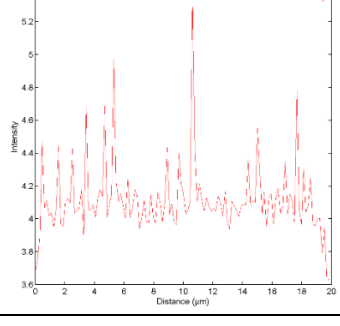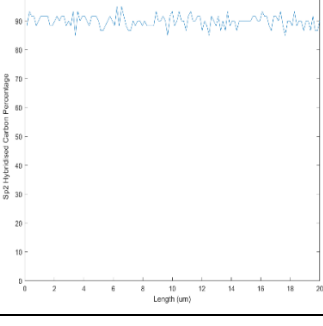
Window mode carbon elemental line scans were acquired using time per step values of 0.1 ms, 0.2 ms, 0.5 ms, 1.0 ms, 2.0 ms, and 5.0 ms. The line scans are shown in Figure 6-15, along with the

SEM image of the area over which the lines were acquired, the hybridisation line scans that were produced from each of the elemental line scans, and the SNR values calculated for each. The 20 μm FOV SEM image shows the sample with three distinct areas that appear to have different colours in the image and are thought to show different flakes of the graphite or ridges within the same flake. The yellow line indicating the line over which the window mode carbon elemental line scans were acquired is shown in the SEM image and crosses all three of these areas. Although it was shown previously that there is no significant impact of electron beam damage on the HOPG samples the elemental line scans were acquired sequentially with the smallest time per step, and thus the shortest acquisition time, obtained first.

The window mode carbon elemental line scan acquired with a time per step of 0.1 ms is shown in Figure 6-15, along with the resultant hybridisation line scan which shows an average of approximately 85 % sp^2 hybridised carbon, but also shows a large variation in the sp^2 content across the surface. The percentage of sp^2 hybridised carbon varies between approximately 20 % and 100 % resulting in a SNR value of 3.3. The variations in the percentages are not consistent across the line, however they do not correspond to the different areas on the SEM image in Figure 6-15, suggesting that the features on the surface are all graphitic but with different morphology.

When the time per step is increased to 0.2 ms the resultant hybridisation line scan is significantly improved, with the percentages showing far less variation and a higher average of approximately 90 % sp^2 hybridised carbon (Figure 6-15). An increase in the time per step to 0.5 ms further reduces the range of sp^2 hybridised carbon percentages observed across the surface to vary between approximately 80 % and 100 %, with an average of approximately 90 %. Doubling the time per step to 1.0 ms maintains an average sp^2 hybridised carbon percentage of approximately 90 % across the line, however the range is reduced and values now vary between approximately 83 % and 98 %.

The hybridisation line scans in Figure 6-15 show that as the time per step continues to increase the variation in the hybridisations determined decreases and the line becomes much more uniform, but maintains an average percentage of approximately 90 %. These results show that ideally a time per step of 5.0 ms would be preferable for obtaining window mode carbon elemental line scans for conversion to sp^2 hybridised carbon percentage line scans. However, using a time per step of 5 ms results in long acquisition times, and it is therefore desirable to use a lower time if the compromise is possible, so the SRN is now examined to determine the improvement in the variance as the time per step value is increased.

TPS (ms)	SEM	Carbon Elemental Line Scan	Hybridisation Line Scan	SNR
0.1				3.27
0.2				5.93
0.5				10.0
1.0				13.0
2.0				22.8
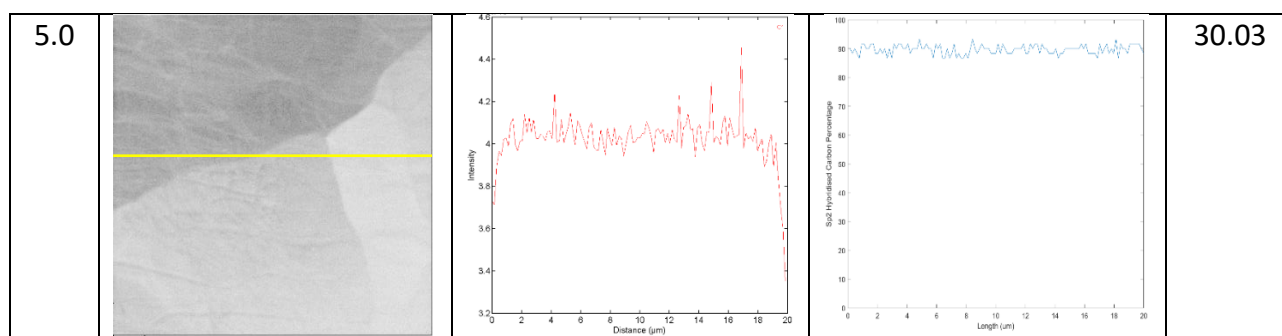
Figure 6-15: SEM images (20 μm FOV), C(KLL) elemental line scans, and hybridisation line scans of HOPG with time per step of 0.1 ms, 0.2 ms, 0.5 ms, 1.0 ms, 2.0 ms, and 5.0 ms.

The SNR values are plotted against the time per step value used to acquire the carbon elemental line scans in Figure 6-16.
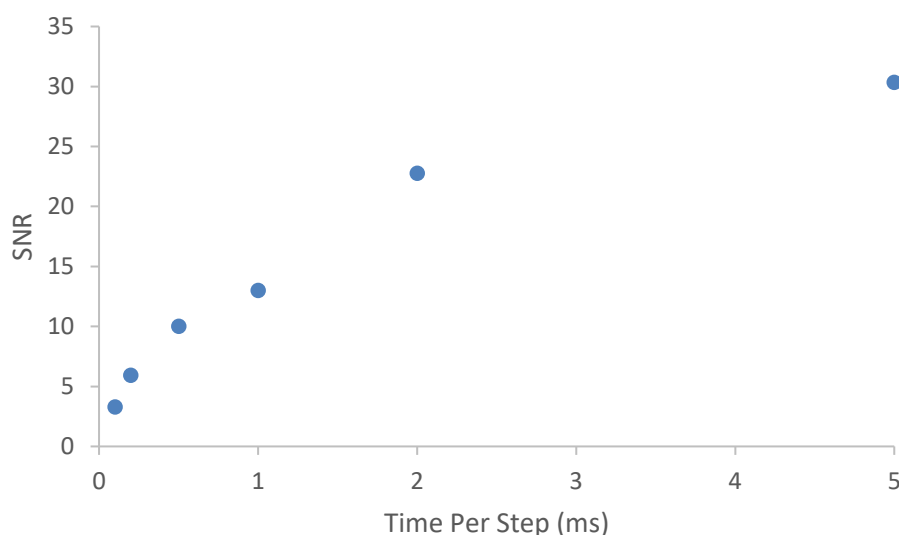
Figure 6-16: Variation in SNR value from hybridisation line scans in Figure 6-15 plotted against the time per step of the C(KLL) spectra used to calculate the hybridisation.

The SNR increases as the time per step value increases, indicating that to obtain the hybridisation line scan that produces the most consistent results a time per step of 5.0 ms should be used. However, as has previously been discussed a high time per step results in an increased acquisition time, and a choice must be made to choose the point at which further improvements to the SNR do not justify the increased cost in time. From Figure 6-16 it can be seen that the SNR approximately doubles when the time per step is increased from 1.0 ms to 2.0 ms, however a further increase in time per step to 5.0 ms does not result in a five-fold increase in SNR. Based on the SNR it is concluded that a time per step of 1.0 ms or 2.0 ms should be used to acquire the carbon elemental line scans. However, the spectra from the carbon elemental line scans must be examined to see if the changes

in the spectral shape between the time per step values are significant.

The spectra from each point of the carbon elemental line scans from Figure 6-15 were averaged, with the resultant spectra shown in Figure 6-17. These averaged spectra show very little difference in the spectral shape between the different time per step values, which is in agreement with the D parameter values in Table 6-5. The D parameter values for spectra acquired with a time per step of 0.2 ms and 0.5 ms were 22.6 eV, while those for all other time per step values tested were 22.8 eV. This difference in D parameter values within the uncertainty of the measurement (0.2 eV) and the variation is therefore not considered to be a significant change.

Examination of spectra from individual points of the carbon elemental line scans shows that the noise in the spectra is larger when the time per step is smaller, and the signal to noise ratio improves as the time per step becomes larger. A time per step value of 1.0 ms appears to be the point at which the noise level becomes minimal and no significant improvement is observed with further time per step increases. Referring back to the hybridisation line scans in Figure 6-15 it can be seen that there is some improvement in the line scans when the time per step continues to be increased above 1.0 ms, however this improvement is not sufficient to justify the increased acquisition time necessary to obtain it.

Consideration of the D parameter values from the spectra at individual points along the line (Table 6-5) shows that for all three points the value approaches 22.8 eV as the time per step increases, although they do not all follow the same trend to reach that value. This is consistent with the improvement in the signal to noise ratios observed in the spectra, as higher levels of noise at the lower step widths is likely to result in larger and more random changes in the maxima and minima positions and improvement in the signal to noise ratio will result in more accurate and consistent determination of the maxima and minima positions.
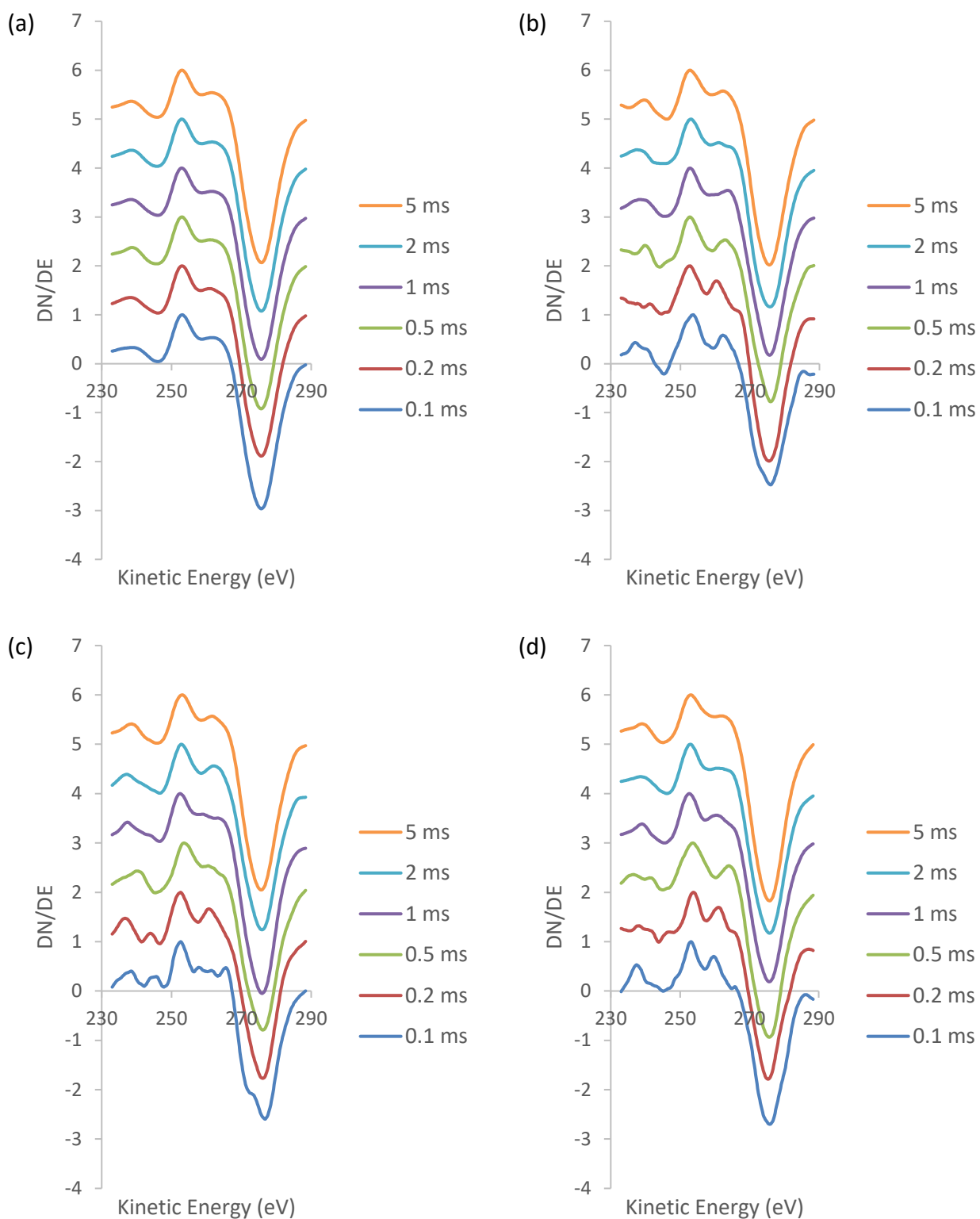
Figure 6-17: C(KLL) spectra taken from (a) the average of all spectra in the line scan, and point (b) 32, (c) 64, and (d) 96 of the carbon elemental line scans. Each plot shows spectra from line scans of HOPG with time per step of 0.1 ms (blue), 0.2 ms (red), 0.5 ms (green), 1.0 ms (purple), 2.0 ms (light blue), and 5.0 ms (orange).

Table 6-5: D Parameter values from each spectrum in Figure 6-17.

Time Per Step (ms)	D Parameter (eV) (Average)	D Parameter (eV) (Point 32)	D Parameter (eV) (Point 64)	D Parameter (eV) (Point 96)
0.1	22.8	22.4	24.2	22.6
0.2	22.6	22.8	23.6	21.6
0.5	22.6	23.2	22.6	21.8
1.0	22.8	22.8	23.4	23.2
2.0	22.8	22.8	23.2	22.8
5.0	22.8	22.8	22.6	22.8

The results in Figure 6-15, Figure 6-16, Figure 6-17, and Table 6-5 combine to show that it is desirable to have a high value for time per step to improve the spectral shape, signal to noise ratio, and therefore the resultant hybridisation line scan. However, the acquisition time required to obtain these spectra is not justified based on the smaller improvements that occur when the time per step continues to increase past a value of 1.0 ms, thus these results suggest that a time per step of 1.0 ms is the optimal value.

6.2.3.2 Time Per Step Optimisation – DLC
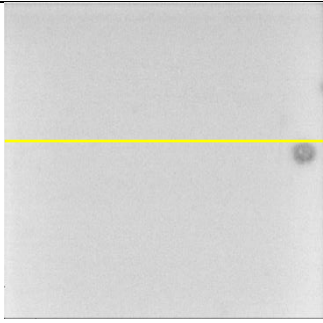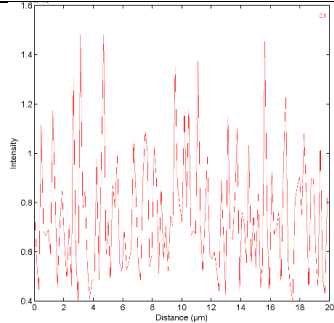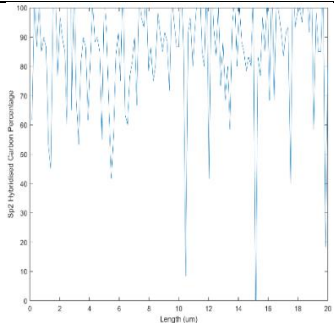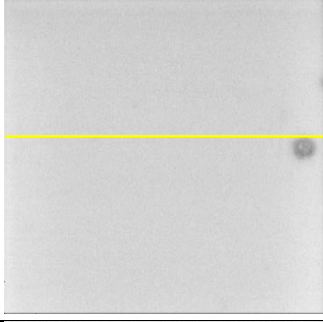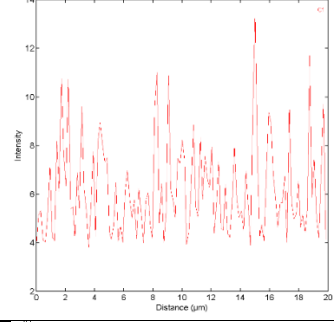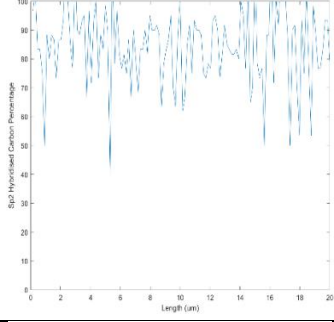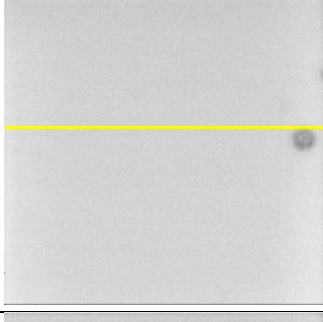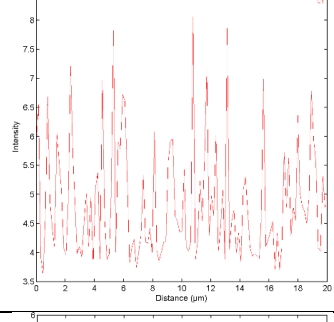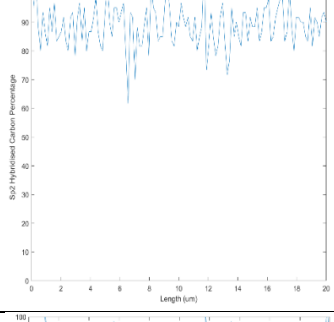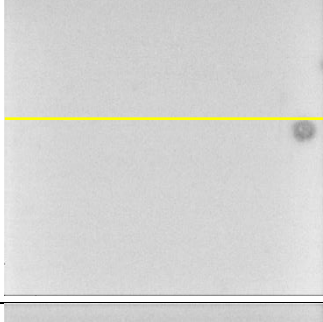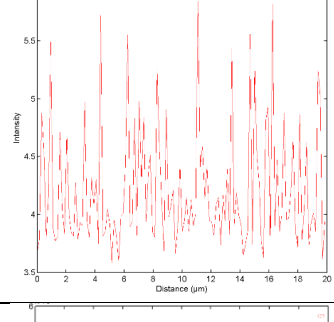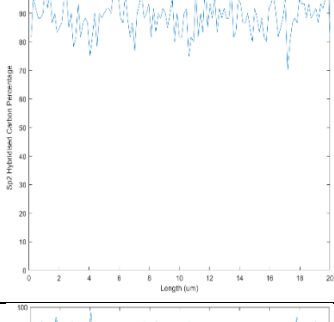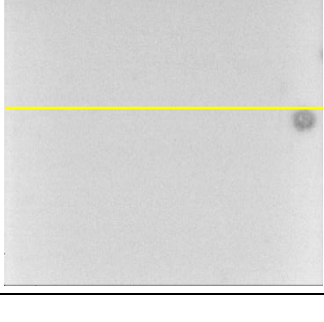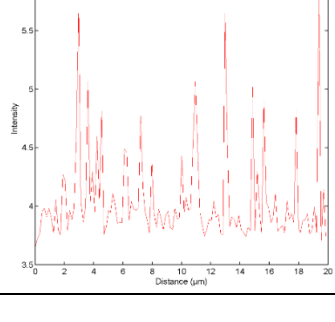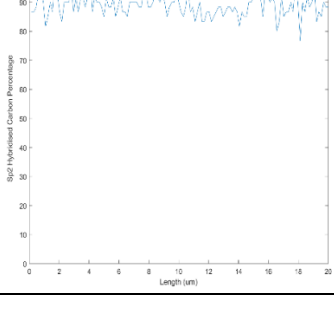
The time per step optimisation tests were repeated with a DLC film, with the resultant line scans shown in Figure 6-18. The SEM image showing the 20 μm FOV area of the film over which these line scans were acquired is also shown in Figure 6-18 and reveals a surface that is almost entirely uniform in colour and texture except for a small darker spot which appears to have several particles in it. The yellow line in the SEM image indicates the line over which the line scans were acquired and runs through the uniform area and along the top of the darker spot. The carbon elemental line scans were acquired sequentially over this line, starting with the scan requiring the shortest acquisition time to minimise the impact of electron beam induced damage altering the carbon present on the surface. The extent of this damage may be higher than that observed previously due to the larger number of scans acquired and the increased scan time for many of these scans.

The window mode carbon elemental line scan acquired with a time per step of 0.1 ms is shown in Figure 6-18, along with the resultant hybridisation line scan and its SNR. This hybridisation line scan has an average sp^2 carbon percentage of approximately 80 % but also has very large variation in the percentages across the surface, with values ranging between 0 % and 100 % and a SNR value of 2.2.

These variations appear random in relation to the surface as they do not match up to any features observed in the SEM image, suggesting that the features on the surface are all composed of DLC but have different morphology that produces variation in the intensities of the SEM image.

As the time per step is increased to 0.2 ms the range in the sp^2 percentage values obtained decreases, with values between 50 % and 100 % observed, however the average slightly increases to approximately 82 %. The nature of the variations still appears to be random, with the largest variations not occurring in the same spots as the previous scan. As the time per step is increased to 0.5 ms the average sp^2 hybridised carbon concentration increases to approximately 88 %. The variation in the percentages is further decreased, with values ranging between 65 % and 100 %. Doubling the time per step to 1.0 ms results in an average sp^2 hybridised carbon percentage of approximately 90 % and a further reduction in the variation, with values ranging between 75 % and 100 %.

This trend of decreasing variation continues as the time per step used to acquire the line scan is increased. The average sp^2 hybridised carbon percentage remains at approximately 90 % with time per step values of 2.0 ms and 5.0 ms, however with a time per step of 5.0 ms the values range between 85 % and 95 % and there is very little variation across the surface. These results suggest that a time per step of 5.0 ms would be the best choice to acquire window mode elemental line scans for the purposes of creating hybridisation line scans. This conclusion is consistent with that made previously with the HOPG sample, however the acquisition time for a scan with a 5.0 ms is larger than is practical and therefore a shorter time per step is needed. The SNR provides further information about the variance in the hybridisation line scans, and is now considered.

TPS (ms)	SEM	Carbon Elemental Line Scan	Hybridisation Line Scan	SNR
0.1				2.21
0.2				3.04
0.5				5.87
1.0				7.42
2.0				9.0

282

| 5.0 | | | | 15.0 |
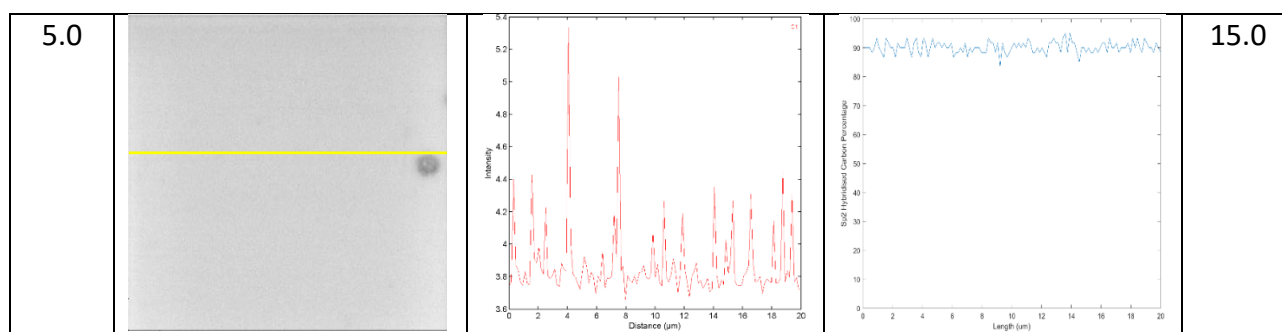
Figure 6-18: SEM images (20 µm FOV), C(KLL) elemental line scans, and hybridisation line scans of a DLC film with time per step of 0.1 ms, 0.2 ms, 0.5 ms, 1.0 ms, 2.0 ms, and 5.0 ms.

The SNR values from the hybridisation line scans are plotted against the time per step value used to acquire the carbon elemental line scan to examine any trend that occurs (Figure 6-19).
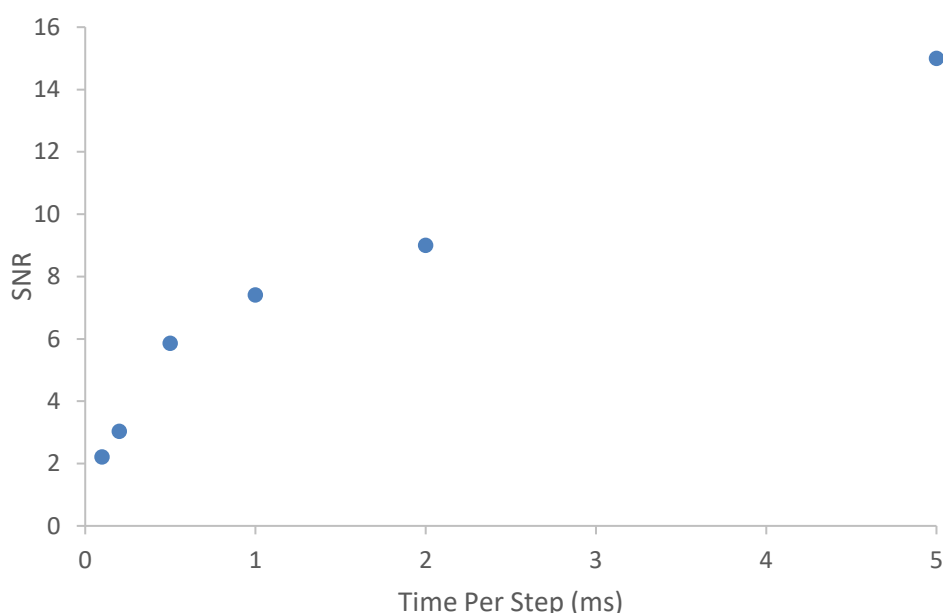
Figure 6-19: Variation in SNR value from hybridisation line scans in Figure 6-18 plotted against the time per step of the C(KLL) spectra used to calculate the hybridisation.

The change in the SNR with variation in time per step value is very similar to that observed previously for HOPG (Figure 6-16). As the time per step increases the SNR also increases, however the trend is not linear. Increasing the time per step from 1.0 ms to 2.0 ms only increases the SNR from 7.4 to 9.0, with a further increase in time per step to 5.0 ms changing the SNR to 15.0. While this doubling of the SNR provides higher quality hybridisation line scans it takes five times longer to acquire, and the improvement that is achieved may not be worth this increased time cost which also will produce increased electron beam induced damage to the surface. The spectra from the window mode elemental line scans are now examined to determine the changes to the signal to noise ratio as the

time per step changes.

When the spectra from each point of the carbon elemental line scans in Figure 6-18 are averaged they appear very similar (Figure 6-20) with both the signal to noise ratio and positions of the maxima and minima showing little change. The D parameter values in Table 6-6 are quite constant as the time per step value is varied, with values of either 22.6 eV or 22. 8 eV determined for each of the time per step values, which is not a significant change as the uncertainty in the measurement is 0.2 eV.

However, when spectra from individual points along the lines are examined differences are observed in the spectral line shape (Figure 6-20). The spectra from three different points along the line all show higher levels of noise when the time per step is low, however as the time per step increases the signal to noise ratio improves and the spectral quality improves, resulting in more accurate D parameter values. While there is some variation in the D parameter values as the time per step changes at each point (Table 6-6) there is an overall trend towards a D parameter value of 22.8 eV as the time per step increases. The values at each point become closer to 22.8 eV when the step width increases beyond 0.5 ms which suggests that this is the minimum time per step value needed to obtain accurate results. As changes in the signal to noise ratio continue to be observed in the spectra with increasing time per step a value of 5.0 ms is preferred. However, the compromise between acquisition time and spectral quality must be examined, and is made more difficult by the electron beam induced damage that occurs to DLC films.

Figure 6-20: C(KLL) spectra taken from (a) the average of all spectra in the line scan, and point (b) 32, (c) 64, and (d) 96 of the carbon elemental line scans. Each plot shows spectra from line scans of a DLC film with time per step of 0.1 ms (blue), 0.2 ms (red), 0.5 ms (green), 1.0 ms (purple), 2.0 ms (light blue), and 5.0 ms (orange).

Table 6-6: D Parameter values from each spectrum in Figure 6-20.

Time Per Step (ms)	D Parameter (eV) (Average)	D Parameter (eV) (Point 32)	D Parameter (eV) (Point 64)	D Parameter (eV) (Point 96)
0.1	22.6	24.6	22.0	24.6
0.2	22.6	23.8	24.2	25.6
0.5	22.8	23.2	22.6	22.6
1.0	22.6	22.8	21.8	23.0
2.0	22.8	22.2	22.8	23.0
5.0	22.8	23.0	22.8	22.6

The results in Figure 6-18, Figure 6-19, Figure 6-20, and Table 6-6 combine to show that a large value for time per step is preferred to improve the spectral shape and signal to noise ratio of the window mode carbon elemental maps. This will result in a more accurate hybridisation line scan, however the balance between the improvement obtained by increasing the time per step and the increased acquisition time must be considered. Based on these factors, it has been concluded that a time per step value of 1.0 ms is the optimal value as further increases in time per step dramatically increase the acquisition time for little improvement to the spectra.

6.2.3.3 Choice of Time Per Step

By systematically varying the time per step used to acquire the window mode carbon elemental line scans shown in Figure 6-15 and Figure 6-18 it has been found that the time per step value has a large impact on the signal to noise ratio of the spectra, and therefore on the D parameter values. A higher level of spectral noise results in a decreased ability to accurately determine the positions of the maxima and minima for each spectrum, and it was found for both HOPG and DLC that a time per step of 1.0 ms is the minimum value that is needed to obtain data with sufficient resolution to find accurate sp^2 hybridised carbon percentages. Therefore, all window mode carbon elemental line scans for the purpose of determining carbon hybridisation will now be acquired with a time per step of 1.0 ms.

6.2.4   Number of Scans Optimisation

When acquiring a line scan a number of spectra are taken and averaged to obtain the final spectrum at each point along the line. The number of scans chosen influences the counting statistics of the acquisition, and therefore the quality of the spectra obtained. The increase in acquisition time must

again be balanced against the resultant improvement to the spectral shape, and to test this carbon elemental line scans were taken sequentially over the same line using 10, 20, 30, and 40 scans for both HOPG and DLC films.

6.2.4.1 Number of Scans Optimisation – HOPG

Window mode carbon elemental line scans were acquired by averaging 10, 20, 30, or 40 scans over the same area of a HOPG sample and are shown in Figure 6-21, along with the SEM image of the area over which the scans were acquired, the resultant hybridisation line scans, and the SNR values from those line scans. The SEM image shows a 20 μm FOV area of HOPG that consists of several graphene flakes which are evident both through appearance of edges and different coloured areas. The yellow line indicating the line over which the window mode carbon elemental line scans were acquired crosses over several of those flakes but otherwise does not cross any features on the surface. The tests were all acquired sequentially over this line in order of increasing acquisition time.

The window mode carbon elemental line scan acquired using an average of 10 scans is shown in Figure 6-21, and the resultant hybridisation line scan shows an average percentage of approximately 90 % sp^2 hybridised carbon across the line but with values varying between approximately 80 % and 100 % to produce a SNR value of 6.43. These changes in hybridisation observed across the surface do not correlate with the features observed in the SEM image and appear to be quite random, which confirms the conclusion that the features are indeed different flakes of HOPG which appear different in the SEM because of the surface morphology.

An increase to 20 scans results in less variation in the sp^2 percentages across the line, with the range decreasing to approximately 85 % to 95 %, still centred around approximately 90 %. Further increases in the number of scans to 30 and 40 scans results in a small improvement in the range, however the average remains around 90 % sp^2 hybridised carbon. The small variations in the percentage of sp^2 hybridised carbon present across the surface do not correlate with any features in the SEM image such as edges of flakes. The SNR of the hybridisation line scans varies with scan number, and will now be examined further.
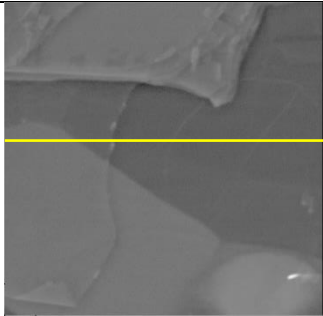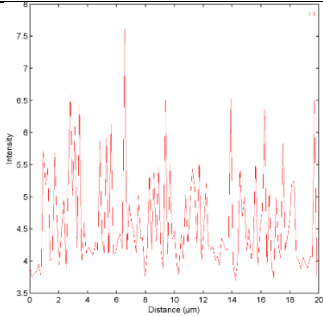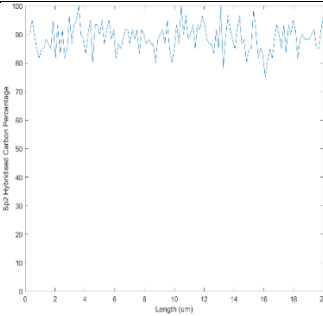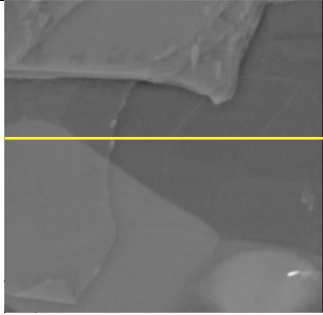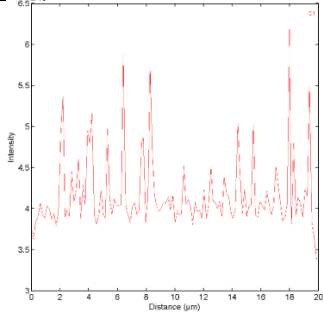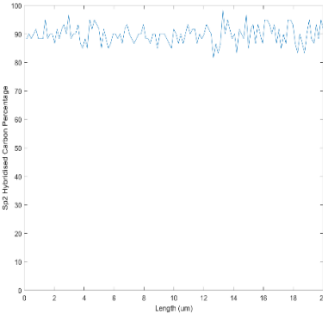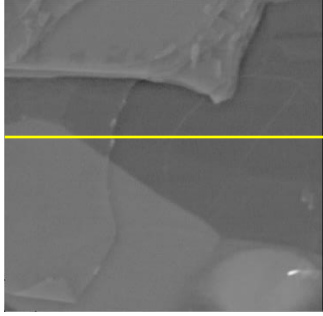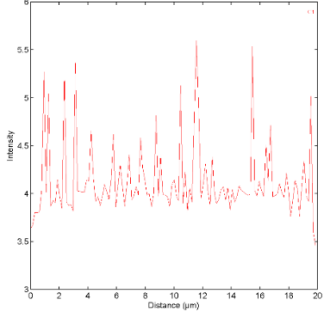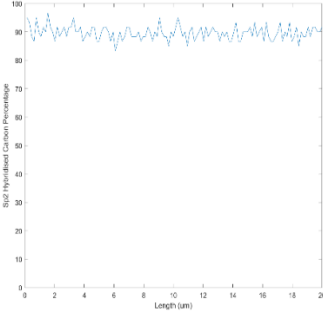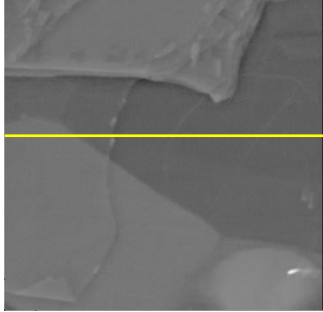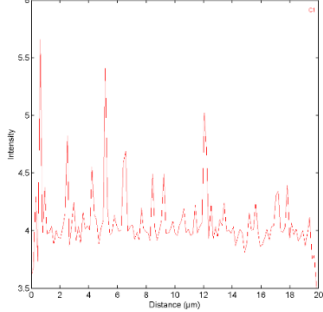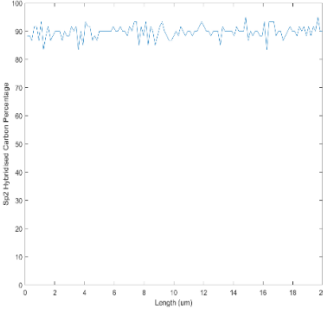
Number of Scans	SEM	Carbon Elemental Line Scan	Hybridisation Line Scan	SNR
10				6.43
20				10.1
30				15.0
40				18.0

Figure 6-21: SEM images (20 μm FOV), C(KLL) elemental line scans, and hybridisation line scans of HOPG with 10, 20, 30, and 30 scans.

The SNR from the hybridisation line scan is plotted against the number of scans averaged during acquisition in Figure 6-22. The SNR increases with a linear trend as the number of scans increases, with 40 scans producing a SNR that is almost double that from 20 scans. These results show that it is desirable to use 30 or 40 scans when acquiring the carbon elemental line scans. The acquisition time increase that occurs with 30 or 40 scans is significant, and therefore the spectra from these line scans need to be examined to determine if this increase in acquisition time produces worthwhile improvement in spectral shape.
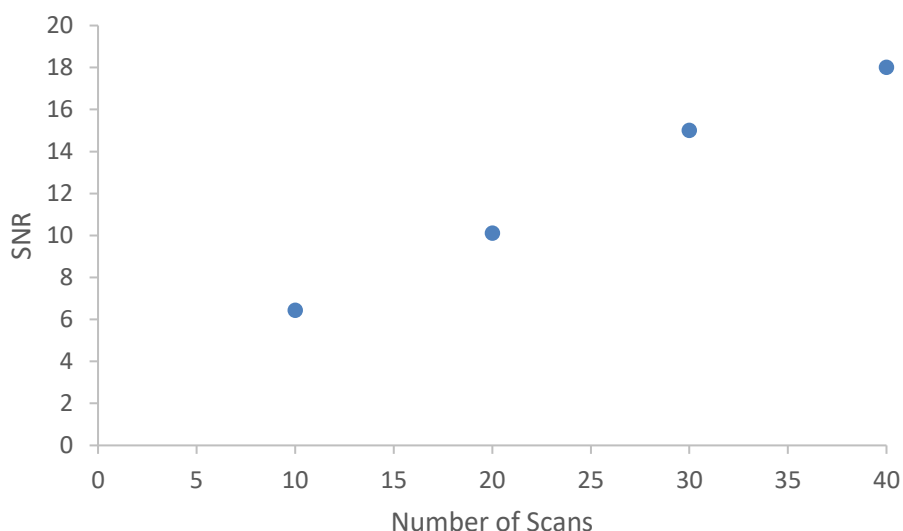
Figure 6-22: Variation in SNR value from hybridisation line scans in Figure 6-21 plotted against the number of scans averaged in the acquisition of the C(KLL) spectra used to calculate the hybridisation.

The spectra from each point of the carbon elemental line scans in Figure 6-21 were averaged and are shown in Figure 6-23 for each number of scans tested. The signal to noise ratio, spectral shape, and width between the maxima and minima appears very similar for each number of scans tested, which is supported by the D parameter values in Table 6-7. The spectrum acquired through the averaging of 10 scans has a D parameter value of 22.6 eV and those using 20, 30, and 40 scans have D parameter values of 22.8 eV. This difference is not considered significant as it falls within the uncertainty of the D parameter measurements (0.2 eV).

Examination of spectra extracted from single points along the window mode carbon elemental line scans show some small differences in the spectral shape and signal to noise ratio (Figure 6-23). The spectral noise is higher when only 10 scans are averaged, however as the number of scans is increased to 20, 30, or 40 there isn't any further improvement observed in the signal to noise ratio. There are some differences in the fine structure of the spectra as the number of scans averaged changes, however the positions of the maxima and minima do not change to a large extent. This is confirmed in the D parameter values in Table 6-7, which do not vary to a large extent but do show some small changes. These changes are not systematic, however the D parameter values trend towards 22.8 eV as the number of scans averaged increases.
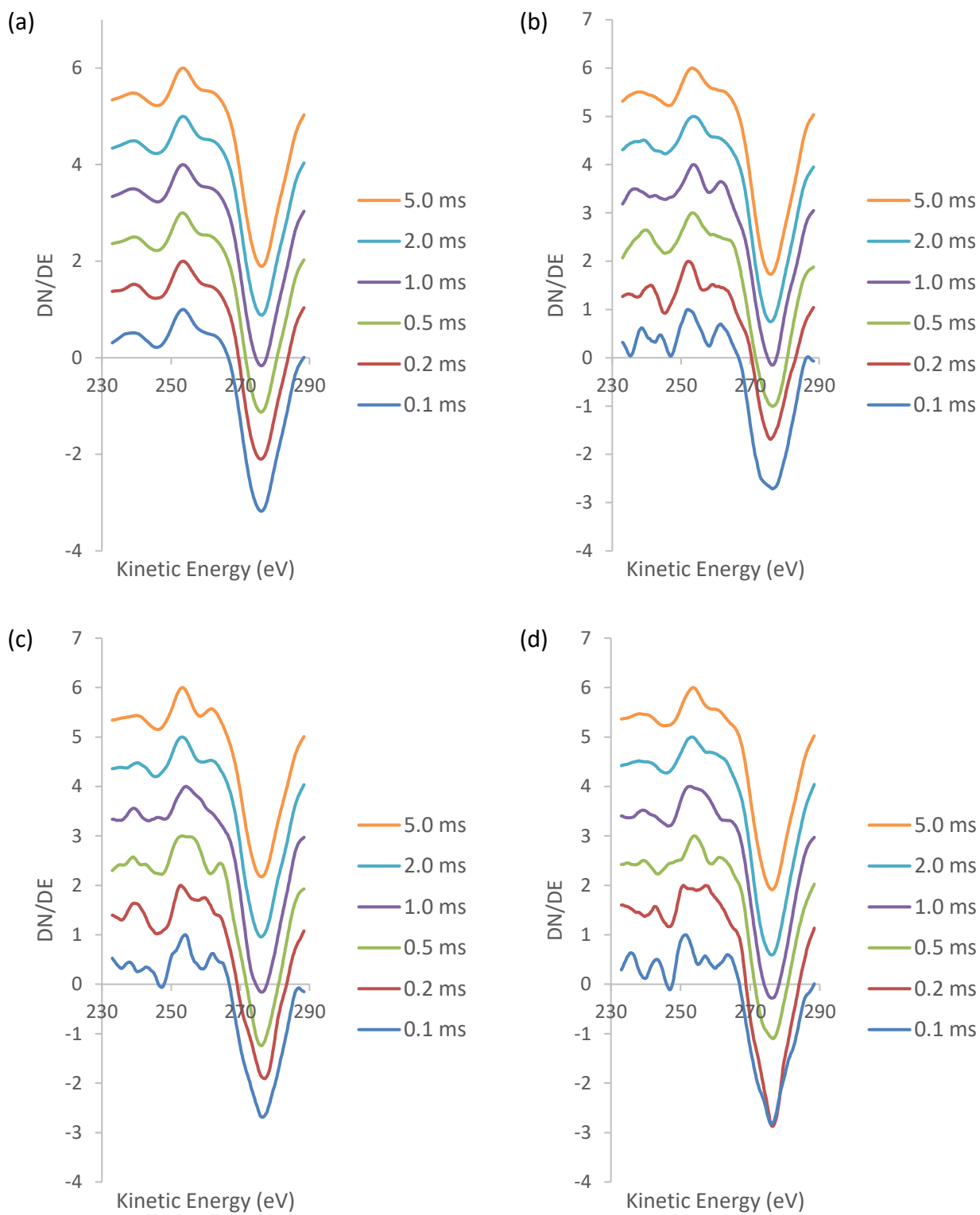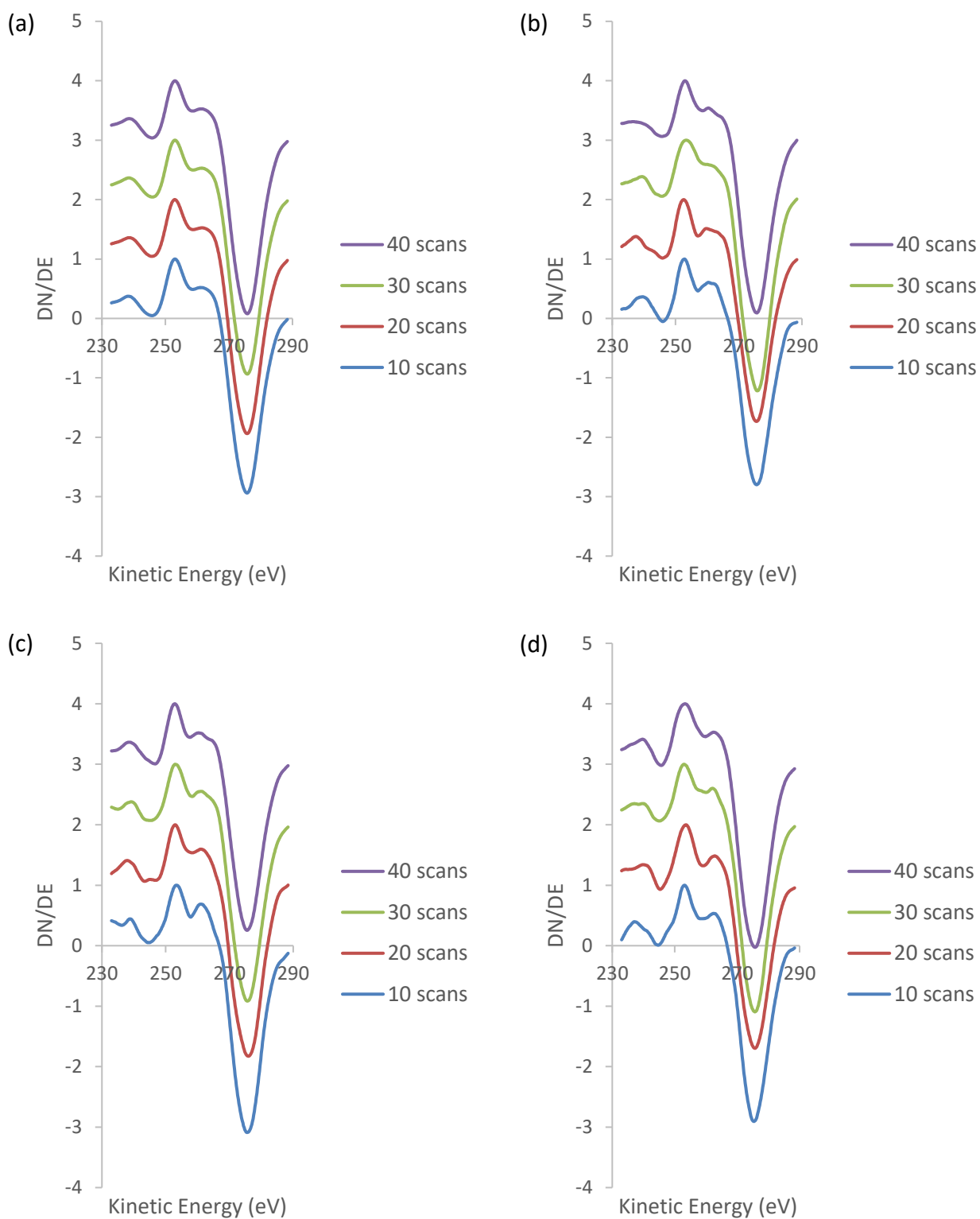
Figure 6-23: C(KLL) spectra taken from (a) the average of all spectra in the line scan, and point (b) 32, (c) 64, and (d) 96 of the carbon elemental line scans. Each plot shows spectra from line scans of HOPG with 10 scans (blue), 20 scans (red), 30 scans (green), and 40 scans (purple).

Table 6-7: D Parameter values from each spectrum in Figure 6-23.

Number of Scans	D Parameter (eV) (Average)	D Parameter (eV) (Point 32)	D Parameter (eV) (Point 64)	D Parameter (eV) (Point 96)
10	22.6	22.8	22.2	22.2
20	22.8	23.0	23.0	22.2
30	22.8	22.4	22.6	22.8
40	22.8	22.8	22.6	22.4

The results from Figure 6-21, Figure 6-22, Figure 6-23, and Table 6-7 combine to show that the number of scans averaged when acquiring the window mode carbon elemental line scans is an important factor in the quality of the spectra produced. An increase in the number of scans results in an improvement in the signal to noise ratio, and therefore an improvement in the determination of the D parameter, however the improvement comes at the cost of increased acquisition time. These results suggest that the optimal number of scans to use is 20, as it reduces the spectral noise significantly over 10 scans but further increases above 20 scans do not produce improvement that justifies the increase in acquisition time.

6.2.4.2 Number of Scans Optimisation – DLC

Window mode carbon elemental line scans were acquired on a DLC film using 10, 20, 30, or 40 scans averaged, with the results shown in Figure 6-24 along with the SEM image of the area over which the scans were acquired and the resultant hybridisation line scans. The 20 µm FOV SEM image shows surface of the DLC film, which appears almost entirely featureless, however there is one particle present near the centre. The yellow line on the SEM image indicates the area over which the line scans were acquired and passes through the featureless area of the surface.

The window mode carbon elemental line scan acquired with an average of 10 scans is shown in Figure 6-24, and the resultant sp^2 hybridised carbon percentage line scan shows an average sp^2 carbon percentage of approximately 85 %, however values vary between approximately 70 % and 100 %. This variation in the hybridisation occurs randomly across the line, with no area showing consistently higher percentages than the other, resulting in a SNR value of 4.45.

Increasing the number of scans to 20 shows a decrease in the range of percentages of sp^2 carbon from approximately 80 % to 100 %, with the average at around 88 %. Further increases in the scan

number continue to reduce the range of percentages observed and the average increases to approximately 90 %, suggesting that some electron beam induced graphitisation is occurring. The SNR is now considered to provide further information on the variation in the hybridisation line scans.

Number of Scans	SEM	Carbon Elemental Line Scan	Hybridisation Line Scan	SNR
10				4.45
20				8.09
30				11.3
40				15.0
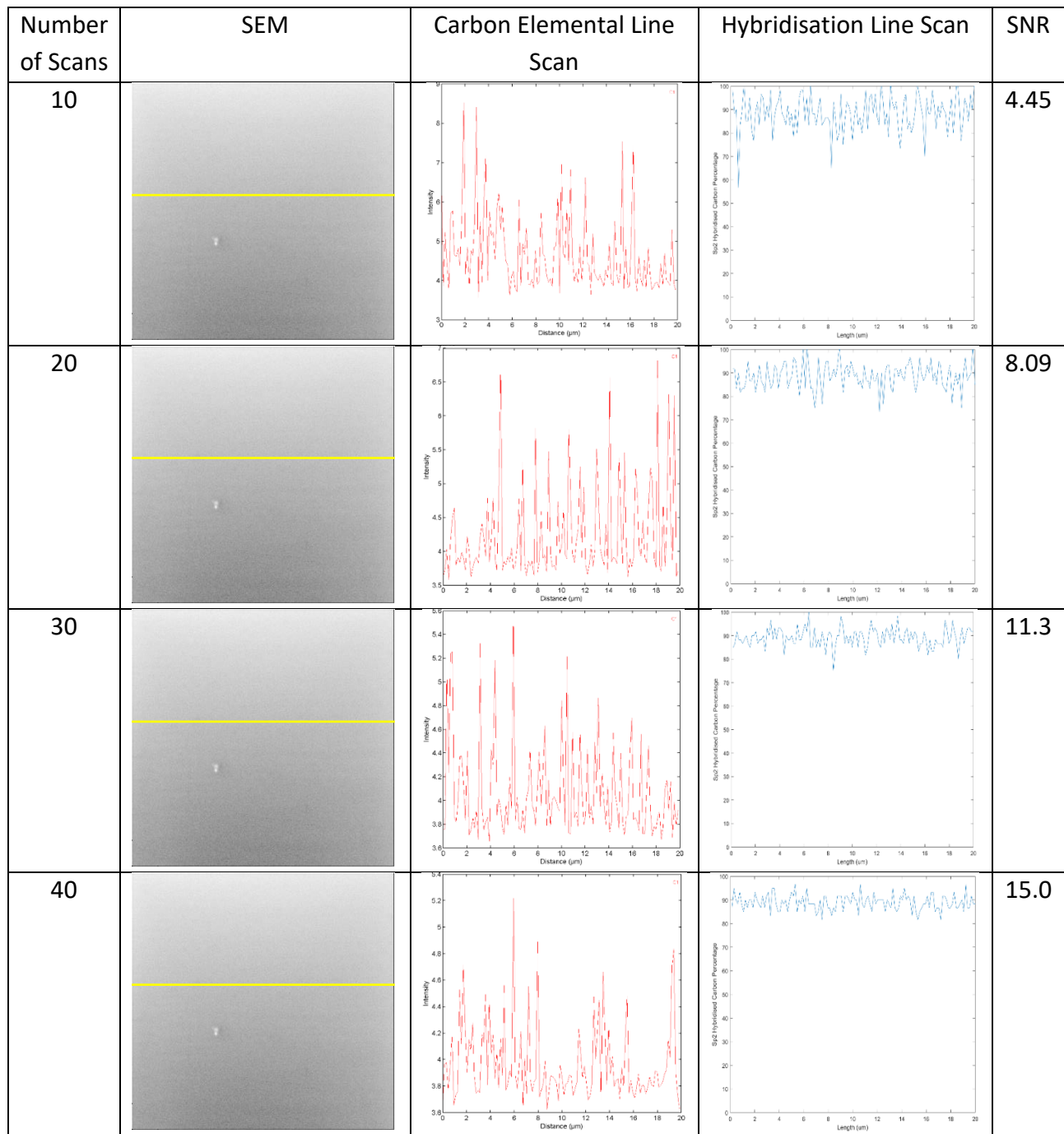
Figure 6-24: SEM images (20 µm FOV), C(KLL) elemental line scans, and hybridisation line scans of a DLC film with 10, 20, 30, and 30 scans.

The variation in SNR value with number of scans averaged during carbon elemental line scan acquisition is plotted in Figure 6-25. There is a linear trend linking an increase in the number of scans used to acquire the line scan and the SNR of the hybridisation line scan, with the SNR almost
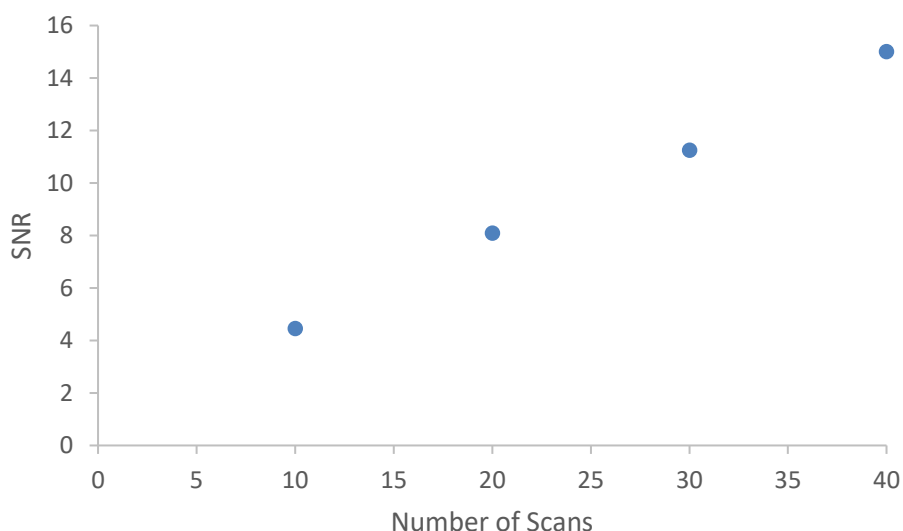
Figure 6-25: Variation in SNR value from hybridisation line scans in Figure 6-24 plotted against the number of scans averaged in the acquisition of the C(KLL) spectra used to calculate the hybridisation.

doubling as the number of scans doubles. This is the same trend that was observed for HOPG (Figure 6-22) and suggests that 30 or 40 scans would be the best number to use. As this increase in the number of scans would result in a much longer acquisition time the spectra extracted from the carbon elemental line scan will be examined to determine if this increase in acquisition time is worthwhile.

The spectra from each point of the carbon elemental line scans in Figure 6-24 are averaged and are shown in Figure 6-26. The spectral shape from each of the numbers of scans tested appears very similar in regards to both the signal to noise ratio and the positions of the maxima and minima. This suggests that the D parameter values for each spectrum will be very similar, which is confirmed in Table 6-8 where it can be seen that the D parameter is 22.6 eV for the 20 scan spectrum, while it is 22.8 eV for all other spectra. The difference between these values is only 0.2 eV, which is the same as the uncertainty in the measurements, and the D parameter values are therefore not significantly different.

However, examination of spectra from individual points along the carbon elemental line scan show some differences for different numbers of scans. Each of the spectra averaged from 10 scans show a higher spectral noise level than those with higher scan numbers as well as a slightly different shape for the maxima and minima. However, the spectral shape does change to a large extent as the number of scans averaged increases past 20 scans. The D parameter values do change somewhat as the scan number increases, with an overall increasing trend observed at all three points. The three

293

points all have slightly different D parameter values but all trend towards 23.0 eV as the number of scans averaged increases.

Figure 6-26: C(KLL) spectra taken from (a) the average of all spectra in the line scan, and point (b) 32, (c) 64, and (d) 96 of the carbon elemental line scans. Each plot shows spectra from line scans of a DLC film with 10 scans (blue), 20 scans (red), 30 scans (green), and 40 scans (purple).

Table 6-8: D Parameter values from each spectrum in Figure 6-26.

Number of Scans	D Parameter (eV) (Average)	D Parameter (eV) (Point 32)	D Parameter (eV) (Point 64)	D Parameter (eV) (Point 96)
10	22.8	22.6	21.2	22.0
20	22.6	22.6	23.0	22.4
30	22.8	22.8	22.2	22.6
40	22.8	23.2	23.2	23.0

The results from Figure 6-24, Figure 6-25, Figure 6-26, and Table 6-8 combine to show the impact of changing the number of scans averaged when acquiring the window mode carbon elemental line scans. An increase in the number of scans used results in an improvement of the signal to noise ratio which makes the positions of the maxima and minima, and therefore the D parameter value, more accurate. This suggests that averaging 40 scans would be the best option for the line scan acquisition, but the acquisition time then becomes very large and for DLC films there is also an increase in the level of electron beam induced damage to the surface. By examining all of the above results it is concluded that an average of 20 scans is a good compromise between spectral shape improvement and acquisition time as it offers the most significant improvement in a reasonable time.

6.2.4.3 Choice of Number of Scans

The window mode carbon elemental line scans in Figure 6-21 and Figure 6-24 show the systematic variation of the number of scans averaged to acquire the line scans. These results show the impact of the number of scans on the signal to noise ratio and spectral shape, and therefore on the D parameter values. An increase in the number of scans improves the signal to noise ratio and makes the positions of the maxima and minima clearer, however the improvement gained when the number of scans goes above 20 for both HOPG and DLC is not large enough to justify the increase in acquisition time. Therefore, all window mode carbon elemental line scans will now be acquired by averaging 20 scans.

6.2.5 Constant Total Scan Time

The previous sections of this chapter have shown optimisation of the scan parameters that produce

the best quality window mode carbon elemental line scans in a reasonable acquisition time. These parameters are a time per step of 1.0 ms, a step width of 0.2 eV, and 20 scans averaged. This combination of parameters results in a total acquisition time of 20 ms at each energy step in the spectra obtained, however there are a range of parameter combinations that can result in this total time at each step. This range of parameters will now be examined to determine if the achieving the same total time in a different way alters the results.

6.2.5.1 Constant Total Scan Time – HOPG

Window mode carbon elemental line scans were acquired on HOPG using a variety of time per step values and numbers of averaged scans such that the total acquisition time at each energy step is 20 ms. These scans are shown in Figure 6-27, along with the 20 μm SEM image of the area of HOPG where the scans were acquired, the resultant hybridisation line scans, and the SNR values of those line scans. The SEM image shows several graphite flakes that have small, slightly darker lines randomly distributed across the surface, which look like slight folds in the graphite sheets. The yellow line in the SEM image indicates the line over which the window mode carbon elemental line scans were acquired and crosses a single graphene flake but also several of the small darker lines.

The sp^2 hybridised carbon percentage line scans in Figure 6-27 all appear very similar, with an average sp^2 content of approximately 90 % and values ranging between approximately 85 % and 95 %. This suggests that the total scan time is what is important, and the parameters used to achieve this total time are not vital. However, when the SNR values are calculated for the hybridisation line scans some variation is observed.
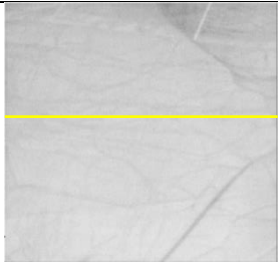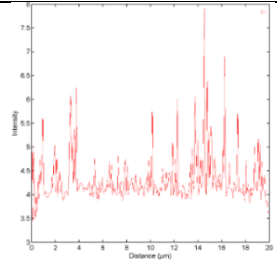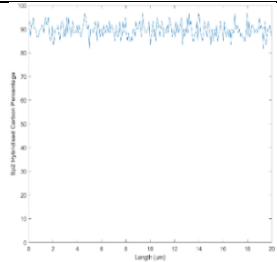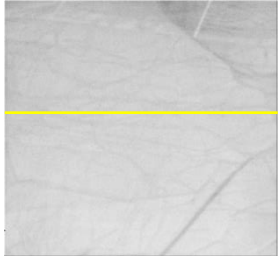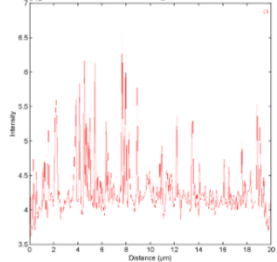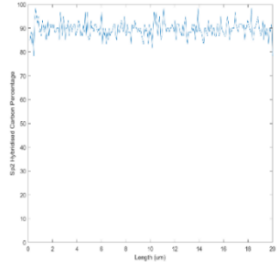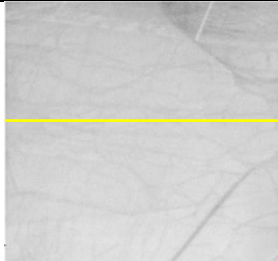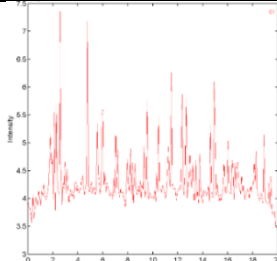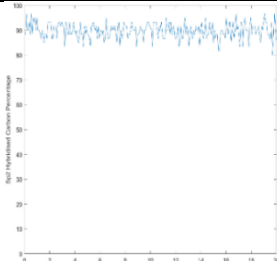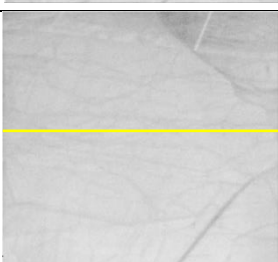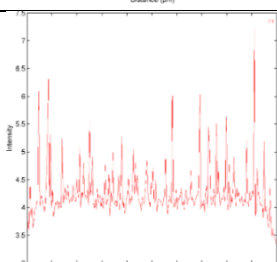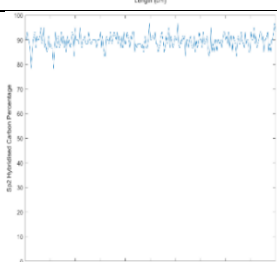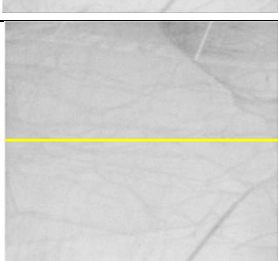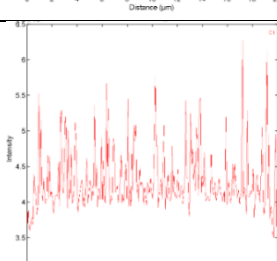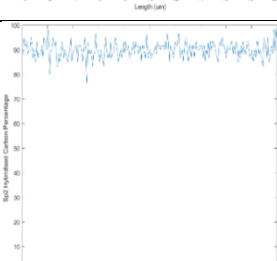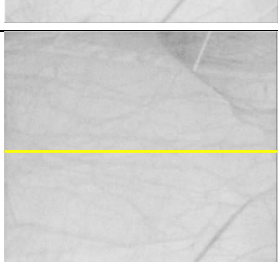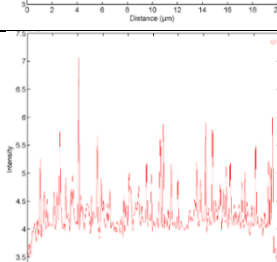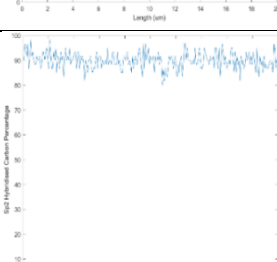
TPS (ms)	Number of Scans	SEM	Carbon Elemental Line Scan	Hybridisation Line Scan	SNR
10	2				10.0
5	4				11.3
2	10				22.5
1	20				18.0
0.5	40				12.9
0.2	100				11.4

Figure 6-27: SEM images (20 µm FOV), C(KLL) elemental line scan, and hybridisation line scans for HOPG taken with various values of time per step and repeat scan numbers such that the total scan acquisition time remains constant.

As there are two variables that are being varied to achieve the same total time one of the variables was chosen to plot with the SNR values to examine any trend that occurs. The time per step variable was chosen, and the result is plotted in Figure 6-28.
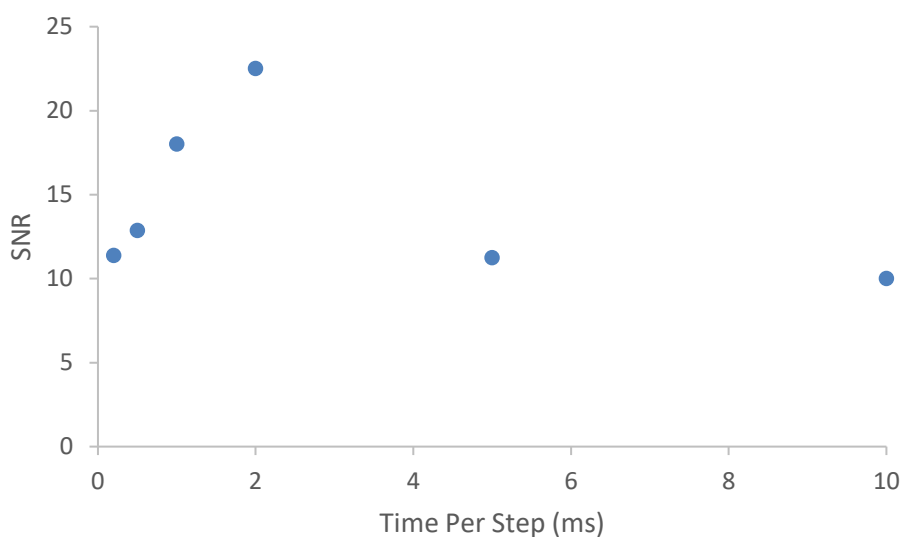
Figure 6-28: Variation in SNR value from hybridisation line scans in Figure 6-27 plotted against the time per step of the C(KLL) spectra used to calculate the hybridisation.

There is an interesting trend that occurs in the SNR as the time per step and number of scans is varied, with the combinations of 1.0 ms time per step and 20 scans or 2.0 ms time per step and 10 scans both producing higher SNR values than any of the other combinations, which suggests that the way that the total dwell time is arrived at is important. However, the spectra obtained in the carbon elemental line scans will be examined to determine if the spectral shape is impacted by these changes in scanning parameter.

The average spectra of each of the carbon elemental line scans in Figure 6-27 are shown in Figure 6-29 and have very similar shapes in terms of the signal to noise ratio and the positions of the maxima and minima. The D parameter values in Table 6-9 also are very similar, with all tests showing a value of 22.8 eV except for that with 1.0 ms time per step averaged 20 scans which has a D parameter value of 22.6 eV, which is not significantly different due to the uncertainty of 0.2 eV in the measurement.

When the spectra from individual points along the line scans are examined some differences are found, however these differences are mainly in the fine structure of the peaks while the signal to noise ratio and positions of the maxima and minima remain fairly constant. The differences in the fine structure show no clear trend, however they are consistent across each point for the same

variable choice.
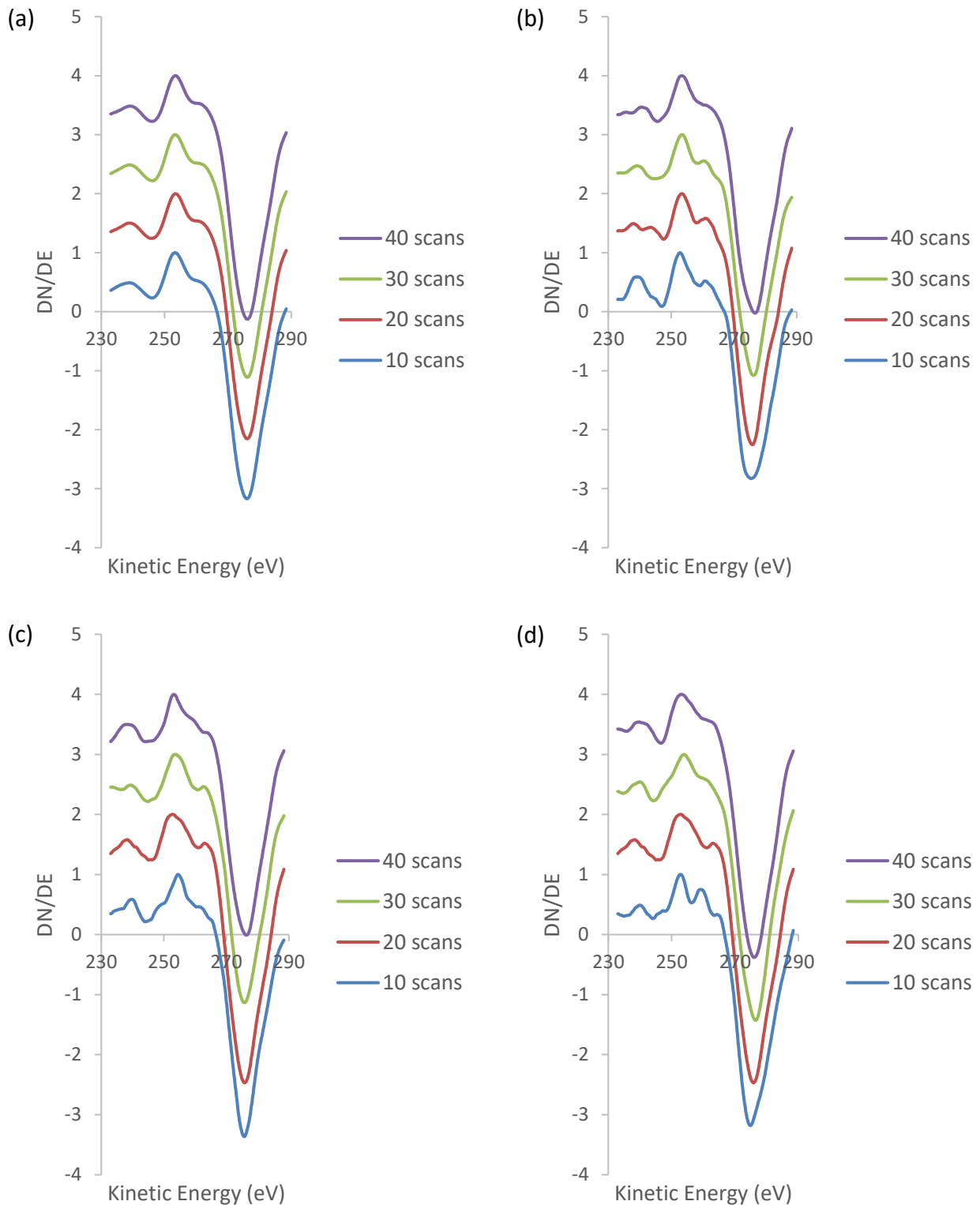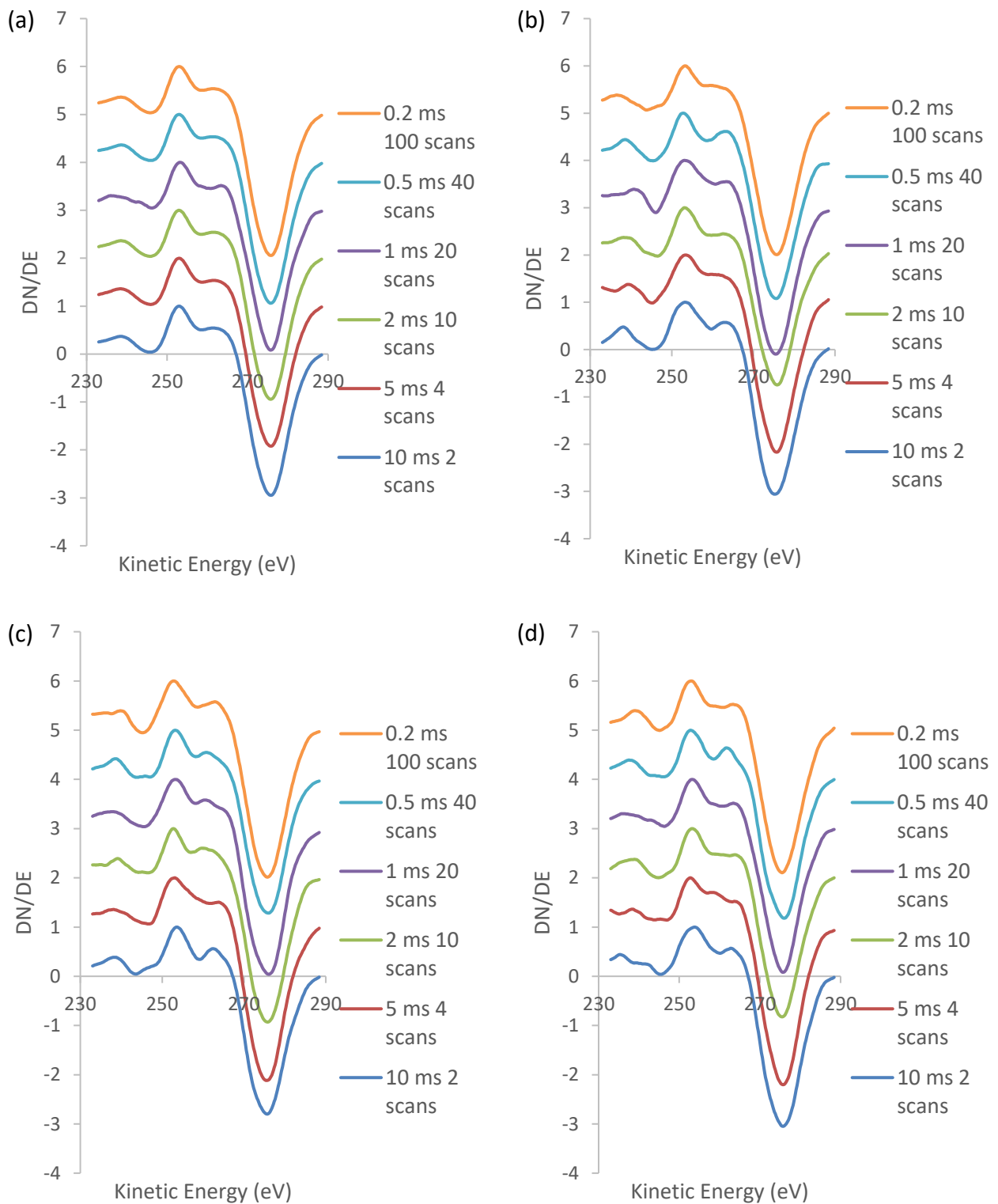

Figure 6-29: C(KLL) spectra taken from (a) the average of all spectra in the line scan, and point (b) 64, (c) 128, and (d) 192 of the line scans of HOPG. Each plot shows spectra with various values of time per step and repeat scan numbers such that the total scan acquisition time remains constant.

When comparing the D parameter values in Table 6-9 it can be seen that there is some variation

when the time per step and number of scans are changed. The D parameter values are around 22.6 eV for parameter choices of 1.0 ms time per step and 20 scans averaged, and it is this pairing that produces the most consistent results. As the pairings go to either extreme, that is, a high time per step and low scan number or a low time per step and high scan number, the results are more varied. This suggests that the middle of the range pairings are the most suitable, and as such it is concluded that the time per step of 1.0 ms and 20 averaged scans are the best choice for acquiring the window mode carbon elemental line scans.
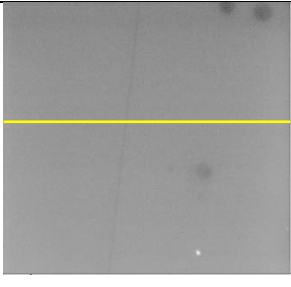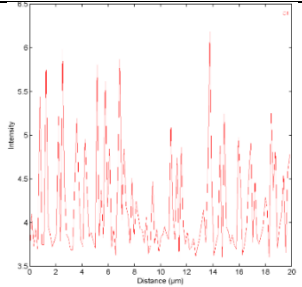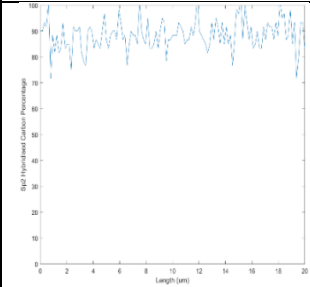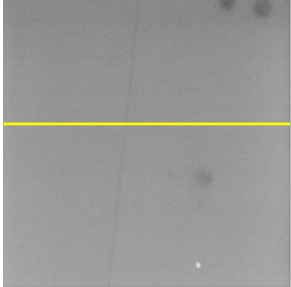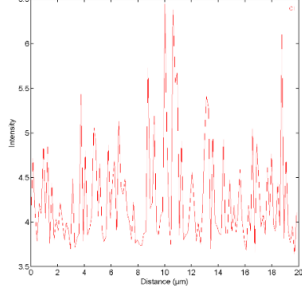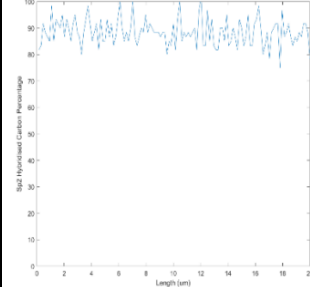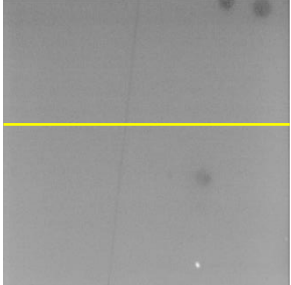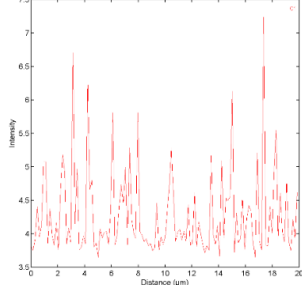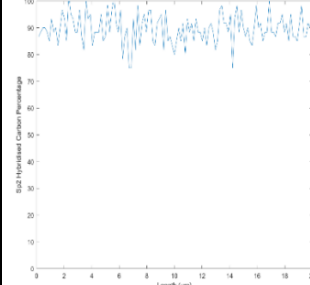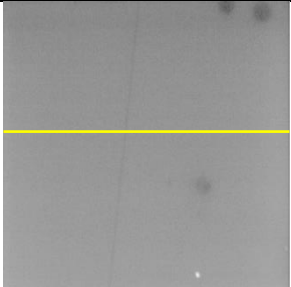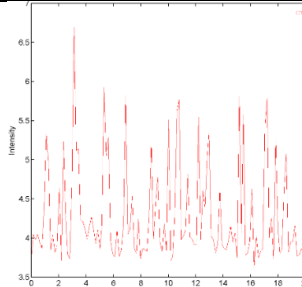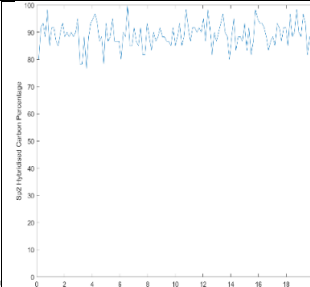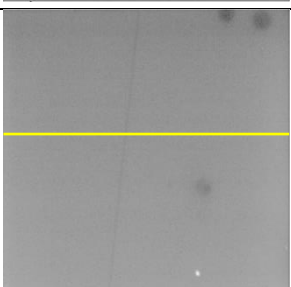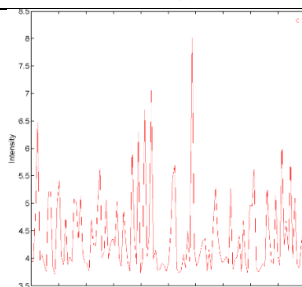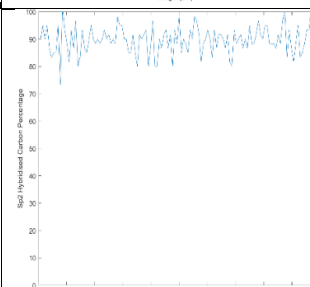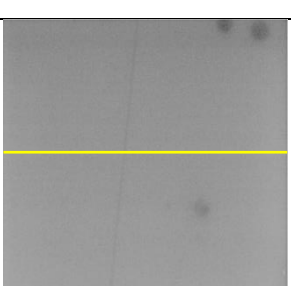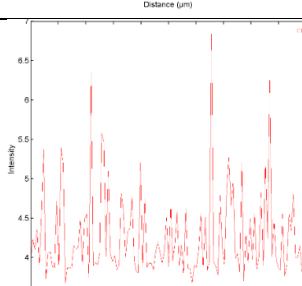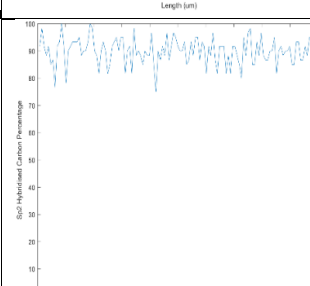
Table 6-9: D Parameter values from each spectrum in Figure 6-29.

Time Per Step (ms)	Number of Scans	D Parameter (eV) (Average)	D Parameter (eV) (Pixel 272)	D Parameter (eV) (Pixel 558)	D Parameter (eV) (Pixel 784)
10	2	22.8	21.8	22.0	22.0
5	4	22.8	22.2	22.4	23.0
2	10	22.8	22.6	23.0	22.2
1	20	22.6	22.6	22.8	22.6
0.5	40	22.8	22.8	22.8	23.2
0.2	100	22.8	22.6	23.0	22.4

Through comparison of the data in Figure 6-27, Figure 6-28, Figure 6-29, and Table 6-9 the influence of changing the time per step and averaged scan number while maintaining the same total acquisition time at each energy value can be observed. It was found that there were some differences in the SNR values and fine structure of the spectra when the time per step and scan numbers were changed, and the most consistent results are obtained using scanning parameters of 1.0 ms time per step and 20 scans averaged.

6.2.5.2 Constant Total Scan Time – DLC

The total scan time was again held constant while varying the time per step and number of scans used to obtain carbon elemental line scans of a DLC sample. The SEM image in Figure 6-30 shows the 20 μm area over which the scans were acquired, which appears to be mostly uniform with the exception of several small darker circles and a large particle. However, the yellow line showing the line where the elemental line scans were acquired does not pass through any of these features. The carbon elemental line scans, the resultant hybridisation line scans, and the SNR values of the hybridisation line scans for all the parameter combinations tested are also shown in Figure 6-30.

TPS (ms)	Number of Scans	SEM	Carbon Elemental Line Scan	Hybridisation Line Scan	SNR
10	2				6.34
5	4				7.50
2	10				7.50
1	20				10.0
0.5	40				7.50
0.2	100				7.50

| 0.1 | 200 | | | | 6.43 |
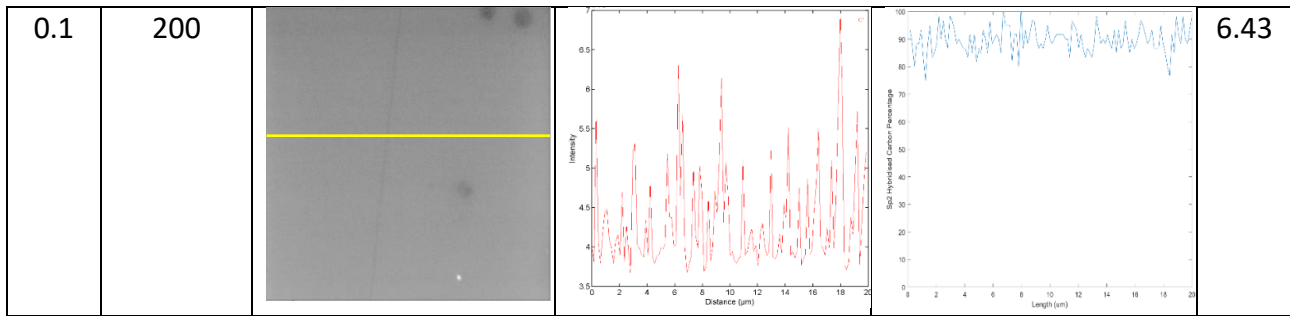
Figure 6-30: SEM images (20 µm FOV), C(KLL) elemental line scan, and hybridisation line scans for a DLC film taken with various values of time per step and repeat scan numbers such that the total scan acquisition time remains constant.

Examination of all the hybridisation line scans shows that there are some differences in the values at each point of the line, but there is no systematic change in either the point values, range of values, or average value when the time per step and number of scans combinations are changed. The average sp^2 hybridised carbon percentage across each line varies between approximately 88 % and 90 %, with values mostly varying between 80 % and 100 %. Based on these line scans it does not appear that using different parameters to achieve the same total acquisition time significantly changes the hybridisation line scan, however there is some difference in the SNR values.

The SNR is plotted against the time per step in Figure 6-31, although both the time per step and number of scans is changing only one of the variables needs to be plotted to examine the trend in the SNR values.
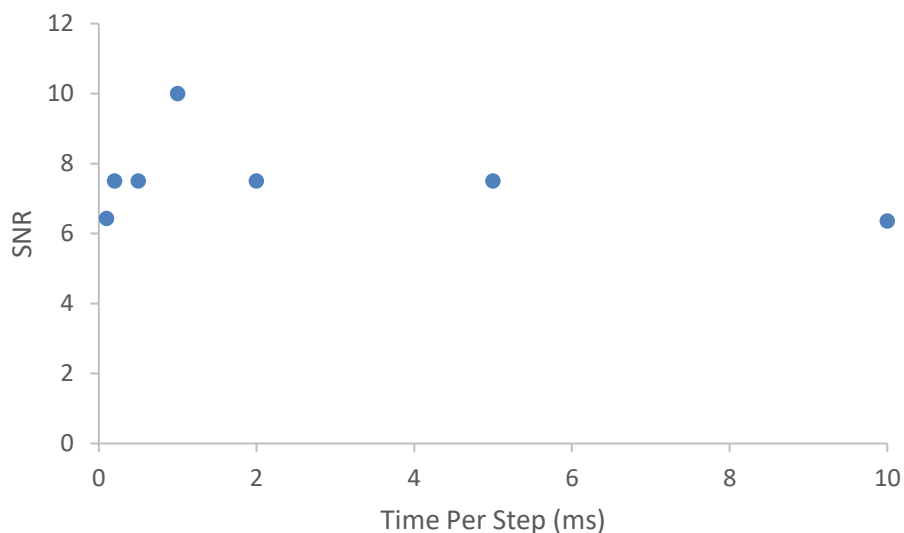
Figure 6-31: Variation in SNR value from hybridisation line scans in Figure 6-30 plotted against the time per step of the C(KLL) spectra used to calculate the hybridisation.

In Figure 6-31 there is one data point that is significantly higher than the others, and this point

corresponds to a combination of 1.0 ms time per step and 20 scans averaged. This result suggests that this combination of scanning parameters leads to the highest quality hybridisation line scans for the same total acquisition time, however examination of the spectra needs to be performed to determine if there are any changes in the spectral shape or signal to noise ratio.

The average spectra produced by averaging every point of each line in Figure 6-30 is shown in Figure 6-32. All of the spectra have very similar line shapes and produce very similar D parameter values, as shown in Table 6-10, where values of 22.6 eV or 22.8 eV are shown for all of the spectra, which is not significant as the uncertainty in the D parameter values is 0.2 eV. Examination of spectra for each parameter combination from individual points on the line (Figure 6-32) show some variations in the line shape, particularly in the fine structure but also in the shape and position of several of the maxima and minima. However, there appears to be no clear trend in any of these changes or in the resultant D parameter values in Table 6-10. Examination of the D parameter values in Figure 6-17 show that the parameter combinations with middle range values show the most consistency between samples. This trend is the same as that reached using the HOPG sample, and suggests that a choice of 1.0 ms time per step and 20 scans is the best pair of parameter values to use.
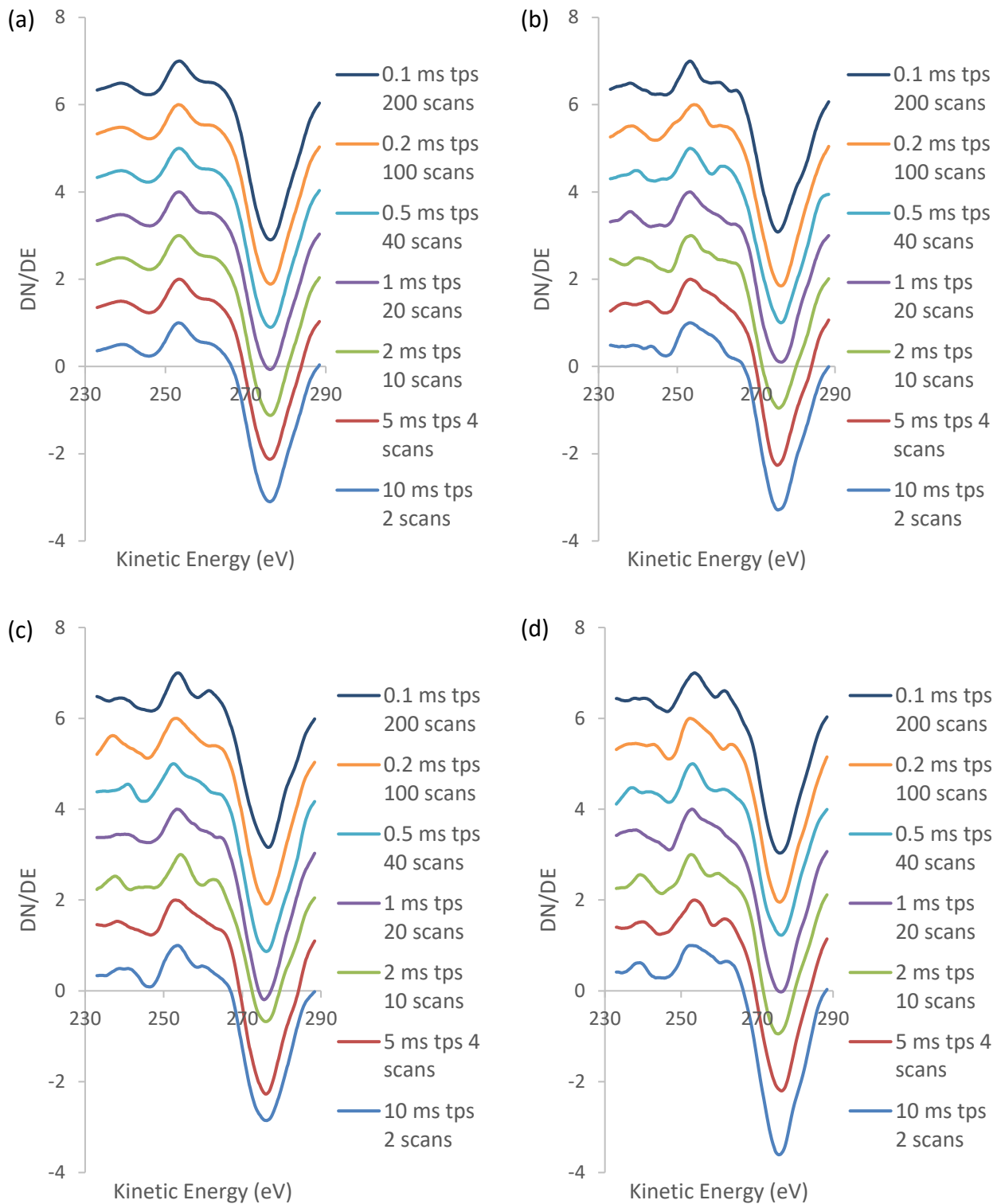
Figure 6-32: C(KLL) spectra taken from (a) the average of all spectra in the line scan, and point (b) 64, (c) 128, and (d) 192 of the line scans of a DLC film. Each plot shows spectra with various values of time per step and repeat scan numbers such that the total scan acquisition time remains constant.

Table 6-10: D Parameter values from each spectrum in Figure 6-32.

Time Per Step (ms)	Number of Scans	D Parameter (eV) (Average)	D Parameter (eV) (Pixel 272)	D Parameter (eV) (Pixel 558)	D Parameter (eV) (Pixel 784)
10	2	22.6	22.4	22.6	23.6
5	4	22.6	22.2	23.0	22.8
2	10	22.8	22.4	21.6	22.8
1	20	22.6	23.2	22.2	23.2
0.5	40	22.8	23.0	23.8	23.4
0.2	100	22.8	21.8	23.0	23.6
0.1	200	22.8	22.4	22.8	22.4

Through examination of the data in Figure 6-30, Figure 6-31, Figure 6-32, and Table 6-10 some differences have been observed in the window mode carbon elemental line scans obtained using different values for time per step or number of scans but the same total acquisition time at each point. This data shows that the highest SNR and highest level of consistency is achieved when a time per step of 1.0 ms and 20 scans averaged are used to obtain the window mode carbon elemental line scans.

6.2.5.3 Parameter Choice for Same Total Scan Time

The window mode carbon elemental line scans in Figure 6-27 and Figure 6-30 were obtained through systematic variation of the time per step and number of scans averaged while maintaining the total acquisition time at each energy point at 20 ms. The results show that there is some variation in the positions of the maxima and minima, and therefore on the D parameter, as the parameters are varied for both HOPG and DLC. It was found that the best SNR and the most consistency is achieved when the parameters are set to values in the middle of their ranges, and it was therefore concluded that the best choice of parameters are 1.0 ms time per step and 20 scans averaged. These parameter values will therefore be used for the acquisition of the window mode carbon elemental line scans for the purpose of creating carbon hybridisation line scans.

6.2.6   Magnification Level Dependence

All of the data shown in this chapter so far has been obtained using a FOV, and therefore a line scan length, of 20 um, as this is the level of magnification that is most useful for examining carbon
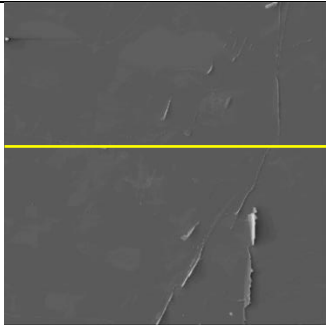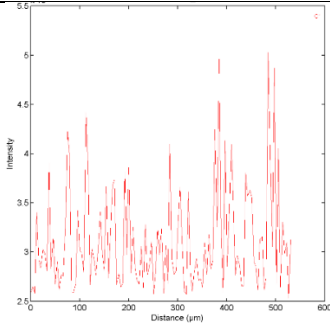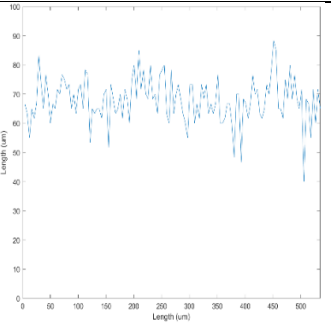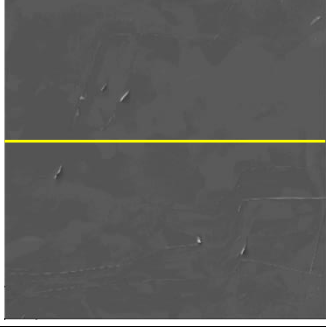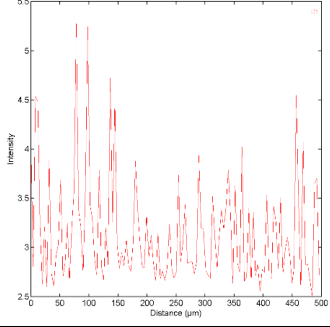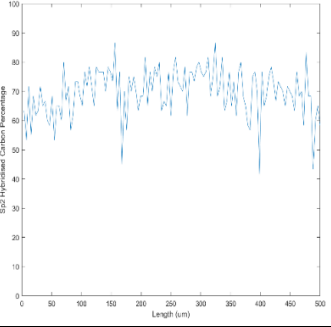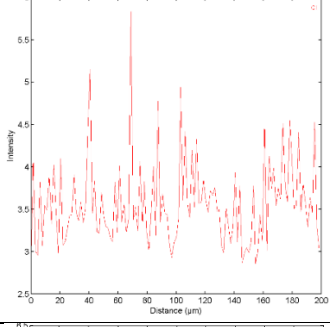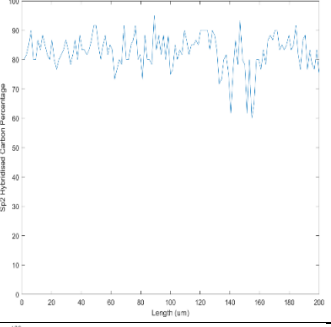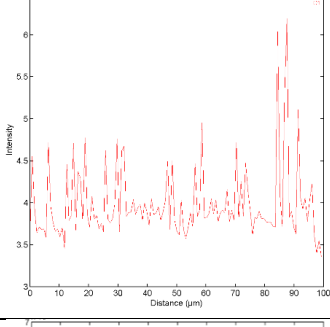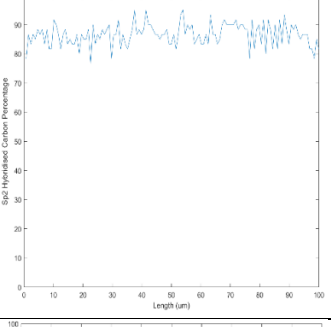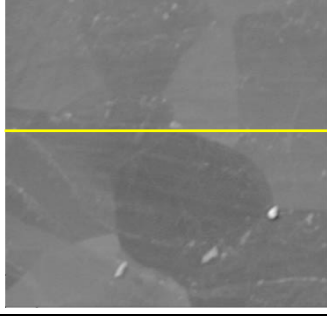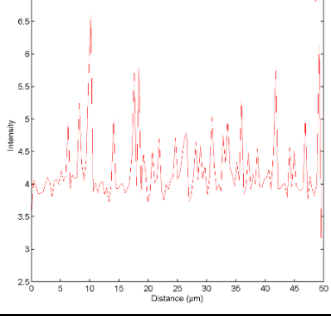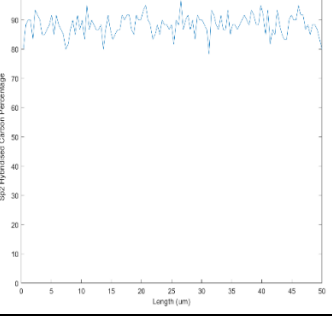
structures such as graphene flakes and nanodiamonds. However, it has been observed that the level of magnification at which the window mode carbon elemental line scans are acquired influences the shape of the spectra obtained, and therefore the D parameter and the sp^2 hybridised carbon percentage value that is calculated. To examine this systematically carbon elemental line scans were collected with FOVs of 535, 500, 200, 100, 50, 20, and 10 µm for both HOPG and DLC.

6.2.6.1 Magnification Level Dependence – HOPG

The SEM image of the 535 µm FOV area examined on a HOPG sample is shown in Figure 6-33, with the yellow line showing the line over which the window mode carbon elemental line scan was taken. This line does not cross any significant features, although it is likely that there are sheet edges and other features that are not visible at this scale. The window mode carbon elemental line scan and resultant hybridisation line scan are also shown in Figure 6-33. The hybridisation shown across this sample is on average approximately 70 % sp^2 hybridised carbon, with values ranging between approximately 50 % and 90 % resulting in a low SNR value of 3.50. The average percentage is much lower than that observed previously for HOPG and the range of the data is much higher, suggesting that at this level of magnification the method used to calculate sp^2 percentage is not accurate. The results for a 500 µm FOV are very similar to the 535 µm FOV, however further increase of magnification to 200 µm results in a significant change in the hybridisation percentages observed.

The SEM image of the 200 µm FOV area is shown in Figure 6-33 and shows that the line over which the carbon elemental scan is acquired is a mostly featureless area, but does cross some areas with slight colour differences that indicates different graphite flakes. The window mode carbon elemental scan and resultant hybridisation line scan are also shown in Figure 6-33 and show an average sp^2 hybridised carbon percentage of approximately 85 % and a range of approximately 65 % to 90 %. These values are much closer to the expected values for HOPG, however the range is much larger than those shown previously for HOPG at higher magnifications.

A further increase in magnification to a FOV of 100 µm shows results that match what is expected based on the previous line scans of HOPG at a high level of magnification. The SEM image, window mode carbon elemental line scan, and resultant hybridisation line scan are shown in Figure 6-33, with the average sp^2 carbon percentage of approximately 88 % and a range of approximately 80 % to 95 %. Increasing the magnification to a FOV of 50 µm results in an average carbon hybridisation percentage of approximately 90 % and a range of approximately 85 % to 95 %, and these numbers are the same when the magnification is further increased to 20 µm and 10 µm (Figure 6-33).

FOV (um)	SEM	Carbon Elemental Line Scan	Hybridisation Line Scan	SNR
535				3.50
500				4.24
200				7.08
100				8.70
50				9.78

| 20 | | | | 11.3 |
| 10 | | | | 12.9 |
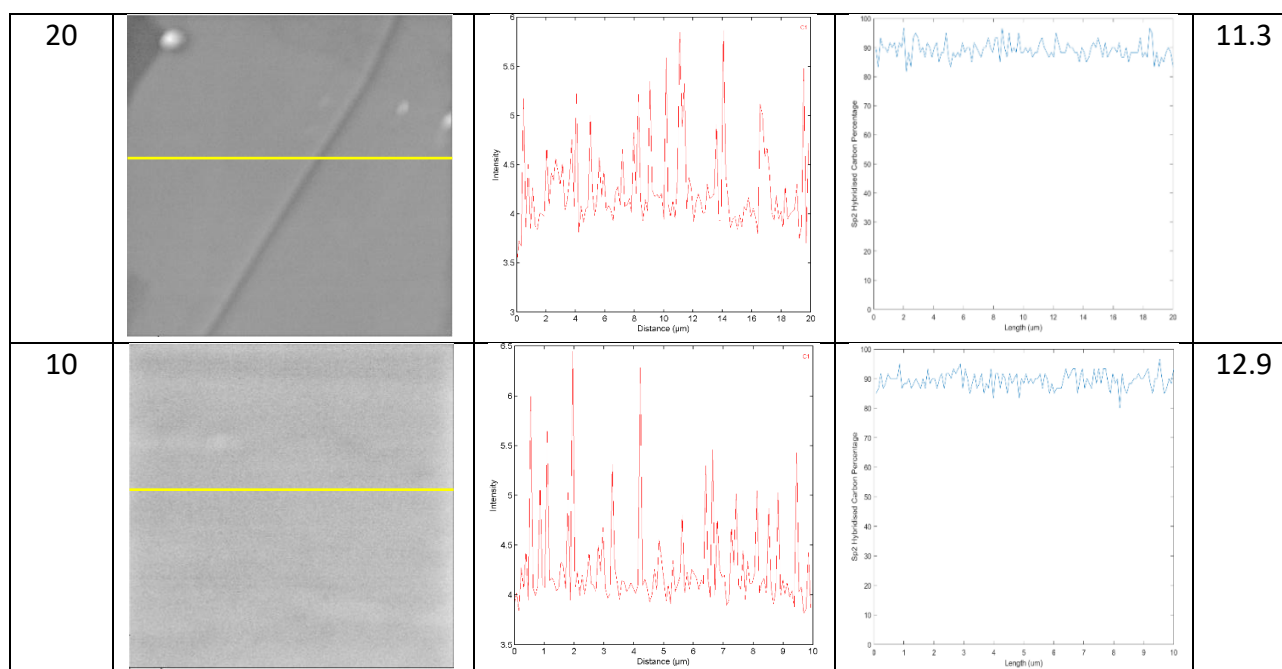
Figure 6-33: SEM images, C(KLL) elemental line scans, and hybridisation line scans for HOPG taken with FOV of 535 um, 500 um, 200 um, 100 um, 50 um, 20 um, and 10 um.

This variation in the average hybridisation percentage and variation results in changes to the SNR ratio, which will now be compared for the different magnification levels in Figure 6-34.
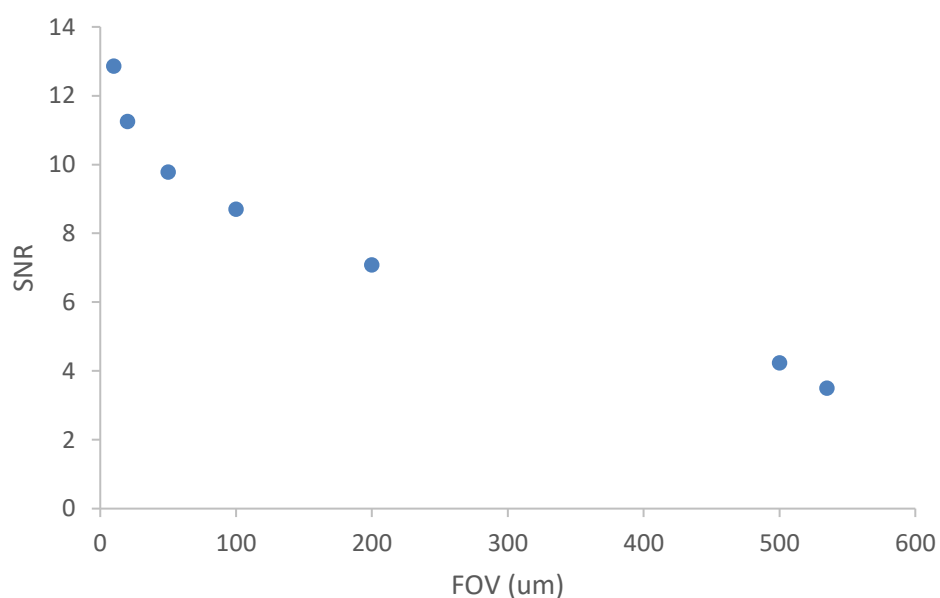
Figure 6-34: Variation in SNR value from hybridisation line scans in Figure 6-33 plotted against the FOV of the hybridisation line scan.

It can be seen in Figure 6-34 that there is a trend of decreasing SNR with increasing FOV, and it is important to note that while changes in the SNR observed in the previous sections were mostly due to changes in the variance of the data, the changes in Figure 6-34 are the result of changes in both

the average and the variance. The hybridisation of the HOPG should be constant regardless of the level of magnification that is used to acquire the line scans, however it is possible that an increased magnification level results in a larger amount of electron beam induced damage occurring as the electron beam is concentrated over a smaller area. To examine this further the spectra from the carbon elemental line scan are compared for each magnification level.

The spectra averaged from each point of the carbon elemental line scans in Figure 6-33 are shown in Figure 6-35. As the FOV increases the spectral shape changes, with the width between the maxima and minima increasing and a shoulder becoming more prominent at the low kinetic energy side of the peak. This trend is also shown in Table 6-11, which shows an increase in D parameter values from 20.2 eV at 535 μm to 22.8 eV at 10 um. Spectra from individual points along the lines show the same trends of increasing peak width and emerging shoulder (Figure 6-35) and increasing D parameter value (Table 6-11) with increasing level of magnification (decreasing FOV). These results show that a FOV of 100 μm or below result in sp^2 hybridisation line scans that give consistent results using the same calibration curve, however at lower magnifications the calibration curve does not appear to provide accurate results. Based on this all samples examined using this technique will be characterised at a FOV of 100 μm or smaller.
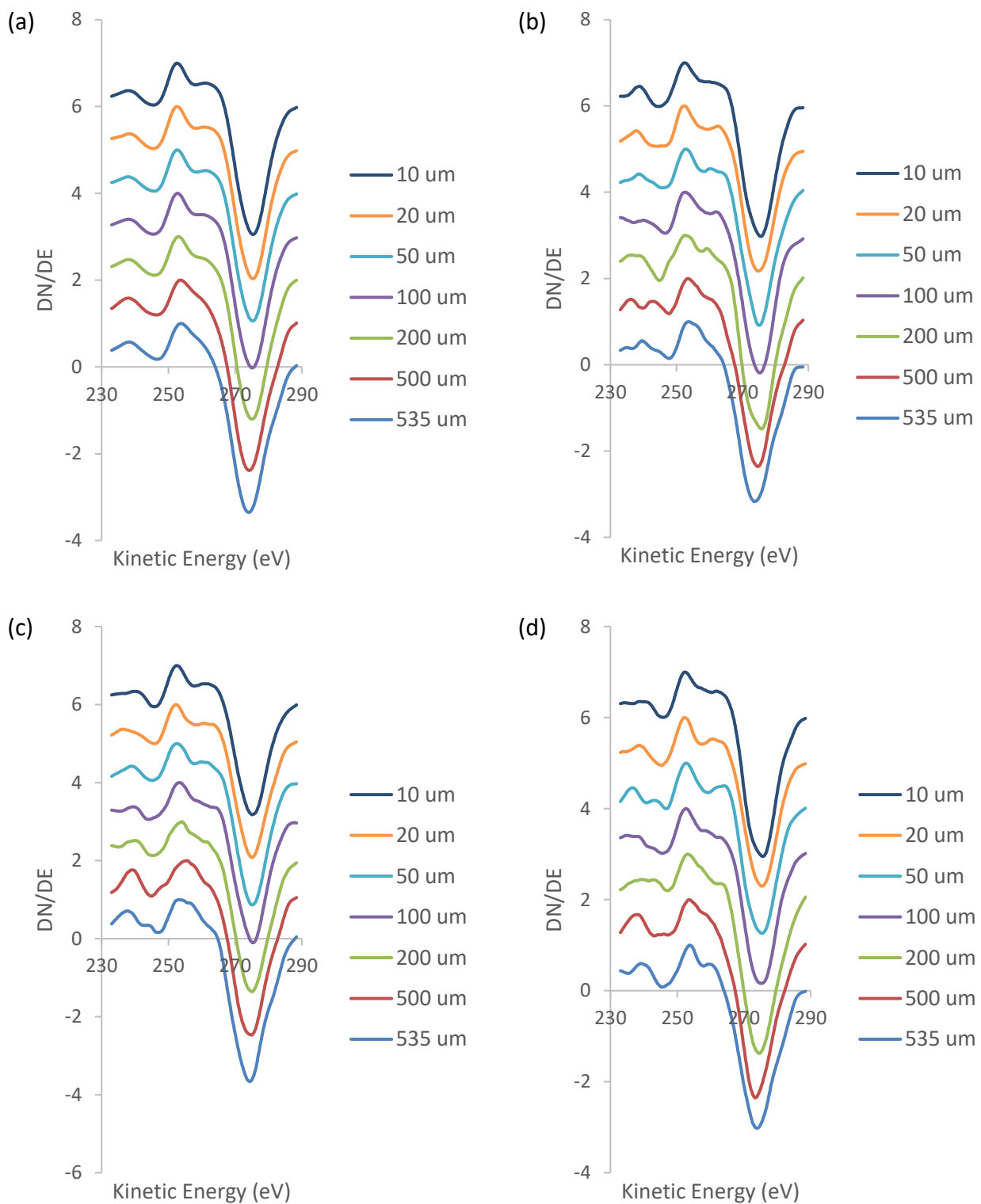
Figure 6-35: C(KLL) spectra taken from (a) the average of all spectra in the line scan, and point (b) 32, (c) 64, and (d) 96 of the 128 point carbon elemental line scans of HOPG. Each plot shows a spectrum from an elemental map with a FOV of 535 μm (blue line), 500 μm (red line), 200 μm (green line), 100 μm (purple line), 50 μm (light blue line), 20 μm (orange line), and 10 μm (dark blue line).

Table 6-11: D Parameter values from each spectrum in Figure 6-35.
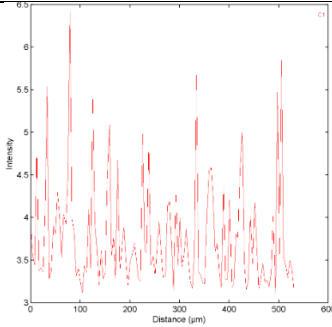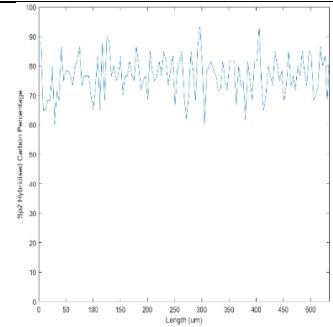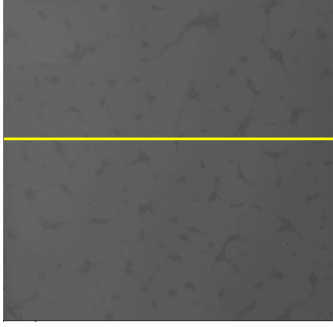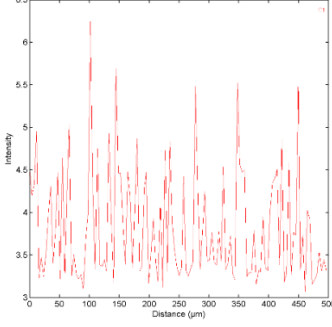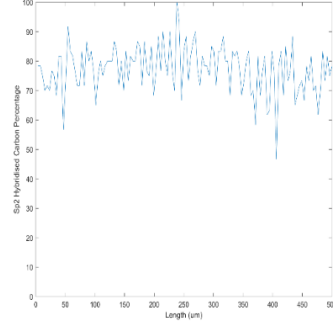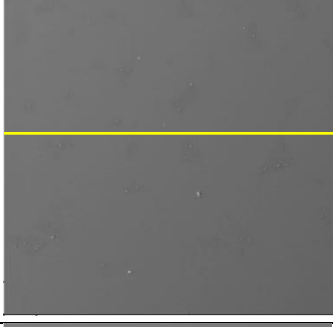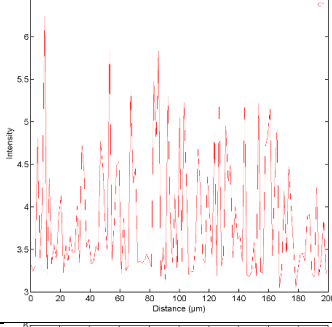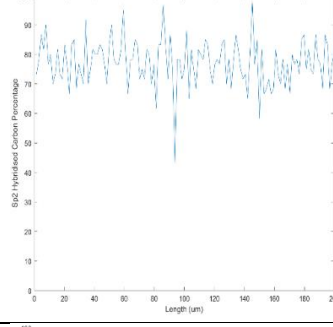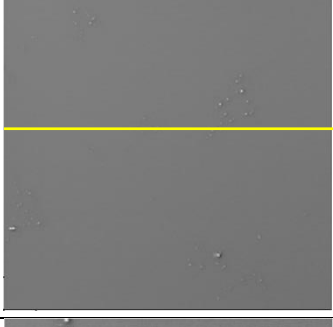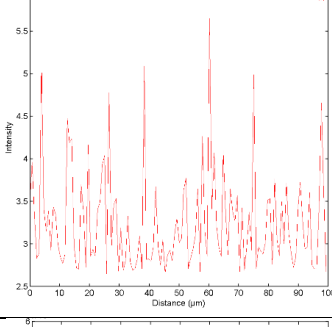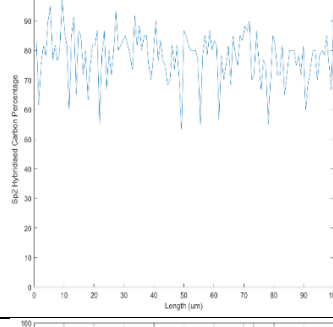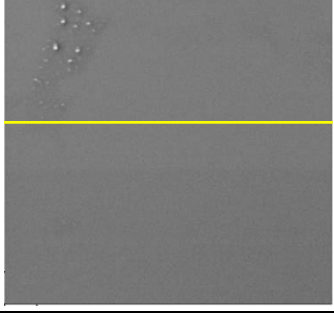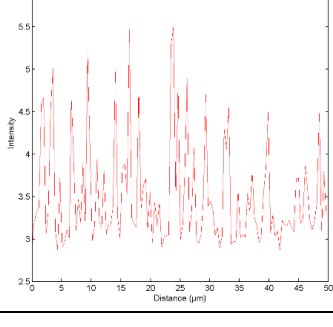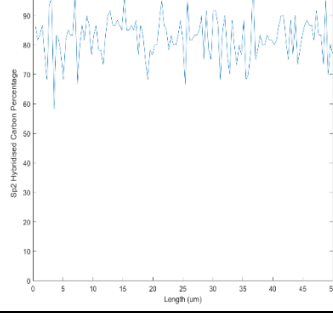
Field of View (um)	D Parameter (eV) (Average)	D Parameter (eV) (Pixel 272)	D Parameter (eV) (Pixel 558)	D Parameter (eV) (Pixel 784)
535	20.2	19.8	21.4	20.0
500	20.6	21.4	19.4	19.8
200	22.0	23.0	21.0	21.4
100	22.4	22.4	22.0	22.6
50	22.6	22.4	22.6	22.8
20	22.8	22.4	22.6	23.2
10	22.8	23.0	22.6	23.2

The results shown in Figure 6-33, Figure 6-34, Figure 6-35, and Table 6-11 combine to show that the shape of the carbon peak changes quite significantly as the level of magnification changes. Based on these results, the calibration curve used to determine the sp^2 hybridised carbon percentage based on the D parameter value does not hold when the FOV is higher than 100 um, and therefore all line scans acquired for the purpose of identifying carbon hybridisation will be acquired using a FOV of 100 μm or lower.

While acquiring all carbon elemental line scans at a low FOV allows for the technique to produce consistent results, it is still important to understand why there is a dependence on the magnification level when the hybridisation of HOPG should not change. To determine whether this is an artefact of the technique or the sample the same magnification level tests need to be performed on a different sample.

6.2.6.2 Magnification Level Dependence - DLC

Hybridisation line scans were acquired for DLC using FOVs ranging between 535 μm and 10 μm to determine if the same dependence occurs as was observed for HOPG. Figure 6-36 shows the 535 μm FOV SEM image of the DLC sample, with the yellow line indicating the line over which the window mode carbon elemental line scan was acquired. The surface is quite uniform with small areas of a darker colour scattered across the surface, with the line crossing several of these areas. The resultant hybridisation line scan shows an average sp^2 carbon percentage of approximately 75 %, with a range of approximately 50 % to 95 %, which is significantly lower than the percentages observed previously at a 20 μm FOV.

FOV (um)	SEM	Carbon Elemental Line Scan	Hybridisation Line Scan	SNR
535				4.39
500				4.44
200				4.71
100				5.06
50				4.67

20				6.21
10				6.92
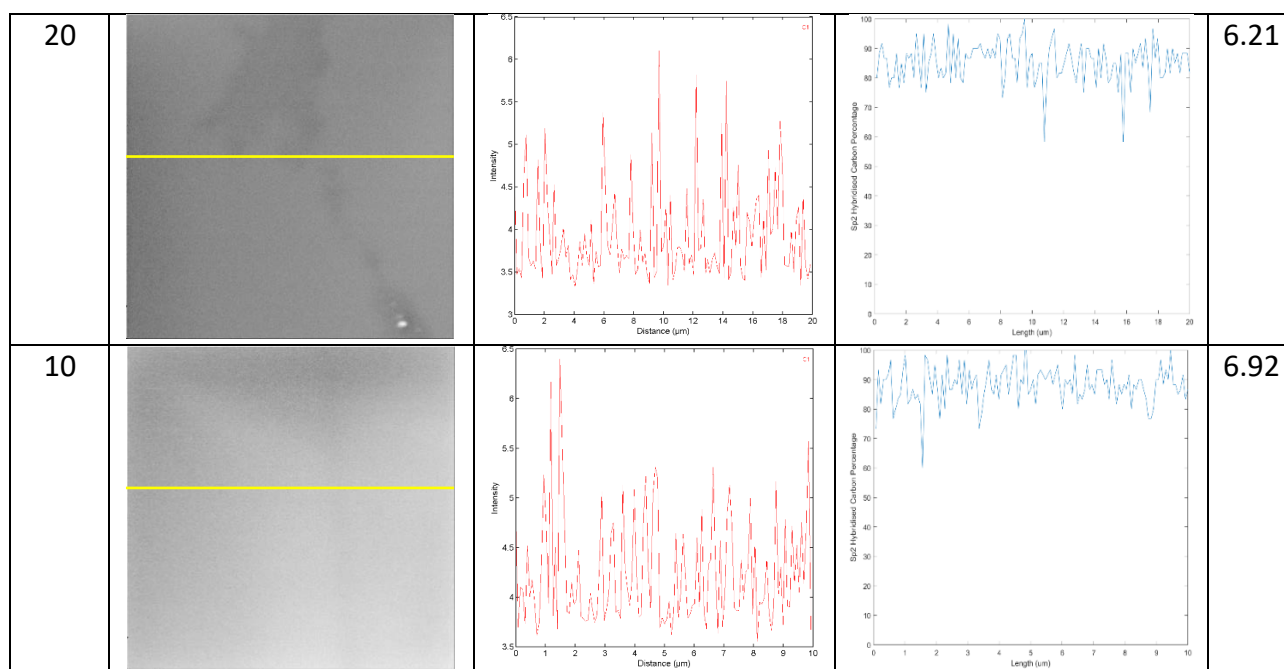
Figure 6-36: SEM images, C(KLL) elemental line scans, and hybridisation line scans for a DLC film taken with FOV of 535 um, 500 um, 200 um, 100 um, 50 um, 20 um, and 10 um.

The 500 μm FOV results (Figure 6-36) show a very similar SEM image and a very similar hybridisation line scan. The results start to change when the FOV is decreased to 200 um. The surface examined at this level of magnification is uniform in colour and structure (Figure 6-36), and results in a hybridisation line scan with an average sp^2 hybridised carbon percentage of approximately 80 % and a range of approximately 60 % to 100 %. The results obtained at a FOV of 100 μm show very similar results to the 200 μm FOV sample (Figure 6-36), however a further increase of magnification results in further changes in the sp^2 hybridised carbon percentage line scans.

SEM images of the DLC film examined at 50 um, 20 um, and 10 μm are also shown in Figure 6-36, along with the window mode carbon elemental line scan and hybridisation line scan at each of these magnification. All three show very similar hybridisation line scans, with an average sp^2 hybridised carbon percentage of approximately 85 % and a range of approximately 75 % to 100 %. These results match those seen for HOPG, and support the conclusions that the calibration curve only holds for levels of magnification that give a FOV of 100 μm or lower. To provide further insight into the phenomena the results the SNR values must be considered.

The SNR values are plotted against the FOV of the hybridisation line scan in Figure 6-37.
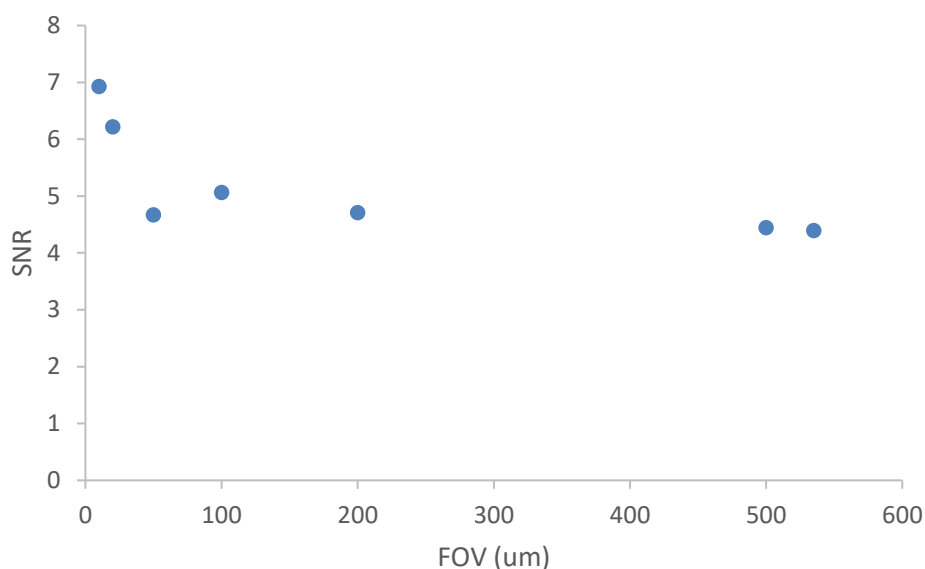
Figure 6-37: Variation in SNR value from hybridisation line scans in Figure 6-36 plotted against the FOV of the hybridisation line scan.

It can be seen in Figure 6-37 that a decrease in the FOV of the hybridisation line scan results in an increase in the SNR, with the increase caused by both an increase in the average hybridisation and a decrease in the range of hybridisation values. While it is expected that there would be some variations in the hybridisation of the DLC film, this variation should occur randomly across the surface and there should not be a change in hybridisation with magnification level. To further examine this effect the spectra from the carbon elemental line scans will be examined.

The average spectra created from each point of the carbon elemental line scans in Figure 6-36 are shown in Figure 6-38, and show an increase in the peak width and an increasing intensity of the shoulder in the lower binding energy side of the peak as the FOV decreases. The D parameter values in Table 6-12 also show this trend, with the 535 μm FOV line scan showing a D parameter value of 21.2 eV while at 10 μm the D parameter value is 22.6 eV. The spectra extracted from individual points in the line scan also show this trend, with the peak width increasing, resulting in the D parameter values increasing as the level of magnification increases. The results show some variation, but overall stabilise more at FOVs of 50 μm or below, suggesting that the calibration curve holds best at these lower FOVs. This agrees with the results shown previously for HOPG, and indicate the same conclusions that suggest that this technique is accurate provided that the FOV is kept to 50 μm or below. All samples characterised with this technique will therefore be examined at these suggested level of magnification.
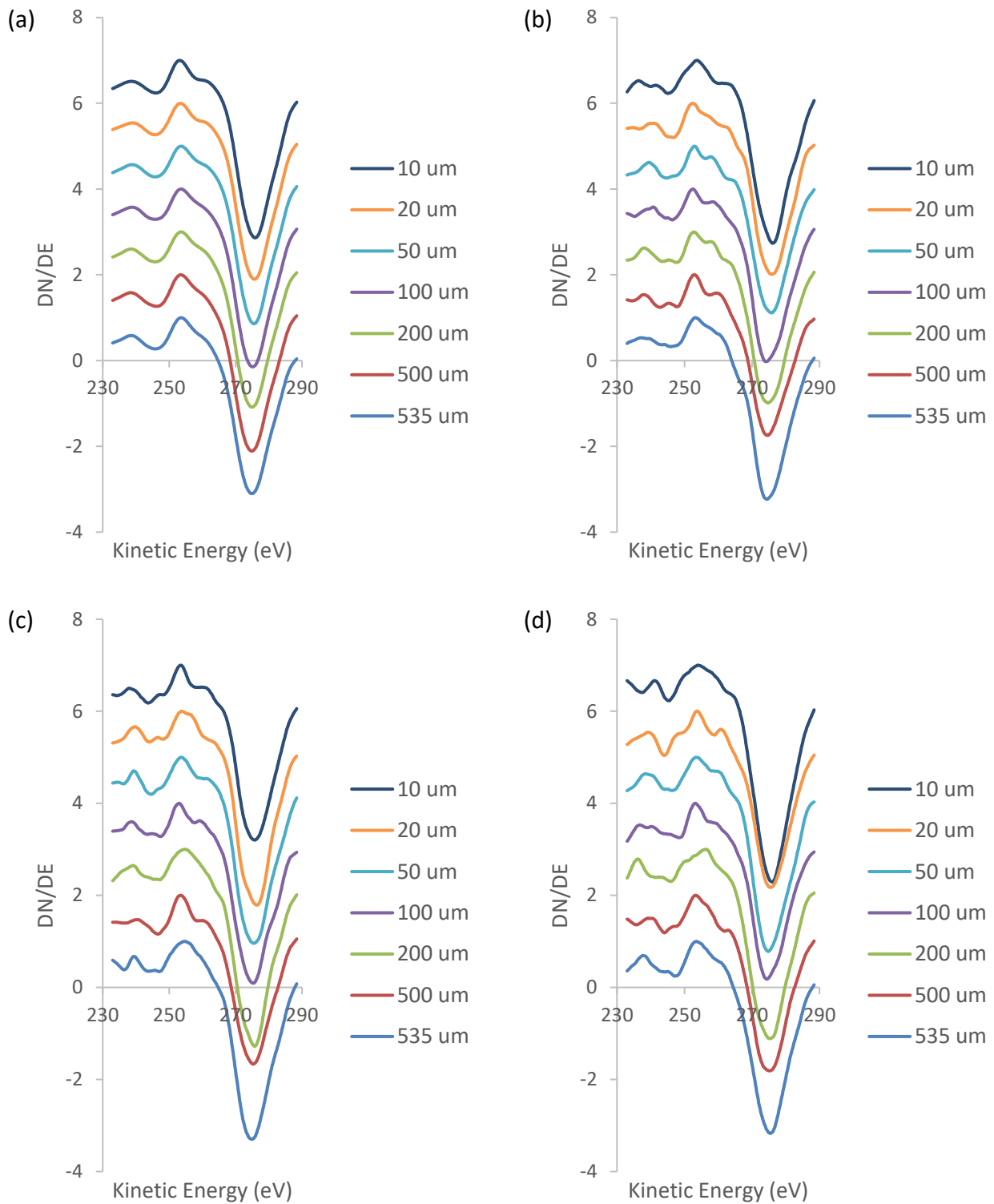
Figure 6-38: C(KLL) spectra taken from (a) the average of all spectra in the line scan, and point (b) 32, (c) 64, and (d) 96 of the 128 point carbon elemental line scans of a DLC film. Each plot shows a spectrum from an elemental map with a FOV of 535 μm (blue line), 500 μm (red line), 200 μm (green line), 100 μm (purple line), 50 μm (light blue line), 20 μm (orange line), and 10 μm (dark blue line).

Table 6-12: D Parameter values from each spectrum in Figure 6-38.

Field of View (um)	D Parameter (eV) (Average)	D Parameter (eV) (Pixel 272)	D Parameter (eV) (Pixel 558)	D Parameter (eV) (Pixel 784)
535	21.2	21.2	20.4	21.8
500	21.2	21.6	22.0	21.8
200	21.4	22.0	21.0	19.0
100	21.6	21.6	22.4	21.2
50	22.0	22.8	21.8	21.4
20	22.2	23.4	22.6	21.6
10	22.6	22.4	22.4	22.0

The results in Figure 6-36, Figure 6-37, Figure 6-38, and Table 6-12 indicate that the level of magnification at which the hybridisation line scans are acquired has an impact on the spectral shape, and therefore on the hybridisations found. For DLC films it was found that below 50 μm the hybridisations determined are stable and can be found using the same calibration curve, however when the magnification is lower the calibration curve does not produce correct results. Based on these results it is concluded that any line scan acquired for the purpose of determining carbon hybridisation must be acquired at a FOV of 50 μm or lower.

As the fine structure of the spectra does not change significantly when the magnification level changes and rather appears that the entire spectrum broadens it is unlikely that the sample itself is the reason for this magnification level dependence.

6.2.6.3 Causes of Magnification Level Dependence

In sections 6.2.6.1 and 6.2.6.2 it was observed that for both HOPG and DLC there is a dependence of the spectra obtained in a carbon elemental line scan on the magnification level at which the scan is acquired. However, as this was observed with both HOPG and DLC with little change to the fine structure of the spectra, the phenomena is not thought to be due to the samples themselves, but rather the result of an artefact of the technique. All scans were acquired with the same scanning parameters so that the only thing that changes is the magnification level, therefore any difference that occurs must be a result of internal mechanisms of the scanning technique rather than user input. These results suggest that there is a difference in how the instrument acquires or processes data acquired at different magnification levels, however what this difference is cannot be

determined from the data presented in sections 6.2.6.1 and 6.2.6.2. Further investigation into this phenomenon is needed to conclusively determine its cause, however it appears that with the current interface to the instrument this phenomenon is beyond the control of the user.

6.2.6.4 Choice of Magnification Level

Comparison of the results in Figure 6-30 and Figure 6-33 for window mode carbon elemental line scans acquired at different magnifications shows that the FOV at which the scan is acquired has a large impact on the shape of the spectra and therefore on the D parameter. When the FOV is large the D parameter of the spectra is smaller for both HOPG and DLC than it is for the smaller FOV, and it has been demonstrated that the calibration curve used to calculate the sp^2 hybridised carbon percentage only holds when the FOV is below 50 um. Based on this conclusion all samples will be examined at a FOV of 50 μm or lower to ensure that the calibration curve holds and the sp^2 hybridised carbon percentages calculated are accurate.

6.3 Carbon Hybridisation Line Scans

Now that optimisation of the hybridisation line scanning technique has been performed and the appropriate scanning parameters selected the technique can be applied to carbon samples to determine their hybridisation. The standards of HOPG and DLC are presented first, followed by the carbon tape substrates, before samples with more than one carbon material, and hence more than one hybridisation, are examined.

6.3.1 Highly Oriented Pyrolytic Graphite

Highly Oriented Pyrolytic Graphite is composed of sp^2 hybridised carbon and is used as a standard for many applications, as has been discussed previously, and is used in this chapter as a control sample and a substrate. In the previous sections of this chapter HOPG has been used as a control to optimise the scan parameters used to acquire window mode carbon elemental line scans to convert to sp^2 hybridised carbon percentage line scans. However, now HOPG is examined using a higher spatial resolution with the optimised scanning parameters.

A 20 μm FOV SEM image of HOPG is shown in Figure 6-39 (a) and shows the yellow line indicating the line over which the line scans were acquired. The SEM image shows a darker coloured area in the upper left corner while the rest of the image is mostly uniform in colour. There is also a line running down the left side of the SEM image which indicates a step edge, and several smaller lighter lines across the surface which indicate small ripples in the graphite sheets. The yellow line crosses

Figure 6-39: (a) SEM image of HOPG (FOV 20 um) with yellow line indicating line scan line, (b) 512 point window mode carbon (red) and oxygen (blue) elemental line scans, (c) 512 point window mode carbon elemental line scan, and (d) 512 point sp^2 hybridised carbon percentage line scan.

over two differently coloured areas in the SEM image but otherwise appears to traverse a uniform area.

The window mode carbon and oxygen elemental line scans acquired across this line are shown in Figure 6-39 (b) and show a surface that is approximately 95 % carbon and 5 % oxygen consistently across the line.

The window mode carbon elemental line scan acquired with the optimised scan parameters and the resultant hybridisation line scan are shown in Figure 6-39 (c) and (d), respectively. The hybridisation line scan shows an average percentage of approximately 90 %, with values ranging between approximately 85 % and 95 %. The average and range do not change across the surface despite the changes in appearance of the HOPG in the SEM image, suggesting that the different colours in the SEM image simply indicate flakes of graphite sitting higher than others but with constant hybridisation composition.

To examine the consistency of the hybridisation line scanning technique multiple samples were acquired, and a second sample of HOPG is shown in the 20 μm FOV SEM image in Figure 6-40 (a). This sample appears much less smooth than that in Figure 6-39, with many small ridges shown as the lighter colour lines in the SEM image, which, due to the morphology sensitivity of SEM, appear to indicate that the top sheet of the graphite is wrinkled up. The yellow line in Figure 6-40 (a)

318

Figure 6-40: (a) SEM image of HOPG (FOV 20 um) with yellow line indicating line scan line, (b) 512 point window mode carbon (red) and oxygen (blue) elemental line scans, (c) 512 point window mode carbon elemental line scan, and (d) 512 point sp^2 hybridised carbon percentage line scan.

indicates the area over which the carbon and oxygen window mode elemental line scans in Figure 6-40 (b) were acquired and passes through many of these ripple features.

The carbon and oxygen elemental lines scan shows the same percentages as the previous sample, with approximately 95 % carbon and 5 % oxygen across the entire line regardless of features shown in the SEM image.

The window mode carbon elemental line scan and resultant hybridisation line scan (Figure 6-40 (c) and (d)) also show very similar results to the previous sample, with an average of approximately 95 % sp^2 hybridised carbon across the surface, again regardless of the features shown in the SEM image. The range of sp^2 hybridised carbon values vary between approximately 85 % and 95 %, which is also consistent with the previous sample.

These results show that the surface is predominately composed of carbon (approximately 95 %) with a small amount of oxygen across the surface (approximately 5 %). The carbon present across the surface is mostly sp^2 hybridised, however a small amount of sp^2 hybridised carbon is present across the surface. Although some different features are visible in the SEM image there are no variations in the elemental or hybridisation composition that corresponds with these positions, and it is therefore concluded that these features are graphitic areas with a different topology making them appear different in the SEM image. These results are what were expected for HOPG based on

319

both the structure of HOPG and previous hybridisation mapping results (section 5.3.1) and therefore provide evidence that the carbon hybridisation line scanning technique is producing accurate results.

6.3.2 Diamond-Like Carbon

Diamond like carbon films were deposited on silicon substrates using PECVD from methane and will be used as a substrate for other carbon materials in this chapter, and is therefore considered here individually to produce standard line scans.

The 20 μm FOV SEM image in Figure 6-41 (a) shows a DLC surface that is mostly uniform in colour and texture but does contain several small dark spots. The yellow line in the SEM image shows the line over which the carbon, oxygen, and silicon elemental line scans in Figure 6-41 (b) were acquired and passes through one small dark spot near the centre of the image, but otherwise passes through an area of the sample that appear uniform.

The carbon, oxygen, and silicon elemental line scans show that the percentages of all three elements are consistent across the surface, with the carbon (red line) percentage at approximately 85 % across the surface, oxygen at approximately 5 %, and silicon at approximately 10 %. This silicon content is much higher than is expected based on the previous characterisation of DLC films. When the spectra used to create the line scans are examined the silicon peak is very small if present at all,

Figure 6-41: (a) SEM image of a DLC film (FOV 20 um) with yellow line indicating line scan line, (b) 512 point window mode carbon (red), oxygen (blue), and silicon (green) elemental line scans, (c) 512 point window mode carbon elemental line scan, and (d) 512 point sp² hybridised carbon percentage line scan.

320

however the MultiPak software, which uses sensitivity factors to create the line scans, calculates the percentage of silicon to be around 10 %. While this is a strange artefact of the technique, it occurs consistently and does not impact the creation of the hybridisation line scans.

Figure 6-41 (c) shows the carbon window mode elemental line scan and the resultant hybridisation line scan is shown in Figure 6-41 (d). The hybridisation line scan shows a sp^2 hybridised carbon content of approximately 90 % across the entire line, which is a similar percentage to that shown in Figure 6-39 and Figure 6-40 for a HOPG surface, however the range of percentages is much higher than those observed for HOPG, with values ranging between approximately 80 % and 100 %. This result is consistent with those shown earlier in this chapter, and also with the results shown in the previous chapter where DLC films were characterised with the carbon hybridisation mapping technique (section 5.3.2).

Another example of a DLC surface is shown Figure 6-42 (a), which is a 20 µm FOV SEM image showing a surface that contains several features. Most of the image appears to be smooth and uniform in colour, however along the upper edge of the image is an irregularly shaped darker region. On the lower left there is an irregularly shaped area that is again darker, and this region also contains several variously sized particles that appear white in the SEM image. The yellow line indicating the area of acquisition for the line scans passes through one of these small particles and also the darker coloured area in the SEM image but otherwise appears very similar.

The carbon, oxygen, and silicon elemental line scans are shown in Figure 6-42 (b) and are consistent with the results shown in Figure 6-41, as are the results shown in Figure 6-42 (c) and (d), which show the carbon elemental line scan and resultant hybridisation line scan, respectively. There are no changes in the hybridisation line scan that correspond with the changes observed in the SEM image which suggests that the DLC surface is consistent despite the difference in appearance of the areas and particle in the SEM image. The consistency in the elemental and hybridisation composition despite the different appearance suggests that the different coloured areas in the SEM image are the result of variations in the topology of the surface.

Figure 6-42: (a) SEM image of a DLC film (FOV 20 um) with yellow line indicating line scan line, (b) 512 point window mode carbon (red), oxygen (blue), and silicon (green) elemental line scans, (c) 512 point window mode carbon elemental line scan, and (d) 512 point sp^2 hybridised carbon percentage line scan.

The results of the hybridisation line scans for the two DLC film samples show consistent results, and also show consistency to the carbon hybridisation maps presented in section 5.3.2. While previous results in this work using XPS and SAM to characterise DLC films showed that they had a high sp^3 hybridised carbon percentage (chapter 4), the results from carbon hybridisation mapping from the same films showed a much higher sp^2 content. The results shown in Figure 6-41 and Figure 6-42 show the same hybridisations as those observed in the optimisation process in section 6.2, which is also higher than that observed in chapter 4.

The reasons for the differences observed cannot be stated with any certainty, but is possibly either the result of the increased interaction of the electron beam with the sample that occurs in a line scan or an artefact of how the instrument acquires and processes spectra depending on whether it is a high resolution spectrum or a line scan.

The results from these samples show a difference to those obtained for the equivalent HOPG case, and provide supporting evidence that the carbon hybridisation line scans are able to distinguish between different hybridisations. The hybridisation line scan also shows results that are consistent with the hybridisation maps seen in section 5.3.2, showing consistency between the two techniques.

322

6.3.3 Carbon Tape

Carbon tape is used as a substrate for the characterisation of graphene flakes and nanodiamonds in this work and is therefore considered here individually for later comparison to other carbon types. The carbon tape has been shown previously to be composed of carbon, oxygen, and silicon, and is expected from the previous carbon hybridisation mapping to have a reasonably high sp^2 hybridised carbon content but show a large amount of variation across the surface.

The carbon tape surface shown in the SEM image (FOV 20 um) in Figure 6-43 (a) shows a surface that is highly textured as indicated by the inconsistency in brightness across the SEM image. The yellow line in the image indicates the area over which the line scans were acquired and crosses over a range of particles and areas between the particles that appear smooth.

The carbon, oxygen, and silicon elemental line scans acquired over this line are shown in Figure 6-43 (b) and show mostly consistent values across the surface despite the changes in the appearance of the carbon tape in the SEM image. The carbon percentage varies between approximately 55 % and 70 %, while oxygen shows values between 20 % and 30 % and silicon between 10 % and 30 %.

The carbon window mode elemental line scan and resultant hybridisation line scan are shown in Figure 6-43 (c) and (d). The hybridisation line scan shows much larger variations in the sp^2 carbon percentage values than any carbon source examined so far, with values ranging between

Figure 6-43: (a) SEM image of carbon tape (FOV 20 um) with yellow line indicating line scan line, (b) 512 point window mode carbon (red), oxygen (blue), and silicon (green) elemental line scans, (c) 512 point window mode carbon elemental line scan, and (d) 512 point sp^2 hybridised carbon percentage line scan.

approximately 60 % and 100 % sp^2 hybridised carbon, with occasional spikes to values as low as 20 %. This variation in values occurs quite consistently across the surface, with no clear correlation between the hybridisation line scan and the SEM image observed.

A second example of a carbon tape surface is shown in Figure 6-44 (a), which displays a SEM image with a 20 µm FOV. This surface appears highly textured across much of the area examined, however it also has some areas that are flatter and more consistent in brightness. The yellow line indicating the line over which the line scans were acquired passes through both flat and textured areas, and these areas show different elemental compositions in the carbon, oxygen, and silicon elemental line scans in Figure 6-44 (b).

The silicon percentage remains constant at approximately 15 % across the whole surface, however there is an increase in the carbon percentage from approximately 60 % to approximately 65 % when the line crosses from a flat area in the SEM image to a textured area. The oxygen concentration has a corresponding decrease in these areas, with the percentage dropping from approximately 25 % in the flat areas to approximately 20 % in the textured areas.

The window mode carbon elemental line scan and resultant hybridisation line scan (Figure 6-44 (c) and (d), respectively) do not show changes with the change in texture of the surface. The sp^2 hybridised carbon percentage ranges between approximately 60 % and 100 % with several

Figure 6-44: (a) SEM image of carbon tape (FOV 20 um) with yellow line indicating line scan line, (b) 512 point window mode carbon (red), oxygen (blue), and silicon (green) elemental line scans, (c) 512 point window mode carbon elemental line scan, and (d) 512 point sp^2 hybridised carbon percentage line scan.

spikes down to values as low as 5 %, which is consistent with the range of values observed in the previous sample.

The results from the two carbon tape samples shown above are consistent with each other and show a wide range of carbon hybridisations across the surface that do not correlate with specific features observed in the SEM images of the areas examined. These results are what was expected as carbon tape is not a uniform substance, and also match the results found using the carbon elemental mapping technique shown in the section 5.3.3. The carbon hybridisation line scanning technique has successfully identified the range of hybridisations present in carbon tape, and will now be applied to more complex samples composed of carbon structures of one hybridisation on a substrate of a different hybridisation.

6.3.4 Nanodiamonds

Nanodiamonds were used in the previous chapter to create samples composed of sp^3 hybridised carbon deposited on substrates of a contrasting hybridisation and were successfully characterised using the hybridisation mapping technique. The same samples will now be characterised using the hybridisation line scanning technique. Samples of nanodiamonds or piranha solution treated nanodiamonds on HOPG and DLC were prepared by dispersing the nanodiamonds in water and drop casting onto the substrates. Samples with a carbon tape substrate were prepared by pressing the nanodiamond powder onto the carbon tape.

6.3.4.1 Nanodiamonds on Highly Oriented Pyrolytic Graphite

The SEM image in Figure 6-45 (a) (FOV 20 um) shows two large clusters of nanoparticles near the centre of the sample, along with several smaller ones scattered around the image. The HOPG substrate appears to be featureless. The yellow line in the SEM image passes through the two large clusters, one of which has a small hole in the centre through which the substrate can be seen, but otherwise passes through the featureless HOPG.

The carbon and oxygen elemental line scans in Figure 6-45 (b) show that the surface is almost entirely carbon, with a uniform concentration of approximately 96 % across the entire line, while the remaining 4 % of the surface is oxygen. This shows that there is no difference in the elemental composition of the nanodiamonds and the HOPG.

The window mode carbon elemental line scan and resultant hybridisation line scan are shown in Figure 6-45 (c) and (d), respectively, and the hybridisation line scan shows clear differences between
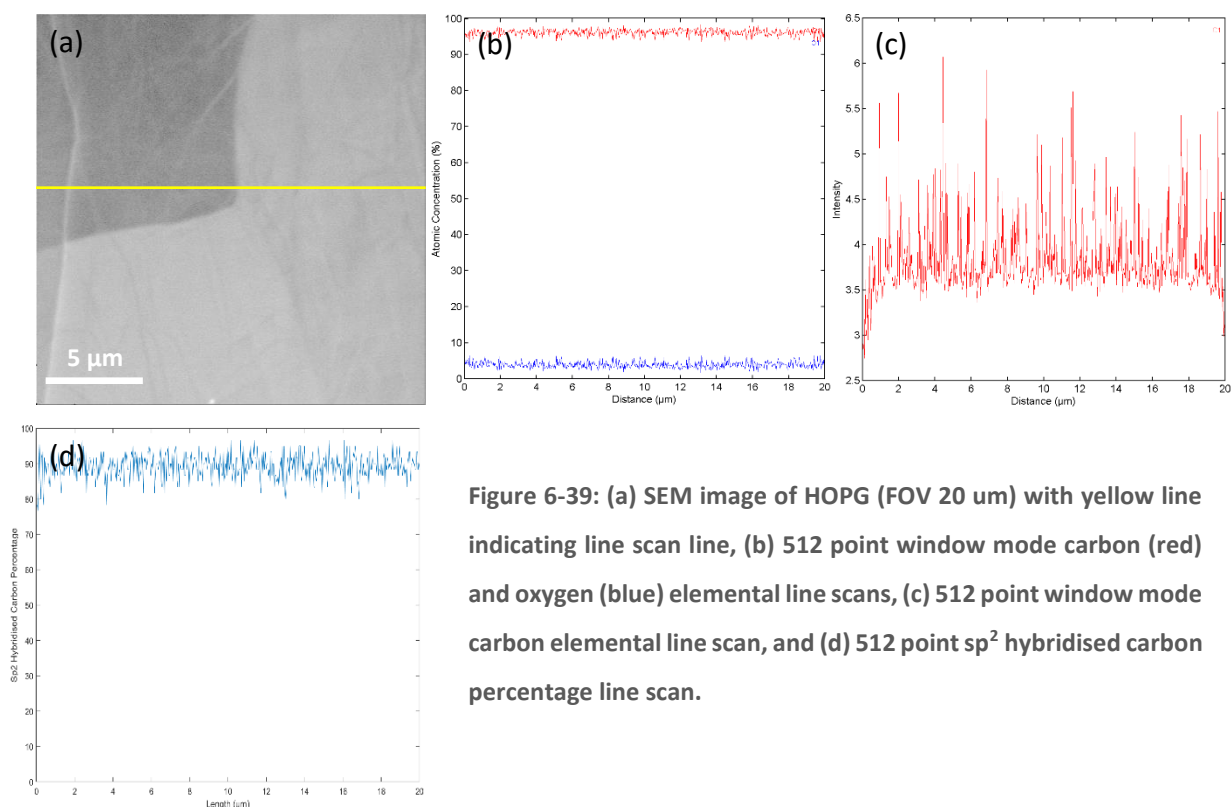
Figure 6-45: (a) SEM image of nanodiamonds on HOPG (FOV 20 um) with yellow line indicating line scan line, (b) 512 point window mode carbon (red) and oxygen (blue) elemental line scans, (c) 512 point window mode carbon elemental line scan, and (d) 512 point sp^2 hybridised carbon percentage line scan.

the areas that correspond to the HOPG substrate and the nanodiamonds in the SEM image. On the areas that line up with the HOPG substrate the *sp*^{2} hybridised carbon percentage is on average approximately 90 %, with a range between approximately 85 % and 95 %, which is the same as the line scans acquired on HOPG previously. However, the areas that correspond to the nanodiamond clusters exhibit much lower *sp*^{2} concentrations, with the minimum reached at approximately 20 % and 10 % for the left and right clusters, respectively. The area corresponding to the hole in the centre of the nanodiamond cluster shows a *sp*^{2} hybridised carbon percentage of 80 % to 90 %, indicating that at those points the surface is HOPG, but perhaps has small amounts of nanodiamond present that isn't easily seen in the SEM image but results in slightly lower *sp*^{2} percentages than would be expected. These results are very similar to those seen in the previous chapter (section 5.3.6.1) when the carbon hybridisation mapping technique was used to analyse the same type of sample, and provides good evidence for the viability of the hybridisation line scanning technique.

A second example of a sample composed of nanodiamonds on HOPG is shown in Figure 6-46 (a), which is a 20 μm FOV SEM image showing a large cluster of nanodiamonds across most of the lower half of the image. There is also several other smaller nanodiamond clusters across the surface, again mostly present in the lower half of the image. The yellow line in the SEM image shows the line over which the line scans were acquired, and passes through the large group of nanodiamond clusters in the centre of the image as well as one of the smaller nanodiamond clusters to the right of the large
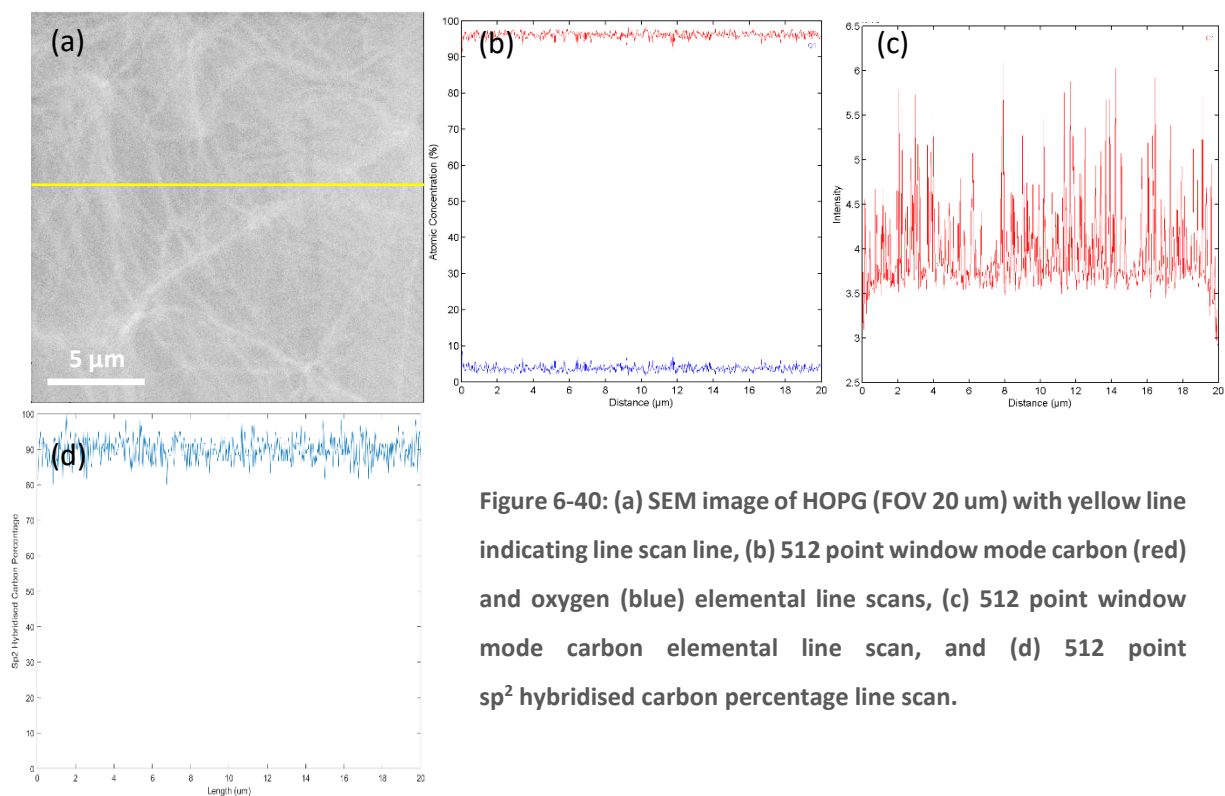
Figure 6-46: (a) SEM image of Nanodiamonds on HOPG (FOV 20 um) with yellow line indicating line scan line, (b) 512 point window mode carbon (red) and oxygen (blue) elemental line scans, (c) 512 point window mode carbon elemental line scan, and (d) 512 point sp^2 hybridised carbon percentage line scan.

cluster and areas of featureless HOPG in between.

The carbon and oxygen elemental line scans are shown in Figure 6-46 (b) and indicate that the concentrations of both elements are quite uniform across the surface. The carbon concentration at approximately 96 % and the oxygen at approximately 4 % across the entire line showing that there is no elemental difference between the HOPG and the nanodiamonds.

A window mode carbon elemental line scan was acquired over this area and converted to a hybridisation line scan, both of which are shown in Figure 6-46 (c) and (d), respectively. The hybridisation line scan shows clear differences between the areas of the sample that are composed of HOPG or nanodiamonds. The section of the line that corresponds to the large group of nanodiamond clusters in the SEM image shows sp^2 hybridised carbon percentages that are as low as 5 %, although there is some variation across this area. This variation is expected as the nanodiamond clusters are not all of a consistent size or distribution, and there are some areas where the HOPG substrate is also being detected because there is either no nanodiamond in that position or the nanodiamond is thin enough that the HOPG substrate underneath is also detected. The smaller cluster that is visible to the right of the large one in the SEM image also shows a difference from the surrounding HOPG in the sp^2 hybridised carbon percentage line scan. This smaller section shows lower sp^2 hybridised carbon percentage than the HOPG, however it is not as low as the larger clusters. As the nanodiamond cluster in this position is smaller and thinner the HOPG substrate

underneath is detected to a larger extent, and therefore the sp^2 hybridised carbon percentage observed along this area is a combination of both the HOPG and nanodiamonds. The remainder of the line crosses what appears to be featureless HOPG and is therefore expected to have a high sp^2 hybridised carbon percentage. The observed percentage is approximately 92 % across these areas, which is slightly lower than the 95 % observed in previous HOPG samples, however the variation is also larger, with percentages ranging between approximately 85 % and 97 %. This slight lowering of the percentage and increase in the range of values suggests that there may be a very thin layer of small nanodiamonds across the HOPG that are not visible in the SEM image. Due to the method used to deposit the nanodiamonds on the HOPG it is likely that there could be a distribution of fine nanodiamonds across the surface. This thin layer may not be clearly visible in the SEM image if the particles are on the nanoscale, but would cause some changes in the hybridisation of the surface relative to that of HOPG.

The hybridisation line scans presented here show a clear difference between the nanodiamonds and HOPG substrate in these samples, with the HOPG showing a sp^2 hybridised carbon percentage of approximately 95 % and the nanodiamonds showing percentages down to approximately 5 %, depending on how thick the nanodiamond is at each point. These results are consistent with those found with the carbon hybridisation mapping technique in the previous chapter (section 5.3.5.1), and present evidence that the carbon hybridisation line scan technique is able to differentiate between different types of carbon on one surface.

6.3.4.2 Nanodiamonds on Diamond-Like Carbon

To further test the capabilities of the hybridisation line scanning technique the same nanodiamonds were also deposited on a substrate of a DLC film grown on silicon. The 20 µm FOV SEM image in Figure 6-47 (a) shows the surface of one such sample, which has a large nanodiamond cluster in the centre of the sample and several smaller nanodiamond clusters to the right of the sample. There are also areas across the entire sample which are lighter in colour than the surrounding DLC substrate. These areas appear to be composed of a fine powder with occasional larger particles scattered through it, and are indicative of a finer nanodiamond powder that has deposited across the sample. The yellow line shows where the line scans were acquired and passes through the large nanodiamond cluster in the centre, as well as some of the smaller clusters to the right and areas of the fine powder and DLC substrate.

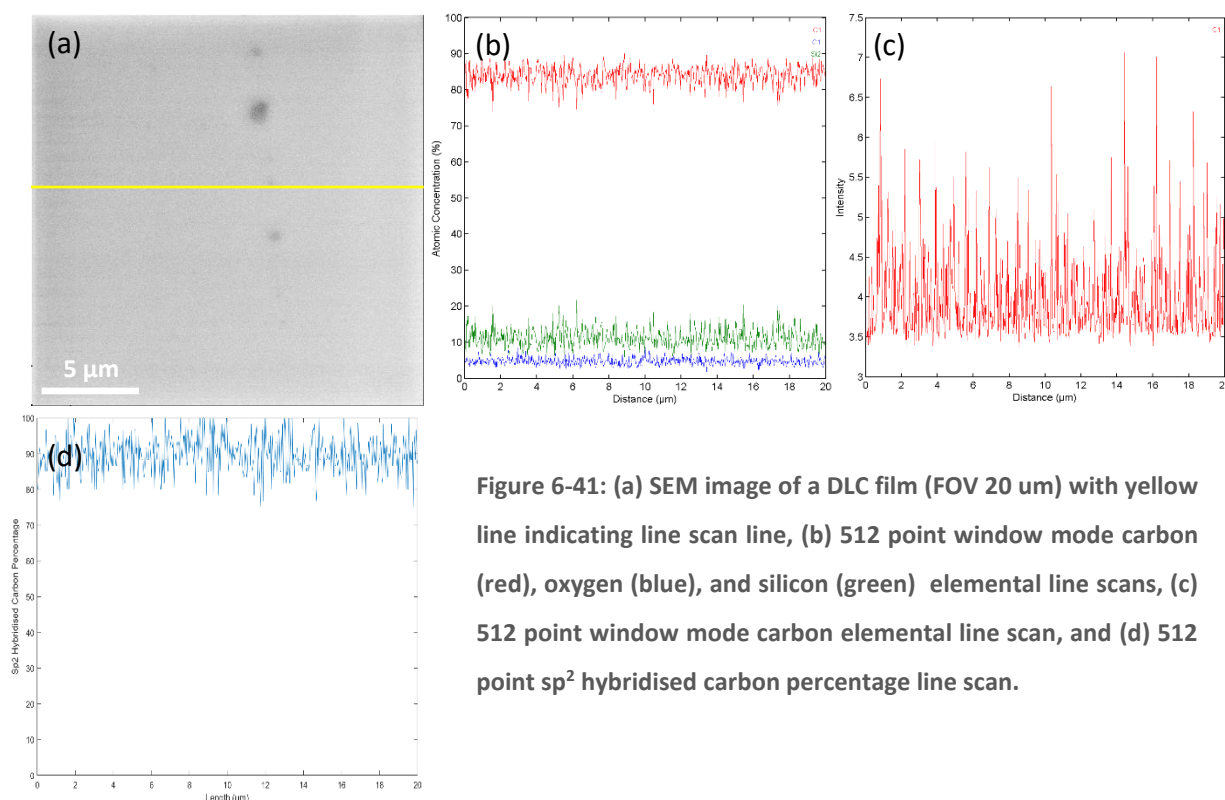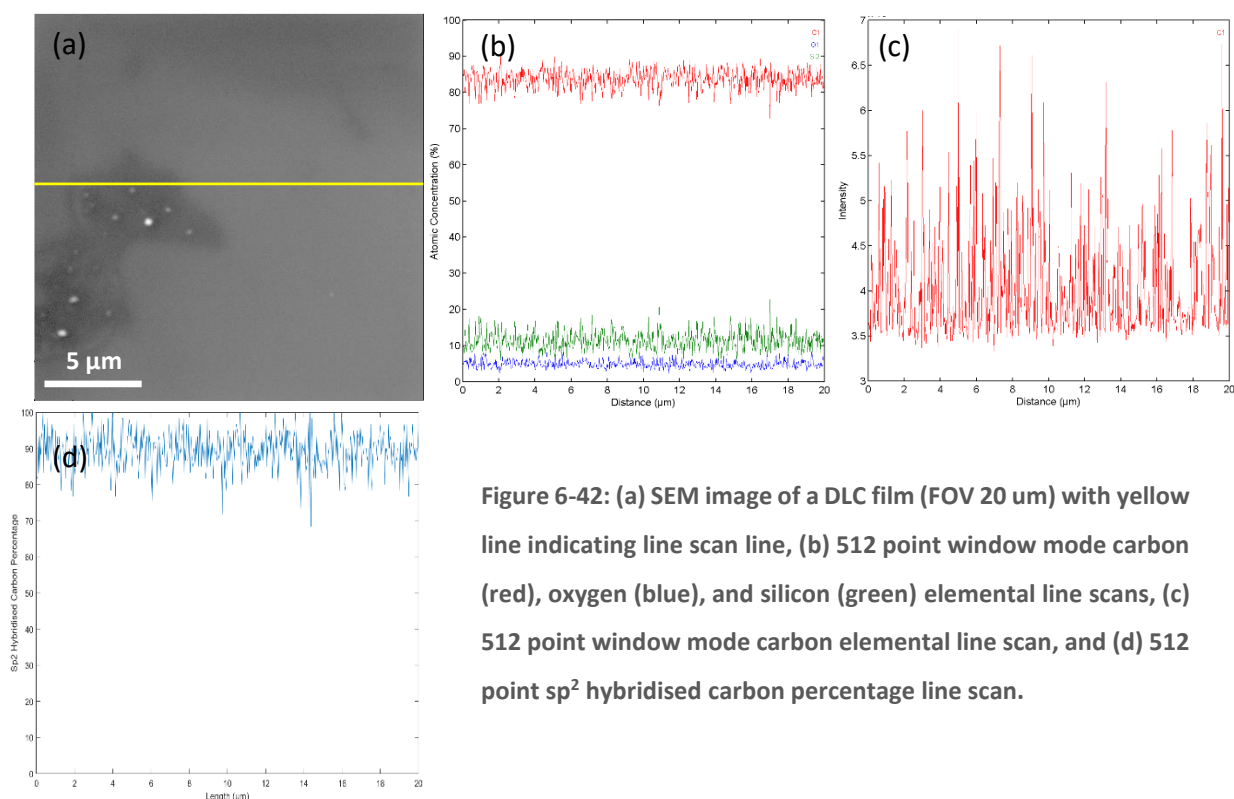The carbon, oxygen, and silicon window mode elemental line scans are shown in Figure 6-47 (b) and

Figure 6-47: (a) SEM image of Nanodiamonds on DLC (FOV 20 um) with yellow line indicating line scan line, (b) 512 point window mode carbon (red), oxygen (blue), and silicon (green) elemental line scans, (c) 512 point window mode carbon elemental line scan, and (d) 512 point sp^2 hybridised carbon percentage line scan.

show that there is some variation across the surface. The carbon percentage is approximately 82 % across the areas of DLC or thin nanodiamond powder but increases to approximately 90 % in the areas corresponding to the nanodiamonds. This corresponds with a decrease in the silicon concentration from approximately 13 % to approximately 10 % in the same areas and a slight decrease in the oxygen concentration from approximately 7 % to approximately 5 %. Examination of the silicon spectra again show a very small or no silicon peak suggesting an artefact of how MultiPak calculates percentages from the sensitivity factors, however this does not affect the creation of a hybridisation line scan.

The window mode carbon elemental line scan and its resultant hybridisation line scan are shown in Figure 6-47 (c) and (d), respectively. There are large differences in the sp^2 hybridised carbon percentage across the line that correlate with the features observed in the SEM image. The large nanodiamond cluster in the centre of the line shows sp^2 hybridised carbon percentages as low as 8 %, as do the smaller nanodiamond clusters across the right of the line. The areas between these clusters shows sp^2 hybridised carbon percentages that are much higher than the nanodiamond areas but are not as high as expected if only DLC is being detected. This is due to the thin nanodiamond powder that is scattered across the sample which is lowering the sp^2 hybridised carbon percentages in these areas as the detected percentage detects both this powder and the underlying DLC. Some areas have a thicker layer of this powder than others, which can be seen in the SEM image by the change in colour and in the sp^2 hybridised carbon percentage map as a

decrease in the sp^2 hybridised carbon percentage.

Another sample of nanodiamonds on DLC is shown in Figure 6-48 (a), which is a 20 μm FOV SEM image showing one large nanodiamond cluster on the right of the image as well as the DLC substrate on the top left and DLC powder on the bottom right with a straight line dividing these areas that runs almost through the centre diagonal. The yellow line passes through all three of these features and indicates the path over which the line scans were acquired.

The carbon, oxygen, and silicon elemental line scans are shown in Figure 6-48 (b) and show very similar results to those seen on the previous sample (Figure 6-47 (b)). The carbon elemental concentration is approximately 83 % on the left side of the line, which corresponds with the DLC area in the SEM image, while the right side of the line where the nanodiamonds are present has a slightly higher carbon concentration of approximately 88 %. This increase in carbon percentage matches the decrease in oxygen and silicon over the same portion of the line, with oxygen at 6 % on the left of the line and 4 % on the right and silicon at 11 % on the left and 8 % on the right.

The window mode carbon elemental line scan over this same line is shown in Figure 6-48 (c) and its corresponding hybridisation line scan is shown in Figure 6-48 (d). This hybridisation line scan shows very clear differences between the areas of the line that correspond to the DLC and the nanodiamonds in the SEM image. The left half of the line scan shows an average sp^2 hybridised
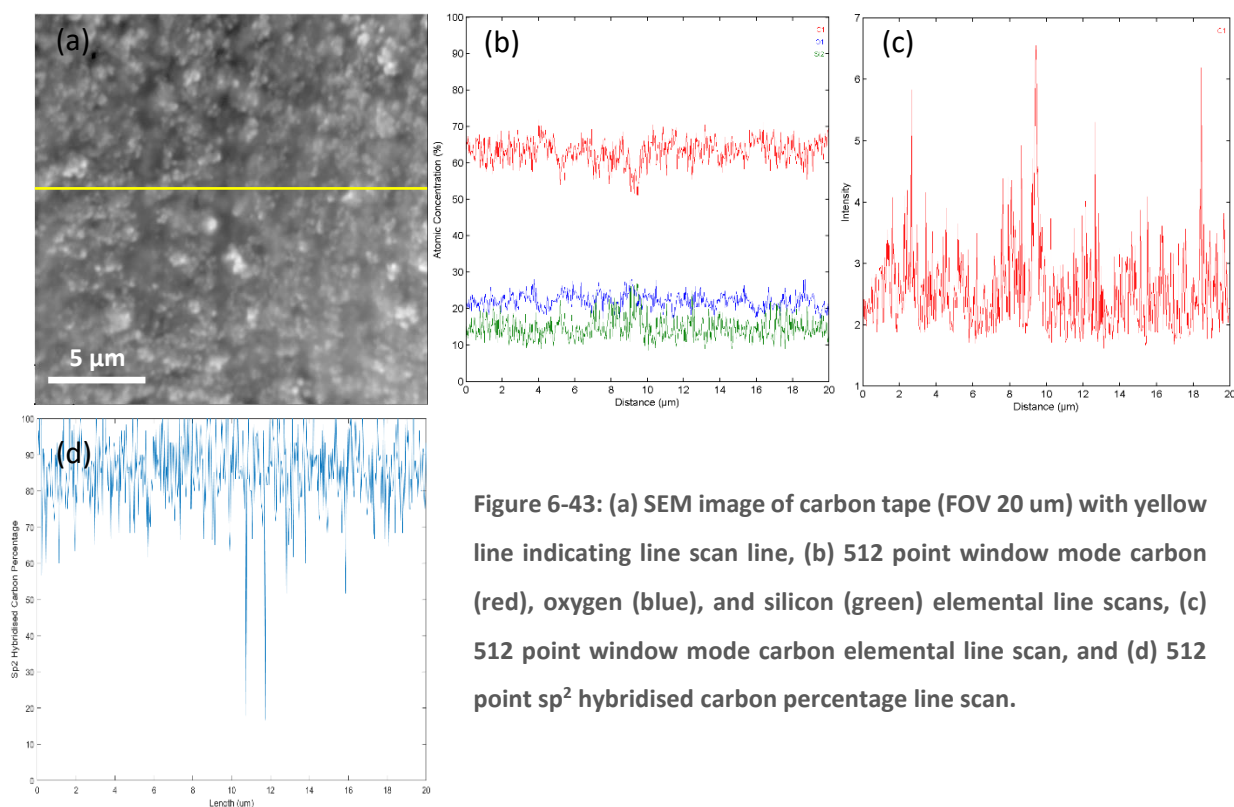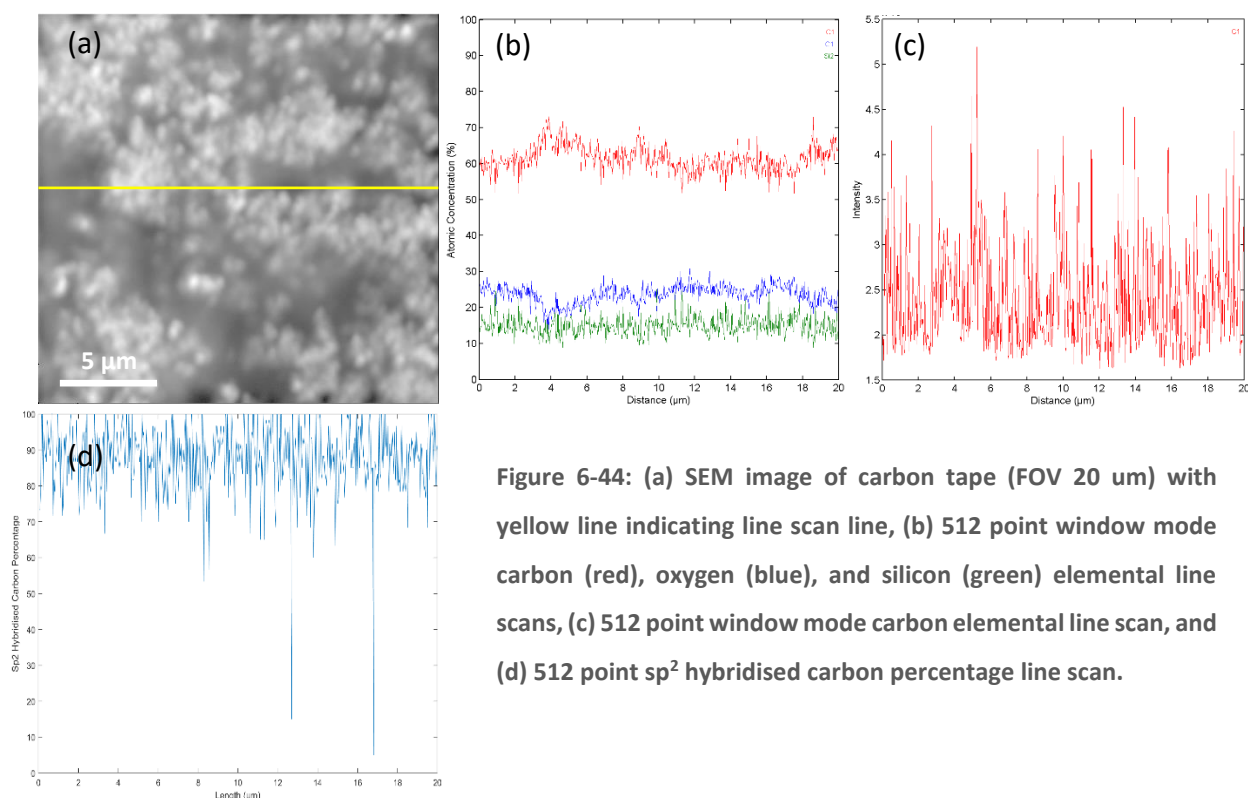

Figure 6-48: (a) SEM image of Nanodiamonds on DLC (FOV 20 um) with yellow line indicating line scan line, (b) 512 point window mode carbon (red), oxygen (blue), and silicon (green) elemental line scans, (c) 512 point window mode carbon elemental line scan, and (d) 512 point sp^2 hybridised carbon percentage line scan.

carbon percentage of approximately 90 %, with values ranging between 80 % and 100 %, which is what was expected from the DLC samples characterised previously. There is an area in the centre of the line scan that correspond to the area of the SEM that shows the thin nanodiamond powder but is not yet to the large nanodiamond cluster, and this area shows a decreased sp^2 hybridised carbon percentage from the DLC area, but is not yet showing the very low percentages that are a result of the larger clusters. This is due to the low thickness of the powder, which is allowing for the DLC film underneath to also be detected at these points, thus showing a sp^2 hybridised carbon percentage that is between that expected form the DLC and the nanodiamonds. Further to the right on the hybridisation line scan is the area that corresponds with the large nanodiamond cluster in the SEM image, which is clearly indicated in the line scan by the low sp^2 hybridised carbon percentage of approximately 10 %. This low percentage is very similar to that observed for the nanodiamonds in the previous sample, thus showing consistency between the samples using this hybridisation line scanning technique.

The hybridisation line scans of nanodiamonds on DLC show that the DLC film has a sp^2 hybridised carbon percentage of approximately 90 % while the nanodiamonds have much lower percentages as low as 10 %. These differences can be very clearly observed in the hybridisation line scan and correspond with the features of the sample observed in the SEM image. These results are also consistent with the results of characterising the same types of sample with the carbon hybridisation mapping technique in the previous chapter (section 5.3.5.2), and show good evidence for the validity and consistency of the carbon hybridisation line scanning technique.

6.3.4.3 Nanodiamonds on Carbon Tape

A sample of nanodiamonds on carbon tape is shown in the 20 µm FOV SEM image in Figure 6-49 (a). The sample shows several medium and large nanodiamond clusters which are mostly located in the bottom left quadrant of the image. The remainder of the sample is the carbon tape substrate, which appears to be highly textured and also has some small particles, which can make it difficult to distinguish between the particles from the carbon tape and the smaller nanodiamond clusters visually. The yellow line in the SEM image indicates the line over which the line scans were acquired and passes through areas of carbon tape (top of the image, left on the line scans) and nanodiamond clusters (bottom of the image, right on the line scans).

The carbon, oxygen, and silicon elemental line scans in Figure 6-49 (b) are not consistent across the entire line, with the elemental concentrations changing as the features in the SEM image change. In
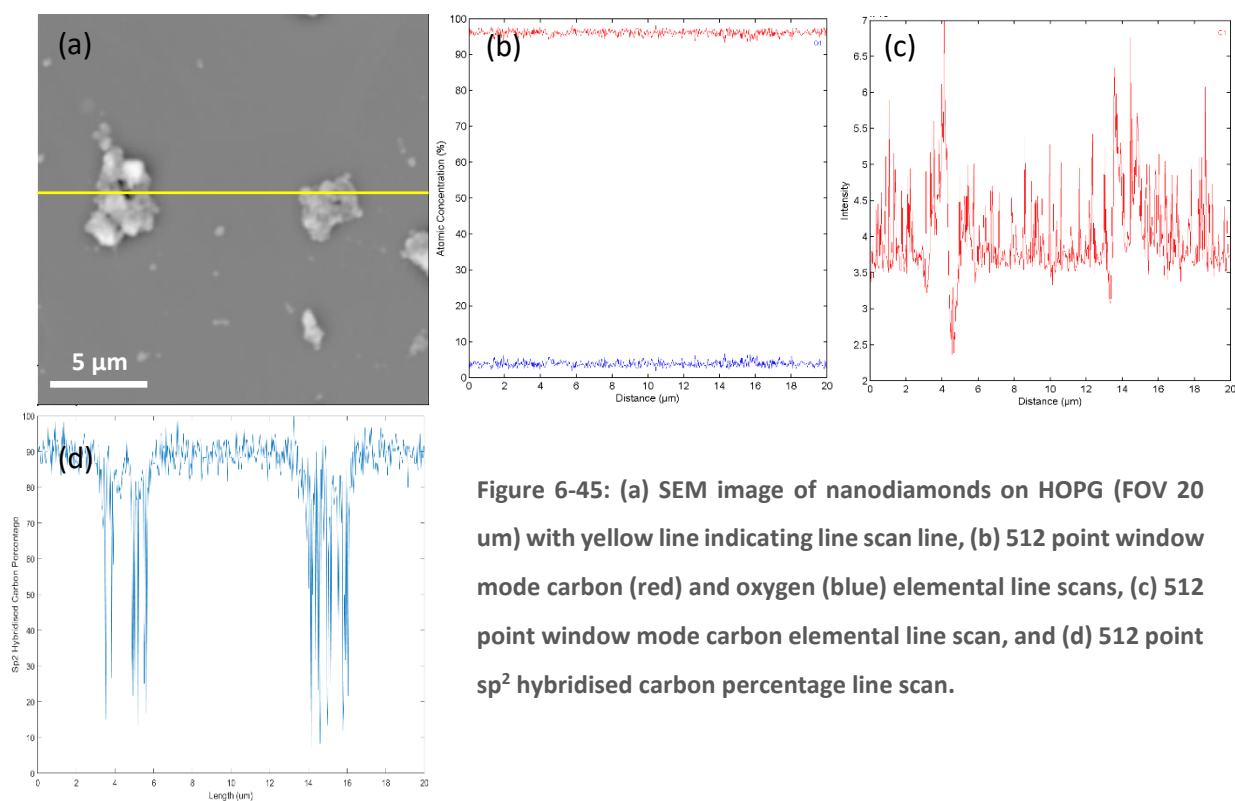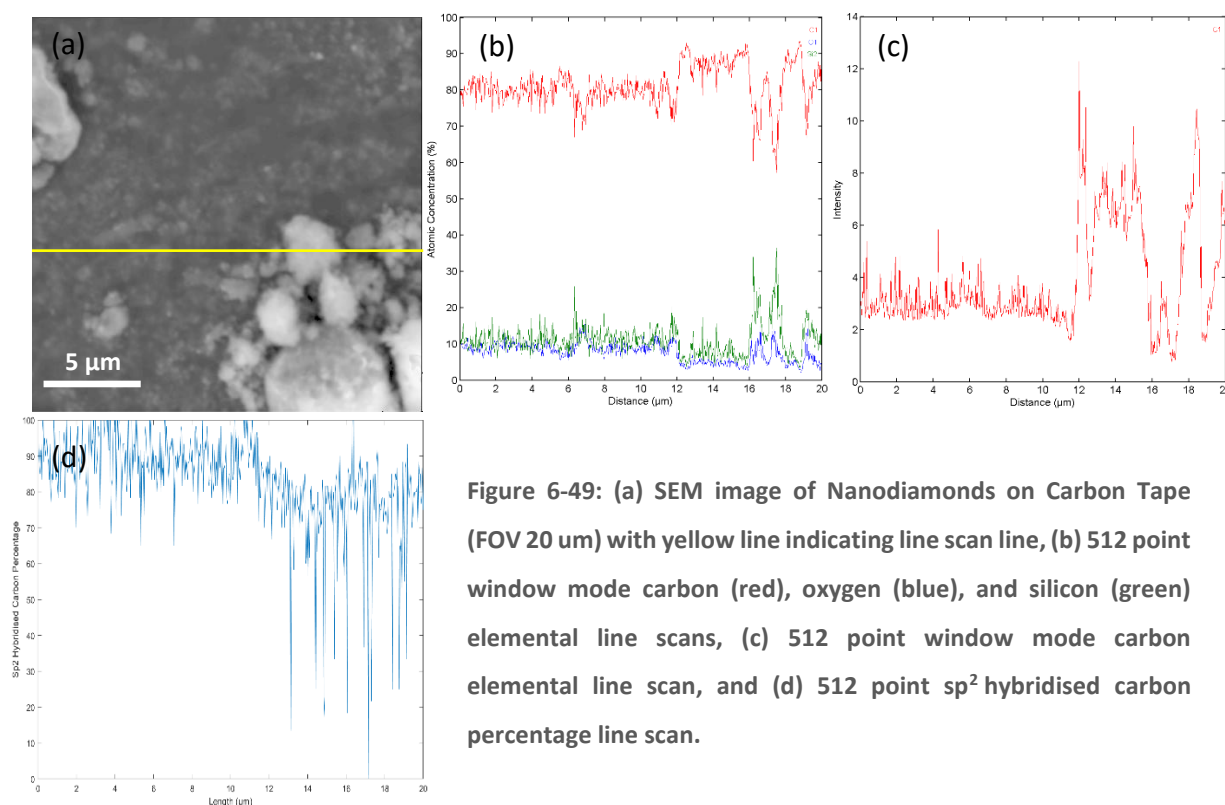
Figure 6-49: (a) SEM image of Nanodiamonds on Carbon Tape (FOV 20 um) with yellow line indicating line scan line, (b) 512 point window mode carbon (red), oxygen (blue), and silicon (green) elemental line scans, (c) 512 point window mode carbon elemental line scan, and (d) 512 point sp^2 hybridised carbon percentage line scan.

the area corresponding to the carbon tape the carbon concentration averages approximately 80 %, while oxygen and silicon average approximately 9 % and 11 %, respectively. As the line passes across the nanodiamond clusters the carbon concentration increases to approximately 90 % with corresponding decreases in the oxygen and silicon concentrations to 4 % and 6 %, respectively. There are also two areas of decreased carbon concentration that correspond with two small gaps between nanodiamond clusters where the carbon substrate is seen.

The window mode carbon elemental line scan and resultant hybridisation line scan are shown in Figure 6-49 (c) and (d), respectively, and also show clear differences between the carbon tape and nanodiamonds. The left half of the line scan corresponds with the carbon tape area in the SEM image and displays sp^2 hybridised carbon percentages that match those expected for carbon tape from the previous samples (Figure 6-43 and Figure 6-44). This region shows an average sp^2 hybridised carbon percentage of approximately 90 % but a large range with values between 70% and 100 % detected in various places along the line. The area on the right of the line scan shows much lower percentages (down to 0 %) which corresponds with the nanodiamonds in the SEM image. This area does not have sp^2 hybridised carbon percentages as consistently low as has been observed in some previous samples, suggesting that these nanodiamond clusters are quite thin and the carbon tape substrate, which has higher sp^2 content, is also being detected at these points.

A second sample of nanodiamonds on carbon tape is shown in Figure 6-50 (a), which is a 20 μm FOV

SEM image of the sample. There are several very large clusters of nanodiamonds on the surface, as well as other medium to large clusters scattered across the surface. The carbon tape substrate is highly textured and has some areas that look very similar to small nanodiamond clusters and again make it difficult to determine the difference visually between these small features. The yellow line in the SEM image shows the acquisition line for the line scans and passes through one large nanodiamond cluster on the left and one medium cluster in the centre, with areas of carbon tape along the rest of the line.

The carbon, oxygen, and silicon elemental line scans are shown in Figure 6-50 (b) and show some elemental difference between the nanodiamonds and carbon tape. The carbon concentration along the areas that corresponds with the carbon tape is approximately 75 %, however in the areas that correspond with the nanodiamond clusters the carbon percentage increases to 90 %. The oxygen and silicon experience reductions in atomic concentration in these areas, with oxygen decreasing from approximately 11 % to 4 % and silicon from 14 % to 6 %.

The window mode carbon elemental line scan (Figure 6-50 (c)) was converted to a hybridisation line scan (Figure 6-50 (d)), which shows clear differences between the regions that correspond to the nanodiamonds and carbon tape in the SEM image. In the left of the line there is a large nanodiamond cluster, and the corresponding area in the hybridisation line scan shows low sp^2 percentages (down to 20 %). A smaller nanodiamond cluster is in the centre of the line, and this area shows a
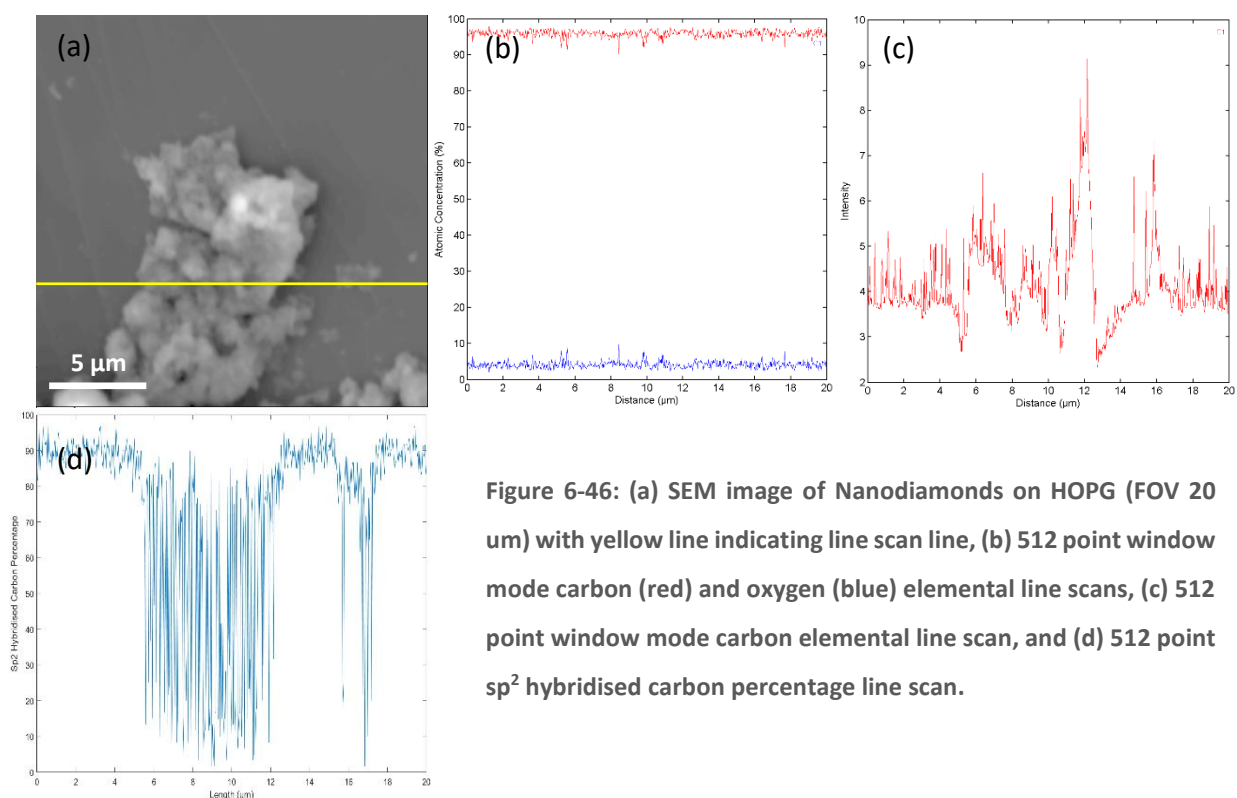

Figure 6-50: (a) SEM image of Nanodiamonds on Carbon Tape (FOV 20 um) with yellow line indicating line scan line, (b) 512 point window mode carbon (red), oxygen (blue), and silicon (green) elemental line scans, (c) 512 point window mode carbon elemental line scan, and (d) 512 point sp^2 hybridised carbon percentage line scan.

sp^2 hybridised carbon percentage of approximately 50 %. This result suggests that the nanodiamond cluster is quite thin and the carbon tape substrate is also being detected in this area. The remainder of the line runs across areas that appear to be carbon tape in the SEM image and show sp^2 hybridised carbon percentages that reflect this. The average sp^2 content in these areas is approximately 85 %, with values ranging from 65 % to 100 %, which is what is expected for carbon tape from previous samples.

The above samples show nanodiamonds with sp^2 hybridised carbon percentages of around 20 % and carbon tape with an average percentage of approximately 85-90 %, which are consistent with results obtained both earlier in this chapter and in the previous chapter, where similar samples were characterised with the carbon hybridisation mapping technique (section 5.3.5.3). These samples therefore supply further evidence for the validity and consistency of the carbon hybridisation line scanning technique and its ability to discern different hybridisations on a surface.

6.3.5   Piranha Solution Treated Nanodiamonds

Piranha solution treated nanodiamonds were also analysed using the hybridisation line scanning technique. These treated nanodiamonds were obtained from the University of Melbourne and underwent a piranha solution treatment as described in the previous chapter. In order to compare these nanodiamonds to the untreated nanodiamonds they were deposited on the same three substrates using the same methods, and the results will be analysed here.

6.3.5.1 Piranha Solution Treated Nanodiamonds on Highly Oriented Pyrolytic Graphite

A sample of piranha solution treated nanodiamonds deposited on HOPG is shown in the 20 μm FOV SEM image in Figure 6-51 (a). This sample shows many small clusters of the piranha solution treated nanodiamonds that are both grouped together and dispersed individually, while the HOPG substrate appears featureless with the exception of differently coloured stripes indicating the presence of different graphene sheets. The yellow line in the SEM image indicates the path over which the line scans were acquired and passes through three nanodiamond clumps and also over areas of HOPG.

Carbon and oxygen elemental line scans are shown in Figure 6-51 (b) and show a sample that has very consistent atomic concentrations across the entire line, with a carbon percentage of approximately 96 % and an oxygen percentage of 4 %, which indicates that the piranha treated nanodiamonds and HOPG have the same elemental composition.

The window mode carbon elemental line scan and resultant hybridisation line scan are shown in

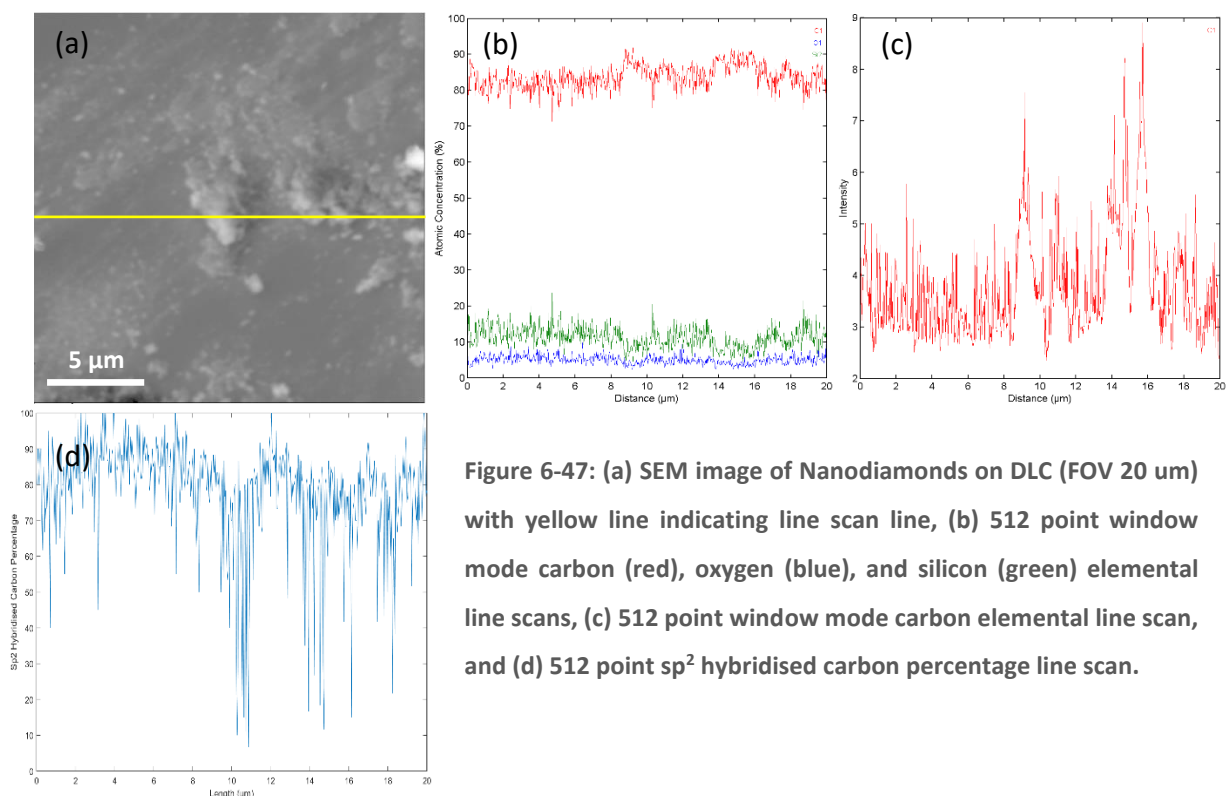Figure 6-51: (a) SEM image of Piranha Solution treated Nanodiamonds on HOPG (FOV 20 um) with yellow line indicating line scan line, (b) 512 point window mode carbon (red) and oxygen (blue) elemental line scans, (c) 512 point window mode carbon elemental line scan, and (d) 512 point sp^2 hybridised carbon percentage line scan.

Figure 6-51 (c) and (d). There are clear differences between the areas of the hybridisation line scan that correspond to the HOPG and the piranha treated nanodiamonds in the SEM image. There are three large clusters of nanodiamonds that the line scan passes over, and at each of these points the sp^2 hybridised carbon percentage decreases down to almost 0 %. The areas that correspond with the HOPG substrate in the line scan show approximately 90 % sp^2 hybridised carbon, which is expected from the previous results. The areas at the edge of the nanodiamond clusters, where the nanodiamonds are thinner, show a sp^2 hybridised carbon percentage between these two extreme values (around 75 %) indicating that both the nanodiamonds and underlying HOPG substrate are being detected at these points.

The SEM image in Figure 6-52 (a) shows a second sample of piranha solution treated nanodiamonds on HOPG. This 20 µm FOV image shows a surface that contains many medium to large clusters of the treated nanodiamonds scattered across the centre and top of the image, with the spaces between showing the featureless HOPG substrate. The yellow line in the SEM image shows the path over which the line scans were acquired and passes through a HOPG area on the left, through a large nanodiamond area in the centre, and again HOPG on the right.

The carbon and oxygen elemental line scans shown in Figure 6-52 (b) indicate uniform elemental concentrations across the surface of approximately 96 % carbon and 4 % oxygen. This result is consistent with the previous sample in Figure 6-51, and indicates that the HOPG and piranha

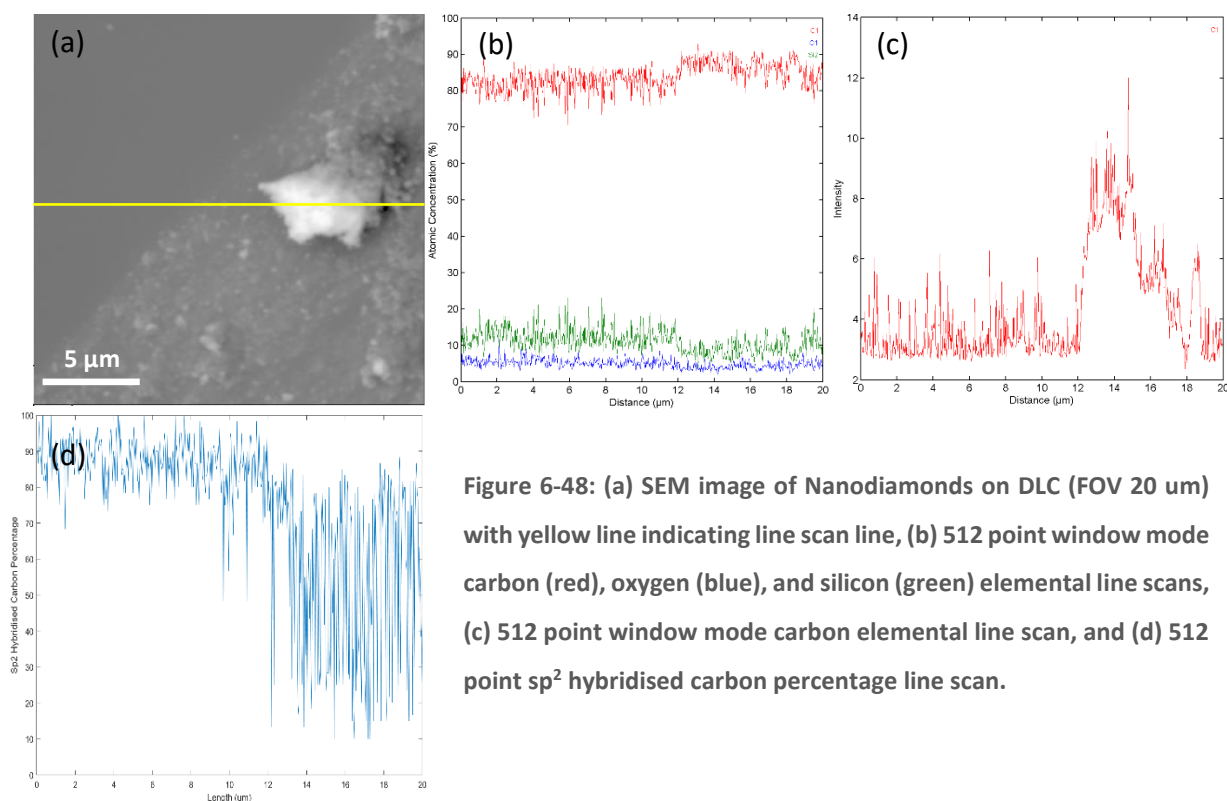Figure 6-52: (a) SEM image of Piranha Solution treated Nanodiamonds on HOPG (FOV 20 um) with yellow line indicating line scan line, (b) 512 point window mode carbon (red) and oxygen (blue) elemental line scans, (c) 512 point window mode carbon elemental line scan, and (d) 512 point sp^2 hybridised carbon percentage line scan.

solution treated nanodiamonds have the same elemental composition.

The window mode carbon elemental line scan and resultant hybridisation line scan are shown in Figure 6-52 (c) and (d), respectively, and show clear differences between the hybridisations of the HOPG and the piranha solution treated nanodiamonds. The areas on the left and right of the hybridisation line scan show a sp^2 hybridised carbon percentage of approximately 90 %, which is expected for HOPG and consistent with the previous results. The area corresponding with the piranha solution treated nanodiamonds has sp^2 hybridised carbon percentages down to 10 %, which is higher than the previous sample but consistent with the untreated nanodiamonds shown previously. Towards the right end of the nanodiamond region of the line scan it can be seen that there is an area of much higher sp^2 hybridised carbon percentage than the rest of that region. When compared to the corresponding position in the SEM image it can be seen that the nanodiamond clusters in this area appear to be much smaller. This suggests that the nanodiamonds in this area are thinner and the HOPG substrate is also being detected along this section of the sp^2 hybridised carbon percentage line scan.

The hybridisation line scans presented for samples composed of piranha solution treated nanodiamonds on HOPG show clear differences between the hybridisation of the two types of carbon. HOPG showed a sp^2 hybridised carbon percentage of approximately 90 % while the piranha solution treated nanodiamonds showed sp^2 carbon content between 0 % and 10 %, depending on

336

how thick the nanodiamond cluster is at that point. These results are consistent with those found in the previous section for the untreated nanodiamonds on HOPG, suggesting that the piranha solution treatment has not significantly changed the hybridisation of the nanodiamonds. These results also provide further evidence for the validity of the carbon hybridisation line scanning technique and its ability to differentiate between different types of carbon on one surface.

6.3.5.2 Piranha Solution Treated Nanodiamonds on Diamond-Like Carbon

The same piranha solution treated nanodiamonds were also deposited on a DLC film grown on silicon. The 20 μm FOV SEM image in Figure 6-53 (a) shows one such sample, which contains a range of differently sized nanodiamond clusters scattered across an otherwise featureless surface. There is also a long, white, string-like feature in the upper left quarter of the image, which is not a feature that is seen in any of the other nanodiamond or DLC samples. Based on the SEM image it is thought that this feature is some sort of contaminate that has deposited on the surface during deposition of the nanodiamonds. The yellow line on the surface indicates the line over which the line scans were acquired and passes through several nanodiamond clusters and areas of substrate but does not pass through the contaminate feature.

The carbon, oxygen, and silicon elemental maps across this line are shown in Figure 6-53 (b) and show some variations in the atomic concentrations across the surface. These variations line up with the features in the SEM image, with the carbon concentration increasing from approximately 83 %
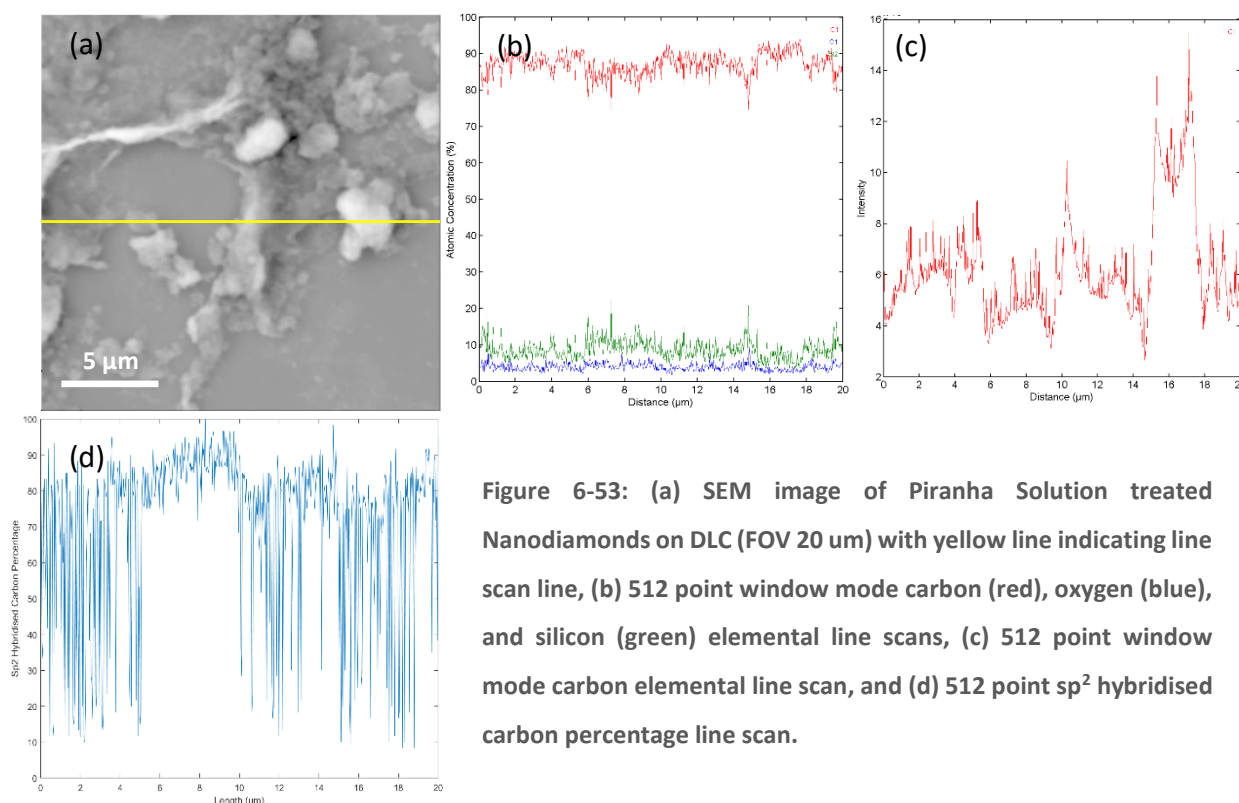
Figure 6-53: (a) SEM image of Piranha Solution treated Nanodiamonds on DLC (FOV 20 um) with yellow line indicating line scan line, (b) 512 point window mode carbon (red), oxygen (blue), and silicon (green) elemental line scans, (c) 512 point window mode carbon elemental line scan, and (d) 512 point sp^2 hybridised carbon percentage line scan.

337

in the DLC film areas to approximately 89 % in the areas that correspond to the piranha solution treated nanodiamond clusters. There is a corresponding decrease in the silicon content in these areas, from approximately 12 % to 8 %, and a small decrease in oxygen from 5 % to 4 %.

The window mode carbon elemental line scan acquired over this same line is shown in Figure 6-53 (c), and the resultant hybridisation line scan is shown in Figure 6-53 (d). The sp^2 hybridised carbon percentage is significantly different in the areas corresponding to the piranha treated nanodiamonds and the DLC film. The area on the left of the line scan corresponds to a nanodiamond cluster in the SEM image and shows percentages of sp^2 hybridised carbon as low as 10 %, as do areas in the centre and right of the line scan which also correspond to nanodiamond clusters in the SEM image. The areas in between show sp^2 hybridised carbon percentages of approximately 85% and correspond to the DLC film areas in the SEM image. This percentage is slightly lower than that observed previously for DLC films, which is likely a result of small nanodiamond particles present on the DLC film that cannot be clearly seen in the SEM image. These percentages correlate with those observed in the previous sample of piranha solution treated nanodiamonds on HOPG and also with the untreated nanodiamonds on DLC.

A second sample of piranha solution treated nanodiamonds in shown in the SEM image in Figure 6-54 (a), which shows many smaller clusters of the nanodiamonds scattered across the surface as well as one group of clusters near the centre of the image. The yellow line indicates the path over which the line scans were acquired, and passes through several individual nanodiamond clusters as well as the large group of nanodiamond clusters and several areas of the DLC film.

The carbon, oxygen, and silicon elemental line scans shown in Figure 6-54 (b) indicate some changes in elemental composition across the line that correspond to some extent with the features in the SEM image. The areas that correspond with the nanodiamonds in the SEM image tend to have a slightly higher carbon concentration, with the concentration increasing from approximately 83 % to approximately 88 %, while there is a corresponding slight decrease in the oxygen and silicon atomic percentages.

The window mode carbon elemental line scan acquired over the same line, and its resultant hybridisation line scan, are shown in Figure 6-54 (c) and (d), respectively. This hybridisation line scan shows clear differences between the areas showing piranha solution treated nanodiamonds and the DLC film. The area on the centre right of the line scan show sp^2 hybridised carbon percentages down
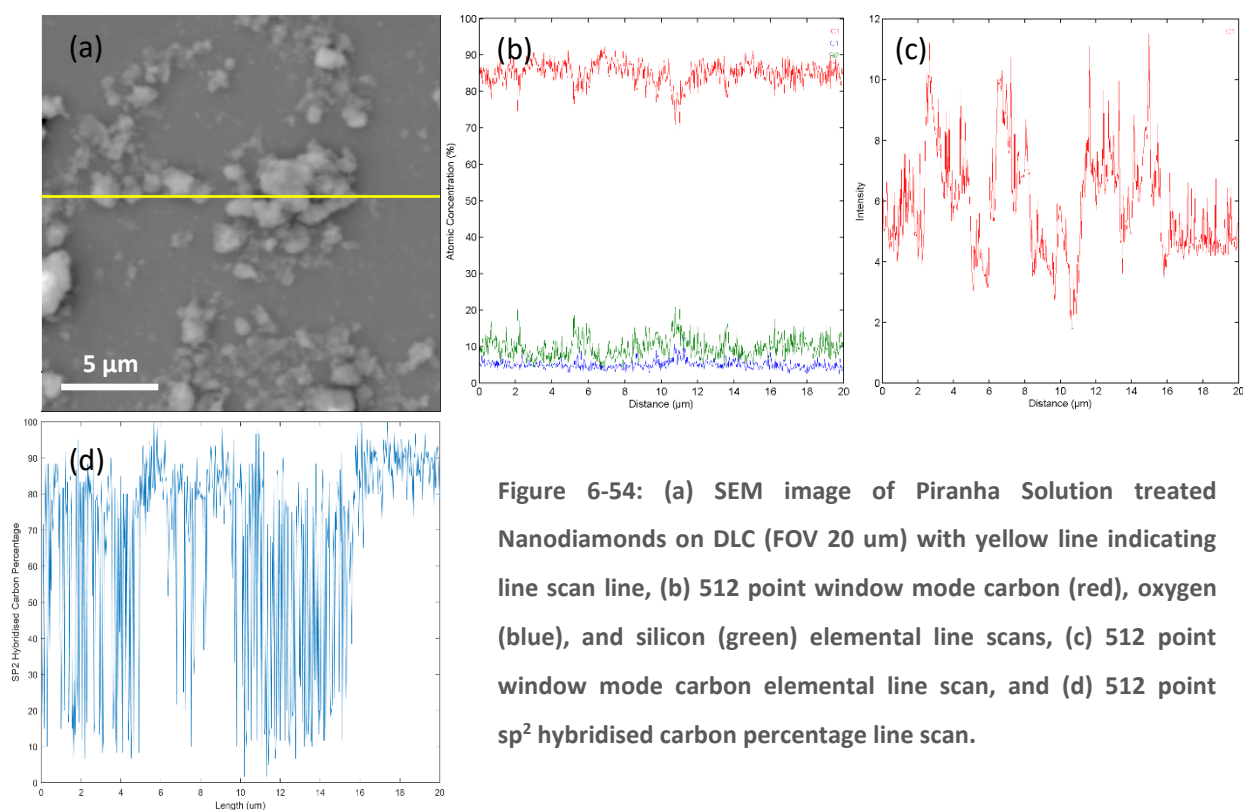
Figure 6-54: (a) SEM image of Piranha Solution treated Nanodiamonds on DLC (FOV 20 um) with yellow line indicating line scan line, (b) 512 point window mode carbon (red), oxygen (blue), and silicon (green) elemental line scans, (c) 512 point window mode carbon elemental line scan, and (d) 512 point sp^2 hybridised carbon percentage line scan.

to approximately 10 %, which matches the percentages seen previously for the piranha solution treated nanodiamonds. This percentage is also seen on the left of the line scan, where several individual nanodiamond clusters are next to each other. There are also small gaps in this section of the line scan where the percentage of sp^2 hybridised carbon is closer to 70 % or 80 %, and these areas line up with the small gaps between the nanodiamond clusters in the SEM image. The area on the right of the line scan has a sp^2 hybridised carbon percentage of approximately 90 %, which is consistent with the percentages seen for DLC films previously.

Samples of piranha solution treated nanodiamonds on DLC films have shown clear differences between the sp^2 hybridised carbon percentages detected in the areas corresponding to the two types of carbon, with the DLC film having a sp^2 content of 85 % to 90 % and the piranha solution treated nanodiamonds having sp^2 hybridised carbon percentages of around 10 %. These results are consistent with those seen in previous samples and suggest that the nanodiamonds have not undergone a significant change in hybridisation after the piranha treatment. These samples provide further evidence for the validity of the hybridisation line scanning technique and its ability to consistently identify the hybridisation of different carbon materials.

6.3.5.3 Piranha Solution Treated Nanodiamonds on Carbon Tape

Piranha solution treated nanodiamonds were also deposited on carbon tape and examined using the carbon hybridisation line scanning technique. The SEM image in Figure 6-55 (a) shows variously
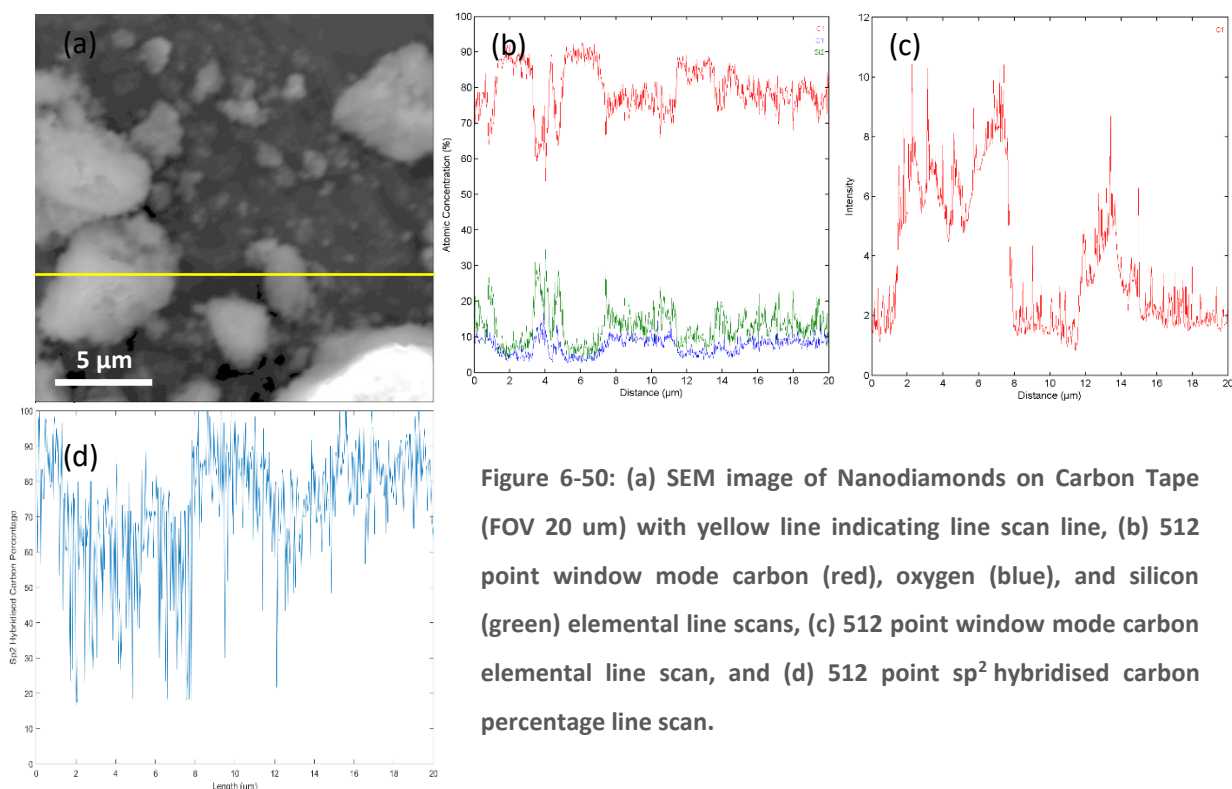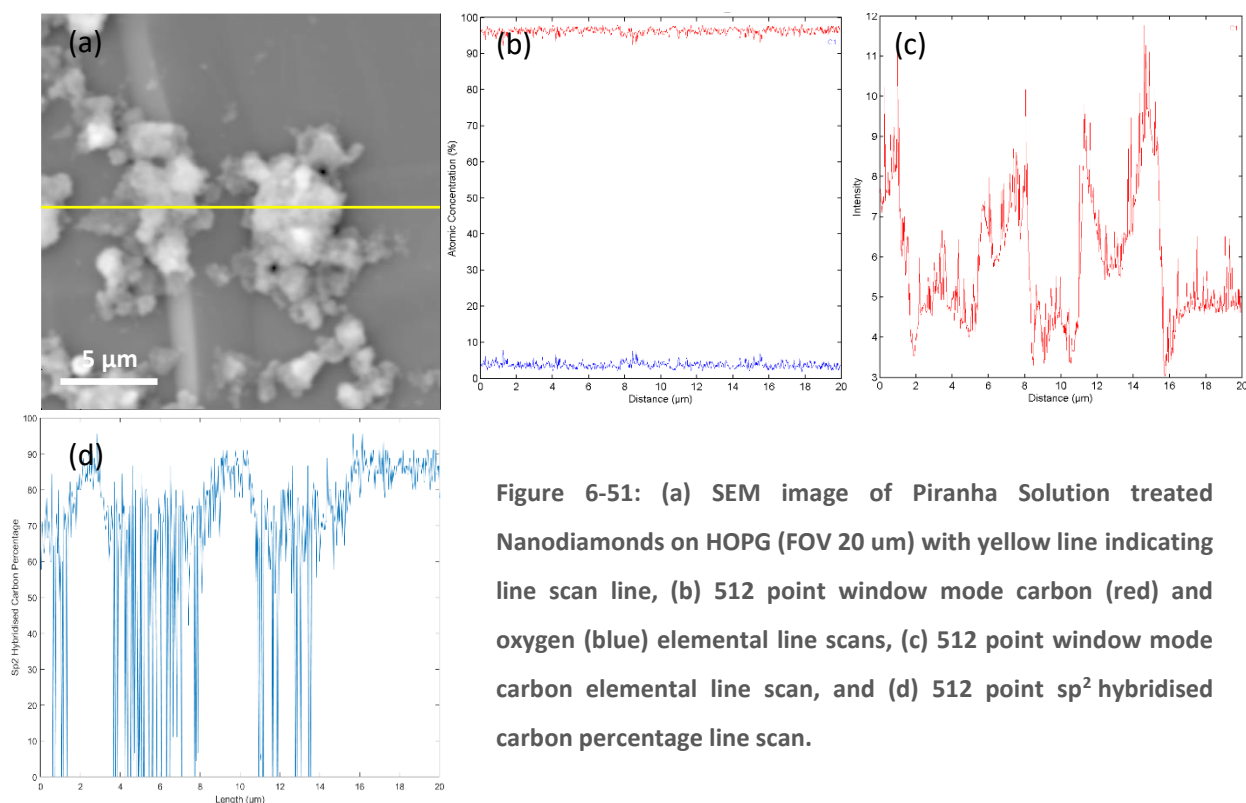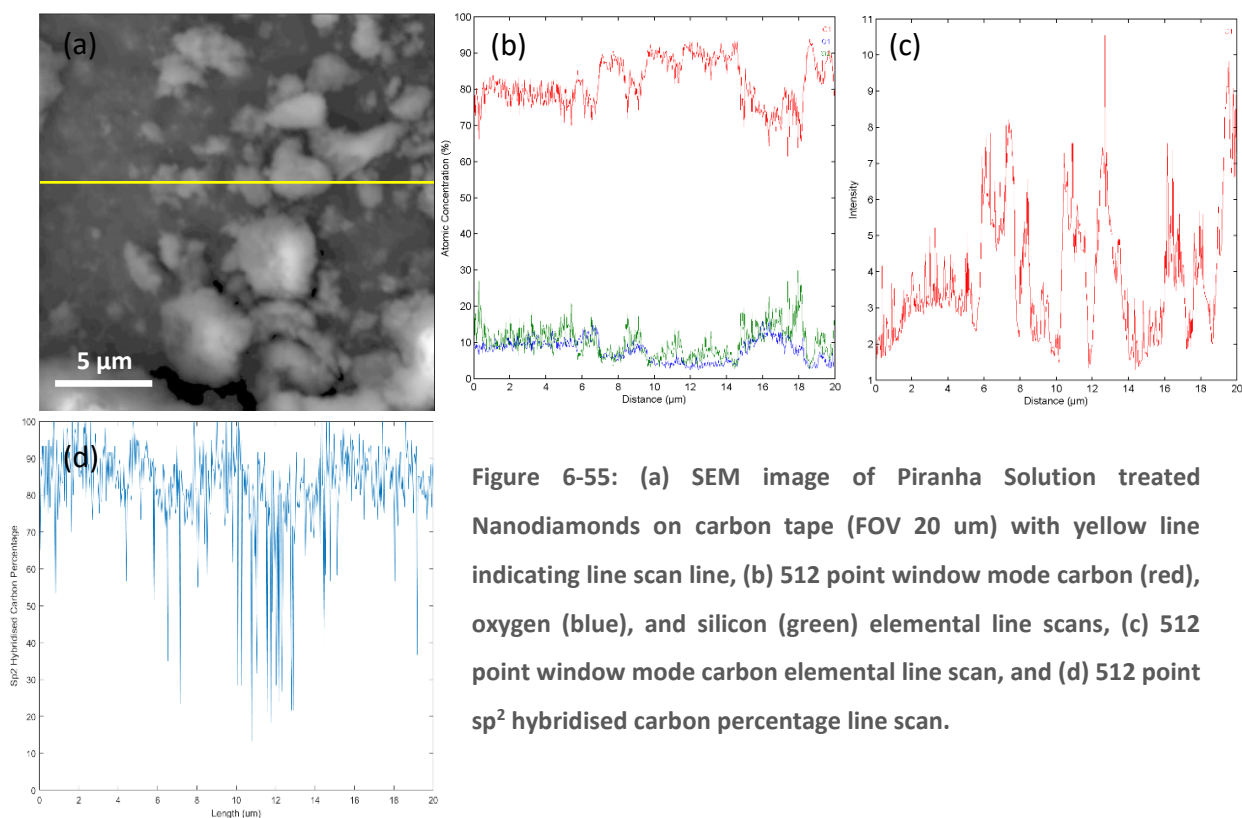
Figure 6-55: (a) SEM image of Piranha Solution treated Nanodiamonds on carbon tape (FOV 20 um) with yellow line indicating line scan line, (b) 512 point window mode carbon (red), oxygen (blue), and silicon (green) elemental line scans, (c) 512 point window mode carbon elemental line scan, and (d) 512 point sp^2 hybridised carbon percentage line scan.

sized clusters of piranha solution treated nanodiamonds scattered across a piece of carbon tape, which is not uniform in appearance. The yellow line indicates the path over which the line scans were acquired and passes through an area of carbon tape at the top before some features in the lower half of the image. Due to the nature of the carbon tape, which appears to be composed of multiple particles as shown previously, it is difficult to identify whether the smaller features observed in the SEM image are from the carbon tape or are smaller nanodiamond clusters.

The carbon, oxygen, and silicon elemental line scans over this line are shown in Figure 6-55 (b) and show a difference in the elemental composition across the surface. The carbon content is higher on the features that appear to be nanodiamond clusters in the SEM image, with the percentage increasing from approximately 80 % to approximately 90 %. There are corresponding decreases in the oxygen and silicon concentrations in these areas, with oxygen decreasing from 9 % to 4 % and silicon decreasing from 11 % to 6 %.

The window mode carbon elemental line scan and corresponding hybridisation line scan are shown in Figure 6-55 (c) and (d). The hybridisation line scan shows differences across the line that correspond with some of the features in the SEM image. The left of the line scan shows sp^2 hybridised carbon percentages of approximately 85 % with a large variation, which matches the results found previously for carbon tape and corresponds with the area that appears to be carbon tape in the SEM image. Further along the line in the SEM image are two small particles that appear

to be piranha solution treated nanodiamonds, and the sp^2 hybridised carbon percentage line scan supports this with a lower sp^2 content than the carbon tape. However, the sp^2 hybridised carbon percentage is not as low as has been previously seen for the piranha solution treated nanodiamonds, which suggests that the clusters are quite small and the carbon tape beneath them is also being detected. The line next crosses a small area that again appears to be carbon tape and shows the same sp^2 hybridised carbon percentage as the previous area, before crossing larger nanodiamond clusters. These clusters are more easily identifiable from the SEM image as their size is larger than the particles observed in carbon tape. The sp^2 hybridised carbon percentage in the corresponding area of the line scan is lower than that found for the carbon tape, with values of around 20 % determined across these features. These values fall within the range detected for the untreated nanodiamonds previously however they are slightly higher than other values determined for the piranha solution treated nanodiamonds previously.

Another sample of piranha solution treated nanodiamonds on carbon tape is shown in the 50 μm FOV SEM image in Figure 6-56 (a). The sample consists of a large variety of sizes of nanodiamond clusters, some of which are large enough to start experiencing charging due to the electron beam, which is shown by the bright white areas in the SEM image. The yellow line in the image passes through many of the smaller nanodiamond clusters in the SEM image, along with areas that appear to show the carbon tape substrate with much smaller nanodiamond clusters on it.
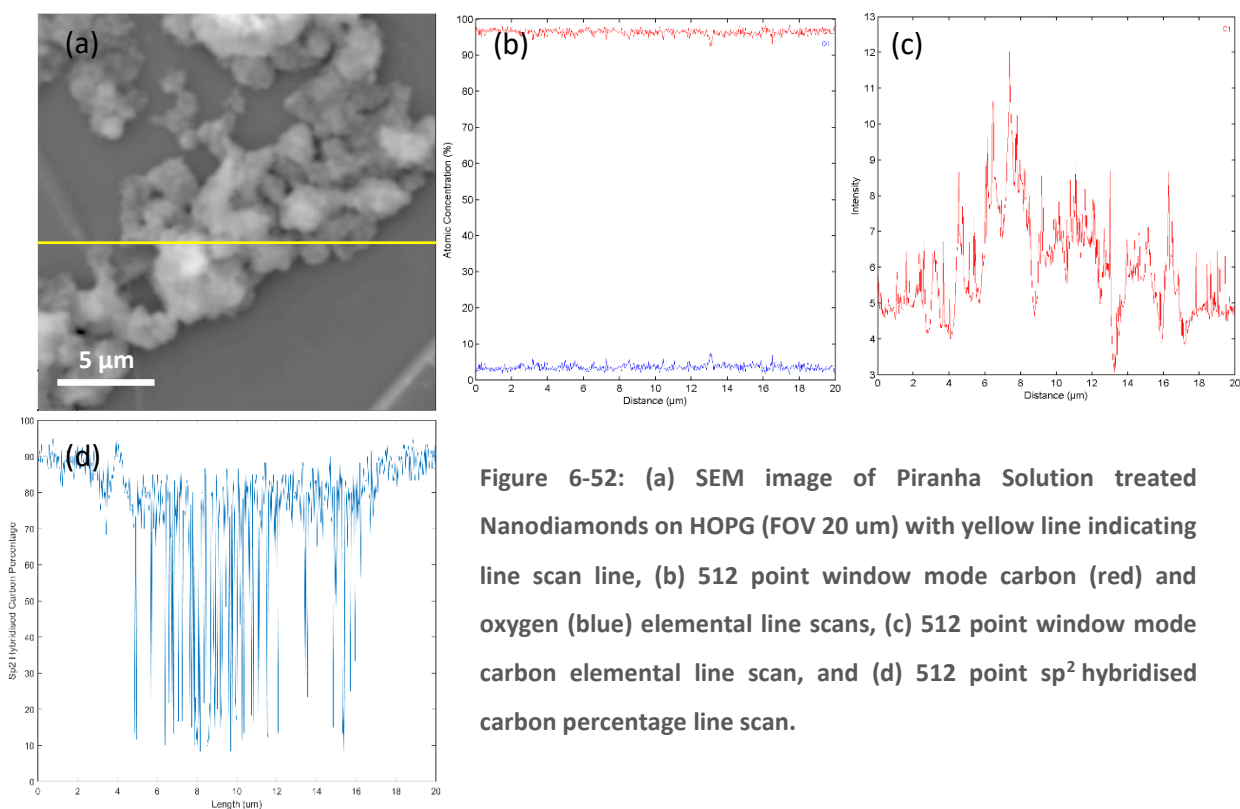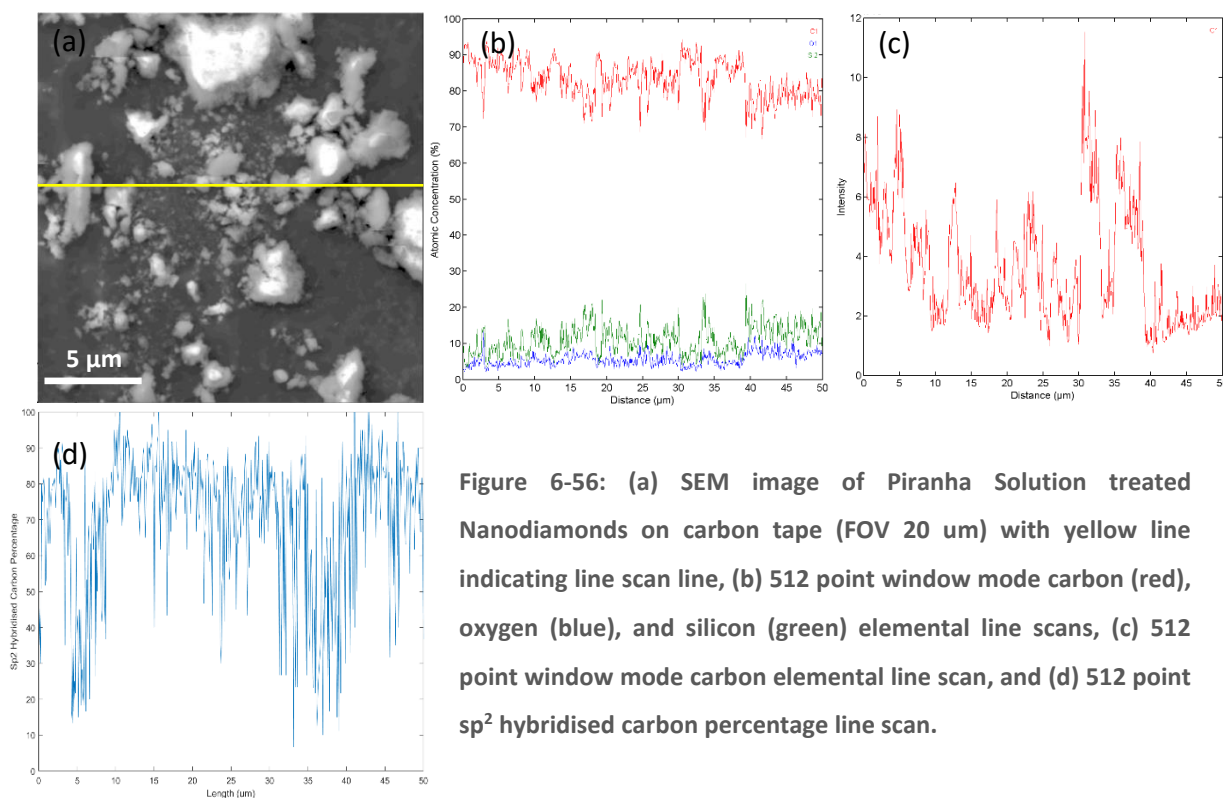

Figure 6-56: (a) SEM image of Piranha Solution treated Nanodiamonds on carbon tape (FOV 20 um) with yellow line indicating line scan line, (b) 512 point window mode carbon (red), oxygen (blue), and silicon (green) elemental line scans, (c) 512 point window mode carbon elemental line scan, and (d) 512 point sp^2 hybridised carbon percentage line scan.

The carbon, oxygen, and silicon elemental line scan for this sample are shown in Figure 6-56 (b) and show a similar trend to the previous sample, with a slight increase in the carbon concentration from approximately 80 % to 90 % in the areas that correspond to the nanodiamond clusters. There is a decrease in the oxygen and silicon percentages in these areas, with oxygen changing from approximately 5 % to approximately 4 % and silicon from approximately 15 % to 6 %.

The window mode carbon elemental line scan and resultant hybridisation line scan are shown in Figure 6-56 (c) and (d), and again show differences between the hybridisations of the different features in the SEM image. There is a small section on the left of the line that shows low sp^2 hybridised carbon percentages of around 15 %, which indicates the presence of piranha solution treated nanodiamonds. When compared to the SEM image this area does match with a large nanodiamond cluster and shows carbon tape with smaller nanodiamond clusters on either side. These areas in the line scan show sp^2 hybridised carbon percentages of 75 % to 95 %, which matches the areas seen previously that has small, thin nanodiamond clusters on top of the carbon tape substrate. As the line continues across the sample it continues to show changes in the sp^2 hybridised carbon content, all of which correlate with the features observed in the SEM image.

Samples of piranha solution treated nanodiamonds on carbon tape have been presented and show clear differences in the hybridisations present across the different features. The piranha solution treated nanodiamonds showed sp^2 hybridised carbon percentages of around 20 %, which is consistent with the previous samples of both the treated and untreated nanodiamonds. The carbon tape was shown to have a sp^2 hybridised carbon content of approximately 85 % but with large variations, which is also consistent with the percentages found for carbon tape when it was considered individually. Similar samples were also examined with the carbon hybridisation mapping technique in the previous chapter (section 5.3.6.3) and showed results consistent with the results found here with the carbon hybridisation line scanning technique. These samples therefore provide further evidence for the validity of the carbon hybridisation line scanning technique and its ability to differentiate between different types of carbon present on one surface.

6.4 Conclusion

The carbon hybridisation mapping technique has been outlined in this chapter and then optimised and successfully applied to samples containing a range of carbon hybridisations. The SAM parameters found to be optimal for acquiring window mode carbon elemental line scans for the purpose of creating hybridisation line scans were a step width of 0.2 eV, a time per step of 1.0 ms,

and 20 scans averaged. It was also found that the level of magnification at which the line scans are acquired has an impact on the results, with the calibration curve for converting the D parameter value to a sp^2 hybridised carbon percentage only producing reliable results when the FOV is 50 μm or lower.

A variety of samples were examined with the optimised hybridisation line scanning technique, including both standards of a single material and mixed samples. Samples that were standards of a single material included HOPG, DLC films, and carbon tape, while samples with mixed hybridisations included nanodiamonds or piranha solution treated nanodiamonds on HOPG, DLC films, or carbon tape. The carbon hybridisation line scanning technique was successfully able to determine the hybridisations of these different features and clearly show these differences in a line scan consistently, thus providing a useful tool for the creation of carbon-based devices with multiple hybridisations.

7 CONCLUSIONS AND FUTURE WORK

7.1 Conclusions

The work presented in this dissertation has focused on two main areas: the growth and modification of carbon materials and the characterisation of the hybridisation of carbon materials with high spatial resolution. The properties of a carbon material depend on its structure and hybridisation, and therefore the ability to tailor the structure to suit a specific purpose will enable the building of carbon-based devices for a range of properties. In order to create devices that are entirely composed of carbon, structures made from different hybridisations of carbon on the same surface are needed, and it is necessary to characterise these structures with spatial resolution. X-ray photoelectron spectroscopy and scanning Auger microscopy were the two techniques used in the characterisation of samples within this work, and were used to determine both the elemental and hybridisation compositions of the samples.

The ability to create or modify carbon materials with a variety of properties is vital for the production of entirely carbon-based devices, and it was therefore this ability that was examined first within this work in chapter 3 by modifying the surface of HOPG using plasma. Two different source gases were chosen for the plasma treatment due to the different ways in which they interact with the sample surface. Oxygen plasma contains species which will react chemically with the HOPG surface, while argon plasma contains larger, more inert species that modify the surface by bombardment. While some studies on the modification of HOPG with oxygen or argon plasma have been performed previously in the literature, the range of plasma deposition parameters and the plasma chamber orientation make the modification possible with the instrument used in this work different from previous studies.

Through systematic studies of the variation of treatment time with both plasma for a range of RF-coupling powers it was found that an increase in time resulted in an increase in the level of oxide formed on the HOPG surface as well as an increase in the conversion of sp^2 hybridised carbon to sp^3 hybridised carbon. The RF-coupling power used to ignite the plasma was found to have a lower effect on the extent of modification of HOPG than the treatment time, with increases above 40 W not showing significant changes in the elemental or hybridisation composition of the samples. The source gas also influenced the extent of modification, with argon plasma treatment resulting in a greater oxide level on the surface than oxygen plasma. The hybridisation of the surface is also

different when the source gas is changed, with argon plasma producing a surface with a much lower sp^2 hybridised carbon percentage. These differences are due to the difference in the way the two plasma interact with the HOPG surface, and the combination of the source gas, RF-coupling power, and treatment time show allow for the level of modification of the HOPG surface to be varied to achieve the desired properties.

The next step in developing the ability to produce carbon with a variety of properties was to grow diamond-like carbon films using plasma enhanced chemical vapour deposition, which was presented in chapter 4. There are several plasma parameters that can be varied to control the plasma conditions, including the pressure, RF-coupling power, and growth time, as well as the source gas(es). When methane is used as the source gas for the deposition an increase in growth time produces a thicker DLC film, as does an increase in RF-coupling power or an increase in source gas pressure. However, no variation in the elemental or hybridisation composition of the film is observed when any of these parameters are varied. Films were also grown with either argon or hydrogen mixed with methane as the source gas. Variation in the methane:argon ratio does not produce any changes in the thickness, elemental, or hybridisation composition of the films, while a change in the methane:hydrogen ratio produces films with constant composition but changes the thickness of the film.

Having established the ability to control the growth or modification of a carbon surface using plasma by varying several plasma parameters, the focus shifted to creating a method for the characterisation of the hybridisation of carbon materials with high spatial resolution. Two techniques for achieving this using scanning Auger microscopy were developed in this work, and demonstrated using a variety of samples.

The first technique developed in chapter 5 was a hybridisation mapping technique, which produces maps of sp^2 hybridised carbon percentage of an area examined using the in-situ SEM in the scanning Auger nanoprobe instrument. This is achieved by acquiring a window mode carbon elemental map of the surface, which contains a full spectrum of the C(KLL) peak within each pixel, and exporting and processing this map in MATLAB. Code was written in MATLAB to smooth and differentiate the spectrum from each pixel, and then calculates the D parameter value of each spectrum, thereby finding the sp^2 hybridised carbon percentage at each pixel of the carbon elemental map. These hybridisation percentages are then displayed as a 2D map, with the intensity value of the original elemental map replaced with the sp^2 hybridised carbon percentage value from that pixel. These

maps show the variation in carbon hybridisation across a surface, and have been applied to samples containing either one type of carbon or two different carbon materials. These materials included HOPG, DLC, carbon tape, and nanodiamonds, and the hybridisation mapping technique was able to identify the hybridisations present in each of these samples, showing a clear correlation with features of the samples shown in the SEM images. The technique was shown to identify hybridisations with a high level of consistency both within the same sample and across different samples, and provides a valuable tool for the creation of carbon-based devices made of areas of different hybridisation.

The hybridisation mapping technique was proven to be very useful for the identification of carbon hybridisation with high spatial resolution, however it does have a drawback in the large acquisition times needed to acquire the data. To provide a compromise between the resolution and acquisition time a second technique was developed in chapter 6 that produces line scans of sp^2 hybridised carbon percentage. These hybridisation line scans can be acquired to a higher spatial resolution than the hybridisation maps, with the compromise that this resolution is only achieved in one dimension. The production of hybridisation line scans occurs in a very similar way to the hybridisation maps, with window mode carbon elemental line scans acquired and then converted to show hybridisation values in MATLAB. The technique was applied to the same samples as the mapping technique, and showed the same ability to distinguish between areas of different hybridisation on the surface with a high level of reproducibility.

The hybridisation mapping and hybridisation line scanning techniques provide important information on micro- and nano-structured carbon materials, allowing for the prediction of the properties present in different areas of the sample based on the hybridisation that is detected. This work has therefore provided a valuable tool for the creation of entirely carbon-based devices, having provided the ability to accurately determine the hybridisation of a carbon surface with high spatial resolution.

7.2   Recommendations for Future Work

This work has provided an insight into the extent of modification that can be induced to a HOPG surface through plasma treatment, however there were some interesting phenomena that were observed that require further examination. The first is the unusual trends that were observed for 50 W argon plasma treated HOPG, which showed an initial increase in the modification of the surface, however increased exposure to the plasma has reduced the level of oxide on the surface.

This experiment should be repeated to confirm the results, and should also be extended by examining longer treatment times to determine if the trend continues. Longer treatment times should also be examined for 30 W and 40 W argon plasma treatments so that comparison of the RF-coupling powers can be performed.

Argon plasma treatments of HOPG have been shown to produce a higher level of oxygen on the surface than oxygen plasma treatments, which has been concluded to be the result of the differing methods of modification that occur from the two plasma treatments. It was also suggested that the increased level of sputtering from the antenna in the plasma chamber with argon plasma over oxygen plasma introduces a higher level of oxygen on the sample surface due to the deposition of iron oxides. This claim can be further investigated by examining the oxygen and iron species more closely, particularly by performing higher resolution XPS on the O $1s$ peak to determine whether the oxygen present on the sample surface is bonded to iron or only to carbon.

The validity of the hybridisation mapping and line scanning techniques has been shown in this work through the examination of a variety of samples, with the different materials shown consistently to have different hybridisations that correlate to the features observed on the surface. Now that the techniques have been shown to work they can be applied to a wider range of samples, such as samples of more than two materials or with patterned surfaces, to provide important information about the structure of carbon-based devices.

A further capability of the SAM technique is the ability to perform characterisation with a variety of angles between the electron beam and the sample (and thus the sample and the spectrometer), allowing for the performance of angle-resolved AES. One drawback of the angle-resolved technique is that as the angle is varied further from perpendicular the intensity of the Auger signal is decreased, decreasing the quality of the spectra and impeding the ability to accurately quantify results. However, now that the optimal scanning parameters for the carbon hybridisation mapping have been determined, it could be possible to perform hybridisation mapping in combination with this angle-resolved technique. This research could help indicate the depth of modification of the surface, and whether the top layer experiences different changes in hybridisation than deeper layers, which has been suggested in some results presented here.

8 REFERENCES

1. Mohideen, M.M., Y. Liu, and S. Ramakrishna, *Recent progress of carbon dots and carbon nanotubes applied in oxygen reduction reaction of fuel cell for transportation.* Applied Energy, 2020. **257**: p. 114027.
2. Hoang, V.C., K. Dave, and V.G. Gomes, *Carbon quantum dot-based composites for energy storage and electrocatalysis: Mechanism, applications and future prospects.* Nano Energy, 2019. **66**: p. 104093.
3. Qin, S., et al., *All-carbon hybrids for high-performance electronics, optoelectronics and energy storage.* Science China Information Sciences, 2019. **62**(12): p. 220403.
4. Yu, H., Y. Xue, and Y. Li, *Graphdiyne and its Assembly Architectures: Synthesis, Functionalization, and Applications.* Advanced Materials, 2019. **31**(42): p. 1803101.
5. Sakamoto, R., et al., *The Accelerating World of Graphdiynes.* Advanced Materials, 2019. **31**(42): p. 1804211.
6. Wang, N., et al., *Graphdiyne-Based Materials: Preparation and Application for Electrochemical Energy Storage.* Advanced Materials, 2019. **31**(42): p. 1803202.
7. Zhang, R., et al., *Flexible Graphene-, Graphene-Oxide-, and Carbon-Nanotube-Based Supercapacitors and Batteries.* Annalen der Physik, 2019. **531**(10): p. 1800507.
8. Selvaraj, M., et al., *Application and prospects of carbon nanostructured materials in water treatment: A review.* Journal of Water Process Engineering, 2020. **33**: p. 100996.
9. Lin, Z., et al., *Carbon Nanomaterial-Based Biosensors: A Review of Design and Applications.* IEEE Nanotechnology Magazine, 2019. **13**(5): p. 4-14.
10. Venkataraman, A., et al., *Carbon Nanotube Assembly and Integration for Applications.* Nanoscale Research Letters, 2019. **14**(1): p. 220.
11. Syama, S. and P.V. Mohanan, *Comprehensive Application of Graphene: Emphasis on Biomedical Concerns.* Nano-Micro Letters, 2019. **11**(1): p. 6.
12. Devi, P., S. Saini, and K.-H. Kim, *The advanced role of carbon quantum dots in nanomedical applications.* Biosensors and Bioelectronics, 2019. **141**: p. 111158.
13. Tinwala, H. and S. Wairkar, *Production, surface modification and biomedical applications of nanodiamonds: A sparkling tool for theranostics.* Materials Science and Engineering: C, 2019. **97**: p. 913-931.
14. Falcao, E.H.L. and F. Wudl, *Carbon allotropes: beyond graphite and diamond.* Journal of Chemical Technology & Biotechnology, 2007. **82**(6): p. 524-531.
15. Esteve, J., M.C. Polo, and G. Sánchez, *Diamond and diamond-like carbon films.* Vacuum, 1999. **52**(1–2): p. 133-139.
16. Lettington, A.H., *Applications of diamond-like carbon thin films.* Carbon, 1998. **36**(5–6): p. 555-560.
17. Soldano, C., A. Mahmood, and E. Dujardin, *Production, properties and potential of graphene.* Carbon, 2010. **48**(8): p. 2127-2150.
18. Brown, T.L., LeMay,H. E., Bursten, B. E., Murphey, C. J., Langford, S. J., Sagatys, D., *Chemistry The Central Science: A Broad Perspective*. 2 ed. 2010, Frenchs Forest, NSW, Australia: Pearson Australia.
19. Flowers, P., Theopold, K., Langley, R., Robinson, W. R., *Chemistry 2e*. 2019, OpenStax.
20. Strekalov, V.N., et al., *Early stages of laser graphitization of diamond.* Applied Physics A, 2003. **76**(4): p. 603-607.
21. Zhu, L., et al., *Study on disordered graphitic nanocarbon under pressure and their transformation into polycrystalline nanodiamond.* Chemical Physics Letters, 2019. **730**: p. 491-496.

22. Lascovich, J.C., R. Giorgi, and S. Scaglione, *Evaluation of the sp2/sp3 ratio in amorphous carbon structure by XPS and XAES.* Applied Surface Science, 1991. **47**(1): p. 17-21.

23. Greil, P., *Perspectives of Nano-Carbon Based Engineering Materials.* Advanced Engineering Materials, 2015. **17**(2): p. 124-137.

24. Eskusson, J., R. Jaaniso, and E. Lust, *Diamond-like phase formation in an amorphous carbon films prepared by periodic pulsed laser deposition and laser irradiation method.* Applied Surface Science, 2009. **255**(15): p. 7104-7108.

25. Haque, A., R. Sachan, and J. Narayan, *Synthesis of diamond nanostructures from carbon nanotube and formation of diamond-CNT hybrid structures.* Carbon, 2019. **150**: p. 388-395.

26. Huang, B.-R., et al., *Effect of XeF laser treatment on structure of nanocrystalline diamond films.* Diamond and Related Materials, 2010. **19**(5–6): p. 445-448.

27. Ruffinatto, S., et al., *Diamond porous membranes: A material toward analytical chemistry.* Diamond and Related Materials, 2015. **55**: p. 123-130.

28. Feng, S., et al., *Porous structure diamond films with super-hydrophilic performance.* Diamond and Related Materials, 2015. **56**: p. 36-41.

29. Grill, A., *Tribology of diamondlike carbon and related materials: an updated review.* Surface and Coatings Technology, 1997. **94–95**: p. 507-513.

30. Girolami, M., et al., *Raman investigation of femtosecond laser-induced graphitic columns in single-crystal diamond.* Applied Physics A, 2014. **117**(1): p. 143-147.

31. Alemanno, E., et al., *Excimer laser-induced diamond graphitization for high-energy nuclear applications.* Applied Physics B, 2013. **113**(3): p. 373-378.

32. Caylar, B., M. Pomorski, and P. Bergonzo, *Laser-processed three dimensional graphitic electrodes for diamond radiation detectors.* Applied Physics Letters, 2013. **103**(4): p. 043504.

33. Lagomarsino, S., et al., *Electrical and Raman-imaging characterization of laser-made electrodes for 3D diamond detectors.* Diamond and Related Materials, 2014. **43**: p. 23-28.

34. Tsubota, M., et al., *High-temperature characteristics of charge collection efficiency using single CVD diamond detectors.* Nuclear Instruments and Methods in Physics Research Section A: Accelerators, Spectrometers, Detectors and Associated Equipment, 2015. **789**: p. 50-56.

35. Angelone, M., et al., *Development of single crystal diamond neutron detectors and test at JET tokamak.* Nuclear Instruments and Methods in Physics Research Section A: Accelerators, Spectrometers, Detectors and Associated Equipment, 2008. **595**(3): p. 616-622.

36. Pillon, M., et al., *Experimental response functions of a single-crystal diamond detector for 5–20.5 MeV neutrons.* Nuclear Instruments and Methods in Physics Research Section A: Accelerators, Spectrometers, Detectors and Associated Equipment, 2011. **640**(1): p. 185-191.

37. Schmid, G.J., et al., *A neutron sensor based on single crystal CVD diamond.* Nuclear Instruments and Methods in Physics Research Section A: Accelerators, Spectrometers, Detectors and Associated Equipment, 2004. **527**(3): p. 554-561.

38. Foulon, F., et al., *Characterisation of CVD diamond detectors used for fast neutron flux monitoring.* Nuclear Instruments and Methods in Physics Research Section A: Accelerators, Spectrometers, Detectors and Associated Equipment, 2002. **476**(1–2): p. 495-499.

39. Alekseyev, A., et al., *Study of natural diamond detector spectrometric properties under neutron irradiation.* Nuclear Instruments and Methods in Physics Research Section A: Accelerators, Spectrometers, Detectors and Associated Equipment, 2002. **476**(1–2): p. 516-521.

40. Krasilnikov, A.V., et al., *Study of d–t neutron energy spectra at JET using natural diamond detectors.* Nuclear Instruments and Methods in Physics Research Section A: Accelerators, Spectrometers, Detectors and Associated Equipment, 2002. **476**(1–2): p. 500-505.

41. Rebai, M., et al., *Fission diamond detector tests at the ISIS spallation neutron source.* Nuclear Physics B - Proceedings Supplements, 2011. **215**(1): p. 313-315.

42. Giacomelli, L., et al., *Diamond detectors for fast neutron irradiation experiments.* Nuclear Physics B - Proceedings Supplements, 2011. **215**(1): p. 242-246.

43. Lukosi, E. and M. Prelas, *Diamond sensor arrays for neutron detection: Preamplifier signal dependence on sensor array configuration.* Radiation Measurements, 2015. **73**: p. 18-25.

44. Kumar, A., et al., *Fabrication and characterization of polycrystalline diamond detectors for fast neutron monitoring.* Nuclear Instruments and Methods in Physics Research Section A: Accelerators, Spectrometers, Detectors and Associated Equipment, 2015. **785**: p. 55-60.

45. Sato, Y., et al., *Radiation hardness of a single crystal CVD diamond detector for MeV energy protons.* Nuclear Instruments and Methods in Physics Research Section A: Accelerators, Spectrometers, Detectors and Associated Equipment, 2015. **784**: p. 147-150.

46. Dueñas, J.A., et al., *Time response of 50 μm thickness single crystal diamond detectors.* Diamond and Related Materials, 2015. **55**: p. 144-148.

47. Chu, P.K. and L. Li, *Characterization of amorphous and nanocrystalline carbon films.* Materials Chemistry and Physics, 2006. **96**(2–3): p. 253-277.

48. Komlenok, M.S., et al., *UV laser induced changes to morphological, optical and electrical properties of conductive nanocrystalline diamond films.* Diamond and Related Materials, 2015. **58**: p. 196-199.

49. Avouris, P. and C. Dimitrakopoulos, *Graphene: synthesis and applications.* Materials Today, 2012. **15**(3): p. 86-97.

50. Iski, E.V., et al., *Graphene at the Atomic-Scale: Synthesis, Characterization, and Modification.* Advanced Functional Materials, 2013. **23**(20): p. 2554-2564.

51. Zhang, X., et al., *Graphene's potential in materials science and engineering.* RSC Advances, 2014. **4**(55): p. 28987-29011.

52. Ferrari, A.C. and D.M. Basko, *Raman spectroscopy as a versatile tool for studying the properties of graphene.* Nat Nano, 2013. **8**(4): p. 235-246.

53. Kim, K.T., J.W. Jung, and W.H. Jo, *Synthesis of graphene nanoribbons with various widths and its application to thin-film transistor.* Carbon, 2013. **63**(0): p. 202-209.

54. Novoselov, K.S., et al., *A roadmap for graphene.* Nature, 2012. **490**(7419): p. 192-200.

55. Sokolov, D.A., et al., *Excimer laser reduction and patterning of graphite oxide.* Carbon, 2013. **53**: p. 81-89.

56. Stankovich, S., et al., *Synthesis of graphene-based nanosheets via chemical reduction of exfoliated graphite oxide.* Carbon, 2007. **45**(7): p. 1558-1565.

57. Rao, C.N.R., H.S.S.R. Matte, and K.S. Subrahmanyam, *Synthesis and Selected Properties of Graphene and Graphene Mimics.* Accounts of Chemical Research, 2013. **46**(1): p. 149-159.

58. Jung, J.-H., et al., *Electro-active graphene–Nafion actuators.* Carbon, 2011. **49**(4): p. 1279-1289.

59. Luo, S., P.T. Hoang, and T. Liu, *Direct laser writing for creating porous graphitic structures and their use for flexible and highly sensitive sensor and sensor arrays.* Carbon, 2016. **96**: p. 522-531.

60. Kurra, N., A.A. Sagade, and G.U. Kulkarni, *Ultrafast Direct Ablative Patterning of HOPG by Single Laser Pulses to Produce Graphene Ribbons.* Advanced Functional Materials, 2011. **21**(20): p. 3836-3842.

61. Lee, J., et al., *Ablation of Graphene Film by Direct Nd:YVO4 Laser Under Various Beaming Conditions.* Journal of Nanoscience and Nanotechnology, 2014. **14**(12): p. 9060-9064.

62. Trusovas, R., et al., *Reduction of graphite oxide to graphene with laser irradiation.* Carbon, 2013. **52**: p. 574-582.

63. Liu, L., et al., *Controlled oxidative functionalization of monolayer graphene by water-vapor*

plasma etching. Carbon, 2012. **50**(8): p. 3039-3044.

64. Zeinalipour-Yazdi, C.D. and D.P. Pullman, *Study of a rhombohedral graphite X-ray filter using the sphere-in-contact model.* Chemical Physics Letters, 2019. **734**: p. 136717.

65. García-Ruiz, A., et al., *Spectroscopic Signatures of Electronic Excitations in Raman Scattering in Thin Films of Rhombohedral Graphite.* Nano Letters, 2019. **19**(9): p. 6152-6156.

66. Jara, A.D., et al., *Purification, application and current market trend of natural graphite: A review.* International Journal of Mining Science and Technology, 2019. **29**(5): p. 671-689.

67. Taylor, J.K., *Fundamental Interactions of RF-Plasma with Highly Oriented Pyrolytic Graphite*, in *School of Physical and Chemical Sciences*. 2014, Flinders University.

68. Paredes, J.I., Martinez-Alonso, A., Tascon, J. M. D., *Atomic Force Microscopy Investigation of the Surface Modification of Highly Oriented Pyrolytic Graphite by Oxygen Plasma.* Journals of Materials Chemistry, 2000. **10**: p. 7.

69. Paredes, J.I., A. Martínez-Alonso, and J.M.D. Tascón, *Comparative study of the air and oxygen plasma oxidation of highly oriented pyrolytic graphite: a scanning tunneling and atomic force microscopy investigation.* Carbon, 2000. **38**(8): p. 1183-1197.

70. Grigonis, A., et al., *Graphitization of amorphous diamond-like carbon films by laser irradiation.* Optical Materials, 2008. **30**(5): p. 749-752.

71. LiBassi, A., et al., *Density, sp3 content and internal layering of DLC films by X-ray reflectivity and electron energy loss spectroscopy.* Diamond and Related Materials, 2000. **9**(3–6): p. 771-776.

72. Bourgoin, D., S. Turgeon, and G.G. Ross, *Characterization of hydrogenated amorphous carbon films produced by plasma-enhanced chemical vapour deposition with various chemical hybridizations.* Thin Solid Films, 1999. **357**(2): p. 246-253.

73. Lascovich, J.C. and S. Scaglione, *Comparison among XAES, PELS and XPS techniques for evaluation of Sp2 percentage in a-C:H.* Applied Surface Science, 1994. **78**(1): p. 17-23.

74. Titantah, J.T. and D. Lamoen, *sp3/sp2 characterization of carbon materials from first-principles calculations: X-ray photoelectron versus high energy electron energy-loss spectroscopy techniques.* Carbon, 2005. **43**(6): p. 1311-1316.

75. Scaglione, S., et al., *Study of the sp2-to-sp3 ratio of dual-ion-beam sputtered hydrogenated amorphous carbon films.* Surface and Coatings Technology, 1991. **47**(1): p. 287-291.

76. Montero, I., et al., *X-ray photoelectron spectroscopy and X-ray-excited Auger electron spectroscopy studies of the initial deposition of hydrogenated amorphous carbon.* Thin Solid Films, 1993. **228**(1–2): p. 72-75.

77. Czyzniewski, A., *Preparation and characterisation of a-C and a-C:H coatings deposited by pulsed magnetron sputtering.* Surface and Coatings Technology, 2009. **203**(8): p. 1027-1033.

78. Zebda, A., et al., *Surface energy and hybridization studies of amorphous carbon surfaces.* Applied Surface Science, 2008. **254**(16): p. 4980-4991.

79. Grill, A., *Electrical and optical properties of diamond-like carbon.* Thin Solid Films, 1999. **355–356**: p. 189-193.

80. Jelínek, M., et al., *Diamond/graphite content and biocompatibility of DLC films fabricated by PLD.* Applied Physics A, 2010. **101**(4): p. 579-583.

81. Coşkun, Ö.D. and T. Zerrin, *Optical, structural and bonding properties of diamond-like amorphous carbon films deposited by DC magnetron sputtering.* Diamond and Related Materials, 2015. **56**: p. 29-35.

82. Catena, A., et al., *Surface morphology and grain analysis of successively industrially grown amorphous hydrogenated carbon films (a-C:H) on silicon.* Applied Surface Science, 2015. **347**: p. 657-667.

83. Hosseini, S.I., et al., *Investigation of the properties of diamond-like carbon thin films deposited by single and dual-mode plasma enhanced chemical vapor deposition.* Thin Solid

Films, 2011. **519**(10): p. 3090-3094.

84. Sharma, A.K., et al., *Structural and tribological characteristics of diamond-like carbon films deposited by pulsed laser ablation.* Materials Science and Engineering: B, 2000. **77**(2): p. 139-143.

85. Casiraghi, C., et al., *Bonding in hydrogenated diamond-like carbon by Raman spectroscopy.* Diamond and Related Materials, 2005. **14**(3–7): p. 1098-1102.

86. Stein, M.F., Ramon, B. C., Marciano, F. R., Lobo, A. O., Trava-Airoldi, V. J., *Thermal Stability Study of Diamond-Like Carbon Films Containing Crystalline Diamond Nanoparticles.* UNIVAP Magazine, 2013. **20**(35): p. 183-190.

87. Mechler, Á., et al., *Excimer laser irradiation induced formation of diamond-like carbon layer on graphite.* Applied Surface Science, 1999. **138–139**: p. 174-178.

88. Kononenko, T.V., et al., *Excimer laser etching of diamond-like carbon films: spalling effect.* Applied Surface Science, 1995. **86**(1–4): p. 234-238.

89. Sohbatzadeh, F., et al., *Characterization of diamond-like carbon thin film synthesized by RF atmospheric pressure plasma Ar/CH4 jet.* Superlattices and Microstructures, 2016. **89**: p. 231-241.

90. Ouchabane, M., et al., *Influence of bias voltage on the structure and deposition mechanism of diamond-like carbon films produced by RF (13.56 MHz) CH4 plasma.* physica status solidi (a), 2010. **207**(10): p. 2311-2318.

91. Grill, A., *Diamond-like carbon: state of the art.* Diamond and Related Materials, 1999. **8**(2–5): p. 428-434.

92. Mizokawa, Y., et al., *Comparison of the CKLL first-derivative auger spectra from XPS and AES using diamond, graphite, SiC and diamond-like-carbon films.* Surface Science, 1987. **182**(3): p. 431-438.

93. Tzeng, S.-S., Y.-J. Wu, and J.-S. Hsu, *The effects of plasma pre-treatment and post-treatment on diamond-like carbon films synthesized by RF plasma enhanced chemical vapor deposition.* Vacuum, 2008. **83**(3): p. 618-621.

94. Dey, R.M., et al., *Substrate bias effects during diamond like carbon film deposition by microwave ECR plasma CVD.* Current Applied Physics, 2008. **8**(1): p. 6-12.

95. Podsvirov, O.A., et al., *Residual stress in diamond-like carbon films: Role of growth conditions and ion irradiation.* Journal of Surface Investigation. X-ray, Synchrotron and Neutron Techniques, 2010. **4**(2): p. 241-244.

96. Ding, X.L., Q.S. Li, and X.H. Kong, *Effect of Repetition Rates of Laser Pulses on Microstructure and Optical Properties of Diamond-Like Carbon Films.* International Journal of Modern Physics B, 2009. **23**(30): p. 5671-5681.

97. Vouagner, D., et al., *Characterization of diamond-like carbon films before and after pulsed laser irradiation.* Applied Surface Science, 2000. **154–155**: p. 201-205.

98. Konishi, T., K. Yukimura, and K. Takaki, *Fabrication of diamond-like carbon films using short-pulse HiPIMS.* Surface and Coatings Technology, 2016. **286**: p. 239-245.

99. Smietana, M., et al., *Substrate effect on the optical properties and thickness of diamond-like carbon films deposited by the RF PACVD method.* Diamond and Related Materials, 2010. **19**(12): p. 1461-1465.

100. Lung, B.H., M.J. Chiang, and M.H. Hon, *Growth characterization and properties of diamond-like carbon films by electron cyclotron resonance chemical vapor deposition.* Thin Solid Films, 2001. **392**(1): p. 16-21.

101. Tian, S., et al., *Highly efficient field emission from nanodiamond films treated by fast reactive ion etching process.* Physica E: Low-dimensional Systems and Nanostructures, 2011. **43**(10): p. 1902-1905.

102. Gutiérrez B, J.M., et al., *High antibacterial properties of DLC film doped with nanodiamond.*

Surface and Coatings Technology, 2019. **375**: p. 395-401.

103. Mousinho, A.P., et al., *Micro-machine fabrication using diamond-like carbon films.* Diamond and Related Materials, 2003. **12**(3–7): p. 1041-1044.

104. Hosseini, S.I., M. Sharifian, and B. Shokri, *Single and dual-mode plasma enhanced chemical vapor deposition of fluorinated diamond-like carbon films.* Surface and Coatings Technology, 2012. **213**: p. 285-290.

105. Singh, S., et al., *Influence of Impinging Ion Energy on the Bonding and Mechanical Characteristics of DLC Films Deposited by Microwave ECR Plasma CVD.* Plasma Processes and Polymers, 2008. **5**(9): p. 853-860.

106. Trava-Airoldi, V.J., et al., *A comparison of DLC film properties obtained by r.f. PACVD, IBAD, and enhanced pulsed-DC PACVD.* Surface and Coatings Technology, 2007. **202**(3): p. 549-554.

107. Hirakuri, K.K., M. Yoshimura, and G. Friedbacher, *Application of DLC films as masks for integrated circuit fabrication.* Diamond and Related Materials, 2003. **12**(3–7): p. 1013-1017.

108. Fu, Y.Q., et al., *Laser micromachining of sputtered DLC films.* Applied Surface Science, 2006. **252**(13): p. 4914-4918.

109. Wang, J., et al., *Microstructure and chemical bond evolution of diamond-like carbon films machined by femtosecond laser.* Applied Surface Science, 2015. **340**: p. 49-55.

110. Fedosenko, G., et al., *Pulsed PECVD deposition of diamond-like carbon films.* Diamond and Related Materials, 2002. **11**(3–6): p. 1047-1052.

111. Choi, W.S., et al., *The effect of RF power on tribological properties of the diamond-like carbon films.* Thin Solid Films, 2005. **475**(1–2): p. 287-290.

112. Nery, R.P.O.S., R.S. Bonelli, and S.S. Camargo, *Evaluation of corrosion resistance of diamond-like carbon films deposited onto AISI 4340 steel.* Journal of Materials Science, 2010. **45**(20): p. 5472-5477.

113. Gronau, R., et al., *Study of the ability to field emission from diamond-like carbon layers and carbon nanotubes.* Vacuum, 2008. **82**(10): p. 962-965.

114. Jelínek, M., et al., *Biocompatibility and sp3/sp2 ratio of laser created DLC films.* Materials Science and Engineering: B, 2010. **169**(1–3): p. 89-93.

115. Corbella, C., et al., *Modifying surface properties of diamond-like carbon films via nanotexturing.* Journal of Physics D: Applied Physics, 2011. **44**(39): p. 395301.

116. Jamshidi, R., Hosseini, S. I., Ahmadizadeh, Y., *Dual-Frequency Plasma Enhanced Chemical Vapor Deposition of Diamond-Like Carbon Thin Films.* Acta Physica Polonica A, 2012. **122**: p. 230-235.

117. Harshavardhan, K.S., R.S. Yalamanchi, and L.K. Rao, *Formation of crystalline diamond from amorphous diamond-like carbon films by pulsed laser irradiation.* Applied Physics Letters, 1989. **55**(4): p. 351-353.

118. Küttel, O.M., et al., *Diamond-like carbon films deposited in a dual microwave-radio-frequency plasma.* Materials Science and Engineering: B, 1992. **11**(1): p. 321-324.

119. Korzec, D., et al., *Hybrid plasma system for diamond-like carbon film deposition.* Surface and Coatings Technology, 2000. **131**(1–3): p. 20-25.

120. Fedosenko, G., et al., *Comparison of diamond-like carbon films synthesized by 2.45 GHz microwave and 13.56 MHz multi-jet radiofrequency plasma sources.* Diamond and Related Materials, 2001. **10**(3–7): p. 920-926.

121. Singh, S.B., et al., *X-ray reflectivity studies on DLC films deposited by microwave ECR CVD: Effect of substrate bias.* Surface and Coatings Technology, 2009. **203**(8): p. 986-991.

122. Ohtsu, Y., et al., *Production of High-Density Capacitively Coupled Plasma with RF Multi-Hollow Cathode and/or High Secondary Electron Emission for DLC Film Preparation.* Plasma Processes and Polymers, 2009. **6**(S1): p. S458-S461.

123. Han, X.G., et al., *Phase transformation of graphite irradiated by high-intensity pulsed ion*

beams. Applied Surface Science, 2007. **253**(12): p. 5425-5430.

124. Hirakuri, K.K., et al., *Thin film characterization of diamond-like carbon films prepared by r.f. plasma chemical vapor deposition.* Thin Solid Films, 1997. **302**(1–2): p. 5-11.

125. Smietana, M., et al., *Influence of RF PACVD process parameters of diamond-like carbon films on optical properties and nano-hardness of the films.* Diamond and Related Materials, 2008. **17**(7–10): p. 1655-1659.

126. Dwivedi, N., et al., *Correlation of sp3 and sp2 fraction of carbon with electrical, optical and nano-mechanical properties of argon-diluted diamond-like carbon films.* Applied Surface Science, 2011. **257**(15): p. 6804-6810.

127. Huang, L.-Y., J. Lu, and K.-W. Xu, *Investigation of the relation between structure and mechanical properties of hydrogenated diamond-like carbon coatings prepared by PECVD.* Materials Science and Engineering: A, 2004. **373**(1–2): p. 45-53.

128. Ishpal, et al., *Investigation of radio frequency plasma for the growth of diamond like carbon films.* Physics of Plasmas, 2012. **19**(3): p. 033515.

129. Kroushawi, F., et al., *Study on the Hydrogenated Diamond-Like Carbon Films Synthesized by RF-PECVD from n-decane.* Journal of Fusion Energy, 2012. **31**(6): p. 581-585.

130. Md. Kamrul, H., P. Bimal Kumar, and H. Akimitsu, *Comparative Study on Chemical Vapor Deposition of Diamond-Like Carbon Films from Methane and Acetylene Using RF Plasma.* Japanese Journal of Applied Physics, 2006. **45**(10S): p. 8398.

131. Konofaos, N., I.P. McClean, and C.B. Thomas, *Characterisation of the Interface States between Amorphous Diamond-Like Carbon Films and (100) Silicon.* physica status solidi (a), 1997. **161**(1): p. 111-123.

132. Romyani, G., J. Tapati, and R. Swati, *Transparent polymer and diamond-like hydrogenated amorphous carbon thin films by PECVD technique.* Journal of Physics D: Applied Physics, 2008. **41**(15): p. 155413.

133. Wang, X., et al., *Comparisons of HFCVD diamond nucleation and growth using different carbon sources.* Diamond and Related Materials, 2015. **54**: p. 26-33.

134. Riccardi, C., et al., *Gaseous precursors of diamond-like carbon films: chemical composition of CH4/Ar plasmas.* Vacuum, 2001. **61**(2–4): p. 211-215.

135. Neuville, S., *The enhancement of interconnected sp3 sites by chemical effects during ta-C film growth.* Diamond and Related Materials, 2002. **11**(10): p. 1721-1730.

136. Kinoshita, H., et al., *Synthesis and mechanical properties of carbon nanotube/diamond-like carbon composite films.* Diamond and Related Materials, 2007. **16**(11): p. 1940-1944.

137. Cicala, G., P. Bruno, and A.M. Losacco, *PECVD of hydrogenated diamond-like carbon films from CH4–Ar mixtures: growth chemistry and material characteristics.* Diamond and Related Materials, 2004. **13**(4–8): p. 1361-1365.

138. Yasumaru, N., K. Miyazaki, and J. Kiuchi, *Glassy carbon layer formed in diamond-like carbon films with femtosecond laser pulses.* Applied Physics A, 2004. **79**(3): p. 425-427.

139. Harris †, P.J.F., *Fullerene-related structure of commercial glassy carbons.* Philosophical Magazine, 2004. **84**(29): p. 3159-3167.

140. Aqel, A., et al., *Carbon nanotubes, science and technology part (I) structure, synthesis and characterisation.* Arabian Journal of Chemistry, 2012. **5**(1): p. 1-23.

141. Belin, T. and F. Epron, *Characterization methods of carbon nanotubes: a review.* Materials Science and Engineering: B, 2005. **119**(2): p. 105-118.

142. Suzuki, S., Y. Watanabe, and S. Heun, *Photoelectron spectroscopy and microscopy of carbon nanotubes.* Current Opinion in Solid State and Materials Science, 2006. **10**(2): p. 53-59.

143. Widmann, C.J., et al., *Fabrication and characterization of single crystalline diamond nanopillars with NV-centers.* Diamond and Related Materials, 2015. **54**: p. 2-8.

144. Jiang, X., et al., *Mechanistic Features of Nanodiamonds in the Lapping of Magnetic Heads.*

The Scientific World Journal, 2014. **2014**: p. 6.

145.	Day, A.H., et al., *Synthetic routes, characterization and photophysical properties of luminescent, surface functionalized nanodiamonds.* Carbon, 2019. **152**: p. 335-343.

146.	Singh, B., et al., *Multi-instrument characterization of five nanodiamond samples: a thorough example of nanomaterial characterization.* Analytical and Bioanalytical Chemistry, 2016. **408**(4): p. 1107-1124.

147.	Jang, D.M., et al., *Hydrogen and carbon monoxide generation from laser-induced graphitized nanodiamonds in water.* Physical Chemistry Chemical Physics, 2013. **15**(19): p. 7155-7160.

148.	Shvidchenko, A.V., et al., *Colloids of detonation nanodiamond particles for advanced applications.* Advances in Colloid and Interface Science, 2019. **268**: p. 64-81.

149.	Gao, Y. and P. Yin, *Determination of crystallite size of nanodiamond by Raman spectroscopy.* Diamond and Related Materials, 2019. **99**: p. 107524.

150.	Perona Martinez, F., et al., *Nanodiamond for Sample Preparation in Proteomics.* Analytical Chemistry, 2019. **91**(15): p. 9800-9805.

151.	Duan, X., et al., *sp2/sp3 Framework from Diamond Nanocrystals: A Key Bridge of Carbonaceous Structure to Carbocatalysis.* ACS Catalysis, 2019. **9**(8): p. 7494-7519.

152.	Exchange, M.N. *What is MEMS Technology?* [cited 2015 15 September]; Available from: https://www.mems-exchange.org/MEMS/what-is.html.

153.	Jin, W.-M. and J.H. Moon, *Supported pyrolysis for lithographically defined 3D carbon microstructures.* Journal of Materials Chemistry, 2011. **21**(38): p. 14456-14460.

154.	Jonnalagadda, K.N. and I. Chasiotis, *Strength and Fracture Resistance of Amorphous Diamond-Like Carbon Films for MEMS.* Journal of Nanomaterials, 2009. **2009**: p. 8.

155.	Choi, S., et al., *Fabrication of graphite nanopillars and nanocones by reactive ion etching.* Thin Solid Films, 2006. **513**(1–2): p. 31-35.

156.	Kononenko, T.V., et al., *Three-dimensional laser writing in diamond bulk.* Diamond and Related Materials, 2011. **20**(2): p. 264-268.

157.	Wang, C. and M. Madou, *From MEMS to NEMS with carbon.* Biosensors and Bioelectronics, 2005. **20**(10): p. 2181-2187.

158.	Kassegne, S., et al., *Electrical impedance, electrochemistry, mechanical stiffness, and hardness tunability in glassy carbon MEMS µECoG electrodes.* Microelectronic Engineering, 2015. **133**(0): p. 36-44.

159.	Moon, J.-M., et al., *Diamond-like carbon electrodes in electrochemical microgravimetry.* Journal of Electroanalytical Chemistry, 1999. **464**(2): p. 230-237.

160.	Mousinho, A.P., et al., *Diamond-like carbon microoptics elements.* Thin Solid Films, 2004. **459**(1–2): p. 145-148.

161.	Gao, W., et al., *Direct laser writing of micro-supercapacitors on hydrated graphite oxide films.* Nat Nano, 2011. **6**(8): p. 496-500.

162.	Nagato, K., et al., *Laser-assisted replication of large-area nanostructures.* Journal of Materials Processing Technology, 2014. **214**(11): p. 2444-2449.

163.	Kononenko, T., et al., *All-carbon detector with buried graphite pillars in CVD diamond.* Applied Physics A, 2014. **114**(2): p. 297-300.

164.	Hauert, R., *A review of modified DLC coatings for biological applications.* Diamond and Related Materials, 2003. **12**(3–7): p. 583-589.

165.	Moldovan, C., et al. *Biomems Microprobe for Electrical Activity Recording of Living Cells*. in *Semiconductor Conference, 2007. CAS 2007. International*. 2007.

166.	Yin, Y., et al., *Surface adsorption and wetting properties of amorphous diamond-like carbon thin films for biomedical applications.* Thin Solid Films, 2008. **516**(16): p. 5157-5161.

167.	Fredriksson, H., D. Chakarov, and B. Kasemo, *Patterning of highly oriented pyrolytic graphite and glassy carbon surfaces by nanolithography and oxygen plasma etching.* Carbon, 2009.

47(5): p. 1335-1342.

168.   Massi, M., et al., *Plasma etching of DLC films for microfluidic channels.* Microelectronics Journal, 2003. **34**(5–8): p. 635-638.

169.   Liu, L., et al., *Nanosphere Lithography for the Fabrication of Ultranarrow Graphene Nanoribbons and On-Chip Bandgap Tuning of Graphene.* Advanced Materials, 2011. **23**(10): p. 1246-1251.

170.   George, A., et al., *Large Area Resist-Free Soft Lithographic Patterning of Graphene.* Small, 2013. **9**(5): p. 711-715.

171.   Joshi-Imre, A. and S. Bauerdick, *Direct-Write Ion Beam Lithography.* Journal of Nanotechnology, 2014. **2014**: p. 26.

172.   Seth, J., et al., *Lithographic application of diamond-like carbon films.* Thin Solid Films, 1995. **254**(1–2): p. 92-95.

173.   Dumitru, G., *Laser Processing of Tribological DLC Films: An Overview*, in *Tribology of Diamond-Like Carbon Films*, C. Donnet and A. Erdemir, Editors. 2008, Springer US. p. 571-590.

174.   Neff, M., et al., *Femtosecond laser writing of buried graphitic structures in bulk diamond.* Applied Physics A, 2009. **97**(3): p. 543-547.

175.   Kononenko, T.V., et al., *Microstructuring of diamond bulk by IR femtosecond laser pulses.* Applied Physics A, 2008. **90**(4): p. 645-651.

176.   Kononenko, T.V., et al., *Femtosecond laser microstructuring in the bulk of diamond.* Diamond and Related Materials, 2009. **18**(2–3): p. 196-199.

177.   Grigonis, A., et al., *Laser-induced transformation of a-C:H thin films.* Vacuum, 2009. **83, Supplement 1**: p. S152-S154.

178.   Grigonis, A., Ž. Rutkunienė, and A. Medvids, *The influence of nanosecond pulse laser irradiation on the properties of a-C:H films.* Vacuum, 2008. **82**(11): p. 1212-1215.

179.   Kononenko, T.V., et al., *Laser-induced spallation in diamond-like carbon films.* Applied Physics A, 2004. **79**(3): p. 543-549.

180.   Kononenko, T.V., et al., *Ablation of CVD diamond with nanosecond laser pulses of UV–IR range1.* Diamond and Related Materials, 1998. **7**(11–12): p. 1623-1627.

181.   Pimenov, S.M., G.A. Shafeev, and E.N. Loubnin, *Laser activation of diamond films for electroless metal plating: Valence band modifications.* Applied Physics Letters, 1996. **68**(3): p. 334-336.

182.   Bachmair, F., et al., *A 3D diamond detector for particle tracking.* Nuclear Instruments and Methods in Physics Research Section A: Accelerators, Spectrometers, Detectors and Associated Equipment, 2015. **786**: p. 97-104.

183.   Kononenko, T.V., A.A. Khomich, and V.I. Konov, *Peculiarities of laser-induced material transformation inside diamond bulk.* Diamond and Related Materials, 2013. **37**: p. 50-54.

184.   Kononenko, T.V., et al., *Graphitization wave in diamond bulk induced by ultrashort laser pulses.* Applied Physics A, 2015: p. 1-10.

185.   Miyazaki, K., et al., *Reflectivity in femtosecond-laser-induced structural changes of diamond-like carbon film.* Applied Physics A, 2005. **80**(1): p. 17-21.

186.   Santagata, A., et al., *Carbon-Based Nanostructures Obtained in Water by Ultrashort Laser Pulses.* The Journal of Physical Chemistry C, 2011. **115**(12): p. 5160-5164.

187.   Grigonis, A., et al., *Modification of the amorphous carbon films by the ns-laser irradiation.* Central European Journal of Physics, 2011. **9**(5): p. 1344.

188.   Yasuhiko, S., et al., *Three-Dimensional Micro- and Nano-Fabrication in Transparent Materials by Femtosecond Laser.* Japanese Journal of Applied Physics, 2005. **44**(7R): p. 4735.

189.   Wang, C.Z., et al., *Laser-Induced Graphitization on a Diamond (111) Surface.* Physical Review Letters, 2000. **85**(19): p. 4092-4095.

190. Gouzman, I., et al., *Irradiation effects induced by reactive and non-reactive low energy ion irradiation of graphite: An electron spectroscopy study.* Surface and Interface Analysis, 1994. **22**(1-12): p. 524-527.

191. Massi, M., et al., *Effects of plasma etching on DLC films.* Thin Solid Films, 1999. **343–344**(0): p. 381-384.

192. Komatsu, Y., A. Alanazi, and K.K. Hirakuri, *Application of diamond-like carbon films to the integrated circuit fabrication process.* Diamond and Related Materials, 1999. **8**(11): p. 2018-2021.

193. Hueso, J.L., et al., *XPS investigation of the reaction of carbon with NO, O2, N2 and H2O plasmas.* Carbon, 2007. **45**(1): p. 89-96.

194. Chen, F.F., *Introduction to Plasma Physics and Controlled Fusion*. 2 ed. Vol. 1: Plasma Physics. 1984: Springer US.

195. Deslandes, A., *RF-Plasma Hydrogenation of sp2-Bonded Carbon Surfaces*, in *School of Chemistry, Physics, and Environmental Sciences*. 2009, Flinders University: Flinders University, Australia.

196. Barlow, A., *Plasma Processing Studies with Application to Carbon Nanotube Fluorination*, in *School of Chemical and Physical Sciences*. 2011, Flinders University: Flinders University. p. 282.

197. Moulder, J.F., Stickle, W. F., Sobol, P. E., Bomben, K. D., *Handbook of X-ray Photelectron Spectroscopy*. 1995, USA: Physical Electronics, Inc.

198. Childs, K.D.C., B. A.; LaVanier, L. A.; Moulder, J. F.; Paul, D. F.; Stickle, W. F.; Watson, D. G., *Handbook of Auger Electron Spectroscopy*. 3rd ed. 1995, Minnesota, USA: Physical Electronics, Inc.

199. Barlow, A.J., et al., *Multivariate Auger Feature Imaging (MAFI) – a new approach towards chemical state identification of novel carbons in XPS imaging.* Surface and Interface Analysis, 2015. **47**(2): p. 173-175.

200. Barlow, A.J., et al., *Chemically specific identification of carbon in XPS imaging using Multivariate Auger Feature Imaging (MAFI).* Carbon, 2016. **107**: p. 190-197.

201. Barclay, M., S.B. Hill, and D.H. Fairbrother, *Use of X-ray photoelectron spectroscopy and spectroscopic ellipsometry to characterize carbonaceous films modified by electrons and hydrogen atoms.* Applied Surface Science, 2019. **479**: p. 557-568.

202. Zhang, X., et al., *Effect of Copper Substrate Surface Orientation on the Reductive Functionalization of Graphene.* Chemistry of Materials, 2019. **31**(21): p. 8639-8648.

203. Inc., M.I. *Application Note: The Basics of Pressure Measurement and Capacitance Manometers*. 2013.

204. Holland, L. and S.M. Ojha, *Deposition of hard and insulating carbonaceous films on an r.f. target in a butane plasma.* Thin Solid Films, 1976. **38**(2): p. L17-L19.

205. Baranov, A.M., et al., *Real time investigation of the initial stages of a-C films growth.* Diamond and Related Materials, 2004. **13**(4–8): p. 1356-1360.

206. Kondrashov, P.E., et al., *Investigation of ultrathin DLC film growth by a novel X-ray reflectivity technique and in situ ellipsometry.* Diamond and Related Materials, 1999. **8**(2–5): p. 532-537.

207. Smietana, M., et al., *Correlation between thickness and optical properties of thin diamond-like carbon films deposited with RF PACVD method.* Materials Science and Engineering: B, 2009. **165**(1–2): p. 132-134.

208. Mutsukura, N., *Deposition of hydrogenated carbon film in a magnetically confined CH4 rf discharge.* Vacuum, 2000. **56**(2): p. 129-132.

209. Grigaliūnas, V., et al., *Nanoimprint lithography using IR laser irradiation.* Applied Surface Science, 2006. **253**(2): p. 646-650.

210. Hofmann, S., *Auger- and X-Ray Photoelecton Spectroscopy in Materials Science*. Springer

Series in Surface Sciences. 2013: Springer-Verlag Berlin Heidelbery.

211. Seah, M.P. and W.A. Dench, *Quantitative electron spectroscopy of surfaces: A standard data base for electron inelastic mean free paths in solids.* Surface and Interface Analysis, 1979. **1**(1): p. 2-11.

212. Tanuma, S., C.J. Powell, and D.R. Penn, *Calculations of electron inelastic mean free paths. IX. Data for 41 elemental solids over the 50 eV to 30 keV range.* Surface and Interface Analysis, 2011. **43**(3): p. 689-713.

213. Baer, D.R. and M.H. Engelhard, *XPS analysis of nanostructured materials and biological surfaces.* Journal of Electron Spectroscopy and Related Phenomena, 2010. **178**: p. 415-432.

214. Mérel, P., et al., *Direct evaluation of the sp3 content in diamond-like-carbon films by XPS.* Applied Surface Science, 1998. **136**(1–2): p. 105-110.

215. Gorham, J.M., et al., *Detecting carbon in carbon: Exploiting differential charging to obtain information on the chemical identity and spatial location of carbon nanotube aggregates in composites by imaging X-ray photoelectron spectroscopy.* Carbon, 2016. **96**: p. 1208-1216.

216. Stojilovic, N., *Why Can't We See Hydrogen in X-ray Photoelectron Spectroscopy?* Journal of Chemical Education, 2012. **89**(10): p. 1331-1332.

217. Jackson, S.T. and R.G. Nuzzo, *Determining hybridization differences for amorphous carbon from the XPS C 1s envelope.* Applied Surface Science, 1995. **90**(2): p. 195-203.

218. Walton, J. and N. Fairley, *Quantitative surface chemical-state microscopy by x-ray photoelectron spectroscopy.* Surface and Interface Analysis, 2004. **36**(1): p. 89-91.

219. Artyushkova, K. and J.E. Fulghum, *Multivariate image analysis methods applied to XPS imaging data sets.* Surface and Interface Analysis, 2002. **33**(3): p. 185-195.

220. Artyushkova, K. and J.E. Fulghum, *Identification of chemical components in XPS spectra and images using multivariate statistical analysis methods.* Journal of Electron Spectroscopy and Related Phenomena, 2001. **121**(1): p. 33-55.

221. Cho, S.H., et al., *The C2H2 gas effect on the growth behavior of remote plasma enhanced CVD SiC:H film.* Journal of Electroceramics, 2006. **17**(2): p. 811-816.

222. Al-Harthi, S., et al., *Unusual surface and edge morphologies, sp2 to sp3 hybridized transformation and electronic damage after Ar+ ion irradiation of few-layer graphene surfaces.* Nanoscale Research Letters, 2012. **7**(1): p. 466.

223. Chien, S.C., et al., *Mechanical properties of amorphous boron carbon nitride films produced by dual gun sputtering.* Diamond and Related Materials, 2003. **12**(9): p. 1463-1471.

224. Dementjev, A.P., M.N. Petukhov, and A.M. Baranov, *The unique capability of X-ray photon spectroscopy and X-ray excited Auger electron spectroscopy in identifying the sp2/sp3 ratio on the surface of growing carbon films.* Diamond and Related Materials, 1998. **7**(10): p. 1534-1538.

225. Cheng, M., et al., *Restoration of graphene from graphene oxide by defect repair.* Carbon, 2012. **50**(7): p. 2581-2587.

226. Larciprete, R., Fabris, S., Sun, T. Lacovig, P, Baraldi, A, and Lizzit, S., *Dual Path Mechanism in the Thermal Reduction of Gra.* Dual Path Mechanism in the Thermal Reduction of Graphene Oxide, 2011.

227. Popescu, S., et al., *Rapid Prototyping of a Low-cost Graphene-based Impedimetric Biosensor.* Procedia Technology, 2017. **27**(Supplement C): p. 274-276.

228. Dick, C.E. and A.C. Lucas, *K-Shell Fluorescence Yields for Light Elements.* Physical Review A, 1970. **2**(3): p. 580-586.

229. Langenberg, A. and J.v. Eck, *Carbon, nitrogen, neon and argon K-shell ionization by proton and helium-ion impact: X-ray emission cross sections and fluorescence yields.* Journal of Physics B: Atomic and Molecular Physics, 1976. **9**(14): p. 2421-2433.

230. Bhalla, R.P., F.D. McDaniel, and G. Lapicki, *Carbon K-shell x-ray and Auger-electron*

production in hydrocarbons and carbon oxides by 0.6--2.0-MeV protons. Physical Review A, 1987. **35**(9): p. 3655-3662.

231. Bhalla, R.P., F.D. McDaniel, and G. Lapicki, *Carbon K-shell X-ray and Auger-electron cross sections and fluorescence yields in benzene bombarded by 0.6 TO 2.0 MeV protons.* Nuclear Instruments and Methods in Physics Research Section B: Beam Interactions with Materials and Atoms, 1987. **24-25**: p. 180-183.

232. Hartmann, E., *X-ray fluorescence yields for light emitter atoms: carbon.* Journal of Physics B: Atomic, Molecular and Optical Physics, 1988. **21**(7): p. 1173-1182.

233. Steffen, H.J., *Use of valence band Auger electron spectroscopy to study thin film growth: oxide and diamond-like carbon films.* Thin Solid Films, 1994. **253**(1): p. 269-276.

234. Lesiak, B., et al., *C sp2/sp3 hybridisations in carbon nanomaterials – XPS and (X)AES study.* Applied Surface Science, 2018. **452**: p. 223-231.

235. Galuska, A.A., H.H. Madden, and R.E. Allred, *Electron spectroscopy of graphite, graphite oxide and amorphous carbon.* Applied Surface Science, 1988. **32**(3): p. 253-272.

236. Mizokawa, Y., et al., *The C KLL first-derivative x-ray photoelectron spectroscopy spectra as a fingerprint of the carbon state and the characterization of diamondlike carbon films.* Journal of Vacuum Science & Technology A, 1987. **5**(5): p. 2809-2813.

237. Parmeter, J.E., D.R. Tallant, and M.P. Siegal, *Thermal Stability Studies of Diamond-Like Carbon Films.* MRS Proceedings, 2011. **349**.

238. Lampert, L., A. Barnum, and J. Jiao, *Towards the Electron Spectroscopy Graphene Fingerprint.* Microscopy and Microanalysis, 2015. **21**(S3): p. 1149-1150.

239. Baitinger, E.M., L.A. Pesin, and A.V. Cherednichenko, *Influence of the type of electron hybridization on the intensity of carbon auger spectra.* Russian Physics Journal, 1996. **39**(8): p. 798-801.

240. Lurie, P.G. and J.M. Wilson, *The diamond surface: II. Secondary electron emission.* Surface Science, 1977. **65**(2): p. 476-498.

241. Günther, S., et al., *Artefact formation in scanning photoelectron emission microscopy.* Ultramicroscopy, 1998. **75**(1): p. 35-51.

242. Tzeng, S.-S., et al., *Influence of nitrogen plasma post-treatment on diamond-like carbon films synthesized by RF plasma enhanced chemical vapor deposition.* Diamond and Related Materials, 2010. **19**(7–9): p. 783-786.

243. Amanatides, E. and D. Mataras, *Electrical and optical properties of CH4/H2 RF plasmas for diamond-like thin film deposition.* Diamond and Related Materials, 2005. **14**(3–7): p. 292-295.

244. Torrengo, S., et al., *XPS and ToF-SIMS investigation of nanocrystalline diamond oxidized surfaces.* Applied Surface Science, 2013. **276**: p. 101-111.

245. Speranza, G., et al., *XPS and UPS in situ study of oxygen thermal desorption from nanocrystalline diamond surface oxidized by different process.* Diamond and Related Materials, 2011. **20**(4): p. 560-563.

A.   APPENDIX A: AUXILIARY INFORMATION FOR XPS AND SAM HIGH RESOLUTION PEAK ANALYSIS

A.1   XPS C 1*s* Peak Analysis

XPS is an extremely useful characterisation technique for nanostructured materials for many reasons [1]. The first is the identification of the elemental composition and chemical environment of sample surfaces, the properties of which are extremely important for nanostructured materials as they dominate over the bulk properties [1]. Secondly, while XPS does not always provide nanoscale resolution in the plane of the surface, it does allow surface sensitivity on the order of several nanometres, thus providing information about the structure and composition of nanofeatures on a surface [1]. In addition, XPS can be used to examine coatings and other layers on particles and nanostructured surfaces [1].

Information about the chemical environments of carbon within a surface can be examined by deconvoluting high-resolution spectra the C1*s* peak into components representing the different chemical states of carbon atom present. In the samples examined in this work, the components include both carbon-carbon bonds and carbon-oxygen bonds, as well as an indication of carbon bonds bordering a vacancy in a carbon lattice. Also described are factors that influence the ability to determine the elemental composition of the surface.

A.1.1   Dependence of XPS Peak Positions on Photon Energy

Many XPS instruments utilise a dual-anode X-ray source, including the instrument used in this work. This allows operation of the instrument at two different excitation energies: Al Kα (1486.6 eV) and Mg Kα (1253.6 eV). The two X-ray lines have different characteristics, including their flux and line width, which make them useful in different situations [2]. It is therefore important to consider these factors, as well as what elements are expected to be present, when deciding which source to use [2]. As some elements will have overlapping peaks, changing the excitation energy can assist in separating these peaks [2]. XPS spectra are plotted as counts versus binding energy, therefore the photoelectron peak position will remain constant between different excitation sources, while the Auger peak has a photon energy dependence [2].

X-rays are generated by accelerating electrons that are thermionically emitted from a filament into a target material made of a pure metal [2]. This results in an X-ray emission spectrum that is a

combination of characteristic X-rays and a bremsstrahlung background, which is a continuous background of X-ray emission that drops off sharply at a wavelength corresponding to the maximum energy possible for a given accelerating voltage, that is, when an electron loses all its kinetic energy through the emission of a single photon [2]. Bremsstrahlung radiation occurs when a charged particle is decelerated by an external force, such as the deceleration of an electron by an atomic nucleus [2]. The emission spectrum peaks are superimposed on this Bremsstrahlung background, with the peaks being characteristic of the target material [2]. The X-ray source used in this work contained an aluminium window to prevent exposure of the samples to this Bremsstrahlung radiation.

The X-rays produced in this way occur when the incident electron has sufficient energy to cause the ejection of a core electron from the target material, for example from the K shell [2, 3]. The hole that is left behind is then filled by another electron from an outer electron shell, which then results in the emission of an X-ray photon with an energy equal to the difference between the two shells involved by X-ray fluorescence [2, 3]. K_α and K_β indicate that the emission is the result of a transition to the K shell from the L shell (α) or the M shell (β), respectively [2]. The K_α line is used in XPS as it the most intense line at the typical accelerating voltages used in common X-ray sources (up to 15 kV) [2].

A.1.2 XPS Peak Widths

The width and shape of XPS spectra peaks are mainly influenced by the X-ray source, the uncertainty in the lifetime of the ionised state, and the resolution of the analyser [2]. In an ideal situation, these factors would all have discrete contributions and the peaks would be single lines [2]. Unfortunately, the peaks in real spectra are quite complex [2].

The characteristics of the X-ray line are the largest factor that influence the width and shape of spectral peaks [2, 3]. The width of the Mg K_α line is 0.70 eV (for α_1=0.36 eV and α_2=0.36 eV), therefore the line width is the result of convolution of the two distinct transitions, $K_{\alpha 1}$ and $K_{\alpha 2}$, although it is generally referred to simply as K_α [2]. The two contributions have the same width, however they have different intensities, with a 2:1 (α_1:α_2) ratio [2]. The main factor in the broadening of these lines is the uncertainty in the lifetime of the hole produced in the ionised level upon impact [2]. This lifetime is in turn influenced by factors such as multiple ionisation processes leading to more than one hole present at any one time and the natural width of the levels themselves [2].

Broadening of the photoelectron peak is caused by both intrinsic and extrinsic mechanisms that affect the kinetic energy of the emitted photoelectron [2]. These include the width of the core level and thermal and phonon broadening [2]. The result of these factors is a distribution of electron velocities coming from a single state [2]. There is also Doppler broadening as a result of the motion of the atom from which the electron is emitted [2]. All atoms have some finite amount of thermal energy, and therefore a velocity, thus the electrons already have some small amount of kinetic energy, which is either added to or subtracted from the kinetic energy that is expected from the energy level gap depending on whether the atom is moving in the same direction as the electron or the opposite [2]. This random motion of atoms results in a normal distribution function of velocities, which results in a broadening of the peak [2].

The width of the photoelectron peak is also influenced by the resolution of the analyser [2]. An electron energy analyser admits electrons with a small range of kinetic energies centred around the set detection energy [2]. In this work a Concentric Hemispherical Analyser (CHA) is used. This type of analyser has several factors that influence the resolution: the radii of the hemispheres, the dimensions of the entrance and exit slits, and the pass energy [2]. It is not practical to have varying radii, therefore the slit widths and pass energy are the two variables that are usually changed [2]. If the radii are fixed, then a reduction in the slit width or pass energy results in increased resolution [2]. However, in the CHA used for this work the slit widths are also fixed, so the pass energy is the only variable that can be adjusted to change the resolution. Even when the pass energy and slit width are reduced, there is still a limit to the level of resolution that can be achieved, which is governed by the width of the exciting line [2]. However, as the slit widths or pass energy is reduced there is also a decrease in signal intensity as there are an increasing number of electrons that fall outside the 'acceptable' energy window and are rejected [2].

A.1.3   XPS Peak Position

The binding energy of an electron within an atom will change when the bonding state or chemical environment changes, which results in a change in the observed spectral peak [4]. These changes can include binding energy, peak width and shape, and valence band changes [4]. The change in binding energy of the peak relative to its position in the pure elemental spectrum is called its chemical shift [4]. When an atom is bonded to an atom with a different electronegativity there is a charge transfer in the atom, with the atom with higher electronegativity becoming more negative, decreasing the binding energy of that atom, while the less electronegative atom will become

positive and have an increase in binding energy [4]. If the chemical shift is smaller than the peak width then the different state appears as a component within the peak rather than a separate peak, and must be deconvoluted to determine what that component is [4].

A.1.4 XPS Peak Fitting

The chemical state of an atom affects its energy levels, which results in a difference in binding energies of the electrons causing peaks in a XPS spectrum to be shifted [2]. The peak for graphitic (sp^2 hybridised) carbon is normally present at 284.5 eV, however if that carbon atom is bonded to an oxygen atom it will be shifted to 285-286 eV, depending on the exact bonding of the atoms [2]. Different atoms bonded to the carbon will cause binding energy shifts of different magnitudes [2]. In addition, the hybridisation of the carbon atom changes the binding energy of the electrons, with sp^3 hybridised carbon having a binding energy that is slightly higher than that of sp^2 hybridised carbon [2].

Often there will be more than one chemical state of an element present in a sample, which results in a convoluted peak [2, 4]. The ability to separate these components depends on the energy separation and analyser resolution [4]. In carbon, the presence of different components presents as a peak with an asymmetric shoulder which is usually present on the higher binding energy side of the peak [2]. To obtain information about the chemical environments of an element the peak must be deconvoluted by subtracting a background and performing synthetic curve fitting [2].

The temporally random collection of single electrons as counts results in the noise present in the XPS spectrum [3]. The percent standard deviation of the counts in any channel is $100/(counts)^{1/2}$, and the signal-to-noise ratio is proportional to the square root of the counting time [3].

The background present in XPS spectra is a result of inelastic collisions of electrons [2, 3]. XPS is performed under Ultra-High Vacuum (UHV) conditions to increase the Inelastic Mean Free Path (IMFP) of the electrons, some will still undergo collisions with neighbouring nuclei or other electrons, resulting in a large range of kinetic energies that are observed as a background signal that increases with increasing binding energy [2]. This results in different background levels on either side of peaks, so the background must be removed before curve fitting can be performed [2].

There are several types of background subtraction that can be applied to spectra [2, 4]. The simplest is a linear subtraction between the end points at either side of the peak [2, 4]. This method is not physically realistic and can introduce errors and asymmetry by not taking into account any variation

in the magnitude of the background across the peak, but can be valid for spectra where the background is relatively small compared to the peaks [2, 4]. In 1972 Shirley introduced a background that increases at a rate that is proportional to the peak intensity, providing that the background and measured intensity are equal on either side of the peak [2]. This method assumes that the background at a given binding energy in the peak spectrum should be proportional to the total amount of (signal) electrons above that energy [4]. The Shirley background does, however, have the potential to misrepresent intensity as being due to inelastic scattering rather than important peak structure [2]. As this is more of a problem for heavy elements where scattering creates larger background variations [2] it is not a concern for this research where the primary elements present are carbon, oxygen, and silicon. There is a third type of background subtraction based on the physical attributes of the sample rather than the mathematical derivation of the Shirley background, which was created by Tougaard [2]. This method takes into account the initial energy distribution function and inelastic electron scattering [4]. While the Tougaard method may be more thorough it requires a large energy range extending 50 eV to the high binding energy side of the peak to get a reasonable fit [4], which dramatically increased the acquisition time of the high resolution peaks. The Shirley background is still widely used due its simplicity and wide availability in peak fitting software [2], and was the background subtraction used in this work.

The shape of peaks in XPS spectra are a combination of Gaussian and Lorentzian curves [2, 4]. The shape of the XPS line and the natural width of the core level both result in a Lorentzian peak shape [2, 4]. The types of broadening mentioned previously all add a Gaussian broadening to this peak shape [2, 4]. When fitting peaks the shape is therefore set as a GL(m) curve, where m is the mixing ratio [2, 4]. For a purely Lorentzian curve m=1, while for a purely Gaussian curve m=0. If a combination is used the fraction m is therefore that of the Lorentzian [2]. For example, in this work a GL(30) shape is used, which is 30 % Gaussian and 70 % Lorentzian [2].

While GL curves fit the basic lineshape of the photoemission process, peaks for conductors are asymmetric, typically skewed with a tail at the higher binding energy side of the peak caused by many-body interactions of the photoelectron with the electrons at the Fermi edge [4]. The Diniach-Sunjic line shape includes an asymmetry factor to account for this [4]. The factor is related to the phase shift for scattering of conducting electrons from the hold potential [4].

The number of atoms of each carbon hybridisation is proportional to the area under each component of the peak divided by its sensitivity factor, which should be the same for each

hybridisation because the sensitivity factors for XPS core level spectra is dependent only on atomic factors and not on the chemical state of the atoms [5].

A.1.5 Quantification from Peak Intensities

Quantitative information about the elemental composition of the sample can be determined by examining the intensity of the spectral peaks, and is usually given as an atomic percent [4]. There are three methods for quantification using intensity [4]. The first is to take into account elemental relative sensitivity factors (E-RDFs) that are derived from the intensities of pure elemental standards [4]. The second method is to use basic physical equations which incorporate appropriate material and instrument parameters [4]. The third method combines the first two, and includes corrections for matrix effects and elemental distributions through the depth of the surface [4]. In this work, the first method is used, with the sensitivity factors being present in the library in CasaXPS, which uses them to perform the calculations from intensity to atomic percent.

The ratio of the intensities of an elemental peak in a sample of unknown concentration (I_A) and that same peak in an elemental reference sample (I_A^0) gives the mole fraction, X_A, of the element A in the unknown sample [3, 4].

$$X_A = \frac{I_A}{I_A^0}$$
(A.1-1)

In a sample with multiple elements the ratio of the atomic concentrations of elements A and B is therefore [3, 4]

$$\frac{X_A}{X_B} = \frac{I_A I_A^0}{I_B I_B^0} = \frac{I_A/S_A}{I_B/S_B} = \frac{I_A}{I_B} S_{B,A}$$
(A.1-2)

Where X_A, X_B, I_A, I_B, I_A^0, and I_B^0 are the mole fractions, the measured intensities, and the standard intensities from pure elemental samples of A and B, respectively [3, 4]. The absolute elemental sensitivity factors are defined as $S_A = I_A^0$ and $S_B = I_B^0$, and the E-RSF for A relative to B is $S_{B,A} = S_B/S_A$ [3, 4].

If there are more than two elements present then this equation can be extended to calculate the mole fraction of an element I, X_i [3, 4]:

$$X_i = \frac{I_i/I_i^0}{\sum_{j=1}^{n}(\frac{I_j}{I_j^0})} = \frac{I_i S_i}{\sum_{j=1}^{n}(\frac{I_j}{S_j})}$$

(A.1-3)

Where the sum of all molar fractions must be equal to unity, and this equation is valid only if all elements are detected [3, 4].

A.1.6   Satellite Peaks

There are many sources of satellite peaks in XPS spectra [3, 4]. If the x-ray source is not monochromated then the peaks from the main x-ray line ($K_{\alpha1,2}$) will be accompanied by satellite peaks from other x-ray lines such as $K_{\alpha3,4}$ [3, 4]. The spectral peaks as a result of this line will have an intensity that is approximately 10 % of that of the $K_{\alpha1,2}$ peak, and sit at a lower binding energy by about 10 eV [4].

X-ray ghost lines occur when x-rays from an element other than the x-ray source anode material are incident on the sample [3]. The most common causes are magnesium contamination in the aluminium anode (or vice versa), copper from the anode base structure, oxidation of the anode, or generation of x-rays in the aluminium foil x-ray window [3].

There may also be broad peaks present as a result of plasmon excitation loss, typically spanning 10-20 eV [3, 4]. These peaks will be present at the higher binding energy side of the main peak, and are the result of discrete energy losses due to collective oscillations in the valence band [3, 4]. Peaks from both surface and bulk plasmon losses are observed separately [3, 4]. The electron density, n_e, in the valence band is related to the bulk plasmon frequency $h\nu_p$ by the relation $h\nu_p \propto (n_e)^{1/2}$ [4]. The two-dimensional oscillations in the surface layers cause the surface plasmon peak, which usually has a lower intensity than that of the bulk plasmon [4]. Additionally, the frequency of the surface plasmon is lower than that of the bulk by about $\sqrt{2}$ [3, 4].

Rearrangement of the electrons after photoemission leads to another type of satellite peak, known as shake-up peaks [3, 4]. The rearrangement can result in an excited state that exists a few eV above the ground state, therefore the photoelectron suffers a loss in kinetic energy of the magnitude of the change and a peak forms at a few eV higher than the main peak [3, 4]. Shake-off peaks occur as a result of interaction of photoelectrons with valence band electrons [3, 4]. Metals with high electron density near the Fermi edge may produce photoelectrons with lower energy by excitations in empty states above the Fermi edge [4]. This results in a tail on the high binding energy side of the

main peak, rather than a discrete loss, and the peak becomes asymmetric [4].

All transitions from levels with total angular momentum higher than s (that is, p, d, f,… shells) will be a doublet peak due to the unpaired electron that is left behind after the photoemission process [3, 4]. This electron will either have a parallel or antiparallel orientation to the orbital momentum, which causes an energy difference, and therefore a doublet peak [3, 4]. The separation between the two peaks of the doublet increases with atomic number, and decreases with higher l values for the same n values [3, 4]. The ratio of the degeneracy (2j+1) of the two peaks is constant, and results in a constant intensity of the doublet peak, which assists in deconvolution [4]. A doublet can also occur for s-peaks (multiplet splitting) when there is an unpaired electron in the valence band or shallow core levels, resulting in a net spin [4]. An exchange interaction can then occur during the emission of a s-electron, resulting in a splitting of the peak [3, 4].

A.1.7 Effects of Nanostructure on XPS Signals

The differences in the inelastic mean free path (IMFP) for electrons in different materials, along with the distribution of electrons that have lost energy, can provide information on the nanostructures of many materials [1]. It is often assumed in XPS analysis that all elements present in the sample are distributed homogenously, however if a surface has nanostructures that is not likely to be true [1]. An understanding of how nanostructures influence the XPS spectra, combined with other knowledge about the nature of the sample, can lead to the determination of structural or elemental distribution information [1]. The XPS spectra for a surface can be influenced by nanostructures in several ways, the first of which is the peak intensities and relative peak intensities of different peaks for the same element, as well as peaks for different peaks, and how these intensities change with emission angle [1]. Additionally, the binding energies of the peaks, the value of the Auger parameter, and the background signals from electrons that have lost energy are all spectral features that can be influenced by nanostructure [1].

As has already been discussed, the escape depth of the photoelectrons, and thus the characterisation depth, vary with the energy of the photoelectrons and the emission angle [1]. This leads to peak ratios that relate to the compositional layering, enrichment, and segregation of elements in the sample surface [1]. When a photoelectron is emitted with a low kinetic energy (high binding energy) the sampling depth is lower than that of higher kinetic energy photoelectrons, enhancing the signal intensities from the elements closest to the surface [1]. Similarly, when the angle of emission is increased the sampling depth is decreased, thus varying the emission angle and

studying the resultant changes in the relative peak intensities provides information about the layering of elements in the sample surfaces, including element enrichment (or depletion) and providing a depth profile through non-destructive methods [1].

Often there are layers above the element of interest in a sample, for example an oxide layer or adventitious carbon contamination, and the presence of these layers will impact the relative intensities of the photoelectron peaks [1]. For example, if a high energy and low energy peak of the same element are compared for a pure elemental sample and a sample with an oxide layer, the ratio of the two peaks can indicate layer thickness [1]. If the higher kinetic energy peak increases relative to the lower kinetic energy peak, that suggests there is less of the element of interest near the surface and indicates the thickness of the oxide layer [1]. Similarly, if a thin film is present (thinner than the sampling depth of its electrons), the ratio of the higher and lower kinetic energy peaks can provide information on the thickness of the film [1].

XPS can be used to determine information about the molecular orientation of ordered molecular assembles and larger molecules with asymmetric elemental distribution [1]. The orientation of ordered molecular assembles can result in shifts in binding energies of spectral peaks, while the orientation of larger molecules mostly impacts the intensity of the peaks due to the sampling depth and layering already discussed [1].

A similar approach can be taken when examining the thickness of coatings on particles [1]. In order to take into account the differences between a flat surface and a surface made up of particles a correction factor can be applied to the calculated layer thickness [1].

The size of particles can also be determined using XPS by using a couple of different methods [1]. The first method is to use the ratios of the peaks from the particles and the support and compare it to a model structure [1]. A second method is to use an equation that relates the signal intensity ratio of the electron peaks of different kinetic energies from the particles [1]. This equation relates the particle cluster size and the IMFPs to the intensities of peaks [1]. It is important to note that both of these methods are only valid when the particles or clusters are somewhat separated from each other on the support surface, and for particles that are smaller than the sampling depth [1].

It has been well established that the XPS spectral peaks for nanoparticles have different binding energies than those for the bulk material of the same element, with shifts of between 0.05 eV and 0.6 eV common [1]. This variation often varies with sufficient regularity that the particle size can be

determined from the binding energy shift [1]. During the photoelectron emission process of electrons from isolated particles there is a Coulomb attraction between the ejected electron and the remaining charged particle [1]. This Coulomb effect suggests that the binding energy of electrons within a nanoparticle would increase as the particle diameter decreases, which has been observed in many cases [1]. Changes in the particles energy levels due to size, lattice strain, charge shifting due to substrate interactions, and final state relaxation effects are also expected to influence the binding energy of the particle [1].

The nanostructure of a sample surface does not only alter the XPS peaks, but also alters the background of the spectrum as the electrons that have lost kinetic energy through inelastic scattering have also had their initial energy altered, and thus the distribution of electrons that cause the background will change [1]. When the distribution of an element within the sample surface changes, the intensity of the photoelectron peak can be the same but the background to the high binding energy side of the peak can be quite different [1]. It has been shown, for example, that as the layer of Cu within a sample shifts further into the sample the high binding energy background will increase [1].

It can be particularly important to know the impact of contamination on nanostructured surfaces due to the high number of atoms that are associated with surfaces or interfaces [1]. Common contaminations include adventitious carbon, impurities introduced in chemical cleaning processes, synthesis, and processing, and can disrupt peak ratios or mask important signals [1]. It is therefore important that great care is taken to ensure that contamination is minimised and that the measured spectra are in fact from the sample and not due to contamination or other artefacts [1].

In order to reduce the errors introduced by inelastic scattering of electrons XPS is normally performed under UHV conditions [1]. However, it is possible that being placed in a vacuum may induce changes in the surface of a sample [1]. This can be tested by cooling the samples and then collecting spectra as a function of time to see how the spectra change as exposure to the vacuum continues [1]. Exposure to air can also change a surface, for example by oxidising a surface or deposition of adventitious carbon, the effects of this can be examined by keeping samples in a N_2 atmosphere prior to XPS characterisation [1]. These environmental effects can induce larger changes on the properties of nanostructured materials due to their high surface area, including the surface structure, phase transformations, chemical stability, polymer structure, and chemical state, which will impact on the XPS spectra [1].

A.2   Auger C(KLL) Peak Analysis

The energy width between the most positive maxima and the most negative minima of the C(KLL) peak in the derivative Auger spectrum has been shown to be indicative of the amounts of sp^2 and sp^3 hybridised carbon present in the sample surface [6]. Graphite has been shown to have a D parameter of 21-23 eV, while diamond has a D parameter of 11-14 eV, and a linear relationship exists between the sp^3 content and the D value [6-8]. An advantage of this method over C $1s$ peak deconvolution is that by examining the width of the differentiated peak, rather than the position, the measurement becomes independent of charging [7].

It has been shown that not only are there differences in the shape of the C(KLL) Auger peaks for different hybridisations, but there is also a difference in the peak intensities [4, 9, 10]. The intensity of the C(KLL) peak decreases with decreasing degree of carbon hybridisation [9]. Diamond has the highest degree of carbon hybridisation (sp^3) and also has the highest peak intensity, followed by graphite (sp^2 hybridised), and finally carbide (sp hybridised) with the lowest peak intensity [9].

Auger peak-to-peak height measurements are very sensitive to changes in line shape, therefore small chemical shifts can make it difficult to perform quantitative analysis [4]. To overcome these issues, the fine structure of the peak can be blurred slightly by lowering the analyser resolution, allowing for a clearer peak maximum and minimum [4]. This can be achieved by overmodulation or increased smoothing and differentiation [4]. Factor analysis can also be used to separate overlapping peaks in derivative AES spectra and determine the effect of chemical shifts [4]. A complication arises when an electron beam is used for the excitation source, as the beam can induce damage to the surface, and effects such as electron stimulated desorption and deposition, beam heating, and charging can occur [4].

A.2.1   Satellite Peaks

Plasmon loss peaks are seen in AES spectra as lines successively mirrored at lower kinetic energy with reduced intensity to the main peak [10, 11]. The plasmon energy gives the interval between the primary and loss peaks, and is typically on the order of 5 to 30 eV [10] [11]. The more prominent of the plasmon loss peaks are the bulk plasmons, while the surface plasmons are present at an energy interval that is approximately the bulk plasmon energy divided by the square root of two [10]. These peaks often make up the majority of the fine structure on the low kinetic energy side of the main peak of many metals, but are not easily observed in non-conductors and are not prominent in all conductors [10][11].

When using a low primary electron energy ionisation loss peaks can be observed at a fixed energy below the elastic peak [10]. The ionisation loss peaks are formed by electrons that have lost energy from ionising atoms near the sample surface [10].

A.2.2 Chemical Information from AES

The chemical environment of an atom influences its local bonding and energy levels, which in turn influences the energy position and shape of its Auger peak [10]. While theoretical predictions of the line shape and energy shifts can be difficult experimental data can be compared to reference samples to determine composition [10]. The energy shifts from chemical influences are often larger in AES than XPS as a result of the extra-atomic relaxation effects that occur in the Auger emission process [10][11]. There are often significant differences in the Auger line shape as a result of chemical environment, including in the fine structure of the low kinetic energy side [10]. For example, the plasmon losses are more prominent in a metal oxide than in the metal [10][11]. The largest changes in the Auger line shape with differing chemical environment are seen for transitions involving valence band electrons [10]. The line shape for the core-valence-valence transitions, such as the C(KVV) transition examined in this work, shows the weighted self-convolution of the valence band density of state [10][11].

A.2.3 Quantification from Peak Intensities

Quantification of the elemental composition of samples using AES is performed by examining the intensity of the Auger peaks, and produces values of atomic percentage for each element involved. This intensity is dependent on a variety of factors, including the electron beam current, the number of atoms per unit volume, the ionization cross section of the core level of the element, the auger transition probability, the IMFP of the electron, and the detector angle and transmission functions [11].

The atomic concentration of a pure element i, X_i^0, has an intensity of I_i^0, and for a sample of unknown concentration of element i the concentration X_i with the pure standard is [11]

$$X_i = \frac{I_i/\rho_i S_i}{I_i^0/\rho_i^0 S_i^0}$$
(A.2-1)

Where ρ is the atomic density and S represents the sensitivity factor of the element, which takes into account the previously mentioned factors that influence the intensity of the peak [11]. A general expression for the atomic percentage of any element within a sample, X_a, is [11]

$$X_a = \frac{N_a}{\sum N_i} = \frac{I_a/S_a}{\sum I_i/S_i} \qquad \text{(A.2-2)}$$

And can be applied for any homogenous sample provided that the ratio of the sensitivity factors is matrix independent for all of the materials within the sample [11]. A heterogeneous sample cannot be characterised as rigorously with this equation as the microscopic character of the sample will influence the quantitative results [11].

A.3   References

1.   Baer, D.R. and M.H. Engelhard, *XPS analysis of nanostructured materials and biological surfaces.* Journal of Electron Spectroscopy and Related Phenomena, 2010. **178**: p. 415-432.
2.   Barlow, A., *Plasma Processing Studies with Application to Carbon Nanotube Fluorination*, in *School of Chemical and Physical Sciences*. 2011, Flinders University: Flinders University. p. 282.
3.   Moulder, J.F., Stickle, W. F., Sobol, P. E., Bomben, K. D., *Handbook of X-ray Photelectron Spectroscopy*. 1995, USA: Physical Electronics, Inc.
4.   Hofmann, S., *Auger- and X-Ray Photoelecton Spectroscopy in Materials Science*. Springer Series in Surface Sciences. 2013: Springer-Verlag Berlin Heidelbery.
5.   Huang, L.-Y., J. Lu, and K.-W. Xu, *Investigation of the relation between structure and mechanical properties of hydrogenated diamond-like carbon coatings prepared by PECVD.* Materials Science and Engineering: A, 2004. **373**(1–2): p. 45-53.
6.   Parmeter, J.E., D.R. Tallant, and M.P. Siegal, *Thermal Stability Studies of Diamond-Like Carbon Films.* MRS Proceedings, 2011. **349**.
7.   Barlow, A.J., et al., *Chemically specific identification of carbon in XPS imaging using Multivariate Auger Feature Imaging (MAFI).* Carbon, 2016. **107**: p. 190-197.
8.   Barlow, A.J., et al., *Multivariate Auger Feature Imaging (MAFI) – a new approach towards chemical state identification of novel carbons in XPS imaging.* Surface and Interface Analysis, 2015. **47**(2): p. 173-175.
9.   Baitinger, E.M., L.A. Pesin, and A.V. Cherednichenko, *Influence of the type of electron hybridization on the intensity of carbon auger spectra.* Russian Physics Journal, 1996. **39**(8): p. 798-801.
10.   Popescu, S., et al., *Rapid Prototyping of a Low-cost Graphene-based Impedimetric Biosensor.* Procedia Technology, 2017. **27**(Supplement C): p. 274-276.
11.   Childs, K.D.C., B. A.; LaVanier, L. A.; Moulder, J. F.; Paul, D. F.; Stickle, W. F.; Watson, D. G., *Handbook of Auger Electron Spectroscopy*. 3rd ed. 1995, Minnesota, USA: Physical Electronics, Inc.

B. APPENDIX B: DATA PROCESSING FOR HYBRIDISATION MAPPING

Neither SmartSoft nor MultiPak allow for extraction of the spectra within these elemental maps, therefore an intermediate program must be used before importing into MATLAB. By opening the .map file in CasaXPS it is converted into a .vms file and can be displayed. The following steps are then used to create an array of spectra:

1. Open the .vms file in CasaXPS. Note that there is a '0' block which will need to be removed. This can be done by clicking on the block to highlight it, then clicking the 'delete' button as shown in Figure 8-1. If this block is not removed, each spectrum extracted from the file will have a data point at (0,0), which will interfere with the subsequent data processing.
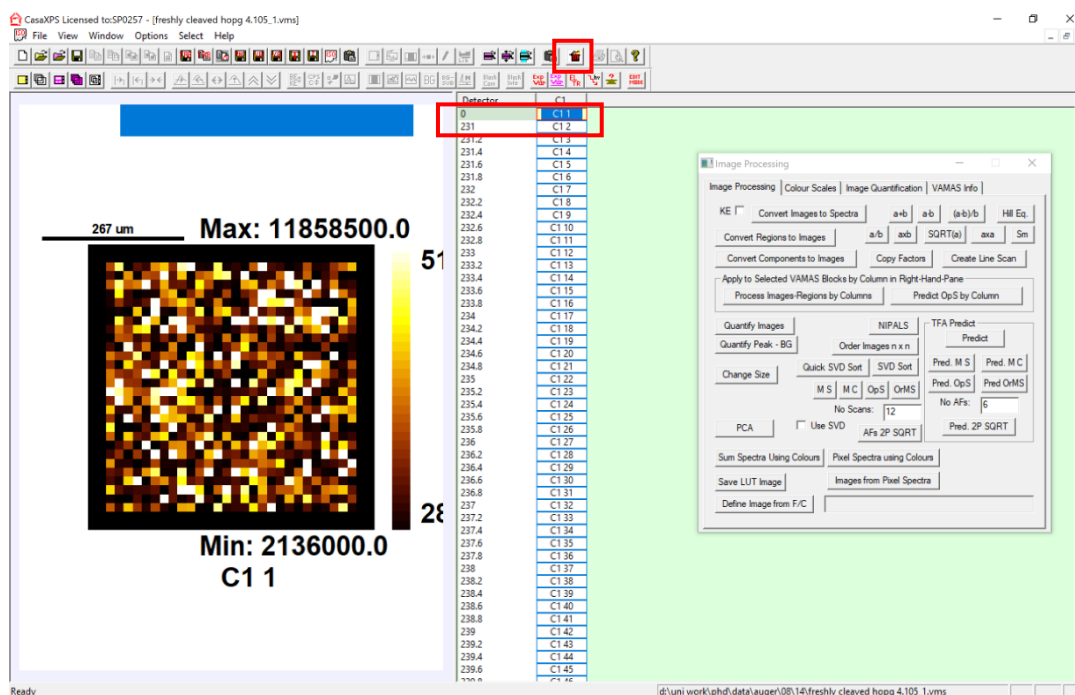
Figure 8-1: '0' VAMAS block and delete button in CasaXPS

2. Select all VAMAS blocks by clicking the top label in the VAMAS blocks window. Overlay the blocks by clicking 'Overlay' in the ribbon menu bar, as shown in Figure 8-2.
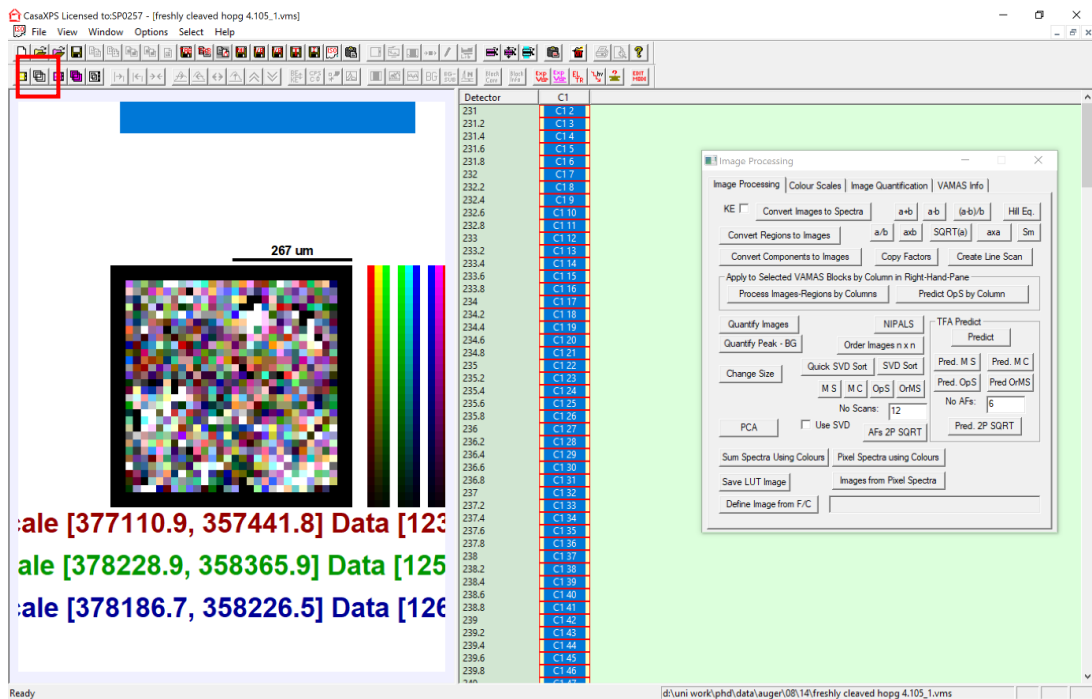
Figure 8-2: 'Overlay' button in CasaXPS

3. Open the 'Image Processing' dialogue box from the 'Options' menu as shown in Figure 8-3.
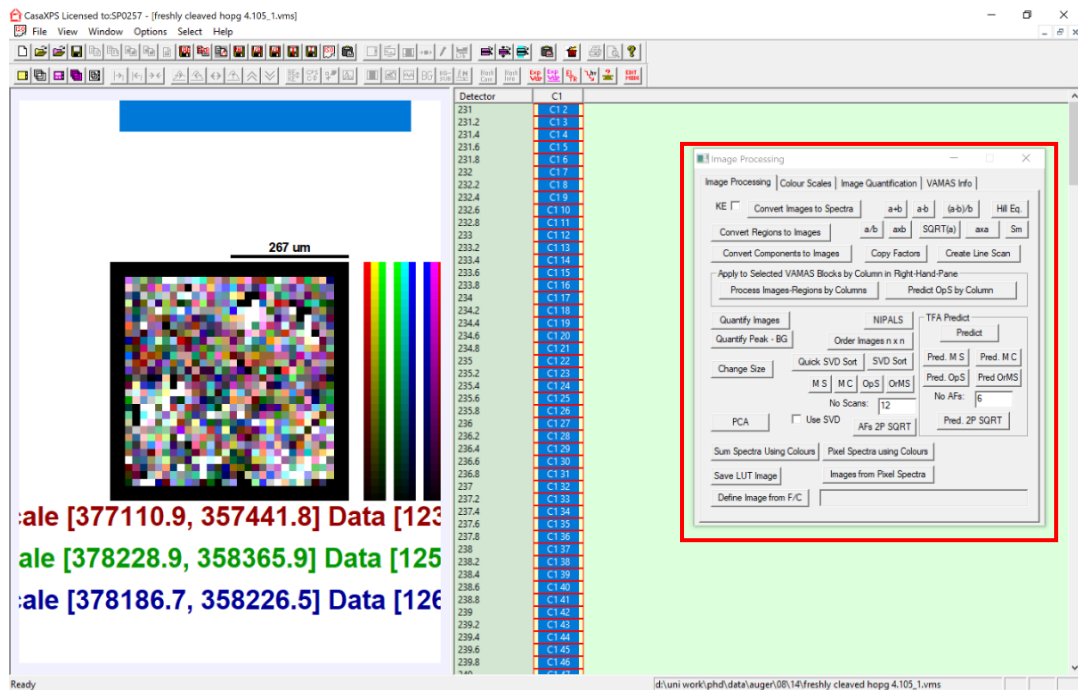
Figure 8-3: 'Image Processing' dialogue box in CasaXPS

4. In the 'Image Processing' tab, click 'Convert Images to Spectra', as shown in Figure 8-4. This will open a new window which shows a spectrum on the left, and a series of VAMAS blocks on the right. Each of the blocks contains all the spectra from one row of the map.
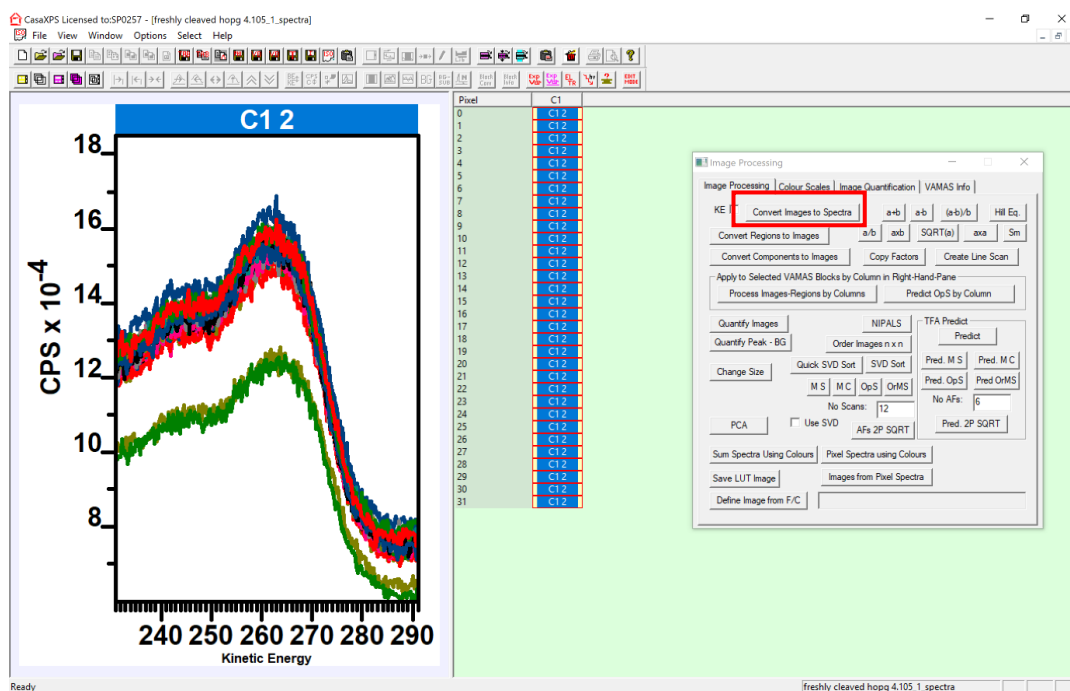
Figure 8-4: 'Convert Images to Spectra' button in CasaXPS.

5. Click on the top label in the VAMAS blocks to highlight all the spectra blocks and then click 'Overlay' in the ribbon menu bar as shown in Figure 8-5.
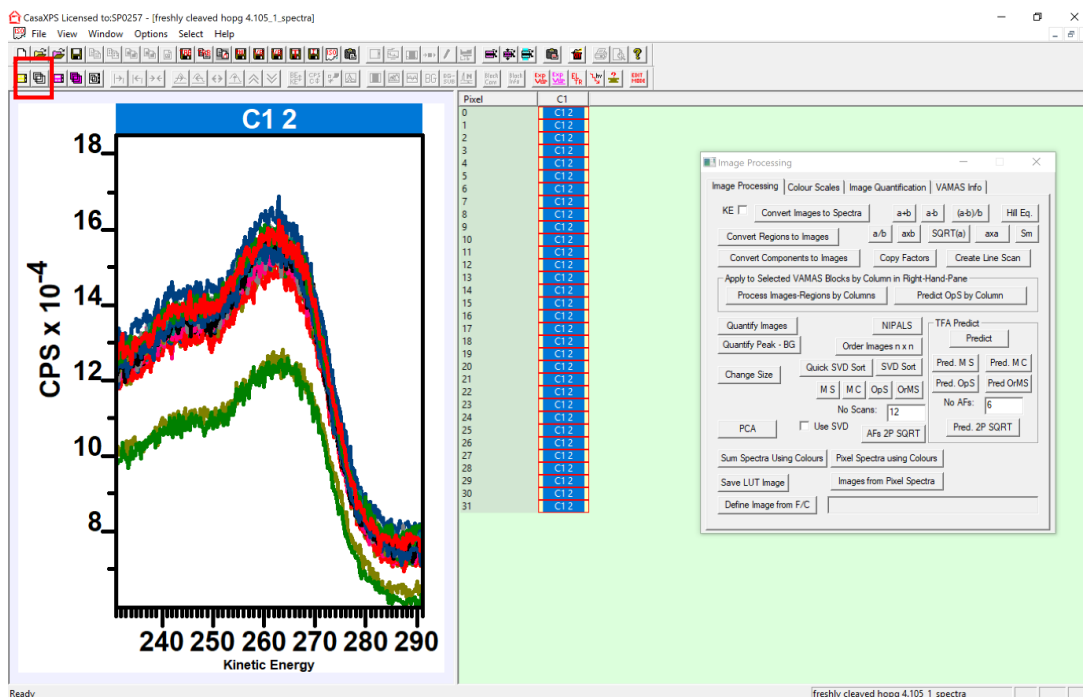
Figure 8-5: 'Overlay' button in CasaXPS.

6. In the 'VAMAS Info' tab of the 'Image Processing' dialogue box select 'Convert CV to VB' as
    shown in Figure 8-6. This converts the corresponding variables to VAMAS blocks and will
    result in each block being split into its contributing spectra. The dataset should now be a
    grid of spectra corresponding to each pixel of the original map, as shown in Figure 8-7.
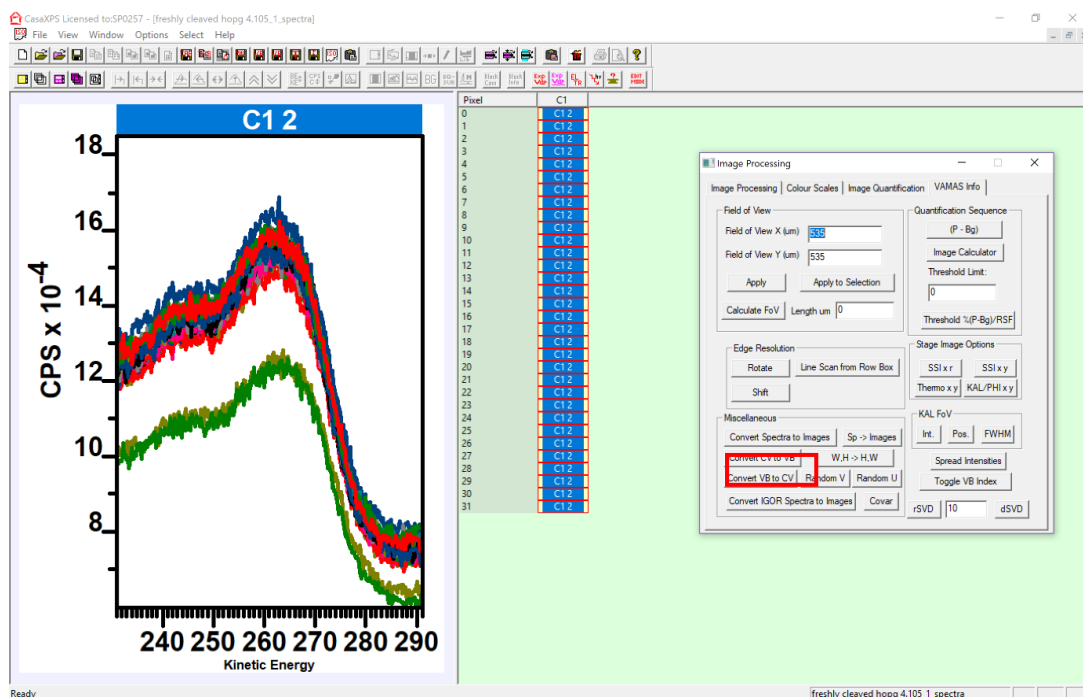
Figure 8-6: 'Convert CV to VB' button in CasaXPS.
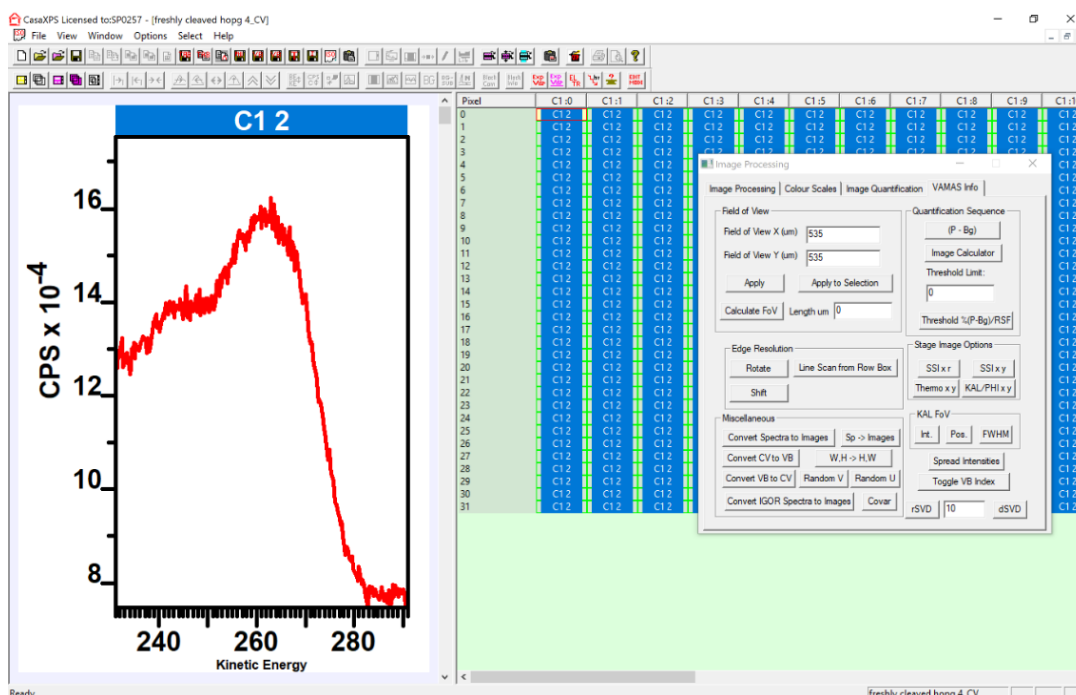
Figure 8-7: Each VAMAS block in CasaXPS now contains the spectrum from a single pixel of the carbon map.

7. The spectra can now be exported as a .txt file by selecting the row(s) desired and clicking the 'Save TAB ASCII' button as shown in Figure 8-8. If the map has a width larger than 32 pixels then the data should be saved in several parts to make importing into MATLAB smoother. For example, if the map is 64 pixels wide then the data should be saved in lots of 20 lines of spectra, and a 128-pixel map should be saved in lots of 10 lines of spectra. Once imported into MATLAB these data sets will be rejoined to form one data set of all spectra. The file should be named according to the lines selected to make it easier to import and identify in MATLAB. Click 'save', then ensure the 'Rows of Tables' button is selected as shown in Figure 8-9, and finally click 'OK'.

The .txt file thus obtained contains the spectra selected as a series of columns, with the format of 'x values, y values, blank column', repeated for the number of spectra in the file. For the purposes of creating the carbon hybridisation map the only columns needed are the columns containing the y values (or raw counts) of each spectrum, therefore code must be written in MATLAB to ensure that only those columns are extracted. The x-values are also needed, but only once and so these values can be saved separately. There are also several lines of header data present that must be ignored when processing the data in MATLAB, which can be done either by not importing those lines when you first import the data into MATLAB, or by including code to ignore these lines as part of the processing code to parse the useful data. The first of these approaches has been taken in this work.
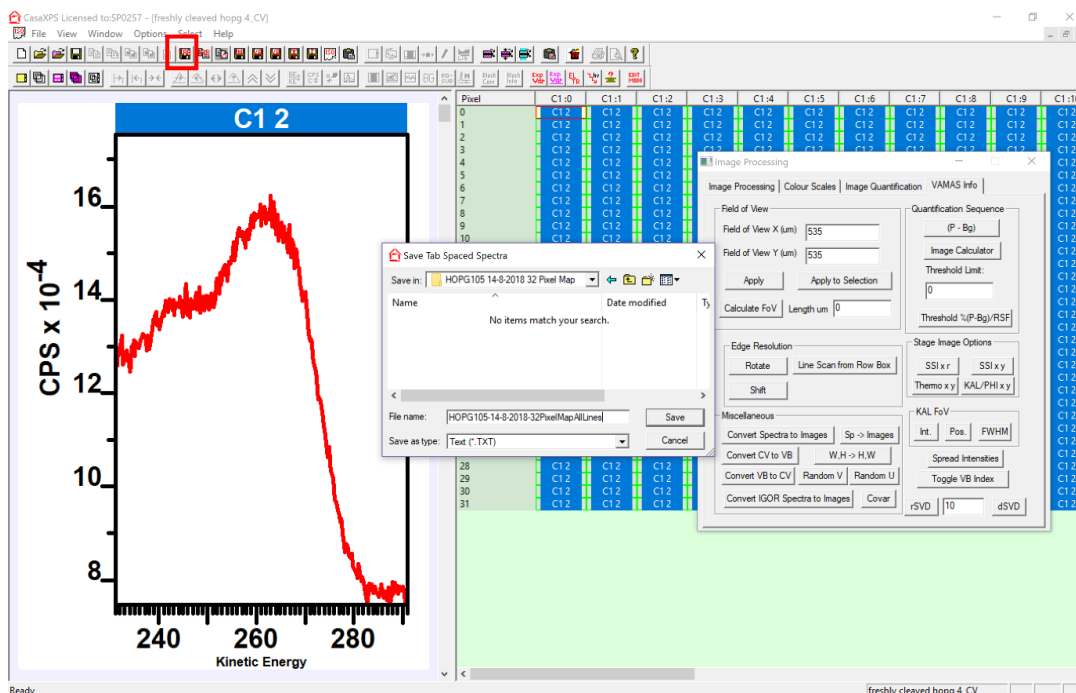
Figure 8-8: 'Save TAB ASCII' button in CasaXPS.
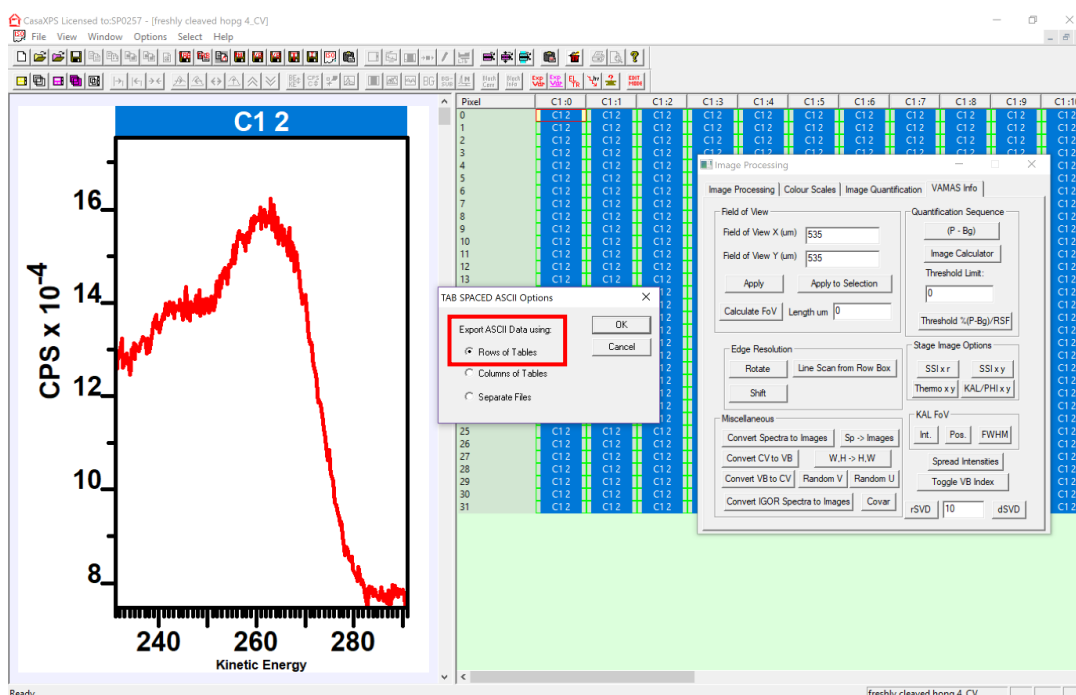
Figure 8-9: 'Rows of Tables' button in CasaXPS.

8. Open the .txt file in excel, then save as a .xlsx file.

9. In MATLAB, open the .xlsx file. When the file loads in the 'Import Data' window, change the output type to 'Numeric Matrix' as shown in Figure 8-10. At this point you can remove the header lines before importing by highlighting the spectra only. Highlight all spectra then

click 'Import Selection'. The selected data will then be imported into the MATLAB Workspace as a matrix.
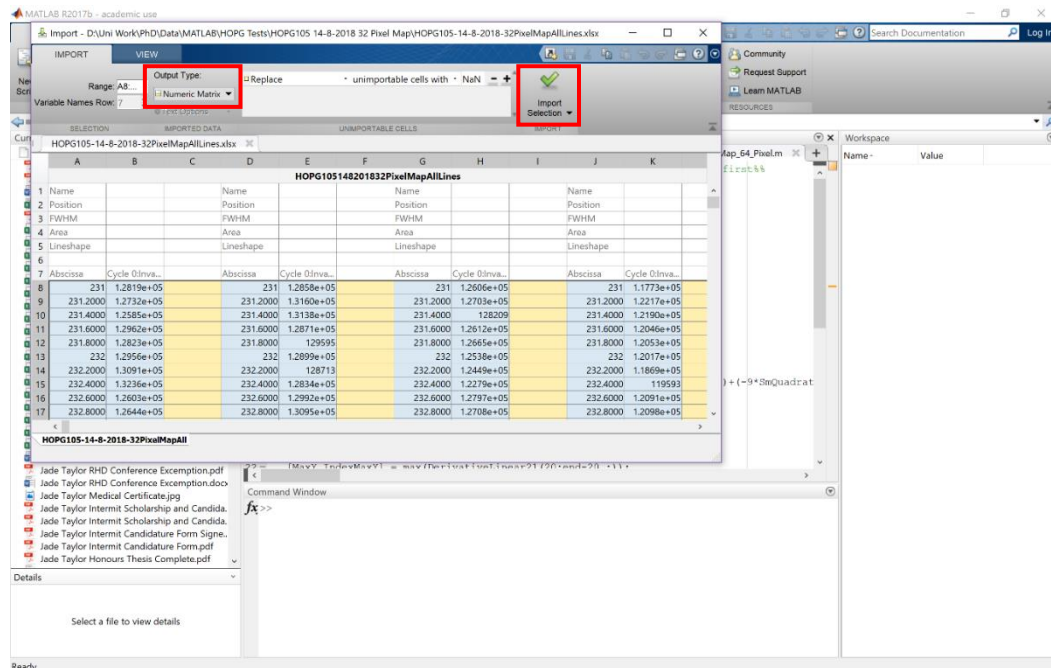
Figure 8-10: 'Input Type' dropbox and 'Input selection' buttons in the MATLAB import window.

This MATRIX should be renamed to 'Map' to match with the MATLAB code used to process the data. This can be done by right clicking on the variable name in the MATLAB workspace, and selecting 'rename'. If there are multiple files being imported as the map has a larger pixel width than 32 pixels then each file should be labelled 'Map1, 'Map2', etc., and the MATLAB code will join these matrices together to form the total 'Map' matrix. With the 'Input Data' window still open, highlight the first column only and import this column, then rename it to 'XValues' as shown in Figure 8-11 and Figure 8-12.

Figure 8-11: Highlighted 'XValues' column to be imported in the MATLAB import window.

Figure 8-12: Renamed variables in the MATLAB Workspace.

As every third column, starting with column 2, is used in the code it is important that each file contains a full multiple of 3 columns so that when they are joined together and code applied the appropriate columns are extracted. However, each imported data set ends with the final column of y values, disrupting this pattern. It is therefore necessary to add an extra column to 'Map1', 'Map2', etc. after importing them but before starting the code. This can easily be achieved by opening the variable in MATLAB, moving to the column to

8

the right of the final data column, and typing 'NaN' (for 'not a number') in the first square. This introduces a new column at the end of the variable, and the format will now match that necessary for the code, as shown in Figure 8-13.
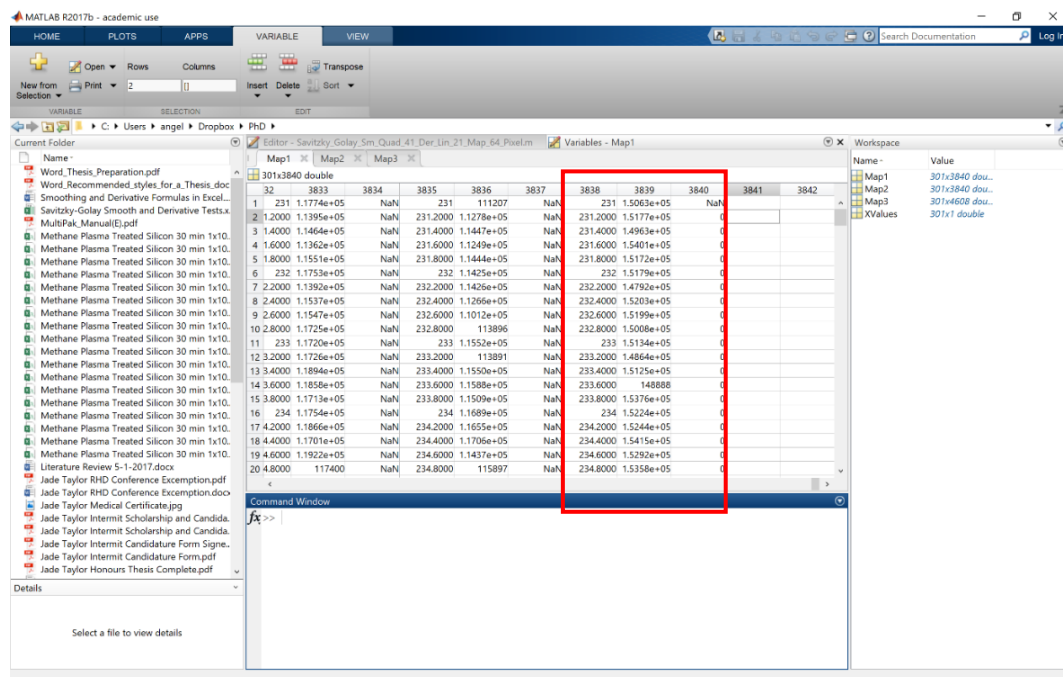
Figure 8-13: Addition of a new column at the end of the 'Map1' variable by adding a 'NaN' cell in the column after the last data column in the MATLAB variable editor.

10. The data is now imported and in the correct format for the hybridisation map to be created by clicking 'run'. The output will be a map of sp^2 hybridisation, and all variables created in the process will now appear in the workspace. The workspace should be saved to avoid having to import the data again, as it is a time-consuming process if something goes wrong.

C. APPENDIX C: MATLAB CODE FOR HYBRIDISATION MAPS WITH HIGHER PIXEL RESOLUTION

C.1 64x64 Pixel Map

The code given in section 5.1.2.1 can be modified to apply to a 64x64 pixel map. The data for the larger map must be imported in parts to reduce the processing time. As such, the data is initially saved in the MATLAB workspace in three parts: 'Map1', 'Map2', and 'Map3'. The data has the form of a three-column repeat: x-values, y-values, and a blank column. The MATLAB code has been written to extract the 'y-values' columns, thus it is important that the repeat is maintained when the 'Map1', 'Map2', and 'Map3' are joined together. However, 'Map1' ends with a column of y-values and 'Map2' begins with a column of x values, thus a blank column needs to be inserted at the end of 'Map1' for the formats to match. This can be done by opening the 'Map1' variable in the editor and entering 'NaN' (for 'not a number') in a new column at the end of the existing data. This process needs to be repeated for 'Map2'. The data will now all be in the correct format when 'Map' is created from the three separate files.

The format of the code after the creation of the 'Map' matrix is the same, however several parts are changed to accommodate the increase in pixels. The first is for the reshaping of the matrix of D parameter values, which must be changed to reshape to a 64x64 matrix. The meshgrid '[A,B]' must also be updated to create a 64x64 pixel grid for the D parameter hybridisation maps to be plotted on. The code for a 64x64 pixel map is therefore:

```
%%Create Map from Map Components - Add extra column to end of each
map first%%
Map = [Map1,Map2,Map3];

%%Select Spectra Columns from Map File%%
Data = Map(:,2:3:end);
X = XValues(20:end-20,:);

%%Smoothing%%Map5
%%sgolayfilt(Data,order,number of points)%%

SmQuadratic41 = sgolayfilt(Data,2,41);

%%Differentiation%%

for k = 11:288
    DerivativeLinear21(k,:) = (1/(770*0.2))*((-10*SmQuadratic41(k-
10,:))+(-9*SmQuadratic41(k-9,:))+(-8*SmQuadratic41(k-8,:))+(-
7*SmQuadratic41(k-7,:))+(-6*SmQuadratic41(k-6,:))+(-
5*SmQuadratic41(k-5,:))+(-4*SmQuadratic41(k-4,:))+(-
```

```matlab
    3*SmQuadratic41(k-3,:))+(-2*SmQuadratic41(k-2,:))+(-
1*SmQuadratic41(k-
1,:))+(0*SmQuadratic41(k,:))+(1*SmQuadratic41(k+1,:))+(2*SmQuadrat
ic41(k+2,:))+(3*SmQuadratic41(k+3,:))+(4*SmQuadratic41(k+4,:))+(5*
SmQuadratic41(k+5,:))+(6*SmQuadratic41(k+6,:))+(7*SmQuadratic41(k+
7,:))+(8*SmQuadratic41(k+8,:))+(9*SmQuadratic41(k+9,:))+(10*SmQuad
ratic41(k+10,:)));
end

%%Map Creation%%

%%Find Max and Min of Each Spectra%%
[MaxY,IndexMaxY] = max(DerivativeLinear21(20:end-20,:));
[MinY,IndexMinY] = min(DerivativeLinear21(20:end-20,:));

%%Find Corresponding X Values%%
XValuesMap = [X(IndexMaxY), X(IndexMinY)];

%%Create Matrix of D%%
DAll = XValuesMap(:,1) - XValuesMap(:,2);
DAllRow = DAll.';
D = reshape(DAllRow,64,64).';

%%Make D positive and Convert to sp2 percentage%%
DPositive = D.*-1;
Dminus14 = DPositive-12;
sp2 = Dminus12./0.12;

%%Create D parameter Map - Reverse y axis once plot is created%%
[A,B] = meshgrid(1:1:64,1:1:64);
Dmap = pcolor(A,B,DPositive);

%%Create sp2 Map - Reverse y axis after figure is made%%
figure
[A,B] = meshgrid(1:1:64,1:1:64);
map = pcolor(A,B,sp2);
```

C.2   128x128 Pixel Map

The MATLAB code can be modified again to accommodate a 128x128 pixel map. The data must
again be imported in sections to help reduce the processing time, and the same process of adding a
column to each data set described for the 64x64 pixel map needs to be followed. The D parameter
matrix reshaping and '[A,B]' meshgrid creation must also be updated to reflect the increase in pixels.
The code for 128x128 pixel map is therefore as follows:

```matlab
%%Create Map from Map Components - Add extra column to end of each
Map first%%
Map                                                         =
[Map1,Map2,Map3,Map4,Map5,Map6,Map7,Map8,Map9,Map10,Map11,Map12,Ma
p13];
```

```matlab
%%Select Spectra Columns from Map File%%
Data = Map(:,2:3:end);
X = XValues(20:end-20,:);

%%Smoothing%%
%%sgolayfilt(Data,order,number of points)%%

SmQuadratic41 = sgolayfilt(Data,2,41);

%%Differentiation%%

for k = 11:288
    DerivativeLinear21(k,:) = (1/(770*0.2))*((-10*SmQuadratic41(k-
10,:))+(-9*SmQuadratic41(k-9,:))+(-8*SmQuadratic41(k-8,:))+(-
7*SmQuadratic41(k-7,:))+(-6*SmQuadratic41(k-6,:))+(-
5*SmQuadratic41(k-5,:))+(-4*SmQuadratic41(k-4,:))+(-
3*SmQuadratic41(k-3,:))+(-2*SmQuadratic41(k-2,:))+(-
1*SmQuadratic41(k-
1,:))+(0*SmQuadratic41(k,:))+(1*SmQuadratic41(k+1,:))+(2*SmQuadrat
ic41(k+2,:))+(3*SmQuadratic41(k+3,:))+(4*SmQuadratic41(k+4,:))+(5*
SmQuadratic41(k+5,:))+(6*SmQuadratic41(k+6,:))+(7*SmQuadratic41(k+
7,:))+(8*SmQuadratic41(k+8,:))+(9*SmQuadratic41(k+9,:))+(10*SmQuad
ratic41(k+10,:)));
end

%%Map Creation%%

%%Find Max and Min of Each Spectra%%
[MaxY,IndexMaxY] = max(DerivativeLinear21(20:end-20,:));
[MinY,IndexMinY] = min(DerivativeLinear21(20:end-20,:));

%%Find Corresponding X Values%%
XValuesMap = [X(IndexMaxY), X(IndexMinY)];

%%Create Matrix of D%%
DAll = XValuesMap(:,1) - XValuesMap(:,2);
DAllRow = DAll.';
D = reshape(DAllRow,128,128).';

%%Make D positive and Convert to sp2 percentage%%
DPositive = D.*-1;
Dminus14 = DPositive-12;
sp2 = Dminus12./0.12;

%%Create D parameter Map - Reverse y axis once plot is created%%
[A,B] = meshgrid(1:1:128,1:1:128);
Dmap = pcolor(A,B,DPositive);

%%Create sp2 Map - Reverse y axis after figure is made%%
[A,B] = meshgrid(1:1:128,1:1:128);
map = pcolor(A,B,sp2);
```

C.3   Higher Pixel Number Maps

The code can continue to be modified to accommodate maps with higher pixel numbers. Maps with

3

pixel numbers higher than 128x128 were not acquired in this work due to the excessive acquisition time that would be required. However, if the code was to be applied to a different system where the collection time required was lowered, for example by not needing the smaller energy step necessary for this work, then larger pixel maps may be feasible and the code could be further modified in the same way as has already been described.

D. APPENDIX D: SAVITZKY-GOLAY SMOOTHING AND DIFFERENTIATION

D.1 Smoothing of Spectroscopic Data

Spectroscopic data is the superposition of quantitative information and random errors of a variety of sources, the latter of which is termed noise [1]. The challenge is to remove as much noise as possible without significant degradation of the spectra [1]. Spectral data is obtained as two columns of numbers, with the independent variable, in this case kinetic energy (SAM) or binding energy (XPS), varying by a fixed interval [1]. Removal of noise from the spectra is often necessary to perform analysis on the data, and is performed on all SAM data in this work.

A moving average is one of the simplest ways to smooth data [1]. This involves taking a subset of data points, adding their values together, and dividing by the number of points to calculate the average value of the centre point [1]. The subset is then moved along the data by dropping the first point at one end of the set and adding the next point at the other end, and the calculation is repeated [1].

The general process of convolution applies a set of convoluting integers (C_i) to the data points (Y_{j+i}), with a normalisation factor (N) applied to the result [1]. The general formula for this is [1]

$$Y_i^* = \frac{\sum_{i=-m}^{i=m} C_i Y_{j+i}}{N} \tag{D.1}$$

Where the index j represents the running index of the ordinate data, and Y_i^* is the new value of Y_j [1]. For the moving average each value of C_i is equal to 1 and N is the number of points used [1]. However, for data with a sharp peak the moving average tends to degrade the end of the peak, and is therefore not suitable [1]. For this type of data a symmetrical function is preferred so that points on either side are considered [1].

If given a set of data with noise, an experimenter would draw a line through these points that seems to give the best fit and remove as much of the noise as possible [1]. This process can be performed numerically by using the method of least squares [1]. This least squares process involves fitting a curve, such as $a_3x^3+a_2x^2+a_1x+a_0=Y$, to the data points, where the a's are chosen such that when each

value of *x* is substituted into the equation the sum of the square of the differences between the calculated numbers, *Y*, and the observed numbers is a minimum for the total of the observations used in determining the coefficients [1].

D.2   Derivation of Savitzky-Golay Coefficients

When survey or high-resolution AES spectra are taken with SmartSoft and opened in MultiPak the programs automatically apply a smoothing and differentiation to the data. The number of points the program uses to perform this processing is set to S9-D5 when the step width is 1.0 eV, and is automatically adjusted so that the range over which the smoothing or differentiation is performed remains the same when the step width is decreased. However, when elemental maps are taken in window mode the spectra obtained are in an undifferentiated form and cannot be differentiated in MultiPak. The smoothing and differentiation must therefore be performed in MATLAB as part of the data processing code, and it is therefore necessary to derive the formulas needed to apply the Savitzky-Golay smoothing over the necessary number of points.

When the step width is 1.0 eV a 9-point quadratic Savitzky-Golay smoothing is applied, however for the work high-resolution C(KLL) spectra and carbon elemental map spectra are acquired with a step width of 0.2 eV. In order for the smoothing to still be applied over a range of 8 eV more points must be considered in the smoothing calculation. To this end, for the spectra considered here a 41-point smoothing formula is used. There is a built in Savitzky-Golay smoothing function in MATLAB, which was used to smooth the spectra used in the maps.

Similarly, the differentiation usually applied is a 5-point linear Savitzky-Golay differentiation, however when the step width is lowered to 0.2 eV a 21-point derivative must be used so that the process is still applied over a range of 4 eV.

Savitzky-Golay smoothing and differentiation is a process of successively applying a linear least squares method to fit a polynomial to a data set [1]. If the data points are equally spaced an analytical solution to the least squares method can be determined and a set of convolution coefficients calculated [1]. Savitzky and Golay were the first to publish tables of these coefficients and the method for calculating them [1]. They performed the calculations for a variety of polynomial orders and point numbers, however there have been some corrections published since this first paper [1, 2].

The mathematical description of the Savitzky-Golay smoothing process is [3]:

$$Y_j^* = \frac{\sum_{i=-m}^{i=m} C_i Y_i + 1}{N}$$ (D.2)

Where

- j is the running index of the ordinate data in the original data table
- Y_i is the original data point
- Y_i^* is the recalculated (smoothed) data point
- m is (2n-1)/2, where n is the number of points specified by the operator
- N is the normalisation factor
- C is the convoluting integer

The same process is used in Savitzky-Golay differentiation is the same as that described in (D.2) for smoothing, however the values of the coefficients C will be different [3].

Consider a data set of n points (x_i,y_i) (j = 1,…,n), where x is an independent variable and y is a datum value. We want to use the linear least squares method to fit a polynomial to the data. The polynomial will be fit to a set of adjacent data points (where m is an odd number and the points are equally separated by an interval h). First we make a change of variable

$$z = \frac{x - \bar{x}}{h}$$ (D.3)

Where $\bar{x}$ is the value of the central point of the subset, and z therefore has values of

$$\frac{1 - m}{2}, …, 0, …, \frac{m - 1}{2}$$

Such that if m=5, z=-2,-1,0,1,2. A polynomial of degree k will be fit to the data, and is defined as

$$Y = a_0 + a_1 z + a_2 z^2 + \cdots + a_k z^k$$ (D.4)

Where the coefficients a_0, a_1, etc. can be calculated by using the ordinary least squares method.

Consider this system as a matrix model where **Y** is a (k+1)x1 matrix, **J** is a mx(k+1) matrix with the values (1, z_i^2, z_i^3,…,z_i^k) in each row for i=1-m, **a** is a (k+1)x1 matrix of the a coefficients, which are

3

unknown and we wish to calculate as accurately as possible, and $\boldsymbol{\varepsilon}$ is a (k+1)x1 matrix of errors, such that

$$Y = Ja + \varepsilon \tag{D.5}$$

$$\begin{bmatrix} y_0 \\ y_1 \\ \vdots \\ y_k \end{bmatrix} = \begin{bmatrix} 1 & z_1 & z_1^2 & \cdots & z_1^k \\ 1 & z_2 & z_2^2 & \cdots & z_2^k \\ \vdots & \vdots & \vdots & \ddots & \vdots \\ 1 & z_m & z_m^2 & \cdots & z_m^k \end{bmatrix} \begin{bmatrix} a_1 \\ a_2 \\ \vdots \\ a_k \end{bmatrix} + \begin{bmatrix} \varepsilon_1 \\ \varepsilon_2 \\ \vdots \\ \varepsilon_k \end{bmatrix}$$

We want to find the values **a** such hat the sum of the squared residuals, **e**, is minimised. By rearranging (D.5) we find the equation for the vector of the residuals **e**.

$$e = Y - Ja \tag{D.6}$$

The sum of squared residuals is therefore

$$\begin{aligned} e^T e &= (Y - Ja)^T (Y - Ja) \\ &= Y^T Y - aJ^T Y - Y^T Ja + a^T J^T Ja \\ &= Y^T Y - 2a^T J^T Y + a^T J^T Ja \end{aligned} \tag{D.7}$$

In order to find the values of **a** that minimise the sum of squared residuals we take the derivative of (D.7) with respect to **a**, and set the result to equal zero.

$$\frac{\partial e^T e}{\partial a} = -2J^T Y + 2J^T Ja = 0 \tag{D.8}$$

Rearranging (D.8) we obtain the 'normal equations':

$$(J^T J)a = J^T Y \tag{D.9}$$

We want to find **a**, so we pre-multiply both sides of (D.9) by the inverse, $(J^TJ)^{-1}$:

$$(J^T J)^{-1}(J^T J)a = (J^T J)^{-1}J^T Y \tag{D.10}$$

By definition, $(J^TJ)^{-1}(J^TJ)=I$, where **I** is the identity matrix, therefore,

$$Ia = (J^T J)^{-1} J^T Y$$

$$a = (J^T J)^{-1} J^T Y$$

(D.11)

Therefore, to find the convolution coefficients, **a**, we solve (D.11). Once we know **a**, we can substitute back into the equation for our polynomial **Y** (D.4). For example, for a cubic polynomial,

$$Y = a_0 + a_1 z + a_2 z^2 + a_3 z^3 = a_0 \qquad at\ z = 0, x = \bar{x}$$

(D.12)

To find the first equation for the first derivative, we differentiate (D.12) with respect to x, and find

$$\frac{dY}{dx} = \frac{1}{h}(a_1 + 2a_2 z + 3a_3 z^2) = \frac{1}{h} a_1 \qquad at\ z = 0, , x = \bar{x}$$

(D.13)

We can also find the second and third derivative,

$$\frac{d^2 Y}{dx^2} = \frac{1}{h^2}(2a_2 + 6a_3 z) = \frac{2}{h^2} a_2 \qquad at\ z = 0, , x = \bar{x}$$

$$\frac{d^2 Y}{dx^2} = \frac{6}{h^3} a_3$$

(D.14)

For example, to calculate the equations for smoothing and differentiation using a 5-point cubic polynomial:

$$J = \begin{bmatrix} 1 & -2 & 4 & -8 \\ 1 & -1 & 1 & -1 \\ 1 & 0 & 0 & 0 \\ 1 & 1 & 1 & 1 \\ 1 & 2 & 4 & 8 \end{bmatrix}, \qquad a = \begin{bmatrix} a_0 \\ a_1 \\ a_2 \\ a_3 \end{bmatrix}, \qquad Y = \begin{bmatrix} y_{j-2} \\ y_{j-1} \\ y_j \\ y_{j+1} \\ y_{j+2} \end{bmatrix}$$

$$\therefore J^T = \begin{bmatrix} 1 & 1 & 1 & 1 & 1 \\ -2 & -1 & 0 & 1 & 2 \\ 4 & 1 & 0 & 1 & 4 \\ -8 & -1 & 0 & 1 & 8 \end{bmatrix}$$

$$\therefore J^T J = \begin{bmatrix} 5 & 0 & 10 & 0 \\ 0 & 10 & 0 & 34 \\ 10 & 0 & 34 & 0 \\ 0 & 34 & 0 & 130 \end{bmatrix}$$

$$\therefore (J^T J)^{-1} = \frac{1}{2520} \begin{bmatrix} 1224 & 0 & -360 & 0 \\ 0 & 2275 & 0 & -595 \\ -360 & 0 & 180 & 0 \\ 0 & -595 & 0 & 175 \end{bmatrix}$$

$$\therefore (J^T J)^{-1} J^T = \frac{1}{2520} \begin{bmatrix} -216 & 864 & 1224 & 864 & -216 \\ 210 & -1680 & 0 & 1680 & -210 \\ 360 & -180 & 360 & -180 & 360 \\ -210 & 420 & 0 & -420 & 210 \end{bmatrix}$$

$$\therefore \begin{bmatrix} a_0 \\ a_1 \\ a_2 \\ a_3 \end{bmatrix} = \frac{1}{2520} \begin{bmatrix} -216 & 864 & 1224 & 864 & -216 \\ 210 & -1680 & 0 & 1680 & -210 \\ 360 & -180 & 360 & -180 & 360 \\ -210 & 420 & 0 & -420 & 210 \end{bmatrix} \begin{bmatrix} y_{j-2} \\ y_{j-1} \\ y_j \\ y_{j+1} \\ y_{j+2} \end{bmatrix} \qquad \text{(D.15)}$$

We can now separate the matrices out to find each a, and simplify:

$$a_0 = \frac{1}{2520} \begin{bmatrix} -216 & 864 & 1224 & 864 & -216 \end{bmatrix} \begin{bmatrix} y_{j-2} \\ y_{j-1} \\ y_j \\ y_{j+1} \\ y_{j+2} \end{bmatrix}$$

$$= \frac{1}{35} \begin{bmatrix} -3 & 12 & 17 & 12 & -3 \end{bmatrix} \begin{bmatrix} y_{j-2} \\ y_{j-1} \\ y_j \\ y_{j+1} \\ y_{j+2} \end{bmatrix}$$

$$= \frac{1}{35} (-3y_{j-2} + 12y_{j-1} + 17y_j + 12y_{j+1} - 3y_{j+2}) \qquad \text{(D.16)}$$

$$a_1 = \frac{1}{2520} [210 \quad -1680 \quad 0 \quad 1680 \quad -210] \begin{bmatrix} y_{j-2} \\ y_{j-1} \\ y_j \\ y_{j+1} \\ y_{j+2} \end{bmatrix}$$

$$= \frac{1}{12} [1 \quad -8 \quad 0 \quad 8 \quad -1] \begin{bmatrix} y_{j-2} \\ y_{j-1} \\ y_j \\ y_{j+1} \\ y_{j+2} \end{bmatrix}$$

$$= \frac{1}{12} (y_{j-2} - 8y_{j-1} + 8y_{j+1} - y_{j+2}) \tag{D.17}$$

$$a_2 = \frac{1}{2520} [360 \quad -180 \quad -360 \quad -180 \quad 360] \begin{bmatrix} y_{j-2} \\ y_{j-1} \\ y_j \\ y_{j+1} \\ y_{j+2} \end{bmatrix}$$

$$= \frac{1}{14} [2 \quad -1 \quad -2 \quad -1 \quad 2] \begin{bmatrix} y_{j-2} \\ y_{j-1} \\ y_j \\ y_{j+1} \\ y_{j+2} \end{bmatrix}$$

$$= \frac{1}{14} (2y_{j-2} - y_{j-1} - 2y_j - y_{j+1} + 2y_{j+2}) \tag{D.18}$$

$$a_3 = \frac{1}{2520} [-210 \quad 420 \quad 0 \quad -420 \quad 210] \begin{bmatrix} y_{j-2} \\ y_{j-1} \\ y_j \\ y_{j+1} \\ y_{j+2} \end{bmatrix}$$

$$= \frac{1}{12} [-1 \quad 2 \quad 0 \quad -2 \quad 1] \begin{bmatrix} y_{j-2} \\ y_{j-1} \\ y_j \\ y_{j+1} \\ y_{j+2} \end{bmatrix}$$

$$= \frac{1}{12} (-y_{j-2} + 2y_{j-1} - 2y_{j+1} + y_{j+2}) \tag{D.19}$$

We therefore have the equation for smoothing with a 5-point cubic by inserting (D.16) into (D.12),

where h=1:

$$Y = \frac{1}{35}\left(-3y_{j-2} + 12y_{j-1} + 17y_j + 12y_{j+1} - 3y_{j+2}\right) \tag{D.20}$$

Similarly, we can find the equation for evaluating the first derivative by substituting (D.17) into (D.13),

$$\frac{dY}{dx} = \frac{1}{12}\left(y_{j-2} - 8y_{j-1} + 8y_{j+1} - y_{j+2}\right) \tag{D.21}$$

In this work a 41-point quadratic smoothing and 21-point linear derivative are applied to the AES spectra. The equations for these processes can be found in the same way as described here.

D.3 References

1. Savitzky, A. and M.J.E. Golay, *Smoothing and Differentiation of Data by Simplified Least Squares Procedures.* Analytical Chemistry, 1964. **36**(8): p. 1627-1639.
2. Steinier, J., Y. Termonia, and J. Deltour, *Smoothing and differentiation of data by simplified least square procedure.* Analytical Chemistry, 1972. **44**(11): p. 1906-1909.
3. Inc, U.-P., *PHI MultiPak Software Manual*. 2017, ULVAC-PHI, INC.: Japan.